

Springer Series in Synergetics

Springer:
COMPLEXITY

Alexander E. Hramov
Alexey A. Koronovskii
Valeri A. Makarov
Alexey N. Pavlov
Evgenia Sitnikova

Wavelets in Neuroscience

 Springer

Springer Complexity

Springer Complexity is an interdisciplinary program publishing the best research and academic-level teaching on both fundamental and applied aspects of complex systems – cutting across all traditional disciplines of the natural and life sciences, engineering, economics, medicine, neuroscience, social and computer science.

Complex Systems are systems that comprise many interacting parts with the ability to generate a new quality of macroscopic collective behavior the manifestations of which are the spontaneous formation of distinctive temporal, spatial or functional structures. Models of such systems can be successfully mapped onto quite diverse “real-life” situations like the climate, the coherent emission of light from lasers, chemical reaction-diffusion systems, biological cellular networks, the dynamics of stock markets and of the internet, earthquake statistics and prediction, freeway traffic, the human brain, or the formation of opinions in social systems, to name just some of the popular applications.

Although their scope and methodologies overlap somewhat, one can distinguish the following main concepts and tools: self-organization, nonlinear dynamics, synergetics, turbulence, dynamical systems, catastrophes, instabilities, stochastic processes, chaos, graphs and networks, cellular automata, adaptive systems, genetic algorithms and computational intelligence.

The three major book publication platforms of the Springer Complexity program are the monograph series “Understanding Complex Systems” focusing on the various applications of complexity, the “Springer Series in Synergetics”, which is devoted to the quantitative theoretical and methodological foundations, and the “SpringerBriefs in Complexity” which are concise and topical working reports, case-studies, surveys, essays and lecture notes of relevance to the field. In addition to the books in these two core series, the program also incorporates individual titles ranging from textbooks to major reference works.

Editorial and Programme Advisory Board

Henry Abarbanel, Institute for Nonlinear Science, University of California, San Diego, USA

Dan Braha, New England Complex Systems Institute and University of Massachusetts Dartmouth, USA

Péter Érdi, Center for Complex Systems Studies, Kalamazoo College, USA and Hungarian Academy of Sciences, Budapest, Hungary

Karl Friston, Institute of Cognitive Neuroscience, University College London, London, UK

Hermann Haken, Center of Synergetics, University of Stuttgart, Stuttgart, Germany

Viktor Jirsa, Centre National de la Recherche Scientifique (CNRS), Université de la Méditerranée, Marseille, France

Janusz Kacprzyk, System Research, Polish Academy of Sciences, Warsaw, Poland

Kunihiko Kaneko, Research Center for Complex Systems Biology, The University of Tokyo, Tokyo, Japan

Scott Kelso, Center for Complex Systems and Brain Sciences, Florida Atlantic University, Boca Raton, USA

Markus Kirkilionis, Mathematics Institute and Centre for Complex Systems, University of Warwick, Coventry, UK

Jürgen Kurths, Nonlinear Dynamics Group, University of Potsdam, Potsdam, Germany

Andrzej Nowak, Department of Psychology, Warsaw University, Poland

Linda Reichl, Center for Complex Quantum Systems, University of Texas, Austin, USA

Peter Schuster, Theoretical Chemistry and Structural Biology, University of Vienna, Vienna, Austria

Frank Schweitzer, System Design, ETH Zurich, Zurich, Switzerland

Didier Sornette, Entrepreneurial Risk, ETH Zurich, Zurich, Switzerland

Stefan Thurner, Section for Science of Complex Systems, Medical University of Vienna, Vienna, Austria

Springer Series in Synergetics

Founding Editor: H. Haken

The Springer Series in Synergetics was founded by Herman Haken in 1977. Since then, the series has evolved into a substantial reference library for the quantitative, theoretical and methodological foundations of the science of complex systems.

Through many enduring classic texts, such as Haken's *Synergetics* and *Information and Self-Organization*, Gardiner's *Handbook of Stochastic Methods*, Risken's *The Fokker Planck-Equation* or Haake's *Quantum Signatures of Chaos*, the series has made, and continues to make, important contributions to shaping the foundations of the field.

The series publishes monographs and graduate-level textbooks of broad and general interest, with a pronounced emphasis on the physico-mathematical approach.

For further volumes:

<http://www.springer.com/series/712>

Alexander E. Hramov • Alexey A. Koronovskii •
Valeri A. Makarov • Alexey N. Pavlov •
Evgenia Sitnikova

Wavelets in Neuroscience

 Springer

Alexander E. Hramov
Alexey A. Koronovskii
Research and Education Center
'Nonlinear Dynamics of Complex
Systems'

Saratov State Technical University
Saratov, Russia

and

Department of Nonlinear Processes
Saratov State University
Saratov, Russia

Alexey N. Pavlov
Physics Department
Saratov State University
Saratov, Russia

and

Research and Education Center
'Nonlinear Dynamics of Complex
Systems'
Saratov State Technical University
Saratov, Russia

Valeri A. Makarov
Department of Applied Mathematics
Complutense University
Madrid, Spain

Evgenia Sitnikova
Institute for Higher Nervous Activity
and Neurophysiology
Russian Academy of Sciences
Moscow, Russia

ISSN 0172-7389

ISBN 978-3-662-43849-7

ISBN 978-3-662-43850-3 (eBook)

DOI 10.1007/978-3-662-43850-3

Springer Heidelberg New York Dordrecht London

Library of Congress Control Number: 2014945977

© Springer-Verlag Berlin Heidelberg 2015

This work is subject to copyright. All rights are reserved by the Publisher, whether the whole or part of the material is concerned, specifically the rights of translation, reprinting, reuse of illustrations, recitation, broadcasting, reproduction on microfilms or in any other physical way, and transmission or information storage and retrieval, electronic adaptation, computer software, or by similar or dissimilar methodology now known or hereafter developed. Exempted from this legal reservation are brief excerpts in connection with reviews or scholarly analysis or material supplied specifically for the purpose of being entered and executed on a computer system, for exclusive use by the purchaser of the work. Duplication of this publication or parts thereof is permitted only under the provisions of the Copyright Law of the Publisher's location, in its current version, and permission for use must always be obtained from Springer. Permissions for use may be obtained through RightsLink at the Copyright Clearance Center. Violations are liable to prosecution under the respective Copyright Law.

The use of general descriptive names, registered names, trademarks, service marks, etc. in this publication does not imply, even in the absence of a specific statement, that such names are exempt from the relevant protective laws and regulations and therefore free for general use.

While the advice and information in this book are believed to be true and accurate at the date of publication, neither the authors nor the editors nor the publisher can accept any legal responsibility for any errors or omissions that may be made. The publisher makes no warranty, express or implied, with respect to the material contained herein.

Printed on acid-free paper

Springer is part of Springer Science+Business Media (www.springer.com)

To our parents

Preface

*If people do not believe that mathematics is simple,
it is only because they do not realize
how complicated life is*

John von Neumann

About 30 years ago Jean Morlet introduced for the first time the notion of a wavelet as a soliton-like function. At the beginning he applied this function to the analysis of backscattered seismic signals, but soon he realized that wavelets have a significantly broader field of possible applications. In 1981, Alexander Grossmann interpreted wavelets as coherent states and gave an elegant proof of Morlet's reconstruction algorithm. Since then this technique has witnessed explosive growth and it now represents a universal mathematical tool with useful applications in many scientific and engineering studies.

Originally wavelets emerged as an alternative to the classical spectral analysis based on the Fourier transform, such as windowed Fourier analysis or the Gabor transform. In order to improve processing of transient components in complex signals, Morlet decided to replace Gabor functions, which have a fixed duration, by new building blocks or time–frequency atoms, which can have an arbitrarily small duration. Later this concept led to new insights and a mathematically rigorous foundation.

Nowadays, there is no doubt that the introduction of wavelets theory was one of the most important events in mathematics over the past few decades. This is probably the only concept that has been applied in practically all fields of basic science. Moreover, wavelets are widely used for image recognition and compression, for analysis and synthesis of complex signals, in studies of turbulent flows and biological data, etc.

This book is devoted to application of wavelet-based methods in neuroscience. We have attempted to illustrate how wavelets may provide new insight into the complex behavior of neural systems at different levels: from the microscopic dynamics of individual cells (e.g., analysis of intracellular recordings) to the

macroscopic level of widespread neuronal networks (e.g., analysis of EEG and MEG recordings). Our main aim has been to show how and where wavelet-based tools can gain an advantage over classical approaches traditionally used in neuroscience. We hope that the logical structure of the book as regards content (from micro to macro scale) represents a new approach to experiential data analysis and could be helpful in everyday use. The book describes several examples obtained by the authors in experimental neuroscience.

The book results from a long-term cooperation between research groups at Saratov State University, Saratov State Technical University, Universidad Complutense de Madrid, and the Moscow Institute of Higher Nervous Activity and Neurophysiology of the Russian Academy of Science. We want to express our sincere gratitude to Prof. V. S. Anishchenko and Prof. D. I. Trubetskov for their constant support, scientific exchange, and interest in our work. We thank our collaborators A. Brazhe, N. Brazhe, D. Dumsky, V. Grubov, G. van Luijtelaar, A. Luttjohann, A. Moreno, E. Mosekilde, A. Nazimov, A. Ovchinnikov, F. Panetsos, C. M. van Rijn, O. Sosnovtseva, A. Tupitsyn, and J. A. Villacorta-Atienza with whom we have worked on different aspects of neural dynamics over the last decade. Our special thanks go to Prof. J. Kurths who has encouraged us to write this book. We acknowledge fruitful discussions with our colleagues A. Balanov, I. Belykh, V. Kazantsev, I. Khovanov, A. Neiman, G. Osipov, V. Ponomarenko, M. Prokhorov, and V. Raevskiy. We also extend our warmest thanks to the Rector of Saratov State Technical University Prof. I. Pleve for support and help with preparation of this book. Finally, we would like to express our sincere gratitude to our families for their constant support and inspiration.

Over the years, our studies in the field of wavelets have been supported by the Russian Foundation of Basic Research (Russia), the Russian Scientific Foundation (Russia), the Ministry of Education and Science of Russian Federation (Russia), the U.S. Civilian Research and Development Education (USA), the BrainGain Smart Mix Program of the Netherlands Ministry of Economic Affairs (the Netherlands), and the Dynasty Foundation (Russia).

Saratov, Russia
 Saratov, Russia
 Madrid, Spain
 Saratov, Russia
 Moscow, Russia
 July 2014

Alexander E. Hramov
 Alexey A. Koronovskii
 Valeri A. Makarov
 Alexey N. Pavlov
 Evgenia Sitnikova

Contents

1	Mathematical Methods of Signal Processing in Neuroscience	1
1.1	General Remarks	1
1.2	Nonstationarity of Neurophysiological Data	2
1.3	Wavelets in Basic Sciences and Neuroscience	4
1.4	Automatic Processing of Experimental Data in Neuroscience	5
1.5	Brain–Computer Interfaces	6
1.6	Topics to Consider	7
	References	9
2	Brief Tour of Wavelet Theory	15
2.1	Introduction	15
2.2	From Fourier Analysis to Wavelets	16
2.3	Continuous Wavelet Transform	26
2.3.1	Main Definitions: Properties of the Continuous Wavelet Transform	26
2.3.2	Mother Wavelets	32
2.3.3	Numerical Implementation of the Continuous Wavelet Transform	35
2.3.4	Visualisation of Wavelet Spectra: Wavelet Spectra of Model Signals	45
2.3.5	Phase of the Wavelet Transform	52
2.4	Discrete Wavelet Transform	63
2.4.1	Comparison of the Discrete and Continuous Wavelet Transforms	63
2.4.2	General Properties	65
	References	72
3	Analysis of Single Neuron Recordings	77
3.1	Introduction	77
3.2	Wavelet Analysis of Intracellular Dynamics	78
3.2.1	Interference Microscopy and Subcellular Dynamics	78

3.2.2	Modulation of High Frequency Oscillation by Low Frequency Processes	80
3.2.3	Double Wavelet Transform and Analysis of Modulation	81
3.2.4	Modulation of Spike Trains by Intrinsic Neuron Dynamics	83
3.3	Information Encoding by Individual Neurons	86
3.3.1	Vibrissae Somatosensory Pathway	86
3.3.2	Classification of Neurons by Firing Patterns	88
3.3.3	Drawbacks of the Traditional Approach to Information Processing	89
3.3.4	Wavelet Transform of Spike Trains	90
3.3.5	Dynamical Stability of the Neuronal Response	93
3.3.6	Stimulus Responses of Trigeminal Neurons	96
3.4	Wavelet Coherence for Spike Trains: A Way to Quantify Functional Connectivity	101
3.4.1	Wavelet Coherence of Two Point Processes	102
3.4.2	Measure of Functional Coupling Between Stimulus and Neuronal Response	104
3.4.3	Functional Connectivity of Gracilis Neurons to Tactile Stimulus	105
	References	117
4	Classification of Neuronal Spikes from Extracellular Recordings	121
4.1	Introduction	121
4.2	General Principles of Spike Sorting	122
4.3	Spike Detection over a Broadband Frequency Activity	124
4.4	Naive Spike Sorting	127
4.5	Principal Component Analysis as Spike-Feature Extractor	130
4.5.1	How It Works	130
4.5.2	Possible Pitfalls	132
4.6	Wavelet Transform as Spike-Feature Extractor	135
4.6.1	Wavelet Spike Classifier	135
4.6.2	Potential Problems	136
4.7	Wavelet Shape-Accounting Classifier	138
4.8	Performance of PCA vs WT for Feature Extraction	139
4.9	Sensitivity of Spike Sorting to Noise	142
4.9.1	Impact of High/Low Frequency Noise on PCA and WT	143
4.9.2	Proper Noise Filtering May Improve Spike Sorting	145
4.10	Optimal Sorting of Spikes with Wavelets and Adaptive Filtering	147
4.10.1	Noise Statistics and Spike Sorting	147
4.10.2	Parametric Wavelet Sorting with Advanced Filtering	148

4.11	Spike Sorting by Artificial Neural Networks	154
4.11.1	General Approach	154
4.11.2	Artificial Neural Networks	156
4.11.3	Training the Artificial Neural Network	159
4.11.4	Algorithm for Spike Sorting Using Neural Networks	160
4.12	Artificial Wavelet Neural Networks for Spike Sorting	163
4.12.1	Structure of Wavelet Neural Networks	164
4.12.2	Wavelet Neural Networks	164
	References	174
5	Wavelet Approach to the Study of Rhythmic Neuronal Activity	177
5.1	Introduction	177
5.2	Basic Principles of Electroencephalography	178
5.2.1	Electrical Biopotential: From Neuron to Brain	179
5.2.2	Application of EEG in Epilepsy Research	180
5.3	General Principles of Time–Frequency Analysis of EEG	182
5.3.1	The Need for Mathematical Analysis of EEG	182
5.3.2	Time–Frequency Analysis of EEG: From Fourier Transform to Wavelets	183
5.3.3	Time–Frequency Analysis of Spike–Wave Discharges by Means of Different Mother Wavelets	187
5.4	Applications of Wavelets in Electroencephalography	195
5.4.1	Time–Frequency Analysis of EEG Structure	196
5.4.2	Automatic Detection of Oscillatory Patterns and Different Rhythms in Pre-recorded EEG	196
5.4.3	Classification of Oscillatory Patterns	197
5.4.4	Real-Time Detection of Oscillatory Patterns in EEG	197
5.4.5	Multichannel EEG Analysis of Synchronization of Brain Activity	198
5.4.6	Artifact Suppression in Multichannel EEG Using Wavelets and Independent Component Analysis	198
5.4.7	Study of Cognitive Processes	199
	References	201
6	Time–Frequency Analysis of EEG: From Theory to Practice	211
6.1	Introduction	211
6.2	Oscillatory Activity Prior to Epileptic Seizures	212
6.2.1	Description of Experiment	212
6.2.2	Time–Frequency Wavelet Analysis of Cortical and Thalamic SWDs	213
6.2.3	Delta and Theta Precursors of SWD as Measured in the Cortex and Thalamus	216
6.3	Time–Frequency Analysis of Sleep Spindles and Spindle-Like Oscillatory Patterns	221
6.3.1	Relationship Between Sleep Spindles, 5–9 Hz Oscillations, and SWDs	221
6.3.2	Experimental Procedure	222

- 6.3.3 Time–Frequency Analysis of Spindle-Like Oscillatory Patterns: Comparison of Different Mother Wavelets 223
- 6.3.4 Intra-spindle Frequency Dynamics in Epileptic and Non-epileptic Rat Strains 231
- 6.3.5 Age-Related Changes in the Time–Frequency Structure of Sleep Spindles 233
- 6.4 Practical Notes Concerning Application of the Continuous Wavelet Transform in Time–Frequency EEG Analysis 235
 - 6.4.1 Complex or Real Mother Wavelet 236
 - 6.4.2 Shape of Mother Wavelet 236
 - 6.4.3 Width of Mother Wavelet 236
- 6.5 Classification of Sleep Spindle Events by Means of Adaptive Wavelet Analysis 237
 - 6.5.1 Construction of Adaptive Wavelet Basis (“Spindle Wavelet”) for Automatic Recognition of Sleep Spindles 237
 - 6.5.2 Identification of Two Spindle Types with the Aid of Two Adaptive “Spindle Wavelets” 239
 - 6.5.3 Two Types of Sleep Spindles and Their Relevance to SWD 240
- 6.6 Synchronous Dynamics of Epileptic Discharges: Application of Time-Scale Synchronization Approach 242
- References 248
- 7 Automatic Diagnostics and Processing of EEG 253**
 - 7.1 Introduction 253
 - 7.2 Automatic Identification of Epileptic Spike–Wave Discharges 255
 - 7.2.1 General Aspects of Automatic SWD Detection in EEG 255
 - 7.2.2 Off-Line Wavelet-Based Algorithm for Automatic Detection of SWDs 256
 - 7.2.3 Performance of the Method 259
 - 7.3 Brain–Computer Interface for On-Line Diagnostics of Epileptic Seizures 260
 - 7.3.1 On-Line SWD Detection Algorithm 260
 - 7.3.2 Experimental Verification of the Algorithm and On-Line SWD Diagnostics 264
 - 7.4 Automatic Detection of Sleep Spindles by Adaptive Wavelets 267
 - 7.5 Automatic Detection and Discrimination of 5–9 Hz Oscillations and Sleep Spindles 271
 - 7.6 On–Off Intermittency of Thalamo–Cortical Oscillations 273
 - 7.6.1 Nonlinear Dynamics of SWDs, Sleep Spindles, and 5–9 Hz Oscillations 273

- 7.6.2 Intermittent Dynamics of SWDs Under the Influence of a Pro-absence Drug (Vigabatrin) 276
- 7.6.3 Mechanisms of Intermittent Behavior in the Thalamo-Cortical Neuronal Network 278
- 7.7 Serial Identification of EEG Patterns Using Adaptive Wavelet Analysis 279
 - 7.7.1 Adaptive Wavelet-Based Technique and the Serial Method..... 280
 - 7.7.2 Experimental Validation of the Serial Method..... 284
- 7.8 Artifact Suppression in Multichannel EEG Using Wavelet-Enhanced Independent Component Analysis..... 286
 - 7.8.1 Independent Component Analysis in EEG Studies..... 287
 - 7.8.2 ICA-Based Artifact Suppression 288
 - 7.8.3 Wavelet-Enhanced ICA (wICA) for Artifact Suppression 290
 - 7.8.4 Data Collection and Numerical Tools for Testing Connectivity 293
 - 7.8.5 Suppression of Artifacts by ICA and wICA Methods..... 295
 - 7.8.6 Recovering Brain Signals in the Presence of Artifacts..... 299
 - 7.8.7 Power Spectrum Distortion 301
 - 7.8.8 Artifact Suppression and Non-local Characteristics Derived from EEG 302
 - 7.8.9 Conclusion 304
- References 306
- 8 Conclusion** 313
 - Reference 314
- Index** 315

Acronyms

ANN	Artificial neural networks
BCI	Brain–computer interface
CNS	Central nervous system
CSD	Current source density
CWT	Continuous wavelet transform
DWT	Discrete wavelet transform
ECoG	Electrocorticogram
EEG	Electroencephalogram
FFT	Fast Fourier transform
GAERS	Genetic rats with absence epilepsy
HF	High frequency
HPF	High-pass filter
ICA	Independent component analysis
icEEG	Intracranial EEG
ISI	Interspike interval
LF	Low frequency
LFP	Local field potential
MEG	Magnetoencephalogram
NN	Neuronal network
OSDS	On-line SWD detection system
PCA	Principal component analysis
PSTH	Peristimulus time histogram
PWAF	Parametric wavelet sorting with advanced filtering
RTN	Reticular thalamic nucleus
rWF	Representative waveform
SD	Standard deviation
sdEEG	Subdural EEG
SI	Somatosensory
SWD	Spike-wave discharge
TC	Thalamocortical
TSS	Time scale synchronization

VPM	Ventroposteromedial
WAG/Rij	Wistar Albino Glaxo/Rijswijk
WF	Waveform
WMSPC	Wavelet method with superparamagnetic clustering
wICA	Wavelet independent component analysis
WNN	Wavelet neuronal network
WPOD	Wavelet power over domain
WSAC	Wavelet shape-accounting classifier
WSC	Wavelet-based spike classifier
WT	Wavelet transform

Chapter 1

Mathematical Methods of Signal Processing in Neuroscience

Abstract This chapter offers a brief introduction to the novel advanced mathematical methods of analysis and processing of neurophysiological data. First, we give the rationale for the development of specific mathematical approaches for decoding information from non-stationary neurophysiological processes with time-varying features. Second, we focus on the development of mathematical methods for automatic processing and analysis of neurophysiological signals, more specifically, in the development of brain–computer interfaces (BCIs). Finally, we give an overview of the main applications of wavelet analysis in neuroscience, from the *microlevel* (the dynamics of individual cells or intracellular processes) to the *macrolevel* (dynamics of large-scale neuronal networks in the brain as a whole, ascertained by analyzing electro- and magnetoencephalograms).

1.1 General Remarks

Neurodynamics is a contemporary branch of interdisciplinary neuroscience that examines mechanisms of the central nervous system based on the mutual experience of chemists, biologists, physicists, mathematicians, and specialists in the nonlinear theory of oscillations, waves, and dynamical chaos [1–6]. Practical applications of modern methods in neuroscience facilitate an interdisciplinary approach to brain functions and attract experts in experimental and theoretical neurobiology, psychophysiology, cognitive neuroscience, biophysics, physics, nonlinear dynamics, etc. This interdisciplinary collaboration provides unique methods for analyzing the functional activity of the central nervous system (CNS) that focus on the basic principles of the neuronal dynamics of individual cells and neural networks.

Recent progress in understanding molecular and ionic mechanisms of neuronal activity [7] encourages further investigation of certain key problems in modern physics, such as exploration of the functional properties and principles of information coding, as well as its representation and the processing of sensory data in the central nervous system. Perception and information processing are

important functions of the CNS. Visual, acoustic, tactile, and gustatory stimuli are transformed by the sensory receptors of the first order neurons into a sequence of electrical pulses. These first-order sensory neurons are therefore involved in primary processing of sensory information [8–12]. Sensory information is then passed through relay stations (brain stem and thalamic nuclei) that transform and convolve the information code, until finally it reaches the cerebral cortex which shapes the “fingerprint” of the external world [13, 14]. At each subsequent stage, the processes of information transfer become increasingly difficult to study. The question of how the totality of nervous impulses (action potentials or spikes) generated by single neurons can reflect the full complexity and diversity of the external world remains one of the biggest challenges in fundamental science [13, 15–17].

Experimental methods have recently been developed for registering the neuronal activity underlying processes of information encoding–decoding at different levels of the nervous system—from molecular changes in membrane properties of receptor cells to changes in the local (electrical) field potentials in the cerebral cortex. Traditional and noninvasive methods for registering electrical brain activity, such as electroencephalography (EEG) with electrodes arranged on the skin of the head, offer several advantages, and this method is still commonly used in neurophysiology and medicine. EEG is often used in various studies of brain functions in humans and animals [18, 19]. There are also invasive methods using implanted electrodes which provide better spatial resolution, and these are advantageous when examining neuronal activity in small groups of neurons in superficial (cortex) and deep (subcortical) structures. Another advantage of invasive recording techniques is that implanted electrodes can also be used for electrical stimulation with different research purposes, e.g., suppression of epileptic discharges [20–22]. The relatively new noninvasive recording technique known as magnetic encephalography (MEG) has become more popular over the last few years, because it provides better spatial resolution than EEG and better quality of signals reflecting brain activity [23–25].

1.2 Nonstationarity of Neurophysiological Data

Despite technical progress in developing new methods of data acquisition in experimental neurophysiology, mathematical methods of experimental data analysis could not be readily applied, and this may impede further progress. In the vast majority of experimental studies in neuroscience, only a few statistical methods of data analysis are used, e.g., calculation of the mean spike frequency, construction of various correlation characteristics and distribution functions, etc. Traditional methods of statistical analysis are undoubtedly useful, but most of them unable to evaluate the relevant information regarding complex processes in the CNS. In order to illustrate this fact, we give an example that demonstrates the response of a sensory neuron to periodic stimulation. From a mechanical point of view, the response of

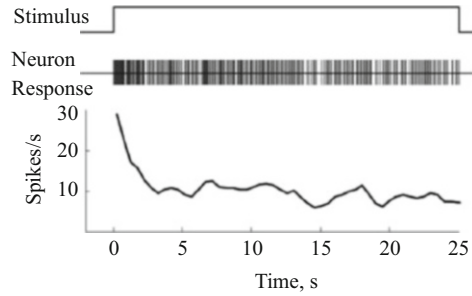


Fig. 1.1 Illustration of adaptation reaction of neuronal firing activity to a repeated stimulation. This neuron was recorded in a rat in the trigeminal sensory nuclear complex which receives tactile information from vibrissae. Stimulation was performed by periodic mechanical deflection of one whisker by a series of short directed air puffs (duration of each air pulse 5 ms). *From top to bottom:* start and end of stimulation by the sequence of periodic impulses, firing activity of a single neuron (train of spikes), and dynamics of the mean spike frequency (averaging over a sliding time window of 500 ms duration)

the neuron to a sequence of equal external stimuli could be identical, so periodic stimulation of a neuron with a series of impulses could elicit a periodic sequence of spikes (action potentials, for example, 2 or 3 spikes per stimulus). However, in the experimental situation, we often obtain time- and activity-dependent variations in the neuron's response (the neuron does not demonstrate an equal response to repeated identical stimuli) which reflect neuronal plasticity. The phenomenon of synaptic neuronal plasticity (the basic mechanism underlying memory and learning) reflects adaptation to external afferent activity modified by the internal characteristics of individual cells and the global dynamics of the wider neuronal network interactions [26, 27]. It is known that a neuron can even stop responding to the next stimulus from a certain moment.

Figure 1.1 illustrates the adaptive response of a neuron of the trigeminal complex to periodic stimulation. Maximum neuron activity (27 spikes/s) is observed at the onset of stimulation; it falls to an average of 10 spikes/s within a few seconds and varies thereafter, exhibiting a slow negative drift. On the one hand, such behavior of a living cell makes it extremely difficult to define characteristic forms/patterns of neural activity associated with the peculiar properties of a given stimulus. On the other hand, such complexity in neuronal activity encourages the development of more relevant (complex) methods of data analysis, in addition to the simple description of statistical characteristics of neuronal responses that is one of the tasks of neurodynamics. We conclude that more specific mathematical methods must be applied, such as wavelets [28–30], the Hilbert–Huang transform [31–33], and the Wigner–Ville transform [34–36], which are more suitable for decoding information about non-stationary processes with time-varying features.

1.3 Wavelets in Basic Sciences and Neuroscience

Wavelet analysis [28, 37–40] is unique in the sense that even the first practical application to neurophysiological data analysis produced prominent results [29, 41–45]. For this reason, it is considered a very powerful analytical tool for studying the dynamics of neural systems.

Wavelet terminology was introduced in the 1980s [37, 46, 47]. This mathematical approach was initially proposed as an alternative to classical spectral analysis based on the Fourier transform. Wavelet theory is considered to be one of the most important events in mathematics of the past decades. Indeed, it appears to be the sole new mathematical concept that was immediately recognized as a tool in practically all branches of basic science (first and foremost, in physics and related disciplines) and many technical fields [30, 48–55]. In fact, introduction of the wavelet theory itself was not entirely unexpected. It was developed to meet the very real needs of experimental investigations, particularly in geophysics and seismology. Contemporary wavelet analysis combines various pre-existing ideas and methods. For example, fast wavelet transform algorithms are based on the subband coding ideology known from radio and electric engineering [56]. Some ideas were borrowed from physics (coherent states [57], etc.) and mathematics (studies on Caldéron–Zygmund integral operators [58]). Wavelet analysis is logically related to the theory of diffusion differential equations [59].

Today, wavelets are widely used for the analysis and synthesis of various signals, image processing and recognition, compression of large volumes of information, digital filtration, the study of fully developed turbulence, and the solution of certain differential equations. This list can certainly be extended [54, 59–67]. The new theory aroused great interest from the very beginning. According to well-known estimates [48], since the 1990s, the number of publications using wavelets in physics has been growing continuously. The number of references to Internet sources containing the term “wavelet” has reached several million. In fundamental science, this mathematical approach is mostly applied to study complex temporally non-stationary or spatially nonhomogeneous nonlinear processes. Wavelet analysis is well adapted for studying the complex structure of signals from living systems, since other traditional computation techniques can be applied only to processes with time (or space)-constant parameters (i.e., stationary in time or spatially homogeneous). Despite the fact that wavelet analysis has long been regarded as a standard tool for studying complex processes and practical application of this method in neuroscience and medicine is just beginning, prognoses for its successful application are rather optimistic. In this monograph we highlight recent advances made by practical application of wavelet in neurodynamics and neurophysiology.

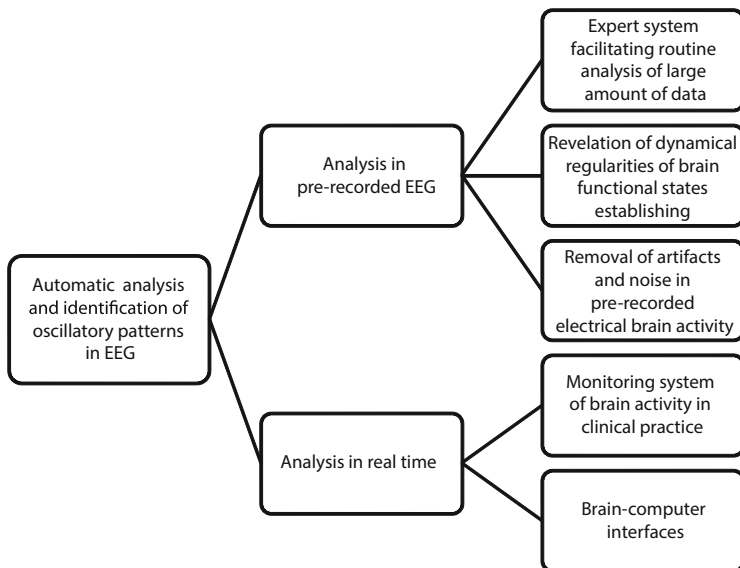


Fig. 1.2 Wavelet-based methods of automatic EEG diagnostics, processing, and analysis

1.4 Automatic Processing of Experimental Data in Neuroscience

An important field of wavelet applications in neurophysiology and neuroscience is the development of methods for automatic processing and analysis of brain signals. Electrical signals that can be recorded from the brain (EEG) represent a linear mixture of coexisting oscillatory components, i.e., nonlinear effects do not complicate the process of recognition. The development of expert systems for automatic EEG analysis is of particular interest for both fundamental neuroscience and clinical practice due to a wide spectrum of possible applications (classified in Fig. 1.2). One must distinguish between on-line and off-line analysis. Automatic (i.e., without the attention and control of an operator) analysis of pre-recorded EEG signals (*off-line* diagnostics) aims to reduce routine work, for example, to suppress artifacts in the recorded EEG. EEG analysis in real time (*on-line*) aims at fast detection of certain EEG events and the organization of closed-loop control systems. Clinically-oriented applications are the most effective field of on-line analysis of neurophysiological signals, including EEG monitoring with predictive diagnostic purposes, e.g., for the suppression of epileptic activity, the so-called spike-wave discharges [20].

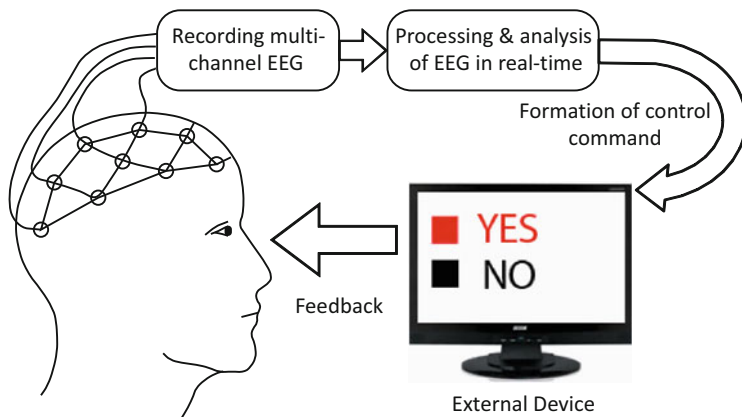


Fig. 1.3 General scheme of a simple brain–computer interface. Modern IBC is a system that registers and analyzes signals of electrical brain activity (usually EEG) from the user and “converts” them into a “machine” command for external device control. The central point of such a system is the development of algorithms for real-time recognition of EEG patterns corresponding to certain cognitive operations. Note the importance of the feedback loop in the BCI. This is necessary to adapt the aforementioned algorithms to recognize the specific patterns of electrical brain activity based on EEG features. Also the operator (user) must learn to evoke and control the relevant mental state, which is impossible without the use of feedback

1.5 Brain–Computer Interfaces

One of the most exciting applications of wavelets is to use it for *mental control* of brain functions, which, as a matter of fact, is a new form of human–computer interaction [68, 69]. The specific dynamics of electrical brain activity characterizes mental activity that includes compilation of imaginary commands (“mental action”). This “mental action” is associated with specific changes in the time–frequency characteristics and spatial structure of EEG [70–73]. In the brain–computer interface, mental control systems must perform the following steps (see Fig. 1.3):

- Recognize and select characteristic changes in the EEG (event-related *oscillatory patterns*).
- Decrypt their meaning (associated with a specific operation).
- Convert this meaning into commands for hardware control.

Mental control systems should be able to solve two main problems. First, the technical problem of precise recognition of an EEG pattern, subsequent formulation of a “command”, and transmission to control. Second, cognitive and psychological tasks in which the operator (a person) should learn to keep specific mental states that can be recognized from analysis of the spatial-temporal structure of his/her EEG. An additional problem is that the system should work in real time. Earlier control systems were suggested to use information about complex physical activity expressed as body movements of the operator, e.g., the trajectory when moving

a hand in the process of equipment handling. These interfaces encountered many problems, including registration of complex information, isolation of relevant information from the general data stream, and correct interpretation. Besides that, such interfaces require a system of sensors for registration of motor activity and a wireless device for data transmission from operator to computer. Therefore, simple brain–computer interfaces (BCI) are of particular interest, such as interfaces that are able to monitor electrical brain activity and detect the mental intentions of the operator. For example, simple stimulus–symbol interfaces conceived by the operator [74, 75] open up new prospects for resolving the problem of mental control.

Thus, algorithms of automatic EEG pattern recognition associated with specific cogitative operations in real time help to effectively perform the first step (pattern recognition) in brain–computer interfaces. Wavelet-based methods are perfectly suited to pattern recognition tasks [76–79].

Note that brain–computer interfaces have already been used as an alternative to traditional devices for inputting information into the computer. So for certain categories of users, for example, people with motor function disabilities, this way of interacting with the computer can improve their quality of life, at least partly, opening the way to a full-fledged life in society [80–83]. One of the first successfully worked BCIs was developed at Emory University by Roy Bakay and Phillip Kennedy, who used implanted depth electrodes in the brain motor center of a paralyzed 53-year-old patient, who was able to move the cursor on a computer screen, and thus communicate with doctors (writing several simple sentences) [84]. Rapid progress in neuroscience and technology suggests that brain–computer interfaces could be widely used for control of artificial limbs, manipulators, and robot technical devices (for example, wheelchairs), and also in the gaming industry [85–88].

1.6 Topics to Consider

A mathematically rigorous description of wavelet analysis can be found in numerous textbooks and monographs (see, for example, [28, 53, 55, 60, 89–93]) as well as in reviews in scientific journals [17, 51, 52, 94]. This book focuses on the new possibilities provided by the wavelet approach for decoding information from signals recorded on the level of individual neurons and groups of neurons, as well as neural network activity. A large number of the aforementioned scientific publications aimed to identify the most important problems in the field of wavelet applications to neurodynamics and neurophysiology. On this topic, we distinguish the following three areas of wavelet applications in neuroscience:

- **Microlevel** (cellular/intracellular)—wavelet analysis of the dynamics of individual cells or intracellular processes.
- **Mesolevel** (groups of cells)—analysis of information processes in small neuronal ensembles.

- **Macrolevel** (brain activity)—analysis of macrodynamics in widespread neural networks (EEG/MEG, neuroimaging data).

This monograph discusses the progress made on each of these levels in a consistent manner. The book contains seven chapters:

- Chapter 2 provides a mathematical introduction to wavelet analysis, including the basic concepts and definitions of wavelet theory, and considers practically significant questions related to effective numerical implementation of the wavelet transform (both, discrete and continuous). Special attention is paid to the importance of the relationship between wavelet and Fourier analysis. This chapter specifically addresses those readers who are not familiar with the mathematical concepts of complex signal processing.

The next two chapters describe methods for wavelet investigation of neurophysiological systems.

- Chapter 3 discusses the application of wavelets for analysis of cellular dynamics at the microscopic level (individual cells or intracellular processes). This chapter also presents the principles for analyzing the information from a single cell, using electrical signals of individual neurons.
- Chapter 4 describes the main aspects of the wavelet analysis of a variety of impulse shapes (action potentials) of individual neurons using extracellular records of single-unit neuronal activity. We consider different approaches to classifying neuronal impulses in terms of their configuration, some based solely on wavelets, and others involving combined methods, such as wavelet neural networks.

The last three chapters of the book consider the macrodynamics of neuronal networks using wavelet analysis of electroencephalograms (EEGs).

- Chapter 5 considers the main definitions and principles of electroencephalography that are required for a better understanding of Chaps. 6 and 7. We describe general physical and mathematical approaches to time–frequency analysis of rhythmic EEG activity using continuous wavelet transforms. We also review some recent achievements of wavelet-based studies of electrical brain activity, including (i) time–frequency analysis of EEG structure, (ii) automatic detection of oscillatory patterns in pre-recorded EEG, (iii) classification of oscillatory patterns, (iv) real-time detection of oscillatory patterns in EEG, (v) detection of synchronous states of electrical brain activity, (vi) artifact suppression/rejection in multichannel EEG, and (vii) the study of cognitive processes.
- Chapter 6 describes some results of time–frequency analysis of EEG structure using the continuous wavelet transform. In this chapter we pay special attention to technical and computational details of time–frequency analysis of neurophysiological signals (EEG of animals and humans). This chapter also presents wavelet analysis of hypersynchronous rhythmic activity in multichannel EEG, characterizing the onset of absence epilepsy in patients.

- Chapter 7 considers basic problems of automatic diagnostics and processing of EEG. We discuss the wavelet-based techniques in order to fully automatize “routine” operations, such as visual inspection of EEG. In addition, we exhibit examples of practical applications of wavelet methods for automatic analysis of pre-recorded EEG and MEG signals (*off-line* diagnostics), and also some examples of EEG analysis in real-time (*on-line*). We also discuss the principles of fast and precise detection of transient events in EEG and the organization of closed-loop control systems that can be used in BCI. Finally, we consider methods of artifact suppression in multichannel EEG based on a combination of wavelets and independent component analysis

This book is based primarily on the fundamental results in neurodynamics obtained recently by the authors—physicists, mathematicians, and biologists in close collaboration with specialists in experimental neurophysiology. At the same time, the book contains a relatively complete bibliography (over 400 sources) characterizing the application of wavelets in neurophysiological research. In general, this book overviews theoretical and practical knowledge and, in our opinion, demonstrates the advantages of powerful analytical tools and novel mathematical methods of signal processing and nonlinear dynamics in order to address neurophysiological problems. Moreover, wavelet analysis helps to reveal important information and facilitates a deeper understanding of the investigated phenomena. More intensive studies in this area can contribute to interdisciplinary interactions between physics, nonlinear dynamics, applied mathematics, and neurophysiology and promote further mutual research in these areas.

References

1. G. Buzsaki, A. Draguhn, Neuronal oscillations in cortical networks. *Science* **304**, 1926 (2004)
2. H.D. Abarbanel, M.I. Rabinovich, A. Selverston, M.V. Bazhenov, R. Huerta, M.M. Sushchik, L.L. Rubchinskii, Synchronisation in neural networks. *Phys.–Usp.* **39**(4), 337 (1996)
3. V.I. Nekorkin, Nonlinear oscillations and waves in neurodynamics. *Phys.–Usp.* **51**(3), 295 (2008)
4. B.P. Bezruchko, V.I. Ponomarenko, M.D. Prokhorov, D.A. Smirnov, P.A. Tass, Modeling nonlinear oscillatory systems and diagnostics of coupling between them using chaotic time series analysis: applications in neurophysiology. *Phys.–Usp.* **51**(3), 304 (2008)
5. M.I. Rabinovich, M.K. Muezzinoglu, Nonlinear dynamics of the brain: emotion and cognition. *Phys.–Usp.* **53**(4), 357 (2010)
6. M.I. Rabinovich, K.J. Friston, P. Varona (eds.), *Principles of Brain Dynamics: Global State Interactions* (MIT, Cambridge, 2012)
7. H.C. Tuckwell, *Introduction to Theoretical Neurobiology* (Cambridge University Press, Cambridge, 1988)
8. W.J. Freeman, *Mass Action in the Nervous System* (Academic, New York, 1975)
9. L.S. da Fernando, Neural mechanisms underlying brain waves: from neural membranes to networks. *Electroencephalogr. Clin. Neurophysiol.* **79**, 81 (1991)
10. G.R. Ivanitskii, A.B. Medvinskii, M.A. Tsyganov, From the dynamics of population autowaves generated by living cells to neuroinformatics. *Physics-Uspekh* **37**(10), 961 (1994)

11. W.J. Freeman, Mesoscopic neurodynamics: from neuron to brain. *J. Physiol. (France)* **94**, 303 (2000)
12. G.N. Borisyuk, R.M. Borisyuk, Y.B. Kazanovich, G.R. Ivanitskii, Models of neural dynamics in brain information processing—the developments of ‘the decade’. *Phys.–Usp.* **45**(10), 1073 (2002)
13. A. Villacorta-Atienza, M.G. Velarde, V.A. Makarov, Compact internal representation of dynamic situations: neural network implementing the causality principle. *Biol. Cybern.* **103**, 285 (2010)
14. V.A. Makarov, A. Villacorta-Atienza, in *Recurrent Neural Networks for Temporal Data Processing* (INTECH’2011, Shanghai), ed. by H. Cardot (2011), pp. 81–102
15. N.P. Castellanos, V.A. Makarov, Recovering EEG brain signals: artifact suppression with wavelet enhanced independent component analysis. *J. Neurosci. Methods* **158**, 300 (2006)
16. A. Villacorta-Atienza, M.G. Velarde, V.A. Makarov, Compact internal representation of dynamic situations: neural network implementing the causality principle. *Biol. Cybern.* **103**, 285 (2010)
17. A.N. Pavlov, A.E. Hramov, A.A. Koronovskii, Y.E. Sitnikova, V.A. Makarov, A.A. Ovchinnikov, Wavelet analysis in neurodynamics. *Phys.–Usp.* **55**(9), 845 (2012)
18. P.L. Nunez, K. Srinivasan, *Electric Fields of the Brain: The Neurophysics of EEG* (Oxford University Press, New York, 1981)
19. E. Niedermeyer, F.L. da Silva, *Electroencephalography: Basic Principles, Clinical Applications, and Related Fields* (Lippincot Williams & Wilkins, Philadelphia, 2004)
20. A. Berenyi, M. Belluscio, D. Mao, G. Buzsaki, Closed-loop control of epilepsy by transcranial electrical stimulation. *Science* **337**(6095), 735 (2012)
21. A. Lutjohann, E.L.M. van Luijtelaar, The dynamics of cortico-thalamo-cortical interactions at the transition from pre-ictal to ictal LFPs in absence epilepsy. *Neurobiol. Dis.* **47**, 49 (2012)
22. A. Lutjohann, J.M. Schoffelen, E.L.M. van Luijtelaar, Peri-ictal network dynamics of spike-wave discharges: phase and spectral characteristics. *Exp. Neurol.* **239**, 235 (2013)
23. M. Hämmäläinen, R. Hari, R.J. Ilmoniemi, J. Knuutila, O.V. Lounasmaa, Magnetoencephalography: theory, instrumentation, and applications to noninvasive studies of the working human brain. *Rev. Mod. Phys.* **65**, 413 (1993)
24. P. Hansen, M. Kringelbach, R. Salmelin (eds.), *MEG: An Introduction to Methods* (Oxford University Press, New York, 2010)
25. I. Westmijse, P. Ossenblok, B. Gunning, E.L.M. van Luijtelaar, Onset and propagation of spike and slow wave discharges in human absence epilepsy: a MEG study. *Epilepsia* **50**, 2538 (2009)
26. E. Ahissar, P.M. Knutsen, Object localization with whiskers. *Biol. Cybern.* **98**, 449 (2008)
27. V.A. Makarov, A.N. Pavlov, A.N. Tupitsyn, F. Panetsos, A. Moreno, Stability of neural firing in the trigeminal nuclei under mechanical whisker stimulation. *Comput. Intell. Neurosci.* **2010**, 340541 (2010)
28. I. Daubechies, *Ten Lectures on Wavelets* (SIAM, Philadelphia, 1992)
29. A. Aldroubi, M. Unser, *Wavelets in Medicine and Biology* (CRC, Boca Raton, 1996)
30. J.C. Van den Berg (eds.), *Wavelets in Physics* (Cambridge University Press, Cambridge, 2004)
31. N.E. Huang, Z. Shen, S.R. Long, A new view of nonlinear water waves: the Hilbert spectrum. *Ann. Rev. Fluid Mech.* **31**, 417 (1999)
32. N.E. Huang, Z. Shen, S.R. Long, M.C. Wu, H.H. Shih, Q. Zheng, N.C. Yen, C.C. Tung, H.H. Liu, The empirical mode decomposition and the Hilbert spectrum for nonlinear and non-stationary time series analysis. *Proc. R. Soc. A: Math. Phys. Eng. Sci.* **454**, 903 (1998)
33. N.E. Huang, Z. Shen, *Hilbert–Huang Transform and Its Applications* (World Scientific, Singapore, 2005)
34. B. Boashash, in *Advances in Spectrum Analysis and Array Processing*, ed. by S. Haykin (Prentice Hall, Englewood Cliffs, 1990), pp. 418–517
35. S. Qian, D. Chen, *Joint Time–Frequency Analysis* (Prentice Hall, Upper Saddle River, 1996)
36. W. Mecklenbrauker, F. Hlawatsch, *The Wigner Distribution: Theory and Applications in Signal Processing* (Elsevier, Amsterdam, 1997)

37. A. Grossman, J. Morlet, Decomposition of Hardy function into square integrable wavelets of constant shape. *SIAM J. Math. Anal.* **15**(4), 273 (1984)
38. M.B. Ruskai, G. Beylkin, R. Coifman, I. Daubechies, S.G. Mallat, Y. Meyer, L. Raphael, *Wavelets and Their Applications and Data Analysis* (Jones and Bartlett, Boston, 1992)
39. Y. Meyer, *Wavelets: Algorithms and Applications* (SIAM, Philadelphia, 1993)
40. Y. Meyer, *Wavelets and Operators* (Cambridge University Press, Cambridge, 1992)
41. J.J. Benedetto, A.I. Zayed, *Sampling, Wavelets, and Tomography* (Birkhäuser, Boston, 2004)
42. J.C. Letelier, P.P. Weber, Spike sorting based on discrete wavelet transform coefficients. *J. Neurosci. Methods* **101**, 93 (2000)
43. E. Hulata, R. Segev, E. Ben-Jacob, A method for spike sorting and detection based on wavelet packets and Shannon's mutual information. *J. Neurosci. Methods* **117**, 1 (2002)
44. Q.R. Quiroga, Z. Nadasdy, Y. Ben-Shaul, Unsupervised spike detection and sorting with wavelets and superparamagnetic clustering. *Neural Comput.* **16**, 1661 (2004)
45. R.Q. Quiroga, A. Kraskov, T. Kreuz, P. Grassberger, Performance of different synchronization measures in real data: a case study on electroencephalographic signals. *Phys. Rev. E* **65**, 041903 (2002)
46. J. Morlet, G. Arens, E. Fourgeau, D. Glard, Wave propagation and sampling theory. Part I. Complex signal and scattering in multilayered media. *Geophysics* **47**(2), 203 (1982)
47. J. Morlet, G. Arens, E. Fourgeau, D. Giard, Wave propagation and sampling theory. Part II. Sampling theory and complex waves. *Geophysics* **47**(2), 222 (1982)
48. P.S. Addison, *The Illustrated Wavelet Transform Handbook: Introductory Theory and Applications in Science Engineering, Medicine and Finance* (Institute of Physics Publishing, Bristol, 2002)
49. G. Kaiser, *A Friendly Guide to Wavelets* (Springer/Birkhauser, Boston, 1994)
50. S.G. Mallat, *A Wavelet Tour of Signal Processing* (Academic, New York, 1998)
51. N.M. Astaf'eva, Wavelet analysis: basic theory and some applications. *Phys.-Usp.* **39**(11), 1085 (1996)
52. I.M. Dremin, O.V. Ivanov, V.A. Nechitailo, Wavelets and their uses. *Phys.-Usp.* **44**(5), 447 (2001)
53. A.A. Koronovskii, A.E. Hramov, *Continuous Wavelet Analysis and Its Applications* (Fizmatlit, Moscow, 2003)
54. V.G. Anfingentov, A.A. Koronovskii, A.E. Hramov, Wavelet analysis and its applications for examination of behaviour of nonlinear dynamical systems of different nature. *BRAS: Phys.* **64**(12), 2383 (2000)
55. B. Torresani, *Continuous Wavelet Transform* (Savoire, Paris, 1995)
56. M. Vetterli, J. Kovacevic, *Wavelets and Subband Coding* (Prentice Hall, Englewood Cliffs, 1995)
57. S.T. Ali, J.P. Antoine, J.P. Gazeau, *Coherent States, Wavelets and Their Generalizations* (Springer, New York, 1999)
58. Y. Meyer, R. Coifman, *Calderon-Zygmund and Multilinear Operators* (Cambridge University Press, Cambridge, 1997)
59. D.E. Postnov, Evaluation of a continuous wavelet transform by solving the Cauchy problem for a system of partial differential equations. *Comput. Math. Math. Phys.* **46**(1), 73 (2006)
60. J.J. Benedetto, M. Frazier, *Wavelets: Mathematics and Applications* (CRC, Boca Raton, 1994)
61. R. Gencay, F. Selcuk, B. Whitcher, *An Introduction to Wavelets and Other Filtering Methods in Finance and Economics* (Academic, San Diego, 2001)
62. T. Strutz, *Bilddatenkompression. Grundlagen, codierung, JPEG, MPEG, wavelets* (Vieweg Braunschweig, Wiesbaden, 2002)
63. J.S. Walker, *A Primer on Wavelets and Their Scientific Applications* (CRC, Boca Raton, 1999)
64. C.L. da Fontoura, J.R.M. Cesar, *Shape Analysis and Classification: Theory and Practice* (CRC, Boca Raton, 2001)
65. S. Jaffard, Y. Meyer, R. Ryan, *Wavelets: Tools for Science and Technology* (SIAM, Philadelphia, 2001)

66. M.V. Wickerhauser, *Adapted Wavelet Analysis from Theory to Software* (A.K. Peters, Wellesley, 1994)
67. E.B. Postnikov, E.A. Lebedeva, Decomposition of strong nonlinear oscillations via modified continuous wavelet transform. *Phys. Rev. E* **82**(5), 057201 (2010)
68. C. Guger, H. Ramoser, G. Pfurtscheller, Real-time EEG analysis for a brain–computer interface (BCI) with subject-specific spatial patterns. *IEEE Trans. Neural Syst. Rehabil. Eng.* **8**(4), 447 (2000)
69. S.G. Mason, G.E. Birch, A general framework for brain–computer interface design. *IEEE Trans. Neural Syst. Rehabil. Eng.* **11**(1), 70 (2003)
70. S. Makeig, S. Enghoff, T.P. Jung, T.J. Sejnowski, A natural basis for efficient brain-actuated control. *IEEE Trans. Neural Syst. Rehabil. Eng.* **8**, 208 (2000)
71. N.E. Sviderskaya, T.N. Dashinskaja, G.V. Taratunova, Spatial organization of EEG activation during the creative processes. *J. High. Nerv. Act.* **51**, 393 (2001)
72. N.E. Sviderskaya, *Spatial Organization of Electroencephalogram* (VGMA Press, Voronezh, 2008)
73. N.E. Sviderskaya, A.G. Antonov, Effect of individual psychological characteristics on the spatial organization of EEG during nonverbally-divergent mindset. *Hum. Physiol.* **34**(5), 34 (2008)
74. L.A. Farwell, E. Donchin, Talking off the top of your head: toward a mental prosthesis utilizing event related brain potentials. *EEG Clin. Neurophysiol.* **70**, 510 (1988)
75. J.N. Mak, Y. Arbel, J.W. Minett, L.M. McCane, B. Yuksel, D. Ryan, D. Thompson, L. Bianchi, D. Erdogmus, Optimizing the P300-based brain–computer interface: current status, limitations and future directions. *J. Neural Eng.* **8**, 025003 (2011)
76. M. Huang, P. Wu, Y. Liu, L. Bi, H. Chen, Application and contrast in brain–computer interface between Hilbert–Huang transform and wavelet transform, in *The 9th International Conference for Young Computer Scientists (ICYCS'08)*, Zhang Jia Jie, 18–21 Nov 2008, pp. 1706–1710
77. M.R. Kousarrizi, A.A. Ghanbari, M. Teshnehlab, M. Aliyari, A. Gharaviri, Feature extraction and classification of EEG signals using wavelet transform, SVM and artificial neural networks for brain–computer interfaces, in *International Joint Conference on Bioinformatics, Systems Biology and Intelligent Computing, 2009 (IJCBS'09)*, Shanghai, 3–5 Aug 2009, pp. 352–355
78. T. Bassani, J.C. Nievola, Pattern recognition for brain–computer interface on disabled subjects using a wavelet transformation, in *IEEE Symposium on Computational Intelligence in Bioinformatics and Computational Biology (CIBCB'08)*, Sun Valley Idaho, 15–17 Sept 2008, pp. 180–186
79. V.M. Vaughan, Guest editorial brain–computer interface technology: a review of the second international meeting. *IEEE Trans. Neural Syst. Rehabil. Eng.* **11**(2), 94 (2003)
80. U. Hoffmann, J.M. Vesin, T. Ebrahimi, K. Diserens, An efficient P300-based brain–computer interface for disabled subjects. *J. Neurosci. Methods* **167**(1), 115 (2008)
81. G. Pires, U. Nunes, M. Castelo-Branco, Comparison of a rowcolumn speller vs. a novel lateral single-character speller: assessment of BCI for severe motor disabled patients. *Clin. Neurophysiol.* **123**, 1168 (2012)
82. N.V. Manyakov, N. Chumerin, A. Combaz, M.M. van Hulle, Comparison of classification methods for P300 brain–computer interface on disabled subjects. *Comput. Intell. Neurosci.* **2011**, 519868 (2011)
83. S. Lu, C. Guan, H. Zhang, Unsupervised brain–computer interface based on intersubject information and online adaptation. *IEEE Trans. Neural Syst. Rehabil. Eng.* **17**, 135 (2009)
84. P.R. Kennedy, R.A. Bakay, Restoration of neural output from a paralyzed patient by a direct brain connection. *Neuroreport* **9**, 1707 (1998)
85. J.R. Wolpaw, Brain–computer interfaces as new brain output pathways. *J. Physiol.* **579**(Part 3), 613 (2007)
86. A.Y. Kaplan, S.L. Shishkin, I.P. Ganin, I.A. Basyul, A.Y. Zhigalov, Adapting the P300-based brain–computer interface for gaming: a review. *IEEE Trans. Comput. Intell. AI Games (Special Issue on Brain/Neuronal–Computer Games Interfaces and Interaction)* **5**(2), 141 (2013)

87. I.P. Ganin, S.P. Shishkin, A.G. Kochetkova, Y.A. Kaplan, Brain–computer interface on the base of “wave P300”: study of the effect of stimulus number in the sequence of their presentation. *Hum. Physiol.* **38**(2), 5 (2012)
88. G. Edlinger, C. Guger, Social environments, mixed communication and goal-oriented control application using a brain–computer interface, in *Proceedings of the International Conference UAHCI 2011*, Orlando. LNCS, vol. 6766 (2011), pp. 545–554
89. D.E. Newland, *An Introduction to Random Vibrations, Spectral and Wavelet Analysis* (Wiley, New York, 1993)
90. M. Holschneider, *Wavelets: An Analysis Tool* (Oxford University Press, Oxford, 1995)
91. C. Blatter, *Wavelets: A Primer* (A.K. Peters, Natick, 1998)
92. M. Farge, J.C. Hunt, J.C. Vassilicos, *Wavelets, Fractals and Fourier Transforms* (Oxford University Press, Oxford, 1995)
93. D.B. Percival, A.T. Walden, *Wavelet Methods for Time Series Analysis* (Cambridge University Press, Cambridge/New York, 2000)
94. B.P. van Milligen, E. Sánchez, T. Estrada, C. Hidalgo, B. Brãnas, B. Carreras, L. Garsia, Wavelet bicoherence: a new turbulence analysis tool. *Phys. Plasmas* **2**(8), 3017 (1995)

Chapter 2

Brief Tour of Wavelet Theory

Abstract In this chapter, the main definitions of wavelet theory are given. To explain the basic ideas of the continuous wavelet transform, we describe a transition from Fourier analysis to wavelets. Mother functions and numerical techniques for implementing the wavelet transform are described. The problem of visualising the results is considered. Finally, features of the discrete wavelet transform are discussed.

2.1 Introduction

As already mentioned in Chap. 1, wavelet analysis constitutes a powerful tool for studying the nonstationary dynamics of nonlinear systems. Although it arose not so long ago [1–3], researchers are already widely using wavelets in different areas of modern science. At present, there are many monographs and reviews devoted to wavelets and their applications in different areas of science and technology, e.g., in physics, biophysics, biology, medicine, economics, meteorology, etc. [4–11]. Thus, wavelet analysis has become an essential mathematical tool, providing effective solution for various problems related to the study and diagnostics of complex nonlinear processes, as well as digital signal processing. Over the past few decades, wavelet analysis has been widely considered as an interdisciplinary technique. One of the most impressive examples of such interdisciplinary cooperation is the application of wavelets to neurodynamics and neurophysiology, where wavelet analysis is increasingly used to examine neurophysiological data as well as to diagnose both normal and pathological processes in neural systems.

In the present chapter, we give a brief mathematical introduction to the wavelet theory. Here we try to explain the main principles of the wavelet transform (for both, the continuous and the discrete form), a method for numerical implementations of the transform, and the potential of wavelets for investigating complex signals associated with physiological processes. With a view to providing easier explanations, we restrict the discussion to simple mathematical examples and models.

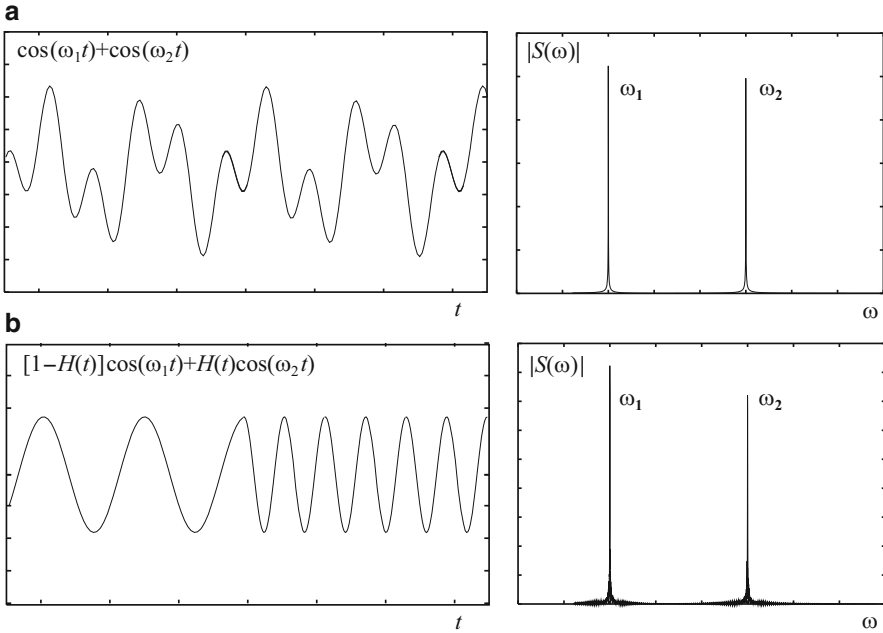


Fig. 2.1 Signals (2.1) and (2.2) and the corresponding Fourier spectra (a) and (b), respectively

2.2 From Fourier Analysis to Wavelets

We begin our considerations with the well-known Fourier transform [5, 12], which to some extent provides the background for the wavelet theory. As a first example, let us consider a signal representing the sum of two harmonic functions with different angular frequencies ω_1 and ω_2 , viz.,

$$x(t) = \cos(\omega_1 t) + \cos(\omega_2 t) . \quad (2.1)$$

The Fourier spectrum of this signal (see Fig. 2.1) is characterized by two sharp peaks corresponding to the frequencies¹ ω_1 and ω_2 . If both components exist permanently, the Fourier spectrum detects their frequencies, providing the researcher with full information about the signal under investigation.

Further, we consider another signal in which the harmonics appear and disappear with time:

$$x(t) = [1 - H(t)] \cos(\omega_1 t) + H(t) \cos(\omega_2 t) , \quad (2.2)$$

¹Note that hereafter we will consider only the positive range of frequencies, since the negative frequency region is the “mirror image” of the positive one and does not provide any additional useful information.

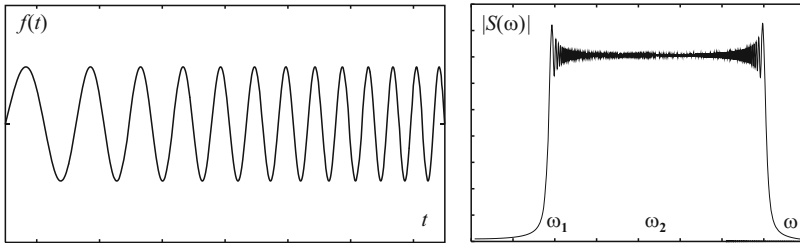


Fig. 2.2 Signal $x(t) = \cos[\omega(t)t]$ with linearly increasing frequency $\omega(t) = \omega_1 + a(\omega_2 - \omega_1)t$ and its Fourier spectrum. Having examined only the spectrum $|S(\omega)|$, one can suppose that the signal contains all frequencies in the range $[\omega_1, 2\omega_2 - \omega_1]$

where

$$H(t) = \begin{cases} 0, & t < 0, \\ 1/2, & t = 0, \\ 1, & t > 0 \end{cases}$$

is the Heaviside function.

Comparing the Fourier spectra² $|S(\omega)|$ of the considered signals (2.1) and (2.2), one can see that they are quite similar (see Fig. 2.1a, b). In other words, the Fourier spectrum is unable to provide enough information about frequencies that can be recognized in the analyzed signal at a given moment of time. The spectrum $|S(\omega)|$ of the signal does not allow one to say whether the signal is a superposition of two harmonic functions or whether it consists of two distinct components existing during clearly different time intervals. In other words, spectral analysis reveals the occurrence of different harmonic components, but it does not provide information related to their time localization. Nevertheless, the Fourier transform is a powerful tool for examining time series produced by systems with constant parameters. The spectral composition of such signals remains unchanged during the whole observation period. On the other hand, if the frequency components appear and disappear with time or if the frequency changes smoothly (see, e.g., Fig. 2.2), another spectral technique is required.

This circumstance is brought about by the core mechanism of the Fourier transform, which performs integration over the whole available signal. From the mathematical point of view, the time interval of integration is infinite³:

$$S(\omega) = \int_{-\infty}^{+\infty} x(t)e^{-i\omega t} dt, \tag{2.3}$$

²More precisely, amplitude spectra of the Fourier transform.

³Of course, in the case of experimental signals or data from numerical simulation, researchers deal with finite time series.

and each frequency component makes a contribution to the spectrum. Thus, using spectral analysis, we can detect characteristic rhythms in the signal, but we are unable to reveal their time localization. In other words, infinite oscillating harmonic functions sine and cosine used within the Fourier transform cannot be applied for localized spectral analysis [13, 14].

As a consequence, if we are going to localize the frequency components in time, we have to pass from integration over the infinite time interval $(-\infty, +\infty)$ to a certain time “window”⁴ with duration $2T$, viz., $[t_0 - T, t_0 + T]$, where t_0 is the time at which we are (locally) defining frequency components in the signal:

$$S(\omega, t_0) = \int_{t_0-T}^{t_0+T} x(t)e^{-i\omega t} dt . \quad (2.4)$$

To evaluate the dynamics of the frequency components over time, we must shift the observation window along the time series. In this case we obtain the instantaneous spectrum depending on t_0 . This spectrum changes as the observation window is moved along the time axis (see Fig. 2.3). Since t_0 is a variable in (2.4), the spectrum $S(\omega, t_0)$ should be considered as a two-dimensional function.

However, this approach with the rectangular window, known as the short-time Fourier transform, also has several limitations [15]. Indeed, the spectrum of a harmonic signal is the δ -function only in the case when the signal is infinite and the integration is performed over the whole infinite time interval. If the signal is finite (or if the integration is performed over a finite time interval), the spectral image of the signal is characterized by the finite width, and the shorter the duration of the signal, the broader its image in the Fourier space. So, using the short-time Fourier transform, one has to operate with the shortest length $2T$ of the observation window to localize the appearance (or disappearance) of the frequency components of the signal more precisely. On the other hand, however, this decreases the resolution of the method in the frequency domain. In other words, the more precisely we define the frequency of the spectral components, the less exactly we can localize this component in time, and vice versa.

If we wish to maintain the possibility of tracing the modifications of the signal with time, but also to reduce the lack of precision in frequency detection, the transform (2.4) needs to be modified. Note also that the short-time Fourier transform performed only once does not give full information about the signal under consideration. A set of transformations performed for the same signal and different widths $2T$ of the observation window is more informative. Indeed, the transformation with a narrow window may be used to localize modifications of the signal in the time domain, whereas the transformation with a broad window can provide information about the frequencies. Of course, this approach is inconvenient,

⁴Here, for simplicity, a rectangular window is used. In a more general case (known as the Gabor transform), we use a window function $g(t)$ that is localized in both the time and frequency domains.

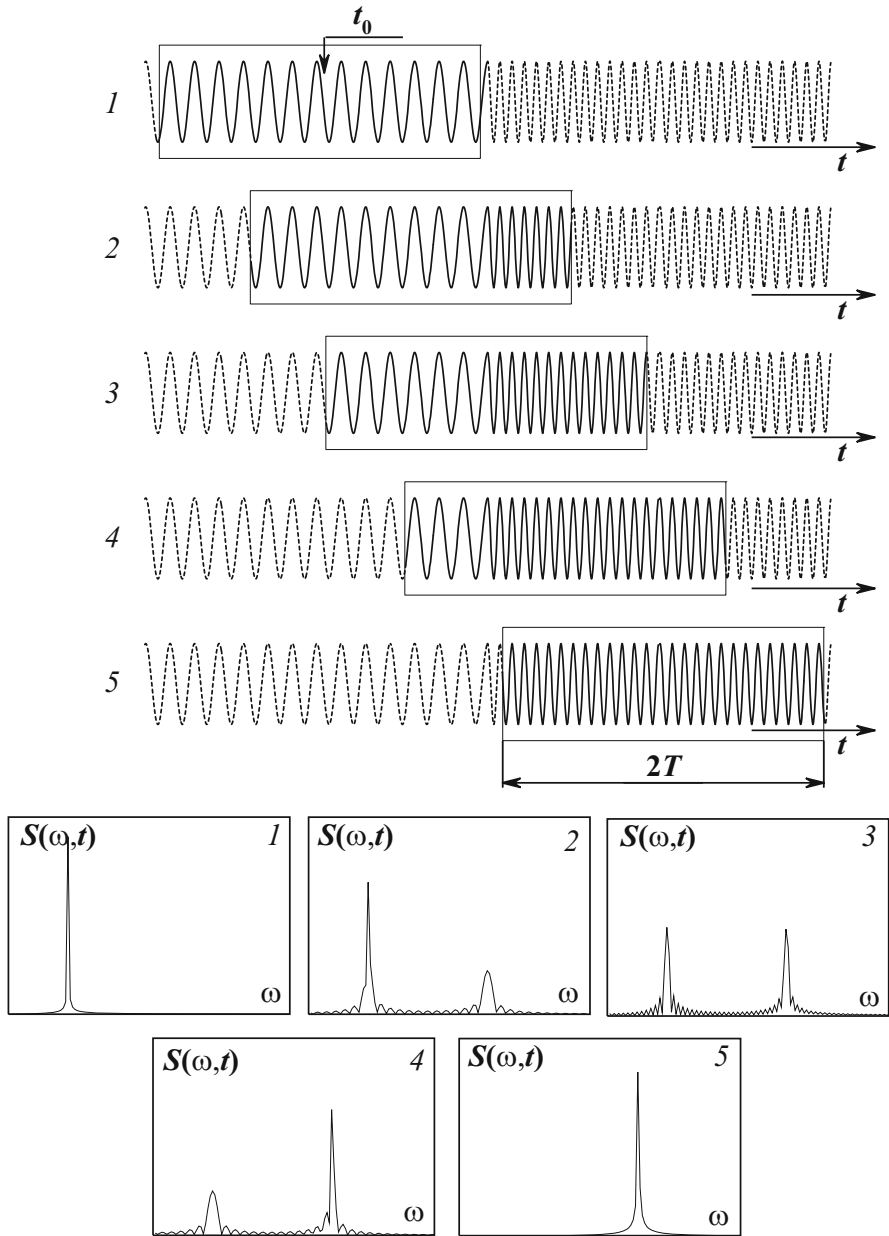
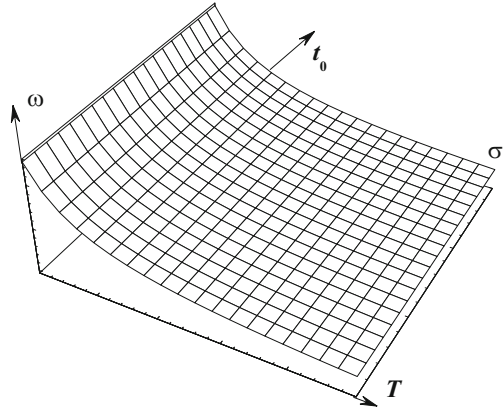


Fig. 2.3 Spectrum $S(\omega, t_0)$ of the signal (2.2) consisting of two consecutive parts of harmonic signals with the different frequencies ω_1 and ω_2 . Five locations of the observation window (rectangle) are shown. Shifting the window along the time series results in a transformation of the spectrum (see bottom of figure)

Fig. 2.4 Surface σ defined in the 3D space $\Omega = (\omega, t_0, T)$ (frequency–time–length of observation window)



since one has to consider a function $S(\omega, t_0, T)$ depending on three variables instead of two, ω and t_0 , and this requires representation in a space of at least four dimensions.

To reduce the number of the variables, one can link the frequency ω of the harmonic filling with the length of the observation window T , e.g., for each value of T one can use $\omega = \omega_n = 2\pi n/T$, where $n \in \mathbb{N}$ is the number of filling periods fitted into the window length. Then, the short-time Fourier transform may be written in the form

$$S(T, t_0) = \int_{t_0-T}^{t_0+T} x(t) \exp\left(-i\frac{2\pi n}{T}t\right) dt, \quad n > 0. \quad (2.5)$$

In fact, in the 3D space (ω, t_0, T) , where the function $S(\omega, t_0, T)$ is defined, a surface σ is introduced and further consideration is carried out at the points belonging to this surface. Obviously, some information is lost in this case, but the remaining data allow us to understand the particularity of the time series under study, since the surface σ covers both the frequency and the time domain (see Fig. 2.4).

Moreover, the length of observation window that is optimal to detect different frequency components of the signal is defined by the corresponding time scales. To pick out the low-frequency components, a longer part of the time series should be used than for analysis of high-frequency oscillations. The relation $\omega_n = 2\pi n/T$ provides a reasonable ratio between the analyzed frequency and the length of the observation window.

Transforming (2.5) for the time series $x(t) = \sin(\omega t)$ results in

$$S(T, t_0) = \frac{2T \sin(\omega T)}{\omega^2 T^2 - 4\pi^2 n^2} [\omega T \sin(\omega t_0) - i2\pi n \cos(\omega t_0)] \exp\left(-i2\pi n \frac{t_0}{T}\right). \quad (2.6)$$

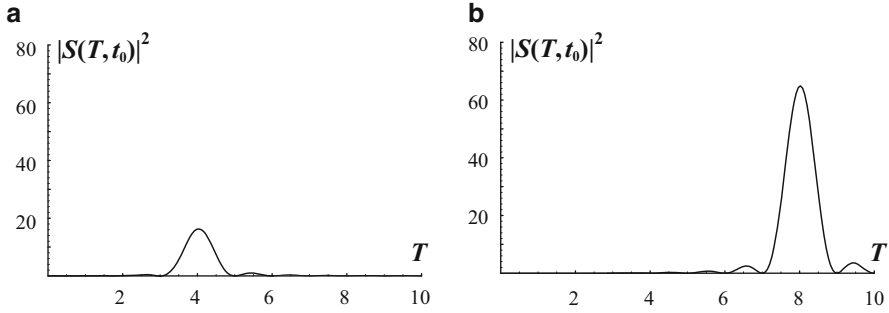


Fig. 2.5 Transformation (2.5) of the signal $x(t) = \sin(\omega t)$ ($\omega = \pi$, $t_0 = 0$) for (a) $n = 2$, (b) $n = 4$

As for the spectral analysis, the result of this transformation is characterized by both real and imagine parts. By analogy with the Fourier transform, there is a reason for considering the square of the absolute value of S , i.e.,

$$|S(T, t_0)|^2 = \frac{4T^2 \sin^2(\omega T)}{(\omega^2 T^2 - 4\pi^2 n^2)^2} \left[\omega^2 T^2 \sin^2(\omega t_0) + 4\pi^2 n^2 \cos^2(\omega t_0) \right]. \quad (2.7)$$

One can see that in this case the quantity of $|S(T, t_0)|^2$ takes its maximal value $4\pi^2 n^2 / \omega^2$ for $T_m = 2\pi n / \omega$ (Fig. 2.5), i.e., as for the Fourier transform, the transformation (2.5) allows detection of the time scale T_m (related to the frequency ω of the signal) corresponding to the main rhythm of the analyzed signal.

There are several important points to be made here. Firstly, for the same signal $x(t) = \sin(\omega t)$ and different values of the parameter n (which is determined as the number of periods of the harmonic function with the corresponding frequency that would fill the integration window of length $2T$), the values T_m corresponding to the maximal magnitude of $|S(T, t_0)|^2$ are different (see Fig. 2.5a, b). This becomes clear when one takes into account the fact that the quantity $|S(T, t_0)|^2$ reaches its maximum when the harmonic filling is characterized by the same frequency ω as the main frequency of the signal under study $x(t)$ (Fig. 2.6). In other words, the quantity $|S(T, t_0)|^2$ is maximal when $T = T_m = 2\pi n / \omega$, where ω is the frequency of the signal $x(t)$ under investigation. In fact, the same situation is also observed for Fourier analysis. Note that the value of T_m (when the quantity $|S(T, t_0)|^2$ becomes maximal) depends on the integration window and, in general, does not coincide with the corresponding time scale of the signal. Note also that the more periods are considered within the integration window, the more clearly the corresponding harmonic in $|S(T, t_0)|^2$ is defined (compare Fig. 2.5a, b). Nevertheless, as a consequence, the length of the integration window corresponding to the maximal value of $|S(T, t_0)|^2$ also increases with the growth of the period number n . As mentioned above, this results in the deterioration of the resolution of the transformation (2.5) in the time domain.

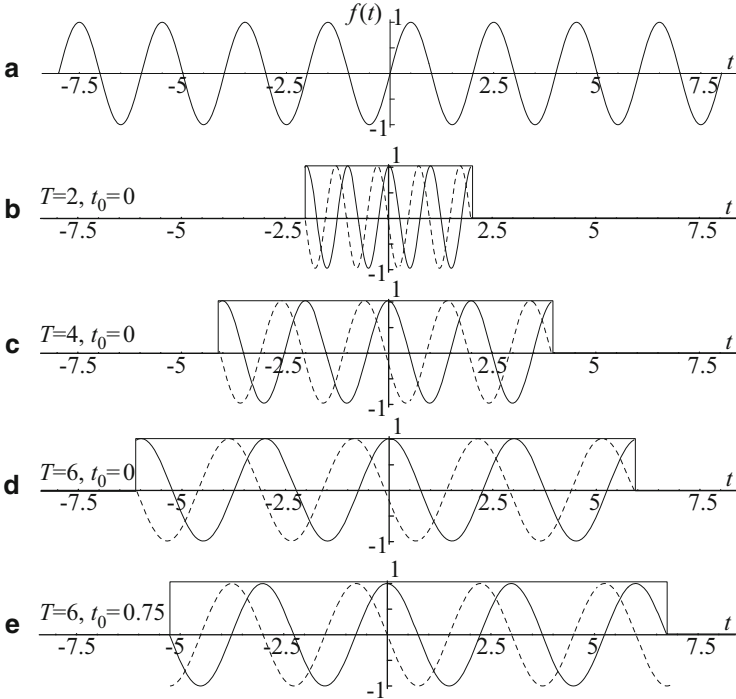
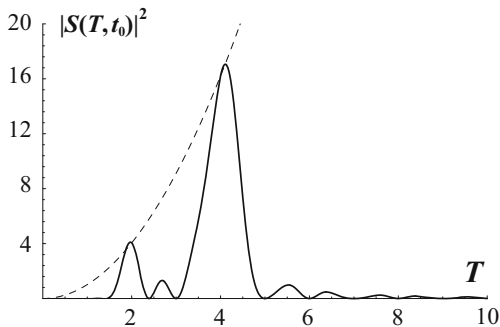


Fig. 2.6 (a) Time series $x(t) = \sin(\pi t)$ and several integration windows (b–d) with different lengths $2T$ and the analyzing harmonic filling $\exp(-i2\pi n/T)$. The real part of the filling is shown by the *solid line*, and the imaginary part by the *dashed line*. The maximal value of $|S(T, t_0)|^2$ is observed for $T = 4$ (c), when the frequency of the filling coincides with the signal frequency ω . (e) Shift of the integration window by the value determined by the second variable t_0

Secondly, one should note that the quantity $S(T, t_0)$ that results from the transformation (2.5) is a function of two variables, i.e., T and t_0 . The parameter T defines the time interval used for the integration and the frequency of the harmonic filling. So the frequency of the analyzing harmonic filling is closely related to the length $2T$ of the window. The variable t_0 determines the time moment associated with the transformation. In fact, it defines a shift of the integration window along the time axis. At the same time, the harmonic filling remains fixed when the integration window is shifted (see Fig. 2.6d, e). In other words, the phase of the filling changes continuously when the integration window is moved along the time axis. To avoid this problem the filling phase should be fixed relative to the observation window by means of the following modification of (2.5):

$$S(T, t_0) = \int_{t_0-T}^{t_0+T} x(t) \exp \left[-i \frac{2\pi n}{T} (t - t_0) \right] dt . \quad (2.8)$$

Fig. 2.7 Transform (2.8) for the signal $x(t) = \sin(\omega_1 t) + \sin(\omega_2 t)$, $\omega_1 = \pi$, $\omega_2 = 2\pi$. The dashed line corresponding to the function T^2 determines the maxima of the corresponding frequency components with unit amplitude



Clearly, changes in the phase of the harmonic filling do not influence the value of $|S(T, t_0)|^2$. For the harmonic signal $x(t) = \sin(\omega t)$, the transform (2.8) gives

$$S(T, t_0) = \frac{2T \sin(\omega T)}{\omega^2 T^2 - 4\pi^2 n^2} \left[\omega T \sin(\omega t_0) - i2\pi n \cos(\omega t_0) \right]. \quad (2.9)$$

It is easy to see that the difference between (2.6) and (2.9) consists only of the factor $\exp(-i2\pi n t_0 / T)$.

Thirdly, one has to take into account the fact that different frequency components of the signal with equal amplitude are detected by the transformation (2.8) in different ways. The corresponding maxima are characterized by different magnitudes. The squares of these maxima are related to each other by

$$\frac{|S_1|^2}{|S_2|^2} = \left(\frac{\omega_2}{\omega_1} \right)^2, \quad (2.10)$$

which may be obtained directly from (2.7). In other words, the lower the frequency, the larger its contribution to the signal spectrum, under the condition that the amplitudes of the considered spectral components are equal (see Fig. 2.7). This means that, if there are two or more components in the signal whose frequencies differ sufficiently from each other, the components with higher frequencies may be missed.

Equation (2.8) may be written in the more general form

$$S(T, t_0) = \int_{-\infty}^{+\infty} x(t) \psi^* \left(\frac{t - t_0}{T} \right) dt, \quad (2.11)$$

where $\psi(\xi)$ is the analyzing function (see Fig. 2.8)

$$\psi(\xi) = [H(\xi + 1) - H(\xi - 1)] e^{i2\pi\xi}, \quad (2.12)$$

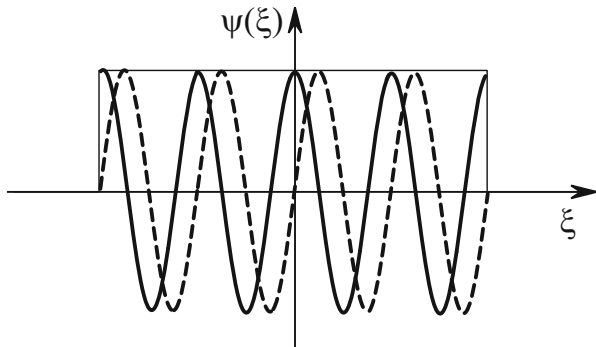


Fig. 2.8 The real (*solid line*) and imaginary (*dashed line*) parts of the sine wavelet (2.12)

and the star hereafter indicates complex conjugation. In fact, (2.11) may already be considered (with some corrections) as the wavelet transform. So we have gone in stages from the Fourier transform to the wavelet analysis.

The transformation (2.11) consists in the expansion and shift of the function $\psi(\xi)$ as described above and shown in Fig. 2.6. In this case the quantity T describes the expansion of the analysing function $\psi(\xi)$, whereas the variable t_0 corresponds to the shift of $\psi(\xi)$ along the time axis. The function $\psi(\xi)$ is known as the mother wavelet, and all other functions $\psi((t - t_0)/T)$ used for other time scales are obtained from it by expansions and shifts. For convenience, a normalization condition is imposed on the mother wavelet:

$$\|\psi\|_{L^2} = \left[\int_{-\infty}^{+\infty} \psi(\xi)\psi^*(\xi)d\xi \right]^{1/2} = 1. \quad (2.13)$$

Taking into account the requirement (2.13), the mother wavelet (2.12), denoted by ψ_0 , should be written in the form

$$\psi_0(\xi) = \frac{H(\xi + 1) - H(\xi - 1)}{\sqrt{2}} e^{i2\pi\xi}. \quad (2.14)$$

The wavelet functions $\psi_0((t - t_0)/T)$ obtained for other time scales by means of the expansion and shift of the mother wavelet ψ_0 do not satisfy the requirement (2.13). To satisfy the normalization condition for every time scale T , a normalization factor depending on the time scale T should be introduced. Then the function $\psi_0(\xi)$ with normalization coefficient $T^{-1/2}$ should be used instead of $\psi(\xi)$ in (2.11):

$$\psi_{T,t_0}(t) = \frac{1}{\sqrt{T}} \psi_0\left(\frac{t - t_0}{T}\right). \quad (2.15)$$

Finally, (2.11) takes the form

$$S(T, t_0) = \frac{1}{\sqrt{T}} \int_{-\infty}^{+\infty} x(t) \psi_0^* \left(\frac{t - t_0}{T} \right) dt . \quad (2.16)$$

Equation (2.16) is the standard form of the continuous wavelet transform introduced in the scientific literature [7, 12, 14, 16–20]. At the end of this section we need also to compare the notation in this section with the one used traditionally in the literature. For the continuous wavelet transform, the time scale is traditionally denoted by s (so in the above consideration, $T \equiv s$), whereas for the wavelet surface being result of the transformation, the symbol W is used, i.e.,

$$W(s, t_0) = \frac{1}{\sqrt{s}} \int_{-\infty}^{+\infty} x(t) \psi_0^* \left(\frac{t - t_0}{s} \right) dt . \quad (2.17)$$

Often, the notion of “frequency” f is considered instead of the “time scale” s since it is more suitable in many studies. In fact, the frequency f used in the wavelet analysis carries the same meaning as the frequency of the Fourier transform. In particular, this approach is commonly used in neuroscience and neurophysiology. At the same time, researchers have to be very careful using the term “frequency” for wavelets, since in general the relationship between the time scale s of the wavelet analysis and the frequency f of the Fourier transform differs from the equation $f = 1/s$, which becomes correct only for special choices of the mother wavelet and its parameters.

So we have moved gradually from the Fourier transform to the wavelet analysis, aiming to expose the underlying ideas of wavelets. By analogy with the Fourier transform, the wavelet analysis expands the given signal $x(t)$ in terms of a certain functional basis. At the same time, the functional bases used for the Fourier and wavelet transforms are not the same. While the infinite-in-time harmonic functions sine and cosine are used in classical spectral analysis, functions ψ_{s,t_0} that are well-localized in both time and frequency (obtained by expansion and shift of the mother wavelet ψ_0) are used in wavelet analysis. These localized functions (wavelets) allow us to examine processes with statistical characteristics that vary in time (or in space), and provide a two-dimensional representation of the signal $x(t)$ when the time and frequency are interpreted as independent variables.

We shall refer to the mother wavelet (2.14) obtained by the gradual transition from the Fourier transform shown in Fig. 2.8 as the sine wavelet. The sine wavelet is not widely used in practical applications (in particular, due to the low level of localization in the frequency domain), but it brings out the main ideas and methodology of continuous wavelet analysis. An important particularity of the wavelet transform is the possibility of using an arbitrary function satisfying certain conditions (which will be discussed in Sect. 2.3) as the mother wavelet.

Finally, note that, besides the continuous wavelet transform, the discrete wavelet transform is also used in many applied problems. General information concerning these two counterparts of the wavelet transform is given below.

2.3 Continuous Wavelet Transform

2.3.1 Main Definitions: Properties of the Continuous Wavelet Transform

In the following, we restrict the class of mother functions to $f \in L^2(\mathbb{R})$. The function space L^2 contains signals with limited energy, i.e., with finite norm $\|f\|_{L^2}$. The continuous wavelet transform (CWT) is performed by convolution of the examined function $f(t)$ with the two parameter wavelet function $\psi_{s,t_0}(t)$, viz.,

$$W(s, t_0) = \int_{-\infty}^{+\infty} f(t) \psi_{s,t_0}^*(t) dt . \quad (2.18)$$

The wavelet function is obtained from the mother wavelet $\psi_0(t)$ by means of an expansion and a shift:

$$\psi_{s,t_0}(t) = \frac{1}{\sqrt{s}} \psi_0\left(\frac{t-t_0}{s}\right) . \quad (2.19)$$

The parameter s , known as the time scale of the wavelet transform ($s \in \mathbb{R}^+$), determines the width of the wavelet in the time domain, whereas the parameter $t_0 \in \mathbb{R}$ specifies the wavelet location on the time axis. The factor $1/\sqrt{s}$ in (2.19) provides the constant unit norm of the wavelets in the function space $L^2(\mathbb{R})$, i.e.,

$$\|\psi_{s,t_0}\|_{L^2} = \|\psi_0\|_{L^2} = 1 , \quad (2.20)$$

where the norm in the space $L^2(\mathbb{R})$ is defined by

$$\|f\|_{L^2} = \left[\int_{-\infty}^{+\infty} |f(x)|^2 dx \right]^{1/2} . \quad (2.21)$$

Below, we will use the following notation for the wavelet functions:

- ψ_0 for the mother wavelet.
- ψ_{s,t_0} for the wavelet function obtained from the mother wavelet ψ_0 by (2.19).

- ψ for the wavelet function obtained from the mother wavelet ψ_0 , for which the normalizing factor is not yet defined, i.e., $\psi = a\psi_0$, where a is unknown.
- Ψ for the wavelet function used in the calculation of the wavelet surface using the fast Fourier transform.

By the Parseval formula, the condition (2.20) implies that

$$\frac{1}{2\pi} \int_{-\infty}^{+\infty} |\hat{\psi}_0(\omega)|^2 d\omega = 1, \quad (2.22)$$

where $\hat{\psi}_0(\omega)$ is the Fourier image of the mother wavelet function

$$\hat{\psi}_0(\omega) = \frac{1}{\sqrt{2\pi}} \int_{-\infty}^{\infty} \psi_0(t) e^{-i\omega t} dt. \quad (2.23)$$

Analogously,

$$\frac{1}{2\pi} \int_{-\infty}^{+\infty} |\hat{\psi}_{s,t_0}(\omega)|^2 d\omega = 1, \quad (2.24)$$

where $\hat{\psi}_{s,t_0}(\omega)$ is the Fourier image of the wavelet function $\psi_{s,t_0}(t)$.

So the continuous wavelet transform maps the space of one-dimensional functions into the two-dimensional (in general, complex) space.

$$W : L^2(\mathbb{R}) \rightarrow \mathbb{C}(\mathbb{R} \times \mathbb{R}^+),$$

and as a consequence, information contained in the wavelet coefficients is abundant. This fact results, e.g., in the presence of a correlation in the wavelet spectrum of a random signal (noise), although this correlation is not actually present in the signal (so this is a consequence of the wavelet transform). This may be considered as a significant disadvantage of the wavelet transform that must be taken into account when wavelet spectra are interpreted.

The mother wavelet can be chosen rather arbitrarily, e.g., as in Sect. 2.2, but it must fulfill several requirements. First of all, we should mention the *boundedness condition*

$$\int_{-\infty}^{+\infty} |\psi_0(t)|^2 dt < \infty. \quad (2.25)$$

Then there is the *localization condition*, according to which the mother wavelet function ψ_0 must be localized in both the time and frequency domains. This condition is satisfied if the function ψ_0 decreases rapidly and is quite regular. As an estimate for good localization and boundedness, the conditions $|\psi_0(t)| < 1/(1 + |t|^n)$ or $|\hat{\psi}_0(\omega)| < 1/(1 + |\omega - \omega_0|^n)$ may be used, where ω_0 is the dominant frequency of the wavelet and the parameter n should be as large as possible [21].

According to the *admissibility condition*, the Fourier image $\hat{\psi}_0(\omega)$ of the mother wavelet $\psi_0(t)$ must obey the condition

$$C_\psi = \int_{-\infty}^{+\infty} \frac{|\hat{\psi}_0(\omega)|^2}{\omega} d\omega < \infty . \quad (2.26)$$

Since in practice only positive frequencies are usually considered, (2.26) can often be replaced by

$$\int_0^{+\infty} \frac{|\hat{\psi}_0(\omega)|^2}{\omega} d\omega = \int_0^{+\infty} \frac{|\hat{\psi}_0(-\omega)|^2}{\omega} d\omega < \infty . \quad (2.27)$$

Note also that, for practical purposes, the condition (2.26) is analogous to the condition of zero mean as a consequence of (2.22):

$$\int_{-\infty}^{+\infty} \psi_0(t) dt = 0 , \quad (2.28)$$

or

$$\hat{\psi}_0(0) = 0 , \quad (2.29)$$

whence the mother wavelet $\psi_0(t)$ must be an oscillatory function.

Sometimes this requirement may be important not only for the zero moment (2.28), but also for the m first moments, i.e.,

$$\int_{-\infty}^{+\infty} t^k \psi_0(t) dt = 0 , \quad k = 0, 1, \dots, m . \quad (2.30)$$

Such m th order wavelets may be used to analyse small-scale fluctuations and high order features by ignoring quite regular (polynomial) components. Indeed, expanding the function $f(t)$ in (2.18) in a Taylor series at t_0 , one obtains

$$\begin{aligned}
W(s, t_0) = \frac{1}{\sqrt{s}} & \left[f(t_0) \int_{-\infty}^{+\infty} \psi_0^* \left(\frac{t-t_0}{s} \right) dt \right. \\
& + f'(t_0) \int_{-\infty}^{+\infty} (t-t_0) \psi_0^* \left(\frac{t-t_0}{s} \right) dt \\
& + \dots + \frac{f^{(n)}(t_0)}{n!} \int_{-\infty}^{+\infty} (t-t_0)^n \psi_0^* \left(\frac{t-t_0}{s} \right) dt + \dots \left. \right].
\end{aligned} \tag{2.31}$$

By (2.30), the first m terms of (2.31) vanish, and as a consequence, they do not contribute to $W(s, t_0)$. Note that it may be enough for practical purposes if (2.30) is approximately satisfied.

If the admissibility condition (2.26) is satisfied, *the inverse wavelet transform* exists (see, e.g., [22] for details):

$$f(t) = \frac{1}{C_\psi} \int_0^{+\infty} \frac{ds}{s^2 \sqrt{s}} \int_{-\infty}^{+\infty} \psi_0 \left(\frac{t-t_0}{s} \right) W(s, t_0) dt_0. \tag{2.32}$$

By analogy with the Fourier power spectrum $P(\omega) = |\hat{f}(\omega)|^2$, the distribution of instantaneous energy over the time scales of the wavelet transform can be introduced by

$$E(s, t_0) = |W(s, t_0)|^2, \tag{2.33}$$

along with the time-averaged integral wavelet spectrum or *scalogram*

$$\langle E(s) \rangle = \frac{1}{T} \int_0^T |W(s, t_0)|^2 dt_0. \tag{2.34}$$

Since the distribution of the wavelet energy is related to the Fourier power spectrum [16] by

$$\langle E(s) \rangle \sim s \int P(\omega) |\hat{\psi}_0(s\omega)|^2 d\omega, \tag{2.35}$$

this means that $\langle E(s) \rangle$ is a smoothed Fourier power spectrum, defined by the Fourier image $\hat{\psi}_0$ of the mother wavelet ψ_0 .

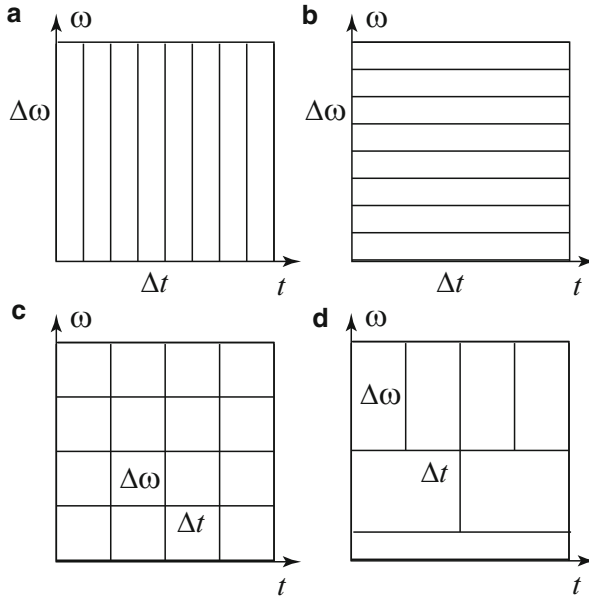
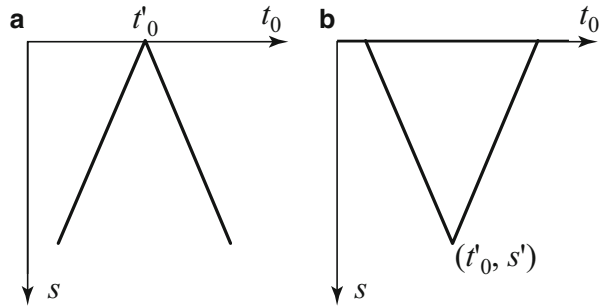


Fig. 2.9 Time-and-frequency localization in the space time t –frequency ω for different transformations. (a) discrete sample (Shannon transform), (b) Fourier transform, (c) short-time Fourier transform, (d) continuous wavelet transform

One important point is the ability of the wavelets to pick out information concerning local properties of a signal. As discussed above (Sect. 2.2), in order to obtain precise information about high-frequency components with good temporal resolution, rather short time intervals must be used. However, extracting information about low-frequency spectral components requires relatively long fragments of time series.

Figure 2.9 illustrates the ability of different transformations to extract localized information. Figure 2.9a shows a segmentation of the time t –frequency ω space for discrete samples of the signal values, when the δ -function plays the role of the basis function (Shannon transform). One can see that this transform provides excellent time resolution, but no frequency information at all can be extracted. In contrast, the Fourier transform is characterized by perfect frequency resolution, but there is no localization in time (see Fig. 2.9b). Figure 2.9c corresponds to the short-time Fourier transform, where the resolution on short and long time scales is determined by the length of the integration window. In the case of the wavelet transform (Fig. 2.9d), the time resolution determined by the width of the wavelet $\psi(t/s)$ decreases with the growth of the time scale s , whereas the frequency resolution determined by the width of the Fourier image of the wavelet $\hat{\psi}(s\omega)$ increases. It provides good time localization for small scales and good frequency resolution for large scales (see Fig. 2.9d).

Fig. 2.10 Influence angle of the wavelet transform on the plane (t_0, s)



So the *main feature* of the wavelet transform which is extremely important when analyzing complex nonstationary processes is the ability to respect the locality of the signal representation, and as a consequence, the ability to reconstruct the signal locally. Importantly, the continuous wavelet transform allows us to determine the contribution of a certain scale at a given moment of time. It also provides the possibility to reconstruct only a part of the signal. In fact, there is a relationship between local properties of the signal and local behavior of the wavelet surface related to this signal. This means that, in order to reconstruct a part of the signal, one has to use the values of the wavelet surface $W(s, t)$ belonging to a certain region called the influence angle (see Fig. 2.10a).

When the wavelet function ψ_0 is well localized in the time interval ΔT for the time scale $s = 1$, the values of the wavelet spectrum corresponding to the time t'_0 are contained in the influence cone bounded by the straight lines $s = 2(t'_0 - t_0)/\Delta T$ and $s = 2(t_0 - t'_0)/\Delta T$. At the same time, the value $W(s', t'_0)$ at point (t'_0, s') depends on the fragment of the time series contained in the same influence cone (see Fig. 2.10b). The longer the analyzed time scale s , the longer the fragment of time series, i.e., high-frequency (or, what comes to the same, short-scale) information is determined by short fragments of the time series, whereas longer fragments of time series should be used for low-frequency components. If the wavelet function ψ_0 provides good localization in the Fourier space, i.e., the Fourier image $\hat{\psi}_0$ of the mother function is concentrated in the frequency band $\Delta\Omega$ around the dominant frequency ω_0 for time scale $s = 1$, the values of the wavelet transform corresponding to the frequency ω' are located in the range of time scales $s \in [(\omega_0 - \Delta\Omega/2)/\omega', (\omega_0 + \Delta\Omega/2)/\omega']$. If $f(t)$ is a locally smooth function, the corresponding values of the wavelet surface are fairly small. When $f(t)$ has a singularity, the magnitude of the wavelet surface increases in its vicinity. Note also that, if the wavelet surface contains artifacts at certain points, they are influenced on the reconstructed signal only locally, in the vicinity of these positions, whereas the inverse Fourier transform spreads these errors over the whole reconstructed signal.

2.3.2 Mother Wavelets

One important problem when using the wavelet transform is the choice of appropriate mother wavelet ψ_0 for analysis of the signal. This choice depends on both the aim of the study and the characteristics of the analyzed signal. Thus, to detect phases of an oscillatory process by means of the wavelet transform, *complex wavelets* are used. In contrast, to reveal self-similarity on different time scales, there is a good reason to use *real wavelets*. Existing traditions as well as intuition and the experience of the researcher may also play an important role when choosing the mother wavelet. This section discusses the main wavelets used in practical applications.

The actual choice of mother wavelet depends on what information is to be extracted from the analyzed signal. Each wavelet function ψ_0 is characterized by different properties that allow us to reveal distinct features of the signal $f(t)$. Figure 2.11 shows the most commonly used wavelets $\psi_0(\eta)$, together with their Fourier images $\hat{\psi}_0(\eta)$. Important characteristics of these wavelets (discussed in detail later) are given in Table 2.1.

One of the most popular complex wavelets used to reveal the time–frequency structure of signals is the Morlet wavelet [3] (see Fig. 2.11)

$$\psi_0(\eta) = \pi^{-1/4} \left(e^{i\omega_0\eta} - e^{-\omega_0^2/2} \right) e^{-\eta^2/2}, \quad (2.36)$$

where ω_0 is the wavelet parameter (often taken as $\omega_0 \sim 2\pi$). The second term in the brackets performs a correction of the wavelet transform for signals with nonzero mean values. When $\omega_0 \gg 0$, the term $e^{-\omega_0^2/2}$ may be neglected, whereas the central frequency (the global maximum of the Fourier image of the wavelet) is conventionally taken to be ω_0 .

In fact, the Morlet wavelet is an analog of the sine wavelet described in Sect. 2.2. Indeed, the Morlet wavelet is a plane wave modulated by a Gaussian function, whereas the sine wavelet is the same plane wave modulated by a rectangular impulse. The functional set obtained on the basis of the Morlet wavelet is well localized in both the time and frequency domains. With growing value of the parameter ω_0 , the resolution in Fourier space increases, whereas the time localization is reduced. This is easily seen from the comparison of Fourier images of the Morlet wavelet obtained for $\omega_0 = 2\pi$ and $\omega_0 = 16$ (see Fig. 2.11a, b). For $\omega_0 = 16$, the Fourier image is narrower, attesting to the better resolution in the frequency domain. However, the time resolution decreases for $\omega_0 = 16$.

Another example of a complex wavelet is the Paul wavelet [23] (Fig. 2.11d)

$$\psi_0(\eta) = \frac{2^m i^m m!}{\sqrt{\pi(2m!)}} (1 - i\eta)^{-(m+1)}, \quad (2.37)$$

where m is the wavelet order corresponding to the number of zero moments.

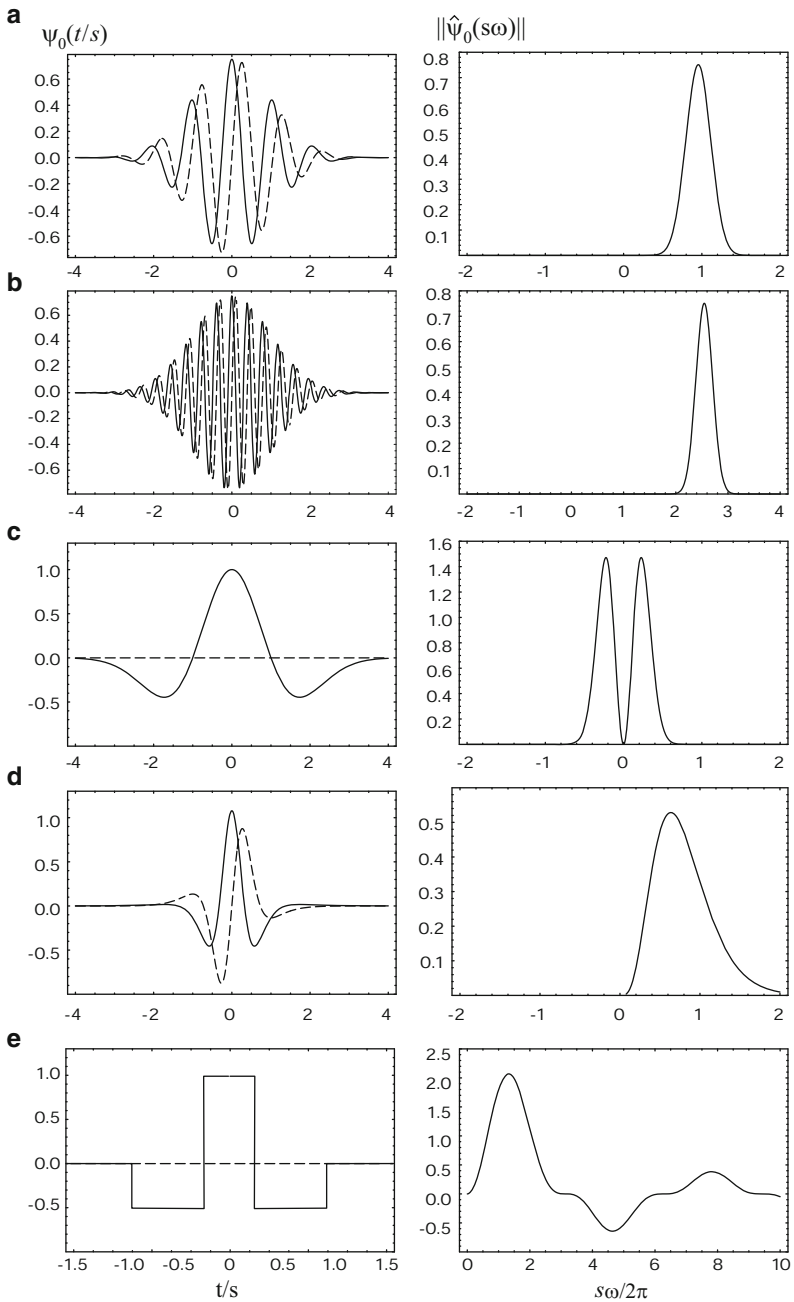


Fig. 2.11 Most commonly used wavelets (*left*) and their Fourier images (*right*). The real part of each wavelet function is shown by a *solid line*, while the *dashed line* illustrates the imaginary part. (a) Morlet wavelet with main frequency $\omega_0 = 2\pi$. (b) Morlet wavelet with $\omega_0 = 16$. (c) MHAT wavelet (DOG wavelet with $m = 2$). (d) Paul wavelet with $m = 4$. (e) FHAT wavelet

Table 2.1 Commonly used wavelets and their main properties. Here $H(x)$ is the Heaviside function, f is the frequency of the Fourier transform, f_s is the frequency of the wavelet transform ($f_s = 1/s$), and τ_s is the width of the region of boundary effects

Wavelet $\psi_0(\eta)$	$\hat{\psi}_0(s\omega)$	τ_s	f/f_s
Morlet $\pi^{-1/4} e^{i\omega_0 \eta} e^{-\eta^2/2}$	$\pi^{-1/4} H(\omega) e^{(s\omega - \omega_0)^2/2}$	$\sqrt{2}s$	$\frac{\omega_0 + \sqrt{2 + \omega_0^2}}{4\pi}$
Paul $\frac{2^m i^m m!}{\sqrt{\pi} (2m!)} (1 - i\eta)^{-(m+1)}$	$\frac{2^m}{\sqrt{m} (2m-1)} H(\omega) (s\omega)^m e^{-s\omega}$	$s/\sqrt{2}$	$\frac{2m+1}{4\pi}$
DOG $\frac{(-1)^{m+1}}{\left[\Gamma\left(m + \frac{1}{2}\right)\right]^{1/2}} \frac{d^m}{d\eta^m} e^{-\eta^2/2}$	$\frac{i^m}{\left[\Gamma\left(m + \frac{1}{2}\right)\right]^{1/2}} (s\omega)^m e^{-(s\omega)^2/2}$	$\sqrt{2}s$	$\frac{\sqrt{m+1/2}}{2\pi}$
FHAT $\begin{cases} 1, & \eta < 1/3, \\ -1/2, & 1/3 < \eta \leq 1, \\ 0, & \eta > 1 \end{cases}$	$3H(s\omega) \left[\frac{\sin(s\omega)}{s\omega} - \frac{\sin(3s\omega)}{3s\omega} \right]$	$\sqrt{2}s$	$3/4$

Among real wavelet functions, the DOG wavelets are widely used (DOG stands for difference of Gaussians) [24]. DOG wavelets are constructed on the basis of derivatives of the Gaussian function (see Fig. 2.11c):

$$\psi_0(\eta) = \frac{(-1)^{m+1}}{\left[\Gamma\left(m + \frac{1}{2}\right)^{0.5}\right]} \frac{d^m}{d\eta^m} \exp\left(\frac{-\eta^2}{2}\right). \quad (2.38)$$

The mother wavelet corresponding to $m = 1$ is called the WAVE wavelet, viz.,

$$\psi_0(\eta) = \eta e^{-\eta^2/2}, \quad (2.39)$$

while $m = 2$ corresponds to the MHAT (Mexican hat) wavelet, viz.,

$$\psi_0(\eta) = (1 - \eta^2) e^{-\eta^2/2}. \quad (2.40)$$

Another real mother wavelet is the discrete FHAT (French hat) wavelet shown in Fig. 2.11e, viz.,

$$\psi_0(\eta) = \begin{cases} 1, & |\eta| < 1/3, \\ -1/2, & 1/3 < |\eta| \leq 1, \\ 0, & |\eta| > 1. \end{cases} \quad (2.41)$$

The simplest discrete wavelet used in many technical applications is the Haar wavelet [25]

$$\psi_0(\eta) = \begin{cases} 1, & 0 \leq \eta < 1/2, \\ -1, & 1/2 \leq \eta < 1, \\ 0, & \eta < 0, \eta \geq 1, \end{cases} \quad (2.42)$$

which will be discussed in detail in Sect. 2.4 on the discrete wavelet transform.

The set of mother wavelets is not restricted to the functions considered here. Other functions are also applied in practice and successfully used in various areas of research. The reader can find additional examples of the mother wavelets as well as ways to construct them, e.g., in [16, 26–30]. In the following chapters of this book, we shall discuss examples of wavelets constructed especially to analyze neurophysiological signals.

2.3.3 Numerical Implementation of the Continuous Wavelet Transform

Since the analytical form of wavelet spectra can be obtained only for the simplest cases such as, e.g., $f(t) = a \sin(\omega t)$, analysis of experimental time requires numerical implementation of the wavelet transform.

When we carry out numerical analysis, we are dealing with time series of a variable $x(t)$ whose values are known only at specified time moments. Typically, the values of $x(t)$ are recorded with equal time span.⁵ Therefore, we shall further consider a time series $\{x_n\}$, where each value x_n is acquired with an equal time interval h , i.e., $x_n = x(hn)$, $n = 0, \dots, N - 1$, where N is the number data points in the time series.

The continuous wavelet transform of the sequence $\{x_n\}$ is defined as the discrete counterpart of the convolution of the analyzed signal and the basis function $\psi(\eta)$ (2.18) which is normalized by the corresponding time scale s and shifted along the time axis by the interval nh . One can then write

$$W(n, s) = \sum_{n'=0}^{N-1} x_{n'} \psi^* \left(\frac{(n' - n)h}{s} \right), \quad (2.43)$$

⁵This is the most typical case in experimental studies. However, data can be acquired in such a way that each data point is related to an arbitrary instant of time. This happens, e.g., for point processes represented by RR intervals of the electrocardiogram [31, 32]. In such a case, the relevant algorithms must be modified [31, 32].

where the normalization coefficient for the discrete analogue of the continuous wavelet transform will be discussed later (see (2.59)). Changing the scale coefficient and the time shift nh , one can localize the dynamics of any particularities of the process $\{x\}$ in the time domain s .

2.3.3.1 Effective Numerical Method for the Continuous Wavelet Transform

Direct calculation of the wavelet transform using (2.43) is not optimal. The simplest and most universal way to optimize the numerical procedure of the wavelet transform is to consider the local nature of the wavelet function (see Fig. 2.10). Indeed, the wavelet function ψ_{s,t_0} is localized within the time interval $t \in [t_0 - T(s), t_0 + T(s)]$. As the function ψ_{s,t_0} is normalized for different time scales, the time localization interval $2T(s)$ depends on the time scale s . Since the wavelet function is supposed to be close to zero with high precision outside this interval, (2.18) may be replaced by

$$W(s, t_0) \simeq \int_{t_0 - T(s)}^{t_0 + T(s)} f(t) \psi_{s,t_0}^*(t) dt . \quad (2.44)$$

The quantity $T(s)$, which also depends on the selected mother wavelet, can be found experimentally for the preassigned precision of numerical calculations. Of course, the higher the value of T , the more accurate the result of the wavelet transform. For the Morlet wavelet, for instance, the optimal length of the time interval related to a reasonable compromise between time duration and accuracy of the performed calculations is estimated as $T(s) = 4s$.

In the discrete form, (2.44) should be rewritten as

$$W(n, s) = \sum_{n' = n - [T(s)/h]}^{n + [T(s)/h]} x_{n'} \psi^* \left(\frac{(n' - n)h}{s} \right) . \quad (2.45)$$

One can see that, for arbitrary values of the analyzed discrete sequence $\{x_n\}$, the values of the wavelet function are invariable for all time moments n , and as a consequence, they can be calculated once and for all in the interval $[-T(s), T(s)]$ with time span h as

$$y_{sn} = \psi^* \left(\frac{nh}{s} \right) , \quad (2.46)$$

keeping this thereafter as the matrix.

So the problem of calculating the wavelet transform is reduced to multiplying two matrixes, viz.,

$$W(n, s) = \sum_{i=-[T(s)/h]}^{[T(s)/h]} x_{n+i} y_{si}, \quad (2.47)$$

which may be done rather quickly.

To perform direct numerical realization of the wavelet transform using (2.43), the sum should be estimated N times for every time scale s , where N is the number of data points. Assuming that $\{x_n\}$ is a complex sequence and the wavelet function has already been calculated in the whole region of possible values, $M = \mathcal{L} \times 8N^2 + O(N)$ arithmetic iterations must be carried out, where \mathcal{L} is the number of time scales s for which the wavelet transformation is applied. Indeed, according to (2.43), N complex multiplications (6 arithmetic operations) and $N - 1$ complex additions (2 arithmetic operations) must be performed at each point of the discrete space with dimension $N \times \mathcal{L}$.

Using (2.47) considerably reduces the required operations, since only

$$M = 8N \times \sum_{i=[s_{\min}/\Delta s]}^{[s_{\max}/\Delta s]} [T(i\Delta s/h)] + O(N) \quad (2.48)$$

operations must be carried out, where s_{\min} and s_{\max} are the minimal and maximal boundaries of the analyzed time scales, and Δs is the discretization step. If $T(s)/h \ll N$, a considerable efficiency gain is obtained. For the Morlet wavelet, the number of required iterations is estimated as

$$M = 64N \times \sum_{i=[s_{\min}/\Delta s]}^{[s_{\max}/\Delta s]} (i\Delta s/h) + O(N). \quad (2.49)$$

2.3.3.2 Numerical Method for the Continuous Wavelet Transform Based on the Fast Fourier Transform

Considering the Fourier images for the initial signal \hat{x}_k and wavelet $\hat{\psi}$ also reduces the number of required operations [8, 16]. By the convolution theorem, one can simultaneously compute all values of $W(n, s)$ ($n = 0, \dots, N - 1$) in the Fourier space for the fixed time scale s using the discrete Fourier transform.

For the sequence $\{x_n\}$, the discrete Fourier transform is estimated as follows

$$\hat{x}_k = \sum_{n=0}^{N-1} x_n e^{-2\pi i k n / N}, \quad (2.50)$$

where $k/(Nh) \in (0, \dots, (N - 1)/(Nh))$ forms the frequency set of initial signal x_n given by the sequence consisting of N points with the time step h .

With a known Fourier image $\hat{\psi}_0(\omega)$ of the mother wavelet $\psi_0(t)$ (see (2.23)), one can easily compute the Fourier image of the function $\psi(t/s)$:

$$\begin{cases} \psi(t) \rightarrow \hat{\psi}(\omega) , \\ \psi(t/s) \rightarrow \hat{\psi}(s\omega) , \end{cases} \quad (2.51)$$

i.e., renormalization of the wavelet function in the Fourier space is taken into account by multiplying the frequency by the scale factor s .

Similarly, using the discrete Fourier transform⁶ one can obtain

$$\begin{aligned} \hat{\Psi}(\omega_k) &= \sum_{n=0}^{N-1} \Psi(nh) e^{-i\omega_k nh} , \\ \hat{\Psi}(s\omega_k) &= \sum_{n=0}^{N-1} \Psi(nh/s) e^{-is\omega_k nh/s} , \end{aligned} \quad (2.52)$$

where the frequency ω_k is given by

$$\omega_k = \frac{2\pi k}{Nh} . \quad (2.53)$$

In the Fourier space, the wavelet transform is written as a simple multiplication of the Fourier image of the signal \hat{x} by the complex conjugated Fourier image $\hat{\Psi}^*$ of the wavelet function. The wavelet surface $W(n, s)$ is obtained by the inverse Fourier transform

$$W(n, s) = \frac{1}{N} \sum_{k=0}^{N-1} \hat{x}_k \hat{\Psi}^*(s\omega_k) e^{i\omega_k nh} . \quad (2.54)$$

When using the approach based on the Fourier images $\{\hat{x}\}$ and $\hat{\psi}$, the wavelet function ψ should be renormalized for each time scale s to correctly compare the wavelet spectra of different signals (and, moreover, the same signal for different time scales s). The aim of this renormalization is to provide the unit energy at each time scale:

$$\hat{\Psi}(s\omega_k) = \left(\frac{s}{h}\right)^{1/2} \hat{\Psi}_0(s\omega_k) . \quad (2.55)$$

⁶Notice the difference between ψ , $\hat{\psi}$ and Ψ , $\hat{\Psi}$ used for the continuous and discrete transforms, respectively.

Finally, the equation for the wavelet surface $W(n, s)$ is written as

$$W(n, s) = \left(\frac{s}{h}\right)^{1/2} \frac{1}{N} \sum_{k=0}^{N-1} \hat{x}_k \hat{\psi}_0^*(s\omega_k) e^{i\omega_k n h} . \quad (2.56)$$

Fourier images of different wavelet functions $\psi_0(\eta)$ are shown in Fig. 2.11 and Table 2.1. Constant factors for each function are chosen according to the normalization condition (the condition of the unit energy)

$$\int_{-\infty}^{\infty} |\hat{\psi}_0(\omega)|^2 d\omega = 1 . \quad (2.57)$$

The analogous condition for the discrete form is

$$\sum_{k=0}^{N-1} |\hat{\psi}(s\omega_k)|^2 = N , \quad (2.58)$$

where N is the number of data points.

If (2.43) is used, the normalization of the wavelet function for the time scale s takes the form

$$\psi\left(\frac{(n' - n)h}{s}\right) = \left(\frac{h}{s}\right)^{1/2} \psi_0\left(\frac{(n' - n)h}{s}\right) , \quad (2.59)$$

where $\psi_0(\eta)$ is the wavelet function obeying the condition $\|\psi\|_{L^2(R)} = 1$, i.e., the wavelet function ψ_0 is also characterized by unit energy. Taking into account (2.59), equation (2.43) should be written in the final form

$$W(n, s) = \left(\frac{h}{s}\right)^{1/2} \sum_{n'=0}^{N-1} x_{n'} \psi_0^*\left(\frac{(n' - n)h}{s}\right) . \quad (2.60)$$

Taking into account (2.56), one can simultaneously obtain the results of the wavelet transform $W(n, s)$ for the fixed value of s and all n , using the fast Fourier transform (FFT) to determine all sums in (2.50) and (2.56). Since the FFT requires only $N \log_2 N$ iterations [33] to calculate the sums (2.50) or (2.56), the whole wavelet surface $W(n, s)$ (for all considered time scales s) is computed with $\mathcal{L} \times N \log_2 N$ iterations.⁷ For a large number of points N , it gives sufficient gain in comparison with the use of (2.60).

⁷Here we do not consider iterations for calculation of the Fourier image of the signal \hat{x} , since this transform should be performed only once.

An important aspect of the wavelet transform is the set of time scales $\{s\}$ used to calculate the wavelet spectrum (2.56). If the mother function represents one from orthogonal wavelets [19, 34], this set of time scales is strongly restricted, whereas for nonorthogonal wavelets the set $\{s\}$ can be arbitrarily chosen in order to acquire more detailed information about the signal. When the FFT procedure is used, the set of time scales is typically considered to be some power of 2:

$$s_l = s_0 2^{l\Delta s}, \quad l = 0, \dots, \mathcal{L}, \quad \mathcal{L} = \frac{\log_2(Nh/s_0)}{\Delta s}. \quad (2.61)$$

Here s_0 is the minimal time scale distinguished when the wavelet transform is applied and \mathcal{L} is the maximal number of time scales used to calculate the wavelet spectrum. The minimal time scale s_0 should be used in such a way that the Fourier period corresponding to this time scale is about $2h$ (see below). The optimal value of Δs is determined mainly by the width $\Delta\Omega$ of the Fourier image of the mother wavelet $\hat{\Psi}_0$. If Δs exceeds $\Delta\Omega/(2\omega_0 - \Delta\Omega)$, the scale resolution of the wavelet transform decreases, since some time scales are excluded from consideration. On the other hand, the choice of a small Δs does not provide essential improvements in the resolution of the wavelet transform (due to the finite width of the wavelet function in the Fourier space). However, it does increase the time required for the calculation.

In the case of the Morlet wavelet with $\omega_0 = 2\pi$, the maximal value of $(\Delta s)_{\max}$ allowing acceptable resolution is about 0.5, whereas for other wavelet functions, e.g., the Paul wavelet, the maximal value of Δs may increase, e.g., $(\Delta s)_{\max} \approx 1.0$ for the Paul wavelet.

The FFT procedure used for the continuous wavelet transform in (2.50) and (2.56) also constrains the length of the considered time series $\{x_n\}$, since for the FFT procedure the number of points in the time series must obey the requirement $N = 2^p$, where p is a natural number. Typically, it is not too difficult to obtain time series with the required number of points. Nevertheless, in several cases, the number of data points is limited and cannot be easily enlarged (e.g., in the case of climatic or geological data).

If the length of such time series is roughly (but less than) 2^p , the properties of the wavelet transform allow one to effectively analyze this data using 2^p points instead of 2^{p-1} . This may be done by forming a surrogate time series in which the first and last $(2^p - N)/2$ points are set equal to constant values, e.g., mean values of the initial time series ($\bar{x} = \sum_n x_n/N$) or zeros. In this case the region of edge effects on the plane (n, s) becomes broader (see next section).

2.3.3.3 Influence of Edge Effects

When a finite time series is used to obtain the wavelet spectrum, the errors in $W(n, s)$ appear near the boundaries of the time axis (i.e., near $n = 0$ and $n = N - 1$) and this results in a distortion of the time–frequency representation of the signal. Firstly, this

is due to the fact that, for the considered time scale s , the wavelet function shifted along the time axis starts going beyond the analysed time series. As a consequence, the $W(n, s)$ values in the vicinity of the time series boundaries become incorrect. Obviously, the region of influence of edge effects becomes broader for longer time scales s (smaller frequencies). Secondly, use of the FFT procedure supposes that the analysed data $\{x\}$ is periodic with period Nh , whereas the considered time series does not usually have this property.

The width τ_s of the edge effect region is determined by the time interval $T(s)$ introduced earlier (see (2.44)). For the Morlet wavelet, the width of the region where edge effects influence the results of the wavelet transform is given by

$$\tau_s = T(s) = 4s . \quad (2.62)$$

There are different ways to suppress unwanted edge effects [8, 16, 35]. One of the most effective solutions of this problem is the formation of a surrogate time series $\{x'_n\}$ with length $2N$ in which the first N points are taken from the initial time series $\{x_n\}$, whereas the next N points starting from $n = N$ are filled by zeros. The resulting surrogate time series $\{x'_n\}$ is further used for the wavelet transform (2.56). Since $N = 2^p$, the FFT procedure can be applied, but for a time series with length 2^{p+1} . This approach reduces the influence of edge effects, and in addition, it is rather fast due to the use of the FFT procedure.⁸

The use of a surrogate time series $\{x'_n\}$ results in the appearance of a large heterogeneity on the boundary of the initial time series x_n . Nevertheless, because half of the surrogate time series consists of constant values (e.g., zeros), the perturbations induced this heterogeneity are in the region of very long time scales, whereas the spectrum of the initial heterogeneity (being sufficiently less than added one from the formal point of view) connected with the influence of the boundaries of the time series is related to the region of time scales of the signal. As a consequence, introducing this kind of heterogeneity results in a decrease in the amplitude $|W|$ of the wavelet spectrum in the vicinity of the boundaries of the time series. Obviously, the longer the part of the surrogate time series filled by zeros, the less the influence of edge effects. The use of surrogate time series with equal lengths of fragments filled by initial values and zeros seems to be an optimal solution in terms of the balance between speed of calculation, internal memory consumption, and accuracy of the wavelet transform in the vicinity of the boundaries of the initial time series x_n [8, 16].

The region of the wavelet spectrum $W(n, s)$ on the plane (n, s) where edge effects are important and cannot be neglected will be referred to as *the region of influence of edge effects*. According to [8], the region of influence of edge effects

⁸For time series with length N , only $\mathcal{L} \times 2N(1 + \log_2 N)$ arithmetic operations are needed to obtain the wavelet surface with the described technique for reducing edge effects.

can be defined using the effective width τ_s of the autocorrelation function, which is calculated for the wavelet power at each time scale s . The value of τ_s is equal to the shift relative to the boundary when the power of the wavelet transform of a time series with edge heterogeneity is halved on the logarithmic scale, i.e., on a linear scale, it corresponds to a power decrease by a factor of e^2 . Such a choice for the boundary of the region associated with edge effects guarantees that these effects can be neglected for times nh , where $(N - n)h > \tau_s$ and $nh > \tau_s$ for the corresponding scales s .

Estimates of the widths τ_s for different mother wavelets are given in Table 2.1 when using the technique of surrogate time series. Comparing the value of τ_s obtained for the Morlet wavelet with the widths of the region of influence of edge effects obtained for the case when these effects have not been suppressed (2.62), one finds that this approach is reasonably effective, allowing effective suppression of the influence of edge effects.

Note also that the value of τ_s characterizing the region of edge effects determines the characteristic time of influence of an isolated peak of large amplitude in the time series on the form of the wavelet power spectrum. Considering the width of the peak in the power spectrum, one can separate, e.g., large-amplitude artifacts in the time series from a permanent harmonic component with the same period.

2.3.3.4 Time Scales of the Continuous Wavelet Transform vs. Frequencies of Fourier Analysis

From Fig. 2.11 one can see that maximum of the Fourier image $\hat{\psi}(s\omega)$ of $\psi(s\omega)$ does not correspond to the frequency $\omega_s = 2\pi f_s$ (where $f_s = 1/s$). In other words, there is no equivalence between frequencies of the Fourier transform (f) and those of the wavelet transform (f_s). Moreover, each mother wavelet is characterized by its own relationship between f and f_s (see Table 2.1). Thus, the Morlet wavelet with $\omega_0 = 2\pi$ is characterized by $f \approx f_s$, and in this case the time scale of the wavelet transform is almost equivalent to the Fourier period. At the same time, for $\omega_0 = 16$, the frequencies f and f_s are already related to each other by $f/f_s = 2.5527$. A similar situation occurs for the MHAT wavelet ($f/f_s = 0.2518$) and the Paul wavelet with $m = 4$ ($f/f_s = 0.7166$). So these relations must be taken into account when the results of the wavelet analysis are compared with the results of the Fourier transform. This is also very important when the wavelet power spectra obtained for different mother wavelets are compared with each other.

A relationship between the frequencies f_s and f may easily be obtained either analytically by substituting the Fourier image of a harmonic signal with known frequency ω_0 , i.e., $\delta(\omega - \omega_0)$ into (2.54) and determining the corresponding time scale s (which may be found as a maximum of the wavelet power spectrum), or numerically, with only one difference, namely that the power spectrum in this case must be calculated with the technique described earlier.

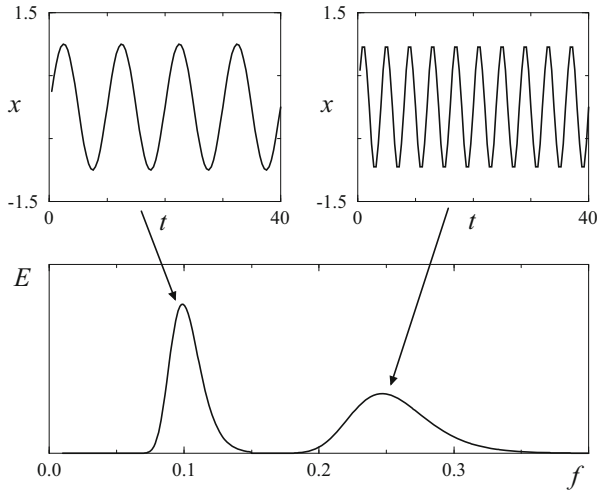


Fig. 2.12 Spectra of two harmonic functions with unit amplitudes and different frequencies, calculated using the Morlet wavelet with $\omega = 2\pi$

2.3.3.5 Normalization of Wavelet Spectrum

In the framework of classical Fourier analysis, the total power of oscillations is equal to the area under the curve of spectral density $|S(f)|^2$, while the magnitude of the peak can be used to determine the amplitude of oscillations with the corresponding frequency. For wavelet analysis, this situation is more complicated. When the total power of the wavelet spectrum is considered, the amplitude cannot be estimated correctly and vice versa. Therefore, depending on the quantity to be obtained, different normalizations of the wavelet spectrum should be used. To illustrate this point, we consider the evaluation of the wavelet spectrum of a harmonic function for different frequencies of oscillation (see Fig. 2.12, where the Morlet wavelet with $\omega_0 = 2\pi$ is used). One can see that the peak in the wavelet spectrum becomes “blurred” with increasing frequency, while its magnitude decreases.

If one needs to calculate the energy associated with a certain frequency band, this effect is not significant, since the increased width of the peak is accompanied by contraction of its amplitude, and the total power of oscillations, i.e., the area under the curve $E(f)$ (see Fig. 2.12), remains unchanged. At the same time, estimating the amplitudes of each sine curve as the square root of the power related to the considered frequency gives different results, and the amplitude decreases with growing frequency f (see also Fig. 2.7 and the corresponding discussion in Sect. 2.2).

To estimate correctly the relationship between the amplitudes of oscillations, a special normalization should be used. For this purpose, the factor $1/\sqrt{s}$ in (2.19) should be replaced by $1/s$. This allows us to determine correct amplitudes for

rhythmic processes with different periods (with a certain constant factor as compared with Fourier analysis), although energy characteristics are preserved. Below (in Fig. 2.15c, d), both normalizations of the wavelet spectrum are given. We thus conclude that the power in a certain frequency band and the amplitudes of characteristic peaks should be considered separately using appropriate normalizations.

2.3.3.6 Signal Reconstruction Based on Wavelet Spectrum

The wavelet transform (2.18) or (2.43) can be considered as a band-pass filter with known frequency characteristic (wavelet function ψ). Therefore, the initial signal can be reconstructed from the wavelet spectrum $W(n, s)$ either through inversion of the convolution product (2.18) or by designing the inverse filter. Such manipulations are relatively easy when one deals with an orthogonal wavelet transform. However, for the continuous wavelet transform, reconstruction of the initial signal $x(t)$ is a serious problem due to the redundancy of information contained in the wavelet surface $W(s, t)$. A simple procedure for signal reconstruction based on knowledge of the wavelet surface for a certain function (the simplest case is the δ -function) is described in [24, 36]. In this case, the time series x_n can be represented by the sum of all coefficients of the wavelet transform on all considered time scales [8, 16]:

$$x_n = \frac{\Delta s \sqrt{h}}{K_\delta \psi_0(0)} \sum_{l=0}^{\mathcal{L}} \frac{W(n, s_l)}{\sqrt{s_l}}, \quad (2.63)$$

where the coefficients $\psi_0(0)$ and $1/\sqrt{s}$ are introduced to obtain the unit energy on each time scale s . For a real signal $\{x_n\} \subset \mathbb{R}$, the inversion formula (2.63) takes the form

$$x_n = \frac{\Delta s \sqrt{h}}{K_\delta \psi_0(0)} \sum_{l=0}^{\mathcal{L}} \frac{\operatorname{Re} \{W(n, s_l)\}}{\sqrt{s_l}}. \quad (2.64)$$

The coefficient K_δ in (2.63) and (2.64) is estimated from the reconstruction of δ -function obtained from its wavelet spectrum, which has been calculated with the mother wavelet $\psi_0(\eta)$. To obtain K_δ one has to construct the time series $x_n = \delta_{n0}$. In this case, the amplitudes of harmonics in the Fourier spectra are constant for all k , $\hat{x}_k = 1/N$. Having substituted \hat{x}_k into (2.54), one finds that the wavelet spectrum at $n = 0$ takes the form

$$W_\delta(s) = \frac{1}{N} \sum_{k=0}^N \hat{\psi}^*(s\omega_k). \quad (2.65)$$

Table 2.2 Characteristics of mother wavelets for the reconstruction of the initial signal from its wavelet spectrum

Wavelet	K_δ	$\psi_0(0)$
Morlet ($\omega_0 = 2\pi$)	0.776	$\pi^{-1/4}$
Paul ($m = 4$)	1.132	1.079
DOG ($m = 2$)	3.541	0.867
DOG ($m = 6$)	1.966	0.884

In this case, the relation for K_δ follows from the inverse formula (2.64)

$$K_\delta = \frac{\Delta s \sqrt{h}}{\psi_0(0)} \sum_{l=0}^{\mathcal{L}} \frac{\operatorname{Re} \{W(n, s_l)\}}{\sqrt{s_l}}. \quad (2.66)$$

Therefore, the parameter K_δ does not depend on the time scale s and remains constant for each mother function ψ_0 . The values of K_δ for commonly used mother wavelets ψ_0 are given in Table 2.2.

Obviously, the total energy of the signal must remain unchanged after the direct and inverse wavelet transforms. This requirement results in an analogue of Parseval's theorem for the wavelet transform, which (in the discrete form) can be written as

$$\sigma^2 = \frac{\Delta s h}{K_\delta N} \sum_{n=0}^N \sum_{l=0}^{\mathcal{L}} \frac{|W(n, s_l)|^2}{s_l}, \quad (2.67)$$

where σ^2 is the standard deviation of the time series. The δ -function is used in (2.67) to reconstruct the initial signal.

Equations (2.63) and (2.67) can be applied to check upon the accuracy of the numerical realization of the wavelet transform. Having obtained information about the accuracy of the numerical calculation of the wavelet spectrum, the minimal time scale and the step along the time axis can be selected to achieve the required accuracy of analysis.

2.3.4 Visualisation of Wavelet Spectra: Wavelet Spectra of Model Signals

In general, the wavelet spectrum $W(t_0, f_s) = |W(t_0, s)|e^{-i\varphi_W(t_0, s)}$ of a 1D signal $x(t)$ can be considered as two surfaces, viz., the surfaces of amplitudes $|W(t, s)|$ and phases $\varphi_W(t, s)$ of the wavelet transform, in the three-dimensional space of time–time scale s /frequency f –amplitude $|W|$ /phase φ_W . In the case where both the mother wavelet and the analysed signal, are real functions, the wavelet spectrum is also a real function. In this section we shall consider only the amplitude spectrum of the wavelet transform $|W(t_0, s)|$, while questions related to the phase of the wavelet transform will be considered in the next.

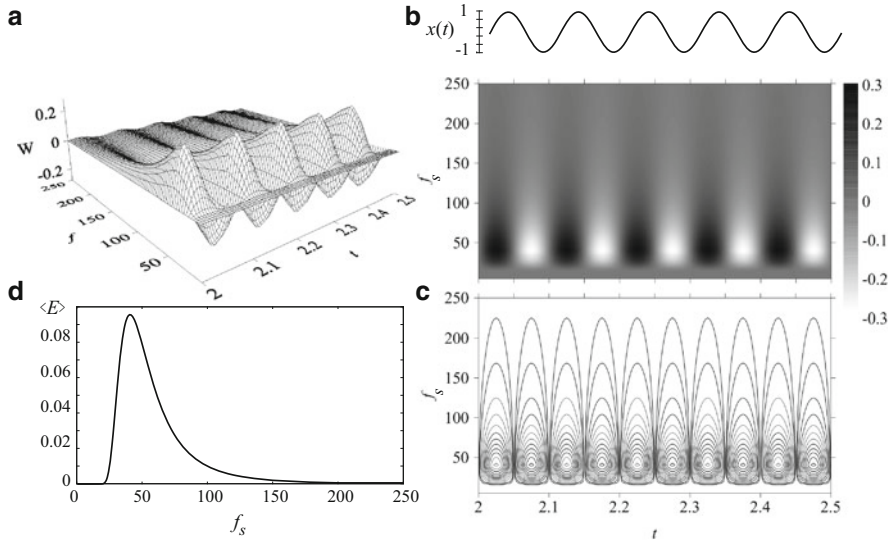


Fig. 2.13 Methods for visualising wavelet spectra. Results of the wavelet transform of a harmonic signal with frequency $f = 10$ for the MHAT wavelet. (a) Three-dimensional representation, (b) projection, and (c) contour curves of the wavelet surface $W(f_s, t)$. (d) Distribution of the total energy $\langle E(f_s) \rangle$ over the wavelet frequencies f_s .

As the simplest model, let us consider the harmonic function $x(t) = \sin(2\pi ft)$, with all calculations performed with the MHAT wavelet. For simplicity, the frequency of the signal is fixed as $f = 10$. The wavelet transform of this function is shown in Fig. 2.13.

In Fig. 2.13a, the wavelet spectrum is shown in the form of a three-dimensional surface. However, this kind of visualization is not often used due to the poor clarity and complicated qualitative interpretation of the results. It is more typical to represent the amplitude wavelet spectrum as the projection of the wavelet surface on the plane (t_0, s) (or (t_0, f_s)) either in the form of contour curves or with shades of gray (see Fig. 2.13b, c, respectively).

The distribution of the energy $\langle E \rangle$ (2.34) over the time scales s (or over the wavelet frequencies f_s) is also very informative. This distribution $\langle E(f_s) \rangle$ is shown for the considered harmonic function $x(t)$ in Fig. 2.13d. Note that the maximum of the distribution corresponds to $f_s \approx 40$, which is in good agreement with the relationship (see Sect. 2.3.3) between the frequency f of the Fourier transform and the wavelet frequency f_s for the MHAT wavelet.

Visual analysis of the wavelet surface provides detailed information concerning the particularities of the signal structure. There is only one characteristic time scale which is constant during the whole time of observation. For multiple-frequency and non-stationary signals, analysis of wavelet surfaces becomes more complicated.

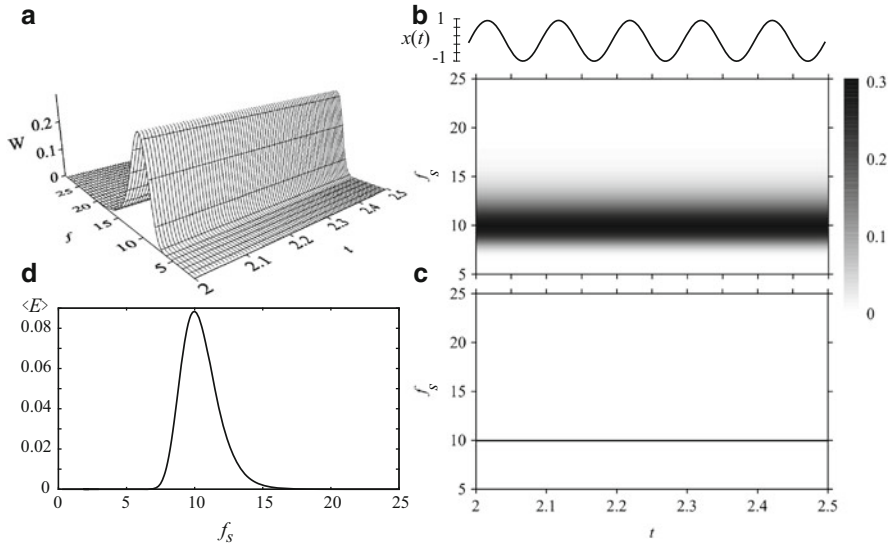


Fig. 2.14 Wavelet transform of the harmonic signal with frequency $f = 10$ for the Morlet wavelet. **(a)** Three-dimensional representation, **(b)** projection, and **(c)** skeleton of the amplitude surface $|W(f_s, t)|$. **(d)** Distribution of the total energy $\langle E(f_s) \rangle$ over the wavelet frequencies f_s

The alternation of light and dark spots in the vicinity of each local maximum or minimum overloads the wavelet spectrum by a large number of details which may be insufficient for understanding the time–frequency structure of the signal under study.

The results are analogous to those shown in Fig. 2.13 and can be obtained with the help of other mother wavelets. For clarity of analysis, complex wavelet functions are preferable (besides eliminating phase information by considering the modulus of the wavelet surface $|W(t_0, s)|$). In particular, the complex Morlet wavelet (2.33) is very useful for analyzing multiple-frequency and non-stationary signals.

Different representations of the corresponding wavelet spectrum of the harmonic signal with the same frequency $f = 10$ are shown in Fig. 2.14. One can see that use of the Morlet mother wavelet gives a clearer wavelet surface than would real wavelets. Indeed, the maximum of the wavelet surface corresponds to the unique rhythm of the signal with frequency $f = 10$. Obviously, contour curves are not convenient in this case. An alternative way of visualizing the wavelet surface, the so-called *skeleton*, may then be used.

The skeleton is a way to visualize results of the wavelet transform by local maxima or minima of the wavelet surface at each time moment. In other words, the skeleton is the plane (t, s) (or (t, f_s)) containing only the peaks of the wavelet energy distribution. This form of information representation is clearer than the 3D representation. For the considered sinusoidal signal, the skeleton gives the

time dependence of the instantaneous frequency shown in Fig. 2.14c. Thus, using the approach described above, one can move from consideration of initial signals to study of the instantaneous frequencies (or time scales) and the instantaneous amplitudes of rhythmic processes, and we shall show in the following chapters that this facilitates analysis of neurophysiological signals.

Note also that the ordinate axis (s or $f_s = 1/s$) is usually shown on a logarithmic scale to represent the data over a wide range of time scales or frequencies.

Since the simple example considered here does not allow us to demonstrate conclusively all the advantages of wavelet analysis, we shall consider in the next few sections several examples of nonstationary signals which are characterized by features that are typical of real neurophysiological signals.

2.3.4.1 Signals with Frequency Switchings

Analysis of oscillations with a frequency of about 0.01 Hz is important when studying the complex dynamics of many physiological processes in living systems. Many rhythms in biology and medicine correspond to the range 10^{-2} – 10^{-1} Hz, and special methods allowing the detailed analysis of signal structure are important, especially for diagnosing the state from experimental data. As mentioned in Sect. 2.2, classical spectral analysis based on the Fourier transform allows us to detect the presence of different rhythms. However, it is impossible to track the time evolution of instantaneous characteristics of these rhythmic processes. Wavelet analysis provides various ways to examine the local properties of signals, including the case of fast changes in the instantaneous frequencies of rhythmic processes. This kind of behavior is typical, e.g., for electroencephalograms, which are characterized by the fast occurrence/disappearance of different rhythms.

A model signal for which the frequency of oscillations changes suddenly is shown in Fig. 2.15. Note that the amplitude of the harmonic function is equal to unity, both before and after switching. Wavelet analysis with the Morlet mother function allows us (with good enough accuracy) to localize time moments when the signal structure is altered. Figure 2.15c, d illustrate the instantaneous distributions of the wavelet energy, both before and after the frequency switches. The maximum of the wavelet power spectrum is shifted after the signal frequency has changed.

Figure 2.15c, d differ only in the type of normalization. The “classical” wavelet transform (Fig. 2.15c) fixes the energy $E(f_s) = |W(f_s, t = t_{fix})|^2$, whereas the normalization used in Fig. 2.15d ensures the equivalence of the amplitudes in the wavelet power spectrum $|W(f_s, t = t_{fix})|^2/s$ if the harmonics are characterized by equal amplitudes. For a detailed discussion of this aspect see the previous section and Fig. 2.11.

Wavelet analysis allows us to correctly localize the moments of switching for series with rather fast frequency variation. Figure 2.16 shows the case when the frequency changes twice during one period of oscillation.

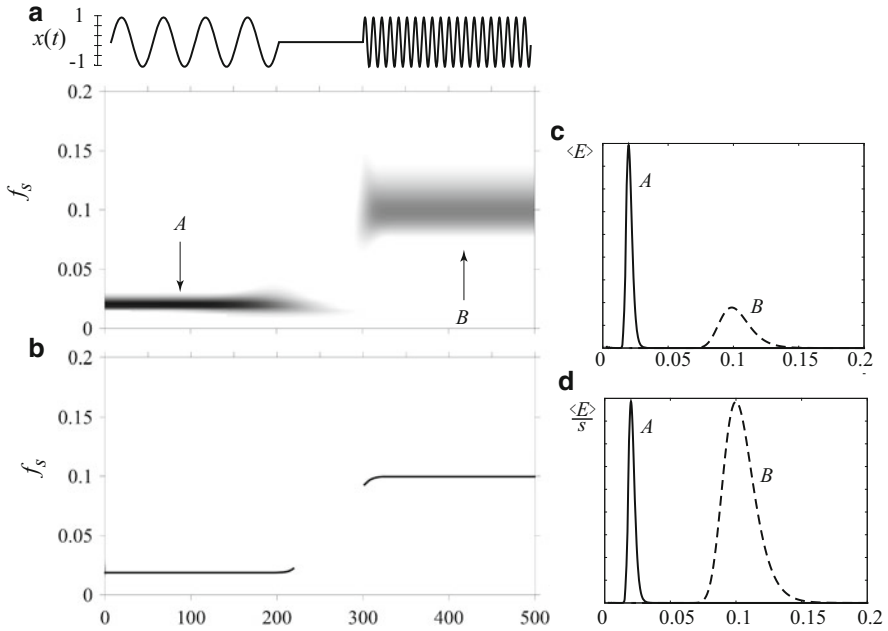


Fig. 2.15 Analysis of a signal with frequency switchings. **(a)** Projection of the wavelet spectrum obtained using the Morlet mother wavelet. **(b)** Skeleton (time dependence of the instantaneous frequency). **(c)** and **(d)** Instantaneous distributions of the wavelet power spectrum (compare with Fig. 2.11) for time moments shown by the *arrows A* and *B*, for a normalization that fixes the energy $E(f_s) = |W(f_s, t = t_{\text{fix}})|^2$ and a normalization ensuring equivalence of the amplitudes in the wavelet power spectrum $|W(f_s, t = t_{\text{fix}})|^2/s$, respectively

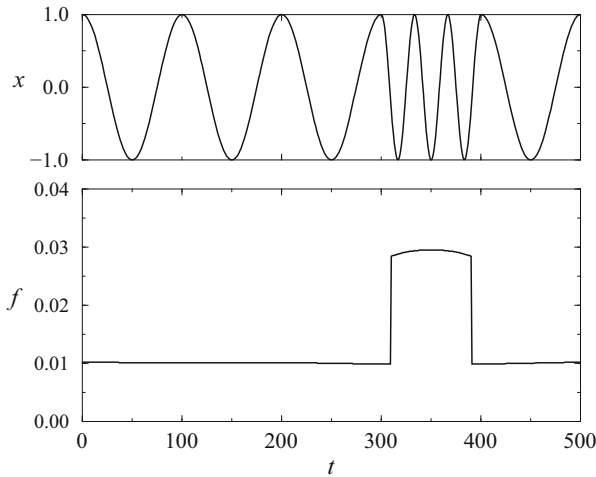


Fig. 2.16 Analysis of a signal with fast evolution of the frequency of the harmonic signal. Analyzed signal and skeleton of the wavelet surface

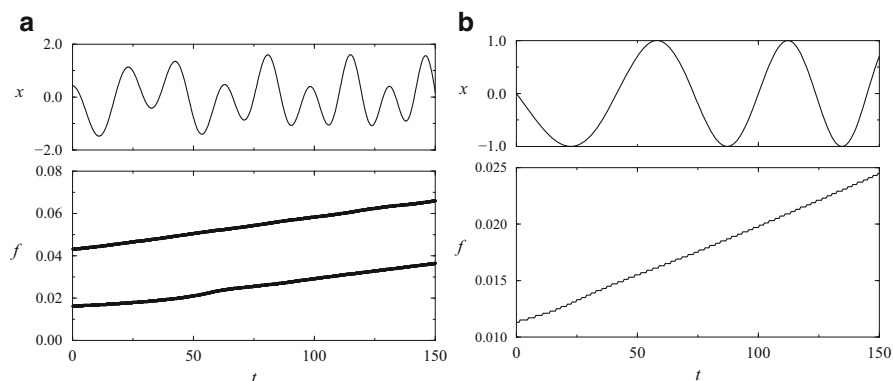


Fig. 2.17 Analysis of chirps. **(a)** Two parallel chirps. **(b)** A chirp whose frequency is approximately doubled during one period of oscillation. Only the skeletons of the wavelet surfaces are shown

2.3.4.2 Signals with Varying Frequency (Chirps)

When we consider neurophysiological signals, frequency variations are typically smooth (in contrast to the sudden frequency switchings of Sect. 2.3.4.1). As a model example, let us consider a chirp signal, i.e., a signal whose frequency changes linearly or, more generally, monotonically in time. Figure 2.17a illustrates the results of the wavelet transform (with the Morlet mother wavelet) of the signal consisting of two “parallel” chirps, viz.,

$$x(t) = \sin [2\pi(f_1 + \Delta f_1 t/2)t] + \sin [2\pi(f_2 + \Delta f_2 t/2)t] ,$$

where $f_1 = f_2/2 = 0.02$, $\Delta f_1 = \Delta f_2 = 1.33 \times 10^{-4}$. For clarity, only the signal $x(t)$ and the corresponding skeleton of the wavelet surface are shown. As one can see, the variations of the instantaneous frequencies described by the linear dependence can easily be identified using the wavelet transform. Thus, wavelet analysis can obtain information concerning the structure of the given signal. This analysis reveals the presence of two chirps in this example.

Although the complex wavelet basis makes it possible to perform local spectral analysis, all characteristics are evaluated within a certain time range corresponding to the wavelet function $\psi_{s,t_0}(t)$. This means that these characteristics are not found absolutely locally, but are obtained as a result of some averaging. Indeed, the averaging procedure leads to decreased accuracy in the estimated instantaneous characteristics, and this accuracy will be less for fast frequency variations. Nevertheless, even for fast variation of the signal properties, the wavelet analysis provides correct results. To illustrate this aspect, a chirp whose frequency is approximately doubled during one period of oscillation is considered in Fig. 2.17b. As one can see, the wavelet analysis with the Morlet wavelet resolves this extremal case with good precision.

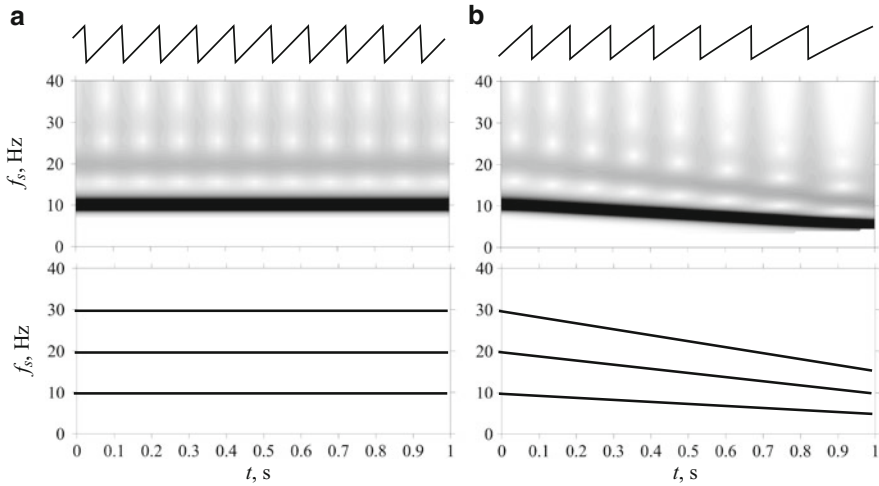


Fig. 2.18 Analysis of signals with complex spectral structure. Model of a sawtooth signal. Wavelet surface and its skeleton for the signal with constant main frequency $f = 10$ GHz (a) and main frequency varying from 10 to 5 GHz (b)

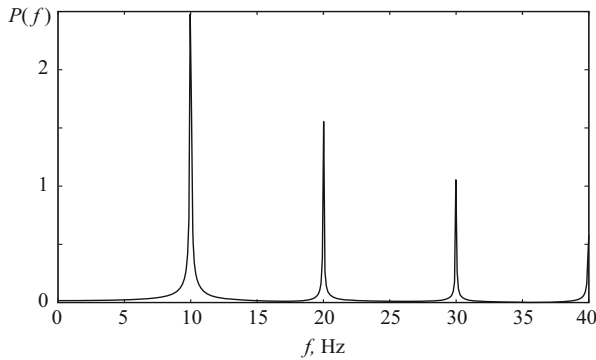


Fig. 2.19 Fourier spectrum of the sawtooth signal shown in Fig. 2.18. One can clearly see the harmonics nf (where $n = 2, 3, 4, \dots$) of the main frequency $f = 1/T = 10$ Hz

2.3.4.3 Processes with Complex Spectral Structure

Wavelet analysis is also a powerful tool for studying complex multiple-frequency signals [16]. To illustrate this aspect of the wavelet transform, we consider a signal representing a multiple-frequency process. Results of the wavelet transform (with the Morlet wavelet) for such a (sawtooth) signal are shown in Fig. 2.18a. The period of the impulses is $T = 0.1$ s. The spectrum of this signal is characterized by higher harmonics of the main frequency, as can be seen from Fig. 2.19.

The wavelet transform nicely reveals the higher harmonics of the main frequency. Indeed, the wavelet spectrum has several stripes corresponding to the frequencies 10, 20, 30 Hz, etc. The skeleton can represent the structure of the signal in a more obvious way, since only the first harmonics can be clearly seen by considering the wavelet surface. Starting from a certain number n , one cannot distinguish higher harmonics of the signals that are caused by their decreasing magnitudes. This example perfectly illustrates differences in the frequency resolution between the Fourier and wavelet analysis. As one can see, Fourier analysis is a more sensitive tool than wavelet analysis for frequencies with small amplitudes.

Note also the growth in the magnitude of the wavelet surface in the region of higher frequencies at times when the initial signal is changing quickly. This kind of behavior is typical and so can be used to localize and select different artifacts of the experimental data. The application of this feature of wavelet analysis to neurophysiological data will be discussed in detail in the following chapters.

Figure 2.18b illustrates the application of the wavelet analysis to a more complicated case where the period of the sawtooth signal grows with time. As one can see from the skeleton estimated for this case, the dynamics of both the main frequency and its higher harmonics can also be precisely estimated. As the main frequency of the sawtooth signal decreases, the skeleton lines come closer together with time. Alternatively, if the main frequency increases, the skeleton lines diverge. These particularities of the wavelet spectra must be taken into account when experimental data are examined.

2.3.5 Phase of the Wavelet Transform

In Sect. 2.3.4, attention was focused on the amplitude and power characteristics of the wavelet spectra. At the same time, if complex wavelets are used, the wavelet surface is also complex, and the quantity $W(s, t)$ is therefore characterized by both the amplitude and the phase

$$\varphi(s, t) = \arg (W(s, t)) . \quad (2.68)$$

Typically, the phase of the wavelet surface is eliminated from consideration and only the amplitude $|W(s, t)|$ is taken into account, in the same way as was done in Sect. 2.3.4. Nevertheless, the phase contains important information about the signal and, roughly speaking, the phase dynamics involves approximately half the information contained in the signal, with phase information being different from information about the amplitude part of the wavelet spectrum.

Indeed, it is more customary to use the amplitude and it is more convenient to deal with, allowing a simple and clear interpretation. Moreover, for many tasks, analysis of amplitudes is quite sufficient to solve research problems. At the same time, this does not mean that the phase does not play an important role, i.e., that it does not deserve attention. There are a broad range of problems in which

phase dynamics is extremely important, e.g., problems involving synchronization phenomena. In this section, we consider the phase and discuss problems where phase analysis can prove useful. We begin our considerations with the phase of the Fourier transform (2.3), in the same way as when the wavelet transform was introduced in Sect. 2.2.

2.3.5.1 Phase of the Fourier Transform

Let us imagine, that the signal under study $f(t)$ is shifted along the time axis by some time interval $f_1(t) = f(t + \tau)$. In this case the result of the Fourier transform of new signal $f_1(t)$ is

$$\begin{aligned} S_1(\omega) &= \int_{-\infty}^{+\infty} f_1(t) e^{-i\omega t} dt = \int_{-\infty}^{+\infty} f(t + \tau) e^{-i\omega t} dt \\ &= e^{i\omega\tau} \int_{-\infty}^{+\infty} f(\xi) e^{-i\omega\xi} d\xi = S(\omega) e^{i\phi(\omega)}, \end{aligned} \quad (2.69)$$

where $S(\omega)$ is the Fourier transform (2.3) of the initial signal $f(t)$ and $\phi(\omega) = \omega\tau$. One can see that the same signal in other reference systems is characterized by Fourier images that are related to each other by (2.69). The amplitudes of these Fourier images are identical, i.e., $|S(\omega)| \equiv |S_1(\omega)|$, but the phases are different:

$$\varphi_1(\omega) = \varphi(\omega) + \omega\tau, \quad (2.70)$$

where $\varphi(\omega) = \arg S(\omega)$, $\varphi_1(\omega) = \arg S_1(\omega)$. Thus, the phase of the signal contains information about the positioning of the signal relative to the time axis, while information about the presence of a certain harmonic and its intensity is completely included in the amplitude part of the Fourier spectrum.

Since the characteristics of the signal are the main subject of interest (but not its position on the time axis), the amplitude part of the Fourier spectrum is used for this kind of task. On the other hand, the question of the position of the signal relative to the coordinate origin of the time axis is very specific and seldom arises in practice.

The situation changes radically when one begins to consider interactions between systems. Since in this case the states of the systems should be considered relative to each other (but not relative to the coordinate origin), the phase difference $\Delta\varphi(\omega)$ of the Fourier spectra must be used rather than the phases:

$$\Delta\varphi(\omega) = \varphi_1(\omega) - \varphi_2(\omega). \quad (2.71)$$

Consideration of the phase difference has been proposed to study synchronization of chaotic oscillators [37–40]. The phase difference between spectral components can be found either directly (see, e.g., [37]) or using the cross-spectrum [41].

2.3.5.2 Phase Synchronization

The wavelet transform with a complex mother function becomes a more useful and effective tool for studying the phase dynamics of the given systems. Besides giving access to the spectral composition of the signal, this approach allows one to track the phase evolution with time. Note that the phase of the oscillations can be obtained without the wavelet transform. For periodic oscillations, the definition of the phase is quite obvious (see, e.g., [42]). But for chaotic oscillations, the definition of the phase becomes more complicated. The concept of chaotic phase synchronization involves consideration of the phases of chaotic interacting systems and we shall discuss it here, since it is closely related to the analysis of phases introduced using wavelet analysis and will be considered below.

Oscillating chaotic systems are widespread in nature [43, 44], but they are characterized by complicated irregular behavior that makes it difficult to study them. Neurophysiological systems are also characterized by intricate dynamics whose characteristics often coincide with, or at least resemble, the characteristics of chaotic systems. Although it is impossible in general to prove that neurophysiological systems are deterministic with chaotic dynamics (moreover stochastic or random behavior must be taken into account), the prospects for studying them from the standpoint of dynamical chaos look quite promising. A wide range of phenomena typical of chaotic oscillators are observed in neurophysiological systems.

One of the most widespread phenomena is the synchronous dynamics of interacting systems. When the systems under study are chaotic, this type of behavior is called *chaotic synchronization*. The concept of the chaotic synchronization is fundamental and deals with different types of synchronous behavior. Several types of chaotic synchronization are known: complete synchronization [45], lag synchronization [46], generalized synchronization [47], noise induced synchronization [48–50], phase synchronization [42], time scale synchronization [51–54], synchronization of spectral components [40], etc.

One of the most important and commonly occurring types of synchronous dynamics is phase synchronization. As pointed out above, phase synchronization is based on the concept of the instantaneous phase $\varphi(t)$ of a chaotic signal [42, 55–57]. In addition, the instantaneous phase is also used to detect the coupling direction of interacting oscillators, which is useful for neurophysiological systems. Note, however, that there is no universal method for defining the phase of a chaotic signal which would be correct for every dynamical system.

The concept of the *attractor* plays an important role in the phase definition. Typically, the oscillating behavior of the system under study is presented in the form of a time series when the observable quantity is shown as a time function. There is another way to represent the oscillating dynamics when the variables characterizing

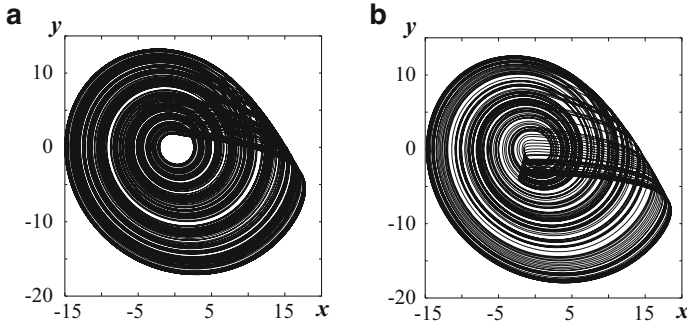


Fig. 2.20 Projections of phase coherent (a) and phase incoherent (b) attractors on the plane (x, y) . The dynamics of the chaotic Rössler system is shown

the system state are plotted as coordinates along axes in a certain space called the *phase space*,⁹ while the time is not shown at all. Although this type of representation of the system dynamics is unusual in biological studies, it is quite useful for solving certain tasks. Each point in the phase space corresponds to a specific state of the system under study and vice versa, with a one-to-one correspondence between the system state and the point in the phase space. The point corresponding to the current state of the system is referred to as the *representation point* and the curve along which the representation point moves is called the *phase trajectory*. A set attracting the representation points as time goes to infinity is an *attractor* of the dynamical system. When the system dynamics is represented in the plane, one speaks of the *projection* of the phase space (the phase trajectory, attractor) on the corresponding plane.¹⁰ Examples of the projections of chaotic attractors are shown in Fig. 2.20.

There are various ways of defining the phase of a chaotic signal. All these ways can be effectively used when the chaotic attractor of the system has simple topology. Such systems are called *systems with well-defined phase* or *systems with phase coherent attractor*. The chaotic attractor for these systems is characterized by the topology when the projection of the phase trajectory on a certain plane of states, e.g., (x, y) , winds around the coordinate origin but does not cross and envelop it (see Fig. 2.20a). In this case the phase $\varphi(t)$ of the chaotic signal may be defined as the angle in the polar coordinate system (x, y) [46, 58], whence

$$\tan \varphi(t) = \frac{y(t)}{x(t)}. \quad (2.72)$$

⁹The dimension of the phase space is equal to the number of quantities required to fully characterize the state of the system under study.

¹⁰Of course, if one deals with a system dimension of 3 or higher.

Since the projection of the phase trajectory does not cross and envelop the coordinate origin, the mean frequency $\overline{\Omega}$ of the chaotic signal, defined as the mean frequency of the phase variation

$$\overline{\Omega} = \lim_{t \rightarrow \infty} \frac{\varphi(t)}{t} = \langle \dot{\varphi}(t) \rangle, \quad (2.73)$$

coincides with the main frequency of the Fourier spectrum $S(f)$ of the system oscillations. If the projection of the phase trajectory envelops or crosses the coordinate origin at certain times, the origin of the coordinate plane is smeared by pieces of the phase trajectory. This kind of chaotic attractor is said to be *phase incoherent* and the system is referred to as a *system with ill-defined phase* (see Fig. 2.20b).

Another way to define the phase of a chaotic signal is to construct the analytical signal [42, 55]

$$\zeta(t) = x(t) + i\tilde{x}(t) = A(t)e^{i\phi(t)}, \quad (2.74)$$

where the function $\tilde{x}(t)$ is the Hilbert transform of $x(t)$, viz.,

$$\tilde{x}(t) = \frac{1}{\pi} \text{PV} \int_{-\infty}^{+\infty} \frac{x(\tau)}{t - \tau} d\tau, \quad (2.75)$$

and PV indicates that the integral is taken in the sense of the Cauchy principal value. The instantaneous phase $\phi(t)$ is defined from (2.74) and (2.75).

The third way to define the instantaneous phase of a chaotic signal is the Poincaré secant surface [42, 55]

$$\phi(t) = 2\pi \frac{t - t_n}{t_{n+1} - t_n} + 2\pi n, \quad t_n \leq t \leq t_{n+1}, \quad (2.76)$$

where t_n is the time of the n th crossing of the secant surface by the trajectory.

Finally, the phase of a chaotic time series can be introduced by means of the continuous wavelet transform [59], but an appropriate wavelet function and parameters must be chosen [60].

The regime of phase synchronization of two coupled chaotic oscillators means that the difference between the instantaneous phases $\phi(t)$ of chaotic signals $\mathbf{x}_{1,2}(t)$ is bounded by some constant, i.e.,

$$|\phi_1(t) - \phi_2(t)| < \text{const}. \quad (2.77)$$

As mentioned above, it is possible to define a mean frequency (2.73), which should be the same for both coupled chaotic systems, i.e., phase locking leads to frequency entrainment. Indeed, according to (2.77) and (2.73), the main frequencies of the synchronized chaotic oscillators must coincide with each other.

Note that, independently of the method used to define it, the phase of a chaotic signal may be located in both the region $\varphi \in (-\infty, \infty)$ and a band of width 2π , e.g., $\varphi \in [-\pi, \pi)$ or $\varphi \in [0, 2\pi)$. To examine the phase-locking condition (2.77), the values $\varphi_{(-\infty, \infty)} \in (-\infty, \infty)$ are more useful. However, in certain circumstances, the bounded phases, e.g., $\varphi_{[0, 2\pi)} \in [0, 2\pi)$, can be used. The two cases are related by

$$\varphi_{[0, 2\pi)} = \varphi_{(-\infty, \infty)} \pmod{2\pi} . \quad (2.78)$$

All these approaches provide correct and similar results for “good” systems with well-defined phase [58]. Indeed, the behavior of the instantaneous phase for the methods (2.72) and (2.76) is very similar within any time range that is less than the characteristic recurrence time. Furthermore, the instantaneous phase defined using the Hilbert transform (2.75) is known to behave for the phase coherent attractor in just the same way as the phases introduced by (2.72) and (2.76) (see, e.g., [58]). These methods involve certain restrictions [61], in particular, for oscillators with ill-defined phase (see, e.g., [61, 62]).¹¹

Obviously, if the examined system is characterized by a well-defined main frequency in the Fourier spectrum and by low background noise, the phase of the signal introduced using one of the above methods will be close to the phase of the corresponding harmonic signal. This is the case when good results can be achieved using the approach of chaotic phase synchronization. If the spectral composition of the signal becomes more complicated, e.g., there are several spectral components with similar amplitudes, the dynamics of the system cannot be correctly described by means of only one phase. In such cases, an approach based on continuous wavelet analysis and the associated concept of time-scale synchronization [52, 53, 65] can be used.

2.3.5.3 Phase of the Wavelet Transform

Since the wavelet surface is complex (if a complex mother wavelet is used), so that

$$W(s, t_0) = |W(s, t_0)|e^{i\varphi(s, t_0)} , \quad (2.79)$$

and since it characterizes the system behavior at each time scale s at the arbitrary time t_0 , the instantaneous phase of the wavelet transform is also automatically defined at each time scale s by

$$\varphi(s, t) = \arg W(s, t) . \quad (2.80)$$

¹¹Nevertheless, the phase synchronization of such systems can usually be detected by means of indirect indications [58, 63] and measurements [64].

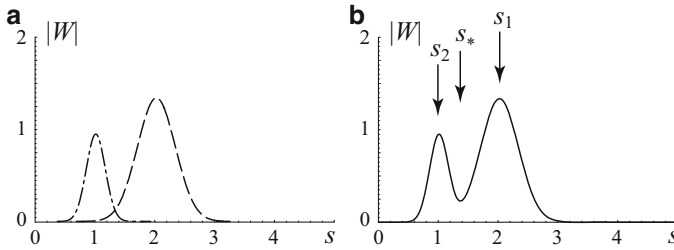


Fig. 2.21 Modulus of the wavelet spectrum for each component of the signal (2.82), showing them separately (a) and for the whole signal (b). The wavelet spectrum of the harmonic function with frequency $\omega_1 = \pi$ is shown in (a) by the dashed line, and the function with frequency $\omega_2 = 2\pi$ by the dotted line

In other words, the behavior of each time scale s can be described by means of its own phase $\phi(s, t)$, this being a continuous function of the time scale s and the time t . Thus, a set of phases $\phi(s, t)$ characterizes the dynamics of the system and can be used to study its behavior.

As in the case of a chaotic signal, the phase defined through the wavelet transform can also be presented in both the range $\varphi \in (-\infty, \infty)$ and a band of width 2π , viz., $\varphi \in [-\pi, \pi)$ or $\varphi \in [0, 2\pi)$. When (2.80) is used, the phase takes values in the 2π band, but there is no problem representing the phase in the infinite range of values.

We begin our considerations of the wavelet phase with a simple signal of the form $f(t) = \sin(\omega t + \phi)$ and transforming it using the Morlet wavelet. In this case the wavelet surface is given by

$$\begin{aligned} W(s, t) &= \sqrt{2\pi s} \pi^{1/4} \sin(\omega t + \phi - i\omega\omega_0 s) e^{-(s^2\omega^2 + \omega_0^2)/2} \\ &\approx \pi^{1/4} \sqrt{\frac{s}{2}} e^{-(\omega s - \omega_0)^2/2} e^{i(\omega t + \phi - \pi/2)}, \end{aligned} \quad (2.81)$$

where $\varphi(s, t) = \omega t + \phi - \pi/2$. As one can see from (2.81), the phase of the wavelet transform does not depend on the time scale and repeats the phase of the initial harmonic signal ($\varphi_{\sin} = \omega t + \phi$) with time lag $-\pi/2$. Note that, in the case of a harmonic signal, the evolution of the phase $\varphi(s, t)$ is the same for all time scales. As for the Fourier spectrum, shifting the signal relative to the time reference point changes the phase $\varphi(s, t)$.

Consider now a signal consisting of two harmonic functions

$$f(t) = \sin \omega_1 t + \sin \omega_2 t, \quad (2.82)$$

where ω_1 is assumed to be π and $\omega_2 = 2\pi$ (see Fig. 2.21). Due to the linearity of the wavelet transform, the wavelet spectrum of the signal (2.82) is defined by

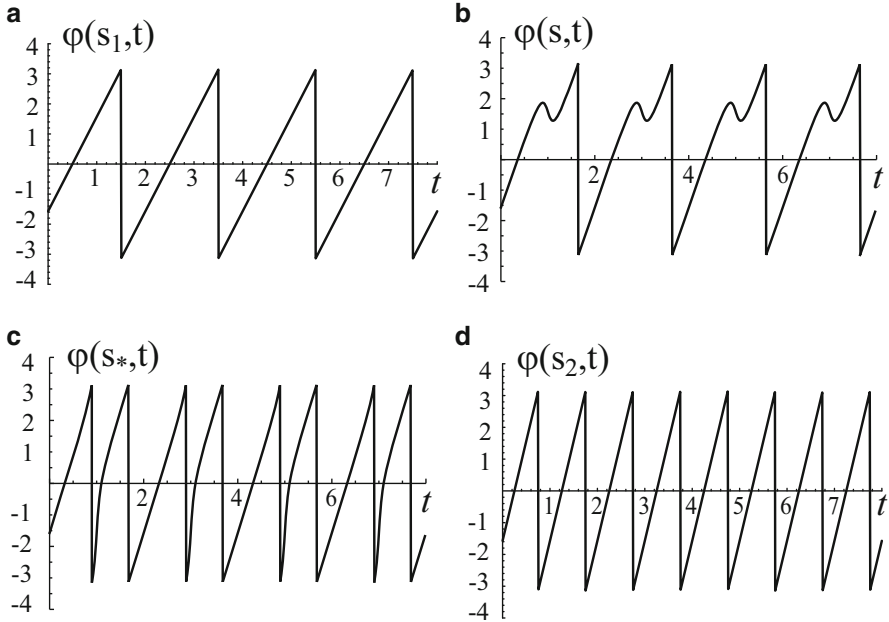


Fig. 2.22 Time dependence of the phase $\varphi(s, t)$ of the wavelet surface $W(s, t)$ for different time scales s : (a) $s_1 = 2.0$, (b) $s = 1.35$, (c) $s_* = 1.325$, (d) $s_2 = 1.0$

$$\begin{aligned}
 W(s, t) &= \sqrt{2\pi s\pi}^{1/4} \sin(\omega_1 t - i\omega_1 \omega_0 s) e^{-(s^2 \omega_1^2 + \omega_0^2)/2} \\
 &\quad + \sqrt{2\pi s\pi}^{1/4} \sin(\omega_2 t - i\omega_2 \omega_0 s) e^{-(s^2 \omega_2^2 + \omega_0^2)/2} \\
 &\approx \pi^{1/4} \sqrt{\frac{s}{2}} \left[e^{-(\omega_1 s - \omega_0)^2/2} e^{i(\omega_1 t - \pi/2)} + e^{-(\omega_2 s - \omega_0)^2/2} e^{i(\omega_2 t - \pi/2)} \right],
 \end{aligned} \tag{2.83}$$

and this spectrum is obviously more complicated.

Figure 2.21a shows the absolute value of the wavelet spectrum of each component of the signal (2.82) separately, while Fig. 2.21b shows the modulus of the wavelet surface of the whole signal (2.82). One can see that each frequency component is characterized by its own maximum of the wavelet surface $|W(s, t)|$, and that the amplitudes of these maxima are different due to the factors discussed in Sect. 2.3.3.5, despite the equivalence of the amplitudes of the sinusoidal functions.

It is intuitively clear that the presence of several spectral components results in the time dependence of the phase dynamics on the time scale of the observation. This statement is illustrated by Fig. 2.22, where the time dependence of the phase $\varphi(s, t)$ of the wavelet surface $W(s, t)$ is shown for different time scales s . Figure 2.22a illustrates the time dependence of the phase $\varphi(s, t)$ for the time scale $s_1 = 2.0$ (see also Fig. 2.21b) corresponding to the lower frequency $\omega_1 = \pi$. Similar dynamics (but with different frequency) is observed for the second time scale $s_2 = 1.0$,

corresponding to the second frequency ω_2 (Fig. 2.22d). Obviously, for intermediate time scales from the range $s \in (s_2, s_1)$, a transition from the behavior shown in Fig. 2.22d to the dynamics shown in Fig. 2.22a should be observed.

This transition is shown in Fig. 2.22b, c. One can see that the amplitude of the wavelet surface decreases with decreasing time scale, namely, in the transition from the time scale s_1 corresponding to the main frequency ω_1 to the time scale s_2 corresponding to the frequency ω_2 . The time dependence of the phase exhibits decreasing segments (Fig. 2.22b) due to the influence of the second harmonic of the signal $f(t)$ (with frequency ω_2), but the harmonic with frequency ω_1 plays the dominant role as before. The time scale s_* separates regions where the phase dynamics is determined by the harmonic with frequency ω_1 or ω_2 , and as a consequence, on this time scale s_* , both harmonics provide equivalent contributions to the phase dynamics (see Fig. 2.22c). Finally, in the range of time scales $s \in (s_1, s_*)$, the phase dynamics is determined by the harmonic with frequency ω_1 .

Thus, considering the phase of the wavelet transform, we have to keep in mind the following:

- For each time scale s of the signal under study, the time-dependent instantaneous phase (2.80) is naturally defined.
- For the selected time scale s' , the dynamics of the phase is defined not only by the frequency component corresponding to this time scale, but also by other harmonics located nearby in the spectrum of the signal and characterized by a large enough amplitude. In other words, on the fixed time scale s' , the phase dynamics can be determined by several components of the Fourier spectrum from a certain frequency band.

It is important to note that one can detect the presence of several frequency components by considering only the amplitude spectrum $|W(s, t)|$ of the wavelet transform, and then defining these frequencies as well (see Fig. 2.21b). However, there are several cases where this cannot be done. Indeed, the wavelet spectrum of the two-frequency signal

$$f(t) = A_1 \sin \omega_1 t + A_2 \sin \omega_2 t , \quad (2.84)$$

where $A_1 = 0.5$, $\omega_1 = 0.9\pi$, $A_2 = 1.25$, and $\omega_2 = \pi$, is characterized by a single maximum exactly in the case of a signal with a single frequency (Fig. 2.23a). This form of the wavelet spectrum is caused by (i) the finite resolution of the wavelet transform in the time space and (ii) the closeness of the coexisting frequency components in the Fourier spectrum of the signal (2.84), as well as the difference between their amplitudes.

Consideration of the phase dynamics allows rather easy detection of nonharmonic dynamics since, in the time scale ranges $s < s_*$ and $s > s_*$, the phase dynamics is different (see Fig. 2.23b). On the time scale $s_2 = 2$, this phenomenon is connected with the dominance of the spectral component with frequency ω_2 (dashed line in Fig. 2.23b) (the phase dynamics thus corresponds here to this component), whereas on the time scale $s_1 = 3$, the main role is played by the

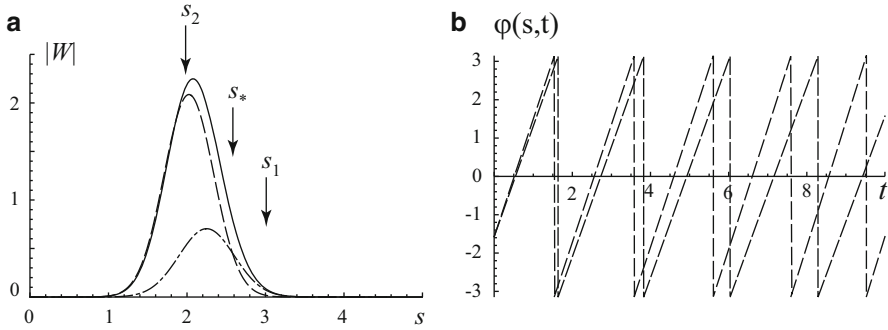


Fig. 2.23 (a) The moduli of the wavelet spectra for each component of the signal (2.84) are shown separately (the wavelet spectrum of the sinusoidal function with frequency $\omega_1 = 0.9\pi$ is shown by the *dotted line*, and that of the function with frequency $\omega_2 = \pi$ by the *dashed line*) and for the whole signal (*solid line*). (b) Time dependencies of the phase $\varphi(s, t)$ for the time scales $s_1 = 3$ (*dotted line*) and $s_2 = 2$ (*dashed line*)

spectral component with frequency ω_1 (which thus determines the behavior of the phase in this case).

2.3.5.4 Time-Scale Synchronization

To end this section let us briefly discuss the concept of time scale synchronization [51–54], based on the examination of the phase dynamics of interacting systems on different time scales. An important feature of the concept of time-scale synchronization is the unification of all types of synchronous behavior of chaotic systems, since all known types of chaotic synchronization (phase synchronization, generalized synchronization, lag synchronization, complete synchronization) can be considered from a unified point of view.

Let us consider the dynamics of two coupled oscillators with complex dynamics. If the time series $\mathbf{x}_{1,2}(t)$ generated by these systems contain the range $s_m \leq s \leq s_b$ of time scales s for which the condition of phase locking

$$|\phi(s_1, t) - \phi(s_2, t)| < \text{const.} \tag{2.85}$$

is satisfied, and if also a part of the wavelet spectrum energy within this range is not equal to zero, viz.,

$$E_{\text{sync}} = \int_{s_m}^{s_b} \langle E(s) \rangle ds > 0, \tag{2.86}$$

we say that *time-scale synchronization* (TSS) takes place between the oscillators.

It is obvious that the classical synchronization of coupled periodic oscillators corresponds to TSS because all time scales in this case are synchronized according to the time scale s , instantaneous phase $\phi_s(t)$, and TSS definitions. The case of chaotic oscillations is more complicated. Nevertheless, if two chaotic oscillators demonstrate any type of synchronized behavior, the time series $\mathbf{x}_{1,2}(t)$ generated by these systems contain time scales s which are correlated with each other for which the phase-locking condition (2.85) and the energy condition (2.86) are satisfied. Therefore, time-scale synchronization is also realized. In other words, complete synchronization, lag synchronization, phase synchronization, and generalized synchronization are particular cases of time-scale synchronization. To detect time-scale synchronization, one can examine the conditions (2.85) and (2.86), both of which should be satisfied for synchronized time scales.

Note that the phase-locking condition (2.85) may be generalized to the case of $m : n$ synchronization. To study this kind of regime, the more general relation

$$|m\varphi_1(s_{n1}, t) - n\varphi_2(s_{m2}, t)| < \text{const.} \quad (2.87)$$

should be examined in different ranges of time scales $s_{n1} \in I_1 = [s_{1l}, \leq s_{1h}]$ and $s_{m2} \in I_2 = [s_{2l}, \leq s_{2h}]$ instead of Eq. (2.85). For ($m : n$) synchronization, the time scale s_{m1} of the first system and correspondingly the time scale s_{n2} of the second system must obey the relation $s_{m2}/s_{n1} = m/n$. The energy condition (2.86) remains unchanged, but different ranges of time scales I_1 and I_2 should be used.

Finally, synchronous dynamics may take place on a time scale changing with time. In this case one, has to check for fulfillment of the condition

$$|\varphi_1(s(t), t) - \varphi_2(s(t), t)| < \text{const.} \quad (2.88)$$

This problem is important when investigating systems whose main rhythm changes with time. In particular, this kind of behavior is typical for physiological systems (see, e.g., [31, 32] where the human cardiovascular system was considered).

A measure of synchronization can also be introduced. This measure $\gamma(t)$ can be defined as that part of the wavelet energy associated with the synchronized time scales:

$$\gamma(t) = \frac{E_{\text{sync}}(t)}{\int_0^{+\infty} E(s, t) ds} \times 100 \% , \quad (2.89)$$

where the numerator is the energy corresponding to the synchronous time scales and the denominator is the total energy of the wavelet spectrum. The value of this measure $\gamma = 100\%$ corresponds to regimes of complete and lag synchronization, while $\gamma = 0$ is evidence of completely asynchronous dynamics. Intermediate values of γ are manifestations of phase synchronous dynamics in a certain range of time scales, when the amplitudes of oscillations may remain uncorrelated. Increasing γ values attest to the expansion of ranges related to synchronous time scales.

Thus, the synchronization measure γ can be used, not only to distinguish between synchronized and nonsynchronized oscillations, but also to characterize the degree of TSS synchronization. Since the synchronization measure depends on time, it can be used to analyze processes leading into or out of the synchronous state.

As a consequence, besides the amplitudes of the wavelet spectrum, the phases (on different time scales) also inform us about the behavior of these complex systems. However, detailed consideration of synchronization theory (in particular, time-scale synchronization based on the continuous wavelet transform) is beyond the scope of this book. The reader can find a detailed description of different aspects of synchronization theory and its applications in [31, 32, 40, 51–54, 65–70].

2.4 Discrete Wavelet Transform

2.4.1 *Comparison of the Discrete and Continuous Wavelet Transforms*

Section 2.3 focused on the continuous wavelet transform, which allows a clear visual representation of the results of signal processing. In contrast to scientific research, many technical applications deal mainly with the discrete wavelet transform. Although it is inferior to the continuous wavelet transform from the viewpoint of visualizing results, the discrete wavelet transform has considerable advantages, such as computational speed, a simpler procedure for the inverse transform, etc. It is important to keep in mind that the discrete wavelet transform is not the discretization of the formula for the continuous wavelet transform (in contrast to the discrete Fourier transform). Differences between the continuous and the discrete wavelet transforms are sufficient to consider them as two different ways for analyzing signal structure.

In the context of the continuous wavelet transform, infinitely differentiable functions represented in analytical form are considered as mother wavelets.¹² As a consequence, these functions are characterized by exponential decay at infinity, and the basis constructed from these wavelets is not orthonormal. Therefore, the continuous wavelet transform provides excessive information, and the values of the wavelet coefficients are correlated. Nevertheless, in several cases, this feature plays a positive role, allowing one to obtain a clearer interpretation of the results, e.g., in the form of skeletons or contour curves [13]. Information obtained from the continuous wavelet transform are more easily analyzed than other ways of studying non-stationary processes (see, e.g., [12, 72]).

¹²For practical purposes, mother wavelets can also be constructed from tabulated segments of time series (see [30, 71]). This subject will be discussed in detail in Sect. 6.3.

Using complex functions, the continuous wavelet transform can be used to study the evolution of such characteristics as the instantaneous amplitude, frequency, and phase of rhythmic processes identified in the signal structure. One may also consider the set of phases corresponding to different spectral components of the signal [51–53, 65]. For these reasons, the continuous wavelet transform is a promising tool for solving many neurophysiological problems. Thus, the continuous wavelet transform is useful in the case when analyzing the synchronous dynamics between neurons or groups of neurons, or diagnosing the presence/absence of rhythmic components in the activity of a neuron group [73].

Although the discrete wavelet transform can use non-orthogonal basis functions (e.g., frames) [19], orthogonal (or almost orthogonal) bases are most commonly used since this allows one to represent the signal more precisely and simplifies the inverse transformation. In contrast to the continuous wavelet transform, the wavelets used in the framework of the discrete wavelet transform have no analytical expression, with the exception of the Haar wavelet (2.42) [18]. The wavelets are specified in the form of matrix coefficients obtained by solving certain equations. In practice, the concrete form of the wavelet function in the explicit form is not considered, and only sets of coefficients are used to define the wavelet. This results in a series of elementary operations that allow the realization of fast algorithms for the discrete wavelet transform. The basis is created using an iterative algorithm that varies the scale and shifts the single function. However, the detailed description of the essential differences between the discrete and continuous wavelet transforms is a mathematical problem that goes beyond the subject of our book, and is discussed, e.g., in [74].

The absence of an analytical expression for wavelets used in the discrete wavelet transform leads to a certain inconvenience with the discrete wavelet transformation. However, this inconvenience is compensated by many useful properties of the discrete wavelet transform. For example, it provides the possibility of using fast algorithms (see, e.g., [75]), which is important for practical purposes, e.g., for coding and transmitting information, or for compressing data. The discrete wavelet transform is used, for instance, in the framework of the JPEG graphic format and the MPEG4 video format, in computer graphics for editing three-dimensional images, etc. The algorithms of the fast discrete transform are applied when processing experimental data.

An important feature of the wavelet transform is shift invariance. This means that, if the signal is shifted along the time axis, the wavelet coefficients are also shifted and, after relabeling, one can find a relationship between the new coefficients and those prior to the shift. This feature is easily illustrated for the continuous wavelet transform, but the relationship between the coefficients on different time scales is more complicated for the discrete wavelet transform. Estimating the wavelet coefficients provides a way to solve the problem of image identification. More efficient algorithms can also be created using a combination of wavelet analysis and neural networks.

The majority of wavelet functions used in the framework of the discrete wavelet transform are irregular. For practical purposes, such properties as the regularity,

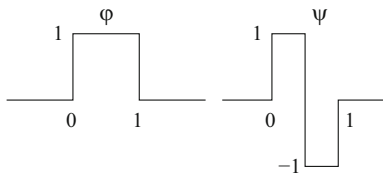
the number of zero moments, and the number of wavelet coefficients exceeding a certain value are important when selecting the wavelet function. A large number of zero moments makes it possible to realize effective data compression, since wavelet coefficients at small scales tend to be zero at those points where the function is rather smooth, and as a consequence, these coefficients may be neglected without significant loss of information. In this case, however, the wavelet function becomes broader and this results in a decreased speed of computing. Thus, the choice of basis function is determined by specific features of the problem to be solved. Typically, the discrete wavelet transform is used to solve technical problems (signal coding, computer graphics, image recognition, etc.), whereas the continuous wavelet transform is applied in scientific studies related to the analysis of complex signals.

Wavelet analysis, as applied to neurodynamics and neurophysiology tasks, provides many possibilities for effective recognition (or identification) of signal shapes. Additionally, wavelets are able to filter noise, artifacts, and random distortions from experimental data. Indeed, neurophysiological data often contain artifacts such as rapid changes in the amplitude and other local variations of the signal, which may be caused by the neurophysiological processes themselves or by equipment failures, external factors, etc. Filters based on the Fourier transform are useless for eliminating artifacts, since information about them is contained in all coefficients of the transform. Filtration with wavelets is more effective, since it is possible (perhaps in automatic regime) to detect, localize, identify, and eliminate artifacts, having analyzed the wavelet coefficients on small scales. Digital filtration based on wavelets can be used to clear noisy signals from experimental data at the preprocessing stage. Wavelets are also widely used to recognize signals with similar shapes in the presence of noise. In neurophysiology, such problems arise in the tasks of EEG pattern recognition, identification of impulse activity of single neurons from extracellular recordings of electric potentials, etc. In other words, the reason for the active use of wavelets in modern studies is that similar problems arise in the digital processing of different signals.

2.4.2 *General Properties*

The continuous wavelet transform discussed in Sect. 2.3 deals with the expansion of the signal $f(t)$ when the basis is obtained from a soliton-like function $\psi(t)$. In this approach, the scale transformation is carried out for only one function (the mother wavelet). The multi-scale analysis is based on a different concept. It uses orthonormalized wavelet bases to characterize the ‘increment of information’ required for the transition from the rough description to the more detailed one [18]. This approach was used for the first time in problems relating to image analysis. It provides successive approximations of the given signal $f(t)$ at different scales. In fact, the signal is approximated for certain intervals, and deviations from the approximating functions are analyzed. The approximating functions are

Fig. 2.24 Scaling function and Haar wavelet



related to each other on different scales and orthogonal to each other with the shift along the time axis. This means that only specific functions can be used for the approximation. To explain the ideology of multi-scale analysis, we introduce the necessary definitions using the Haar wavelet as the most simple example.

To analyze the successive approximations for the signal on different scales, the approximating functions should be chosen to satisfy an additional requirement imposed by the relationship between the approximating functions on different scales. In the ideal case, it is better to use a single function $\varphi(t)$ to approximate the signal on both the large and small scales. Further, the detailed analysis of the signal structure is carried out at the selected scale with the wavelet $\psi(t)$. The function $\varphi(t)$ is called the *scaling function* or *father wavelet*. For the scaling function, the following property is fulfilled:

$$\int_{-\infty}^{\infty} \varphi(t) dt = 1 , \quad (2.90)$$

i.e., its mean value is not equal to zero as for the mother wavelet $\psi(t)$. The functions $\varphi(t)$ and $\psi(t)$ of the Haar wavelet are shown in Fig. 2.24. Scaling of the functions $\varphi(t)$ and $\psi(t)$ results in the equations

$$\begin{aligned} \varphi(t) &= \varphi(2t) + \varphi(2t - 1) , \\ \psi(t) &= \varphi(2t) - \varphi(2t - 1) , \end{aligned} \quad (2.91)$$

from which the difference between these functions is clear. When the signal is analyzed, the functions $\varphi(t)$ and $\psi(t)$ play the role of high-pass and low-pass filters, respectively.

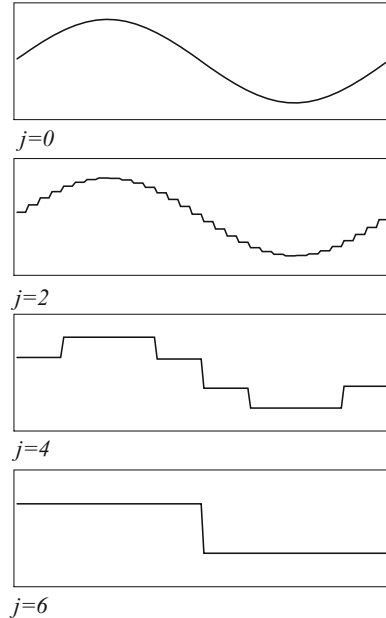
By analogy with the basis of the continuous wavelet transform, we introduce the notation

$$\varphi_{j,k}(t) = \frac{1}{2^{j/2}} \varphi\left(\frac{t}{2^j} - k\right) . \quad (2.92)$$

For the given values of the scale and shift, characterized by the parameters j and k , the approximation coefficients of the signal $x(t)$ are

$$s_{j,k} = \int_{-\infty}^{\infty} x(t) \varphi_{j,k}(t) dt . \quad (2.93)$$

Fig. 2.25 Approximation of the harmonic function on different levels of resolution j



For the selected scale the resulting coefficients are referred to as the *discrete approximation* of the signal on the scale j . Summing the scaling functions with the corresponding coefficients provides the so-called *continuous approximation* of the signal $x(t)$ at the selected scale [76]:

$$x_j(t) = \sum_{k=-\infty}^{\infty} s_{j,k} \varphi_{j,k}(t) . \tag{2.94}$$

On small scales, this continuous approximation is very close to the initial signal $x(t)$.

As an illustration, let us consider the approximation of one period of the harmonic function shown in Fig. 2.25. Using the Haar scaling function means that on different scales the signal is replaced by the averaged values. For large j , it results in a very rough representation of the harmonic function, but for the maximum possible resolution level $j = 0$ (determined by the discretization step), the continuous approximation tends to the initial signal $x(t)$.

Using the Haar wavelet, we thus have a simple illustration of the main idea of multi-scale analysis, namely the construction of a set of approximating function spaces. In fact, we are dealing with the histogram approximation of the signal, with the orthogonal complements adding more details on the smallest scales [76]. Figure 2.26 shows examples of the calculation of two successive approximations and the complement to the second of these.

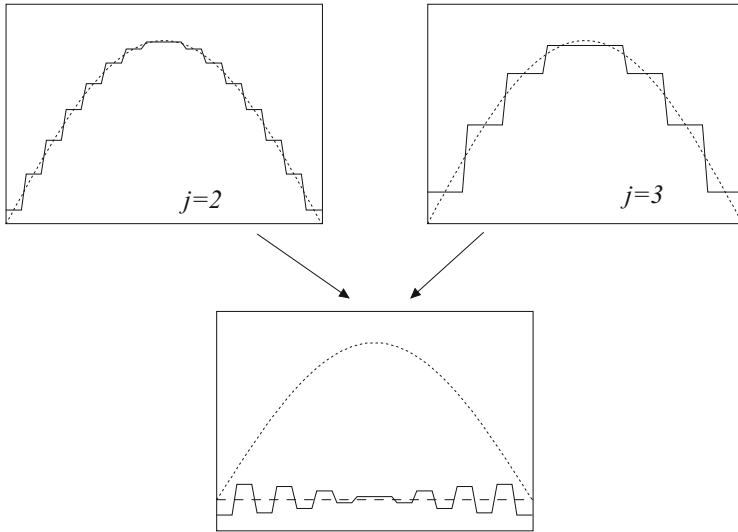


Fig. 2.26 Approximations of a half period of the harmonic function on the scales $j = 2$ and $j = 3$, together with the complement to the approximation on the scale $j = 3$, allowing one to move to the next scale

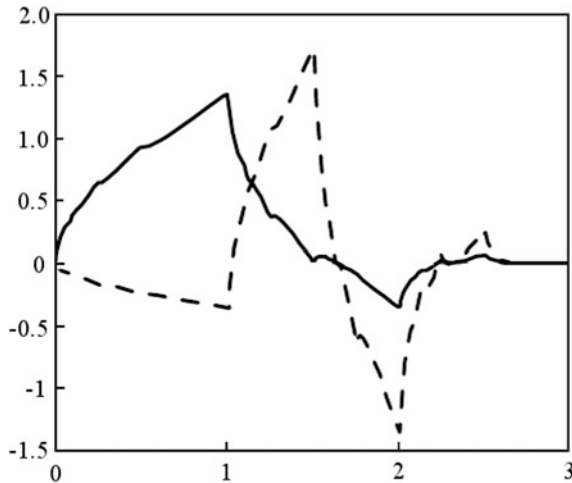


Fig. 2.27 Scaling function (solid line) and the Daubechies wavelet D^4 (dashed line)

Wavelets and the corresponding scaling functions used in practice are usually characterized by a more complicated form (see, e.g., Fig. 2.27). However, all equations written for Haar wavelets remain applicable with other bases. We thus pursue our discussion of the simplest case, assuming that the results can be extended to other wavelets.

The concept of continuous approximation can reveal a trend in the analysed process at the selected scale, with further detailed wavelet-based analysis of fluctuations relative to this trend. On a certain arbitrary scale, any function $x(t) \in L^2(\mathbb{R})$ can be expanded in a series

$$x(t) = \sum_k s_{j_n,k} \varphi_{j_n,k}(t) + \sum_{j \leq j_n} \sum_k d_{j,k} \psi_{j,k}(t), \quad (2.95)$$

where

$$d_{j,k} = \int_{-\infty}^{\infty} x(t) \psi_{j,k}(t) dt \quad (2.96)$$

are the wavelet coefficients. The first sum is the approximation of $x(t)$, whereas the second sum provides the details of this function on different scales.

For the selected scale j_n , one can write

$$x(t) = x_{j_n}(t) + \sum_{j \leq j_n} \mu_j(t), \quad (2.97)$$

whereas the function

$$\mu_j(t) = \sum_k d_{j,k} \psi_{j,k}(t) \quad (2.98)$$

characterizes the detailed structure of the signal on the scale j . According to (2.97), one obtains

$$x_{j-1}(t) = x_j(t) + \mu_j(t), \quad (2.99)$$

i.e., if the detailing function $\mu_j(t)$ of the signal is added to the approximation on the selected scale j (this characterizes fluctuations relative to the approximated trend), the approximation on the next, more precise level of resolution ($j - 1$) is obtained. This is the main idea of multi-scale analysis.

In general, the relationship between the functions $\varphi(t)$ and $\psi(t)$ and their scaled and shifted modifications can be written in the form

$$\begin{aligned} \varphi(t) &= \sqrt{2} \sum_{k=0}^{2M-1} h_k \varphi(2t - k), \\ \psi(t) &= \sqrt{2} \sum_{k=0}^{2M-1} g_k \varphi(2t - k), \end{aligned} \quad (2.100)$$

where the factor $\sqrt{2}$ is connected with the traditional form of the fast algorithms and normalization of the functions $\varphi_{j,k}(t)$ and $\psi_{j,k}(t)$, whereas the parameter M determines the wavelet length, e.g., $M = 1$ for the Haar wavelet. Note also the relationship between the coefficients h_k and g_k [76]:

$$g_k = (-1)^k h_{2M-k-1} . \quad (2.101)$$

These coefficients are determined from general properties of the scaling functions and wavelets.

As an example, let us consider calculation of the coefficients for the case $M = 2$. Since the relatively shifted scaling functions are orthogonal, we have

$$\int_{-\infty}^{\infty} \varphi(t)\varphi(t-l)dt = \delta_{0l} . \quad (2.102)$$

Using (2.100), a first restriction on the coefficients h_k is obtained:

$$\sum_k h_k h_{k+2l} = \delta_{0l} . \quad (2.103)$$

The condition

$$\int_{-\infty}^{\infty} t^n \psi(t)dt = 0 , \quad (2.104)$$

excluding slow nonstationarity (the polynomial trend) for $n = 0, \dots, M - 1$ gives

$$\sum_k k^n g_k = \sum_k (-1)^k k^n h_k = 0 . \quad (2.105)$$

Finally, from the normalization condition (2.90), one obtains

$$\sum_k h_k = \sqrt{2} . \quad (2.106)$$

In the particular case ($M = 2$), the last three equations written in explicit form result in the system

$$\left. \begin{aligned} h_0 h_2 + h_1 h_3 &= 0 , \\ h_0 - h_1 + h_2 - h_3 &= 0 , \\ -h_1 + 2h_2 - 3h_3 &= 0 , \\ h_0 + h_1 + h_2 + h_3 &= \sqrt{2} . \end{aligned} \right\} \quad (2.107)$$

For the sequence $x(i)$ consisting of eight elements, the pyramidal expansion is implemented as follows. First, after multiplying the vector

$$\left[x_1 \ x_2 \ x_3 \ x_4 \ x_5 \ x_6 \ x_7 \ x_8 \right]^T \quad (2.110)$$

corresponding to the scale $j = 0$ by the 8×8 matrix (2.109), the set of coefficients s and d are obtained:

$$\left[s_{11} \ d_{11} \ s_{12} \ d_{12} \ s_{13} \ d_{13} \ s_{14} \ d_{14} \right]^T . \quad (2.111)$$

The coefficients $d_{j,k}$ are not used in the following transformations and they should therefore be separated by reorganizing the vector elements

$$\left[s_{11} \ s_{12} \ s_{13} \ s_{14} \mid d_{11} \ d_{12} \ d_{13} \ d_{14} \right]^T . \quad (2.112)$$

Secondly, the 4×4 matrix (2.109) multiplies the vector of s -coefficients to give the vector

$$\left[s_{21} \ d_{21} \ s_{22} \ d_{22} \mid d_{11} \ d_{12} \ d_{13} \ d_{14} \right]^T . \quad (2.113)$$

Rearranging the coefficients, one obtains

$$\left[s_{21} \ s_{22} \mid d_{21} \ d_{22} \mid d_{11} \ d_{12} \ d_{13} \ d_{14} \right]^T . \quad (2.114)$$

Thus, the wavelet coefficients characterizing the signal at different scales are separated. The resulting coefficients can be used for signal recognition, e.g., to recognize the impulse activity of single neurons from the common activity of the neuron ensemble which is considered in the next chapter.

References

1. J. Morlet, G. Arens, E. Fourgeau, D. Glard, Wave propagation and sampling theory. Part I: complex signal and scattering in multilayered media. *Geophysics* **47**(2), 203 (1982)
2. J. Morlet, G. Arens, E. Fourgeau, D. Giard, Wave propagation and sampling theory. Part II: sampling theory and complex waves. *Geophysics* **47**(2), 222 (1982)
3. A. Grossman, J. Morlet, Decomposition of Hardy function into square integrable wavelets of constant shape. *SIAM J. Math. Anal.* **15**(4), 273 (1984)
4. M. Holschneider, *Wavelets: An Analysis Tool* (Oxford University Press, Oxford, 1995)
5. M. Farge, J.C. Hunt, J.C. Vassilicos, *Wavelets, Fractals and Fourier Transforms* (Oxford University Press, Oxford, 1995)
6. A. Aldroubi, M. Unser, *Wavelets in Medicine and Biology* (CRC, Boca Raton, 1996)
7. R.T. Ogden, *Essential Wavelets for Statistical Applications and Data Analysis* (Birkhäuser, Boston/Berlin, 1997)
8. C. Torrence, G.P. Compo, A practical guide to wavelet analysis. *Bull. Am. Meteorol. Soc.* **79**, 61 (1998)

9. D.A. Yuen, A.P. Vincent, M. Kido, L. Vecsey, Geophysical applications of multidimensional filtering with wavelets. *Pure Appl. Geophys.* **159**, 2285 (2001)
10. J.C. van den Berg, *Wavelets in Physics* (Cambridge University Press, Cambridge, 2004)
11. R. Gencay, F. Selcuk, B. Whitcher, *An Introduction to Wavelets and Other Filtering Methods in Finance and Economics* (Academic, San Diego, 2001)
12. R. Carmonia, *Practical Time–Frequency Analysis* (Academic, New York, 1998)
13. S.G. Mallat, *A Wavelet Tour of Signal Processing* (Academic, New York, 1998)
14. M.B. Ruskai, G. Beylkin, R. Coifman, I. Daubechies, S.G. Mallat, Y. Meyer, L. Raphael, *Wavelets and Their Applications and Data Analysis* (Jones and Bartlett, Boston, 1992)
15. G. Kaiser, *A Friendly Guide to Wavelets* (Springer/Birkhauser, Boston, 1994)
16. A.A. Koronovskii, A.E. Hramov, *Continuous Wavelet Analysis and Its Applications* (Fizmatlit, Moscow, 2003)
17. C. Blatter, *Wavelets: A Primer* (A.K. Peters, Natick, 1998)
18. Y. Meyer, *Wavelets: Algorithms and Applications* (SIAM, Philadelphia, 1993)
19. I. Daubechies, *Ten Lectures on Wavelets* (SIAM, Philadelphia, 1992)
20. Y. Meyer, *Wavelets and Operators* (Cambridge University Press, Cambridge, 1992)
21. N.M. Astafyeva, Wavelet analysis: spectral analysis of local perturbations. *Appl. Nonlinear Dyn.* **4**(2), 3 (1996)
22. J.C. Goswami, A.K. Chan, *Fundamentals of Wavelets: Theory, Algorithms, and Applications* (Wiley, Hoboken, 2011)
23. T. Paul, Function analytic on half-plane as quantum mechanical states. *J. Math. Phys.* **24**(25), 136 (1984)
24. M. Farge, Wavelet transforms and their applications to turbulence. *Annu. Rev. Fluid Mech.* **24**, 395 (1992)
25. P. Sliwinski, *Nonlinear System Identification by Haar Wavelets* (Springer, Berlin/Heidelberg, 2013)
26. I. Daubechies, The wavelet transform, time–frequency localization and signal analysis. *IEEE Trans. Inf. Theory* **36**, 961–1004 (1990)
27. S.G. Mallat, Multiresolution approximation and wavelet orthonormal bases of $L^2(R)$. *Trans. Am. Math. Soc.* **315**, 69 (1989)
28. P.G. Lemarie, Y. Meyer, Ondelettes et bases hilbertiennes. *Revista Matemática Iberoamericana* **2**, 1 (1986)
29. G. Battle, A block spin construction of ondelettes. Part 1. *Commun. Math. Phys.* **110**, 607 (1987)
30. V.A. Gusev, A.A. Koronovskii, A.E. Hramov, Application of adaptive wavelet bases to analysis of nonlinear systems with chaotic dynamics. *Tech. Phys. Lett.* **29**(18), 61 (2003)
31. A.E. Hramov, A.A. Koronovskii, V.I. Ponomarenko, M.D. Prokhorov, Detecting synchronization of self-sustained oscillators by external driving with varying frequency. *Phys. Rev. E* **73**(2), 026208 (2006)
32. A.E. Hramov, A.A. Koronovskii, V.I. Ponomarenko, M.D. Prokhorov, Detection of synchronization from univariate data using wavelet transform. *Phys. Rev. E* **75**(5), 056207 (2007)
33. R.K. Otnes, L. Enochson, *Applied Time Series Analysis* (Wiley, New York/Chichester/Toronto, 1978)
34. I. Daubechies, Orthogonal bases of compactly supported wavelets. *Comput. Appl. Math.* **41**(7), 906 (1988)
35. S.D. Meyers, B.G. Kelly, J.J. O’Brien, An introduction to wavelet analysis in oceanography and meteorology: with application to the dispersion of Yanai waves. *Mon. Weather Rev.* **121**, 2858 (1993)
36. M. Farge, E. Coirand, Y. Meyer, F. Pascal, Improved predictability of two dimensional turbulent flows using wavelet packet compression. *Fluid Dyn. Res.* **10**, 229 (1992)
37. V.S. Anishchenko, T.E. Vadivasova, D.E. Postnov, M.A. Safonova, Synchronization of chaos. *Int. J. Bifurc. Chaos* **2**(3), 633 (1992)
38. N.F. Rulkov, A.R. Volkovskii, A. Rodriguez-Lozano, E. Del Rio, M.G. Velarde, Synchronous chaotic behaviour of a response oscillator with chaotic driving. *Chaos Solitons Fractals* **4**, 201 (1994)

39. A. Shabunin, V. Astakhov, J. Kurths, Quantitative analysis of chaotic synchronization by means of coherence. *Phys. Rev. E* **72**(1), 016218 (2005)
40. A.E. Hramov, A.A. Koronovskii, M.K. Kurovskaya, O.I. Moskalenko, Synchronization of spectral components and its regularities in chaotic dynamical systems. *Phys. Rev. E* **71**(5), 056204 (2005)
41. I. Noda, Y. Ozaki, *Two-Dimensional Correlation Spectroscopy: Applications in Vibrational and Optical Spectroscopy* (Wiley, Chichester, 2002)
42. A.S. Pikovsky, M.G. Rosenblum, J. Kurths, Phase synchronisation in regular and chaotic systems. *Int. J. Bifurc. Chaos* **10**(10), 2291 (2000)
43. P. Bergé, Y. Pomeau, C. Vidal, *L'Ordre dans le Chaos* (Hermann, Paris, 1988)
44. F.C. Moon, *Chaotic Vibrations: An Introduction for Applied Scientists and Engineers* (Wiley, Hoboken, 2004)
45. L.M. Pecora, T.L. Carroll, Synchronization in chaotic systems. *Phys. Rev. Lett.* **64**(8), 821 (1990)
46. M.G. Rosenblum, A.S. Pikovsky, J. Kurths, From phase to lag synchronization in coupled chaotic oscillators. *Phys. Rev. Lett.* **78**(22), 4193 (1997)
47. N.F. Rulkov, M.M. Sushchik, L.S. Tsimring, H.D. Abarbanel, Generalized synchronization of chaos in directionally coupled chaotic systems. *Phys. Rev. E* **51**(2), 980 (1995)
48. S. Fahy, D.R. Hamann, Transition from chaotic to nonchaotic behavior in randomly driven systems. *Phys. Rev. Lett.* **69**(5), 761 (1992)
49. A. Maritan, J.R. Banavar, Chaos, noise and synchronization. *Phys. Rev. Lett.* **72**(10), 1451 (1994)
50. R. Toral, C.R. Mirasso, E. Hernández-García, O. Piro, Analytical and numerical studies of noise-induced synchronization of chaotic systems. *Chaos Interdiscip. J. Nonlinear Sci.* **11**(3), 665 (2001)
51. A.A. Koronovskii, A.E. Hramov, Wavelet transform analysis of the chaotic synchronization of dynamical systems. *JETP Lett.* **79**(7), 316 (2004)
52. A.E. Hramov, A.A. Koronovskii, An approach to chaotic synchronization. *Chaos Interdiscip. J. Nonlinear Sci.* **14**(3), 603 (2004)
53. A.E. Hramov, A.A. Koronovskii, Time scale synchronization of chaotic oscillators. *Phys. D* **206**(3–4), 252 (2005)
54. A.E. Hramov, A.A. Koronovskii, P.V. Popov, I.S. Rempen, Chaotic synchronization of coupled electron–wave systems with backward waves. *Chaos Interdiscip. J. Nonlinear Sci.* **15**(1), 013705 (2005)
55. M.G. Rosenblum, A.S. Pikovsky, J. Kurths, Phase synchronization of chaotic oscillators. *Phys. Rev. Lett.* **76**(11), 1804 (1996)
56. G.V. Osipov, A.S. Pikovsky, M.G. Rosenblum, J. Kurths, Phase synchronization effect in a lattice of nonidentical Rössler oscillators. *Phys. Rev. E* **55**(3), 2353 (1997)
57. M.G. Rosenblum, J. Kurths, in *Nonlinear Analysis of Physiological Data*, ed. by H. Kantz, J. Kurths (Springer, Berlin, 1998), pp. 91–99
58. A.S. Pikovsky, M.G. Rosenblum, G.V. Osipov, J. Kurths, Phase synchronization of chaotic oscillators by external driving. *Phys. D* **104**(4), 219 (1997)
59. J.P. Lachaux, et al., Studying single-trials of the phase synchronization activity in the brain. *Int. J. Bifurc. Chaos* **10**(10), 2429 (2000)
60. R.Q. Quiroga, A. Kraskov, T. Kreuz, P. Grassberger, Performance of different synchronization measures in real data: a case study on electroencephalographic signals. *Phys. Rev. E* **65**, 041903 (2002)
61. V.S. Anishchenko, T.E. Vadivasova, Relationship between frequency and phase characteristics. Two criteria of synchronization. *J. Commun. Technol. Electron.* **49**, 69 (2004)
62. A.S. Pikovsky, M.G. Rosenblum, J. Kurths, *Synchronization: A Universal Concept in Nonlinear Sciences* (Cambridge University Press, Cambridge, 2001)
63. A.S. Pikovsky, M.G. Rosenblum, J. Kurths, Synchronization in a population of globally coupled chaotic oscillators. *Europhys. Lett.* **34**(3), 165 (1996)

64. M.G. Rosenblum, A.S. Pikovsky, J. Kurths, Locking-based frequency measurement and synchronization of chaotic oscillators with complex dynamics. *Phys. Rev. Lett.* **89**(26), 264102 (2002)
65. A.E. Hramov, A.A. Koronovskii, Y. Levin, Synchronization of chaotic oscillator time scales. *J. Exp. Theor. Phys.* **127**(4), 886 (2005)
66. L. Glass, M.C. Mackey, *From Clocks to Chaos: The Rhythms of Life* (Princeton University Press, Princeton, 1988)
67. S. Boccaletti, J. Kurths, G.V. Osipov, D.L. Valladares, C.S. Zhou, The synchronization of chaotic systems. *Phys. Rep.* **366**, 1 (2002)
68. A.G. Balanov, N.B. Janson, D.E. Postnov, O.V. Sosnovtseva, *Synchronization: From Simple to Complex* (Springer, Berlin, 2009)
69. A.A. Koronovskii, A.A. Ovchinnikov, A.E. Hramov, Experimental study of the time-scale synchronization in the presence of noise. *Phys. Wave Phenom.* **18**(4), 262 (2010)
70. R.A. Filatov, A.E. Hramov, A.A. Koronovskii, Chaotic synchronization in coupled spatially extended beam-plasma systems. *Phys. Lett. A* **358**, 301 (2006)
71. E. Sitnikova, A.E. Hramov, A.A. Koronovskii, E.L. Luijtelaar, Sleep spindles and spike-wave discharges in EEG: their generic features, similarities and distinctions disclosed with Fourier transform and continuous wavelet analysis. *J. Neurosci. Methods* **180**, 304 (2009)
72. P. Flandrin, Some aspects of non-stationary signal processing with emphasis on time-frequency and time-scale methods, in *Wavelets*, ed. by J.M. Combes, A. Grossmann, Ph. Tchamitchian (Springer, Berlin/Heidelberg, 1989), pp. 68–98
73. G. Buzsaki, A. Draguhn, Neuronal oscillations in cortical networks. *Science* **304**, 1926 (2004)
74. P.S. Addison, *The Illustrated Wavelet Transform Handbook: Introductory Theory and Applications in Science Engineering, Medicine and Finance* (Institute of Physics Publishing, Bristol, 2002)
75. M. Vetterli, J. Kovacevic, *Wavelets and Subband Coding* (Prentice Hall, New York, 1995)
76. I.M. Dremmin, O.V. Ivanov, V.A. Nechitailo, Wavelets and their uses. *Physics-Uspokhi* **44**(5), 447 (2001)

Chapter 3

Analysis of Single Neuron Recordings

Abstract In this chapter, we consider several practical problems where wavelets provide information about the dynamics of neuronal systems that cannot be obtained with ordinary frequency or time domain methods. We discuss the possibility of studying intracellular dynamics and information encoding by individual neurons. We characterize the dynamical stability of the neuronal response and propose an approach to quantify wavelet coherence.

3.1 Introduction

The central nervous system (CNS) of living beings processes a large amount of sensory information that is received through interaction with the external world. A study of how this information is encoded, represented, and processed is one of the most important problems in the natural sciences.

Optical, sonic, tactile, and other stimuli are encoded by the corresponding receptors into sequences of electrical pulses (spikes) that are transferred to the first neurons, i.e. to the areas of the CNS that carry out preprocessing. Sensory information passes through several other processing stages before reaching the cortex, where an internal representation (or image) of the external world is formed.

The complexity of experimental studies of the corresponding processes increases significantly with each subsequent stage. Though the molecular and ionic mechanisms underlying encoding are rather well understood [1, 2], the properties of spike trains as information carriers remain less clear: How do these trains reflect the enormous complexity and variety of the external world? There are many open questions regarding the principles of information encoding by individual neurons and their networks, even at the initial information processing stage.

In Chap. 2 we provided a short introduction to the theory and practice of wavelet analysis. Let us now apply this knowledge to several practical problems in which wavelets can offer information about the dynamics of neuronal systems that would be inaccessible to ordinary frequency or time domain methods.

In general, these problems can be separated into groups depending on the chosen mathematical approach, i.e., either the continuous or the discrete wavelet transform. However, as already mentioned, both approaches can provide useful information about the object under study, although this information may differ. Therefore, a better choice is to separate tasks according to the subject of research. In our case it is reasonable to sort out problems according to the spatial scale and complexity of the analyzed signals. In this chapter we shall deal with single neuron recordings, i.e., signals recorded from one neuron, even if it is a part of a network. We shall also consider different types of recording: in studies of intracellular dynamics we work with continuous signals (data from interference microscopy), whereas for the investigation of information processing we use spike trains (point processes) extracted from extracellular single unit recordings.

3.2 Wavelet Analysis of Intracellular Dynamics

At the single neuron level, cell activity includes a large number of biochemical processes that occur on different time scales in the membrane and in the cell cytoplasm. Traditional experimental approaches such as, e.g., fluorescent microscopy, intracellular recordings of the membrane potential, and patch-clamping provide ways to analyze features of biochemical, metabolic, and electrical processes. Often, however, they are highly invasive and may have a significant impact on the intracellular dynamics.

Since intracellular dynamics can be extremely rich and manifests itself on different time scales, the wavelet approach proves very useful. It can provide information about the interplay between different processes and help to achieve a deeper understanding of intracellular regulatory mechanisms. In this section we discuss a study of intracellular dynamics using interference microscopy and wavelet-based techniques.

3.2.1 *Interference Microscopy and Subcellular Dynamics*

Interference microscopy measures the optical path difference between the beam transmitted through an object and a reference beam [3, 4]. The resulting value is normalized to the wavelength to estimate the so-called phase height of the object, which is given by

$$\Phi = \frac{\phi_0 - \phi_{\text{obj}}}{2\pi} \frac{\lambda}{2} - \Phi_0, \quad (3.1)$$

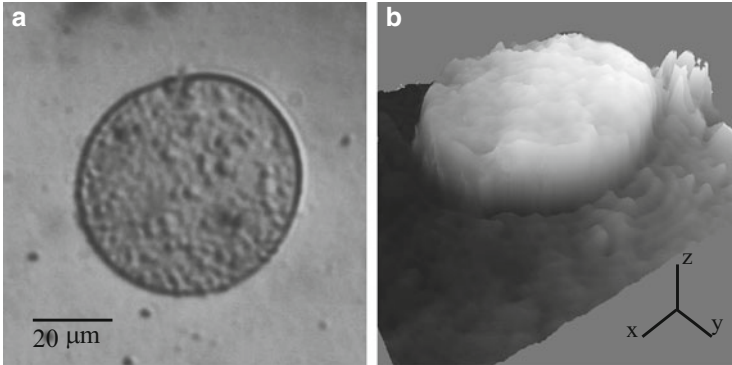


Fig. 3.1 Isolated pond snail neuron. (a) Optical photograph of the neuron. (b) Phase height landscape of the same neuron obtained by interference microscopy (wavelength $\lambda = 532$ nm). Bars in the x and y directions correspond to $10 \mu\text{m}$, and the bar in the z direction corresponds to a phase height of 200 nm (for details, see [5])

where ϕ_0 is the initial phase, ϕ_{obj} is the phase shift that occurs after the laser beam is transmitted through the analyzed object, λ is the laser wavelength, and Φ_0 is a constant shift of the phase height depending on the selected reference point.

For inhomogeneous objects characterized by a refractive index that varies along the vertical direction z , the phase height is estimated as

$$\Phi(x, y) = \int_0^Z [n_{\text{obj}}(x, y, z) - n_s] dz - \Phi_0, \quad (3.2)$$

where n_s is the constant refractive index of the physiological saline and $n_{\text{obj}}(x, y, z)$ is the refractive index of the cell at a point (x, y, z) placed at the distance z from the mirror. The integration limit Z is selected to be above the whole object.

By scanning a cell in the horizontal (x, y) plane, the interference microscope measures the phase height landscape $\Phi(x, y)$. Figure 3.1 shows side-by-side an example of an optical photograph and a phase height landscape of an isolated pond snail neuron. Movements of, e.g., organelles in the cell change $n_{\text{obj}}(x, y, z)$, and hence the phase height in the corresponding place. By scanning a cell many times with constant time interval, we can obtain frames as in a movie. The resulting dynamics of the phase height $\Phi(x, y; t)$ can then be used to monitor different intracellular processes.

Here we consider results obtained from experiments performed with isolated neurons from the buccal ganglia of the pond snail *L. stagnalis*. We measured the phase height at a single point (x, y) inside the cell. Figure 3.2a shows the power spectrum of such a signal. It exhibits a number of characteristic frequencies near 0.1, 0.3, 0.6, 1.2, and 3.0 Hz. These rhythms are caused by movements of protein macromolecules, changes in ion concentration near the membrane, fluctuations in the membrane potential, etc. Many of these intracellular processes interact with one other.

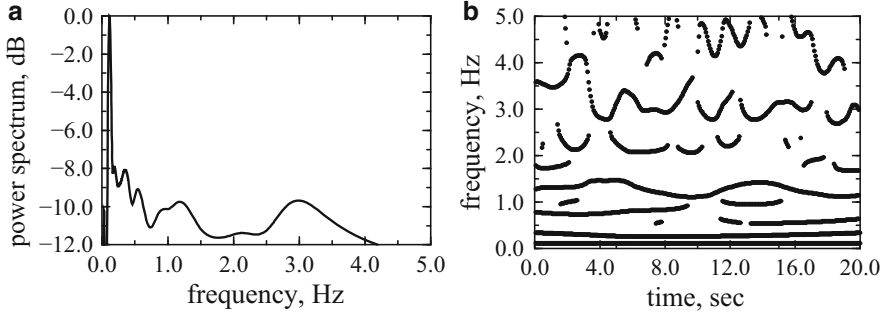


Fig. 3.2 Analysis of the phase height dynamics reflecting intracellular processes. **(a)** Energy spectrum exhibiting several peaks. Frequency peaks correspond to different rhythmic components in the intracellular dynamics. **(b)** Extracted ridges of the wavelet coefficients, obtained after the wavelet transform of the phase height

3.2.2 Modulation of High Frequency Oscillation by Low Frequency Processes

To reveal possible interactions between different rhythmic components, we applied the continuous wavelet transform with the Morlet mother function to the phase height signal. Then we identified instantaneous frequencies and amplitudes of rhythmic contributions.

Figure 3.2b illustrates a typical example of the dynamics of instantaneous frequencies. Rhythmic components in the range from 0.1 to 0.3 Hz have almost constant frequency, while instantaneous frequencies of rhythms near 1 and 3 Hz show slow oscillations [5, 6]. Thus, the processes characterized by long time scales modulate high-frequency oscillations of the phase height. This type of modulation is a well-known phenomenon in living systems. As an example, we can mention the modulation of the heart rate by breathing. The duration of beat-to-beat intervals varies at different stages of the breathing process.

There exist several types of low frequency modulation of a high-frequency process. During modulation, the amplitude $A(t)$ and/or the frequency $\omega(t)$ of a fast oscillation $x(t)$ can vary with the frequency of a slow process $z(t)$.

In the case of so-called amplitude modulation (AM), we can write

$$A(t) = A_0 + \Delta A z(t), \quad (3.3)$$

where A_0 is the base-line amplitude of the fast oscillation and ΔA is the maximal deviation of the amplitude (for convenience, we assume that $|z(t)| \leq 1$). A single-tone modulated signal (with single frequency ω_0) is given by

$$x(t) = A(t) \cos(\omega_0 t + \varphi_0) = A_0 [1 + m_a z(t)] \cos(\omega_0 t + \varphi_0), \quad (3.4)$$

where $m_a = \Delta A/A_0$ is called the amplitude modulation index or the modulation depth, and φ_0 is the initial phase. The modulation depth is a bounded constant with $m_a \in [0, 1]$. If $m_a = 0$, then no modulation exists, whereas $m_a = 1$ corresponds to maximal modulation when the signal amplitude occasionally goes to zero.

Frequency modulation (FM) is another type of modulation. In this case the instantaneous frequency of the signal $x(t)$ can be written as

$$\omega(t) = \omega_0 + \Delta\omega z(t) \quad (3.5)$$

where ω_0 is the base frequency and $\Delta\omega$ is the maximal deviation of the frequency. Then an FM signal can be written as

$$x(t) = A_0 \cos[\Psi(t) + \varphi_0], \quad \Psi(t) = \int_0^t \omega(s) ds, \quad (3.6)$$

or using (3.5),

$$x(t) = A_0 \cos\left[\omega_0 t + \varphi_0 + \Delta\omega \int_0^t z(s) ds\right]. \quad (3.7)$$

In the case of a single-tone FM-signal $z(t) = \cos(\Omega t + \Phi_0)$ and therefore

$$x(t) = A_0 \cos\left[\omega_0 t + \varphi_0 + m_f \sin(\Omega t + \Phi_0)\right], \quad (3.8)$$

where $m_f = \Delta\omega/\Omega$ is the frequency modulation index, which characterizes the depth of modulation of the FM signal, which can take values greater than 1.

In terms of modulation, the processes of slowly varying frequency ridges shown in Fig. 3.2b can be classified as FM processes.

3.2.3 Double Wavelet Transform and Analysis of Modulation

The nonstationary dynamics which is frequently observed in living systems always has multi-tone oscillations. Then the equations describing modulated processes become complicated and the values used to compute modulation indexes become time-dependent. To describe such phenomena and their structure, a double wavelet transform has been proposed [7].

First, we apply an ordinary wavelet transform to the analyzed signal. Then the second wavelet transform is applied to signals constructed from instantaneous frequencies (or amplitudes) of modulated rhythmic processes. Again, as in the first wavelet transform, CWT coefficients are estimated and the ridges of the wavelet energy are identified. Since the wavelet transform is applied twice, this method has been called the double-wavelet analysis [7]. A similar idea called the *secondary*

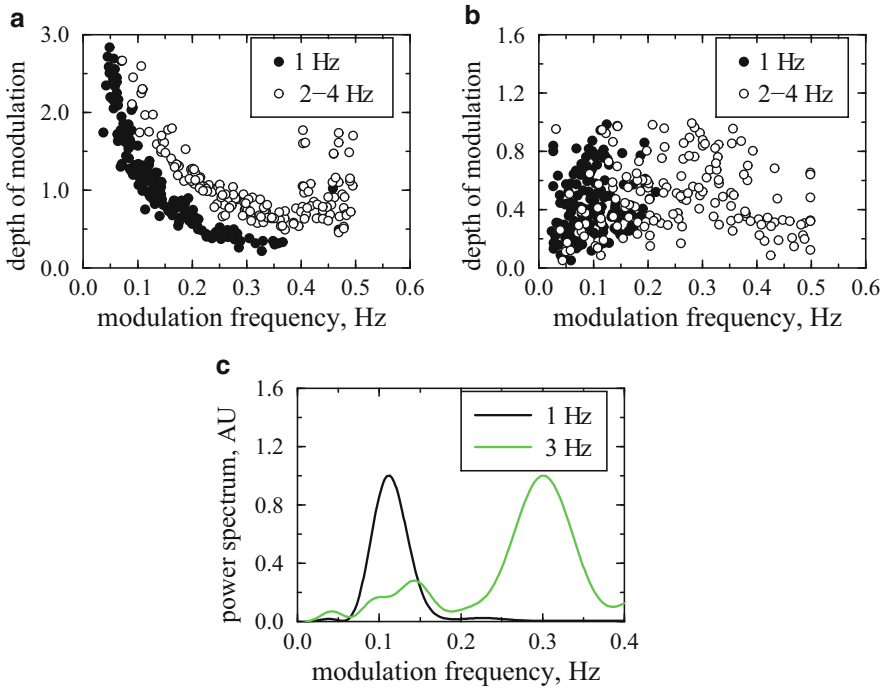


Fig. 3.3 Double wavelet analysis of the phase height dynamics of single cells. **(a)** Frequency modulation of 1 and 2–4 Hz rhythmic components by slow processes. Modulation depth vs frequency of the slow process. **(b)** The same as in **(a)**, but for amplitude modulation. **(c)** Typical normalized spectra of the modulation processes

wavelet transform has been proposed independently by Addison and Watson [8]. This approach allows one to obtain a time series for such characteristics as the amplitude (or frequency) deviation, time-varying modulation indexes, and local spectra of modulation [9].

In addition to the FM process shown in Fig. 3.2b, analysis of the phase height dynamics can reveal FM modulation of the amplitude of high-frequency oscillations by slower dynamics. To obtain statistical information about features of AM and FM phenomena in the dynamics of intracellular processes, we repeated the above described experiments 200 times [5]. Then for each measurement we estimated the modulation frequencies and modulation indexes (modulation depths) using the double-wavelet technique.

Figures 3.3a and b illustrate the distributions of the modulation indexes for FM and AM, respectively. In the FM case, there is clear difference between the two rhythms. The modulation depth is higher for the 2–4 Hz oscillation. In the AM case the 2–4 Hz rhythm generally has a higher modulation frequency. Figure 3.3c shows a typical example of the power spectra of the modulation processes for

each rhythm. Thus, the rhythmic components near 1 and 3 Hz are modulated by different intracellular processes. The rhythm near 1 Hz is mainly modulated by a process with ultralow frequency around 0.1 Hz, while the 3 Hz rhythm is modulated by a higher-frequency dynamics.

In conclusion, the double wavelet analysis revealed the presence of an interaction between slow and fast rhythmic intracellular processes. This interaction occurs in the form of modulation. We associate low-frequency dynamics with processes occurring in the plasma membrane, while high-frequency processes are associated with cytoplasmic events. Evidence for such an assumption is discussed in [10]. Thus, low-frequency oscillations are significantly more pronounced in the membrane region than in the centre of neurons, while the 20–25 Hz rhythms display the opposite behaviour [6]. Moreover, independent experiments on the same type of neurons demonstrated the existence of rhythmic dynamics. In particular, it has been established [11] that frequencies in the range of 0.2–0.4 Hz depend on the activity of Ca^{2+} channels. It has also been found [12] that neurons in invertebrates possess intrinsic electrical activity with frequencies 1 and 1.5–3 Hz. The suggestion about the origin of high frequencies (20–25 Hz) from cytoplasm processes accords with experimental data on vesicle movements in neurons (8–40 Hz) obtained by light-scattering measurements [13].

We note that the double-wavelet approach allows a better understanding of neuron functions and features of intracellular dynamics, both under normal conditions and under different external influences. This approach provides quantitative measures characterizing the interplay among intracellular processes and allows one to diagnose changes in this interplay when there are external influences (see, e.g., [6]).

3.2.4 *Modulation of Spike Trains by Intrinsic Neuron Dynamics*

Neurons encode and exchange information in the form of spike trains. Figure 3.4a shows a typical example of the extracellular potential recorded in the vicinity of a projecting neuron in the gracilis nucleus. The trace has a number of spikes (short pulses) that are clearly distinguishable over the background activity. In Chap. 4, we shall discuss the problem of spike identification and sorting in more detail. Here we just cross-check that all spikes belong to the same cell. This can be done by superposing spikes (Fig. 3.4b). We can verify that all of them have a similar shape and hence can be classified as emitted by only one neuron.

The first part of the recording corresponds to spontaneous neuron dynamics (no external stimulation), while the second represents the neuron response to stimuli (a slight pricking of the rat foreleg with frequency of 1 Hz). We observe that the stimulation drastically changes the firing rate of the neuron. Moreover, the structure of neural firing shows some signs of modulation. The analysis of modulation

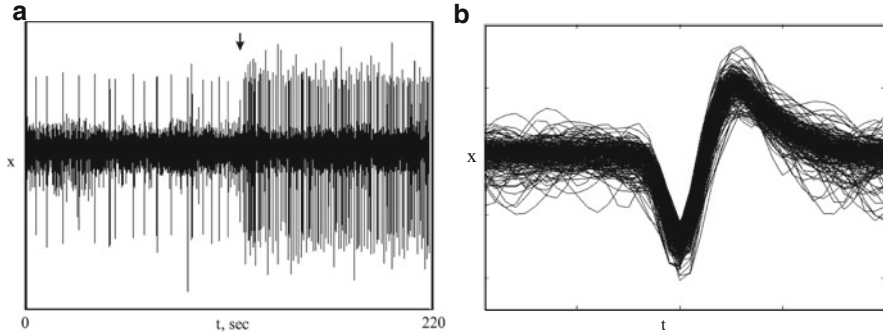


Fig. 3.4 Experimental recording of spiking activity in a single neuron. (a) Extracellular potential with spikes generated by only one projecting neuron in the gracilis nucleus of a rat. The *arrow* marks the beginning of external (tactile) stimulus. (b) Superposed spikes exhibit the same shape, which confirms that they belong to the same neuron

phenomena discussed in Sect. 3.2.3 can also be applied to this spike train. In general, this approach can lead to a deeper understanding of the information encoding used by neurons.

The structure of interspike intervals without external stimulation is quite irregular, whereas under stimulation a well pronounced rhythm appears at the frequency of the external stimulation (Fig. 3.5a, b). To reveal the time dynamics of different rhythms in the spike train, we apply the wavelet transform (with the Morlet mother wavelet) to interspike intervals. The spontaneous neuron dynamics exhibits several rhythms. The two most powerful of these correspond to 8 and 20 s interspike intervals (Fig. 3.5a, c, peaks at 0.05 and 0.125 Hz). Under stimulation, a clear peak appears in the power spectrum at the driving frequency of 1 Hz and the ultralow frequency (0.05 Hz) disappears. However, the low-frequency dynamics observed under spontaneous conditions remains in the spectrum (Fig. 3.5b).

Figure 3.5c, d show the time–frequency spectrograms. Under control conditions (spontaneous firing), there are several rhythms whose frequencies “float” around certain mean values. The sensory stimulus excites a new oscillation at 1 Hz, which again shows some oscillations. Thus, the neuron has some intrinsic dynamics even under stimulation. This provides evidence for a nonlinear interaction between the rhythmic components in neuron dynamics and raises an open question: Is it possible to describe the process of information encoding in terms of frequency modulation?

Indeed, one possible interpretation of the oscillation observed in the main 1 Hz rhythm (Fig. 3.5d) can be given in terms of frequency modulation. The idea is that the intrinsic slow dynamics of the neuron modulates the stimulus driven frequency. Therefore, information encoding by this neuron is not trivial, but includes additional features describing the neuronal state, feedbacks, and even some temporal history of oscillations. On the basis of this hypothesis, modulation features such as the central frequency, depth index, etc., can be estimated using the double-wavelet technique (Sect. 3.2.3).

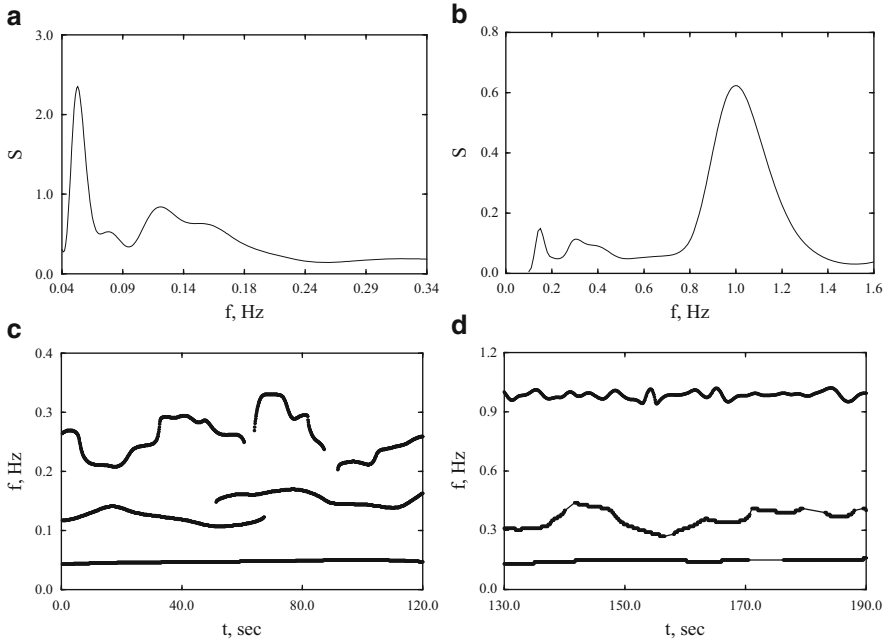


Fig. 3.5 Analysis of interspike intervals in the neuronal spike train shown in Fig. 3.4. **(a)** and **(b)** Power spectra under spontaneous conditions and under stimulation, respectively. **(c)** and **(d)** Time–frequency dynamics of wavelet ridges under spontaneous conditions and under stimulation, respectively

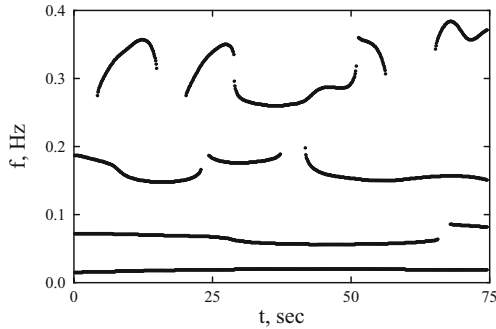


Fig. 3.6 Rhythmic components taking part in the frequency modulation of the neuron response to the 1 Hz stimulus

The instantaneous frequency around 1 Hz is considered as a new signal for the CWT. As a result, all rhythms occurring in the modulation will be revealed and the depth of modulation can be estimated separately for each rhythm. Figure 3.6 shows that the structure of low-frequency modulating signals is quite similar to

the spontaneous dynamics of the neuron. This indirectly confirms the hypothesis. However, physiological interpretation of the observed phenomena and direct ways of testing the hypothesis require more detailed analysis.

3.3 Information Encoding by Individual Neurons

In Sect. 3.2.4, we saw that neurons can encode sensory stimuli in a rather complex way. Besides extrinsic stimuli, some intrinsic neuronal dynamics enters the output spike train transmitted to further relay stations of the central nervous system. Let us now consider information encoding in more detail.

3.3.1 *Vibrissae Somatosensory Pathway*

The rodent vibrissae system is one of the most widely used experimental models for the study of sensory information handling. The rat perceives the main information by means of the vibrissal pad or “whiskers” (Fig. 3.7a). This is a highly specialized and sensitive piece of apparatus that conveys tactile signals via the trigeminal system to the animal’s brain (Fig. 3.7b) [14].

The four longest vibrissae, called straddlers, are labeled by the letters α , β , γ , and δ . The other vibrissae are placed on the upper lip in five rows labeled by the letters A , B , C , D , and E . In each row, the vibrissae are numbered, e.g., A_1 , A_2 , etc. The length of the vibrissae varies from 30–50 to 4–5 mm, thus providing simultaneous contact of their tips with a tangible surface of an object during whisker movements. The different lengths and widths of vibrissae provide them with different oscillatory features. This allows them to cover the wide range of frequencies required for effective perception of objects with different tactile characteristics.

Rats actively use their whiskers to detect and localize objects, and also to discriminate surface textures. By sweeping the whiskers at rates between 5–20 Hz, they can localize and identify objects within a few whisking cycles or even with a single vibrissa [15]. Thus relatively short temporal, but not spatial mechanical information, dominates in the object detection.

Mechanical encoding of different textures is attributed to the whisker resonance. The vibration amplitude across the whisker array codifies the texture (see, e.g., [16]). It occurs also in awake rats and shapes natural whisker vibration. However, it seems that textures are not encoded by the differential resonance. Instead, slip–stick events contribute to a kinetic signature for texture in the whisker system, which suggests the presence of temporal structure in neural spike trains under these experimental conditions [17]. Thus the efficacy of the sensory information transmission and processing in the time domain resides in the possibility for multiple cells to generate coherent responses to a stimulus, which constitutes the neural code.

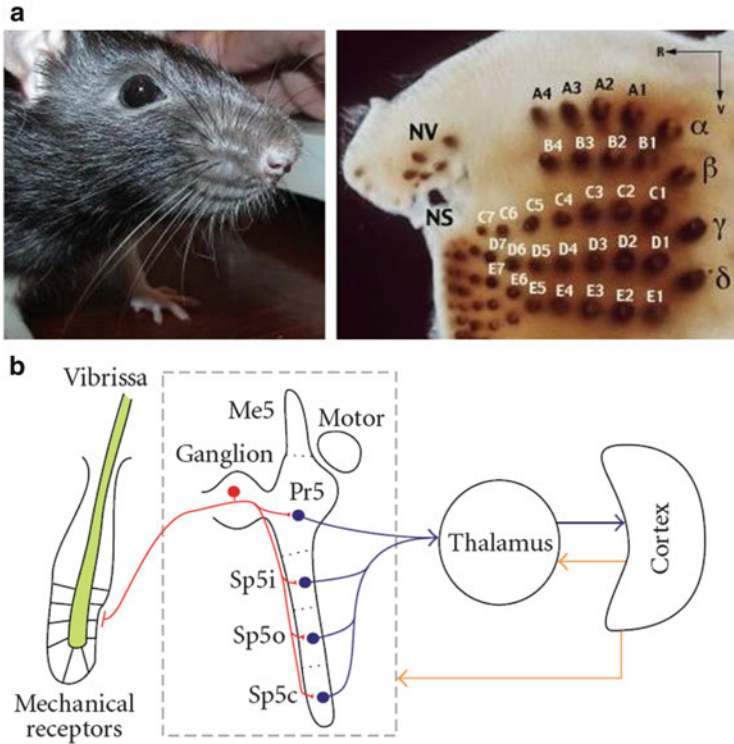


Fig. 3.7 Rat vibrissae system. (a) Illustration of vibrissae and their labeling. (b) Sketch of the main steps in the pathway of tactile information processing

Although there has been much discussion about what type of neural code is employed by each individual neuron or neuron group, growing experimental evidence shows that the same neuron may use different coding schemes (see reviews in [18, 19]). The temporal correlation of multiple cell discharges has also been found important for information transmission to the cortex and its modulation by corticofugal feedback (see, e.g., [20–22]).

Somatosensory information from the whiskers arrives at the trigeminal complex, organized into one motor and three sensory nuclei, including the principal nucleus or principalis (Pr5), the spinal nucleus (Sp5), and the mesencephalic nucleus (Fig. 3.7b). In turn, Sp5 consists of three subnuclei called oralis (Sp5o), interparialis (Sp5i), and caudalis (Sp5c). Information from Pr5 and Sp5 goes to the contralateral thalamus (VPM) and then to the primary somatosensory (SI) cortex. There is also a feedback monosynaptic projection with an extremely precise somatotopy from SI to the trigeminal nuclei.

Over the whole pathway, primary afferents and neurons form spatial structures called barrelettes, berreloids, and barrels in the trigeminal complex, VPM, and SI, respectively. These spatial structures replicate the patterned arrangement of the whisker follicles on the snout (for details see, e.g., [23–26]).

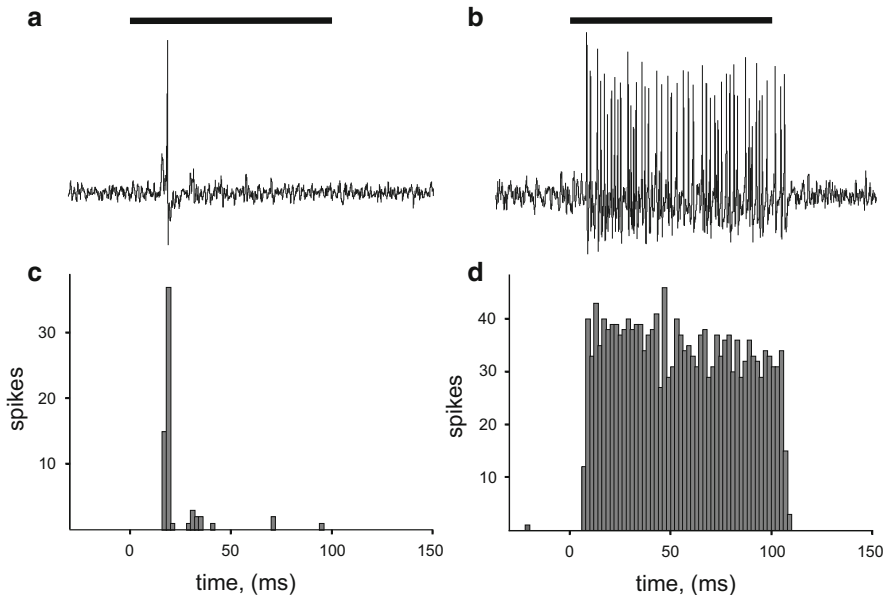


Fig. 3.8 Classification of neurons into phasic and tonic types, according to their response to a long stimulus. (a) Typical response of a phasic neuron to a single stimulus. The extracellular potential recorded in the trigeminal nucleus is shown. The *upper horizontal bar* corresponds to the duration of the stimulus. (c) Peristimulus histogram of a phasic neuron made over 50 identical stimuli (2 ms bin). (b) and (d) The same as in (a) and (c), but for a tonic neuron

3.3.2 Classification of Neurons by Firing Patterns

In electrophysiological studies, the classification of neurons according to their firing patterns for spontaneous activity and under stimulation is widely accepted. Neurons can be divided into three groups according to their mean firing rate (MFR) under spontaneous conditions: silent neurons (SN) with $\text{MFR} < 0.1$ spikes/s, low-frequency (LF) neurons with $0.1 < \text{MFR} < 1.5$ spikes/s, and high-frequency (HF) neurons with $\text{MFR} > 1.5$ spikes/s.

For tactile whisker stimulation, short air puffs directed toward a single vibrissa are usually used. This kind of stimulation produces vibrations of the individual whisker similar to real behavioral conditions. In experiments, the duration of air puffs can be varied. We used three values: short 10 ms, intermediate 50 ms, and long 100 ms pulses. Trigeminal neurons fired from 1 to 8 spikes in response to each onset of tactile stimulation of 10 and 50 ms duration. For the long (100 ms) stimulus, some of the neurons produced from 20 to 40 spikes.

Taking into account the neural responses to the 100 ms stimuli, we can classify all neurons into tonic and phasic [27]. Figure 3.8 shows an example of each neuronal type. Phasic neurons (PhN) generate a few spikes under a change of stimulus phase,

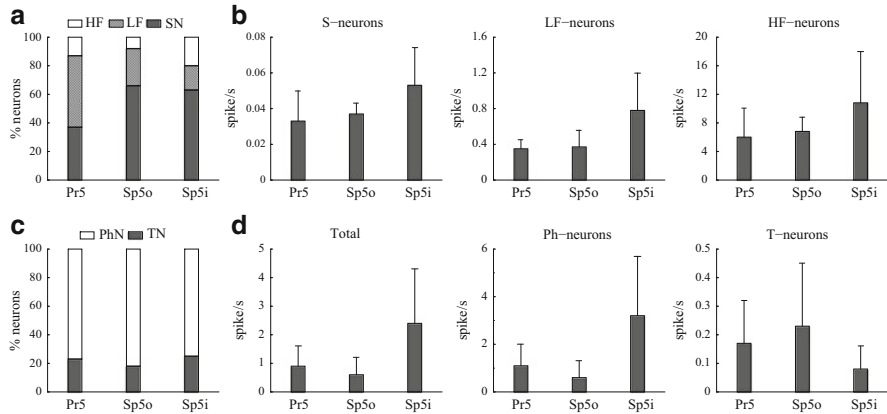


Fig. 3.9 Statistical properties of neurons in Pr5, Sp5i, and Sp5o trigeminal nuclei. (a) Distribution of neurons according to spontaneous activity: SN silent, LF low frequency, and HF high-frequency neurons. (b) Mean spiking frequencies of SN, LF, and HF cells. (c) Distribution of neurons according to the type of response to whisker stimulation: TN tonic and PhN phasic neurons. (d) Mean spiking frequencies for entire population, phasic, and tonic neurons

i.e., at the beginning and/or the end of the stimulus (Fig. 3.8a, c). Tonic neurons (TN) produce large spike trains lasting for the whole stimulation period (Fig. 3.8b, d).

According to the standard electrophysiological analysis, the three nuclei have a quite different percentage of SN, LF, and HF cells (Fig. 3.9a). There is also some deviation in the mean firing frequencies among the nuclei (Fig. 3.9b). Thus there is a difference in the spontaneous neural activity among the nuclei.

The three nuclei have similar percentages of tonic and phasic cells (Fig. 3.9c), and hence no conclusions about dissimilarities among them can be drawn solely on the basis of the type of response to stimulation.

Nevertheless, the Sp5i nucleus appears to be different from the Pr5 and Sp5o, which in turn have some degree of similarity. Indeed, analysis of the firing rate reveals:

- Similarly low spiking frequency among neurons from Pr5 and Sp5o compared with Sp5i neurons for all (SN, LF, and HF) groups (Fig. 3.9b).
- PhN cells from Pr5 and Sp5o nuclei have 2–3 times lower frequency than those from Sp5i (Fig. 3.9d). The opposite behavior is observed for T-neurons.

3.3.3 Drawbacks of the Traditional Approach to Information Processing

In Fig. 1.1, we already gave an example of the firing dynamics of a Pr5 neuron under periodic stimulation of a vibrissa in its receptive field. Even under the condition

of a completely repeatable stimulus, the neuronal response is far from being constant. During the first few seconds, the neuron exhibits a maximal firing rate (about 27 spikes/s), but the rate then quickly falls to about 10 spikes/s, and further fluctuates for more than 20 s. The neuron behavior is thus essentially nonstationary. However, most traditional approaches, such as peristimulus histograms, ignore this observation.

Traditional analysis of neural spike trains has often been performed assuming that segments of the experimental time series are approximately stationary and that such segments can be studied by means of statistical techniques such as correlation measures or Fourier analysis (see, e.g., [28–30]). This approach is obviously useful if the nonstationarity has a time scale longer than the rhythms of interest. However, this is not always the case. Instantaneous frequencies of various rhythmic components can exhibit complex irregular fluctuations, that is, the nonstationarity may be associated with higher frequencies as well. Previous results [20] have shown that Fourier analysis is hardly applicable in such conditions. An alternative is to use the wavelet technique, which can be successfully applied to analyze the temporal structure of neuronal spiking over a wide range of time scales [9, 20].

3.3.4 Wavelet Transform of Spike Trains

For information processing it is reasonable to assume that neurons produce and exchange stereotypical events or spikes. Thus, only the timings of the spike occurrences carry a message. Consequently, before applying any analysis, spikes in experimental data should be identified and sorted among different neurons. This procedure will be discussed in detail in Chap. 4. Here we assume that this problem has already been solved.

Figure 3.10a illustrates a typical example of a high-pass filtered extracellular recording ($f_{\text{cut}} = 300 \text{ Hz}$) made in a Pr5 nucleus. Four spikes coming from a single cell can be seen by the naked eye. However, in more complex situations, advanced spike sorting techniques must be used, including those based on the wavelet transform. The results of data preprocessing given in this section are based on the wavelet shape-accounting classifier (WSAC) (see Sect. 4.4).

Once spikes of a single cell have been identified, they can be represented as a series of δ -functions, viz.,

$$n(t) = \sum \delta(t - t_i) , \quad (3.9)$$

where $\{t_i\}$ is a set of time instants corresponding to spike firing (Fig. 3.10a). Then we can apply the continuous wavelet transform to the signal (3.9).

Let us consider the CWT with the Morlet function. The timescale s plays the role of the period of the rhythmic component. Given a characteristic timescale

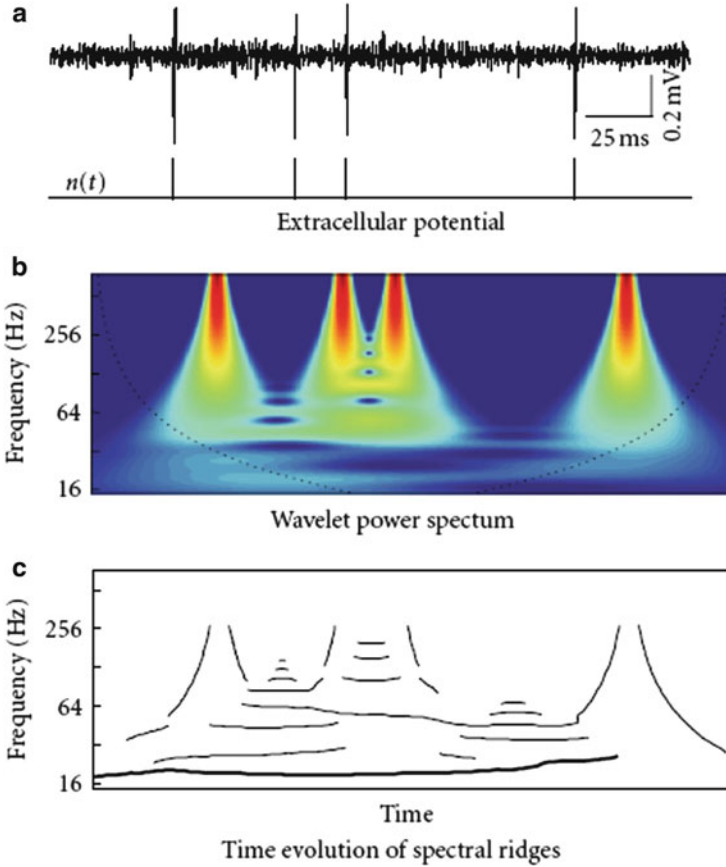


Fig. 3.10 Wavelet analysis of a spike train. (a) Conversion of extracellular recording into a spike train $n(t)$. (b) Energy density $E(f, t)$ of the spike train (color from blue to red corresponds to the spectrum magnitude). The dashed black curve defines the cone of influence where edge effects cannot be neglected. (c) Time evolution of spectral “ridges” $F_k(t)$. The thick curve corresponds to the main (most prominent and stable) ridge, whose central frequency oscillates in time at around 20 Hz

(e.g., the period) s , the resolution of the wavelet in the time and frequency domains is given by

$$\delta t = ck_0s, \quad \delta\omega = \frac{c}{k_0s}, \quad (3.10)$$

where c is a constant of the order of unity. There is a trade-off between the frequency and time resolutions: small values of k_0 provide better time resolution, whereas large values of k_0 improve frequency resolution. The commonly adopted value is $k_0 = 1$ and the limit $k_0 \rightarrow \infty$ corresponds to the Fourier transform. Sometimes, especially for the analysis of spike trains, $k_0 = 2$ can be more suitable.

Equation (3.9) allows us to estimate the wavelet coefficients analytically:

$$W(s, t_0) = \frac{1}{\sqrt{s}} \sum_i e^{-i2\pi(t_i - t_0)/s} e^{-(t_i - t_0)^2 / 2k_0^2 s^2}. \quad (3.11)$$

Using the wavelet transform (3.11), we can perform the time–frequency analysis of rhythmic components hidden in the spike train. The wavelet coefficients can be considered as a parameterized function $W_p(t_0)$, where t_0 plays the role of time. It is convenient to introduce the following normalization of the energy density:

$$E(s, t_0) = \frac{1}{\sqrt{\pi r k_0 s}} |W(s, t_0)|^2, \quad (3.12)$$

where r is the mean firing rate (the normalization of the energy spectrum per spike simplifies comparison of neurons with different firing rates). For biophysical convenience, instead of (3.12), its frequency counterpart $E(f, t)$ is often considered. This is obtained by substituting $s = 1/f$ ($k_0 = 1$).

$E(f, t)$ represents a surface in 3D space whose sections at fixed times provide information about the local energy spectra. Figure 3.10b is a 2D plot of the energy density of the spike train shown in Fig. 3.10a. Each spike produces a broad frequency spectrum. The existence of rhythms in the spike train leads to the appearance of “ridges” in the 3D energy surface, associated with the rhythmic contributions. These ridges, oriented along the time axis, identify the spectral content of the spike train at any given time moment.

Thus, the dynamics of rhythmic components hidden in a spike train is reflected in the time evolution of spectral ridges. To construct spectral ridges, a search for local maxima of the energy spectrum $E(f, t^0)$ at time t^0 is performed (Fig. 3.10b), thus obtaining a set of 2D functions of time $F_k(t)$, where the subindex corresponds to the number of the ridge (Fig. 3.10c).

Spectral ridges can appear and disappear in time, and they can also oscillate (Fig. 3.10c). Oscillations indicate the presence of a given rhythm in the spiking dynamics of a neuron and its modulation by other rhythms (e.g., due to a high frequency jitter in the spike timings). If a neuron generates a stereotypic response to periodic stimulation (i.e., the same pattern for each stimulus event), then its instantaneous frequency associated with the stimulus rhythm remains constant. We thus obtain a “perfect” (continuous and straight) spectral ridge at the stimulus frequency.

Deviation from the stereotypic response associated with “missing” or “extra” spikes, or with changes in the interspike intervals, causes temporal variations in the instantaneous frequency and even disappearance of the ridge, as happens in Fig. 3.10c. Moreover, the greater the fluctuation of the instantaneous frequency, the more significant the differences in the neuronal response. Thus, following the time evolution of the instantaneous frequency of spectral peaks (i.e., the spectral ridge) enables one to study the stability and stationarity of neuronal responses to a tonic stimulus.

To quantify the stability of the neuronal response, the following measure can be considered:

$$\text{St} = \frac{1}{\sigma_0}, \quad (3.13)$$

where σ_0 is the standard deviation of the time evolution of the main spectral ridge $F_0(t)$ found in the vicinity of the stimulus frequency.

To evaluate St for a spike train, its energy density (3.12) is estimated. Then for a fixed time t^0 (changed with a 5 ms time bin), we search for the energy maximum in the frequency range $f_{\text{stim}} \pm 5\%$. The resulting frequency is assigned as $F_0(t^0)$. Finally, the standard deviation of F_0 yields St.

3.3.5 Dynamical Stability of the Neuronal Response

In this section we test the methodology proposed in Sect. 3.3.4 on simulated neuronal responses to external stimuli. To do so, we consider three neurons embedded in a network and receiving the same periodic (1 Hz) sequence of 50 stimuli. Depending on the current network state and its dynamics, the neuronal responses may have different variability, i.e., the firing patterns provoked by each stimulus event may have different degrees of repeatability.

We simulated neuronal responses under three different conditions:

- N1: Constant in time strong variability. The neuron responds to each stimulus by generating 3–5 phasic spikes (3.9 ± 1.2 std) with fluctuating spike timings (8 ms std).
- N2: Changing (small) variability. The neuron generates a spike train similar to N1, but the firing rate decays linearly (from 5 spikes per stimulus at the beginning to about 2.5 at the end).
- N3: Increasing (intermediate) variability. The spike train is similar to N2, but the fluctuation in spike timings increases from 0 at the beginning to about 40 ms std at the end.

The response pattern of the first neuron has a stationary distribution, whereas those of the second and third neurons are similar to the experimentally observed adaptability to the stimulus (Fig. 1.1). Their firing rates decay in time. The difference between the neurons N2 and N3 is in the variability of the spike timings. The neuron N2 has constant fluctuations, whereas the magnitude of the fluctuations for N3 increases with time.

Figure 3.11a shows a 5 s epoch of the stimulus and spike trains of the three neurons. Applying the traditional peristimulus time interval analysis, we obtain roughly the same peristimulus time histograms (PSTHs). All histograms have three peaks at latencies 20, 50, and 90 ms, corresponding to the neuronal phasic response to the stimulus, and are hardly distinguishable. Thus, PSTH fails to quantify the

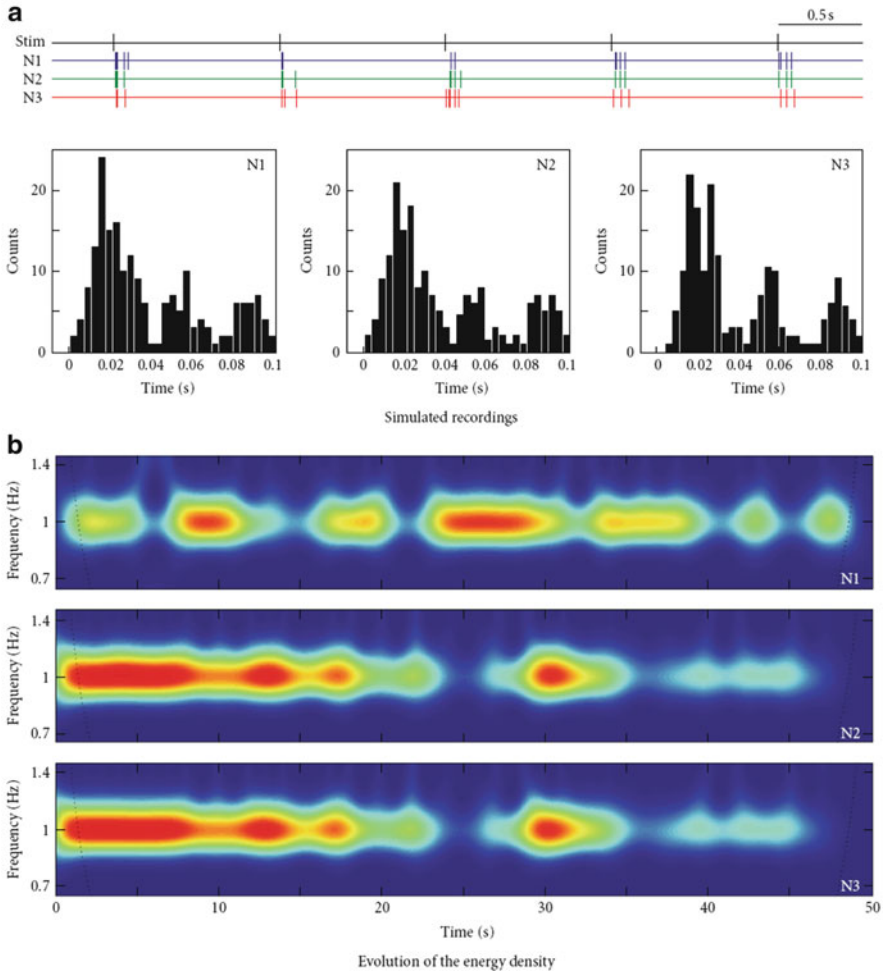


Fig. 3.11 Quantification of the dynamical stability of the stimulus response patterns for three neurons. **(a)** Stimulus and spike trains of three neurons (only 5 s epoch is shown). The three neurons have almost the same PSTHs, but their firing dynamics is significantly different (see the main text). **(b)** Wavelet energy spectra of the spike trains in the stimulus frequency band (*color from blue to red corresponds to the spectrum magnitude*)

differences in behavior exhibited by the neurons, as expected. Not much additional information is provided by the raster plot (not shown).

The wavelet energy spectrum of the first spike train differs significantly from the spectra of N2 and N3, which are very similar (Fig. 3.11b). Fluctuations in the spectral magnitude of the 1 Hz rhythm reflect changes in the strength of the neuronal response at that frequency. Loosely speaking, it is proportional to the number of spikes generated per stimulus. The spectral magnitude of the train N1 fluctuates

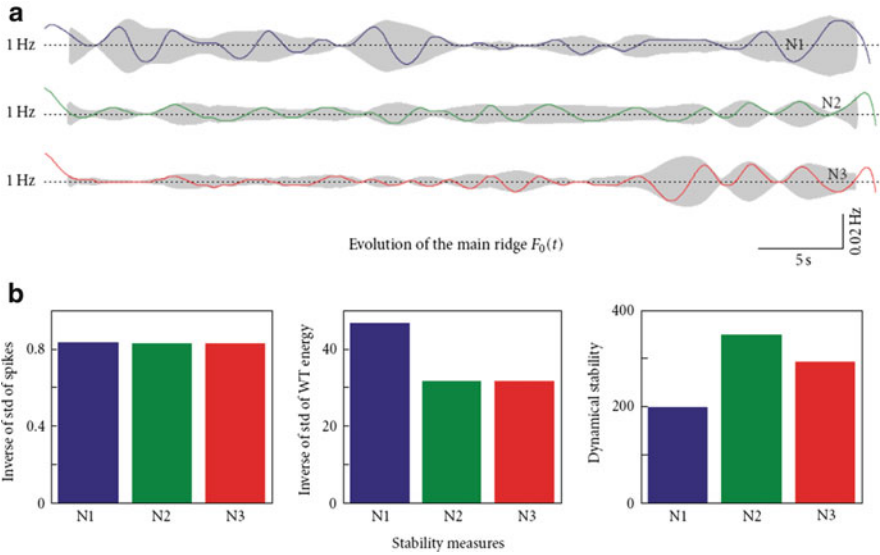


Fig. 3.12 Quantification of the dynamical stability of the stimulus response patterns for three neurons. **(a)** Time evolution of the main spectral ridges for the three spike trains. *Shaded areas* correspond to the envelopes of $F_0(t)$ (obtained by the Hilbert transform). **(b)** Different response stability measures. *Left*: Reciprocal of the standard deviation of the number of spikes. *Center*: Reciprocal of the standard deviation of the magnitude of the energy density at 1 Hz. *Right*: Dynamical stability factor S . The latter characteristic reveals distinctions in the stimulus responses of the neurons

around the mean value, which agrees with the stationary nature of the firing patterns of this neuron. The energy magnitude of N2 and N3 decays in time, again as expected from the decaying firing rate of these neurons.

Figure 3.12a shows the time evolution of the main spectral ridges $F_0(t)$ (corresponding to $f_{\text{stim}} = 1$ Hz) for the three neurons. This provides information about the phase (temporal) relationships between spikes in the firing patterns and reveals differences in the three cases. The instantaneous frequency of N1 displays large stationary deviations from 1 Hz due to the constant variability of spike timings and “missing” spikes. The ridge of N2 has smaller deviations, especially in the first half of the recording, where the neuronal response was more consistent (in the number of generated spikes). N3 shows the smallest ridge variability (close to zero by construction) at the beginning of the stimulation, but growing progressively toward the end. The difference with N2 is explained by the overtime increasing variability of the N3 spike timings.

It is noteworthy that the time evolution of the spectral magnitude (Fig. 3.11b) and the ridge dynamics (Fig. 3.12a) provides complementary information about the firing patterns. Indeed, a strong neuronal response with a similar number of spikes produces a quite stable, high magnitude spectral ridge. If the variability of spike timings is much lower than the reciprocal of the ridge frequency (interstimulus

intervals), then it makes little contribution to the ridge height. However, this high-frequency dynamics will affect the instantaneous ridge frequency and, consequently, will be visible in the $F_0(t)$ plot.

Let us now check the different measures of the response stability of the neurons N1–N3 that can be derived from the spike trains and their wavelet analysis. First, the standard deviations of the number of spikes elicited by each stimulus were calculated. Similar characteristics have been used for quantification of the frequency-dependent response in VPM and SI neurons [31]. Figure 3.12b (left inset) shows that the reciprocal of the standard deviation (i.e., $1/\text{std}$ number of spikes) is the same for all neurons, hence this measure cannot distinguish dynamical differences in their responses.

Figure 3.12b (middle inset) shows the reciprocal of the standard deviation of the magnitude of the energy density (corresponding to Fig. 3.11b) at the stimulus frequency. This measure differentiates the responses of N1 from those of N2 and N3. The lower value for N2 and N3 is mostly due to the trend in the energy magnitude in these cases. Detrending the energy density functions raises the measure to 74 for N2 and N3 and does not affect its value for N1. Thus, the energy magnitude-based measure can be a good predictor of a neural rate code, but it cannot pick up the variability in the spike timings.

Finally, Fig. 3.12b (right inset) shows the dynamical stability measure (3.13) evaluated for the three neurons. This measure correctly quantifies the differences in stability of the firing patterns among all three neurons.

3.3.6 Stimulus Responses of Trigeminal Neurons

The examples described in this section are based on experiments performed on anesthetized (urethane, 1.5 g/kg) Wistar rats of either sex weighing 200–250 g. The experimental procedure is similar to that described in the work by Moreno et al. [32]. Animals were placed in a stereotaxic device that allowed easy access to the vibrissae. Recordings were obtained using tungsten microelectrodes directed vertically into the Pr5, Sp5i, and Sp5o nuclei.

Once an electrode had been put in place, the vibrissae were manually stimulated by means of a thin brush to determine their receptive fields. The vibrissa maximally activating a neuron near the electrode was further used for mechanical stimulation. Free whisker movements were generated by air puffs directed at one vibrissa only and signals were not recorded when other vibrissae exhibited any vibration. Air pulses were generated by a pneumatic pressure pump (Picospritzer III, Parker Inst. TX) and delivered via a silicon tube of diameter 0.5 mm, positioned at 10–12 mm perpendicularly to the vibrissa:

- Stimulus protocol S1: Three separate sequences of 50 air puffs lasting 10, 50, or 100 ms each with 1 s interpuff intervals were delivered at the neuron's receptive fields.

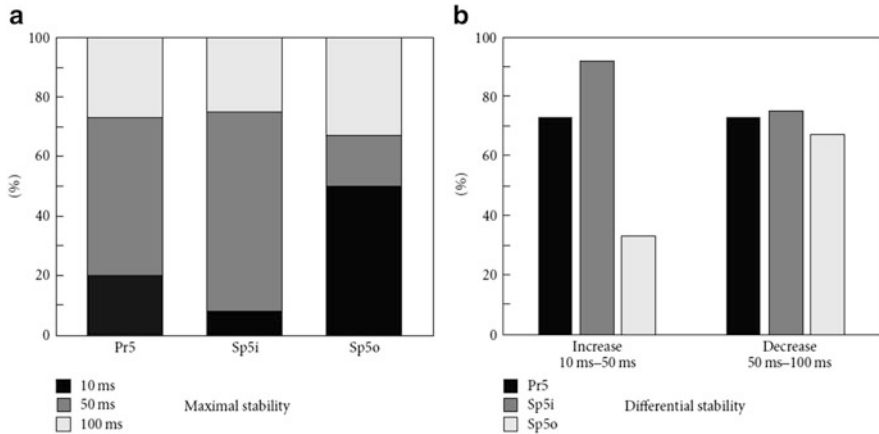


Fig. 3.13 Population analysis of the dynamical stability of the neuronal response patterns under variation of the air puff duration (stimulus protocol S1). **(a)** Percentage of cells showing maximal stability for 10, 50, or 100 ms stimuli. Neurons from Pr5 and Sp5i “prefer” 50 ms, whereas Sp5o shows better stability for shorter (10 ms) stimuli. **(b)** Percentage of neurons showing an increase (*left*) or decrease (*right*) in the response stability under increasing stimulus duration

- Stimulus protocol S2: Air puffs of fixed duration (10 ms), but with different stimulation frequency, ranging from 1 to 30 Hz, were delivered at the neuron’s receptive fields. During the course of individual experiments, the frequency was randomly changed. The whole duration of stimulation at a given frequency was 50 s.

The extracellular potential was amplified, sampled at 20 kHz, passed through the band-pass filter (0.3–3.0 kHz), and then analyzed using the special software Spike 2 and custom packages written in Matlab. For the wavelet analysis, we selected only those neurons whose extracellularly recorded spikes were well isolated from the activity of the other neurons.

3.3.6.1 Effect of Stimulus Duration (Protocol S1)

The stability parameter St was calculated for all selected neurons and the three stimulus durations. In addition, we determined the stimulus duration (10, 50, or 100 ms) that provides the maximally stable response pattern for each neuron. To describe quantitative changes in the stability parameter when the stimulus duration increases ($10 \rightarrow 50 \rightarrow 100$ ms), the neurons satisfying the conditions $St_{50} > St_{10}$ and $St_{50} < St_{100}$ were counted. Figure 3.13 and Table 3.1 summarize the results.

In the case of Pr5 neurons, the stability parameter St is likely to be maximal for the middle stimulus duration (50 ms, Fig. 3.13a). The most stable response is observed for 53 % of all cells with the 50 ms stimulus. The remaining 27 and 20 % of cells respond stably to 100 and 10 ms stimuli, respectively.

Table 3.1 Comparative analysis of the stability of neural response patterns evoked by tactile whisker stimulation by air puffs of different duration (10, 50, and 100 ms) for neurons from Pr5, Sp5i, and Sp5o nuclei

	Maximal S (%)			Increase in S (%) ($S_{50} > S_{10}$)	Decrease in S (%) ($S_{50} > S_{100}$)
	10 ms	50 ms	100 ms		
Pr5	20	53	27	73	73
Sp5i	8	67	25	92	75
Sp5o	50	17	33	33	67

Quite similar behavior occurs for Sp5i neurons. Here even more cells (67 %) “prefer” stimuli of intermediate duration. This is achieved mostly by decreasing the cell population showing a better response to the shortest 10 ms stimuli (8 %).

Sp5o neurons typically behave differently. The maximally stable response pattern for 50 ms stimulation was observed for only 17 % of the cells. Meanwhile, half of the neurons showed better stability for the shortest stimulation (10 ms). The proportion of the cells with better response to the 100 ms stimuli was about 33 %, a little bit higher than for Pr5 and Sp5i neurons.

Figure 3.13b shows differential stability characteristics. For 73 % of Pr5 neurons, responses to 50 ms stimulation are more stable than those to air puffs of 10 ms duration. In the case of Sp5i neurons, the value of St increases at the transition 10 \rightarrow 50 ms for about 92 % of cells. Thus, Pr5 and Sp5i neurons are characterized by a rather similar type of reaction to variation of the stimulus duration. However, different behavior is observed for Sp5o neurons. Only for 33 % of cells did St increase with the stimulus duration (from 10 to 50 ms). If the stimulus duration increases further (50 \rightarrow 100 ms), about 70 % of neurons from all nuclei display a decrease in their response stability.

Thus the protocol S1 allowed us to conclude that:

- The stability of response patterns depends on the stimulus duration, that is, neurons process stimuli of different duration in different ways.
- There exist significant changes in the types of responses for Pr5, Sp5i, and Sp5o neurons. The most reliable responses are achieved in Pr5 and Sp5i for 50 ms stimulus and in Sp5o for 10 ms.

3.3.6.2 Effect of Stimulus Frequency (Protocol S2)

Let us now discuss effects of the stimulation frequency (protocol S2). It has been found that all trigeminal neurons can be subdivided into three groups by their type of response to the frequency content of the stimulus. Figure 3.14 shows the stability measure as a function of the stimulus frequency $St(f_{stim})$ for three representative cells. By analogy with the filter terminology, we will refer to the three basic types of neuronal response as low-pass, band-pass, and no dependence.

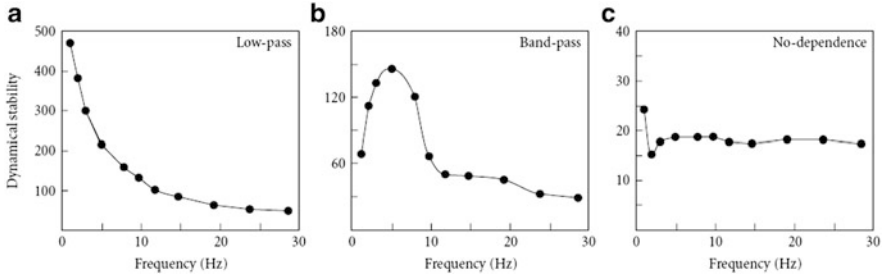


Fig. 3.14 Three main types of behavior of the dynamical stability of neuronal responses to the frequency of a tonic stimulus $St(f_{stim})$: low-pass (*left*), band-pass (*center*), and no dependence (*right*)

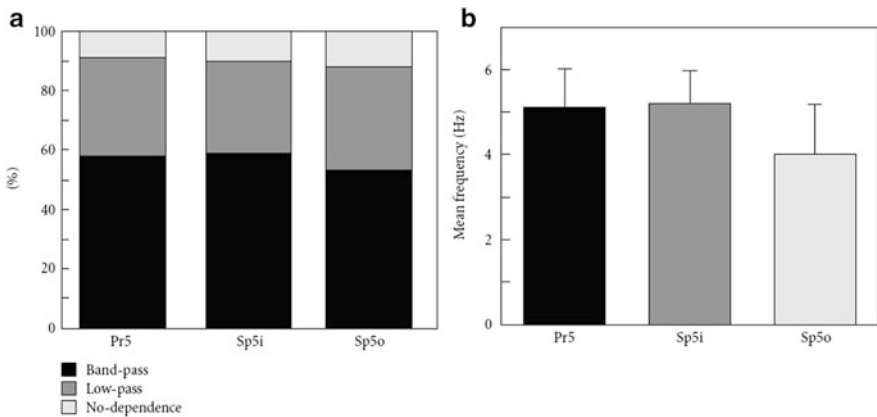


Fig. 3.15 Population analysis of the dynamical stability of neuronal responses under variation of the stimulus frequency (stimulus protocol S2). (a) Percentage of cells showing different “filtering” characteristics in Pr5, Sp5i, and Sp5o nuclei. (b) Mean central frequencies of band-pass neurons

In all nuclei, band-pass is the most frequent cell behavior. It occurs in 58, 59, and 53 % of neurons in Pr5, Sp5i, and Sp5o, respectively (Fig. 3.15a). The low-pass reaction is observed for 33, 31, and 35 % of neurons from Pr5, Sp5i, and Sp5o, respectively. Finally, 9, 10, and 12 % of cells in the corresponding nuclei are characterized by the no-dependence reaction. Thus, there are small population distinctions in the frequency filtering properties of Pr5, Sp5i, and Sp5o nuclei.

For band-pass type responses, the mean central frequency was determined (mean \pm s.e.): 5.1 ± 0.9 Hz (Pr5), 5.2 ± 0.8 Hz (Sp5i), and 4.0 ± 1.3 Hz (Sp5o) (Fig. 3.15b). Thus, neurons in Pr5 and Sp5i nuclei have the same central frequency, whereas cells in Sp5o typically show a smaller value of the stabilization frequency.

3.3.6.3 Biophysical Interpretation

For effective stimulus perception, information specific to the object should be invariant to the details of the whisking motion. Therefore, flexibility and adaptability in the processing of the whisker vibrations are required. Experiments *in vitro* [33] demonstrated that neurons in the barrel cortex do indeed adapt their input–output function, in such a way that the gain rescales, depending on the range of the current stimulus distribution. In this section, it has been shown that *in vivo* accommodation of firing patterns to stimulus characteristics can be quantified by the stability measure St , which was used to study neuronal responses in the trigeminal nuclei evoked by tactile whisker stimulation.

Analysis of the time evolution of frequency ridges in the wavelet space can be used to identify the variable frequency content in a neural spike train under essentially nonstationary conditions of sensory information processing. The method allows an integral quantification of the variability in the number of phasic spikes and in the spike timings. It takes into account changes at the stimulus time scale and also at significantly shorter time scales. The validity of the method has been cross-checked using simulated spike trains resembling properties of real recordings (Fig. 3.11).

A fundamental issue in neural coding is the role of variation of spike timings in information processing. Indirectly, this can be tested by an artificial jittering of the spike timings and its influence on the derived measures (see, e.g., [34, 35]). The stability measure St can be used to provide a direct answer to the question: how stable or repeatable are the firing patterns produced by a neuron for each stimulation. If the stability measure is high, then the spike patterns are highly repeatable during the whole recording, and consequently, such a neuron is likely to be using a kind of temporal code. Conversely, low stability suggests high variability in the spike patterns and points to a rate code or the presence of a complex dynamics, for example, involving local and global feedback and fast adaptation.

Recent results [34] demonstrate that the trigeminal ganglion neurons use temporal code. Here, using the dynamical stability measure, it has been shown that neurons in Pr5, Sp5i, and Sp5o nuclei can vary their response stability according to the stimulus characteristics, for example, the stimulus duration (Fig. 3.13). Thus the trigeminal neurons adapt their coding scheme to the stimulus characteristics, and there is a continuous oscillation between the two extremes, the temporal and rate codes. This conclusion is indirectly supported by the presence of an extensive network locally connecting neurons in the trigeminal nuclei and the global corticofugal projections, so that the global network dynamics can modify the stimulus-evoked patterns of each individual neuron.

It is known that the frequency of whisker movements plays an important role in effective perception (see, e.g., [36, 37]). Previous results showed the presence of resonance properties in the firing of thalamic and cortical neurons (see the review in [16]). Indeed, the stimulation of a vibrissa at a given frequency can be related to

its vibration during perception. Then the surface discrimination requires fine-tuning of the system and a series of impulses deflecting the vibrissa can be considered as a single entity. Therefore, we expect an effective band-pass amplification (or filtration) of the stimuli in a given frequency band by some cells. It was found that more than half (about 57 %) of neurons in the trigeminal nuclei have this property. Finally, the remaining 10 % of cells have no pronounced dependence on the stimulus frequency, and these neurons probably perform a different task, not directly linked to stimulus codification and transmission. Besides, their stability factors are usually extremely low (e.g., in Fig. 3.14, $St_{low} \approx 500$, $St_{band} \approx 150$, whereas $St_{no_dep} \approx 18$), which also suggests that stimulus processing is not their primary role.

The percentage of neurons showing low-pass, band-pass, and no-dependence behavior is quite similar across different nuclei (Fig. 3.15a). This suggests that the number of neurons specializing in different tasks (e.g., border or texture detection) is also similar in Pr5, Sp5i, and Sp5o nuclei. The mean “optimal” stimulation frequencies of the band-pass neurons is about 5 Hz for Pr5 and Sp5i and about 4 Hz in Sp5o. These frequencies are close to the lower end of the frequency scale for whisker movements in active exploration (4–12 Hz) [38]. These results correlate with studies of the amplitude of averaged neuronal responses in the somatosensory cortex, where similar filtration properties have been found [31]. Thus, we can suppose that at least some of the filtration properties observed for neurons in the somatosensory cortex can be influenced by analogous responses generated by neurons in the trigeminal complex.

3.4 Wavelet Coherence for Spike Trains: A Way to Quantify Functional Connectivity

A very common method to track temporal coupling or functional association between stimulus and neural response is the peristimulus time histogram, which characterizes the cross-correlation between two point processes, i.e., stimulus events and the neural spike train [28]. On the one hand, the PSTH examines temporal changes in the amount of generated spikes triggered by the stimulus. On the other, analyses in the frequency domain can provide a more concise description of the temporal correlation of the oscillatory patterns in spike trains.

In the frequency domain, spectral coherence is a well-established standard tool to analyze the linear relationship between two (usually continuous) signals by determining the correlation between their spectra. A high spectral coherence suggests the presence of a functional association between, e.g., the stimulus and the neural response in the corresponding frequency band. Starting from this concept, several modifications of the coherence measure have been suggested (see e.g., [39–41]).

Although the above-mentioned measures have been shown to be very useful for different problems in neuroscience, they suffer from the assumption of stationarity

of the neural response and do not account for dynamical changes in associations (coupling) between stimulus and neural response. Indeed, any analysis based entirely on time averaging (PSTH) or on the Fourier transform (spectral coherence) ignores all temporal variations in the functional coupling between tactile stimulation and neural response. An additional temporal resolution is essential and demands replacement of the classical Fourier (spectral) coherence by other methods. There have been successful attempts to adapt Fourier-based methods to short time signals, for example, by means of orthonormal sliding windows [42–44], which are similar to the classical Gabor transform [45].

Wavelet analysis is a significantly more powerful tool that offers a reasonable compromise between temporal and frequency resolutions. The wavelet transform has been used to analyze brain signals from the very beginning in neuroscience. Most of its applications have been to electroencephalographic recordings (see, e.g., [46–53]).

The first studies of wavelet coherence go back to the beginning of this century [54–57]. In a similar way to spectral coherence, wavelet coherence informs about the functional coupling between, e.g., the stimulus and neural response, but it also provides the temporal structure of the coupling. The use of the wavelet transform for analysis of neural spike trains recorded in the trigeminal nuclei under tactile whisker stimulation is illustrated in [9, 58].

In this section, we quantify the wavelet coherence (i.e., functional association) of the gracile neural response to tactile stimulation, and show that activation of the SI cortex leads to a dynamical (i.e., time-varying) alteration of the neuronal response characteristics mediated by the corticofugal pathway. For this purpose, we shall consider how wavelet coherence can be used to investigate the dynamical properties of neural spike trains and to evaluate dynamical changes in the neural response to tactile stimulation in the gracilis nucleus provoked by activation of the corticofugal feedback from the SI cortex.

3.4.1 Wavelet Coherence of Two Point Processes

PSTH and ordinary spectral coherence usually provide little information about the time–frequency contents of a spike train. Some insight can be obtained by the traditional dot-raster display. Although the raster display can capture important temporal characteristics of the neural stimulus response, it is merely a visual tool, i.e., no measure of stability of the neural response can be derived directly. Moreover, a correct comparison of raster displays generated by several neurons with essentially different firing rates is difficult, if not impossible. This leads eventually to a problem in generalizing results over the neuronal population. Meanwhile, the wavelet technique offers a natural way to study the temporal structure of neural stimulus response coherence.

A spectral representation of a spike train can generally be obtained by the Fourier transform. However, this transformation is known to have difficulties in dealing

with point processes [29]. To overcome some of these difficulties, the multitaper Fourier transform has been advocated in the literature [30]. Although the multitaper transform usually provides a good estimate of the power spectrum, in the case of excessively periodic spike trains (e.g., under experimental conditions of periodic stimulation), it may fail to represent the spectral density consistently. The wavelet transform can be used as an alternative way to perform spectral analysis.

As we saw in Sect. 3.3.4, a spike train can be represented as a sum of delta functions (3.9). Then the wavelet power spectrum of the spike train can be defined by (3.11) and (3.12). The global wavelet spectrum can be obtained from (3.12) by time-averaging the local (time-dependent) spectrum:

$$E_G(s) = \frac{1}{T} \int_0^T E(s, t_0) dt_0, \quad (3.14)$$

where T is the time length of the spike train. The global spectrum (3.14) provides an unbiased and consistent estimate of the true power spectrum [59].

This approach ensures that the mean energy in a random spike train is homogeneously distributed over all interspike intervals $E_G(s) = 1$. This is similar to the spectrum of white noise. Consequently, we quantify the power distribution in the train under study in units of the power of the random spike train with the same mean firing rate. Energy below (above) 1 means that the probability of spike patterns with the given scale s is below (above) the probability of such a pattern in the random spike train.

When dealing with two spike trains N and M , by analogy with the Fourier cross-spectrum, we can introduce the following wavelet cross-spectrum:

$$W_{NM}(s, t_0) = \frac{W_N W_M^*}{k_0 \sqrt{\pi r_N r_M}}, \quad (3.15)$$

where W_N and W_M are the wavelet transforms of the trains N and M , respectively. Then a normalized measure of association between the two spike trains is the wavelet coherence [54]

$$C_{NM}(s, t_0) = \frac{|S[W_{NM}(s, t_0)/s]|^2}{S[E_N(s, t_0)/s] S[E_M(s, t_0)/s]}, \quad (3.16)$$

where S is a smoothing operator (for details see [54, 60]). The coherence definition (3.16) may give artificially high values for the coherence in the case of infinitesimally small values of the power spectrum of either signal or both signals, i.e., when $E(s^*, t_0^*) \approx 0$. To avoid this problem in numerical calculations, a thresholding procedure can be used, setting the coherence to zero when either of the power values is below a certain threshold.

3.4.2 Measure of Functional Coupling Between Stimulus and Neuronal Response

3.4.2.1 Coherence in the Stimulus Frequency Band

To study the functional coupling between the stimulus and the neuronal response we can use (3.16) with N the train of stimulus events and M the neuronal spike train. Because we are interested in studying the functional coupling with stimulus events, which are periodic, we will focus on the frequency band corresponding to the stimulus frequency, i.e., on $f = 1$ Hz, which is associated with the scale $s = 1$ s. To successfully resolve the stimulus-induced frequency contents in the neural response with minimal loss in time resolution, we set $k_0 = 2$. Then from (3.10), $\delta\omega \approx 1/2$ and $\delta t \approx 2$. Although the wavelet transform uses the time scale (period) s as a parameter, to address the frequency contents, we shall use the frequency as the parameter, defined formally by $f = 1/s$.

To quantify the variation of the functional coupling among stimuli and neural response, we average the neural stimulus coherence over scales in a narrow band around the stimulus frequency. An estimate of the band limits can be obtained from (3.10), viz., $f \in [(1-c/2\pi k_0), (1+c/2\pi k_0)]$, which gives 0.83–1.16 Hz for $c = 2$. We shall refer to this frequency band as the stimulus frequency band. Obtained this way, the coherence is a function of time

$$C(t) = \frac{1}{s_2 - s_1} \int_{s_1}^{s_2} C_{NM}(s, t) ds, \quad (3.17)$$

which is then used to evaluate the power spectrum by the conventional Fourier transform.

3.4.2.2 Statistical Significance

Two linearly independent spike trains have insignificant coherence $C_{NM}(s, t_0) \approx 0$, whereas $C_{NM}(s, t_0) = 1$ indicates a perfect linear relationship between the spike trains at the scale s and localization t_0 .

Although a large coherence amplitude usually indicates the presence of a consistent phase relationship (coupling) between two spike trains in a given time interval, it is also possible that this is a random variation in the spike trains. One should therefore cross-check the statistical significance of the observed coherence.

The statistical significance of the wavelet coherence can be assessed relative to the null hypotheses that the two spike trains generated by independent stationary processes with given distributions of interspike intervals (ISIs) are not coherent. To evaluate the significance level, we use a surrogate data test [61, 62] with Monte Carlo simulation to establish a 95% confidence interval. The surrogate spike trains are obtained from the original one by randomizing phase relations, keeping other

first-order characteristics intact. We shuffle the ISIs and evaluate coherence among the surrogate spike trains. To conclude positively about the connectivity between the stimulus train and the neuronal response, their coherence should be higher than the resulting significance level.

3.4.2.3 Mean Characteristics Describing Effects of Cortical Stimulation

To examine the effect of cortical stimulation on the coherence of neural response to stimulus, we average the local coherences over time and the stimulus frequency band

$$C_{\text{ctr}}^{\text{m}} = \langle C_{\text{ctr}}(t) \rangle_t, \quad C_{\text{AESC}}^{\text{m}} = \langle C_{\text{AESC}}(t) \rangle_t, \quad (3.18)$$

where $C_{\text{ctr}}(t)$ and $C_{\text{AESC}}(t)$ are the coherences in the stimulus frequency band in the control and after the SI cortex stimulation conditions, respectively. For convenience we also introduce the overall mean coherence $C^{\text{m}} = (C_{\text{AESC}}^{\text{m}} + C_{\text{ctr}}^{\text{m}})/2$. First, we recall that $C_{\text{ctr}}(t)$ and $C_{\text{AESC}}(t)$ are bounded functions of time and thus the maximal increment $\delta C^{\text{m}} = C_{\text{AESC}}^{\text{m}} - C_{\text{ctr}}^{\text{m}}$ depends on the overall mean coherence and cannot exceed the value $2(1 - C^{\text{m}})$. Thus the higher the overall mean coherence, the lower the coherence increment can be. Then we guess a linear model

$$|\delta C^{\text{m}}| = \alpha(1 - C^{\text{m}}), \quad (3.19)$$

where α is a constant to be identified from the data.

Then for a given value of the wavelet coherence, by using (3.19) we can evaluate the expectation of the absolute value of the coherence increment. If the observed increment is much smaller than the expectation, we can question its significance (i.e., no effect). To decide positively on the presence of an effect on the stimulus coherence provoked by the SI cortex stimulation, we require the experimentally observed increment δC^{m} to be at least 50 % of the expectation value, i.e., $|\delta C^{\text{m}}| \geq 0.5\alpha(1 - C^{\text{m}})$. Then we have a coherence increase or I-effect for positive δC^{m} and a decrease or D-effect for negative values.

3.4.3 Functional Connectivity of Gracilis Neurons to Tactile Stimulus

The analyzed data set consisted of 29 extracellular recordings (spike trains) of unitary neuronal activity from the gracilis nucleus measured at three different epochs:

- Spontaneous firing.
- Responses to periodic stimulation (1 Hz rate) of the neuronal receptive field (control conditions).

- Responses to periodic stimulation (1 Hz rate) of the neuronal receptive field after electrical stimulation of the SI cortex (AESC conditions).

All neurons were identified as projecting to the thalamus [20]. The analyzed neurons showed a low spontaneous activity with mean firing rate 1.1 ± 0.4 spikes/s (range 0–10 spikes/s) whose pattern coincided with the firing characteristics of projecting neurons described previously [63, 64].

3.4.3.1 Example of Wavelet Analysis

First, let us illustrate the wavelet analysis of a representative neural spike train. Figure 3.16a shows the spike train during three different experimental epochs (for illustration purposes, we selected a neuron with a considerable spontaneous activity). Under spontaneous conditions, the neuron exhibits an irregular spiking pattern with a slight peak at 70 ms, manifested in the autocorrelation histogram (ACH, Fig. 3.16b, left). Mechanical stimulation under the control conditions elicited a well-pronounced neuron response with 25 ms peak latency, followed by a weakly rhythmic firing with 120 ms period (Fig. 3.16b, middle). Electrical stimulation of the SI cortex facilitated the neural response to the tactile stimulation. The response in the PSTH became more prominent (Fig. 3.16b, right). However, neither the response latency nor the mean firing rate (21.1 vs. 23.7 spike/s) varied much relative to the control conditions. Furthermore, the weak oscillatory behavior observed in the tail of the PSTH under control conditions disappeared.

The wavelet power spectrum (Fig. 3.16c, left) confirms the irregularity of spontaneous firing observed in the ACH. There are many oscillatory rhythms localized in both the time and frequency domains with essentially erratic distribution. Thus spiking activity has no well-defined dominant periodic activity (although there is a feeble and not-persistent-in-time power peak at 14 Hz). The distribution of the power under control conditions (Fig. 3.16c, middle) shows a consistent peak in the stimulus frequency band (from 0.83 to 1.16 Hz, between the two dotted horizontal lines). This peak indicates the presence of the stimulus-evoked rhythm in the neural firing. We also note that the peak amplitude (power) is not persistent in time, but instead exhibits a low-frequency oscillation (<0.3 Hz). This oscillation of the spectral power suggests that the neural response to the same tactile stimulation is not stable (identical) throughout time, but instead has some variability, i.e., the neuron fires essentially different numbers of spikes with different ISIs in response to the same stimulus events during the stimulation epoch. We also observe some increase in the spectral power around 8 Hz, consistent with the oscillations (120 ms period) observed in the corresponding PSTH (Fig. 3.16b, middle). In accordance with the stimulus response facilitation observed in the PSTH after electrical cortex stimulation, the power peak at the stimulus frequency band became even more pronounced (Fig. 3.16c, right). Now we have a continuous practically black island going through the whole stimulation epoch in the stimulus frequency band. Notice, however, that the ultralow-frequency oscillation of the power is weaker, but still

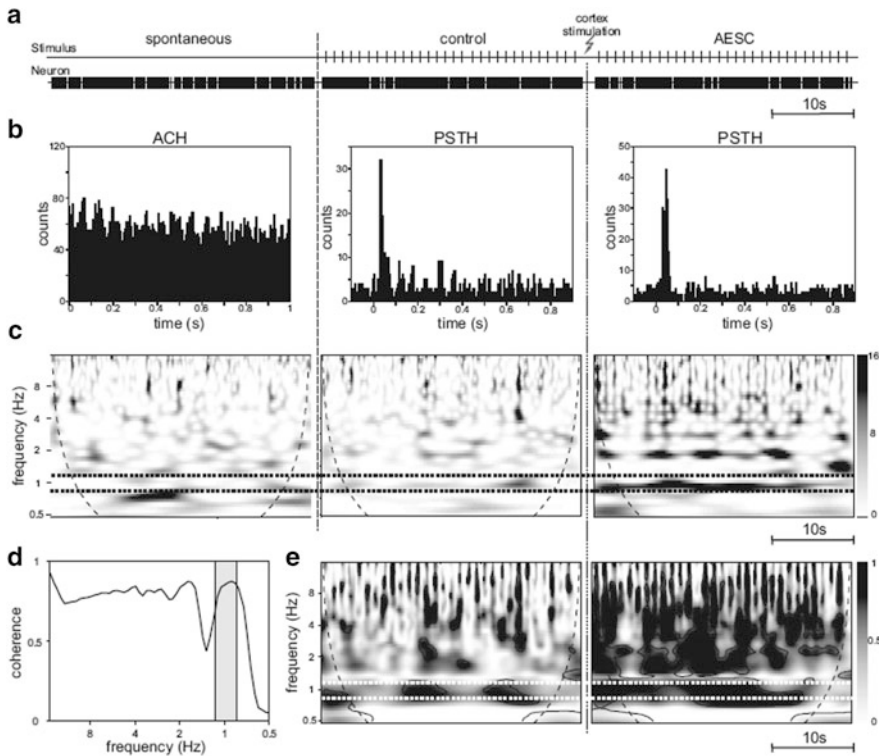


Fig. 3.16 Wavelet spectral and coherence analysis of experimental spike trains. **(a)** Stimulus events and neural spike trains during three experimental epochs: spontaneous activity, control 32 s tactile stimulation delivered to the neuron receptive field at 1 Hz rate, and the same tactile stimulation repeated after electrical stimulation of the somatosensory (SI) cortex (AESC). **(b)** Autocorrelation (ACH) and peristimulus time histograms (PSTHs) for the corresponding epochs. **(c)** Wavelet power spectra of the neural spike train for the corresponding epochs. The x -axis corresponds to the localization z (time), whereas the oscillation frequency from 0.5 to 15 Hz is plotted along the y -axis on a logarithmic scale. *Gray intensity* is equivalent to wavelet spectral power. *Dashed lines* define the cone of influence and *horizontal dotted lines* delimit the stimulus frequency band 0.83–1.16 Hz. **(d)** Level of statistical significance for the wavelet coherence obtained by the surrogate data test. Coherence above the curve is deemed significant. The *gray region* is the frequency band of interest (around the stimulus frequency). **(e)** Wavelet coherence of the neural spike train to tactile stimulation events for the control epoch and after SI cortex stimulation. *Solid black lines* delimit islands of statistically significant coherence (the stripe between two dotted lines is of interest). *Gray intensity* corresponds to the strength of the stimulus coherence of the neural response

exists. Besides, there is a significant increase in the power of harmonics of the 1 Hz rhythm and, on average, a greater presence of oscillations in the domain of higher frequencies.

To quantify how coherent (reliable) the neural response to the stimulus events is, we evaluated the wavelet coherence of the neural spike train and stimulus events.

To decide on the statistical significance of the observed coherence level, i.e., on the presence of functional associations (coupling) between the stimulus and neural response, we performed a surrogate data test by randomizing phase relationships between two signals. Figure 3.16d shows a statistical significance curve ($P = 0.05$) for the frequency range observed in the neural spike train. Coherence above the curve is deemed statistically significant, although if the area of the significant islands is small enough (5%), then the conclusion regarding the coherent response should be made carefully.

Figure 3.16e illustrates the wavelet coherence of the tactile stimulus events and evoked neural response. Because the tactile stimulation is periodic (i.e., has only one frequency), we shall refer to the stimulus frequency band only (delimited by dotted lines in Fig. 3.16e) when speaking about the response coherence. During the control stimulation epoch, we observe three islands of significant coherence in the stimulus frequency band (Fig. 3.16e, left). This provides evidence for the presence of the stimulus–response association previously observed in the corresponding PSTH. However, we also find that the association or stimulus response coupling is not constant, but an oscillatory function of time. Notice also that the neural power spectrum in the corresponding frequency band was not very strong (Fig. 3.16c, middle). However, the coherence clearly reveals the functional coupling between the neural firing dynamics and stimulus events. The stimulus coherence of the neural response becomes stronger after electrical stimulation of the somatosensory cortex (Fig. 3.16e, right). As we observed earlier in the wavelet power spectra (Fig. 3.16c, middle and right), the stimulus coherence also suffers from ultralow-frequency oscillations.

Thus for a given neuron we observed two phenomena:

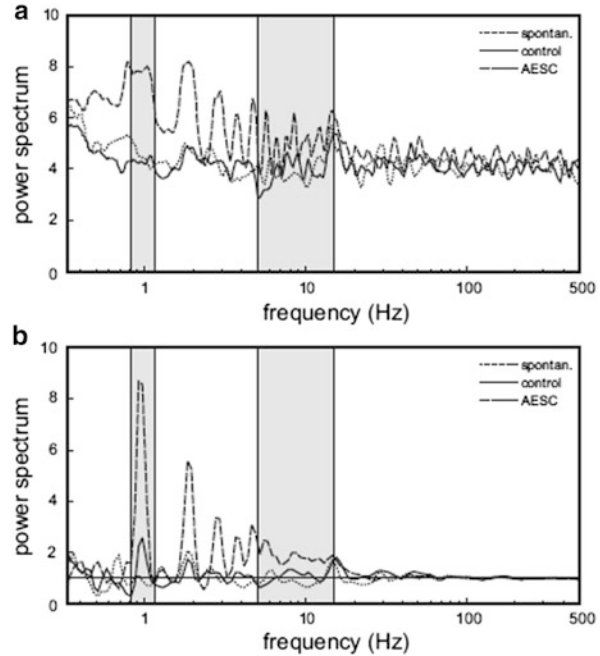
- The strength of the functional stimulus–neural response coupling is amplified by the electrical stimulation of the SI cortex.
- The coupling strength is a dynamical quantity, slowly oscillating in time, that can temporarily fall below the significant level.

The latter implies that the stimulus–response association may be temporarily lost for a single neuron.

3.4.3.2 Pitfalls of Fourier Spectrum and Wavelet Spectral Analysis

To illustrate possible pitfalls in the interpretation of the Fourier power spectrum, we first evaluated the power spectrum through the multitaper Fourier transform of the neural spike train shown in Fig. 3.16a. In accordance with the irregularity of firings under spontaneous conditions, the Fourier spectrum (Fig. 3.17a) is essentially flat with a peak at 14 Hz corresponding to the periodicity observed earlier in the ACH (Fig. 3.16b, left). However, for the control stimulation epoch, the overall spectral distribution is quite similar to that of the spontaneous spectrum, and it lacks a peak at 1 Hz corresponding to the neuron response at the stimulus frequency. In contrast, due to the excessive periodicity of the neural response, after the electrical

Fig. 3.17 Spectral analysis of spike train (corresponding to Fig. 3.16a) for three different epochs: spontaneous activity (*dotted line*), control tactile stimulation (*solid line*), and tactile stimulation preceded by electrical stimulation of the SI cortex (*dashed line*, AESC). *Gray regions* delimit the alpha frequency band ranging from 5 to 15 Hz, and the stimulus frequency band 0.83–1.16 Hz. **(a)** Power spectra obtained by the multitaper Fourier transform. **(b)** Global wavelet power spectra for the same epochs



stimulation of the SI cortex, we observed an unreasonably wide peak around 1 Hz, followed by many strong harmonics contaminating the high-frequency range. Thus the Fourier transform of a spike train may fail to consistently represent its spectral density.

We then used the wavelet transform as an alternative way to perform spectral analysis. Figure 3.17b shows the global wavelet power spectra of the neuron-firing counterpart to the Fourier spectra. The wavelet spectra are much more consistent with the oscillatory rhythms suggested by the previous analysis of spike trains by the ACH and PSTHs. According to the normalization used in (3.12), the unit power density corresponds to the power spectrum of a spike train with randomly distributed ISIs, which we refer to briefly as a random spike train. Then a spectral power above (or below) unity indicates the presence (or absence) of the corresponding rhythm in the spike train with statistical power higher than just a random ratio.

During spontaneous activity, the power spectrum of the neuron firing only slightly deviates from the spectrum of the random train across all frequency bands (Fig. 3.17b, dotted line). In agreement with the weak rhythm observed in the ACH (Fig. 3.16b, left), the global wavelet spectrum also has a small peak at 14 Hz. We also detected peaks at about 0.7 and 1.9 Hz. Going back to the complete wavelet spectrum (Fig. 3.16c, left), we find that the latter peaks are due to strong episodic events localized between 4 and 7 s and between 10 and 16 s from the beginning, respectively. Thus spontaneous firing can be characterized as random, showing no strong persistent specific frequencies. Under the control tactile stimulation, we

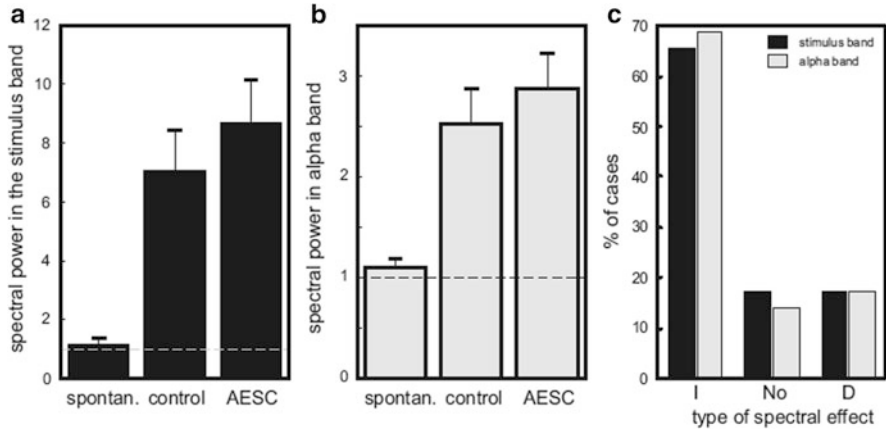


Fig. 3.18 Spectral characteristics of gracile projecting neurons in the stimulus and alpha frequency bands. **(a)** Mean power of the global wavelet spectrum and its SE in the stimulus frequency band for spontaneous conditions and during response to tactile stimulation under control conditions and after electrical stimulation of the SI cortex (AESC). **(b)** Same as **(a)**, but for the alpha frequency band. **(c)** Statistics of the types of spectral effect of the electrical stimulation of the SI cortex for 2 frequency bands. I, No, and D stand for increase, no effect, and decrease in the spectral power, respectively. *Black* and *gray bars* correspond to the stimulus and alpha frequency bands, respectively

observed a strong peak in the stimulus frequency band (Fig. 3.17b, solid line). Note that the peak is quite narrow and has a harmonic at 2 Hz. Stimulation of the SI cortex boosts the amplitude of the power peak in the stimulus frequency band, and we also observed an important enhancement of the power in the band ranging from about 5 to 15 Hz. For higher frequencies (>15 Hz), there is no significant deviation of the power density from 1, whereas for the range <5 Hz, the harmonics of the stimulus frequency rhythm are manifested in the power spectrum. Accordingly, we define the second frequency band of interest (5–15 Hz), which we shall refer to briefly as the alpha frequency band. Thus, at the single-neuron level used in this study, we found that the frequency band corresponding to the evoked neural spiking activity is localized in the stimulus and alpha frequency bands.

3.4.3.3 Population Properties of Spectral Power

To assess statistical properties of the observed changes in the spectral power of the neuronal firing, we compared the global wavelet power spectra under spontaneous conditions and under tactile stimulation in the control and after the SI cortex stimulation conditions. Figure 3.18 summarizes the results.

The overall mean power under spontaneous conditions corresponds to the power of the random spike train, in both the stimulus and the alpha frequency bands (Fig. 3.18a, b, spontaneous). This confirms that the firing pattern of projecting

neurons in the gracilis nucleus is essentially random. Stimulation of the neuron receptive fields boosts the mean power concentrated in both the alpha and the stimulus frequency bands (Fig. 3.18a, b, control), although the increase in the stimulus band is much stronger (7 vs. 2.5 times). Electrical stimulation of the SI cortex raises the power concentrated in these frequency bands even higher (Fig. 3.18a, b, AESC). However, on average, the latter enhancement is not so drastic. The effect of electrical stimulation lasted between 15 and 30 min, after which the neurons recovered their activity.

A balanced one-way ANOVA ensures that the mean spectral powers in three different epochs are significantly different with P values $2.5e-5$ for the stimulus frequency band and $2.7e-5$ for the alpha band. A multiple-comparison test shows that the values of the power during tactile stimulation under control conditions and after SI cortex stimulation conditions differ significantly from the power of spontaneous firing in both frequency bands, and that they are statistically indistinguishable from each other.

Although the mean spectral power across both frequency bands does not differ significantly between tactile stimulations under control conditions and after electrical stimulation of the SI cortex (Fig. 3.18a, b), in the majority of experiments we observed an increase in the power provoked by cortex stimulation. This result agrees with the previously reported facilitation of the stimulus response provoked by SI cortex stimulation [65–68]. To quantify the percentage of neurons exhibiting different types of effects of stimulation of the SI cortex, we evaluated the number of increases in the spectral power (I-effects), the number of cases when the difference was negligible (no-effects), and the number of decreases (D-effects). To decide on the type of the effect we used the relative increment of the power in the given frequency band, viz.,

$$\Delta E = \frac{E_{\text{AESC}} - E_{\text{cntr}}}{(E_{\text{AESC}} + E_{\text{cntr}})/2}, \quad (3.20)$$

where E_{cntr} and E_{AESC} are the spectral power under control conditions and after SI cortex stimulation conditions. If the absolute increment was $<5\%$, we assigned no-effect, otherwise, according to the sign of the increment, we decided on an I- or D-effect.

Figure 3.18c shows that, after stimulation of the SI cortex, in the majority of cases (66 and 69% for the stimulus and alpha frequency bands, respectively), the power of firing does indeed increase in both frequency bands, i.e., we have an I-effect of cortex stimulation. In 17% of cases for the stimulus band and 14% for the alpha band, cortex stimulation had no effect on the spectral characteristics of the neural response. Finally, in 17% of cases, for both bands, the spectral effect of cortex stimulation was negative, i.e., the power diminished.

Thus tactile stimulation leads to a significant enhancement of the power of neuron firing, in both the alpha and the stimulus frequency bands. In addition, electrical stimulation of the SI cortex amplifies the spectral power in these bands for about two thirds of the neurons in the gracilis nucleus. We also conclude that facilitation of the

neural response by the corticofugal pathway occurs not only through an increase in the number of spikes elicited by the stimulus, but also through the ordering of the response pattern.

3.4.3.4 Effect of Cortex Stimulation on Response Coherence

Let us recall that coherence is a normalized measure of the cross-spectrum of two signals. It thus has meaning in the frequency bands presented in both the neural spike train and the stimulus. The latter has the fixed frequency of 1 Hz (up to negligible variations due to the experimental setup). Accordingly, we study the wavelet coherence of the neural response to tactile stimulation in the stimulus frequency band only, whose limits were set to 0.83–1.16 Hz.

To study the effect of cortex stimulation on the neural response coherence in the gracilis nucleus, we evaluate the mean stimulus coherences in the control C_{ctr}^m and after electrical stimulation of the SI cortex C_{AESC}^m . Figure 3.19a shows the absolute value of the coherence increment $|\delta C^m| = |C_{\text{AESC}}^m - C_{\text{ctr}}^m|$ as a function of the mean overall coherence $C^m = (C_{\text{AESC}}^m + C_{\text{ctr}}^m)/2$ for the experimental data set. Not surprisingly, the plot shows a strong linear tendency of the coherence increment to be smaller for higher values of the overall mean coherence. By fitting the model (3.19) to the data in the least-squares sense, we obtain $\alpha = 0.41$ (solid straight line in Fig. 3.19a). Thus for a given value of the wavelet coherence, by using (3.19), we can evaluate the expectation of the absolute value of the coherence increment and define the effect (No, I, or D) provoked by cortical stimulation (Fig. 3.19a).

Figure 3.19b shows the percentage of different types of effects of electrical stimulation of the SI cortex on the tactile stimulus coherence of neuron firing in gracile projecting neurons. In the majority of cases (59%), electrical stimulation of the SI cortex facilitates a more reliable (higher coherence) neural response to the tactile stimulus. In 24 and 17% of cases, we had no effect or a decrease in coherence, respectively. The observed relative increment of the coherence value for I- and D-effects was about the same, namely, 13 and 15%, respectively (Fig. 3.19c).

We note that the positive increment in the coherence (reliability of the neuron response to tactile stimulation) was observed in a slightly lower number of cases than the increment of power in the stimulus frequency band (59% in Fig. 3.19b vs. 66% in Fig. 3.18c), which confirms the statement made earlier that an increase in the spectral power is not necessarily accompanied by an increase in the coherence. Moreover, this suggests possible subtle changes occurring in the stimulus response pattern due to the corticofugal pathway, instead of a simple increase in the firing rate.

To cross-check whether the increment in the wavelet stimulus coherence correlates with conventional characteristics of neural activity, we plotted an increment in the mean firing rate $\delta FR = FR_{\text{AESC}} - FR_{\text{ctr}}$ and an increment in the amplitude of the response peak in the PSTH $\Delta A_{\text{PSTH}} = A_{\text{AESC}} - A_{\text{ctr}}$ versus δC^m (Fig. 3.20). In these plots, a data point belonging to quadrant I or quadrant III

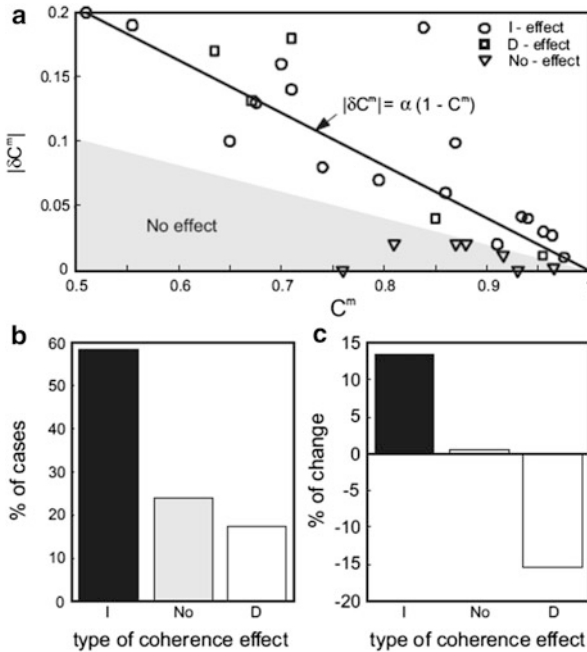


Fig. 3.19 Effect of the electrical activation of the SI cortex on the wavelet coherence (reliability) of the response of projecting neurons in the gracilis nucleus to tactile stimulation of their receptive fields (RFs). (a) The absolute value of the coherence increment δC^m as a function of the mean overall coherence C^m shows a strong linear tendency. The solid straight line is the best fit of the data to the model (3.19). The gray region delimits the no-effect region (data points shown by triangles), where the experimentally observed value of the coherence increment is $<50\%$ of the expectation. Circles and squares correspond to I (increase) and D (decrease) effects of electrical cortex stimulation on the stimulus response coherence. (b) Percentage of neurons exhibiting I, No, and D types of effect. (c) Relative changes (increase or decrease) in the coherence for I and D effects

corresponds to a positive correlation between the corresponding measures, i.e., an increase or decrease in coherence is associated with an analogous effect in the other characteristic, whereas quadrants II and IV establish the contrary effect or anticorrelation. According to the above-described findings, we expected that an enhancement of the reliability of the neural response to tactile stimulation (i.e., $\delta C^m > 0$) would not necessarily be reflected in the neuron firing rate, but it seems reasonable to expect a better peaking of the PSTH and consequently $\Delta A_{PSTH} > 0$.

Indeed, Fig. 3.20a shows that the data points in the case of the mean firing rate are distributed quite arbitrarily over the plane—the linear fit of the data confirms this. The straight line and its 95% confidence interval are essentially horizontal, showing no significant correlation between the measures. A different picture is observed for the increment in the amplitude of the PSTH peak (Fig. 3.20b). The best-fit line and its 95% confidence interval have a notably positive slope. Thus, as expected, we

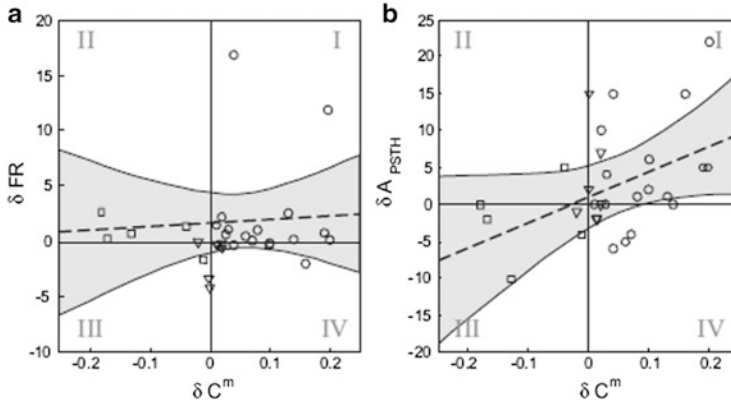


Fig. 3.20 Increment in the mean neural firing rate (a) and the amplitude of the PSTH peak (b) vs. the increment in the neural stimulus response coherence. Quadrants I and III correspond to positive correlation between two characteristics (i.e., increase or decrease of one characteristic is accompanied by the same effect in the other), whereas quadrants II and IV correspond to negative or anticorrelation (i.e., when the effect in one characteristic is contrary to the effect in the other). *Dashed straight lines* and *gray regions* containing them show the best linear fits of the data and their 95 % confidence limits. The direction and position of the fits imply the absence of correlation between the firing rate and coherence measures, and a positive correlation of the amplitude of the PSTH peak and coherence measures. However, note the presence of cases where changes in the PSTH amplitude do not correspond to changes in the coherence

have a positive correlation for the changes provoked by electrical stimulation of the SI cortex between the coherence and the amplitude of the PSTH peak. However, we note that an enhancement (or reduction) of the stimulus coherence is not always accompanied by an increase (or decrease) in the PSTH amplitude. This means that, for a considerable number of experiments the PSTH measure fails to predict the effect of changes in the coherence of the neural response to the tactile stimulus.

3.4.3.5 Variable Functional Coupling to Stimulus

In Fig. 3.16e, we observed qualitatively that tactile stimulus coherence oscillates slowly in time, both for the control experimental conditions and after electrical stimulation of the SI cortex. Let us now quantify these oscillations and study their possible functional role.

Figure 3.21a shows two strips cut out of the corresponding coherence functions in the stimulus frequency band that is shown in Fig. 3.16e between two horizontal dotted lines. To examine the mean coherence and its modulation in time, we average the local coherence over the stimulus frequency band. The resulting time series for the control $C_{\text{ctr}}(t)$ and after SI cortex stimulation $C_{\text{AESC}}(t)$ give a measure of the reliability of the neuron response to stimulation events throughout the corresponding stimulation epoch (Fig. 3.21a, bottom). At the beginning of the stimulation epochs

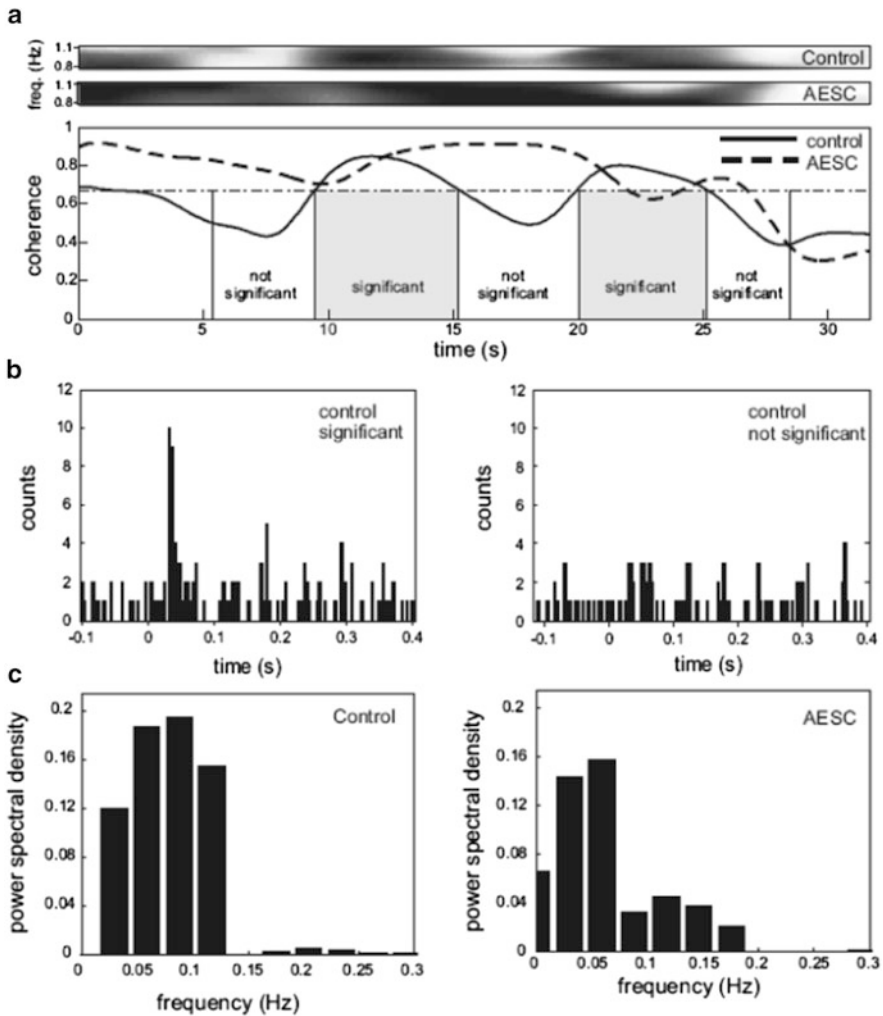


Fig. 3.21 Oscillatory behavior of the wavelet coherence of the neural response to tactile stimulation events in the stimulus frequency band. **(a)** *Top strips* show coherences evaluated in the stimulus frequency band 0.83–1.16 Hz (corresponding to those shown in Fig. 3.16e between horizontal dotted lines) for the control and after electrical stimulation of the SI cortex (AESC) for the representative neuron. *Gray intensity* corresponds to the local coherence value. Zero on the time axis corresponds to the beginning of each epoch. *Bottom: Thick curves* show the integral (averaged over the stimulus frequency band) wavelet stimulus coherence of the neuron response throughout the stimulation epochs. The *thin dash-dotted horizontal line* defines the level of statistical significance for coherence under control stimulation conditions. According to the statistical significance, we define time windows of significant (*gray boxes*) and nonsignificant (*white boxes*) coherence. **(b)** PSTHs of the neural response under control conditions, evaluated over time windows with coherence above (*left*) and below (*right*) the significance level. In the windows of coherent response, the neuron shows a pronounced peak, whereas it loses the stimulus correlation outside the coherence windows. **(c)** Fourier power spectra of the oscillation of the wavelet coherences under control conditions and after SI cortex stimulation (AESC)

(up to ~ 20 s), the stimulus response coherence is higher after electrical cortex stimulation than under the control conditions. The two characteristics then both exhibit some decay (i.e., the neuron firing becomes less stimulus coherent) and no substantial difference between the coherence values is observed. Over all the stimulation epochs, we observed a slow oscillation of relatively large amplitude. We note that the period of slow oscillation is much longer than the wavelet temporal resolution (about 10–15 vs. 2 s), which ensures correct identification of the coherence oscillatory behavior.

The observed oscillation may have a functional role. Indeed, for the control stimulation epoch the coherence falls temporarily below the significance level (Fig. 3.16e, left and Fig. 3.21a, bottom). We can thus define time windows (segments) with coherence above or below the level of statistical significance. In Fig. 3.21a, these windows are shown by white and gray boxes, so that the total length of the significant and nonsignificant segments is the same. Obviously, in windows with high coherence, the neuron should exhibit a strong functional stimulus–response relationship. However, when the stimulus coherence is not significant, this functional association may be lost. The “raw” PSTH (Fig. 3.16b, middle) does not provide evidence for this phenomenon. However, by splitting the spike train into two parts according to the significance of the observed coherence, we do indeed observe an essential difference in the PSTHs (Fig. 3.21b). In regions with significant coherence, the neuron exhibits a well-pronounced stimulus response (Fig. 3.21b, left), whereas its firing becomes practically uncorrelated with the stimulus in the time windows of nonsignificant coherence (Fig. 3.21b, right). We can interpret this behavior as a temporal loss of functional connectivity between the tactile stimulus and the neuron. We also note that electrical stimulation of the SI cortex increases the stimulus–response coherence and that it stays above the level of significance during practically the whole stimulation epoch. Only after about 27 s does the coherence become nonsignificant. In such an “alerted” state, the neuron maintains functional coupling to the sensory stimulus, sending coherent spikes to the thalamus.

Figure 3.21c shows Fourier power spectral densities for the ultralow-frequency oscillation of the stimulus coherence in the control and after cortex stimulation. In the first case, the spectrum has a peak at 0.09 Hz, whereas after SI cortex stimulation, the peak shifts to a lower frequency (0.06 Hz) and becomes smaller.

Figure 3.22 shows the mean frequency and power of the coherence oscillations averaged over the neuron population during tactile stimulation under control conditions and after electrical cortex stimulation. The mean frequency under control conditions was 0.065 Hz, which is slightly lower than the oscillation frequency of 0.068 Hz after cortex stimulation. However, there is no statistically confirmed significant difference between the two means. Similarly, the mean oscillation power is slightly (but not significantly) higher in the case of tactile stimulation preceded by electrical stimulation of the SI cortex. The mean frequency and amplitude of the ultralow-frequency oscillations averaged over the neural population are not affected by the electrical stimulation of the SI cortex.

Thus, the possibility of studying the temporal structure of the stimulus–response coherence allowed us to describe ultraslow fluctuations in the tactile responses of

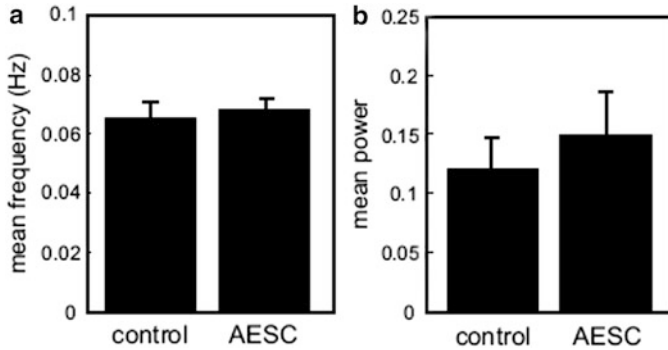


Fig. 3.22 Statistical properties of the ultraslow oscillations of the stimulus response coherence of projecting neurons in the gracilis nucleus under control conditions and after electrical stimulation of the SI cortex (AESC). **(a)** Mean oscillation frequency. **(b)** Mean oscillation power

single projecting neurons. We note that such oscillations are not directly observable either in the Fourier spectrum or in the PSTH of the neural response. Instead, they represent slow modulation of the coherence (or reliability) of the neural response to the tactile stimulation over a long timescale, i.e., the neuron fires essentially a different number of spikes with different ISIs for the same stimulus events during the stimulation epoch. Besides observing a facilitation of the tactile stimulus–neural response functional coupling by the electrical stimulation of the SI cortex, we have provided evidence that the functional coupling between the sensory stimulus input and neural response oscillates slowly in time. During this oscillation, the stimulus coherence can temporarily fall below the significant level. This means that the stimulus–response association may be temporarily lost for a single neuron. This phenomenon suggests that information processing in the gracilis nucleus occurs on the network level, which may be “energetically” beneficial for the system. The mean frequency of the observed coherence oscillation was about 0.07 Hz. Oscillations in the same frequency band (0.02–0.2 Hz) have been reported in studies of human EEG [69]. The authors showed that large-scale ultraslow oscillations in widespread cortical regions may represent a cyclic modulation of cortical gross excitability. This ultraslow oscillation of cortical activity might be transferred to the gracilis nucleus through the corticofugal projections, thus modulating tactile responses.

References

1. H.C. Tuckwell, *Introduction to Theoretical Neurobiology* (Cambridge University Press, Cambridge, 1988)
2. E.R. Kandel, J.H. Schwartz, T.M. Jessell, *Principles of Neural Science*, 4th edn. (McGraw-Hill, New York, 2000)
3. V.A. Andreev, K.V. Indukaev, The problem of sub-Rayleigh resolution in interference microscopy. *J. Russian Laser Res.* **24**, 220 (2003)

4. V.P. Tychinskii, Coherent phase microscopy of intracellular processes. *Phys. Usp.* **44**, 683 (2001)
5. O.V. Sosnovtseva, A.N. Pavlov, N.A. Brazhe, A.R. Brazhe, L.A. Erokhova, G.V. Maksimov, E. Mosekilde, Interference microscopy under double-wavelet analysis: a new approach to studying cell dynamics. *Phys. Rev. Lett.* **94**, 218103 (2005)
6. N.A. Brazhe, A.R. Brazhe, A.N. Pavlov, L.A. Erokhova, A.I. Yusipovich, G.V. Maksimov, E. Mosekilde, O.V. Sosnovtseva, Unraveling cell processes: interference imaging weaved with data analysis. *J. Biol. Phys.* **32**, 191 (2006)
7. O.V. Sosnovtseva, A.N. Pavlov, E. Mosekilde, N.-H. Holstein–Rathlou, D.J. Marsh, Double-wavelet approach to study frequency and amplitude modulation in renal autoregulation. *Phys. Rev. E* **70**, 031915 (2004)
8. P.S. Addison, J.N. Watson, Secondary transform decoupling of shifted nonstationary signal modulation components. *Int. J. Wavelets, Multiresolution Inf. Process.* **2**, 43 (2004)
9. A.N. Pavlov, V.A. Makarov, E. Mosekilde, O.V. Sosnovtseva, Application of wavelet-based tools to study the dynamics of biological processes. *Brief. Bioinformatics* **7**, 375 (2006)
10. A.R. Brazhe, N.A. Brazhe, A.N. Pavlov, G.V. Maksimov, E. Mosekilde, O.V. Sosnovtseva, Interference microscopy for cellular studies, in *Handbook of Research on Systems Biology Applications in Medicine* (IGI Global, 2008), pp. 653–669. ISBN: 978-1-60566-076-9
11. A. Szucs, G. Molnar, K. Rozsa, Periodic and oscillatory firing patterns in identified nerve cells of *Lymnaea stagnalis* L. *Acta Biol. Hungar.* **50**, 269 (1999)
12. A. Schutt, T.H. Bullock, E. Basar, Odor input generates similar to 1.5 Hz and similar to 3 Hz spectral peaks in the helix pedal ganglion. *Brain Res.* **879**, 73 (2000)
13. D. Landowne, L.B. Cohen, Changes in light scattering during synaptic activity in the electric organ of the skate *Raia erinacea*. *Biol. Bull.* **137**, 407 (1969)
14. I. Darian-Smith, The trigeminal system, in *Handbook of Sensory Physiology*, ed. by A. Iggo (Springer, Berlin, 1973), p. 271
15. S.B. Mehta, D. Whitmer, R. Figueroa, B.A. Williams, D. Kleinfeld, Active spatial perception in the vibrissa scanning sensorimotor system. *PLoS Biol.* **5**, 309 (2007)
16. C.I. Moore, Frequency-dependent processing in the vibrissa sensory system. *J. Neurophysiol.* **91**, 2390 (2004)
17. J. Wolfe, D.N. Hill, S. Pahlavan, P.J. Drew, D. Kleinfeld, D.E. Feldman, Texture coding in the rat whisker system: slip–stick versus differential resonance. *PLoS Biol.* **6**, 1661 (2008)
18. E. Ahissar, P.M. Knutsen, Object localization with whiskers. *Biol. Cybern.* **98**, 449 (2008)
19. P.M. Knutsen, E. Ahissar, Orthogonal coding of object location. *Trends Neurosci.* **32**, 101 (2009)
20. N.P. Castellanos, E. Malmierca, A. Nuñez, V.A. Makarov, Corticofugal modulation of the tactile response coherence of projecting neurons in the gracilis nucleus. *J. Neurophysiol.* **98**, 2537 (2007)
21. E. Malmierca, N.P. Castellanos, V.A. Makarov, A. Nuñez, Corticofugal modulation of tactile responses of neurons in the spinal trigeminal nucleus. A mathematical analysis, in *Advancing Artificial Intelligence Through Biological Process Applications*, ed. by A.B. Porto, A. Pazos, W. Buño (Idea Group, Hershey, 2009)
22. E. Malmierca, N.P. Castellanos, A. Nuñez-Medina, V.A. Makarov, A. Nuñez, Neuron synchronization in the rat gracilis nucleus facilitates sensory transmission in the somatosensory pathway. *Eur. J. Neurosci.* **30**, 593 (2009)
23. R.L. Smith, The ascending fiber projections from the principal sensory trigeminal nucleus in the rat. *J. Comp. Neurol.* **148**, 423 (1973)
24. M. Peschanski, Trigeminal afferents to the diencephalons in the rat. *Neuroscience* **12**, 465 (1984)
25. P.M. Ma, The barrelettes-architectonic vibrissal representations in the brainstem trigeminal complex of the mouse. Normal structural organization. *J. Comp. Neurol.* **309**, 161 (1991)
26. M.H. Friedberg, S.M. Lee, F.F. Ebner, The contribution of the principal and spinal trigeminal nuclei to the receptive field properties of thalamic VPM neurons in the rat. *J. Neurocytol.* **33**, 75 (2004)

27. P. Veinante, M. Deschenes, Single-cell study of motor cortex projections to the barrel field in rats. *J. Neurosci.* **19**, 5085 (1999)
28. D.H. Perkel, G.L. Gerstein, G.P. Moore, Neuronal spike trains and stochastic point processes. *Biophys. J.* **7**, 419 (1967)
29. D.R. Brillinger, Comparative aspects of the study of ordinary time series and of point processes, in *Developments in Statistics*, ed. by P.R. Krishnaiah (Academic, New York, 1978), p. 33
30. M.R. Jarvis, P.P. Mitra, Sampling properties of the spectrum and coherency of sequences of action potentials. *Neural Comput.* **13**, 717 (2001)
31. C.E. Garabedian, S.R. Jones, M.M. Merzenich, A. Dale, C.I. Moore, Band-pass response properties of rat SI neurons. *J. Neurophysiol.* **90**, 1379 (2003)
32. A. Moreno, V. Garcia-Gonzalez, A. Sanchez-Jimenez, F. Panetsos, Principalis, oralis and interparietalis responses to whisker movements provoked by air jets in rats. *NeuroReport* **16**, 1569 (2005)
33. M. Díaz-Quesada, M. Maravall, Intrinsic mechanisms for adaptive gain rescaling in barrel cortex. *J. Neurosci.* **28**, 696 (2008)
34. L.M. Jones, D.A. Depireux, D.J. Simons, A. Keller, Robust temporal coding in the trigeminal system. *Science* **304**, 1986 (2004)
35. S.G. Sadeghi, M.J. Chacron, M.C. Taylor, K.E. Cullen, Neural variability, detection thresholds, and information transmission in the vestibular system. *J. Neurosci.* **27**, 771 (2007)
36. G.E. Carvell, D.J. Simons, Task- and subject-related differences in sensorimotor behavior during active touch. *Somatosens. Motor Res.* **12**, 1 (1995)
37. M.A. Harvey, R. Bermejo, H.P. Zeigler, Discriminative whisking in the head-fixed rat: optoelectronic monitoring during tactile detection and discrimination tasks. *Somatosens. Motor Res.* **18**, 211 (2001)
38. W.I. Welker, Analysis of sniffing of the albino rats. *Behaviour* **22**, 223 (1964)
39. L. Baccalá, K. Sameshima, Overcoming the limitations of correlation analysis for many simultaneously processed neural structures. *Biol. Cybern.* **84**, 463 (2001)
40. R. Dahlhaus, M. Eichler, J. Sandkühler, Identification of synaptic connections in neural ensembles by graphical models. *J. Neurosci. Methods* **77**, 93 (1997)
41. A. Korzeniewska, M. Manczak, M. Kaminski, K. Blinowska, S. Kasicki, Determination of information flow direction among brain structures by a modified Directed Transfer Function method (dDTF). *J. Neurosci. Methods* **125**, 195 (2003)
42. M. Bayram, R. Baraniuk, Multiple window time–frequency analysis, in *Proceedings of IEEE-SP International Symposium on Time–Frequency and Time-Scale Analysis*, Paris, p. 173 (1996)
43. E.G. Lovett, K.M. Ropella, Time–frequency coherence analysis of atrial fibrillation termination during procainamide administration. *Ann. Biomed. Eng.* **25**, 975 (1997)
44. Y. Xu, S. Haykin, R.J. Racine, Multiple window time–frequency analysis of EEG using Slepian sequences and Hermite functions. *IEEE Trans. Biomed. Eng.* **46**, 861 (1999)
45. S. Mallat, *A Wavelet Tour of Signal Processing* (Academic, New York, 1999)
46. M. Alegre, A. Labarga, I. Gurtubay, J. Iriarte, A. Malanda, J. Artieda, Movement related changes in cortical oscillatory activity in ballistic, sustained and negative movements. *Exp. Brain Res.* **148**, 17 (2003)
47. N.P. Castellanos, V.A. Makarov, Recovering EEG brain signals: artifact suppression with wavelet enhanced independent component analysis. *J. Neurosci. Methods* **158**, 300 (2006)
48. H. Goelz, R. Jones, P. Bones, Wavelet analysis of transient biomedical signals and its application to detection of epileptiform activity in the EEG. *Clin. Electroencephalogr.* **31**, 181 (2000)
49. V.T. Mäkinen, P.J.C. May, H. Tiitinen, Spectral characterization of ongoing and auditory event-related brain processes. *Neurol. Clin. Neurophysiol.* **104**, 3 (2004)
50. F. Mormann, J. Fell, N. Axmacher, B. Weber, K. Lehnertz, C. Elger, Phase/amplitude reset and theta–gamma interaction in the human medial temporal lobe during a continuous word recognition memory task. *Hippocampus* **15**, 890 (2005)
51. A. Murata, An attempt to evaluate mental workload using wavelet transform of EEG. *Hum. Factors* **47**, 498 (2005)

52. R. Quian Quiroga, H. Garcia, Single-trial event-related potentials with wavelet denoising. *Clin. Neurophysiol.* **114**, 376 (2003)
53. S. Schiff, A. Aldroubi, M. Unser, S. Sato, Fast wavelet transformation of EEG. *Electroencephalogr. Clin. Neurophysiol.* **91**, 442 (1994)
54. A. Grinsted, J.C. Moore, S. Jevrejeva, Application of the cross wavelet transform and wavelet coherence to geophysical time series. *Nonlinear Process. Geophys.* **11**, 561 (2004)
55. A. Klein, T. Sauer, A. Jedynek, W. Skrandies, Conventional and wavelet coherence applied to sensory-evoked electrical brain activity. *IEEE Trans. Biomed. Eng.* **53**, 266 (2006)
56. J.P. Lachaux, A. Lutz, D. Rudrauf, D. Cosmelli, M. Le Van Quyen, J. Martinerie, F.J. Varela, Estimating the time-course of coherence between single-trial brain signals: an introduction to wavelet coherence. *Clin. Neurophysiol.* **32**, 157 (2002)
57. M. Le Van Quyen, J. Foucher, J.P. Lachaux, E. Rodriguez, A. Lutz, J. Martinerie, F.J. Varela, Comparison of Hilbert transform and wavelet methods for the analysis of neuronal synchrony. *J. Neurosci. Methods* **111**, 83 (2001)
58. A. Pavlov, V. Makarov, I. Makarova, F. Panetsos, Sorting of neural spikes: when wavelet based methods outperform principal component analysis. *Nat. Comput.* **6**, 269 (2007)
59. D.P. Percival, On estimation of the wavelet variance. *Biometrika* **82**, 619 (1995)
60. C. Torrence, P.J. Webster, The annual cycle of persistence in the El Niño-Southern Oscillation. *Quarterly J. R. Meteorol. Soc.* **124**, 1985 (1998)
61. J.V. Schreiber, A. Schmitz, Surrogate time series. *Physica D* **142**, 646 (2000)
62. J. Theiler, S. Eubank, A. Longtin, B. Galdrikian, D. Farmer, Detecting nonlinear structure in time series. *Physica D* **58**, 77 (1992)
63. A. Nunéz, F. Panetsos, C. Avendaño, Rhythmic neuronal interactions and synchronization in the rat dorsal column nuclei. *Neuroscience* **100**, 599 (2000)
64. F. Panetsos, A. Nunéz, C. Avendaño, Electrophysiological effects of temporary deafferentation on two characterized cell types in the nucleus gracilis of the rat. *Eur. J. Neurosci.* **9**, 563 (1997)
65. J. Aguilar, C. Rivadulla, C. Soto, A. Canedo, New corticocuneate cellular mechanisms underlying the modulation of cutaneous ascending transmission in anesthetized cats. *J. Neurophysiol.* **89**, 3328 (2003)
66. A. Canedo, J. Aguilar, Spatial and cortical influences exerted on cuneothalamic and thalamo-cortical neurons of the cat. *Eur. J. Neurosci.* **12**, 2515 (2000)
67. E. Malmierca, A. Nuñez, Corticofugal action on somatosensory response properties of rat nucleus gracilis cells. *Brain Res.* **810**, 172 (1998)
68. E. Malmierca, A. Nuñez, Primary somatosensory cortex modulation of tactile responses in nucleus gracilis cells of rats. *Eur. J. Neurosci.* **19**, 1572 (2004)
69. C.J.M. Vanhatalo, M.D. Palva, J.W. Holmes, J. Miller, K. Voipio, A. Kaila, Infralow oscillations modulate excitability and interictal epileptic activity in the human cortex during sleep. *Proc. Natl. Acad. Sci. U. S. A.* **101**, 5053 (2004)

Chapter 4

Classification of Neuronal Spikes from Extracellular Recordings

Abstract In this chapter, we consider the problem of spike separation from extracellularly recorded action potentials, which is important when studying the dynamics of small groups of neurons. We discuss general principles of spike sorting and propose several wavelet-based techniques to improve the quality of spike separation, including an approach for optimal sorting with wavelets and filtering techniques. Finally, we consider the application of artificial neural networks to solve this problem.

4.1 Introduction

Most of the neurons in the brain communicate by sending and receiving short-lasting electrical pulses, so-called action potentials or spikes. When analyzing the cooperative behavior of a neuronal ensemble or studying the neural code, spikes are thought to be stereotypical events. Hence it is not the shape of each spike waveform but the precise timing of spike firing that matters for this analysis. Then we can speak about spike trains generated by neurons as of a multivariate point process. Many contemporary studies of neuronal activity rely on the analysis of spike trains. One may seek different correlations among neurons or behavioral correlates, spatial and temporal patterns, firing synchronization phenomena, etc. For example, this is especially relevant for the analysis of neuronal responses in the first relay stations of the brain to external tactile stimuli, i.e., the way neurons process different external inputs and the temporal sequences of spikes they generate [1,2]. In particular, it has been shown that spiking of single neurons in the gracilis nucleus in response to a stimulus may not always be faithful, while the neuronal group does reliably transmit the stimulus to the next neural nuclei.

Spiking activity can be recorded by a single microelectrode or microelectrode array immersed in a nervous tissue. The vast majority of in vivo electrophysiological experiments use so-called extracellular recordings, i.e., an electrode (inside the nervous tissue) detects electrical activity of neurons from a distance. Then several

neurons near the electrode tip can produce spikes of different amplitude and shape (for more detail see, e.g., [3]). Consequently, one experimental recording (extracellular electric potential) may contain a mixture of spikes generated by different neurons. Then the experimentalist must identify and sort or separate spikes due to different neurons. Ideally all spikes produced by a single neuron should be assigned to one group or cluster. Errors occur when spikes belonging to other neurons are grouped together with the spikes of the target neuron (so-called false positives) or when some spikes emitted by that neuron are not included in its group (false negatives).

Finally, the quality and reliability of any subsequent analysis of spike trains, cooperative neuronal behavior, or single neuron activity depends on the quality of solution of the spike sorting problem. It has been shown that the quality of spike sorting by a human operator is significantly below the estimated optimum [4]. Besides, the amount of data generated by modern experimental setups is truly enormous and continues to grow. In a typical experiment one can easily get more than 10^4 spikes recorded by a single electrode tip. Modern multielectrode arrays can have hundreds of tips, which multiplies the amount of information to be processed. For all these reasons, there is a growing demand to develop automatic techniques for spike sorting.

It is typically assumed that each neuron generates spikes of the same shape and amplitude, while signals from different cells have some individual peculiarities (even though their signatures may be quite similar). Although this assumption may be significantly compromised (e.g., in a burst, each subsequent spike is usually smaller than the previous one), it is reasonably reliable for many practical cases and we shall accept it throughout this chapter.

Nowadays, there exist a number of numerical tools for spike sorting (see, e.g., [3, 5, 6, 8–14], and references therein). In this chapter we shall provide a brief overview, while paying attention to methods involving the wavelet transform and comparing them to the standard techniques most widely used in experimental labs. Although existing methods show good performance on preselected data sets [15–22], the best procedure for spike feature extraction is still a challenging issue.

4.2 General Principles of Spike Sorting

Figure 4.1a sketches a typical setup with a linear multi-electrode lowered to the rat hippocampus along the main axis of the pyramidal neurons. The electrode spans several hippocampal subfields, including CA1 and CA3 regions. As we mentioned above, in vivo electrophysiological experiments usually provide recordings of the extracellular field potential that contains multi-unitary activity coming from nearby neurons. This activity, besides spikes, contains low-frequency oscillations (<1 kHz), so-called local field potentials (LFPs) produced by synaptic currents in principal cells (Fig. 4.1b). LFPs can have significantly higher amplitude than the spikes. These oscillations can be considered as a *noise* from the standpoint of spike sorting.

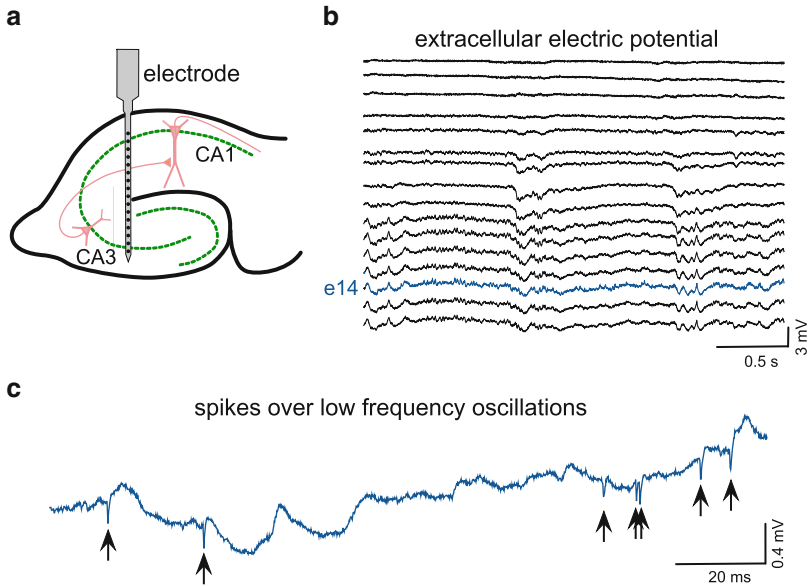


Fig. 4.1 Example of extracellular recordings in the CA1–CA3 regions of the rat hippocampus. (a) Sketch of the recording setup. A linear micro-electrode with 16 tips is lowered into the hippocampus along the main cell axis. (b) Epoch of electrical potentials recorded by the electrode (16 traces). (c) Zoomed trace from the electrode tip #14. Several neuronal spikes can be observed with the naked eye (*arrows*)

However, LFPs have great importance when studying information processing (see, e.g., [23, 24] and references therein). Figure 4.1c shows a short epoch of a recording where we see low-frequency oscillations and fast spikes. LFPs generally have a broad-band spectrum, which significantly overlaps with the spectrum of a typical spike. However, even with the naked eye, we can distinguish at least high amplitude spikes and conclude that they may not be produced by the same neuron.

Although details of different spike sorting techniques may differ significantly, the vast majority of known methods go through a number of common steps. These steps can be independent, or some of them can be included in a single procedure for improving the quality of spike sorting. Some methods can also skip some steps. However, to obtain a good understanding of the problem of spike sorting, it is useful to separate it into four steps (Fig. 4.2).

Steps I and III are the most challenging. In Sect. 4.10, these two problems will be solved together. Concerning step III, there are two types of method: empirical and model-based. In step IV, the researcher should determine the number of different groups (neurons) and the membership of the spikes in these groups.

There are also many clustering algorithms (see, e.g., [25, 26]) showing different performances on different data sets. As a matter of fact, the final performance of spike sorting is largely defined by the quality of the extracted spike features.

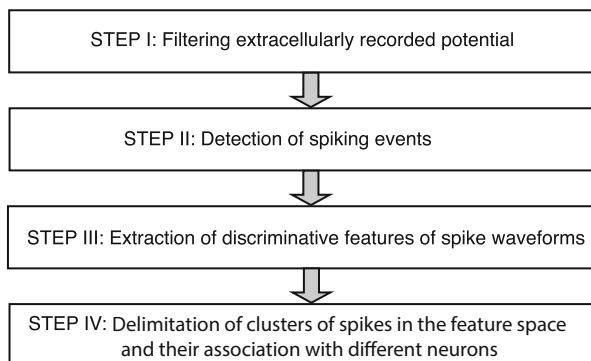


Fig. 4.2 Common steps in spike sorting

Currently available methods for feature extraction may be divided into groups, including:

- Naive, threshold based.
- Principal component analysis (PCA).
- Wavelet transform (WT).

The first two methods are the most widely used now, but the third technique has been shown to be superior and is becoming more popular [10–12].

4.3 Spike Detection over a Broadband Frequency Activity

In the spike sorting procedure mentioned above (Fig. 4.2), step I (filtering the extracellular potential) is usually intended to suppress noise and facilitate step II (detection of spiking events). A straightforward way to identify spikes is then to apply a high-pass filter (HPF) to the raw recording. However, this may significantly distort spike waveforms and create additional difficulties for the ensuing spike sorting. Besides, the operator must set the cutoff frequency, which is not always obvious (we shall discuss this problem in detail in Sects. 4.9 and 4.10). Figure 4.3a–c shows an example application of HPF with different cutoff frequencies to a recording containing high amplitude low frequency activity. Obviously, filtering reduces the noise: the more aggressive the filter, the lower the noise. However, the spike amplitude is also reduced, so we may even decrease the signal-to-noise ratio (Fig. 4.3c). More importantly, the spike shape may be significantly distorted.

A better choice in the case of linear multi-electrode recordings (Fig. 4.1) may be the so-called current source density (CSD) analysis. This is based on modeling the field potential using Maxwell’s equations [27]. In its simplest form, the CSD can be written as

$$J(t, x) = -\sigma \nabla^2 V(t, x), \quad (4.1)$$

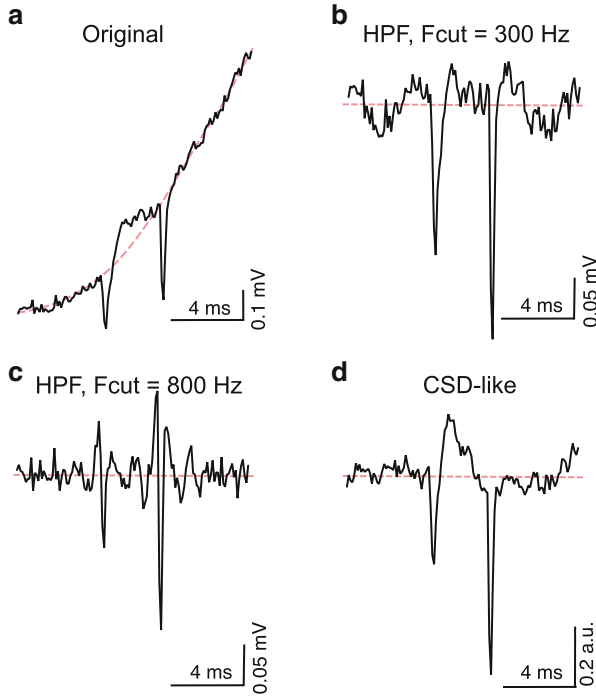


Fig. 4.3 Attenuation of low-frequency oscillations in extracellular recordings. **(a)** Original electric potential with strong low-frequency oscillation (*red dashed curve*). **(b)** High-pass filtering with cutoff frequency $F_{\text{cut}} = 300$ Hz. Spiking activity stands out above the noise. However, spike amplitudes decrease and spike shapes are distorted. **(c)** Same as in **(b)**, but with more aggressive filtering, $F_{\text{cut}} = 800$ Hz. **(d)** CSD-based method emphasizing local currents corresponding to spikes without disturbing their shapes

where $V(t, x)$ is the extracellular (recorded) potential, σ is the (ohmic) conductivity of the extracellular space, and $J(t, x)$ is the CSD. Since spikes are local events, while LFPs usually have large spatial extent, evaluation of the CSD from experimental data can spotlight spikes over LFPs.

For practical reasons we can approximate the second spatial derivative in (4.1) at the j th electrode by finite differences (this is especially useful in laminar brain structures like the hippocampus):

$$\tilde{J}_j(t) = -V_{j+1}(t) + 2V_j(t) - V_{j-1}(t), \quad (4.2)$$

where $V_j(t)$ is the voltage recorded at the j th electrode (without loss of generality, we assumed $\sigma = 1$ in (4.2)). Then \tilde{J}_j can be used for spike detection and sorting. Figure 4.3d shows the currents produced by spiking activity. Note that we now avoid the need to adjust any filter parameters and obtain the true shape of the spikes, but in terms of the CSD.

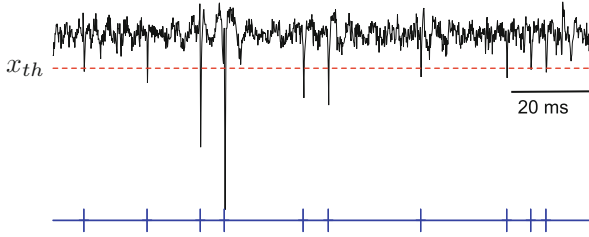


Fig. 4.4 Detection of spikes by thresholding. Events that go through the threshold (*red dashed line*) are marked as spikes ($x_{th} = -3\sigma_x$). The detected spikes are then used for sorting

Let $x(t)$ be the preprocessed signal containing spikes (either high-pass filtered $V(t)$ or CSD-like $\tilde{J}(t)$, Fig. 4.3). Once $x(t)$ has been obtained, we have to select events corresponding to spikes. In other words, we aim to distinguish spikes from the background activity. This is often done by amplitude thresholding. If $x(t)$ crosses a threshold x_{th} (in one selected direction), we mark this event as a spike. More complex detection algorithms are sometimes applied. For example, power detection, in contrast to $x(t)$, uses the quadratic quantity

$$y(t) = \int H(t - \tau)x^2(\tau) d\tau, \quad (4.3)$$

where H is some smoothing kernel (in the simplest case $H(t) = \delta(t)$).

Changing the threshold level x_{th} allows us to regulate the trend between missed spikes (so-called *false negatives*, going undetected) and the number of events occurring due to random fluctuations (*false positives*, which are non-existent spikes). Ideally, the threshold should be selected in such a way as to minimize the total error. As a rule of thumb $x_{th} \approx -3\sigma_x$, where σ_x is the standard deviation of $x(t)$ (Fig. 4.4).

Finally, we obtain a set of spikes:

$$\Omega = \left\{ (t_j, x_j(t)) \mid t \in [t_j, t_j + T] \right\}, \quad (4.4)$$

where t_j are the times of the spikes and T is a time window or duration of spikes (usually $T \approx 1\text{--}2$ ms). For correct spike sorting, all spikes should be aligned in the set Ω . This is usually done in such a way that the maxima (or minima) of all spike waveforms are at the same distance from the beginning of the corresponding spike.

In experimental recordings, each spike waveform $x_j(t)$ is discretized with the time step $\Delta t = 1/F_s$, where F_s is the sampling rate. For adequate spike sampling, F_s should be sufficiently high. $F_s = 20$ kHz is usually acceptable. Then the discretized spikes can be considered as vectors in an m -dimensional space:

$$x_j = (x_{j1}, \dots, x_{jm})^T \in \mathbb{R}^m, \quad (4.5)$$

where $m = T/\Delta t$ is the length of the spikes. Finally, we can construct a data matrix

$$X = [x_1 \ x_2 \ \dots \ x_N] \in \mathcal{M}_{m \times N}(\mathbb{R}) \quad (4.6)$$

containing all spikes. Each column of X describes one spike waveform and the column number corresponds to the number of the spike in the set Ω . Hence we can work with the set

$$\Omega = \left\{ X, \{t_j\}_{j=1}^N \right\}. \quad (4.7)$$

4.4 Naive Spike Sorting

Once a set of events (spikes) Ω (4.7) has been obtained, we must decide how many classes (neurons) there are and separate spikes between them. Comparing spike waveforms, one can resolve this problem with some degree of reliability. However, in practice, spike sorting represents a complicated task due to the high level of background noise, variability of spike waveforms, the fact that distinctions between spikes of different neurons are frequently not well-pronounced, and so on. For example, in Fig. 4.5, at least two groups of spikes are observable by the naked eye, but a reliable inference needs more careful investigation.

Mathematically speaking, each spike is a point in an m -dimensional space (4.5). Since m is quite big (usually $m = 30\text{--}70$), the curse of dimensionality is the major obstacle for clustering spikes in such a multidimensional space. Hence some method is required to reduce the dimension of the representation space. In this section, we describe the simplest (but sometimes very useful) approach to the dimension reduction problem.

Extracellularly recorded signals can be treated as a mixture of spikes produced by several neurons and different sources of fluctuations or noise. Figure 4.6 illustrates a model of this process. The recorded signal is then given by

$$V(t) = \sum_{n=1}^N v_n(t) + \sum_{k=1}^K \xi_k(t). \quad (4.8)$$

The simplest approach to the problem of spike sorting is amplitude thresholding. The amplitude is one of the most important characteristics of spikes. It is assumed a priori that each neuron generates signals of the same shape, and that this shape does not change significantly over time. If the electrode is placed near one neuron, then its spikes will be significantly higher than spikes of distant neural cells and the background activity. In this case it becomes possible to identify at least one type of spikes with amplitude thresholding (e.g., spikes B in Fig. 4.5). Spikes of different heights can be separated by selecting different thresholds (spikes A and B in Fig. 4.5). The advantage of this method is that it requires minimal equipment

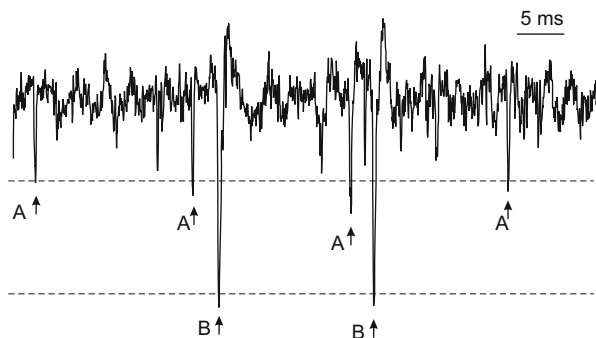


Fig. 4.5 A typical example of the extracellular potential recorded from the rodent hippocampus. The simplest way to sort spikes (marked by *arrows*) is by amplitude thresholding (two *dashed lines*)

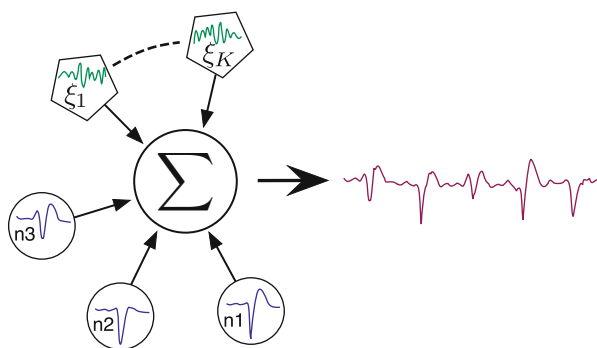


Fig. 4.6 An illustration of the spike sorting problem. The extracellularly recorded signal is a sum of spikes generated by neurons 1–3 and fluctuations produced by noise sources ξ_1, \dots, ξ_K .

and can be implemented on-line during recordings. In some cases this approach provides quite precise information, adequate for the research at hand, and no further improvements are required. One obvious disadvantage is that the amplitude is not the only feature of a spike. Spikes of different neurons may have similar amplitudes but, e.g., different widths. Then the quality of spike sorting by amplitude thresholding decays drastically.

To test the quality of spike sorting one can use a superimposed plot of all spikes belonging to a single cluster (Fig. 4.7). If the spikes belonging to one class have basically the same form (up to small variations induced by noise), then we can conclude that the sorting is good enough (Fig. 4.7a). The existence of a spike class with clearly different spike shapes (Fig. 4.7b) means that the method is unable to accurately resolve spikes and other techniques should be applied. However, this method usually works when the number of spikes is relatively small. In the case of big data sets (thousands of spikes), other methods based on electrophysiological and anatomical criteria should be applied (for details see, e.g., [7]).

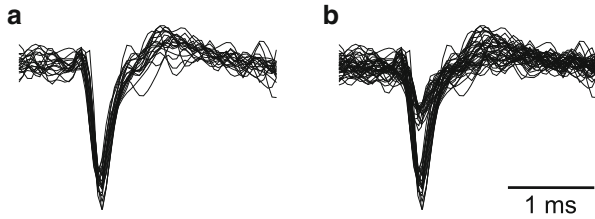


Fig. 4.7 Controlling the quality of spike sorting by spike superposition. **(a)** Good separation. Spikes of only one class (shape) appear in the plot. **(b)** Bad separation. Spikes of two different classes are merged

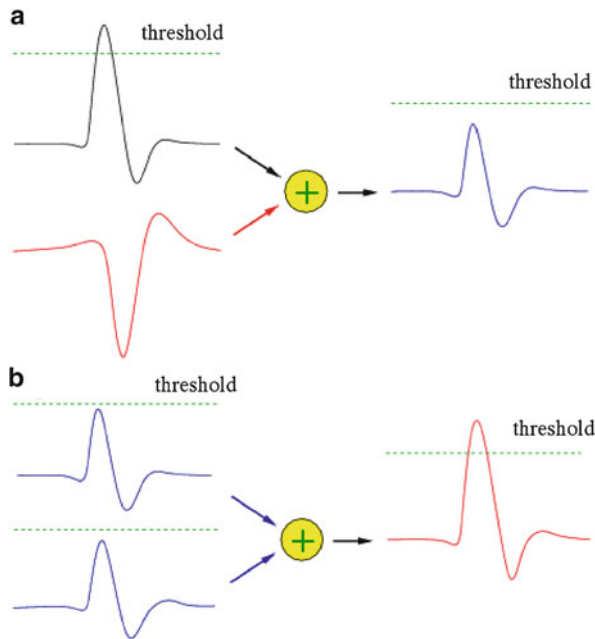


Fig. 4.8 Spike sorting errors due to spike overlap

Besides the background noise, which can be considered as a normally distributed process (or sometimes a Poisson distribution), the amplitude can vary due to possible overlapping if two different neurons fire simultaneously or within a small time window. When the maximum of one spike coincides with the minimum (or, more generally, with the negative phase) of another spike, then the resulting signal may not reach the threshold (Fig. 4.8a). The number of such events can be estimated approximately as follows:

$$N_{\text{missed}} \sim \nu \tau^- , \tag{4.9}$$

where ν is the mean firing rate of neurons and τ^- is the mean duration of the negative phase.

Another possible error occurs when two independent spikes with small amplitudes add together and the threshold is crossed by the resulting signal (Fig. 4.8b). Denoting the firing rates of spikes as ν_1 and ν_2 , we can estimate the error rate in this case as

$$N_{\text{wrong}} \sim \nu_1 \nu_2 \tau_1 \tau_2, \quad (4.10)$$

where τ_1, τ_2 are the spike durations.

These two types of error are typical for amplitude thresholding. Besides the possibility of doubled spikes, one can also consider noisy events with high enough amplitudes to affect the amplitude of spikes. The shape-accounting techniques discussed in the remaining part of this chapter are more robust against these errors. Nevertheless, false positive and false negative errors appear for any spike-sorting technique, but their number is typically much lower than for amplitude thresholding.

In order to perform a more detailed description of spike features, besides amplitude, additional characteristics such as duration, height of local extrema, etc., can also be used. Such an ad hoc approach based on the geometrical description of spikes was widely used in spike-sorting techniques developed early on [28–30]. As a rule, the more characteristics are employed for spike description, the better the spike sorting that can be achieved. However, these techniques are subjective and usually provide suboptimal spike sorting. In the following sections, we discuss spike-sorting techniques based on an integral analysis of spike waveforms.

4.5 Principal Component Analysis as Spike-Feature Extractor

Principal component analysis (PCA) is a simple but significantly more powerful tool for spike sorting [31–35]. This approach can be considered as a particular case of factor analysis [36]. It is widely used for image recognition [37], noise reduction [38], reduction of dimensions in dynamical models without significant loss of information, e.g., for mathematical description of turbulent flows [39], and so on.

4.5.1 How It Works

PCA estimates a set of orthogonal vectors for the matrix (4.6), the so-called principal components $\{c_i\}_{i=1}^N$. These are eigenvectors of the covariance matrix constructed from the data $c_i = (c_{i1}, \dots, c_{im})^T \in \mathbb{R}^m$. Then each spike x_j can be represented as

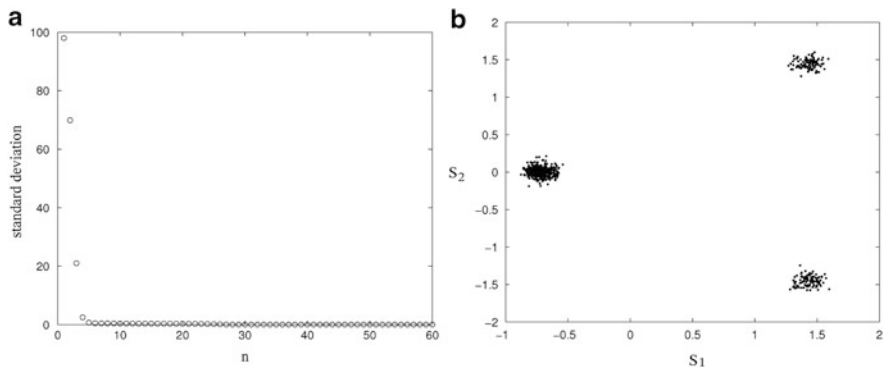


Fig. 4.9 Principal component analysis of spikes of three different classes. **(a)** Standard deviations of the scores vs the number of the principal component. **(b)** Plane of the first two principal components. Three clusters are easily distinguishable

a weighted sum of the principal component vectors with the corresponding weights or scale factors, so called scores S_{ij} , which are evaluated by the scalar product

$$S_{ij} = (c_i^T, x_j) \equiv \sum_k c_{ik} x_{jk} . \quad (4.11)$$

Thus we decompose each spike into an orthogonal set of principal components:

$$x_j = \sum_{i=1}^N S_{ij} c_i . \quad (4.12)$$

Then the scores S_{ij} can be considered as features describing the j th spike.

To illustrate the use of PCA for spike sorting, we generated an artificial set of spikes that consisted of a series of three repeated waveforms extracted from experimental data (with random order of the waveforms), corrupted by noise with Poisson distribution. By analogy with Lewicki [3], we consider the standard deviation of the scores in the direction of each principal component (Fig. 4.9). If $\lambda_1, \lambda_2, \dots$ are the variances in the directions of the principal components, we can estimate the percentage of the data variation that is accounted for by the first k components as $100(\lambda_1 + \lambda_2 + \dots + \lambda_k) / \sum_i \lambda_i$. Figure 4.9 illustrates the standard deviation of scores versus the number of the principal component. The first three components characterize the main changes in the spike shapes. They account for about 80% of the variance in the data. This suggests that, for reasonably faithful description of spikes, one can use just the first few principal components.

There are different approaches for selecting the number of principal components to retain, i.e., deciding which components are important and which can be excluded without losing important information (see, e.g., [40, 41]). For instance, the method proposed by Cattell [41] examines the explained variance (Fig. 4.9a) and searches for

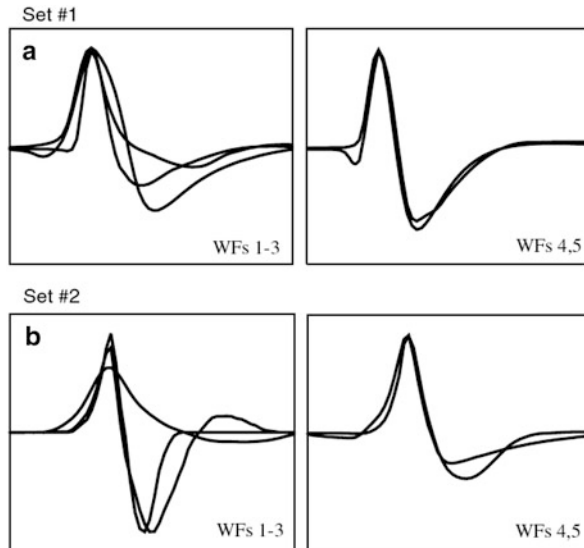


Fig. 4.10 Original spike waveforms used to generate two data sets (sets #1 and #2). We use three clearly different waveforms (WFs 1–3) and two similar waveforms (WFs 4 and 5). The difference between the similar WFs appears on short time scales for set #1 and on longer time scales for set #2

the point where the decrease in the standard deviation vs the number of the principal component becomes the slowest (the so-called elbow criterion). Components to the right of this point can be excluded without loss of important information.

In practice, using the first two ($N = 2$ in (4.12)) or sometimes three components turns out to be optimal. These components have eigenvalues larger than the background noise. Consequently, they account for the most important information about the shapes of the action potentials, while higher components are usually very noisy and provide no information about the shape of the spikes. Other components provide either an insignificant improvement or even decrease the accuracy of spike sorting. The score of the first two components typically enables acceptable spike sorting with much better performance than the method of amplitude thresholding (or at least equivalent). For instance, in the case shown in Fig. 4.9b, the performance of the method is 100%, i.e., all ‘recorded’ spikes are correctly assigned to three neurons.

4.5.2 Possible Pitfalls

In contrast to the amplitude approach, disadvantages with the PCA-based method are less obvious and can be revealed only in comparative analysis of different techniques for spike sorting. For illustrative purposes, we generated two semi-simulated data sets (Fig. 4.10), both consisting of 500 spikes of five different

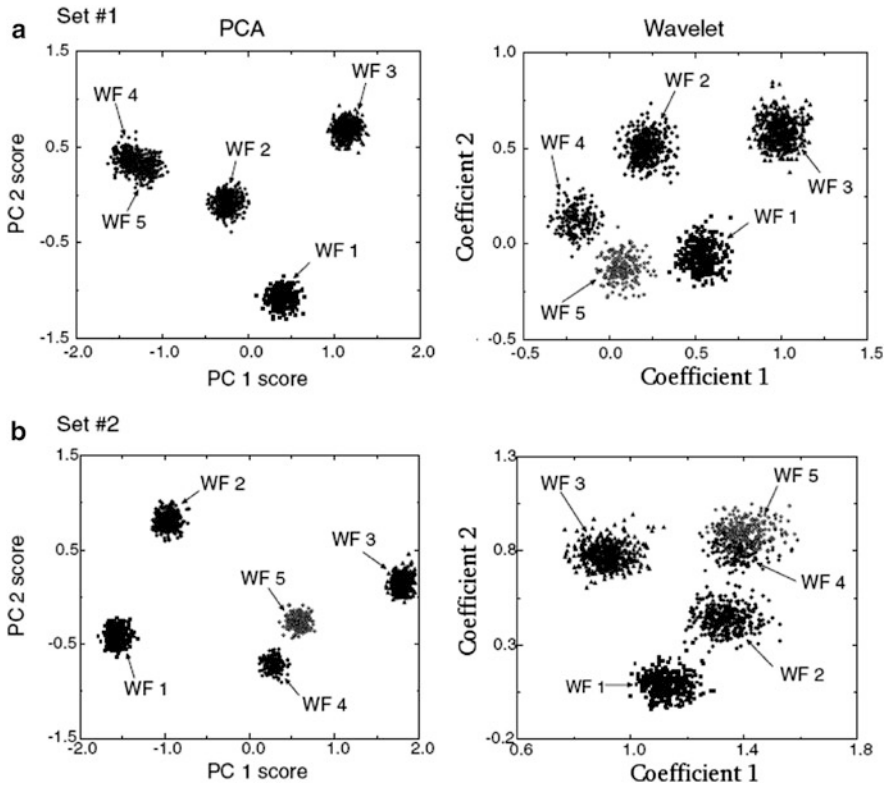


Fig. 4.11 Sorting of the data sets shown in Fig. 4.10 by PCA and wavelet techniques. (a) The wavelet-based approach outperforms the spike separation by PCA for set #1. In the PCA feature space, the spikes of WFs 1–3 are clearly clustered, but WFs 4 and 5 (*open* and *solid circles*, respectively) are mixed together. The wavelet space provides five well separated clusters for all spikes (WFs 1–5). (b) The PCA method provides better separation of set #2, than the WSC method. The chosen suboptimal wavelet coefficients exhibit multi-modal distributions allowing separation of clearly different spikes (WFs 1–3), but not similar WFs 4 and 5

waveforms. The original spike waveforms were selected from electrophysiological recordings. The two sets have three clearly different waveforms (WFs 1–3) and two similar ones (WFs 4, 5). Similar waveforms in set #1 exhibit differences only on short time scales, while WFs 4 and 5 in set #2 show a more pronounced difference on longer time scales. To simulate the noisy background, we mixed a colored noise, band-pass (300 Hz–3.0 kHz) filtered Poisson process, with the noise-free spike waveforms.

Spike sorting of set #1 by PCA reveals four different clusters (Fig. 4.11a). Three clusters correspond to spikes of WFs 1–3, thereby confirming the potential of the PCA approach. However, the fourth cluster contains a mixture of spikes of the two similar waveforms (WFs 4 and 5). Analysis of the first principal components proves that the difference between WFs 4 and 5 is not reflected by them. Thus a problem

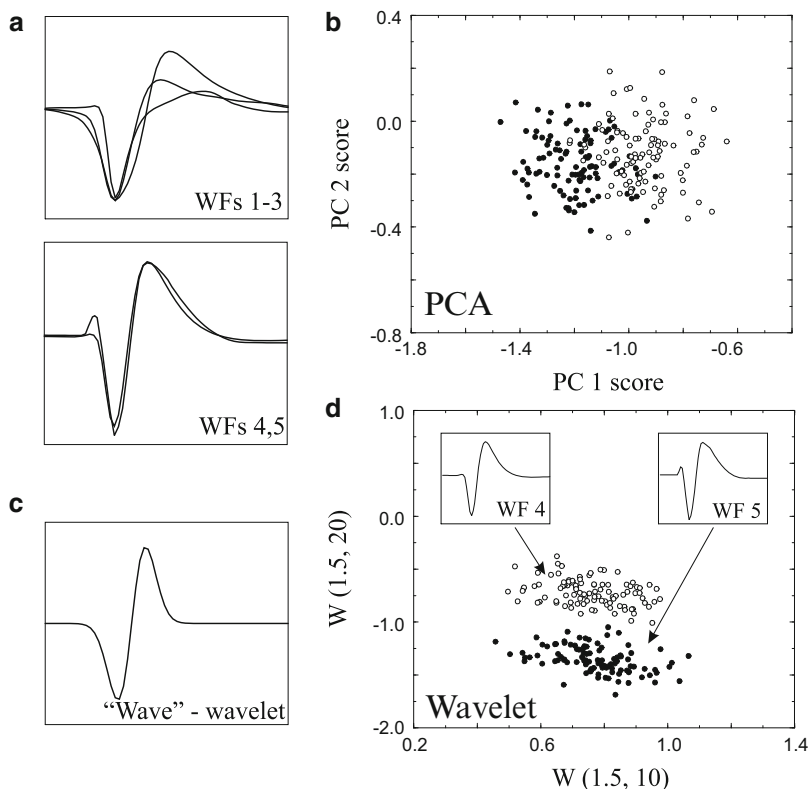


Fig. 4.12 An example where the wavelet-based approach outperforms the spike separation by the PCA. (a) Original spike waveforms used for generation of the data set (set #3). We use three clearly different waveforms (WF 1–3) and two similar waveforms (WF 4 and 5). The difference between the two similar WFs appears on small time scales. (b) Feature space of the first two principal components. A zoomed region corresponding to the fourth cluster is shown. Spikes of two waveforms (*open* and *solid circles* for WFs 4 and 5, respectively) are mixed, and an acceptable separation is impossible. (c) The “Wave”, i.e., the function chosen for wavelet analysis. (d) Zoomed region corresponding to the fourth and fifth clusters (WFs 4 and 5) in the wavelet space. Two clearly distinct clouds are formed, and separation is possible with high fidelity

with the PCA method may occur when, among different spike waveforms, there are two types with similar shapes and clearly expressed distinctions appearing only on small time scales (set #1 in Fig. 4.10). Such distinctions are not usually reflected in the first principal components, and consequently the method fails to separate such spikes.

In order to confirm this conclusion, we considered the other test data set, i.e., data set #3, consisting of 500 spikes of five different waveforms (Fig. 4.12a) corrupted by noise. Application of the PCA to this data set again reveals four different clusters. First, three clusters correspond to spikes of the WFs 1–3, thereby demonstrating the potential of the PCA approach. However, the fourth cluster contains a mixture of

spikes of two similar waveforms: WFs 4 and 5 (Fig. 4.12b). Analysis of the principal components confirms that the difference between WFs 4 and 5 is not reflected in the first two of them. Thus, PCA-based methods may fail to separate spikes with differences appearing on small scales.

4.6 Wavelet Transform as Spike-Feature Extractor

The wavelet approach [10–12] represents the spike waveform $x_j(t)$ by coefficients of the WT. In the case of the continuous wavelet transform [13, 14], the coefficients are associated with selected values of the time localization t_0 and the scale s . In its most general form, the continuous WT of a spike waveform reads

$$W_j(s, t_0) = \frac{1}{\sqrt{s}} \int_0^T x_j(t) \psi_{s,t_0}(t) dt, \quad (4.13)$$

where T is the spike duration (typically 1–2 ms), and

$$\psi_{s,t_0}(t) = \psi\left(\frac{t - t_0}{s}\right)$$

is a translated and scaled mother wavelet.

The main wavelet-based techniques for spike sorting (e.g., [10–12]) use the discrete wavelet transform, since this provides a quick decomposition of a spike with fewer coefficients. Let us consider, e.g., an approach proposed by Letelier and Weber [10].

4.6.1 Wavelet Spike Classifier

The WT of a spike can be considered as a set of filters with different bandwidth. Then the value of the energy found in a specific frequency band for each spike is considered as its feature. This idea was first adopted in the framework of the wavelet-based spike classifier (WSC) [10]. This approach is based on the standard pyramidal expansion algorithm (see Fig. 2.28, Sect. 2.4). The coefficients of the spike decomposition in the basis of Daubechies wavelets are used as features for spike sorting.

For illustrative purposes, we can consider a more general case, namely, application of both the continuous and the discrete wavelet transform, depending on the researcher's choice. We shall consider here the continuous WT, because it is simpler and allows for a detailed representation of the results. In particular, it becomes possible to discuss the problem of optimization of spike features in terms of a surface of the wavelet coefficients, which is a more illustrative approach.

With the tuning parameter s in (4.13), one can successfully resolve the multi-scale structure of the data sets #1 (Fig. 4.10a) and #3 (Fig. 4.12a). Indeed, the WSC technique finds all five clusters, including those corresponding to WFs 4 and 5 (Figs. 4.11a and 4.12d).

In the case where spike waveforms have a multi-scale structure with significant characteristics appearing on small scales, as in the data sets #1 and #3 used in Figs. 4.10a and 4.12a, the wavelets are able to resolve these features. Indeed, application of the wavelet technique to the data set of Fig. 4.11a shows that this approach finds all five clusters. Figure 4.12d also illustrates a good separation of WFs 4 and 5 into two clusters, where the PCA had difficulties (Fig. 4.12b).

4.6.2 *Potential Problems*

Although the WT is potentially more powerful than PCA, there are a number of inherent problems restricting its broader application for spike sorting. Here we discuss the main ones among them: an arbitrary choice of mother wavelet and selection of the best wavelet coefficients:

- Apparently, the results of the analysis, e.g., the wavelet coefficients, depend on the mother wavelet ψ . Generally, there is no standard answer about how to choose the mother wavelet in a particular case. Thus, the performance of the method for a given mother wavelet may vary considerably from one data set to another. For spike separation, different mother wavelets have been advocated: Daubechies [10], Coiflet [11], and Haar [12]. Possible advantages of one or the other depend on the particular spike waveforms of the analyzed data set, and no a priori recommendation can be given about which mother wavelet will perform better. Successful classification can be achieved by selecting a mother wavelet similar in shape to the spike waveforms. For instance, in the example shown in Fig. 4.12, to obtain a good separation, we used the Wave wavelet (Fig. 4.12c), which is visually very similar to WFs 4 and 5 (Fig. 4.12a).
- Let us assume that the mother wavelet has been selected somehow. Then the WT of spike waveforms is performed, thus obtaining a number of different wavelet coefficients for each spike (usually 64 in the case of the DWT and even more for the CWT). In contrast to PCA, these coefficients are not ordered, and making the right choice among them for spike sorting is a challenging problem. Different authors have suggested different procedures for coefficient selection. Among others, we can list: large standard deviation, large mean values, and multi-modal distribution [10]. There is also a more complicated, but at the same time mathematically better justified method based on information theory [11]. However, there is no single universal approach for the choice of WT features capable of providing the best classification in every case, and a counterexample can always be found. Difficulties occur especially when the analyzed data contains spiking activity of many neurons, and among them there are both clearly different and rather similar types of spike waveforms.

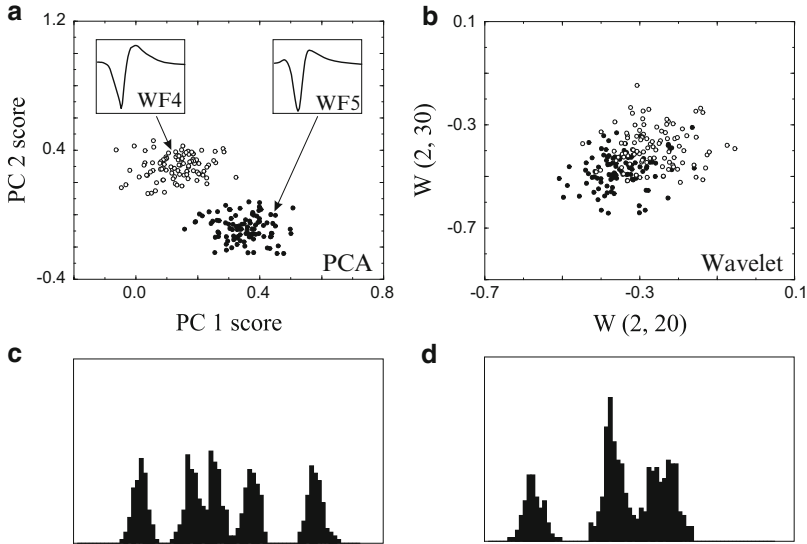


Fig. 4.13 A case where the PCA provides better separation than the wavelet technique. As in Fig. 4.12, we use a data set with spikes of three clearly different and two similar waveforms. However, the difference between similar spikes is not so pronounced now, and is not on small scales (set #4). (a) Principal components show a good separation of spikes of WF4 and WF5 (*open* and *solid circles*, respectively). (b) Wavelet classification. The chosen wavelet coefficients exhibit multi-modal distributions allowing separation of clearly different spikes. However, separation of WF4 and 5 is not achieved. (c) and (d) Histogram of spike density along the first component score (c) and one of the wavelet coefficients (d). The wavelet coefficient exhibits a multi-modal distribution, but the number of peaks (four in (d)) corresponding to clusters is less than in the PCA case (five in (c))

To illustrate the kind of problems that may be encountered, we again generated test data sets #2 and #4 (Figs. 4.10b and 4.13a) with more pronounced differences between the WFs 4 and 5 and with no clear distinctions on small scales. This helps the PCA to separate all spike groups, including those of similar waveforms (Figs. 4.11b and 4.13a). According to one of the wavelet coefficient selection procedures [10], the features used for classification should show a multi-modal distribution. However, in many practical cases, a multi-modal distribution is obtained for many different wavelet coefficients and there is no clue about how to perform an automatic comparison in order to select the most informative ones. An example of such a quasi-arbitrary (unsuccessful) choice of coefficients is illustrated in Fig. 4.13b. Although the chosen wavelet coefficients have multi-modal distributions (Fig. 4.13d), allowing separation of the first three clearly different spike waveforms, the wavelet approach gives a worse classification of two similar waveforms than the one provided by the PCA (Fig. 4.13a, c).

4.7 Wavelet Shape-Accounting Classifier

With a view to improving the wavelet-based extraction of discriminative spike features, let us consider a three-step approach based on a combination of the PCA and wavelet techniques [13, 14]. This algorithm, which we shall refer to as the wavelet shape-accounting classifier (WSAC), works as follows:

- Find representative waveforms (rWFs).
- Search for wavelet parameters (s, t_0) maximizing the distances between the rWFs in the wavelet space.
- Evaluate the wavelet coefficients for the resulting parameter sets for all neuronal spikes $W_i(s^*, t_0^*)$.

To demonstrate the method we start with a typical situation frequently encountered when processing real electrophysiological recordings. A conventional method of spike feature extraction, e.g., PCA, gives two poorly separated overlapping clouds (Fig. 4.14a). For the sake of simplicity, we suppose that these clouds consist of spikes of two neurons (or spikes of one neuron and other possibly noisy spike-like pulses). Our goal is to improve the separability of the two clouds and hence to reduce the number of wrongly classified spikes.

First, we localize the cloud centers S_k ($k = 1, 2$), i.e., the positions of the spike density maxima in the PCA space (step 1). Then we average the spike waveforms over spikes falling in a small neighborhood of each cloud center (insets in Fig. 4.14a):

$$x_{\text{rWF}k} = \bar{x}_{j \in \omega}, \quad \omega = \{j \in [1, N] : \|S_j - S_k\| < \epsilon\}. \quad (4.14)$$

The mean or representative waveforms (rWFs) thus obtained approximate noise-free spike waveforms of the two neurons. Here we assume that each neuron emits spikes of the same shape that are linearly mixed with noise at the electrode, so that the noise impact near the cloud centers is minimal and gets canceled by averaging.

Second, we apply the WT to $x_{\text{rWF}1}$, $x_{\text{rWF}2}$ and search for a set of parameters (s^*, t_0^*) that maximizes the distance $|W_{\text{rWF}1}(s^*, t_0^*) - W_{\text{rWF}2}(s^*, t_0^*)|$ (step 2). Figure 4.14b shows the distance between rWFs in the wavelet space as a function of the scale s for different values of t_0 . Frequently, crucial differences between spike waveforms occur at the beginning and the end of firing. To better account for the spike morphology, we search separately for the maximal distance in the first and second halves of the spike time window. Circles in Fig. 4.14b mark two points (one for each half window) where the distance between the representative waveforms is maximal.

Third, we apply the WT for all spikes x_j , using the parameter sets (s^*, t_0^*) found above (step 3). The resulting coefficients are the new spike features (Fig. 4.14c). Visually, the clouds corresponding to two neurons are better delimited in the wavelet plane than in the PCA space (compare Fig. 4.14a, c). Indeed, the histogram of the distribution of spike features in the wavelet spaces (WSAC method) exhibits

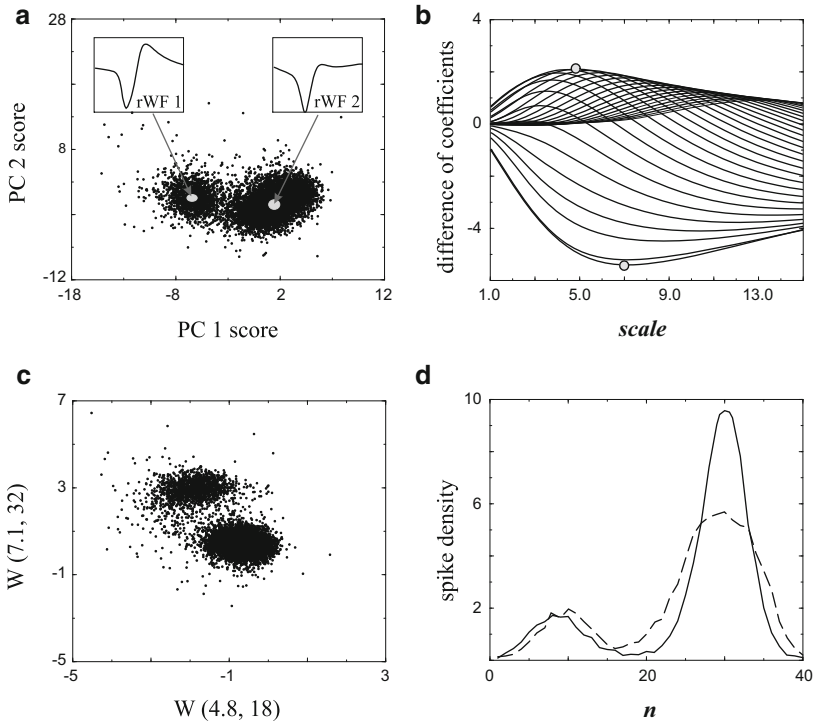


Fig. 4.14 Working principle of the WSAC method. (a) Two overlapping clouds correspond to spikes of different types on the PCA plane. *Insets* show representative spike waveforms obtained by averaging over neighborhoods of the cloud centers. (b) Difference between wavelet coefficients for the representative spikes as a function of scale. *Circles* mark the coefficient pairs ($s = 4.8$, $t_0 = 18$ and $s = 7.1$, $t_0 = 32$) that correspond to the most prominent distinctions between rWF1 and rWF2. (c) New spike feature space. The resulting coefficients are used. (d) Spike density along the clouds. Peaks correspond to the centers of the clouds. The *dashed line* corresponds to the PCA space and the *solid line* shows the results obtained in the wavelet space. The later distribution shows better separated and more prominent peaks resulting in a better localization of spikes of different waveforms in feature space (compare the clouds in (a) and (c))

significantly more pronounced peaks than the PCA method (Fig. 4.14d). This means that one can now better delimit clouds and considerably reduce classification errors arising from misclassification of spikes in the overlapping part of the clouds.

4.8 Performance of PCA vs WT for Feature Extraction

We tested the proposed approach on three different data sets (S1, S2, and S3). Each data set is obtained in the following way. We take two experimental electrophysiological recordings. One of the recordings is selected in such a way that spikes of one type can be easily separated from the rest by the conventional thresholding

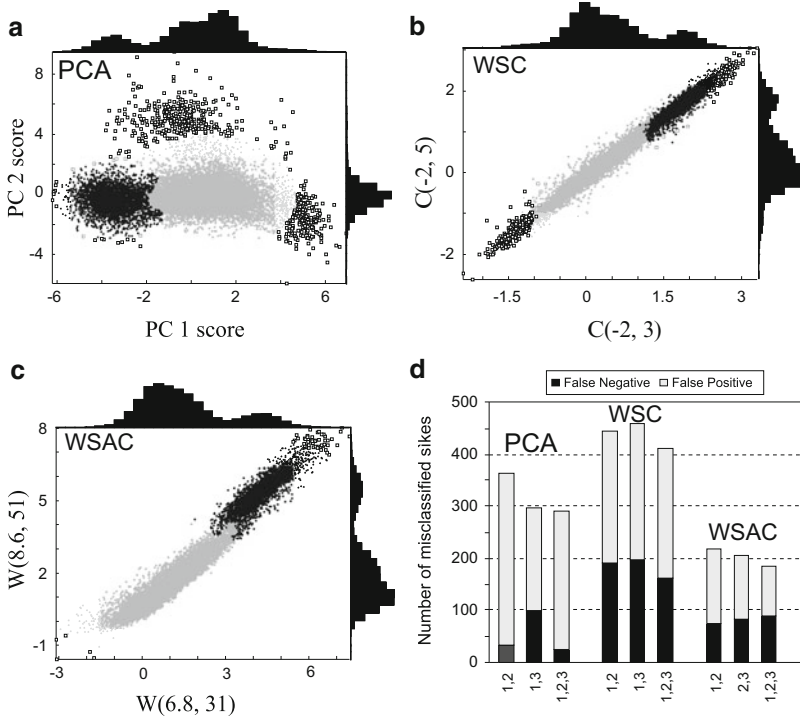


Fig. 4.15 Results of spike separation by different methods for the data set S1. **(a)** Projection of the feature space for the PCA onto its first two components, and corresponding histograms of spike densities. *Black points* correspond to spikes classified as belonging to the targeting cluster. **(b)** The same as in **(a)**, but for the WSC method. **(c)** The same as in **(a)**, but for the WSAC method. **(d)** Number of misclassified spikes for the different methods and for different spike feature subsets used for classification

method (Sect. 4.4). These spikes are then mixed with another experimental recording displaying complex spiking activity. On the one hand, this procedure allows one to keep all characteristics essential to a real electrophysiological experiment (level and type of noise, spike waveform variation, etc.), and on the other hand, we possess a priori information about the membership of spikes for one target cluster formed by the “additional” spikes. Hence, we can estimate the classification error for the given cluster.

The generated data sets were used as an input to three feature extraction algorithms discussed above: PCA, WSC, and WSAC. Then clustering was performed using the superparamagnetic method [42], and the number of misclassified spikes was estimated.

Figure 4.15 illustrates results obtained for the data set S1 consisting of 16,568 spike waveforms, including 3,069 “additional” spikes. The PCA gives two clusters (Fig. 4.15a) shown in black and gray, corresponding to the additional (targeting) and the original action potentials, respectively. Squares mark unclassified spikes that are

not related to either of the clusters. Classification of spikes by the three first PCs gives 290 misclassified spikes: 24 false negative and 266 false positive, i.e., 0.8 and 8.6 % of the total number of spikes in this cluster. The histograms of spike densities for each coordinate in the feature space show a bimodal distribution for the PC1, and a unimodal distribution for the PC2. The former allows separation of different waveforms into two clusters, while the latter does not actually provide additional information for spike classification.

Figure 4.15b illustrates the results of spike sorting performed by the WSC method [10]. Following the authors' recommendations, we chose for classification the wavelet coefficients showing the largest standard deviations, the largest values, and the bimodal distributions. Note that, in contrast to the PCA, the histograms in Fig. 4.15b are both bimodal, so they actually provide useful information for spike sorting. However, for the considered example, we obtain a higher classification error: 410 misclassified spikes (5.2 % of false negative and 8.1 % of false positive). Thus a quasi-arbitrary choice of wavelet coefficients satisfying the given recommendations did not lead to an improvement in spike sorting as compared with the PCA method.

Figure 4.15c shows the results of the spike classification obtained using the WSAC method. We found that three pairs of coefficients (s^* , t^*), namely, (6.8, 31), (8.6, 51), and (6.2, 20), maximize the difference between the characteristic spike shapes. These sets were used for spike sorting, which provided the best results: 185 or 2.8 % of false negatives and 3.1 % of false positives.

Figure 4.15d shows the results of spike classification using the three methods for different combinations of features used in each particular technique. For instance, classification performed using the first two principal components gives 364 errors (first bar in Fig. 4.15d), whereas the same done with PC1 and PC3 results in 296 errors. This means that, in this case, PC3 describes the variation in the data set better than PC2. Using all three components slightly improves the classification, resulting in 290 errors. Considering WSC, we note that each coefficient improves the results of classifications, but the overall performance is the worst among all the methods. On average, the WSAC approach gives the minimal classification error for any combination of spike features.

Table 4.1 summarizes the results obtained for all data sets. We also include classification errors obtained by the WMSPC method based on the approach proposed by Quian Quiroga et al. [12]. This approach performs considerably better for the set S2, while showing poor performance for S1 and S3.

Hence, regarding the question of when wavelet-based methods outperform the PCA, we have shown that the main advantage of WT techniques reveals itself when dealing with the detailed structure of experimental signals over a broad range of scales. Considering the WT approach as a *mathematical microscope*, the following interpretation can be given: wavelets can resolve fine details of a signal structure, but we need to choose the focal point and resolution of this "microscope" appropriately. From the mathematical viewpoint, this means that the selection of wavelet parameters responsible for resolution and focusing is of crucial importance.

Table 4.1 Classification error rates for all data sets and different methods (percentage of misclassified spikes out of the total number of spikes in the cluster)

	S1			S2			S3		
	FN	FP	Sum	FN	FP	Sum	FN	FP	Sum
PCA	0.8	8.6	9.5	41.6	11.8	53.4	0.1	2.6	2.7
WSC	5.2	8.1	13.3	34.2	13.8	48.0	6.7	2.9	9.6
WMSPC	7.5	8.9	16.4	28.7	0.8	29.5	9.5	4.4	13.9
WSAC	2.8	3.1	5.9	26.4	8.2	34.6	1.8	0.3	2.1

FN and FP denote *false negative* and *false positive* errors

If they are selected successfully, the “microscope” can elucidate the differences in spike waveforms.

This is why the problem of selecting the optimal wavelet coefficients is an important trend in the problem of spike separation. In contrast to PCA-based methods, where the first principal component scores are used as spike features due to their natural order, optimal selection of features within the framework of WT techniques is a significantly more complicated procedure.

There are at least two cases where wavelet-based techniques are potentially preferable to PCA:

- When there is small-scale structure in the waveforms that is not reflected in the first principal components.
- When there is strong enough low-frequency noise, since this significantly diminishes the performance of the PCA method, whereas noise statistics are less critical for wavelets.

In other situations, the considered WT-based approaches give comparable results to PCA.

4.9 Sensitivity of Spike Sorting to Noise

Sensitivity of spike sorting to noise statistics is an important problem for any approach. Extracellular recordings of neural activity contain different kinds of noise, from Johnson noise in the electrode and electronics, through the background activity of distant neurons and electrode micromovement, to variation of action potentials due to physiological processes in the cell dynamics.

Obviously, the quality of the spike separation is degraded by increasing noise intensity, although robustness against the noise level may be different for different methods. Another, more important question we address here is how the efficacy of the method depends on the frequency band of the noise. Indeed, when the noise frequency band lies far outside the frequency band of a spike spectrum (about 300–3,000 Hz), the noise can be easily filtered out by applying high-pass and/or low-pass filters, thus eliminating the impact of the noise on spike separation. However, when

the noise frequency band overlaps with the spike spectrum, the use of filters becomes worthless, and the advantages of one or another method can become significant. This kind of overlap can happen, for example, when recording certain neurons from a densely populated brain region and spikes from more distant neurons (far enough away and consequently of low enough amplitude to be included as spikes for separation, but close enough that their effect is noticeable) are confused with noise.

In this section, we study and compare the performance of the PCA and the wavelet technique with regard to the noise statistics, assuming an overlap between the spike spectrum and the noise frequency band. We discuss how the quality of spike separation depends on the frequency band of the experimental noise.

4.9.1 Impact of High/Low Frequency Noise on PCA and WT

Quantities used as features for spike separation in the PCA and WT techniques are often related to rather different time scales. This suggests that PCA and WT may show different degrees of robustness against noise with different statistics.

The wavelet coefficients $W(s, t_0)$ used for spike classification are typically related to rather small values of the scale parameter s . Therefore we expect the coefficients to be distorted mainly by fluctuations in the frequency band associated with the scale parameter value. Relatively slower or faster fluctuations should not have an essential influence (in the case of additive noise). The latter means that separation of several types of spikes by the WT approach should have a maximal classification error for noise with high-frequency dynamics.

Another situation is expected for PCA. This approach quantifies spike features on large scales for entire waveforms. The low-frequency noise appearing on the time scales of the first principal components disperses spikes in the PCA feature space. The high-frequency noise mainly affects high principal components that are not considered for spike separation. As a result, the PCA method should exhibit a classification error that decreases with the frequency band of the presented fluctuations.

To check these conjectures, we generated data sets consisting of 2,000 spikes of two different types (two neurons). Then we mixed spike waveforms with colored noise of a certain frequency band, and finally we performed spike sorting on the resulting data sets.

The colored noise was obtained by band-pass filtering of a Poisson random process. Choosing different values of the central frequency f_{noise} of the band-pass filter, which defines the base noise frequency, and fixing the filter width ($\Delta f_{\text{noise}} = 700 \text{ Hz}$), we estimated the classification error for each spike-sorting technique. Noise with base frequency lower than the main frequency of the spike spectrum (about 1 kHz) was considered to be low frequency, while fluctuations with $f_{\text{noise}} > 1 \text{ kHz}$ were considered to be the high-frequency noise. For wavelet sorting, we used the WSC method [10], but other methods show qualitatively similar results.

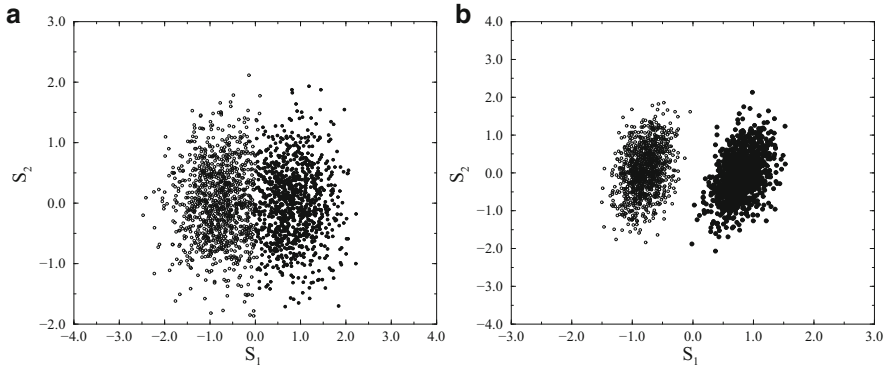


Fig. 4.16 PCA feature space of spike waveforms contaminated by noise. (a) Low-frequency noise, $f_{\text{noise}} = 500$ Hz. (b) High-frequency noise, $f_{\text{noise}} = 2,500$ Hz

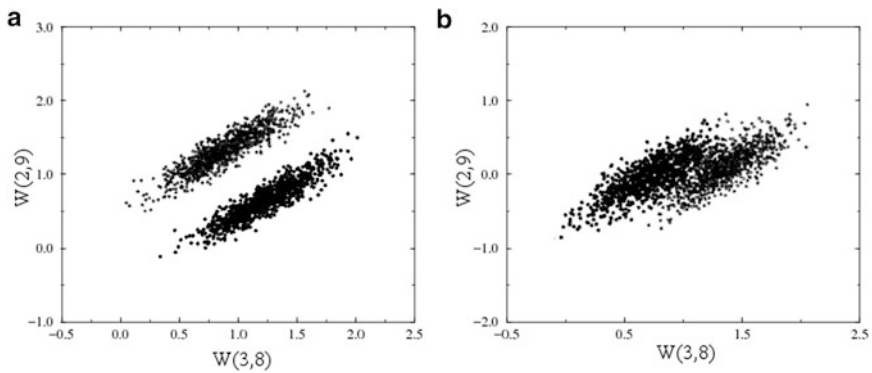


Fig. 4.17 WT feature space of spike waveforms contaminated by noise. (a) Low-frequency noise, $f_{\text{noise}} = 500$ Hz. (b) High-frequency noise, $f_{\text{noise}} = 2,500$ Hz

Figure 4.16 shows that the presence of slow fluctuations is more critical for PCA than the high-frequency dynamics. In the case of high-frequency noise, clusters are well distinguished ($f_{\text{noise}} = 2,500$ Hz, Fig. 4.16b), whereas they are less pronounced for a slower random process ($f_{\text{noise}} = 500$ Hz, Fig. 4.16a). In contrast, spike sorting using the wavelet technique shows good performance in the case of low-frequency noise (Fig. 4.17a, $f_{\text{noise}} = 500$ Hz), but performance is diminished for high-frequency noise (Fig. 4.17b, $f_{\text{noise}} = 2,500$ Hz).

We repeated spike sorting for a different base noise frequency. Figure 4.18 summarizes our results. The error of spike sorting using PCA clearly decreases with the base noise frequency (Fig. 4.18a). Spike separation using the wavelet technique shows a bell-like resonance curve. The worst classification is achieved for an intermediate noise frequency (around 2 kHz). Thus, the spike classification error is sensitive to the noise statistics.

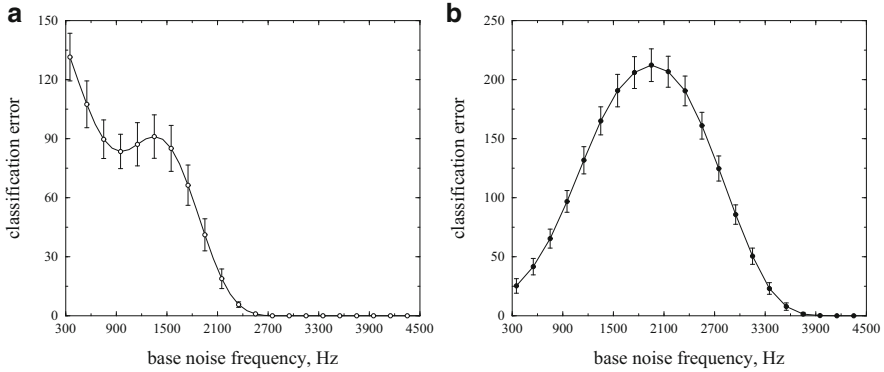


Fig. 4.18 Classification error versus base noise frequency for PCA (a) and the WT technique (b)

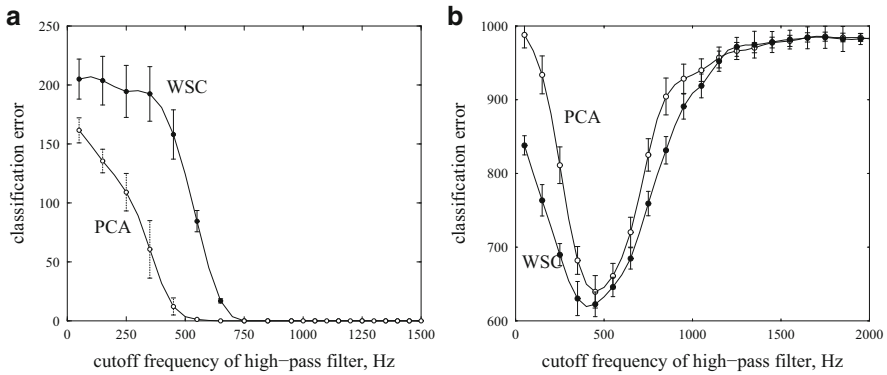


Fig. 4.19 Classification error versus cutoff frequency of a high-pass filter in the case of non-overlapping (a) and overlapping (b) power spectra of noise and spikes. The noise intensity is higher in (b)

4.9.2 Proper Noise Filtering May Improve Spike Sorting

The results shown in Fig. 4.18 provide a clue that the quality of spike sorting may be increased by smart data preprocessing, i.e., noise filtering. In particular, when the noise frequency band lies far outside the frequency band of the spike spectrum, the noise can be easily filtered out by applying high- and/or low-pass filters, thereby eliminating the noise impact on the spike separation. Figure 4.19a illustrates this simple situation.

In order to choose an optimal value for the filter cutoff frequency, one must estimate the power spectra of noise and spikes. But in order to provide a better separation of action potentials, rather than the latter spectrum, it seems to be even more useful to evaluate the spectrum of the difference between the typical (averaged) spike waveforms. Choosing the cutoff frequency of the high-pass filter

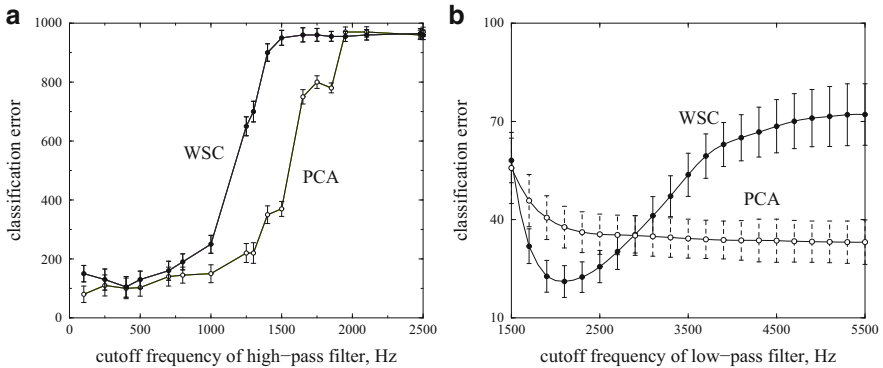


Fig. 4.20 (a) Classification error of the PCA and WT techniques versus the cutoff frequency of a high-pass filter in the case of overlapping power spectra of noise and spikes (low noise intensity). (b) The same, but for low-pass filtered spikes

higher than the range of fluctuations, we obtain clear spike sorting (Fig. 4.19a). Note that the classification error remains the same here, even when the cutoff frequency lies inside the spike spectrum: the filtering changes the waveform shapes, but these changes are the same for each type of spike, so the waveforms can be well separated. Similar results can be obtained if the frequency band of the noise is higher than the frequency band of the spike dynamics. The noise intensity does not have a crucial impact on the selection of the optimal cutoff frequency here.

In practice, however, a significantly more complicated situation is typically encountered. Usually the noise spectrum overlaps significantly with the spike spectrum and the choice of filter parameters becomes less obvious.

In order to seek for the best filtering strategy, we filtered waveforms using elliptic IIR zero-phase filter. Figure 4.19b illustrates an example of how the classification results depend on the cutoff frequency of a high-pass filter for overlapping power spectra. In contrast to the previous case (Fig. 4.19a), we cannot take bigger values of the cutoff frequency here due to the increasing classification error. An optimal value of the given frequency probably depends on both the noise intensity and the strength of spectrum overlap. In particular, this optimum may not be well expressed for rather low noise intensity (Fig. 4.20a), while the choice of filter parameters becomes more critical in the case of intense noise. According to Fig. 4.20b, a cutoff frequency around 400 Hz provides the best spike separation here.

Let us now consider how the use of a low-pass filter influences the quality of spike sorting. Figure 4.20b shows the dependence of the total classification error on the cutoff frequency of the low-pass filter. Indeed, the classification error for the WT technique has a minimum at frequencies around 2.2 kHz and then rapidly increases. For the PCA, the error first decreases gradually to 2 kHz, then remains almost constant. This suggests that low-pass filtering of spikes is worthless for PCA, and is essential for the WT, where to be on the safe side we recommend a cutoff frequency in the range 2.5–3 kHz.

4.10 Optimal Sorting of Spikes with Wavelets and Adaptive Filtering

In the vast majority of spike sorting methods, experimental noise is reduced by a standard filtering prior to extraction of spike features. This procedure does not account for the noise statistics, nor for the spike signatures. Standard techniques like amplitude thresholding and PCA have a long history, and well established recipes for optimal filtering. Their performance usually reaches a maximum for a high-pass filter at 0.3–1 kHz. However, this may not be the case for the WT technique (Fig. 4.20). Then a different filtering approach may be superior.

As we shall see in this section, the performance of the WT method can be significantly improved by incorporating the filtering step into the problem of selecting the optimal feature set. In other words, signal filtering and spike feature extraction can be done in a single step. The parametric wavelet sorting with advanced filtering (PWF) approach was proposed to exploit this idea [43].

4.10.1 Noise Statistics and Spike Sorting

To illustrate how the noise statistics affects the spike-sorting performance, we generated semi-artificial data sets. Each data set consisted of (1,000+1,000) spikes of two different neurons. The original spike waveforms were selected from electrophysiological recordings in the hippocampus. To simulate the effect of the noisy background, we mixed colored noise (a band-pass filtered Poisson process) of a certain frequency band with spike waveforms. We used these data sets for spike sorting and then estimated the performance through the error rate, i.e., the ratio of misclassified spikes to the total number of spikes.

Figure 4.21a shows the error rate as a function of the base noise frequency. In accordance with previous results (Sect. 4.9), the PCA method gives a high error rate for low-frequency noise and then progressively increases performance for high-frequency noise.

As a representative approach for wavelet-based methods, we use the WSC technique. This method exhibits significantly different behavior. The error rate has a well-pronounced peak at an intermediate noise frequency (about 2 kHz). Compared with PCA, the wavelet technique is a better option for sorting spikes contaminated by low-frequency noise ($f_{\text{noise}} < 800$ Hz).

In order to find the best filtering strategy, we filter waveforms, varying the cutoff frequency of the LPF, and then perform spike classification on the filtered data. Here we use white noise passed through the LPF with a varying cutoff frequency. Filtering generally reduces the error rate. However, it affects the PCA and WT methods differently (Fig. 4.21a). Indeed, the classification error for the WT technique has a minimum at a filter frequency around 2.2 kHz and then increases rapidly. For PCA, the error gradually decreases upto 2 kHz and then remains practically constant.

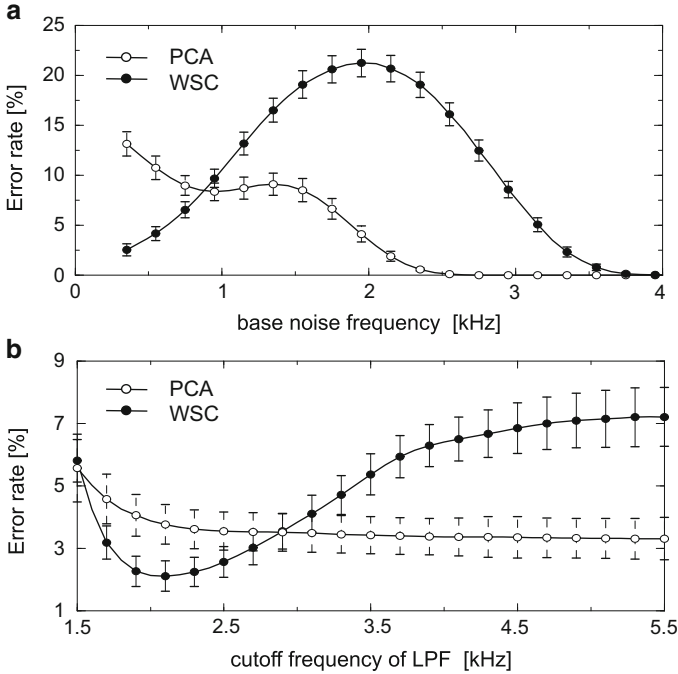


Fig. 4.21 (a) Error rate of spike sorting versus base noise frequency. (b) Error rate after low-pass filtering of spikes

This suggests that low-pass filtering of spikes is worthless for PCA, but it may be essential for WT methods, where the cutoff frequency should be appropriately selected.

4.10.2 Parametric Wavelet Sorting with Advanced Filtering

We now discuss the details of optimal spike sorting using the wavelet technique.

4.10.2.1 Derivation of PWAFF Method

We start from a data set of $N + M$ spikes of two different neurons, contaminated by noise. Denoting the original noise-free spike waveforms by $w_A(t)$ and $w_B(t)$, the recorded spikes can be written as

$$x_j(t) = \xi_j(t) + \begin{cases} w_A(t), & j = 1, 2, \dots, N, \\ w_B(t), & j = N + 1, \dots, N + M. \end{cases} \quad (4.15)$$

where we have assumed without loss of generality that the spikes are ordered. Here, $\{\xi_j\}$ are colored noise sources, mutually uncorrelated and with the same statistics (i.e., spectrum).

Applying the WT (4.13) to the spike waveform $x_j(t)$ for a selected parameter set (s, t_0) , we obtain

$$W_j(s, t_0) = \eta_j + \begin{cases} W_A, & j = 1, 2, \dots, N, \\ W_B, & j = N + 1, \dots, N + M, \end{cases} \quad (4.16)$$

where we have put

$$\eta_j(s, t_0) = \frac{1}{\sqrt{s}} \int_0^T \xi_j \psi_{s, t_0} dt, \quad (4.17)$$

$$W_{A,B}(s, t_0) = \frac{1}{\sqrt{s}} \int_0^T w_{A,B} \psi_{s, t_0} dt. \quad (4.18)$$

In (4.16), the $\eta_i(s, t_0)$ represent a kind of measurement noise and $W_{A,B}$ are the WT coefficients of the corresponding noise-free spikes.

The coefficients W_j can now be used for sorting. The aim is to separate them blindly into two clusters or groups with the lowest possible error rate. In our case, the sorting is achieved by selecting a threshold W_{th} and assigning spikes with $W_j < W_{th}$ to neuron *A*, and the others to neuron *B* (Fig. 4.22). This makes sense if the $\{W_j\}$ have a bimodal distribution, otherwise when, e.g., the noise is too strong or the parameters (s, t_0) are not optimal and no bimodal distribution exists, spike sorting is meaningless.

Let us now assume that the measurement noise is approximately Gaussian with standard deviation σ . We denote the half distance between the noise-free spikes in the wavelet space by

$$\hat{W} = \frac{W_B - W_A}{2} = \frac{1}{2\sqrt{s}} \int_0^T (w_B - w_A) \psi_{s, t_0} dt. \quad (4.19)$$

Without loss of generality, we can shift the origin and set $\hat{W} \equiv W_B = -W_A$. Then the probability density distribution of $\{W_j\}$ reads

$$h(W) = \frac{M}{\sqrt{2\pi}\sigma} \left\{ \gamma \exp \left[-\frac{(W + \hat{W})^2}{2\sigma^2} \right] + \exp \left[-\frac{(W - \hat{W})^2}{2\sigma^2} \right] \right\}, \quad (4.20)$$

where $\gamma = N/M$ is the ratio of the numbers of spikes emitted by the neurons. Then the minimum of the total number of misclassified spikes is attained for

$$W_{th} = \frac{\sigma^2}{2\hat{W}} \ln \gamma. \quad (4.21)$$

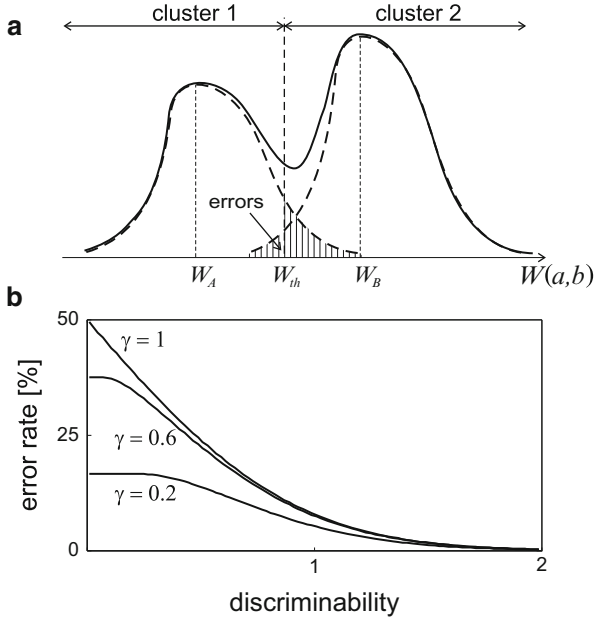


Fig. 4.22 (a) Histogram of the distribution of the WT coefficients W_i describing noisy spikes of two neurons. *Dashed curves* depict the histograms of single neurons. Classification errors appear in the overlap region. (b) Minimal error rate given by (4.22) as a function of the discriminability for several different values of γ

Note that the optimal threshold value ($\gamma \neq 1$) does not generally correspond to the position of the minimum in the histogram. Finally, the theoretical minimum of the error rate is given by

$$R_{\min} = \frac{\gamma \operatorname{erfc}\left(\Delta + \frac{\ln \gamma}{4\Delta}\right) + \operatorname{erfc}\left(\Delta - \frac{\ln \gamma}{4\Delta}\right)}{2(1 + \gamma)}, \quad (4.22)$$

where erfc is the complimentary error function, and

$$\Delta = \frac{\hat{W}}{\sqrt{2}\sigma} \quad (4.23)$$

is the *discriminability coefficient*. Accordingly, the error rate is a two-parameter function of γ and Δ that decays with an increase in Δ (Fig. 4.22b). The ratio γ of the spike numbers is fixed by experiment, so the only remaining freedom is the discriminability Δ .

Let us now explore ways to improve the discriminability. Selecting (s, t_0) appropriately, we can maximize the value of \hat{W} which, for constant σ , increases Δ .

However, as we shall show, the scaling parameter s has a nontrivial effect on the standard deviation σ of the noise, and consequently also on Δ .

The experimental noise $\xi(t)$ of a limited frequency band Ω_{noise} can be represented by a sum of harmonics:

$$\xi_j = \sum_{\Omega_{\text{noise}}} A(\omega_k) \cos(\omega_k t + \phi_{kj}) , \quad (4.24)$$

where ω_k and ϕ_{kj} are the frequency and random phase of the corresponding harmonic, and $A(\omega)$ defines the noise amplitude spectrum. Using the Haar wavelet (advocated for spike sorting in [12]), we obtain the WT of the experimental noise (4.24):

$$\eta_j = -\frac{4}{\sqrt{s}} \sum_k \frac{A(\omega_k)}{\omega_k} \sin \phi_{kj} \sin^2 \frac{s\omega_k}{4} . \quad (4.25)$$

Note that the statistical properties of η do not depend on the localization parameter t_0 . Then the variance of the measurement noise reads:

$$\sigma^2(s, \Omega_{\text{noise}}) = \frac{8}{s} \sum_k \frac{A^2(\omega_k)}{\omega_k^2} \sin^4 \frac{s\omega_k}{4} . \quad (4.26)$$

Thus the discriminability may depend nontrivially on the parameters (s, t_0) , the spike waveforms, and the spectral characteristics of the experimental noise. A natural way to change the noise spectrum is to filter the signal. Denoting the cutoff frequency of the filter by f_c , we finally reduce the problem of optimal spike sorting to *searching for the parameter set (s, t_0, f_c) which maximizes the discriminability:*

$$\arg \max_{s, t_0, f_c} \frac{\hat{W}}{\sqrt{2}\sigma} . \quad (4.27)$$

Note that our problem statement is more general than conventional methods relying on a search for the best parameter set for the WT alone. By including spike filtering in the problem of optimal spike sorting, we account for the specific noise of the individual experiment and potentially provide the best possible spike classification. Moreover, other methods of WT parameter selection are based on empirical analysis of the experimental distribution of the WT coefficients, while the PWF method is parametric.

4.10.2.2 Implementation of the PWF Method

Under experimental conditions, we have no a priori knowledge of the noise-free spikes, nor the spectrum of the experimental noise. To estimate these and optimally sort spikes, we propose the following algorithm:

1. **Estimate the noise-free spike waveforms.** Applying a conventional algorithm, e.g., PCA, we find peaks in the distribution of spike features and average spike waveforms in the vicinity of each peak, thus estimating $w_{A,B}$.
2. **Estimate the spectrum of the experimental noise $P(\omega)$.** A good approximation is the spectrum of the whole extracellular signal.
3. **Find an optimal parameter set (s^*, t_0^*, f_c^*) maximizing the discriminability.** For a given (s, t_0, f_c) :

- Filter the signal representing the waveform difference $(w_B - w_A)$ and evaluate \hat{W} .
- Evaluate

$$A^2(\omega) = P(\omega)H^2(\omega) ,$$

where H is the filter magnitude response, and then σ .

- Evaluate the discriminability, $\hat{W} / \sqrt{2}\sigma$.

Find the maximum

$$(s^*, t_0^*, f_c^*) = \arg \max_{s, t_0, f_c} \Delta(s, t_0, f_c) .$$

4. **Filter spikes with f_c^* and calculate $W_i(s^*, t_0^*)$.**
5. **Sort spikes according to the coefficients W_i .**

Note that the proposed method can be very efficient for large data sets. Steps 1–3 do not depend on the number of spikes and the WT of the whole data set is evaluated only once. Moreover, the algorithm allows the use of more than one feature set for sorting. At step 3, we can obtain more than one extremum, and then perform step 4 for all of them. In this way, we describe each spike with more than one feature (wavelet coefficient) and can use them together for spike sorting in step 5.

4.10.2.3 Algorithm Performance

To test the algorithm, we employ simulated data sets differing by noise statistics and spike waveforms. Figure 4.23 shows an application of the algorithm to the data set #1. The discriminability has a strong peak at a surprisingly low frequency $f_c = 100$ Hz (Fig. 4.23a). With such aggressive filtering, the difference \hat{W} between the noise-free spikes in the wavelet space is small, but at the same time, we almost completely filter out the noise, thereby gaining in performance.

Figure 4.23b shows histograms of the distribution of spike features (see also Fig. 4.22a). The PCA method involves a significant overlap of the spikes of two neurons and the resulting error rate is 5.5%. To find the best possible classification with the conventional WT, we *search exhaustively* through all pairs (s, t_0) for a set minimizing the error rate. Note that this is not possible in any real situation without a priori knowledge of the spike clusters. This procedure yields the absolute minimum

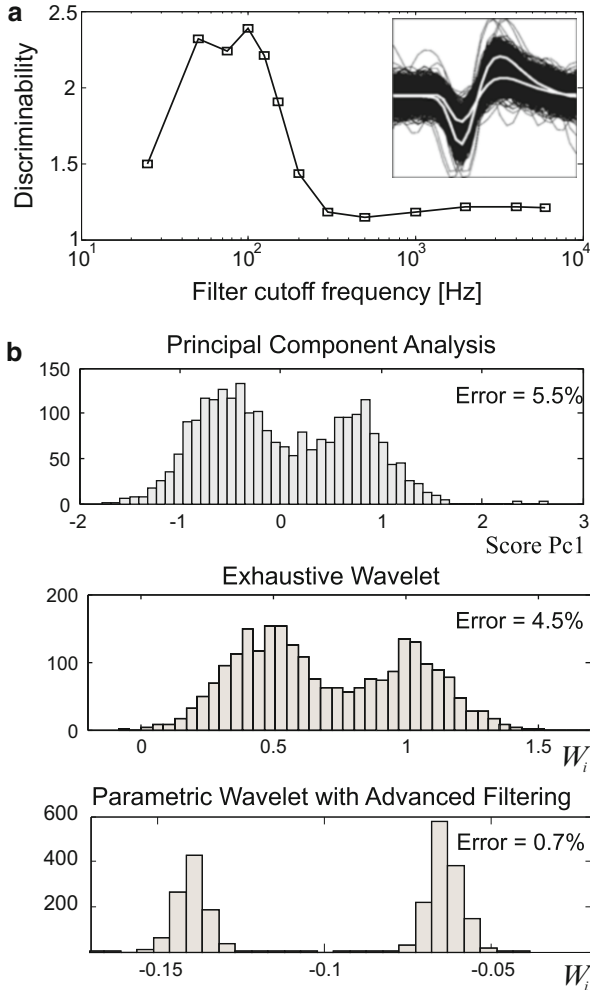


Fig. 4.23 Sorting of data set #1. (a) Discriminability Δ vs cutoff frequency of an LPF. For the maximal $\Delta = 2.39$, the theoretical minimum of the error rate is 0.3%. *Inset*: Superposed experimental spike waveforms and noise free spikes (*white*). (b) Distributions of spike features for different methods: PCA, exhaustive wavelet, and PWAf

of classification errors that can be achieved by any empirical WT-based method. The exhaustive wavelet gives a bit better classification than PCA, achieving a 4.5% error (Fig. 4.23b).

The PWAf method is significantly superior, with an error rate of 0.7%, which is quite close to the theoretical minimum. This confirms the hypothesis that intelligent filtering is essential for wavelet methods.

Table 4.2 Error rate for spike sorting by different algorithms with simulated and experimental data sets

Data set	PCA (%)	Exhaustive wavelet (%)	PWAF (%)
Simulated #1	5.5	4.5	0.7
Simulated #2	28.0	5.5	1.7
Experiment #1	11.1	7.0	3.4
Experiment #2	12.2	7.3	6.8

We performed the same procedure for another data set (Table 4.2) that was selected to exhibit differences between noise-free spikes at small time scales. This is a case where the wavelet technique has an advantage over the PCA method. Indeed exhaustive wavelet and PWAF yield a much better classification than PCA.

We now test the PWAF method on real measurements. Extracellular recordings were made using tetrode electrodes. Their design permits recording of the same neuron by two or more electrode tips (for details see [4]). In rare cases, two electrode tips capture high-amplitude spikes generated by a single neuron in addition to simultaneous multi-neuronal activity. Among many experimental recordings, we selected two data sets where these conditions were satisfied. For these data sets relating voltage traces of the two channels, we sort spikes manually with high fidelity. Then using this information, we estimate the error rate of the automatic methods. Table 4.2 summarizes the results, showing once again that the PWAF method is superior.

4.11 Spike Sorting by Artificial Neural Networks

We now discuss applications of artificial neural networks [44–48] for spike sorting, including combined approaches based on wavelets and neural networks.

4.11.1 General Approach

Here we use the wavelet multiscale decomposition of spikes as an input to a neural network. For spike decomposition, the discrete wavelet transform is used as a tool to characterize the structure of complex signals over a broad range of time scales. Figure 4.24 depicts an example of a three-level DWT of a typical spike waveform $x(t)$. The series of coefficients s_1 – s_3 correspond to the approximation of $x(t)$ at three levels, whereas d_1 – d_3 represent details. Then the set $[s_3, d_1, d_2, d_3]$, used as input to a neural network, uniquely represents the original spike waveform $x(t)$ in the wavelet space.

In general, DWT provides quite a large number of coefficient-features for each spike (equal to the spike length, e.g., 64). Not all of them are relevant for spike

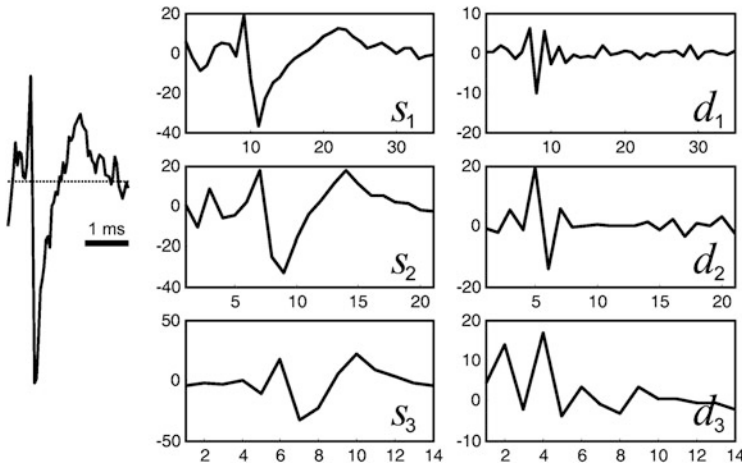


Fig. 4.24 Multilevel decomposition of a typical spike waveform using the D^4 wavelet

sorting, others may contain duplicated information. Thus for efficient spike sorting, a dimension reduction is required, and for this purpose we use neural networks.

Let us assume that some multilayer feedforward neural network receives as input spike waveform features extracted by the wavelet technique described above (Fig. 4.25). The network should be trained in such a way that, at the output, we can read out a *few compound* features best discriminating the spikes [44]. Then the problem of spike sorting becomes trivial and simple clustering algorithms, e.g., *k-means*, can be used. We thus formulate the following algorithm for spike sorting:

- Detect spikes that exceed the level of experimental noise by thresholding the high-pass-filtered recorded potential (Fig. 4.5, $f_{\text{cut}} = 100\text{--}300\text{ Hz}$, $V_{\text{th}} = 3 \cdot \text{MAD}$ (mean absolute deviation)).
- Apply DWT to the selected waveforms (Fig. 4.24). We assume that each waveform has 64 data points and use the D^4 orthonormal Daubechies wavelet, performing a pyramidal decomposition of the waveforms.
- Remove wavelet coefficients fluctuating around zero mean value, since these coefficients are strongly influenced by noise.
- Process the remaining wavelet coefficients by a 3-layer feedforward neural network.

After applying the algorithm, we expect to obtain several clusters grouping spikes in the low-dimensional feature space (Fig. 4.25). The most challenging problem in this algorithm is how to select an appropriate network and how to train it [45–48].

In general, training algorithms can be subdivided into two groups: supervised and unsupervised learning. Supervised learning, i.e., with a “teacher”, usually gives better results. However, within this framework, the learning procedure requires a priori knowledge of all standard spikes, i.e., denoised typical spikes generated by all neurons, which is hardly going to be available in a real experiment.

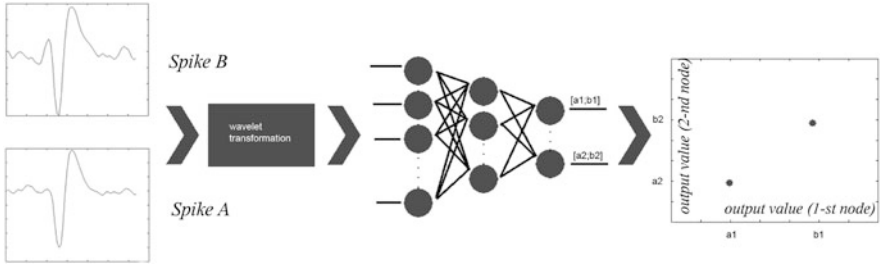


Fig. 4.25 General scheme for spike sorting using the wavelet transform and neural networks. Different spikes are wavelet transformed and the resulting coefficient features are fed into a network which finally represents the spikes in a low-dimensional space. The network should be trained in such a way that spikes of different neurons are grouped into clusters located far away from each other

At the present time, there exist different algorithms for unsupervised learning (without a “teacher”) [46, 47]. These algorithms have been shown to be successful in image recognition, but their reliability depends significantly on the noise level and the data set. Consequently, their use for spike sorting may not be effective. In the present approach, we thus use a kind of supervised learning algorithm, which we shall describe later.

Setting the network structure for a recognition problem is often simply a matter of experience on the part of the researcher. The selected three-layer network in Fig. 4.25 is just one among many. However, several circumstances should be taken into account. The feedforward network representing a multilayer perceptron [49] is one of the most studied in the literature. The choice of the number of layers and units in each layer is a compromise between network stability and plasticity. More complex networks possess better adaptation, but they may be unstable in the recognition process. Concerning the number of units (neurons), we use 64, 32, and 2 units in the first, second, and third layers, respectively. The number of units in the first layer is fixed by the number of data points available for each waveform, whereas the output layer has only two units, corresponding to the lowest useful dimension for clustering (clustering in 1D usually has much lower performance).

4.11.2 Artificial Neural Networks

Following on from the brief sketch given in Sect. 4.11.1, let us now discuss approaches based on ANN in more detail. We continue to use a 3-layer perceptron (Fig. 4.26). In the theory of ANNs, neuron nodes are typically described by the McCulloch–Pitts equations [50]. The state of the neuron j in layer k , denoted by y_{jk} , is given by

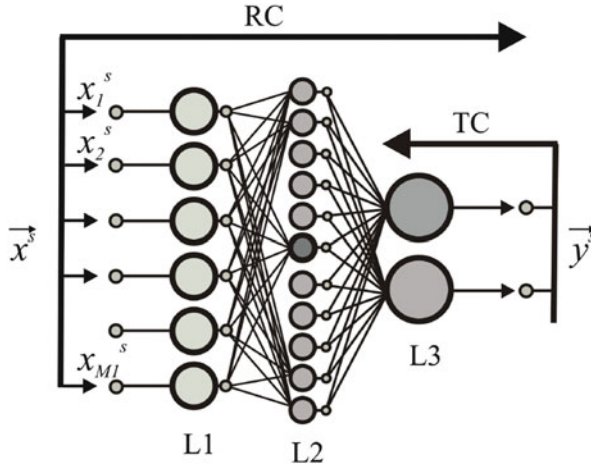


Fig. 4.26 Artificial neural network in the form of a 3-layer perceptron

$$y_{jk} = F(v_{jk}), \quad v_{jk} = \sum_{i=1}^{M_k} \omega_{ijk} y_{ik-1} - \theta_{jk}, \quad j \in [1, N_k], \quad (4.28)$$

where $F(x)$ is the activation function, and in fact, usually $F(x) = \alpha \tanh(\beta x)$, while ω_{ijk} are the synaptic weights defining connections of the neuron with other neurons in the previous layer, and θ_{jk} is the threshold for activation of the neuron. Finally, M_k and N_k are the numbers of synapses and neurons, respectively, in layer k .

The learning of such a multilayer structure assumes an appropriate tuning of the thresholds $\{\theta_{jk}\}$ and synaptic coefficients $\{\omega_{ink}\}$, in such a way that input vectors \mathbf{x}^s would be mapped to predefined output vectors \mathbf{y}^s . As the learning technique, we shall consider algorithms based on the backward propagation of errors. This approach uses minimization of the error functional over the parameters ω_{ijk} and θ_{jk} , viz.,

$$E = \frac{1}{2} \sum_{j=1}^{N_k} (y_{jk} - y_j^s)^2, \quad (4.29)$$

where y_{j3} represents the vector of output values obtained in the process of recognition of the input vector \mathbf{x}^s using the neural network, and \mathbf{y}^s is the known vector. The minimization procedure is based on the convex property of E . In order to reach a minimum of the function, one can move against the gradient of E . Let $\mathbf{P} = \{\dots \omega_{ijk} \dots; \dots \theta_{jk} \dots\}$ be the vector whose components are the synaptic coefficients and threshold levels of the neural network. Then we have to find $\arg \min_{\mathbf{P}} E(\mathbf{P})$. This can be done by the following iterative procedure:

$$\mathbf{P}^{(1)} = \mathbf{P}^{(0)} - \mathbf{e}_j h \frac{\partial E(\mathbf{P}^{(0)})}{\partial P_j^{(0)}} , \quad (4.30)$$

where $h > 0$ is a small constant known as the learning rate (the learning is performed for one component at a time). Then the minimum of the scalar error function (4.29), using all components $\{\omega_{ijk}\}$, $\{\theta_{jk}\}$, corresponds to

$$\begin{aligned} \frac{\partial E}{\partial \omega_{ijk}} &= \frac{\partial E}{\partial y_{jk}} \frac{\partial y_{jk}}{\partial v_{jk}} \frac{\partial v_{jk}}{\partial \omega_{ijk}} = 0 , \\ \frac{\partial E}{\partial \theta_{jk}} &= \frac{\partial E}{\partial y_{jk}} \frac{\partial y_{jk}}{\partial v_{jk}} \frac{\partial v_{jk}}{\partial \theta_{jk}} = 0 , \\ y_{jk} &= \alpha \tanh(\beta v_{jk}) . \end{aligned} \quad (4.31)$$

The coefficients of the neural network (Fig. 4.26) are corrected using (4.28), (4.29), and (4.31):

$$\begin{aligned} \frac{\partial E}{\partial \omega_{ij3}} &= y_{i2} \frac{\beta}{\alpha} (y_{j3} - y_j^s) (\alpha - y_{j3}) (\alpha + y_{j3}) , \\ \frac{\partial E}{\partial \theta_{j3}} &= (-1) \frac{\beta}{\alpha} (y_{j3} - y_j^s) (\alpha - y_{j3}) (\alpha + y_{j3}) , \\ \frac{\partial E}{\partial \omega_{ij2}} &= y_{i1} \frac{\beta}{\alpha} (\alpha - y_{j2}) (\alpha + y_{j2}) \sum_{n=1}^{N_3} \omega_{jn3} \frac{\beta}{\alpha} (y_{n3} - y_n^s) (\alpha - y_{n3}) (\alpha + y_{n3}) , \end{aligned} \quad (4.32)$$

$$\frac{\partial E}{\partial \theta_{j2}} = (-1) \frac{\beta}{\alpha} (\alpha - y_{j2}) (\alpha + y_{j2}) \sum_{n=1}^{N_3} \omega_{jn3} \frac{\beta}{\alpha} (y_{n3} - y_n^s) (\alpha - y_{n3}) (\alpha + y_{n3}) ,$$

$$\begin{aligned} \frac{\partial E}{\partial \omega_{ij1}} &= x_i \frac{\beta}{\alpha} (\alpha - y_{j1}) (\alpha + y_{j1}) \\ &\quad \times \sum_{m=1}^{N_2} \omega_{jm2} \frac{\beta}{\alpha} (\alpha^2 - y_{m2}^2) \sum_{n=1}^{N_3} \omega_{mn3} \frac{\beta}{\alpha} (y_{n3} - y_n^s) (\alpha^2 - y_{n3}^2) , \end{aligned}$$

$$\begin{aligned} \frac{\partial E}{\partial \theta_{j1}} &= (-1) \frac{\beta}{\alpha} (\alpha - y_{j1}) (\alpha + y_{j1}) \\ &\quad \times \sum_{m=1}^{N_2} \omega_{jm2} \frac{\beta}{\alpha} (\alpha^2 - y_{m2}^2) \sum_{n=1}^{N_3} \omega_{mn3} \frac{\beta}{\alpha} (y_{n3} - y_n^s) (\alpha^2 - y_{n3}^2) , \end{aligned}$$

$$\omega_{ijk}^{(1)} = \omega_{ijk}^{(0)} - h_k \left. \frac{\partial E}{\partial \omega_{ijk}} \right|^{(0)} , \quad \theta_{jk}^{(1)} = \theta_{jk}^{(0)} - h_k \left. \frac{\partial E}{\partial \theta_{jk}} \right|^{(0)} .$$

4.11.3 Training the Artificial Neural Network

Let us now describe the supervised network training. We denote the input and output vectors by w and y , respectively. In our particular case $w \in \mathbb{R}^{64}$ represents a spike waveform in the DWT space and $y \in \mathbb{R}^2$ is the reduced set of discriminating spike features. We then construct a set of vector pairs (w_j, y_j) , $(j = 1, \dots, n)$ for n spikes, and say that the network is trained if, when presenting vector w_j at the input, we receive y_j at the output for any $j \in [1, n]$. To achieve this we have to adjust the synaptic weights of the interneuron couplings.

4.11.3.1 Delta Rule

The simplest learning algorithm for a two-layer network consists in several steps and uses iterative adjustment of weights for each neuron in the network. In the first step all weights are randomly initialized. In the second step we present a vector w_j to the input of the network and receive some vector z_j at the output. Then the error of the network response is

$$\delta_j = y_j - z_j . \quad (4.33)$$

In the third step the coupling weights are modified proportionally to the obtained error. We employ the following delta-rule learning:

$$V_{t+1} = V_t + \nu w_j \delta_j^T , \quad (4.34)$$

where V_t is the weight vector at the learning step t and $\nu > 0$ is a small constant defining the learning rate. The learning is performed until convergence is achieved. The learning contains several epochs and is deemed finished if either (a) the weights do not change, or (b) the full absolute error (a sum over all vectors) becomes less than some fixed value.

4.11.3.2 Back Propagation of Errors

When training a multilayer network, the delta-rule described above is not applicable, since the outputs of the internal layers are unknown. In this case the method of back propagation of errors is usually used. This method allows one to obtain the errors for the internal layers. In the learning process, information is passed from the input layer to the output layer, while the error propagates in the opposite direction.

The method estimates the gradient of the error within the network and performs a correction on the coupling weights. It consists of two stages. In the first stage, forward propagation of the input signal is performed to estimate output activations. Then, differences between output activations and the teacher output are estimated

to obtain deltas for all neurons in the hidden layers. In the second stage, the gradient for each weight is computed by multiplying its output delta and input activation. Further, the weight is reduced by analogy with (4.34).

Details of the method are given in [44–48]. We shall illustrate this approach for different examples of neural networks.

4.11.4 Algorithm for Spike Sorting Using Neural Networks

When sorting experimental spikes, the main problem is lack of information about the number of clusters and about the noise-free standard spikes. Thus we cannot apply the above algorithm for network training directly. To overcome this difficulty, we use the algorithm for finding representative waveforms discussed in Sect. 4.7. Finally, the spike-sorting algorithm is as follows (Fig. 4.27):

- Detect spikes that exceed the level of experimental noise.
- Obtain information about the noise statistics and perform preliminary spike sorting using PCA or the wavelet transform.
- Select regions in the feature space with a high density of spikes and obtain the mean spike shapes.
- Apply the wavelet transform to the mean spike waveforms.
- Train the neural network using the wavelet coefficients computed in the previous step.
- Sort the experimental spikes with the resulting network parameters.

Thus for network training, we use spike waveforms corresponding to the centers of the clusters obtained using preliminary spike clustering by a conventional method, e.g., PCA or wavelet transform. As the standard output of the network, we use vectors obtained in the feature space of the mean waveforms [51].

In order to test the spike-sorting abilities of this approach, we created a semi-simulated data set. Two different but rather similar spike waveforms (Fig. 4.25, spikes A and B) were selected from a real extracellular recording. We then generated a series consisting of 946 spikes for each repeated waveform and added colored noise to the data. The noise characteristics were similar to those observed experimentally. As a result, we obtain a signal similar to a real extracellular recording, but with a priori knowledge about the membership of each spike in one or the other group.

The use of preselected standard spikes without experimental noise enables the simplest supervised learning using the back propagation of errors algorithm. We used 64 wavelet coefficients as the learning sequence w_j for the first spike waveform and the same number for the second spike waveform. As a result, the learning algorithm contained 64 epochs. As mentioned above, the network should provide the most effective spike clustering, so the standard output vectors y_i associated with the two waveforms should be markedly different. They can be appropriately chosen. Here we used $y_1 = [0.1, 0.1]$ and $y_2 = [0.5, 0.5]$. Once the learning procedure has

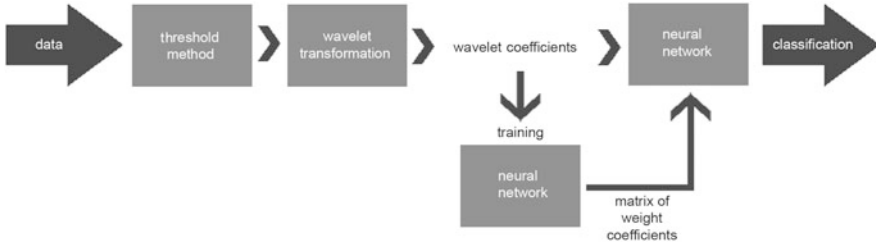


Fig. 4.27 Block diagram for the proposed method of spike sorting

been finished, the network can be used to separate noisy data. DWTs of all spike waveforms are used as input to the trained network, thus providing pairs (y_1, y_2) for each spike. For the final data clustering, we used the k-means algorithm. Then the clustering error is the number of wrongly classified spikes relative to the total number of spikes.

Figure 4.28 illustrates the performance of the proposed approach for spike sorting in the presence of color noise with a fixed bandwidth of 500 Hz and varying central frequency. The classification error grows slightly from 0.7 % for low-frequency noise ($f_c = 250$ Hz) to about 1.5 % for noise for the central frequency 1 kHz, and then it remains constant.

We now test the approach with real electrophysiological recordings. Following the proposed algorithm, we performed preliminary spike sorting using the wavelet spike classifier. Figure 4.29a illustrates the clustering results in the wavelet space. The data are organized into three partially overlapping clusters. For each cluster, we selected 50 points located closest to the spike density peaks in the feature plane. Averaging over 50 spikes provided the representative spike waveforms for three neurons. Using these waveforms, we trained the neural network. Then the full set of spikes was passed through the neural network. Figure 4.29b shows the network output, i.e., the plane (y_1, y_2) . Again all spikes formed three clusters. However, in the network output space, cluster overlapping was significantly reduced. This facilitates clustering (e.g., using k-means), and presumably reduces the number of misclassified spikes.

In conclusion, the considered approach combines the wavelet transform and artificial neural networks. The wavelet analysis allows us to reveal characteristic features in the shapes of spike waveforms. As we have shown in previous sections, WT is potentially a more powerful technique than PCA. However, the selection of the most informative features and rejection of noisy ones in WT approaches is a challenging problem. The use of neural networks provides an automatic solution to this problem (through training). The trained network automatically selects appropriate combinations of the most discriminative features from the whole set. It effectively projects wavelet coefficients into a low dimensional space (2D in our case), significantly improving the separability of spikes generated by different neurons.

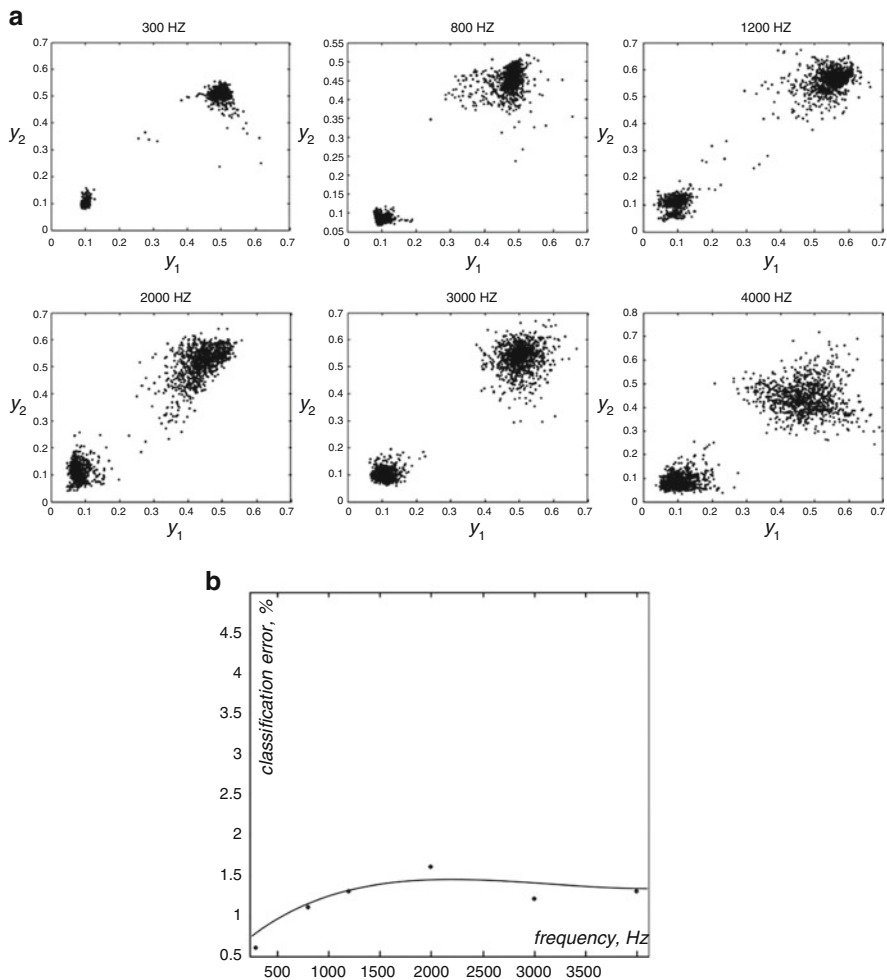


Fig. 4.28 Sorting of semi-simulated spikes. **(a)** (y_1, y_2) -planes representing spikes for different central noise frequencies. **(b)** Classification error vs central noise frequency (noise band 500 Hz)

We tested the proposed approach with semi-simulated and real electrophysiological data. We showed that the use of neural networks can significantly improve the preliminary classification obtained using PCA scores or wavelet coefficients. Reliability of the spike clustering also has been shown for the case of several clusters in the feature space of wavelet coefficients. The considered examples demonstrate the superior performance of the present approach over conventional PCA and wavelet techniques.

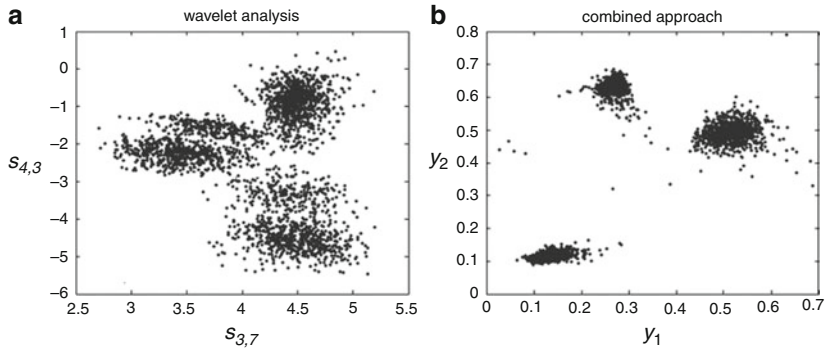


Fig. 4.29 Clustering of electrophysiological spikes by a conventional wavelet method (a) and by the proposed combined approach (b)

4.12 Artificial Wavelet Neural Networks for Spike Sorting

In Sect. 4.11, we showed that the approach based on a combination of the wavelet transform and artificial neural networks can reduce errors in automatic spike sorting. However, it also has some limitations.

On the one hand, this approach can outperform standard neural networks because the integration of a time–frequency representation (using wavelets) into the structure of the recognition algorithm allows an initial preprocessing of the data used as input for the neural network. In this context, the wavelets used in the data preprocessing stage provide a way to select characteristics that can be used by the neural network to better distinguish signals of different types. On the other hand, this method assumes no variation of wavelet parameters in the learning phase. For this reason, the efficacy of the method depends on the initial selection of the parameters, i.e., the results of the data preprocessing.

In the learning phase, there is a loss of connection with the selection of WT parameters since, in the approach considered here, these parameters are not adjusted in the course of the learning procedure. If these parameters are selected sub-optimally, then the situation cannot be further improved. It has been shown that this circumstance strongly influences the final result of image recognition (and consequently of spike sorting), because the personal experience of a researcher becomes one of the key factors. In order to reduce the influence of subjective factors, one can extend the learning phase and include additional tuning of the wavelet parameters, depending on the quality of recognition. This approach is used with the so-called *wavelet neural networks* (WNN) (see, e.g., [52–56]).

4.12.1 Structure of Wavelet Neural Networks

The structure of a WNN and its analytic description is similar to standard neural networks. A WNN can be treated as an extended perceptron that includes two parts: a wavelet transform for revealing typical features of signals and an artificial neural network for image recognition using the selected features.

The first part includes wavelet nodes where wavelet functions (e.g., the Morlet function) are used instead of the classical logistic function. These wavelets reveal features of signals on different independent scales. The procedure begins with obtaining wavelet coefficients from raw data that reflect typical features of the analyzed signal. These coefficients represent an input for the second part of the algorithm when final recognition is performed. One feature of WNNs is the possibility of selecting wavelet coefficients in the course of learning, besides correcting the synaptic coefficients.

WNNs constitute one of the most promising approaches for recognition of spike waveforms. We shall thus discuss this approach in more detail. Since WNN is an extension of standard ANN (Fig. 4.26), we shall briefly discuss some aspects of signal classification with different variants of WNNs (Figs. 4.30–4.32).

4.12.2 Wavelet Neural Networks

Figure 4.30 shows the simplest variant of WNN. It does not require one to include the wavelet part of the WNN in the learning process. To obtain a mathematical description of this WNN, we shall consider discretization of the CWT and the basic functions WAVE and MHAT.

When computing the continuous wavelet transform of a signal $x(t)$, we shall use the discrete values of the scale parameter $s = 2^j$ and the WAVE function as mother wavelet, written in the form

$$\psi(\rho, q, t) = (\rho t - q) \exp \left[-\frac{(\rho t - q)^2}{2} \right]. \quad (4.35)$$

The process of computing wavelet coefficients will be rewritten as follows:

$$C_{jk} = W \left(\frac{1}{2^j}, \frac{k}{2^j} \right) \approx 2^{j/2} \Delta t \sum_{n=0}^{N-1} x(n \Delta t) \psi(\rho_j n - q_k), \quad \rho_j = 2^j \Delta t, \quad q_k = k \rho_j. \quad (4.36)$$

The signal decomposition over the wavelet basis can be treated as the formal inclusion of an additional layer of NN nodes that will contain wavelet coefficients in the synapses. Thresholds of such nodes are switched off, and the activation function is a simple linear function. For the neuron l of the first wavelet layer, we obtain

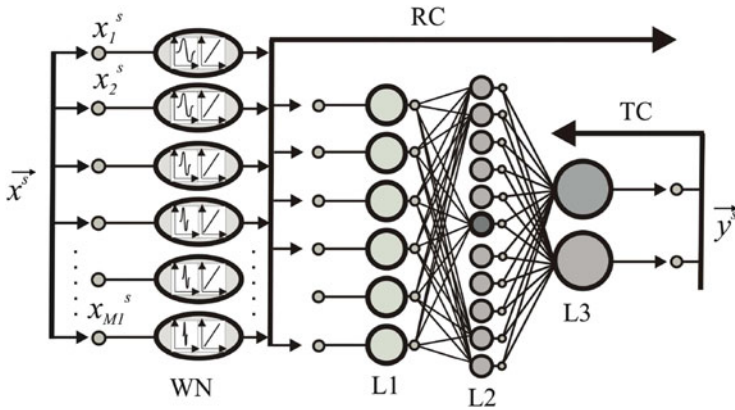


Fig. 4.30 First type of WNN

$$y_{l1} = \alpha v_{l1} - \beta, \quad v_{l1} = \sum_{n=0}^{N-1} x_n w_{nl1},$$

$$w_{nl1} = \psi(\rho_j n - q_k) = (\rho_j n - q_k) \exp \left[-\frac{(\rho_j n - q_k)^2}{2} \right], \quad (4.37)$$

for

$$1 \leq l \leq NN_f, \quad j = \left[\frac{l}{N} \right], \quad k = \left[\left\{ \frac{l}{N} \right\} N \right],$$

where y_{l1} is the reaction of neuron l from the first layer after receiving the vector \mathbf{x} , N_f corresponds to the maximal frequency in the power spectrum, and the integer values j, k quantify the scale and translation parameters. In Eq. 4.37 square and curly brackets denote the integer and fractional parts of the number, respectively. According to (4.37), each neuron of the first layer is associated with the given parameters of the wavelet transform. If the neural network (Fig. 4.26) is added to this layer, one of the simplest variants of the WNN of the first type is obtained (Fig. 4.30). This variant does not require differentiation of the wavelets, and its practical realization is quite simple.

The second type of WNN (Fig. 4.31) assumes a more complex computing algorithm within the framework of which the wavelet function is used in the synaptic part of the first layer and should satisfy the differentiation condition for including wavelet nodes in the learning algorithm. Coefficients of the wavelet transform carry information about the relation between the input vector and a given type of signal, and this is why an additional layer with wavelet functions integrated into the synaptic part seems to be useful. According to the model neuron (4.28), mathematical operations in the synaptic part are analogous to the discretized version

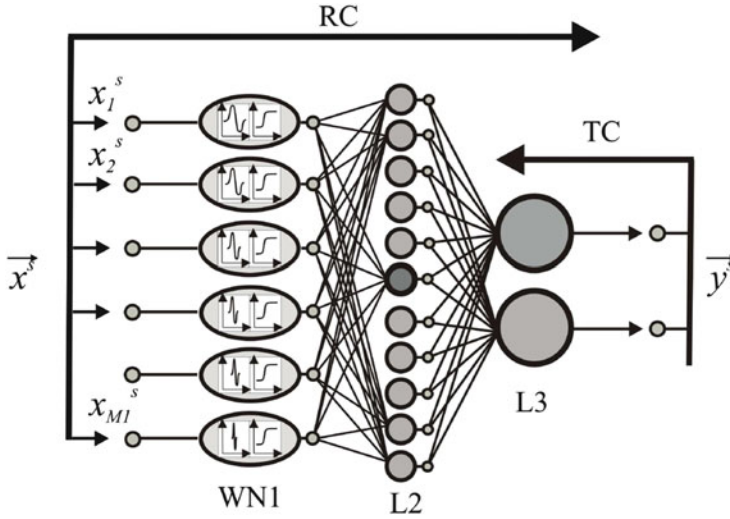


Fig. 4.31 Second type of WNN

of the wavelet transform (4.36), but the decomposition is provided using another basis of functions. If the wavelet function ψ is included in both the recognition and the learning cycles, then a layer of “wavelet nodes” is obtained, where synaptic coefficients are given by the translation and scale parameters of the corresponding function ψ .

Let us show how the procedure of learning and recognition will be written for the WNN shown in Fig. 4.31. The first layer includes a decomposition of the input vector in the basis of wavelet functions. The following layers are organized according to the standard scheme shown in Fig. 4.26. The additional layer of this WNN is described by the following equations:

$$\begin{aligned}
 y_{j1} &= \alpha \tanh \left[\beta \left(\sum_{i=1}^{M_1} x_i w_{ij1} - \theta_{j1} \right) \right], & w_{ij1} &= (\rho_j i - q_j) \exp \left[-\frac{(\rho_j i - q_j)^2}{2} \right], \\
 y_{j2} &= \alpha \tanh \left[\beta \left(\sum_{i=1}^{M_2} y_{i1} \omega_{ij2} - \theta_{j2} \right) \right], & y_{j3} &= \alpha \tanh \left[\beta \left(\sum_{i=1}^{M_3} y_{i2} \omega_{ij3} - \theta_{j3} \right) \right].
 \end{aligned}
 \tag{4.38}$$

Two variants can be considered for the functioning of the wavelet layer, namely, the cases of linear and nonlinear activation function, where (4.38) corresponds to the latter. The learning procedure for this WNN assumes correction of the following parameters: the translation parameter ρ_j and the scale parameter q_j of the wavelet function $\psi(t)$ in the first layer, the thresholds θ_{j1} of formal neurons in the first layer, the synaptic coefficients ω_{ij2} , ω_{ij3} , and the thresholds θ_{j2} , θ_{j3} of the remaining neural layers. The learning process follows the scheme

$$\begin{aligned} \frac{\partial E}{\partial \rho_j} &= \frac{\partial y_{j1}}{\partial v_{j1}} \frac{\partial v_{j1}}{\partial \rho_j} \sum_{m=1}^{N_2} \omega_{jm2} \frac{\beta}{\alpha} (\alpha^2 - y_{m2}^2) \sum_{n=1}^{N_3} \omega_{mn3} \frac{\beta}{\alpha} (\alpha^2 - y_{n3}^2) (y_{n3} - y_n^s), \\ \frac{\partial E}{\partial q_j} &= \frac{\partial y_{j1}}{\partial v_{j1}} \frac{\partial v_{j1}}{\partial q_j} \sum_{m=1}^{N_2} \omega_{jm2} \frac{\beta}{\alpha} (\alpha^2 - y_{m2}^2) \sum_{n=1}^{N_3} \omega_{mn3} \frac{\beta}{\alpha} (\alpha^2 - y_{n3}^2) (y_{n3} - y_n^s), \\ \frac{\partial E}{\partial \theta_{j1}} &= (-1) \frac{\beta}{\alpha} (\alpha - y_{j1}) (\alpha + y_{j1}) \\ &\quad \times \sum_{m=1}^{N_2} \omega_{jm2} \frac{\beta}{\alpha} (\alpha^2 - y_{m2}^2) \sum_{n=1}^{N_3} \omega_{mn3} \frac{\beta}{\alpha} (\alpha^2 - y_{n3}^2) (y_{n3} - y_n^s), \\ \frac{\partial E}{\partial \omega_{ij2}} &= y_{i1} \frac{\beta}{\alpha} (\alpha - y_{j2}) (\alpha + y_{j2}) \sum_{n=1}^{N_3} \omega_{jn3} \frac{\beta}{\alpha} (y_{n3} - y_n^s) (\alpha - y_{n3}) (\alpha + y_{n3}), \\ \frac{\partial E}{\partial \theta_{j2}} &= (-1) \frac{\beta}{\alpha} (\alpha - y_{j2}) (\alpha + y_{j2}) \sum_{n=1}^{N_3} \omega_{jn3} \frac{\beta}{\alpha} (y_{n3} - y_n^s) (\alpha - y_{n3}) (\alpha + y_{n3}), \quad (4.39) \\ \frac{\partial E}{\partial \omega_{ij3}} &= y_{i2} \frac{\beta}{\alpha} (y_{j3} - y_j^s) (\alpha - y_{j3}) (\alpha + y_{j3}), \\ \frac{\partial E}{\partial \theta_{j3}} &= (-1) \frac{\beta}{\alpha} (y_{j3} - y_j^s) (\alpha - y_{j3}) (\alpha + y_{j3}), \\ \rho_j^{(1)} &= \rho_j^{(0)} - h_1 \left. \frac{\partial E}{\partial \rho_j} \right|^{(0)}, \quad \theta_{jk}^{(1)} = \theta_{jk}^{(0)} - h_k \left. \frac{\partial E}{\partial \theta_{jk}} \right|^{(0)}, \\ q_j^{(1)} &= q_j^{(0)} - h_1 \left. \frac{\partial E}{\partial q_j} \right|^{(0)}, \quad \omega_{ijk}^{(1)} = \omega_{ijk}^{(0)} - h_k \left. \frac{\partial E}{\partial \omega_{ijk}} \right|^{(0)}. \end{aligned}$$

The values of derivatives $(\partial y_{j1}/\partial v_{j1})(\partial v_{j1}/\partial \rho_j)$ are estimated depending on the selection of the activation function and the wavelet. Let us consider the WAVE and MHAT wavelets as activation functions:

$$\psi(t) = \begin{cases} t \exp\left(-\frac{t^2}{2}\right), & \text{WAVE,} \\ (1 - t^2) \exp\left(-\frac{t^2}{2}\right), & \text{MHAT.} \end{cases} \quad (4.40)$$

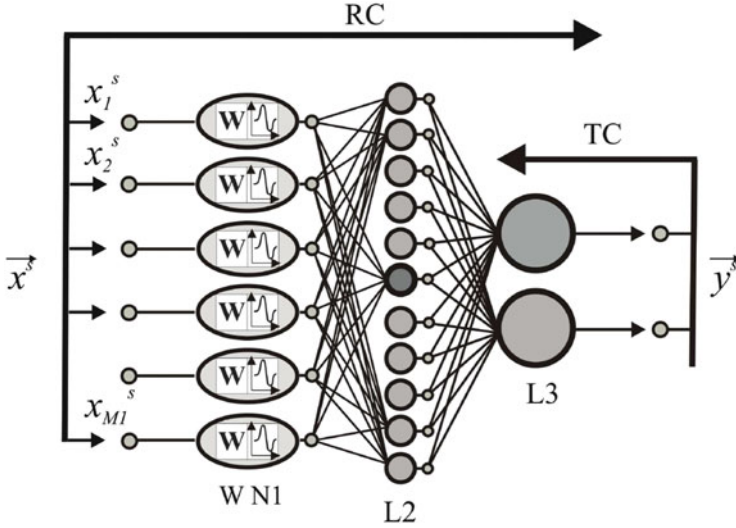


Fig. 4.32 Third type of WNN

The general structure of the WNN constructed on the basis of the 3-layer neural network with the WAVE wavelet in the first layer is shown in Fig. 4.31.

The third type of WNN (Fig. 4.32) includes the wavelet functions as activation functions in the first layer. Let us consider a 3-layer neural network with the activation function $\psi(t)$ in the first layer (Fig. 4.32). The coefficients of this WNN are corrected according to the following equations:

$$\frac{\partial E}{\partial \omega_{ij3}} = y_{i2} \frac{\beta}{\alpha} (y_{j3} - y_j^s) (\alpha - y_{j3}) (\alpha + y_{j3}),$$

$$\frac{\partial E}{\partial \theta_{j3}} = (-1) \frac{\beta}{\alpha} (y_{j3} - y_j^s) (\alpha - y_{j3}) (\alpha + y_{j3}),$$

$$\frac{\partial E}{\partial \omega_{ij2}} = y_{i1} \frac{\beta}{\alpha} (\alpha - y_{j2}) (\alpha + y_{j2}) \sum_{n=1}^{N_3} \omega_{jn3} \frac{\beta}{\alpha} (y_{n3} - y_n^s) (\alpha - y_{n3}) (\alpha + y_{n3}),$$

$$\frac{\partial E}{\partial \theta_{j2}} = (-1) \frac{\beta}{\alpha} (\alpha - y_{j2}) (\alpha + y_{j2}) \sum_{n=1}^{N_3} \omega_{jn3} \frac{\beta}{\alpha} (y_{n3} - y_n^s) (\alpha - y_{n3}) (\alpha + y_{n3}), \quad (4.41)$$

$$\frac{\partial E}{\partial \omega_{ij1}} = x_i \frac{\partial \psi(\rho_j v_{j1} - q_j)}{\partial v_{j1}} \sum_{m=1}^{N_2} \omega_{jm2} \frac{\beta}{\alpha} (\alpha^2 - y_{m2}^2) \sum_{n=1}^{N_3} \omega_{mn3} \frac{\beta}{\alpha} (\alpha^2 - y_{n3}^2) (y_{n3} - y_n^s),$$

$$\frac{\partial E}{\partial \theta_{j1}} = (-1) \frac{\partial \psi(\rho_j v_{j1} - q_j)}{\partial v_{j1}} \sum_{m=1}^{N_2} \omega_{jm2} \frac{\beta}{\alpha} (\alpha^2 - y_{m2}^2) \sum_{n=1}^{N_3} \omega_{mn3} \frac{\beta}{\alpha} (\alpha^2 - y_{n3}^2) (y_{n3} - y_n^s),$$

$$\frac{\partial E}{\partial \rho_j} = \frac{\partial \psi(\rho_j v_{j1} - q_j)}{\partial \rho_j} \sum_{m=1}^{N_2} \omega_{jm2} \frac{\beta}{\alpha} (\alpha^2 - y_{m2}^2) \sum_{n=1}^{N_3} \omega_{mn3} \frac{\beta}{\alpha} (\alpha^2 - y_{n3}^2) (y_{n3} - y_n^s),$$

$$\frac{\partial E}{\partial q_j} = \frac{\partial \psi(\rho_j v_{j1} - q_j)}{\partial q_j} \sum_{m=1}^{N_2} \omega_{jm2} \frac{\beta}{\alpha} (\alpha^2 - y_{m2}^2) \sum_{n=1}^{N_3} \omega_{mn3} \frac{\beta}{\alpha} (\alpha^2 - y_{n3}^2) (y_{n3} - y_n^s),$$

$$\omega_{ijk}^{(1)} = \omega_{ijk}^{(0)} - h_k \left. \frac{\partial E}{\partial \omega_{ijk}} \right|^{(0)}, \quad 1 \leq i \leq M_k, \quad 1 \leq j \leq N_k, \quad k = 1, 2, 3,$$

$$\rho_j^{(1)} = \rho_j^{(0)} - h_1 \left. \frac{\partial E}{\partial \rho_j} \right|^{(0)}, \quad \theta_{jk}^{(1)} = \theta_{jk}^{(0)} - h_k \left. \frac{\partial E}{\partial \theta_{jk}} \right|^{(0)}, \quad q_j^{(1)} = q_j^{(0)} - h_1 \left. \frac{\partial E}{\partial q_j} \right|^{(0)}.$$

The learning rules for all considered WNNs (Figs. 4.30–4.32) are generalized as the following computing algorithm:

- Select initial values of the synaptic coefficients and thresholds of the neural network and wavelet coefficients.
- Recognition based on testing data sets that contain signals of several types is provided for a random sequence of signals of different type. After recognition, the error is estimated and the coefficients of NN and WNN are corrected.
- Recognition and correction are repeated in several stages (“epochs”). The number of stages is chosen depending on the features of the recognized objects.

4.12.2.1 Performance of WNNs

To compare the efficacy of different types of WNNs and to analyze spike-sorting errors, we used two types of waveforms produced by real neurons. Two different waveforms were extracted from extracellular recordings of electrical activity of neural ensembles. The quality of spike identification was controlled using tetrode microelectrodes that allow registration of extracellular potentials in four closely located points (about 30 μm apart) thus providing multichannel recordings of neural activity. A more detailed description of the experimental data can be found in [14, 43]. Further, test signals were generated, including a random sequence of impulses of both types with added noise. Figure 4.33 shows an example of the corresponding test signal. A 3-layer perceptron (Fig. 4.26) contained a number of parameters indicated in Table 4.3. Parameters of the WNNs are given in Table 4.4.

Fig. 4.33 Fragment of a test signal used to compare the efficiency of different recognition approaches

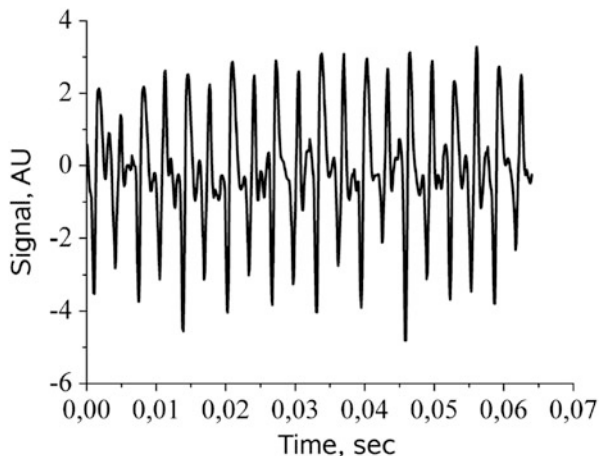


Table 4.3 Parameters of the neural network (Fig. 4.26)

#	Parameter	Description
1	Number of layers	3
2	Number of neurons in the 1st layer	16
3	Number of neurons in the 2nd layer	250
4	Number of neurons in the 3rd layer	2
5	Activation function	$F(x) = \alpha \tanh(\beta x)$, $\alpha = 6.0$, $\beta = 0.45$
6	Number of learning epochs	1,000
7	Number of types \times spikes	2×250
8	Learning step of neurons from layer i	$h_1 = 0.0003$, $h_2 = 0.0002$, $h_3 = 0.0001$
9	Initial values of coefficients	Random values equally distributed in the range $[-0.001, 0.001]$
10	Maximal \times minimal value of the output vector	-6.0×5.0

In the course of learning, the considered neural networks solved the problem of signal identification in the presence of fluctuations within different frequency bands. As the first test, a narrow-band noise (1/20 from the maximal frequency in the power spectrum) was applied because, according to Sect. 4.4, the efficiency of techniques strongly depends on the spectral properties of the presented fluctuations. Experiments were performed using ANN (Fig. 4.26) by changing the frequency band of the presented noise added to the signal (Fig. 4.33). The results are shown in Fig. 4.34. According to this figure, the quality of recognition depends heavily on the frequency band of the fluctuations. The error is maximal for the central frequency of the noise, viz., 600–700 Hz. In general, the classification error takes larger values in the low-frequency area compared with the central frequency of the analyzed signal (about 1.0–1.5 kHz) and approaches zero in the high-frequency area. The test was performed using a series of 3,610,000 generated spikes (each consisting of 32 data points) with frequency band 250 Hz.

Table 4.4 Parameters of the WNNs (Figs. 4.30–4.32)

#	Parameter	Description
1	Wavelet function	$\psi(t) = te^{-t^2/2}$, $\psi(t) = (1 - t^2)e^{-t^2/2}$
2	Type of WNN	<ul style="list-style-type: none"> – WNN of the first type (not including learning procedure for the wavelet layer) – WNN of the second type (including learning procedure for the wavelet layer with linear and nonlinear activation function) – WNN of the third type (including wavelet function as activation function)
3	Number of layers used for learning (in general case)	3
4	Number of neurons in the 1st layer	16
5	Number of neurons in the 2nd layer	250
6	Number of neurons in the 3rd layer	2
7	Activation function	$F(x) = \alpha \text{th}(\beta x)$
8	Number of epochs	1,000
9	Number of types \times spikes	2×250
10	Learning step of neurons from layer i	$h_i \in [0.000001, 0.005]$
11	Initial values of coefficients	Random values equally distributed in the range $[-0.001, 0.001]$
12	Maximal \times minimal value of the output vector	-6.0×5.0

Another situation is observed for fluctuations in the middle and high frequency range. The identification error is small and an increase in the noise intensity (at least, up to the value 0.6 of the signal energy) does not lead to any remarkable increase in the error. This allows us to conclude that the NN can be treated as a filter with characteristics that are adjusted in the course of learning. According to Fig. 4.34a, effective filtering and further recognition are possible only when fluctuations are associated with the middle and higher frequencies as compared with the mean frequency of the recognized signal. Figure 4.34b illustrates an increase in the mean error (as a result of averaging over the whole range of f_c). The mean error increases for higher noise intensities, but the rate of this increase and absolute values of the error depend on the type of NN used. Thus, application of WNNs typically improves recognition accuracy.

Analogous test experiments were performed for WNNs of different types. All variants of wavelet neural networks (Figs. 4.30–4.32) were analyzed using the two basic functions WAVE and MHAT. Additionally, for WNN of the second type (Fig. 4.31), both linear and nonlinear activation functions were considered (Table 4.5). Testing was performed using the same data (Fig. 4.33) to compare the errors of the various methods under identical conditions.

This investigation showed that results obtained with WNNs correspond to the results obtained for the classical ANN (Fig. 4.26), but that wavelet nodes enable

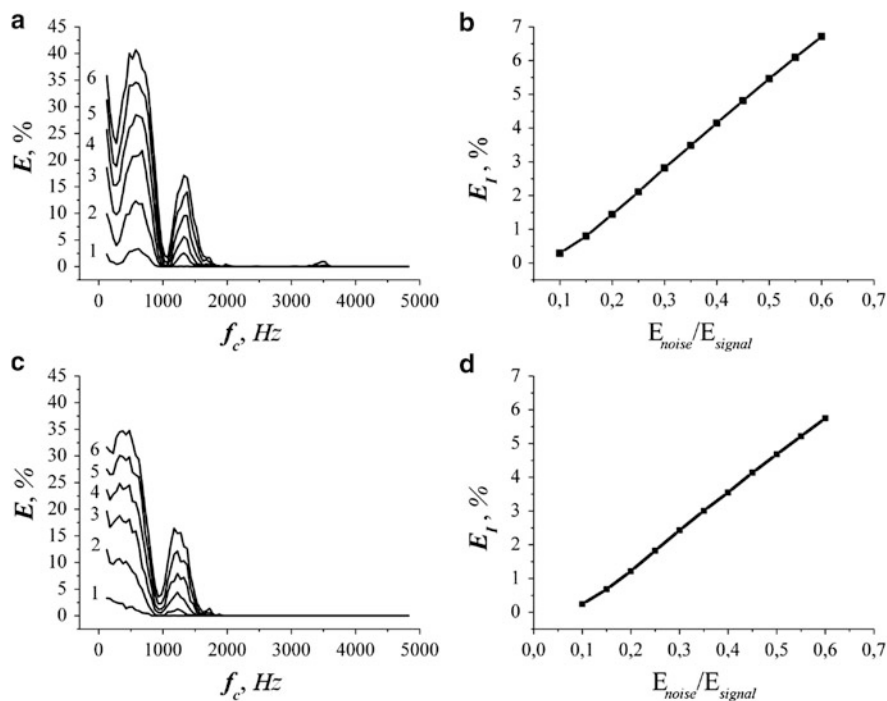


Fig. 4.34 Estimation of the identification error for a standard neural network (**a** and **b**) and WNN of the second type (**c** and **d**) with the MHAT function and nonlinear activation function for different values of the ratio of energies E_{noise}/E_{signal} : 0.1 (1), 0.2 (2), 0.3 (3), 0.4 (4), 0.5 (5), 0.6 (6). Dependencies of the recognition error (**a** and **c**) on the central frequency of narrow-band noise and of the mean error versus the relative intensity of fluctuations (**b** and **d**)

Table 4.5 Neural networks used for spike recognition

#	Type of the used network
1	Standard NN
2	WNN of the first type with WAVE function
3	WNN of the first type with MHAT function
4	WNN of the second type with WAVE function and linear activation
5	WNN of the second type with WAVE function and nonlinear activation
6	WNN of the second type with MHAT function and linear activation
7	WNN of the second type with MHAT function and nonlinear activation
8	WNN of the third type with WAVE function
9	WNN of the third type with MHAT function

error reduction in the presence of noise. Let us consider the corresponding results for the WNN of the second type. Application of the linear activation function within this WNN simplifies computations and does not use thresholds, i.e., it provides a

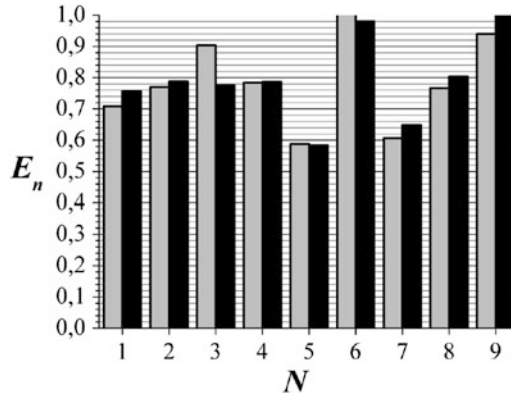


Fig. 4.35 Comparison of efficiency of spike recognition with the neural networks. Error is normalized to the maximal value. Error for the case $E_{\text{noise}}/E_{\text{signal}} = 0.6$ is shown by *gray color*, and coefficient of the increase of error is shown by *black color*

much quicker learning as compared with the nonlinear activation function. The more nonlinear elements are included in the WNN, the more time is required for learning.

According to Fig. 4.34, application of WNNs reduces the maximal error by about 5% (for the case $E_{\text{noise}}/E_{\text{signal}} = 0.6$) and the mean error by about 1%. These results are obtained for the case of narrow-band noise. With an increased frequency band of fluctuations, the quality of recognition with WNN may be significantly improved, and the dependence of the error on the frequency band changes. As another test, the case of noise with a broader frequency band (1 kHz) was considered. This test was performed using a series of 3,040,000 generated spikes (each consisting of 32 data points).

Instead of visual comparison between the graphics (similar to Fig. 4.34), we use two numerical measures: error at fixed signal-to-noise ratio and the coefficient of the increase in the mean error with the noise intensity. Nine NNs (see Table 4.5) were compared using these measures (Fig. 4.35).

According to the results obtained, we can conclude that the most effective recognition techniques are WNN of the second type with nonlinear activation function (variants 5 and 7 in Table 4.5). Let us note that this conclusion is based on the processing of a large number of experiments performed *in vivo* with the trigeminal complex of rats. Less effective results are obtained for WNNs 6 and 9. In the latter case, the accuracy is less than for the standard approach (variant 1). Likewise, for WNNs 2, 3, 4, and 8, no essential improvement was revealed in the results compared with the standard NN. This may be explained by the nonlinearity of WNN, which requires appropriate adjustment using special techniques. The less effective results for some WNNs (e.g., 6 and 9) confirm that the adjustment of WNNs with linear activation functions requires special techniques or complicating the NN structure.

We considered in more detail the WNN of the second type, which is typically not used in practical applications due to the more complicated learning procedure. This WNN requires a learning process about seven times larger compared with the standard NN. However, it provides better recognition in the presence of noise (by about 16 % compared with the classical NN), which counterbalances the extra computing time.

References

1. N.P. Castellanos, E. Malmierca, A. Nunez, V.A. Makarov, Corticofugal modulation of the tactile response coherence of projecting neurons in the gracilis nucleus. *J. Neurophysiol.* **98**(5), 2537 (2007)
2. V.A. Makarov, A.N. Pavlov, A.N. Tupitsyn, F. Panetsos, A. Moreno, Stability of neural firing in the trigeminal nuclei under mechanical whisker stimulation. *Comput. Intell. Neurosci.* **2010**, 340541 (2010)
3. M. Lewicki, A review of methods for spike sorting: the detection and classification of neural potentials. *Netw. Comput. Neural Syst.* **9**, R53 (1998)
4. K. Harris, D. Henze, J. Csicsvari, H. Hirase, G. Buzsaki, Accuracy of tetrode spike separation as determined by simultaneous intracellular and extracellular measurements. *J. Neurophysiol.* **84**, 401 (2000)
5. B. Wheeler, W. Heetderks, A comparison of techniques for classification of multiple neural signals. *IEEE Trans. Biomed. Eng.* **29**, 752 (1982)
6. B. Wheeler, *Automatic Discrimination of Single Units* (CRC, Boca Raton, 1999)
7. J. Csicsvari, H. Hirase, A. Czurko, G. Buzsaki, Reliability and state dependence of pyramidal cell–interneuron synapses in the hippocampus: an ensemble approach in the behaving rat. *Neuron* **21**, 179 (1998)
8. S. Shoham, M.R. Fellows, R.A. Normann, Robust, automatic spike sorting using mixtures of multivariate t -distributions. *J. Neurosci. Methods* **127**, 111 (2003)
9. G. Buzsaki, Large-scale recording of neuronal ensembles. *Nat. Neurosci.* **7**, 446 (2004)
10. J. Letelier, P. Weber, Spike sorting based on discrete wavelet transform coefficients. *J. Neurosci. Methods* **101**, 93 (2000)
11. E. Hulata, R. Segev, E. Ben-Jacob, A method for spike sorting and detection based on wavelet packets and Shannon’s mutual information. *J. Neurosci. Methods* **117**, 1 (2002)
12. R. Quian Quiroga, Z. Nadasdy, Y. Ben-Shaul, Unsupervised spike detection and sorting with wavelets and superparamagnetic clustering. *Neural Comput.* **16**, 1661 (2004)
13. A.N. Pavlov, V.A. Makarov, I. Makarova, F. Panetsos, Separation of extracellular spikes: when wavelet based methods outperform the principal component analysis, in *Mechanisms, Symbols, and Models Underlying Cognition*, ed. by J. Mira, J.R. Alvarez. Lecture Notes in Computer Science (Springer, Berlin/Heidelberg, 2005), p. 123
14. A.N. Pavlov, V.A. Makarov, I. Makarova, F. Panetsos, Sorting of neural spikes: when wavelet based methods outperform principal component analysis. *Nat. Comput.* **6**, 269 (2007)
15. E.M. Schmidt, Computer separation of multi-unit neuroelectric data: a review. *J. Neurosci. Methods* **12**, 95 (1984)
16. C.M. Gray, P.E. Maldonado, M. Wilson, B. McNaughton, Tetrodes markedly improve the reliability and yield of multiple single-unit isolation from multi-unit recordings in cat striate cortex. *J. Neurosci. Methods* **63**, 43 (1995)
17. M. Salganicoff, M. Sarna, L. Sax, G.L. Gerstein, Unsupervised waveform classification for multi-neuron recordings: a real-time, software-based system. I. Algorithms and implementation. *J. Neurosci. Methods* **25**, 181 (1988)

18. M.F. Sarna, P. Gochin, J. Kaltenbach, M. Salganicoff, G.L. Gerstein, Unsupervised waveform classification for multi-neuron recordings: a real-time, software-based system. II. Performance comparison to other sorters. *J. Neurosci. Methods* **25**, 189 (1988)
19. G. Zouridakis, D. Tam, Multi-unit spike discrimination using wavelet transforms. *Comput. Biol. Med.* **27**, 9 (1997)
20. K. Kim, S. Kim, A wavelet-based method for action potential detection from extracellular neural signal recording with low signal-to-noise ratio. *IEEE Trans. Biomed. Eng.* **50**, 999 (2003)
21. M.S. Fee, P.P. Mitra, D. Kleinfeld, Automatic sorting of multiple unit neuronal signals in the presence of anisotropic and non-Gaussian variability. *J. Neurophysiol.* **76**, 3823 (1996)
22. R.K. Snider, A.B. Bonds, Classification of non-stationary neural signals. *J. Neurosci. Methods* **84**, 155 (1998)
23. V.A. Makarov, J. Makarova, O. Herreras, Compact internal representation of dynamic situations: neural network implementing the causality principle. *J. Comput. Neurosci.* **29**, 445 (2010)
24. A. Fernandez-Ruiz, V.A. Makarov, N. Benito, O. Herreras, Schaffer-specific local field potentials reflect discrete excitatory events at gamma frequency that may fire postsynaptic hippocampal CA1 units. *J. Neurosci.* **32**, 5165 (2012)
25. L. Kaufman, P.J. Rousseeuw, *Finding Groups in Data: An Introduction to Cluster Analysis* (Wiley-Interscience, New York, 1990)
26. G.M. Downs, J.M. Barnard, Clustering methods and their uses in computational chemistry. *Rev. Comput. Chem.* **18**, 1 (2002)
27. J.A. Freeman, C. Nicholson, Experimental optimization of current-source density technique for anuran cerebellum. *J. Neurophysiol.* **38**, 369 (1975)
28. W. Simon, The real-time sorting of neuro-electric action potentials in multiple unit studies. *Electro-Encephalogr. Clin. Neurophysiol.* **18**, 192 (1965)
29. J. Feldman, F. Roberge, Computer detection and analysis of neuronal spike sequences. *Informatics* **9**, 185 (1971)
30. G. Dinning, A.C. Sanderson, Real-time classification of multiunit neural signals using reduced feature sets. *IEEE Trans. Biomed. Eng.* **28**, 804 (1981)
31. J. Eggermont, W. Epping, A. Aertsen, Stimulus dependent neural correlations in the auditory midbrain of the grassfrog. *Biol. Cybern.* **47**, 103 (1983)
32. E. Glaser, W. Marks, On-line separation of interleaved neuronal pulse sequences. *Data Acquisition Process. Biol. Med.* **5**, 137 (1968)
33. E. Glaser, Separation of neuronal activity by waveform analysis, in *Advances in Biomedical Engineering*, vol. 1 (Academic, New York, 1971), p. 77
34. G. Gerstein, W. Clark, Simultaneous studies of firing patterns in several neurons. *Science* **143**, 1325 (1964)
35. G. Gerstein, M. Bloom, I. Espinosa, S. Evanczuk, M. Turner, Design of a laboratory for multineuron studies. *IEEE Trans. Syst. Cybern.* **13**, 668 (1983)
36. W.W. Cooley, P.R. Lohnes, *Multivariate Data Analysis* (Wiley, New York, 1971)
37. K. Rao, P. Yip (eds.), *The Transform and Data Compression Handbook* (CRC, Baton Rouge, 2001)
38. D.D. Muresan, T.W. Parks, Adaptive principal components and image denoising. *IEEE Int. Conf. Image Process.* **1**, 101 (2003)
39. I.T. Jolliffe, *Principal Component Analysis* (Springer, New York, 2002)
40. H.F. Kaiser, The application of electronic computers to factor analysis. *Educ. Psychol. Meas.* **20**, 141 (1960)
41. R.B. Cattell, The scree test for the number of factors. *Multivar. Behav. Res.* **1**, 245 (1966)
42. M. Blatt, S. Wiseman, E. Domany, Superparamagnetic clustering of data. *Phys. Rev. Lett.* **76**, 3251 (1996)
43. V.A. Makarov, A.N. Pavlov, A.N. Tupitsyn, Optimal sorting of neural spikes with wavelet and filtering techniques. *Proc. SPIE* **6855**, 68550M (2008)

44. D.E. Rumelhart, G.E. Hinton, R.J. Williams, Learning internal representations by error propagation, in *Parallel Distributed Processing*, vol. 1 (MIT, Cambridge, 1986)
45. S. Haykin, *Neural Networks. A Comprehensive Foundation* (Prentice Hall, Upper Saddle River, 1999)
46. T. Kohonen, *Selforganization and Associative Memory* (Springer, New York, 1989)
47. J. Hopfield, D. Tank, Neural computation of decision in optimization problems. *Biol. Cybern.* **52**, 141 (1985)
48. R. Callan, *The Essence of Neural Networks* (Prentice Hall, London, 1999)
49. F. Rosenblatt, Two theorems of statistical separability in the perceptron, in *Mechanisation of Thought Processes*, vol. 1 (HM Stationery Office, London, 1959), p. 421
50. W. McCulloch, W. Pitts, A logical calculus of the ideas immanent in nervous activity. *Bull. Math. Biophys.* **7**, 115 (1943)
51. A.N. Tupitsyn, A.N. Pavlov, V.A. Makarov, Separation of extracellular spikes with wavelets and neural networks. *Proc. SPIE* **7176**, 71760M (2009)
52. T. Kugarajah, Q. Zhang, Multidimensional wavelet frames. *IEEE Trans. Neural Netw.* **6**, 1552 (1995)
53. H. Szu, B. Telfer, J. Garcia, Wavelet transforms and neural networks for compression and recognition. *Neural Netw.* **9**, 695 (1996)
54. Y. Cheng, B. Chen, F. Shiau, Adaptive wavelet network control design for nonlinear systems. *Proc. Natl. Sci. Counc. Repub. China (A)* **22**, 783 (1998)
55. P.R. Chang, W. Fu, M. Yi, Short term load forecasting using wavelet networks. *Eng. Intell. Syst. Electr. Eng. Commun.* **6**, 217 (1998)
56. L. Cao, Y. Hong, H. Fang, G. He, Predicting chaotic time-series with wavelet networks. *Physica D* **85**, 225 (1995)

Chapter 5

Wavelet Approach to the Study of Rhythmic Neuronal Activity

Abstract This chapter considers the main definitions and principles of electroencephalography that are needed to get a good grasp of Chaps. 6 and 7. We describe the general physical and mathematical approaches to time–frequency analysis of rhythmic EEG activity using the continuous wavelet transform. Besides that, we review some recent achievements of wavelet-based studies of electrical brain activity, including (i) time–frequency analysis of EEG structure, (ii) automatic detection of oscillatory patterns in pre-recorded EEG, (iii) classification of oscillatory patterns, (iv) real-time detection of oscillatory patterns in EEG, (v) detection of synchronous states of electrical brain activity, (vi) artifact suppression/rejection in multichannel EEG, (vii) the study of cognitive processes.

5.1 Introduction

Let us take the next step in the application of wavelet analysis to neurophysiology and consider practical aspects of this mathematical tool for retrieving information about rhythmic brain activity. From a physical viewpoint, the brain is an extremely complex object, consisting of a huge number of elements (neurons) with their own oscillatory dynamics, organized in networks with complex topologies [1–8]. The traditional and highly effective method for studying electrical brain activity is based on registration of electroencephalograms (EEG), which sum the average electrical fields of synaptically interconnected neuronal ensembles located in the vicinity of the recording electrode. In humans, EEG is usually recorded by small metal disks (electrodes or sensors), placed on the scalp. In rats, EEG is usually recorded by intracranial electrodes implanted at the cortical surface or in deep subcortical structures, and this approach can procure more detailed information about electrical activity in relatively small groups of neurons.

Chapters 6 and 7 will discuss different aspects of time–frequency characteristics of EEG and the main results from continuous wavelet analysis of EEG as regards automatic processing of EEG recordings, i.e., the development of new

techniques to remove the need for routine visual inspection of EEG and diminish subjective factors. Nowadays, advanced practical methods for automatic processing of multi-channel EEG data are given a high priority in modern neuroscience. For example, wavelet-based EEG analysis can be used to identify functional relationships between various brain areas, to explore underlying mechanisms of different types of rhythmic brain activity, and to better understand the fundamental principles of brain function. Moreover, EEG comprises a wide variety of rhythms and periodic oscillations, whose frequencies are important characteristics of the functional activity of neuronal structures [3, 9–11]. The frequency content of the EEG recorded in the local brain area depends on the functional activity of this area and its interactions with other areas. New mathematical approaches have important theoretical significance for the study of rhythmic brain activity, underlying, for example, integrative (cognitive) functions of the brain. In addition to that, these new approaches can be widely applied in practical work, for example, in developing effective diagnostic tools and monitoring systems in clinics, in specific brain–computer interfaces, etc. [12–18].

This chapter provides a brief introduction to wavelet analysis of EEG. It starts with the basic definitions and principles of electroencephalography in order to give the reader a better understanding of subsequent chapters. In general, this chapter describes the physical and mathematical bases of the wavelet transform used to investigate rhythmic brain activity.

5.2 Basic Principles of Electroencephalography

EEG is an acronym for electroencephalogram (*electro* = electrical signals, *encephalo* = the brain, *graph* = a recording).

Electroencephalogram. Record of electrical activity of the brain taken by means of electrodes placed on the surface of the head, unless otherwise specified [19].

Electroencephalogram. Electrical potentials recorded from the brain, directly or through overlying tissues [20].

Electroneurophysiology has a history of more than 100 years [21]. In 1875, a Liverpool physician and medical school lecturer Richard Caton first demonstrated that electrical signals could be measured directly from the surface of the animal brain. The father of clinical electroencephalography, the German psychiatrist Hans Berger, recorded electrical activity from human brain and introduced the term ‘electroencephalogram’. The first published EEG data from humans appeared in 1929, when Hans Berger published a paper in which he presented 73 recordings [22, 23].

Between Caton and Berger, Adolph Beck in 1890 [24] found that sensory stimuli (flashes or sounds) induced slow changes in electrical brain activity (slow wave response, evoked potentials). Fleischl von Marxow [25] made a similar observation. A Russian scientist, Vasili Yakovlevich Danilevsky, in his doctoral thesis (1877),

described electrical brain activity in dogs. Another Russian physiologist, Nikolai Evgenjevich Wedensky, recorded electrical activity from peripheral nerves and the central nervous system using a telephone (the results were published in his master's thesis in 1884). In 1913, Vladimir V. Pravdich-Neminsky published photographic recordings of electrical brain activity in dogs and introduced the term *electrocerebrogram*.

From that time, electroencephalographic investigations have led to major advances in studying sleep and epilepsy. Electroencephalography is the most popular method for the analysis of spontaneous brain oscillations and evoked (event-related) potentials, and changes in electrical brain activity during anesthesia and sleep, during sensory perception, and during voluntary activity, etc. Nowadays, EEG investigation has become a necessary part of clinical practice for the diagnosis and prognosis of various neural disorders, especially in epileptic patients.

Several spontaneous rhythms are encountered in EEGs of animals and humans during different behavioral states, whereas peculiar (paroxysmal) patterns appear in EEG during epileptic seizures. Mechanisms that underlie spontaneous rhythmic activity in the brain were studied by V.Ya. Danilevsky [26] and A. Beck [24], who described EEG desynchronization in animals, by I.M. Sechenov, who found spontaneous rhythms in medulla oblongata in the frog, and by H. Berger, who described alpha and beta rhythms in human EEGs.

5.2.1 Electrical Biopotential: From Neuron to Brain

According to the traditional viewpoint, brain functions are associated with continuous processes of integration and disintegration of functional associations within neuronal circuits. These neural associations are temporary and they represent synchronized network activity of neuronal assemblies located in different parts of the brain. Although neural associations are functional, they have an anatomical substrate, viz., synaptic contacts between neurons. Neural connections can be readily reorganized, so different neural circuits can be linked together into a single unit, a so-called functional system. A functional system is a neuronal entity that accomplishes specific functions [27] and disintegrates when the result has been successfully achieved. One of the signs of neuronal integration is synchronization of local electrical field potentials. Synchronized neuronal activity can be recorded locally in the brain, for instance, at the surface of the cerebral cortex, by means of an invasive intracranial electrocorticogram, or on the scalp by non-invasive extracranial EEG [9]. An EEG contains a variety of rhythms and periodic oscillations whose frequencies provide important information about functional activity of the neural system. The state when different brain areas sustain oscillations with the same frequency is called the neuronal synchronization state. It accounts for the processes of neuronal association and information exchange between these brain areas [28, 29]. Synchronization of rhythmic activity in multi-channel EEG can manifest the binding processes (active associations) between neurons and neuronal ensembles [30].

Synchronization between some cortical areas characterizes normal cognitive brain functions. Pathological processes in the central nervous system can selectively increase the level of synchronization between interconnected brain structures. Abnormally high synchronization can underlie seizure activity that can be recorded in EEG as hypersynchronized rhythms. In particular, absence epilepsy, which is analyzed by means of wavelets in Chaps. 6 and 7, results from hypersynchronization of the thalamo-cortical network. Up to now, thalamo-cortical interactions have not been fully explored because they require invasive implantation of electrodes in the thalamus (intracranial EEG). This operation could not be performed on patients with absence epilepsy for ethical reasons (the patients do not have clinical indications for this operation).

During the last decade, non-invasive neuro-imaging and neuro-mapping techniques, such as magnetic resonance imaging (MRI), positron emission tomography, and photoemission computer tomography have been widely used in patients with absence epilepsy. These modern methods have several disadvantages, the main one being that the time resolution is too low and there is no reliable procedure for processing the resulting data. An additional problem with neuro-imaging data comes from the fact that reconstruction of neuronal activity is based on indirect measurements, such as changes in the hemodynamic response, tissue metabolism, blood flow, and blood oxygen saturation, etc. These processes are influenced by many factors, besides neuronal processes. The absence of effective tools for analysis of neuro-imaging data and the high probability of errors in reconstruction of neuronal activity often lead to false conclusions. Thus, two different approaches to analysis of MRI signals during absence epilepsy may lead to different results [31].

In this situation, EEG is preferable in humans as a reliable, cheap, and easily available technique, and application of EEG in animals can be extended by implanting intracranial electrodes in deep structures. Chapter 7 presents the results of time–frequency wavelet analysis (continuous wavelet transform) of electrical activity in the cortex and thalamus during absence epilepsy in animals with a genetic predisposition to this disease.

5.2.2 Application of EEG in Epilepsy Research

Since this monograph focuses on features of the wavelet-based analysis of brain dynamics in animals and patients with epilepsy, we briefly discuss the practical application of EEG in epileptology. Fifteen years before H. Berger published his landmark report (1929), in which he described spontaneous electrical activity in the human brain, N. Cybulski and S. Jelenska-Macieszyna [32] at the University of Krakow in Poland published the first photographs of paroxysmal activity during experimental focal seizures in dogs (cited in [21]). In 1931, H. Berger demonstrated the first recordings of spike-and-wave activity obtained in epileptic patients (Fig. 5.1). Two years later, in 1933, he published an EEG recording during

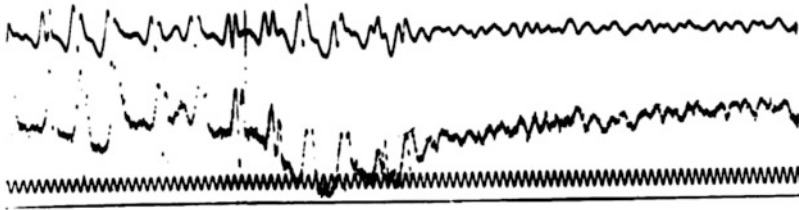


Fig. 5.1 EEG record made by H. Berger in an 18-year-old girl during a seizure. High voltage spike-and-wave complexes appear with a frequency of about 3 per second (From [21])

a brief episode of “simple automatic activity with no other movement” (cited in [21]). Note that it was H. Berger who first suggested applying EEG in clinical practice (cited in [33]).

In 1935, Frederick Gibbs, Hallowell Davis, and William G. Lennox at Boston City Hospital demonstrated spike-and-wave complexes in EEG that manifested clinical absence seizures [34]. Since that time, clinical application of EEG has increased rapidly and the EEG recording technique has been profoundly improved. Over the years, EEG has helped in making short- and long-term prognoses of various neurological and psychiatric disorders. EEG investigation is necessary for the diagnosis of epilepsy (especially in patients with atypical epileptic syndromes), and it also offers important prognostic information.

In clinical practice, EEG is recorded with open and closed eyes using special techniques to provoke epileptic activity (such as photo-stimulation, hyperventilation). Comparative analysis of EEG shape during the states with open and closed eyes provides the most important information. Some paroxysmal activity appears only when the eyes are open, and some under closed eye conditions or immediately at the moment of opening/closing the eyes (alpha rhythm can mask the abnormal activity that can be seen in EEG, when the eyes are open and the alpha rhythm is suppressed). Only in about 50 % of adult patients with epilepsy can photo-stimulation and hyperventilation provoke epileptic activity in EEG during the waking state. This percentage can be increased up to 92 % if 4 consecutive EEG sessions are used. EEG monitoring during sleep increases the chances of identifying epilepsy in patients (from 50 % up to about 80 %).

The area of clinical application of EEG is rather broad. Changes in EEG structure can be used to evaluate the effectiveness of drug medication. Changes in EEG may also carry prognostic information and can be for short- or long-term prediction of neurological diseases.

Routine non-invasive EEG studies provide an opportunity to localize sources of epileptic activity and to determine which areas of the brain could benefit from surgical correction. In complicated cases, localization of pathological brain areas requires intracranial recordings with deep electrodes placed under the dura mater. Electrical activity recorded intracranially from the surface of the cortex is called an electrocorticogram (ECoG), or alternatively, a subdural EEG (sdEEG), or an intracranial EEG (icEEG). An advantage of ECoG over EEG is its high

spatial resolution (ECoG reflects the local electrical field potential). Furthermore, high-frequency components are present in ECoG, but they are reduced in EEG, since the electrical current passes through high-resistance structures, such as meninges, bone, soft tissue, and the scalp. Despite the harmful effect of the invasive procedure, ECoG still remains a standard for the localization of epileptic focus, and it is often used before surgical treatment of epilepsy, when pharmacological treatment appears ineffective. We hope that, in the future, invasive methods will be excluded from clinical practice, to be replaced by new effective noninvasive brain imaging techniques. These new noninvasive methods should provide a high quality of data (spatial resolution and information content), whilst remaining as simple and cheap as possible, and should be easily combined with subsequent data processing techniques.

5.3 General Principles of Time–Frequency Analysis of EEG

5.3.1 The Need for Mathematical Analysis of EEG

Since the days of Hans Berger, the method for recording the EEG has improved substantially. Progress in this area was achieved by development of engineering and computer technologies. The ink recorder was replaced by the digital recording system, which was able to record multi-channel EEG with high temporal resolution. In fact, the availability of analog EEG data made it necessary to find a new approach to the analysis of digital recordings, where the EEG signal is represented as a sequence of discrete values of the electric potential measured in the millisecond range. (In this book, we usually operate with the sample rate 1,024 Hz, i.e., a discretization step of $1/(1,024 \text{ Hz})$, or approximately 1 ms.) Digital recording systems with high-capacity and digital memory meant that one could operate with large volumes of information and perform the subsequent analysis of the EEG. Nowadays, it is necessary to find better ways to store, share, and analyze EEG data.

New computer technologies promote an interdisciplinary approach to the investigation of brain functions under normal conditions and in pathological cases. EEG studies are still attractive for experts in experimental and theoretical neurobiology, psychophysiology, cognitive neuroscience, biophysics, physics, nonlinear dynamics, etc. There is an interdisciplinary field of knowledge called neuroinformatics and computational neuroscience that combines mathematical methods of neural network modeling, time–frequency and structural analysis of neuronal signals, the theory of dynamic chaos, and nonlinear dynamics. The interdisciplinary approach to EEG analysis led to the development of unique methods which helped to unravel certain mechanisms of perception and sensorimotor integration (see, e.g., [35–37]), and to understand some fundamental aspects of sleep, epilepsy (e.g., [7, 38]) and cognitive functions [39].

It is profitable to apply powerful tools of physics and mathematics to EEG analysis. However, interpreting the results of mathematical analysis in the context of neurobiology is often a complex and ambiguous matter. Any result derived from the mathematical analysis of EEG, which may look obvious to the mathematician, can appear meaningless to the physiologist. Difficulties in interpreting the results of mathematical analysis may be caused by a considerable gap in understanding between the biological and mathematical sciences. We believe that new knowledge resulting from cooperation between these disciplines will help to solve many mysteries about brain functions. But success in this venture is only possible through close cooperation (despite all the difficulties) between theory and practice, i.e., between experts in the exact sciences (applied mathematics, physics, nonlinear dynamics, etc.) and practitioners in neurophysiology. Without a deep understanding of the physiological basis of the problem, it would be impossible to develop adequate mathematical tools for further processing and analysis of the relevant experimental EEG records, at least such as would be easily acceptable to physiologists [40].

An interdisciplinary approach is beneficial for any research, but in neurophysiology it is particularly important, because the subject of study—the brain—is an extremely complex one. A better understanding of brain functions requires the cooperation of biologists, physicists, chemists, mathematicians, information specialists, and even the humanities—philosophers, linguists, and so on. One thing is certain: the key to the success of such an interdisciplinary trend in modern neuroscience is the clarity and meaningfulness of the statements of physiological problems.

5.3.2 Time–Frequency Analysis of EEG: From Fourier Transform to Wavelets

The main difficulty with the practical application of physical and mathematical approaches in neuroscience is the strict compliance with the conditions under which the mathematical operations can be considered to be correct and justified with regard to the answers they provide to the relevant questions.

In terms of physics and mathematics, an EEG record is a time series which appears as a sequence of amplitude values for a certain quantity (in the case of EEG, it is a measure of electrical potential), measured at discrete points of time. This representation allows one to take advantage of the considerable theoretical basis of time series analysis developed in mathematics, physics, and nonlinear dynamics, as well as the powerful mathematical tools of statistical analysis.

Among the methods widely used for EEG analysis, we should note the methods of time domain measurements. This concerns primarily auto- and cross-correlation analysis, which should be considered as statistical methods. In the frequency domain (Fourier space), attention should be paid to spectral or Fourier analysis and wavelet

analysis (applicable in both the time and frequency domains). The latter approach is of particular interest in this book. It is relatively new and has been successfully applied in neurodynamics and neurophysiology.

In contrast, the spectral (frequency) analysis of EEG recordings is still widely used in clinical practice, as well as in neuroscience. The fast Fourier transform (FFT) or its modifications are typically used for neurophysiological signals [41–43]. EEG spectral analysis results are usually presented in the form of a power spectrum, in which the frequency content of EEG is depicted as the power value of each frequency component.

The Fourier transform can only be applied to stationary signals, which are infinite in time. The term “stationary” means that the spectral composition and statistical characteristics of the signal do not change over time. However, EEG is essentially a non-stationary signal, whose characteristics change over time.¹ In particular, certain rhythms constantly appear and disappear in EEG. Each of them is characterized by its own frequency in Fourier space and by a typical form in the time domain.

In order to illustrate all the characteristics mentioned above, Fig. 5.2 gives an example of an electrical activity record from the frontal cortex of a WAG/Rij rat with a genetic predisposition to absence epilepsy.² Large variations can be observed in both the amplitude and the frequency parameters of EEG, even in this short fragment. Firstly, one can select the segments of background activity, so-called desynchronized EEG (area F in Fig. 5.2). Secondly, in this EEG segment, the periods that differ from the background EEG by the amplitude, shape, and characteristic frequency can be easily distinguished. Hereinafter we will refer to such EEG fragments as oscillatory patterns. The oscillatory patterns can be classified by shape and by frequency composition. These two classifications are traditionally used by neurophysiologists for analysis and “decoding” of EEG [42, 47]. Taken together, they represent an accurate formal tool for analysis and classification of EEG rhythms. In the signal shown in Fig. 5.2, several oscillatory EEG events are highlighted, such as sleep spindles, short episodes of 5–9 Hz oscillatory activity, K-complexes (delta waves followed by a sleep spindle), and spike–wave discharges (SS, TR, K, SWD, respectively).

Thus, different rhythmic and oscillatory patterns can be distinguished in EEG. In other words, EEG is characterized by a complex time–frequency structure [1]. Traditional electroencephalography subdivides the frequency content of EEG in several bands from about 0.5 to 200–500 Hz (Fig. 5.3a). The presence of EEG oscillations with certain frequencies (frequency bands) is associated with certain states of vigilance (specific brain activity), so the frequency characteristics of EEG

¹Although the non-stationarity of EEG signals causes difficulties for spectral analysis, Fourier transform algorithms have been successfully adapted to EEG analysis (see, e.g., the technical manual [44]).

²WAG/Rij rats are a special inbred line with a genetic predisposition to absence epilepsy [45, 46]. This animal model of epilepsy will be discussed in Sect. 5.3.3, and also in the following chapters of the book.

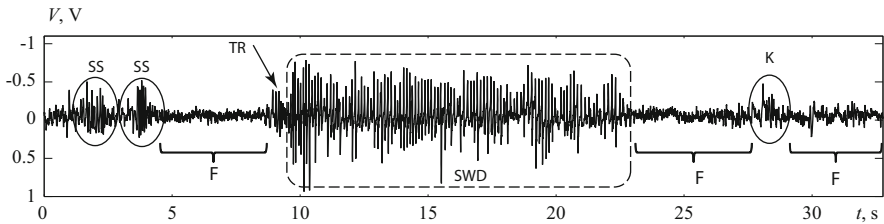


Fig. 5.2 A typical fragment of EEG recorded in the frontal cortex in a WAG/Rij rat, illustrating the non-stationarity of the signal. Selected areas are: spike-wave discharge SWD, sleep spindle SS, short episode of 5–9 Hz activity (in the theta range) TR, K-complex denoted by K, and background activity denoted by F

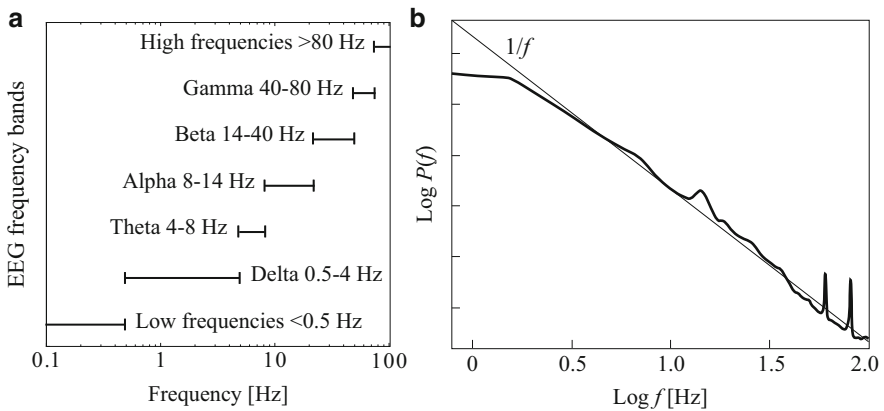


Fig. 5.3 (a) EEG frequency bands distinguished by traditional electroencephalography. (b) Power spectrum of an EEG recorded from the human right frontal lobe during sleep (Figures are based on the data from [1])

correspond roughly to specific brain functions [48–50]. EEG oscillations with different frequencies can co-exist in one structure or present the same time in different brain structures [49, 51, 52].

The spectral power density P of an EEG signal is inversely proportional to the frequency f (see Fig. 5.3b). The observed $1/f$ law of the spectral power suggests that the system exhibits self-organized critical dynamics [1, 53, 54], where disturbances at low frequencies result in sequential transmission of oscillation energy at high frequencies [55, 56]. So high-frequency EEG events superimpose on low-frequency oscillations in EEG [49, 51, 57].

These properties of oscillations are determined by the physical architecture of the neuronal network, as well as by the limited propagation speed of electrical signals between neurons due to synaptic delay [58]. Since the majority of neuronal connections are local (small in size [59]), the period of oscillation depends on the size of neuronal ensembles involved in the oscillatory activity. High-frequency

oscillations in EEG (which often manifest cognitive processes [60]) are underlain by synchronous activity in relatively small neural networks that occupy a limited region of space, while relatively widespread neural networks are involved in low-frequency oscillatory activity [49, 61]. Considering spatial and temporal scales of neuronal network activity, the relationship between network anatomy and frequency of oscillations (which reflects brain activity) should be taken into account.

It is obvious that analysis of complex non-stationary signals, such as electroencephalograms, requires specific methods with good resolution in both the frequency and time domains. Before the introduction and development of wavelet analysis, the only method to study the time–frequency structure of non-stationary signals was the short-time Fourier transform (2.4) considered in Sect. 2.2. In practice, two types of short-time Fourier transform procedure were used to analyze neurophysiological signals.

The first approach was based on the decomposition of the non-stationary EEG signal into fragments of length $2T$, where signal parameters did not change with time, i.e., the EEG fragments were treated as stationary. These EEG fragments overlapped in order to minimize the undesirable effect of boundary artifacts. This procedure could provide the power spectrum at any given time. The second method was based on multiplying the EEG signal by a given window function, e.g., Gauss function, Hamming window, Hann window, etc., which takes a nonzero value for some short period of time. In fact, the Fourier transform (2.3) was performed in a short time interval corresponding to the width of the selected window function. Then the window function was shifted along the time axis, and the next interval of EEG provided the major contribution to the resulting spectrum. The fixed time window is the main disadvantage of the short-time Fourier transform (as already discussed in Chap. 2). Furthermore, the window size could not be adapted to the local properties of the signal.

The mathematical apparatus of the wavelet transform provides a better alternative to the Fourier transform which is free from the above-mentioned shortcomings. From the various physical applications of wavelets, it is well known (see, e.g., [62–68]) that wavelet analysis is well suited for studying non-stationary signals. It is characterized by the following important features:

- It decomposes the signals in the time and frequency domains, which allows us to localize the particularities of a signal in both domains.
- It is suitable for short intervals. One can effectively analyze a short time series containing a small number of characteristic periods of oscillatory activity.
- It is flexible. One can choose the wavelet basis that best takes into account the peculiarities of the analyzed data.
- It is less sensitive to noise. Wavelets are highly effective for analyzing “noisy” data, i.e., signals in which important information is superposed with additive noise.

These advantages make wavelet analysis attractive for studying EEG signals, which are characterized by non-stationarity, the simultaneous presence of oscillatory activity with different shapes and frequencies (which requires an adaptive approach

to examining the EEG structure), a high level of noise, and a relatively short length (either due to the limited time of registration or short duration of fast processes in the brain) [69–72].

The significant advantage of wavelets is that the analysis is not limited to the selected time scale of the observation. Indeed, since the frequency of a signal is inversely proportional to its period, the information about high-frequency components could be obtained from the relatively small time intervals, whereas information about low-frequency components could be obtained from the longer periods of time.

5.3.3 Time–Frequency Analysis of Spike–Wave Discharges by Means of Different Mother Wavelets

Here we discuss the application of wavelet analysis to the description of the structure of the spike–wave discharges in EEG. As pointed out above, in the structure of the EEG, one can distinguish different forms of rhythmic activity and oscillatory patterns which reflect the nature of the neural activity and hence the functional state of the brain. Importantly, many pathological processes in the brain may also be manifested in EEG. For example, during epilepsy, which is characterized by the hypersynchronous activity of brain neurons [45, 73], there are high-amplitude EEG discharges of characteristic shape [74, 75].

There are many types of epileptic disorder (more than 30), and each of them corresponds to a specific epileptic EEG pattern. At the same time, there are difficulties in the diagnosis of certain types of epilepsy, and as a consequence, these diseases remain unnoticed. According to World Health Organization data, about 1 % of the world’s population suffers from epilepsy and more than 30 % of patients do not receive health care [75, 76]. In this section we focus on absence epilepsy (petit mal or childhood absence epilepsy), which is a common neurological disease, the main clinical manifestation of which is a brief loss of consciousness with the absence of the convulsive component (the automatisms of the mimic muscles may be observed) [74, 76]. The attack of absence epilepsy (lower level of consciousness) can last from a few seconds to tens of seconds. Epileptic seizure is accompanied by high-amplitude spike–wave discharges in EEG [75, 76]. Spike–wave discharges (SWD) consist of a relatively high-frequency component (the spike) with peak amplitude significantly exceeding the background activity and the low-frequency “wave” [77].

There are several rat lines with a genetic predisposition to absence epilepsy [45], such as the WAG/Rij rats used in our study. Electroencephalographical and clinical signs of absence epilepsy can be observed in 90 % of WAG/Rij rats [45], and epileptic activity is known to increase progressively with age. Despite some differences in the manifestation of absence epilepsy in WAG/Rij rats and human patients (such as different age-related dynamics and the main frequency of SWD),

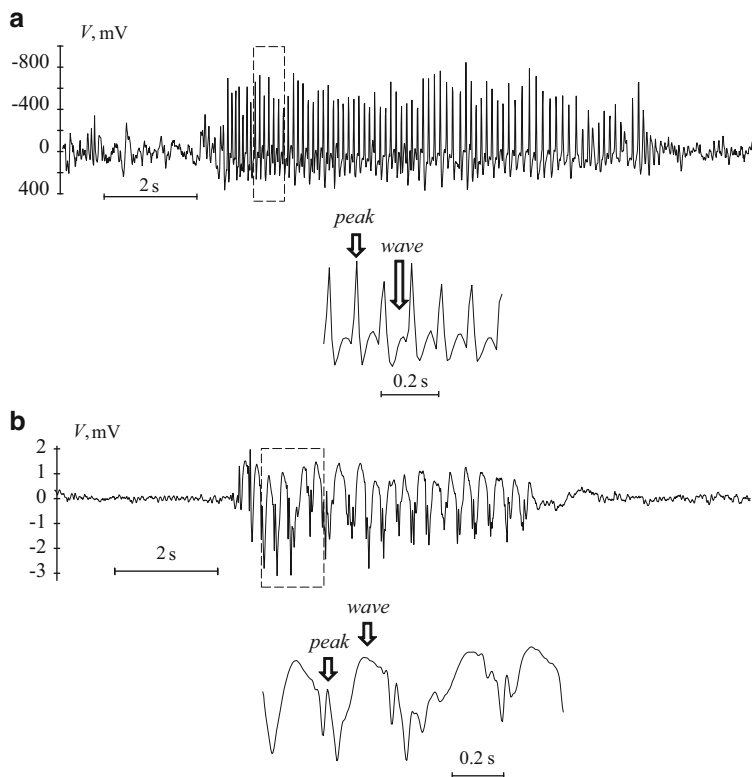


Fig. 5.4 EEG fragments with typical spike–wave discharges as recorded in a WAG/Rij rat (a) and in a human patient with absence epilepsy (b)

the WAG/Rij rat model is recognized as reliable, since the clinical manifestations and response to drugs in WAG/Rij rats is similar to that in patients with absence epilepsy [45].

Figure 5.4 shows typical EEG fragments with spontaneous SWD, as recorded in a symptomatic WAG/Rij rat (Fig. 5.4a) and for a human patient suffering from absence epilepsy (Fig. 5.4b). In the WAG/Rij rat (1 year old), EEG was recorded intracranially by means of an electrode implanted at the surface of the frontal cortex. In the male patient (23 years old), EEG was recorded extracranially with skin electrodes attached to the frontal cortex (F4 electrode in the right hemisphere in the system 10–20 [78], see Sect. 6.6 for details). Enlarged fragments at the bottom of each EEG illustrate the detailed structure of spike–wave discharges with the typical fast (spike) and slow (wave) components. In the human EEG, the spikes are not pronounced, mainly because the signal was recorded at the surface of the skull, and hence relatively far from the source of electrical brain activity.

In the rest of this section, we consider in depth the wavelet analysis of spike–wave discharges in humans and the WAG/Rij rat by means of different types of mother

wavelets (see Sect. 2.3.2). We start by considering the use of the *complex* Morlet wavelet for the continuous wavelet analysis of the SWD. Equation (5.1) gives the formula for the complex mother wavelet:

$$\psi_0(\eta) = \pi^{-1/4} e^{i\omega_0\eta} e^{-\eta^2/2}, \quad (5.1)$$

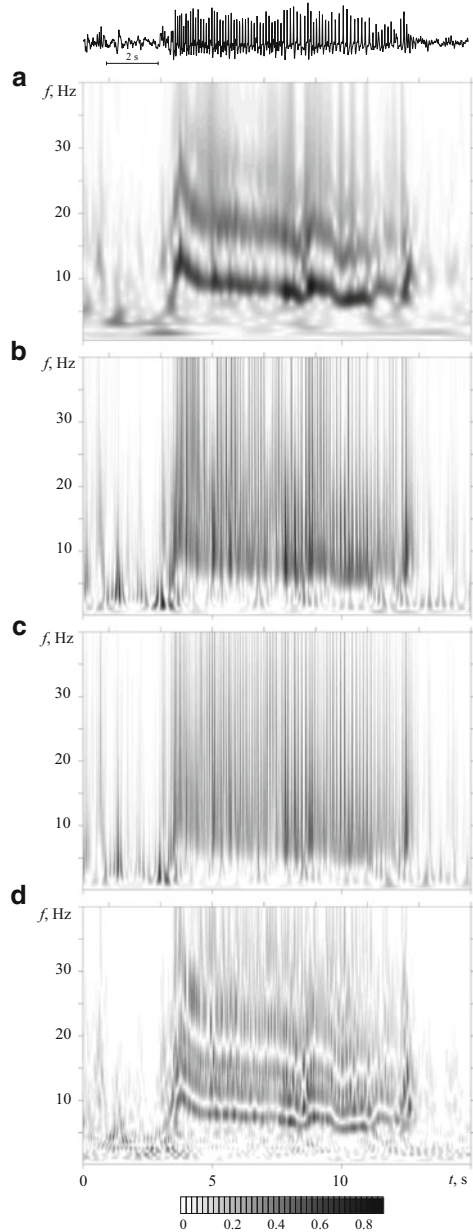
where the second term in the brackets of (2.33) is neglected and $\omega_0 = 2\pi$.

Figures 5.5a and 5.6a show the wavelet spectra of a spike–wave discharge as computed with the aid of the Morlet wavelet in the WAG/Rij rat and in a human patient with absence epilepsy, respectively. In the wavelet spectrum of the rat SWD, the complex frequency dynamics during an epileptic event is clearly visible. In order to identify the frequency dynamics of the SWD, Fig. 5.7a displays the skeleton of the wavelet surface shown in Fig. 5.5a. Typically, the frequency of spontaneous SWD is approximately 12–15 Hz at the beginning, but it decreases rapidly to ~ 10 Hz during the first 300 ms and becomes stable at ~ 10 Hz with fluctuations of 1–3 Hz, while the period of fluctuations lasts approximately 0.7 s. In general, there is a steady trend towards a decrease in frequency to 7–8 Hz at the end of the SWD [79, 80]. The way the SWD frequency dynamics is determined with the help of wavelet analysis from a large volume of experimental data is further discussed in Sect. 6.2.

Analysis of the skeletons of the wavelet surface reveals that there are three first harmonics of the SWD fundamental frequency (shown in Fig. 5.7a) located in the range of 7–15 Hz, and that they tend to decrease in time. This kind of spectrum with higher harmonics is typical for signals with complex shape and sharp peak components (compare with Fig. 2.18, which shows a model pulse signal whose spectrum contains higher harmonics, and see also the discussion in Sect. 2.3.4). It should be noted that the frequency composition of a spike–wave discharge changes very quickly (during one or two oscillation periods). As a consequence, the methods given in [80] could not be used effectively to detect the time–frequency structure of SWDs.

The wavelet spectrum of the SWD in a patient with absence epilepsy is similar to what was found in a rat (see Fig. 5.6). The wavelet spectra of SWDs in humans and in animals differ quantitatively, since the frequency of the human SWD lies in the range 3–4 Hz, which is lower than the frequency in a rat. However, the tendency for a rapid decrease of the main frequency from the beginning to the end of the SWD, and further stabilization of the frequency in the middle of the discharge, is observed in both rats and humans. This can be seen clearly in the skeleton of wavelet spectrum (see Fig. 5.7b). Note also that, in humans, the wavelet spectrum and its skeleton display less pronounced higher harmonics of the main frequency in comparison with the rat. Therefore, in the skeleton of the wavelet spectrum in humans, only the dynamics of the second harmonic can be traced (Fig. 5.7b). This can be accounted for by a *smoother* form of SWD in humans, i.e., low spike amplitudes, which contribute mainly to the dynamics of high frequencies in EEG (the appearance of higher harmonics) during SWD.

Fig. 5.5 Wavelet spectra of a typical spike–wave discharge in WAG/Rij rats, as computed with the aid of different mother wavelets: complex Morlet wavelet with $\omega_0 = 2\pi$ (**a**), real MHAT wavelet (**b**), WAVE wavelet (**c**), and modified Morlet wavelet (**d**)



It should be noted that the complex Morlet wavelet provides the optimal relationship between resolution in the frequency and time domains, and can be successfully used to analyze the fine time–frequency structure and dynamics of the fundamental frequency of complex non-stationary neurophysiological signals.

Fig. 5.6 Wavelet spectra of a typical spike–wave discharge in a person with absence epilepsy, as computed with the aid of different mother wavelets: complex Morlet wavelet with $\omega_0 = 2\pi$ (a), real MHAT wavelet (b), WAVE wavelet (c), and modified Morlet wavelet (d)

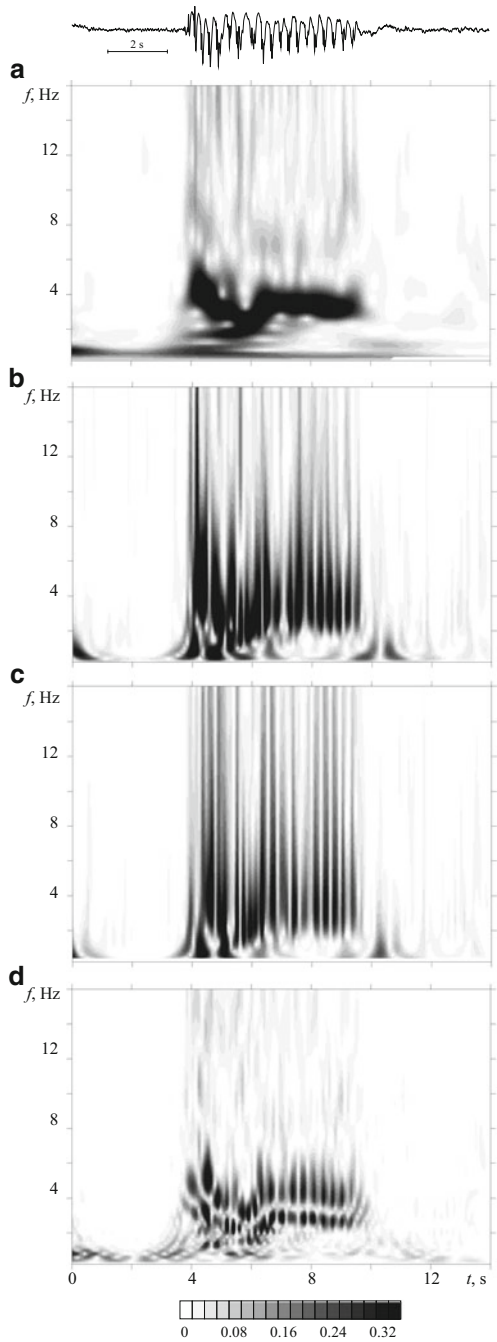
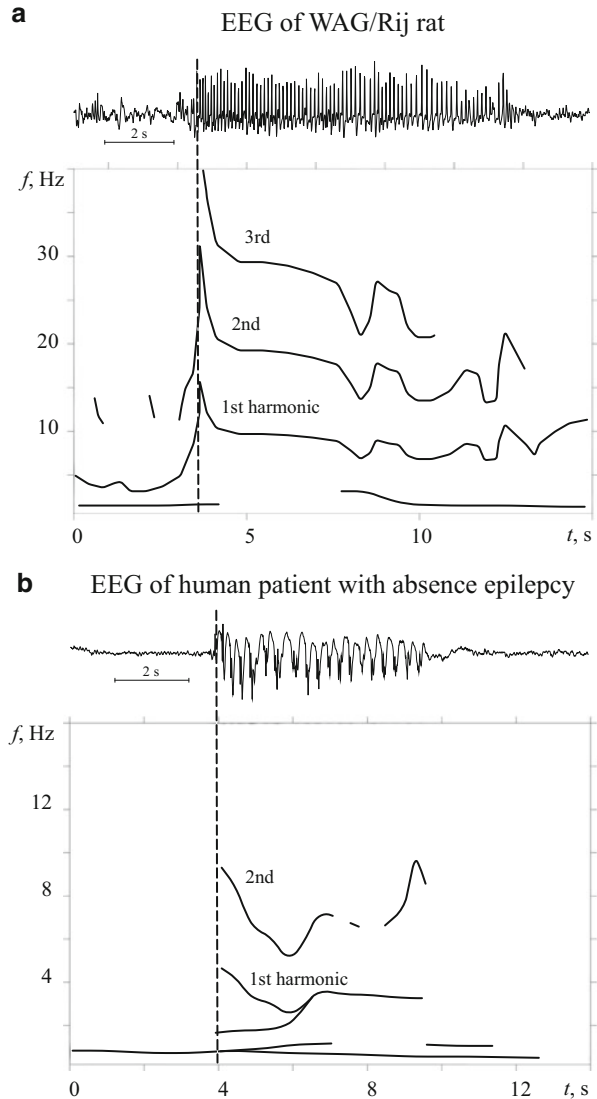


Fig. 5.7 Skeletons of the wavelet spectrum of typical spike–wave discharges obtained with the aid of the complex Morlet wavelet ($\omega_0 = 2\pi$). **(a)** Skeleton of a spike–wave discharge in the WAG/Rij rat. **(b)** Skeleton of the discharge in a human EEG. In skeletons, only peaks exceeding the threshold that corresponds to the amplitude of the wavelet spectrum of the background EEG are shown. Harmonics of oscillations during the spike–wave discharge are marked by numbers. The *vertical dashed line* marks the onset of the SWD



For example, wavelet analysis has been successfully used to identify and describe the dynamics of the intrinsic SWD frequency. The dynamics of EEG frequencies described in this way reflects the functional activity of widespread neuronal networks during the process of initiation and termination of the SWD, which is important for understanding epileptogenesis mechanisms.

We turn now to the analysis of spike–wave discharges by means of *real mother wavelets*. Figures 5.5 and 5.6 illustrate the modulus $|W(f_s, t)|$ of wavelet spectrum coefficients obtained with the help of the standard real mother MHAT (2.40) and

WAVE (2.39) wavelets. The figures show the EEG with SWD in a WAG/Rij rat (Fig. 5.5b, c) and in a human (Fig. 5.6b, c). In order to convert the wavelet frequencies f_s into the frequencies f of the Fourier transform, we determine the relationship between f and f_s in the way discussed in Sect. 2.3.3 (see the ratio f/f_s in Table 2.1).

Indeed, the wavelet spectra obtained by means of the MHAT or WAVE wavelets are characterized by the low-frequency resolution and, as a consequence, the higher harmonics and their frequency dynamics are not clearly distinguished from the background dynamics of the main frequency. At the same time, the characteristic features of these real wavelets lead to sharp peaks in the wavelet spectrum, so any EEG event with a sharp waveform produces intense amplitude bursts in the frequency range of interest in the wavelet spectrum. The disadvantage of real wavelets is the complexity involved in determining the main frequencies in the wavelet spectrum, because the maxima and minima of the wavelet surface correspond to an increase/decrease in the EEG amplitude. Obviously, this form of wavelet spectrum of the SWD does not properly display the particularities of the signal, nor the dynamics of its frequency and amplitude. An advantage of the WAVE and MHAT wavelets is good time resolution, which allows one to track the rapid increase in amplitude of the wavelet spectrum and the moment when the examined rhythm appears in the EEG. However, due to the poor frequency resolution, sharp changes in amplitude of the wavelet spectra could be missed, and that complicates the analysis of the time–frequency structure of the signal. The above remarks concerning real wavelets are valid for the analysis of both animal and human epileptic EEG.

As an example application of real wavelets in EEG analysis, we mention the paper [81], which proposed a real wavelet mother function constructed on the basis of the Morlet wavelet, especially for the analysis of spike–wave discharges in WAG/Rij rats. This modified Morlet wavelet zeroizes the amplitude of the wavelet transform coefficients corresponding to the fundamental EEG frequency in the time and frequency domains.

The modified real Morlet wavelet used in [79, 81] has the form

$$\psi_0(\eta) = \eta \cos(\Omega\eta)e^{-\eta^2/2}, \quad (5.2)$$

where the parameter $\Omega = 5$. It can be shown [82] that the particularity of this mother wavelet is that the frequencies $f_{s\max}$ corresponding to the maximum of the wavelet surface $|W|$ built with the classic wavelet basis satisfy the condition $|W(f_{s\max}, t)| = 0$ when the modified basis (5.2) is used. So in this case the dynamics of the fundamental frequencies in the EEG is not determined by the presence of local maxima as we saw earlier (Chap. 2), but by the zero values of the wavelet surface (see Figs. 5.5d and 5.6d). The modified real Morlet wavelet (5.2) was used to analyze the dynamics of frequency characteristics of typical SWD in patients with child absence epilepsy, juvenile absence, or juvenile myoclonic epilepsy, as well as to study the effect of various pharmacological substances on the time–frequency structure of epileptic discharges.

Comparative analysis of results obtained with the modified real Morlet wavelet (5.2) and standard complex Morlet wavelet (5.1) did not reveal any advantages with the modified wavelet basis. Moreover, application of the real Morlet wavelet in the continuous wavelet transform may just obscure features in the wavelet spectrum, especially when the amplitude of the fundamental frequency was close to its maximum or did not reach the maximum. In this case, the wavelet coefficients were close to zero, which was not convenient for digital signal processing and introduced undesirable difficulties in the automatic processing of the wavelet spectra. Modification of the mother wavelet function is potentially beneficial for signal analysis, because it helps to adjust the method to solve specific problems and expands the area of practical application of the wavelet transform. However, considering the ambiguities associated with real wavelet basis functions, we will modify the complex (not real) wavelet basis function in this book, and demonstrate some profitable features of the modified Morlet wavelet constructed on the basis of the standard complex mother Morlet wavelet function (5.1), which provides good resolution in both the time and frequency domains.

The effects of pharmacological treatment on the structure of spike-wave discharges in WAG/Rij rats, as observed by means of wavelet analysis with a modified real Morlet wavelet, are presented in [82, 83]. This study led to the following conclusions, which could be taken into account in clinical practice (antiepileptic drug treatment).

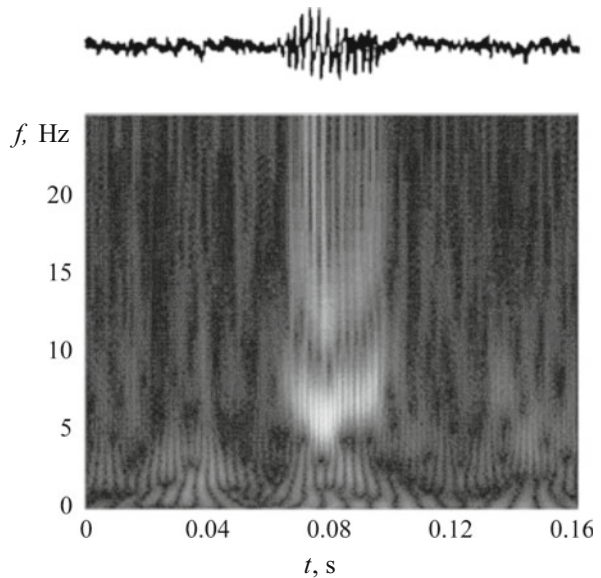
Haloperidol (an antipsychotic drug) in small doses reinforces absence epilepsy and causes numerous short spike-wave discharges in EEG. Rats under low doses of Haloperidol had an SWD of mean duration of 5 s, characterized by a rapid change in intrinsic frequency from 15 Hz at the beginning to 5 Hz at the end of the SWD. In high doses, Haloperidol induces long-lasting spike-wave discharges with relatively low frequency, which varied between 6 and 9 Hz with two types of modulation with periods 0.5–0.6 and 3–6 s.

Vigabatrin (drug of choice for antiepileptic medication, anticonvulsant) in small doses greatly increases the duration of SWDs (up to 20–45 s). Under vigabatrin treatment, the SWD started with short bursts of oscillatory activity with frequency 17–20 Hz, and then the frequency decreased to 5 Hz, and gradually reached a plateau of 8–9 Hz. The main frequency of spike-wave discharges fluctuated between 4.5–5 and 8–9 Hz, and the major changes in frequency occurred approximately every 2 s.

Ketamine (a drug with an anesthetic and analgesic action) caused a biphasic effect on spike-wave discharges. In the first phase, the number of discharges was reduced, and during the second phase, short and long spike-wave discharges were usually observed. The short-lasting discharges had a head-tail waveform (see Fig. 5.8). The “head” consisted of high-amplitude spike-wave complexes with frequency 6–7 Hz and a duration of 1–1.5 s, whereas the “tail” was formed by low-amplitude oscillations with a frequency about 9 Hz and duration 1–3 s.

In general, antiepileptic drug therapy altered the frequency characteristics of SWDs, which are associated with changes in the neuronal network mechanisms of absence epilepsy. These changes underlie the basic mechanisms of absence epilepsy and, in particular, mechanisms involved in suppression of seizure activity.

Fig. 5.8 Short-lasting SWD in WAG/Rij rat under the influence of ketamine (From [83]). The SWD has a specific waveform in EEG (*top*) with two parts, namely a “head” with frequency 6–7 Hz and “tail” with a frequency of about 9 Hz. The corresponding wavelet surface obtained with the modified Morlet wavelet (*bottom*) shows the time–frequency profile of this phenomena



5.4 Applications of Wavelets in Electroencephalography

An EEG contains many different rhythmic components whose frequencies provide important information about functional activity in different brain structures. As already discussed, wavelet analysis is well suited to study complex processes with time-varying characteristics, and it is widely used for time–frequency analysis of EEG data (non-stationary signals that include a variety of oscillatory patterns with significantly different waveforms and frequencies). Furthermore, the presence of a high level of noise and the short duration of EEG recordings cause additional difficulties in EEG analysis [20, 68–70, 72].

Careful attention should be paid to the specific forms of rhythmic activity associated with specific brain and behavioral functions (episodes of epileptic activity, sleep, etc.). It is known that rhythmic components in EEG reflect the synchronous dynamics of a huge number of neurons integrated into ensembles [77, 84, 85], and studies of rhythmic brain activity using wavelets are closely related to an important task of nonlinear dynamics, viz., the study of synchronous behavior in networks with complex topology [4–6, 86].

Sections 5.4.1–5.4.7 overview the most important and actively developed applications of wavelets in studies of electrical brain activity and in diagnostics based on EEG. In the heading of each part, we indicate the first and most important works from our point of view, but the bibliography given here is obviously incomplete due to the large number of publications.

5.4.1 Time–Frequency Analysis of EEG Structure

One of the most obvious applications of wavelets in neurophysiology and electroencephalography is identification of certain EEG patterns and analysis of the time–frequency structure of EEG signals [18, 42, 43, 80, 82, 83, 87–110]. This application takes into account the basic properties of wavelets and the main areas of their use. The first wavelet-based studies in neurobiology aimed to analyze characteristic time–frequency features of various patterns in EEG [43, 87, 89]. Subsequently, specific methods were developed to estimate different statistical characteristics of non-stationary signals such as time-varying wavelet coherence, wavelet entropy, etc. [109–114]. Wavelet-based studies were directed towards determining particular interactions between the cardiovascular system and the CNS using experimental data (ECoG and EEG) [115–117]. One of the most effective applications of wavelets could be found in papers [81, 82, 91, 93, 104] with close attention to pathological electrical brain activity characterized by short duration and complex frequency content (see Sect. 5.3.3), such as spontaneous epileptic spike-wave discharges in EEG. Wavelet analysis has also been used to identify the influences of medication on the time–frequency structure of SWDs [83] and to describe the structure of characteristic “precursors” of epileptic activity [101]. Wavelet-based methods were also used to study other forms of oscillatory activity (oscillatory patterns) in EEG, in particular, sleep spindles and 5–9 Hz oscillations [107].

Some aspects of time–frequency analysis of EEG, novel neurophysiological results obtained using this analysis, interpretations, and conclusions are described in Sects. 5.3.3, 6.2, and 6.3.

5.4.2 Automatic Detection of Oscillatory Patterns and Different Rhythms in Pre-recorded EEG

Simple methods of automatic pattern recognition in EEG (e.g., the threshold method, method of templates, simple neural networks, etc.) often failed to be successful because of high noise levels, nonstationarity of EEG signals, and/or the highly variable time–frequency structure of oscillatory EEG events [107, 118–125].

The following properties of wavelet analysis benefit its application in the automatic processing of EEG data:

1. A representation of the time–frequency structure of signals that enables one to localize signal features simultaneously in the time and frequency domains.
2. Effective analysis of short time series containing small numbers of characteristic oscillations, as required for automatic diagnostics of short-lasting events in EEG.
3. Flexibility in the choice of basis function for signal decomposition, a prerequisite for successfully adjusting the mathematical apparatus of wavelet analysis to the signal properties.

4. Highly effective analysis of noisy data, i.e., processes comprising a sum of useful signals and additive noise.

Currently, there is a quite general approach to automatic processing of pre-recorded EEG data using estimates of wavelet energy in characteristic frequency bands (with standard mother wavelets and adaptive wavelet bases) [107, 120]. This method has been successfully used to analyze the structure of sleep spindles in EEG, i.e., short episodes of rhythmic activity in the EEG (see details in Sect. 7.4).

Automatic data processing methods facilitated further progress in the study of the time-dependent dynamics of various rhythmic components in EEG. For instance, it was shown that epileptic brain activity in WAG/Rij rats is an intermittent process corresponding to on–off intermittency [120]. A similar intermittent dynamics was also found in sleep spindles [107]. This type of dynamical behavior was observed in coupled chaotic oscillators and in networks of nonlinear units at the boundary of the synchronization region [126–131]. On–off intermittent behavior in neuronal networks and applications of oscillation and wavelet theory can provide a deeper understanding of the dynamics of epileptic activity and, in particular, the underlying mechanisms of epileptogenesis. Later on, we shall describe examples of successful applications of wavelets in this field (see Sects. 7.2 and 7.5).

5.4.3 *Classification of Oscillatory Patterns*

The development of standardized databases of characteristic electroencephalograph patterns is an important fundamental and applied problem [70, 80, 97, 107, 117, 132–140]. A relatively new approach to classification and standardization of oscillatory EEG patterns, similar to the *template matching technique*, constructs complex adaptive wavelet bases from original EEG segments [80]. This procedure was effective for identification and classification of spindle-like oscillatory events in EEG. In particular, this method was used to describe “spike–wave spindles” that occurred during desynchronization of EEG and were considered as an immature form of epileptic spike–wave discharges that combined some properties of sleep spindles and SWD [80]. More details will be given in Sect. 6.5.

5.4.4 *Real-Time Detection of Oscillatory Patterns in EEG*

Online identification of characteristic oscillatory patterns in EEG is one of the most interesting and intensively studied problems [141–145]. Further progress in this area is important for monitoring human brain activity, and also for the development of special brain–computer interfaces. One difficulty in identification of EEG patterns relates to the problem of selectivity (different EEG patterns have similar spectra). It is difficult to develop a universal method for online diagnostics of oscillatory

patterns in EEG due to the nonstationarity of experimental data. Application of wavelets for online diagnostics in EEG may help to overcome this problem of nonstationarity, and we shall discuss examples of how a wavelet-based method provides a way to monitor seizure activity in the brain [144]. Let us note that current methods for extracting characteristic EEG patterns using wavelets are increasingly used in developing prototypes of brain–computer interfaces [137, 143, 146]. An advantage and at the same time a disadvantage of these approaches is the use of the discrete wavelet transform. Although it provides quick signal processing, allowing online analysis of a large amount of experimental data, it is less appropriate for flexible recognition of different patterns in EEG. Approaches like those described in [144] which use the continuous wavelet transform can improve the quality of recognition. Section 7.3 describes an algorithm for automatic online detection of spike–wave discharges.

5.4.5 *Multichannel EEG Analysis of Synchronization of Brain Activity*

It is known that different areas of the cerebral cortex often exhibit synchronous activity in both normal states (e.g., during cognitive activity) and pathological states (Parkinson’s disease, epilepsy, paranoid schizophrenia, etc.) [65, 95, 142, 147–154]. As shown in Sect. 2.3.5, the corresponding synchronous dynamics can be analyzed using continuous wavelet analysis with complex mother functions in an approach known as the *time-scale synchronization* [155, 156]. This has been used to study synchronization phenomena in different kinds of system [157–162].

Application of the continuous wavelet transform for analysis of multichannel EEG revealed periods of synchronization in short and noisy data. Besides, synchronization of time scales is quite stable to errors when estimating the characteristic frequencies of analyzed processes and this is important for automatic processing of experimental neurophysiological data.

The discussed method has recently been successfully applied to reveal synchronization between different brain areas during spike–wave discharges (absence epilepsy) in humans and animals. It has also been used to analyze brain activity during cognitive tasks. Section 6.6 describes the most interesting results relating to the sequential involvement of different brain regions in the synchronization process during epileptic discharges.

5.4.6 *Artifact Suppression in Multichannel EEG Using Wavelets and Independent Component Analysis*

Analysis of EEG essentially becomes complicated due to the presence of different artifacts, in particular high-amplitude EEG components associated with eye movements, blinking, muscle activity, etc. [68, 87, 163–170]. Currently, wavelets have

become a popular technique for artifact suppression [68, 169, 170]. For example, a new approach known as wavelet-enhanced independent component analysis (wICA) [167] has been applied to suppress artifacts caused by blinking eyes and heart beats. It is important to note that wICA resulted in a tenfold reduction of movement artifacts in EEG without significant influence on neuronal signals. This advantage can be used to develop algorithms for automatic artifact rejection in EEG. Section 7.8 describes peculiarities of the wICA approach.

5.4.7 Study of Cognitive Processes

In addition to analysis of pathological dynamics in EEG, the wavelet transform is widely used in studies of cognitive processes [11, 143, 154, 171–174]. Thus, interactions between different areas of the cerebral cortex were investigated during cognitive tasks in [171]. This study aimed to assess the strength of intracortical interactions using the degree of synchronization of electrical EEG activity expressed in different brain areas. It used a wavelet-based correlation method to measure the degree of synchronization during short time intervals (comparable with the duration of mental operations, i.e., up to 100 ms).

The discrete wavelet transform with Daubechies functions was used in [173] to study spectral powers in the alpha and beta frequency bands in different brain areas of healthy subjects who were solving simple arithmetic tasks. The continuous wavelet transform of EEG data has been intensively used to study rapid cognitive processes underlying the process of human face recognition. Short fragments of EEG (800 ms) were analyzed in [174] after emotionally valenced stimuli (expression of angry and neutral faces). Analysis was performed using the Morlet function with estimation of wavelet coefficients in the frequency range $\Delta f = 1\text{--}30\text{ Hz}$, reflecting the amplitude dynamics of cortical potentials in the corresponding frequency range Δf . Statistical analysis of rhythmic components in the evoked EEG activity was carried out in the alpha and theta frequency bands. It was shown that individual differences in the perception of facial expressions correlated with wavelet coefficients in the above-mentioned frequency ranges. Thus, changes in the alpha and theta bands were important at the stage of stimulus perception. Emotional reaction is associated with theta activity. Based on wavelet analysis, Yakovenko et al. [174] suggested that emotional expressions are accompanied by different cortico-subcortical interactions among different humans and at different stages of the experiment.

Finally, cognitive processes of human brain activity, accompanied by changes in the waveform of evoked potentials in the EEG, were analyzed in [154] using wavelets. Let us consider this work in more detail. The *evoked potential* represents a structured fluctuation of electrical brain activity in response to external stimulus [175]. Eight components of the evoked potential are traditionally introduced, taking into account their polarity (P positive, N negative) and the latency, i.e., the time delay from the onset of the stimulus. It is important to note that the evoked

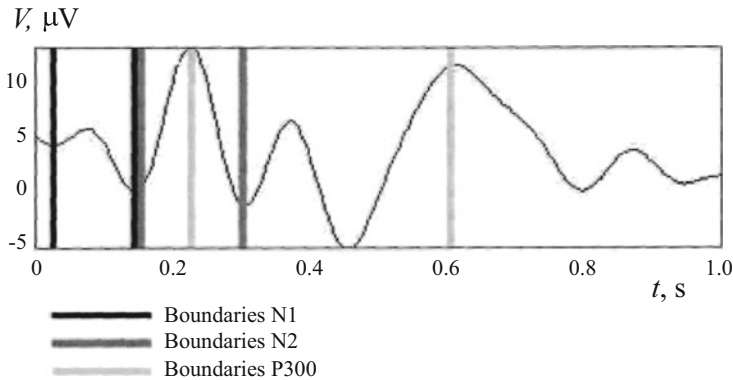


Fig. 5.9 Waveform of acoustically evoked potential and ranges of the “cognitive” components $N1$, $N2$, and $P300$ (From [154])

potential of a certain modality (visual, auditory, somatosensory) is recorded at the corresponding projection area of the neocortex. Potentials at other brain regions are secondary (associative) and may differ in waveform, latent period, and amplitude. For example, the spatial organization of an acoustically evoked potential reflects the following stages of cognitive processes:

- Non-arbitrary perception—component $N1$,
- Transition from non-arbitrary to arbitrary perception—component $N2$,
- Information processing and decision regarding significance—component $P300$.

The purpose of the paper [154] was to develop an effective method for evaluating phase synchronization to analyze acoustically evoked potentials in healthy human subjects. It was shown that, in situations that do not require concentration (e.g., listening to sounds), spatial organization of the components of acoustically evoked potentials had a diffuse character. Phase synchronization indexes fluctuated over the range 0.5–0.8 and took similar values in all components $N1$, $N2$, and $P300$ (see Fig. 5.9, reproduced from [154], which shows a typical waveform of the acoustically evoked potential and variation of the “cognitive” components $N1$, $N2$ and $P300$). Higher phase synchronization indexes in the studied components were found in the frontal or temporal areas of the right hemisphere. Concentration (elicited by auditory stimuli) increased this index up to 0.9 in components $N1$ and $P300$ (see Fig. 5.10). The highest degree of synchronization was observed between associative areas of the cortex (frontal, central, and parietal), between the hemispheres (often diagonally), with a shift in the direction of the left hemisphere.

The described changes in the phase synchronization reflect the process of selective involvement of the above-mentioned areas of neocortex in cognitive (acoustic) tasks. Romanov et al. [154] used the good temporal resolution of the wavelet transform in order to extract information about quick changes in the shape of the electric potential (evoked potential) during mental activity. Wavelet analysis

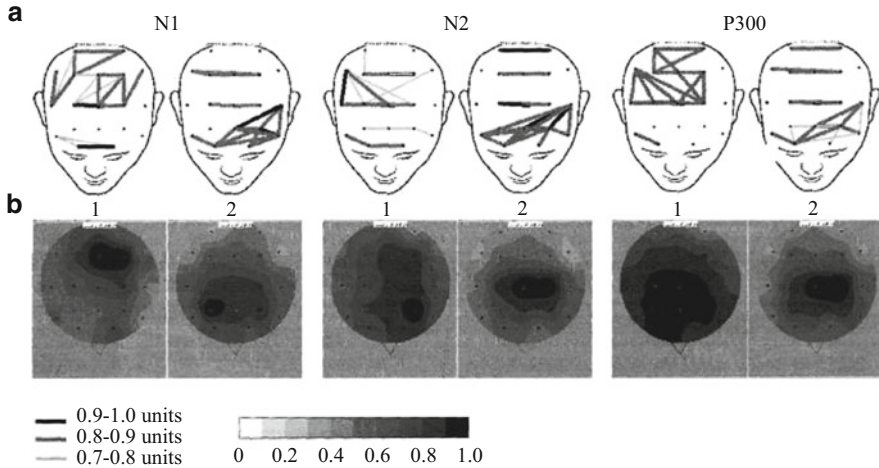


Fig. 5.10 Changes of phase synchronization (**a**) and wavelet power (**b**) while listening to sounds (1) and while counting auditory stimuli (2) in the same subject (From [154])

is thus in demand in psychophysiology, where it is often necessary to analyze short fragments of EEG and rapid processes of human brain activity.

References

1. G. Buzsaki, A. Draguhn, Oscillations in cortical networks. *Science* **304**, 1926 (2004)
2. V.I. Nekorkin, Nonlinear oscillations and waves in neurodynamics. *Phys.-Usp.* **51**, 295 (2008)
3. H.D. Abarbanel, M.I. Rabinovich, A. Selverston, M.V. Bazhenov, R. Huerta, M.M. Sushchik, L.L. Rubchinsky, Synchronisation in neural networks. *Phys.-Usp.* **39**, 337 (1996)
4. D.M. Zenett, A.S. Mikhailov, Mutual synchronization in ensembles of globally coupled neural networks. *Phys. Rev. E* **58**(1), 872 (1998)
5. S.H. Strogatz, Exploring complex networks. *Nature* **410**, 268 (2001)
6. S. Boccaletti, V. Latora, V. Moreno, M. Chavez, D.U. Hwang, Complex networks: structure and dynamics. *Phys. Rep.* **424**, 175 (2006)
7. A. Destexhe, T.J. Sejnowski, *Thalamocortical Assemblies* (Cambridge University Press, Cambridge, 2001)
8. F. Lopes da Silva, Neural mechanisms underlying brain waves: from neural membranes to networks. *Electroencephalogr. Clin. Neurophys.* **79**, 81 (1991)
9. M.N. Livanov, *The Spatial Organization of Processes in the Brain* (Nauka, Moscow, 1972)
10. S.M. Osovetz, D.A. Ginzburg et al., Electrical activity of the brain: mechanisms and interpretation. *Phys.-Usp.* **26**, 801 (1983)
11. N.E. Sviderskaya, *Synchronous Electrical Activity of the Brain and Mental Processes* (Nauka, Moscow, 1987)
12. P. Naatanen, *Attention and Brain Function* (Moscow State University Press, Moscow, 1998)
13. N.E. Sviderskaia, T.N. Dashchinskaia, G.V. Taratynova, EEG spatial organization and activation of creative processes. *J. High. Nerv. Act.* **51**, 393 (2001)

14. J.R. Wolpaw, N. Birbaumer, D.J. McFarland, G. Pfurtscheller, T.M. Vaughan, Brain-computer interfaces for communication and control. *Clin. Neurophys.* **113**, 767 (2002)
15. C. Guger, G. Edlinger, W. Harkam, I. Niedermayer, G. Pfurtscheller, How many people are able to operate an EEG-based brain-computer interface (BCI)? *IEEE Trans. Rehabil. Eng.* **11**, 145 (2003)
16. G.A. Ivanitskii, R.A. Naumov, S.A. Roik, A.M. Ivanitskii, How to determine what is the brain doing by means of his electric potentials? Stable EEG patterns in the performance of cognitive tasks. *Artif. Intell. Quest.* **1**, 93 (2008)
17. A. Kaplan, J.J. Lim, K.S. Jin, B.W. Park, J.G. Byeon, S.U. Tarasova, Unconscious operant conditioning in the paradigm of brain-computer interface based on color perception. *Int. J. Neurosci.* **115**, 781 (2005)
18. E. Sitnikova, A.A. Koronovskii, A.E. Hramov, Analysis of epileptic activity of brain in case of absence epilepsy: applied aspects of nonlinear dynamics. *Appl. Nonlinear Dyn.* **19**(6), 173 (2011)
19. International Federation of Societies for Electroencephalography and Clinical Neurophysiology, A glossary of terms most commonly used by clinical electroencephalographers. *Electroencephalogr. Clin. Neurophysiol.* **37**, 538 (1974)
20. F. Lopes da Silva, *Encyclopedia of the Human Brain* (Elsevier Science, New York, 2002), pp. 146–147
21. E.S. Goldensohn, R.J. Porter, P.A. Schwartzkroin, The American Epilepsy Society: an historic perspective on 50 years of advances in research. *Epilepsia* **38**(1), 124 (1997)
22. H. Berger, Über das elektroencephalogramm des menschen. *Archiv für Psychiatrie und Nervenkrankheiten* **87**, 527 (1929)
23. R. Jung, Sensory research in historical perspective: some philosophical foundations of perception. *Comprehensive physiology* 2011. In: *Supplement 3: Handbook of Physiology, The Nervous System, Sensory Processes* (American Physiological Society, Washington, DC, First published in print 1984), pp. 1–74. doi:10.1002/cphy.cp010301
24. A. Beck, Die Ströme der Nervenzentren. *Zentralbl. Physiol.* **4**, 572 (1890)
25. E.F. von Marxow, Mittheilung, betreffend die Physiologie der Hirnrinde. *Centralblatt für Physiologie* **4**(#18), 36 (1890)
26. V. Ya. Danilevsky, *Study of Physiological Effect of Electricity on Distance* (Kharkov Veterinary Institute Press, Kharkov, 1900)
27. P.K. Anokhin, *Biology and Neurophysiology of the Conditioned Reflex* (Medicine, Moscow, 1968)
28. M.N. Livanov, T.A. Korolkova, G.M. Frenkel, Electrophysiological studies of higher nervous activity. *J. High. Nerv. Act.* **1**(4), 521 (1951)
29. M.N. Livanov, *Spatio-Temporal Organization of the Potentials and Systemic Activity of the Brain: Selected Works* (Nauka, Moscow, 1989)
30. V.S. Rusinov, *Physiology* (Science, Leningrad, 1954), pp. 235–256
31. A. Labate, R.S. Briellmann, D.E. Abbott, A.B. Waites, G.D. Jackson, Typical childhood absence seizures are associated with thalamic activation. *Epileptic Disord.* **7** (4), 373 (2005)
32. N. Cybulski, S. Jeleńska-Macieszyna, Prady czynnościowe kory mózgowej. *Bull. Int. Acad. Cracovie.* **B**, 776 (1914)
33. J.D. Bronzino, *The Biomedical Engineering Handbook* (CRC, Boca Raton, 1995)
34. F.A. Gibbs, H. Davis, W.G. Lennox, The electroencephalogram in epilepsy and in conditions of impaired consciousness. *Arch. Neurol. Psychiatry* (Chicago) **34**, 1133 (2002)
35. W.J. Freeman, *Mass Action in the Nervous System* (Academic, New York, 1975)
36. E. Basar, *Brain Function and Oscillations. II. Integrative Brain Function. Neurophysiology and Cognitive Processes* (Springer, Berlin/Heidelberg, 1999)
37. M.A. Nicolelis, E.E. Fanselow, Thalamocortical optimization of tactile processing according to behavioral state. *Nat. Neurosci.* **5**, 517 (2002)
38. M. Steriade, *Neuronal Substrates of Sleep and Epilepsy* (Cambridge University Press, Cambridge, 2003)

39. E. Basar, *EEG-Brain Dynamics. Relation Between EEG and Evoked Potentials* (Elsevier, Amsterdam, 1980)
40. A.M. Ivanitskii, A.I. Lebedev, Unlocking the secrets of the brain rhythms. *J. High. Nerv. Act.* **57**(5), 636 (2007)
41. S.L. Marple, *Digital Spectral Analysis with Applications* (Prentice-Hall, Englewood Cliffs, 1987)
42. E. Huupponen, W.D. Clercq, G. Gomez-Herrero, A. Saastamoinen, K. Egiazarian, A. Varri, B. Vanrumste, A. Vergult, S. Van Huffel, W. Van Paesschen, J. Hasan, S.L. Himanen, Determination of dominant simulated spindle frequency with different methods. *J. Neurosci. Methods* **156**, 275 (2006)
43. A.M. Bianchi, L.T. Mainardi, S. Cerutti, Time–frequency analysis of biomedical signals. *Trans. Inst. Meas. Control* **15**, 215 (2000)
44. A.B. Ritter, S.S. Reisman, B.B. Michniak, *Biomedical Engineering Principles* (CRC/Taylor & Francis, Boca Raton, 2005)
45. A.M. Coenen, E.L. Van Luijtelaar, The WAG/Rij rat model for absence epilepsy: age and sex factors. *Epilepsy Res.* **1**(5), 297 (1987)
46. A.M. Coenen, E.L. Van Luijtelaar, Pharmacological dissociation of EEG and behavior: a basic problem in sleep–wake classification. *Sleep* **14**, 464 (1991)
47. M. Steriade, M. Deschenes, The thalamus as a neuronal oscillator. *Brain Res. Rev.* **8**, 1 (1984)
48. W. Klimesch, Memory processes, brain oscillations and EEG synchronization. *Brain Res. Rev.* **29**, 169 (1999)
49. J. Csicsvari, B. Jamieson, K.D. Wise, G. Buzsaki, Mechanisms of gamma oscillations in the hippocampus of the behaving rat. *Neuron* **37**, 311 (2003)
50. N. Kopell, G.B. Ermentrout, R.D. Whittington, M. Traub, Gamma rhythms and beta rhythms have different synchronization properties. *Proc. Natl. Acad. Sci. U. S. A.* **97**, 1867 (2000)
51. A.K. Engel, P. Fries, W. Singer, Dynamic predictions: oscillations and synchrony in top–down processing. *Nat. Rev. Neurosci.* **2**, 704 (2001)
52. M. Penttonen, G. Buzsaki, Natural logarithmic relationship between brain oscillators. *Thalamus Relat. Syst.* **2**, 145 (2003)
53. K. Linkenkaer-Hansen, V.V. Nikouline, J.M. Palva, R.J. Ilmoniemi, Long-range temporal correlations and scaling behavior in human brain oscillations. *J. Neurosci.* **21**(4), 1370 (2001)
54. D.R. Chialvo, Critical brain networks. *Physica A* **340**(4), 756 (2004)
55. P. Bak, C. Tang, K. Wiesenfeld, Self-organized criticality: an explanation of $1/f$ noise. *Phys. Rev. Lett.* **59**, 381 (1987)
56. P. Bak, M. Paczuski, Complexity, contingency, and criticality. *Proc. Natl. Acad. Sci. U. S. A.* **92**(15), 6689 (1995)
57. A. Sirota, J. Csicsvari, D. Buhl, G. Buzsaki, Communication between neocortex and hippocampus during sleep in rodents. *Proc. Natl. Acad. Sci. U. S. A.* **100**, 2065 (2003)
58. P.L. Nunez, *Neocortical Dynamics and Human EEG Rhythms* (Oxford University Press, New York, 1992)
59. V. Braitenberg, A. Schuetz, *Cortex: Statistics and Geometry of Neuronal Connectivity*, 2nd edn. (Springer, Heidelberg, 1998)
60. V.N. Dumenko, *High-Frequency Components of the EEG and Instrumental Learning* (Nauka, Moscow, 2006)
61. M. Steriade, Impact of network activities on neuronal properties in corticothalamic systems. *J. Neurophysiol.* **86**, 1 (2001)
62. N.M. Astafeva, Wavelet analysis: basic theory and some applications. *Phys.-Usp.* **39**, 1085 (1996)
63. A.A. Koronovskii, V.I. Ponomarenko, M.D. Prokhorov, A.E. Hramov, Method of studying the synchronization of self-sustained oscillations using continuous wavelet analysis of univariant data. *Tech. Phys.* **52**(9), 1106 (2007)
64. A.A. Koronovskii, A.E. Hramov, *Continuous Wavelet Analysis and Its Applications* (Fizmatlit, Moscow, 2003)

65. R.Q. Quiroga, A. Kraskov, T. Kreuz, P. Grassberger, Performance of different synchronization measures in real data: a case study on electroencephalographic signals. *Phys. Rev. E* **65**, 041903 (2002)
66. E.B. Postnikov, E.A. Lebedeva, Decomposition of strong nonlinear oscillations via modified continuous wavelet transform. *Phys. Rev. E* **82**(5), 057201 (2010)
67. E.B. Postnikov, On precision of wavelet phase synchronization of chaotic systems. *J. Exp. Theor. Phys.* **105**(3), 652 (2007)
68. R. Quiroga, H. Garcia, Single-trial event-related potentials with wavelet denoising. *Clin. Neurophysiol.* **114**, 376 (2003)
69. W.H. Drinkenburg, E.L. Luijtelaaar, W.J. van Schaijk, A.M. Coenen, Aberrant transients in the EEG of epileptic rats: a spectral analytical approach. *Physiol. Behav.* **54**, 779 (1993)
70. P.J. Durka, From wavelets to adaptive approximations: time–frequency parametrization of EEG. *IEEE Trans. Biomed. Eng.* **2**, 1 (2003)
71. N.E. Sviderskaya, *The Spatial Organization of the Electroencephalogram* (Voronezh State Medical Academy Publishing, Voronezh, 2008)
72. W.J. Freeman, C. Skarda, Spatial EEC patterns, non-linear dynamics and perception: the neo-Sherringtonian view. *Brain Res. Rev.* **10**, 145 (1985)
73. J. Laidlaw, A. Richens, D. Chadwick, *A Textbook of Epilepsy*, 4th edn. (Churchill Livingstone, London, 1993)
74. E.L. Van Luijtelaaar, A.M. Coenen, Two types of electrocortical paroxysms in an inbred strain of rats. *Neurosci. Lett.* **70**(3), 393 (1986)
75. National Institute of Neurological Disorders and Stroke, *Seizure and Epilepsy: Hope Through Research* (National Institute of Neurological Disorders and Stroke, Bethesda, 2001). Available from: www.ninds.nih.gov/health_and_medical/pubs/seizures_and_epilepsy_htr.htm
76. R.J. Porter, in *A Textbook of Epilepsy*, ed. by J. Laidlaw, A. Richens, D. Chadwick, 4th edn. (Churchill Livingstone, London, 1993), pp. 1–22
77. E. Sitnikova, E.L. Van Luijtelaaar, Cortical and thalamic coherence during spike–wave seizures in WAG/Rij rats. *Epilepsy Res.* **71**(2–3), 159 (2006)
78. V.V. Gnezditsky, *Inverse Problem of EEG and Clinical Electroencephalography* (Taganrog, Taganrog Radiotechnical State University Press, 2000)
79. A.V. Gabova, D.Yu. Bosnyakova, M.S. Bosnyakov, A.B. Shatskova, G.D. Kuznetsova, Frequency temporal structure of peak-wave discharges of genetic absence epilepsy. *Dokl. Biol. Sci.* **396**, 194 (2004)
80. E. Sitnikova, A.E. Hramov, A.A. Koronovskii, E.L. Luijtelaaar, Sleep spindles and spike–wave discharges in EEG: their generic features, similarities and distinctions disclosed with Fourier transform and continuous wavelet analysis. *J. Neurosci. Methods* **180**, 304 (2009)
81. D. Bosnyakova, A. Gabova, A. Zharikova, V. Gnezditski, G. Kuznetsova, G. van Luijtelaaar, Some peculiarities of time–frequency dynamics of spike–wave discharges in humans and rats. *Pharmacol. Biochem. Behav.* **118**(8), 1736 (2007)
82. D. Bosnyakova, A. Gabova, G. Kuznetsova, Y. Obukhov, I. Midzyanovskaya, D. Salonin, C.M. Rijn, A.M. Coenen, L. Tuomisto, G. van Luijtelaaar, Time–frequency analysis of spike–wave discharges using a modified wavelet transform. *J. Neurosci. Methods* **1654**(1–2), 80 (2006)
83. I. Midzyanovskaya, D. Salonin, D. Bosnyakova, G. Kuznetsova, E.L.M. van Luijtelaaar, The multiple effects of ketamine on electroencephalographic activity and behavior in WAG/Rij rats. *Pharmacol. Biochem. Behav.* **79**, 83 (2004)
84. M. Steriade, *Neuronal Substrates of Sleep and Epilepsy* (Cambridge University Press, Cambridge, 2003)
85. M. Steriade, D.A. McCormick, T.J. Sejnowski, Thalamocortical oscillations in the sleeping and aroused brain. *Science* **262**, 679 (1993)
86. A.K. Kryukov, G.V. Osipov, A.V. Polovinkin, J. Kurths, Synchronous regimes in ensembles of coupled Bonhoeffer–van der Pol oscillators. *Phys. Rev. E* **79**(4), 046209 (2009)

87. S. Schiff, A. Aldroubi, M. Unser, S. Sato, Fast wavelet transformation of EEG. *Electroencephalogr. Clin. Neurophysiol.* **91**, 442 (1994)
88. M. Jobert, C. Tismer, E. Poiseau, H. Schulz, Wavelets: a new tool in sleep biosignal analysis. *J. Sleep Res.* **3**, 223 (1994)
89. J. Muthuswamy, N.V. Thakor, Spectral analysis methods for neurological signals. *J. Neurosci. Methods* **83**, 1 (1998)
90. E. Duzel, R. Habib, B. Schott, A. Schoenfeld, N. Lobaugh, A.R. McIntosh, M. Scholz, H.J. Heinze, A multivariate, spatiotemporal analysis of electromagnetic time–frequency data of recognition memory. *NeuroImage* **18**, 185 (2003)
91. O.A. Rosso, S. Blanco, A. Rabinowicz, Wavelet analysis of generalized tonic–clonic epileptic seizures. *Signal Process.* **83**, 1275 (2003)
92. M. Latka, Z. Was, A. Kozik, J. West, Wavelet analysis of epileptic spikes. *Phys. Rev. E* **67**, 052902 (2003)
93. H. Adeli, Z. Zhou, N. Dadmehr, Analyses of EEG records in an epileptic patient using wavelet transform. *J. Neurosci. Methods* **123**, 69 (2003)
94. H.R. Mosheni, M.B. Shamsollahi, Seizure detection in EEG signals: a comparison of different approaches. *IEEE Int. Conf. Eng. Med. Biol. Soc.* **1**, 53 (2006)
95. H. Carlqvist, V.V. Nikulin, J.O. Strömberg, T. Brismar, Amplitude and phase relationship between alpha and beta oscillations in the human electroencephalogram. *Med. Biol. Eng. Comput.* **43**, 599 (2005)
96. A. Duru, A. Ademoglu, T. Demiralp, Analysis of brain electrical topography by spatio-temporal wavelet decomposition. *Math. Comput. Modell.* **49**, 2224 (2009)
97. S. Slobounov, C. Cao, W. Sebastianelli, Differential effect of first versus second concussive episodes on wavelet information. *Clin. Neurophysiol.* **120**, 862 (2009)
98. O.A. Rosso, M.T. Martin, A. Figliola, K. Keller, A. Plastino, EEG analysis using wavelet-based information tools. *J. Neurosci. Methods* **153**, 163 (2006)
99. M.K. van Vugt, P.B. Sederberg, M.J. Kahana, Comparison of spectral analysis methods for characterizing brain oscillations. *J. Neurosci. Methods* **162**, 49 (2007)
100. H. Adeli, S. Ghosh-Dastidar, N. Dadmehr, A spatio-temporal wavelet–chaos methodology for EEG-based diagnosis of Alzheimer’s disease. *Neurosci. Lett.* **444**, 190 (2008)
101. E.L.M. van Luijtelaar, A.E. Hramov, E. Sitnikova, A.A. Koronovskii, Spike–wave discharges in WAG/Rij rats are preceded by delta and theta precursor activity in cortex and thalamus. *Clin. Neurophysiol.* **122**, 687 (2011)
102. S.V. Bozhokin, N.B. Suvorov, Wavelet analysis of transient processes in EEG photic. *Biomed. Electron.* **3**, 13 (2008)
103. V.V. Grubov, A.A. Ovchinnikov, E.Yu. Sitnikova, A.A. Koronovskii, A.E. Hramov, Wavelet analysis of sleep spindles on EEG and development of method for their automatic diagnostic. *Appl. Nonlinear Dyn.* **19**(4), 91 (2011)
104. G. Ouyang, X. Li, Y. Li, X. Guan, Application of wavelet-based similarity analysis to epileptic seizures prediction. *Comput. Biol. Med.* **37**, 430 (2007)
105. T. Conlon, H.J. Ruskin, M. Crane, Seizure characterisation using frequency-dependent multivariate dynamics. *Med. Biol. Eng. Comput.* **39**, 760 (2009)
106. C.D. Avanzo, V. Tarantinob, P. Bisiacchib, G. Sparacinoa, A wavelet methodology for EEG time–frequency analysis in a time discrimination task. *Int. J. Bioelectromagn.* **11**(4), 185 (2009)
107. E. Sitnikova, A.E. Hramov, V.V. Grubov, A.A. Ovchinnikov, A.A. Koronovsky, On–off intermittency of thalamo-cortical oscillations in the electroencephalogram of rats with genetic predisposition to absence epilepsy. *Brain Res.* **1436**, 147 (2012)
108. Z. Zhang, H. Kawabatab, Z.Q. Liuc, Electroencephalogram analysis using fast wavelet transform. *Comput. Biol. Med.* **31**, 429 (2001)
109. Y. Zhan, D. Halliday, P. Jiang, X. Liu, J. Feng, Detecting time-dependent coherence between non-stationary electrophysiological signal: a combined statistical and time–frequency approach. *J. Neurosci. Methods* **156**, 322 (2006)

110. O.C. Zalay, E.E. Kang, M. Cotic, P.L. Carlen, L. Berj, B.L. Bardakjian, A wavelet packet-based algorithm for the extraction of neural rhythms. *Ann. Biomed. Eng.* **37**, 595 (2009)
111. Y. Mizuno-Matsumoto, S. Ukai, S. Date, T. Kaishima, M. Takeda, S. Tamura, T. Inouyre, Wavelet-crosscorrelation analysis: non-stationary analysis of neurophysiology signals. *Brain Topogr.* **17**(4), 237 (2005)
112. V.T. Makinen, P.J. May, H. Tiitinen, The use of stationarity and nonstationarity in the detection and analysis of neural oscillations. *NeuroImage* **28**, 389 (2005)
113. J.P. Lachaux et al., Estimating the time-course of coherence between single-trial brain signals: an introduction to wavelet coherence. *Neurophysiol. Clin.* **32**(3), 157 (2002)
114. R.Q. Quiroga, O.A. Rosso, E. Base, M. Schurmann, Wavelet entropy in event-related potentials: a new method shows ordering of EEG oscillations. *Biol. Cybern.* **84**, 291 (2001)
115. A. Stefanovska, Coupled oscillators. Complex but not complicated cardiovascular and brain interactions. *IEEE Eng. Med. Biol. Mag.* **11–12**, 25 (2007)
116. B. Musizza, A. Stefanovska, P.V. McClintock, M. Palus, J. Petrovcic, S. Ribaric, F.F. Bajrovic, Interactions between cardiac, respiratory and EEG- δ oscillations in rats during anaesthesia. *J. Physiol.* **580**, 315 (2007)
117. M. Sakai, D. Wei, Separation of electrocardiographic and encephalographic components based on signal averaging and wavelet shrinkage techniques. *Comput. Biol. Med.* **39**, 620 (2009)
118. A.A. Koronovskii, I.M. Minyukhin, A.A. Tyschenko, A.E. Hramov, I.S. Midzyanovskaya, E.Yu. Sitnikova, E.L. Van Lujtelaar, C.M. Rijn, Application of continuous wavelet transform to analysis of intermittent behavior. *Appl. Nonlinear Dyn.* **15**(4), 34 (2007)
119. E. Glassman, A wavelet-like filter based on neuron action potentials for analysis of human scalp electroencephalographs. *IEEE Trans. Biomed. Eng.* **52**(11), 1851 (2005)
120. A.E. Hramov, A.A. Koronovskii, I.S. Midzyanovskaya, E. Sitnikova, C.M. Rijn, On-off intermittency in time series of spontaneous paroxysmal activity in rats with genetic absence epilepsy. *Chaos Int. J. Nonlinear Sci.* **16**, 043111 (2006)
121. K.P. Indiradevi, E. Elias, P.S. Sathidevi, S.D. Nayak, K. Radhakrishnan, A multi-level wavelet approach for automatic detection of epileptic spikes in the electroencephalogram. *Comput. Biol. Med.* **38**, 805 (2008)
122. S.S. Talathi, D.U. Hwang, M.L. Spano, J. Simonotto, M.D. Furman, S.D. Myers, J.T. Winters, W.L. Ditto, P.R. Carney, Non-parametric early seizure detection in an animal model of temporal lobe epilepsy. *J. Neural Eng.* **5**, 85 (2008)
123. H. Ocak, Automatic detection of epileptic seizures in EEG using discrete wavelet transform and approximate entropy. *Expert Syst. Appl.* **36**, 2027 (2009)
124. A.A. Koronovskii, E.L. Van Lujtelaar, A.A. Ovchinnikov, E. Sitnikova, A.E. Hramov, Diagnostics and analysis of oscillatory neuronal network activity of brain with continuous wavelet analysis. *Appl. Nonlinear Dyn.* **19**(1), 86 (2011)
125. N. Acir, C. Güzeliş, Automatic recognition of sleep spindles in EEG via radial basis support vector machine based on a modified feature selection algorithm. *Neural Comput. Appl.* **14**, 56 (2005)
126. J. Shuai, K. Wong, Noise and synchronization in chaotic neural networks. *Phys. Rev. E* **57**(6), 7002 (1993)
127. C.M. Kim, Mechanism of chaos synchronization and on-off intermittency. *Phys. Rev. E* **56**(3, part B), 3697 (1997)
128. F. Xie, G. Hu, Z. Qu, On-off intermittency in a coupled-map lattice system. *Phys. Rev. E* **52**(2), R1265 (1995)
129. F. Xie, G. Hu, Transient on-off intermittency in a coupled map lattice system. *Phys. Rev. E* **53**(1), 1232 (1996)
130. H.L. Yang, E.J. Ding, On-off intermittency in random map lattices. *Phys. Rev. E* **50**(5), R3295 (1994)
131. A.E. Hramov, A.A. Koronovskii, Intermittent generalized synchronization in unidirectionally coupled chaotic oscillators. *Europhys. Lett.* **70**(2), 169 (2005)

132. D. Cvetkovic, E.D. Übeyli, I. Cosic, Wavelet transform feature extraction from human PPG, ECG, and EEG signal responses to ELF PEMF exposures: a pilot study. *Digit. Signal Process.* **18**, 861 (2008)
133. K. Polat, S. Güneş, A novel data reduction method: distance based data reduction and its application to classification of epileptiform EEG signals. *Appl. Math. Comput.* **200**, 10 (2008)
134. A.B. Geva, D.H. Kerem, Forecasting generalized epileptic seizures from the EEG signal by wavelet analysis and dynamic unsupervised fuzzy clustering. *IEEE Trans. Biomed. Eng.* **45**(10), 1205 (1998)
135. H. Ocak, Optimal classification of epileptic seizures in EEG using wavelet analysis and genetic algorithm. *Signal Process.* **88**, 1858 (2008)
136. N.T. Abdullaev, O. Dyshin, H.Z. Samedova, Automatic classification of electroencephalograms based on their wavelet packet processing. *Biomed. Electron.* **6**, 34 (2009)
137. W.Y. Hsu, Y.N. Sun, EEG-based motor imagery analysis using weighted wavelet transform features. *J. Neurosci. Methods* **176**, 310 (2009)
138. M.R. Kousarrizi, A.A. Ghanbari, M. Teshnehlav, M. Aliyari, A. Gharaviri, Feature extraction and classification of EEG signals using wavelet transform, SVM and artificial neural networks for brain-computer interfaces, in *International Joint Conference on Bioinformatics, Systems Biology and Intelligent Computing, 2009 (IJCBS '09)*, Shanghai, 3–5 Aug 2009, pp. 352–355
139. L. Ke, R. Li, Classification of EEG signals by multi-scale filtering and PCA, in *IEEE International Conference on Intelligent Computing and Intelligent Systems (ICIS 2009)*, Phoenix, 20–22 Nov 2009, pp. 362–366
140. L. Li, D. Xiong, X. Wu, Classification of imaginary movements in ECoG, in *5th International Conference on Bioinformatics and Biomedical Engineering (iCBBE)*, Wuhan, 10–12 May 2011, pp. 1–3
141. K. Kiymik, I. Güler, A. Dizibüyüka, M. Akin, Comparison of STFT and wavelet transform methods idetermining epileptic seizure activit in EEG signals for real-time application. *Comput. Biol. Med.* **35**, 603 (2005)
142. C. Brunner, R. Scherer, B. Graimann, G. Supp, G. Pfurtscheller, Online control of a brain-computer interface using phase synchronization. *IEEE Trans. Biomed. Eng.* **53**, 2501 (2006)
143. Z. Wu, D. Yao, Frequency detection with stability coefficient for steady-state visual evoked potential (SSVEP)-based BCIs. *J. Neural Eng.* **5**, 36 (2008)
144. A.A. Ovchinnikov, A. Luttjohann, A.E. Hramov, G. van Luijtelaar, An algorithm for real-time detection of spike-wave discharges in rodents. *J. Neurosci. Methods* **194**, 172 (2010)
145. A.A. Ovchinnikov, A.E. Hramov, A. Luttjehann, A.A. Koronovskii, G. van Luijtelaar, Method for diagnostics of characteristic patterns of observable time series and its real-time experimental implementation for neurophysiological signals. *Tech. Phys.* **56**(1), 1 (2011)
146. W. Ting, Y. Guo-zheng, S. Hong, EEG feature extraction based on wavelet packet decomposition for brain computer. *Measurement* **41**, 618 (2008)
147. J.P. Lachaux et al., Studying single trials of the phase synchronization activity in the brain. *Int. J. Bifurc. Chaos* **10**(10), 2429 (2000)
148. M.L. Quyen, J. Foucher, J.P. Lachaux, E. Rodriguez, A. Lutz, J. Martinerie, F.J. Varela, Comparison of Hilbert transform and wavelet methods for the analysis of neuronal synchrony. *J. Neurosci. Methods* **111**, 83 (2001)
149. P. Gong, A.R. Nikolaev, C. van Leeuwen, Intermittent dynamics underlying the intrinsic fluctuations of the collective synchronization patterns in electrocortical activity. *Phys. Rev. E* **76**(1), 011904 (2007)
150. A.R. Nikolaev, G. Pulin, C. van Leeuwen, Evoked phase synchronization between adjacent high-density electrodes in human scalp EEG: duration and time course related to behavior. *Clin. Neurophysiol.* **116**, 2403 (2005)
151. D. Alexander, C. Trengove, J. Wright, P. Boord, E. Gordon, Measurement of phase gradients in the EEG. *J. Neurosci. Methods* **156**, 111 (2006)
152. P. Bob, M. Palus, M. Susta, K. Glaslova, EEG phase synchronization in patients with paranoid schizophrenia. *Neurosci. Lett.* **447**, 73 (2008)

153. M. Teplan, K. Susmakova, M. Palus, M. Vejmlka, Phase synchronization in human EEG during audio-visual stimulation. *Electromagn. Biol. Med.* **28**(1), 80 (2009)
154. A.S. Romanov, E.V. Sharov, O. Kuznetsova, L.B. Oknina, P.E. Volinsky, G.A. Schekutev, Possibilities of wavelet synchronization method in assessing long-latency components of the acoustic evoked potential of a healthy person. *J. High. Nerv. Act.* **61**(1), 112 (2011)
155. A.E. Hramov, A.A. Koronovskii, An approach to chaotic synchronization. *Chaos Int. J. Nonlinear Sci.* **14**(3), 603 (2004)
156. A.E. Hramov, A.A. Koronovskii, Time-scale synchronization of chaotic oscillators. *Physica D* **206**(3–4), 252 (2005)
157. R.A. Filatov, A.E. Hramov, A.A. Koronovskii, Chaotic synchronization in coupled spatially extended beam-plasma systems. *Phys. Lett. A* **358**, 301 (2006)
158. A.E. Hramov, A.A. Koronovskii, P.V. Popov, I.S. Rempen, Chaotic synchronization of coupled electron-wave systems with backward waves. *Chaos Int. J. Nonlinear Sci.* **15**(1), 013705 (2005)
159. A.E. Hramov, A.A. Koronovskii, V.I. Ponomarenko, M.D. Prokhorov, Detecting synchronization of self-sustained oscillators by external driving with varying frequency. *Phys. Rev. E* **73**(2), 026208 (2006)
160. A.E. Hramov, A.A. Koronovskii, V.I. Ponomarenko, M.D. Prokhorov, Detection of synchronization from univariate data using wavelet transform. *Phys. Rev. E* **75**(5), 056207 (2007)
161. A.E. Hramov, A.A. Koronovskii, Y. Levin, Synchronization of chaotic oscillator time scales. *J. Exp. Theor. Phys.* **127**(4), 886 (2005)
162. A.E. Hramov, A.A. Koronovskii, V.I. Ponomarenko, M.D. Prokhorov, in *Proceedings of International Symposium "Topical Problems of Nonlinear Wave Physics". Part 1. Nonlinear Dynamics: Theory and Applications*, St. Petersburg/N. Novgorod, 2–9 Aug 2005, ed. by V.I. Nekorkin (Nizhnij Novgorod, 2005), p. 33
163. M. Alegre, A. Labarga, I. Gurtubay, J. Iriarte, A. Malanda, J. Artieda, Movement-related changes in cortical oscillatory activity in ballistic, sustained and negative movements. *Exp. Brain Res.* **148**, 17 (2003)
164. H. Goelz, R. Jones, P. Bones, Wavelet analysis of transient biomedical signals and its application to detection of epileptiform activity in the EEG. *Clin. Neurophysiol.* **31**, 181 (2000)
165. A. Murata, An attempt to evaluate mental workload using wavelet transform of EEG. *Hum. Factors* **47**, 498 (2005)
166. X. Wan, K. Iwata, J. Riera, T. Ozaki, M. Kitamura, R. Kawashima, Artifact reduction for EEG/fMRI recordings: nonlinear reduction of ballistocardiogram artifacts. *Clin. Neurophysiol.* **117**, 1 (2006)
167. N.P. Castellanos, V.A. Makarov, Recovering EEG brain signals: artifact suppression with wavelet enhanced independent component analysis. *J. Neurosci. Methods* **158**, 300 (2006)
168. V. Krishnaveni, S. Jayaraman, L. Anitha, K. Ramadoss, Removal of ocular artifacts from EEG using adaptive thresholding of wavelet coefficients. *J. Neural Eng.* **3**, 338 (2006)
169. J.A. Jiang, C.F. Chao, M.G. Chiu, R.G. Lee, C.L. Tseng, R. Lin, An automatic analysis method for detecting and eliminating ECG artifacts in EEG. *Comput. Biol. Med.* **37**, 1660 (2007)
170. H. Leung, K. Schindler, A.Y. Chan, A.Y. Lau, K. Lau, E.H. Ng, K.S. Wong, Wavelet-denoising of electroencephalogram and the absolute slope method: a new tool to improve electroencephalographic localization and lateralization. *Clin. Neurophysiol.* **120**, 1273 (2009)
171. A.R. Nikolaev, G.A. Ivanitskii, A.M. Ivanitskii, A new method of studying cortical interactions in short time intervals: cortical connections during search for word associations. *J. High. Nerv. Act.* **50**(1), 44 (2000)
172. L. Bonfiglio, S. Sello, P. Andre, M.C. Carboncini, P. Arrighi, B. Rossi, Blink-related delta oscillations in the resting-state EEG: a wavelet analysis. *Neurosci. Lett.* **449**, 57 (2009)
173. X. Yu, J. Zhang, D. Xie, J. Wang, C. Zhang, Relationship between scalp potential and autonomic nervous activity during a mental arithmetic task. *Auton. Neurosci. Basic Clin.* **146**, 81 (2009)

174. I.A. Yakovenko, E.A. Cheremushkin, M.K. Kozlov, Analysis of induced electrical activity of the cerebral cortex using wavelet transform at different stages of the installation on the emotional expression. *J. High. Nerv. Act.* **60**, 409 (2010)
175. D. Regan, *Human Brain Electrophysiology: Evoked Potentials and Evoked Magnetic Fields in Science and Medicine* (Elsevier, New York, 1989)

Chapter 6

Time–Frequency Analysis of EEG: From Theory to Practice

Abstract This chapter describes some specific results of time–frequency analysis of EEG using the continuous wavelet transform. In this chapter we pay special attention to technical and computational details of time–frequency analysis of neurophysiological signals, i.e., produced by electrical brain activity in animals and humans. This chapter also presents continuous wavelet analysis of hyper-synchronous rhythmic activity in multichannel EEG, characterizing the onset of absence epilepsy in patients.

6.1 Introduction

In this chapter we consider the continuous wavelet transform as an appropriate method for time–frequency analysis of the EEG signal. The fact that there is no requirement of stationarity is an advantage in using the CWT to characterize short non-stationary events in the EEG of animals and humans, such as episodes of spindle and spike–wave activity, in which the signal-to-noise ratio is low [1–3, 6]. The present chapter also addresses the problem of individual variability and irregularity of the EEG pattern of SWD and sleep spindle events that would be solved by selecting optimal template wavelet functions. From a technical point of view, these results provide a clue as to the selective identification, classification, and statistical description of several types of phasic events in the EEG. More details for automatic EEG processing can be found in Chap. 7.

Let us just describe how Chap. 6 is organised. We begin with the outcomes presented in Sect. 5.3.3 concerning the time–frequency characteristics of the spike–wave discharges in EEG as recorded in the WAG/Rij rat model of absence epilepsy. First, we discuss the selective analysis of low-frequency (delta and theta) precursors of epileptic SWD events (Sect. 6.2). Second, we focus on non-epileptic oscillatory EEG patterns in epileptic rats and demonstrate some peculiarities of the time–frequency structure of sleep spindles (Sect. 6.3). Third, we provide an algorithm for classifying sleep spindles based on a specially constructed adaptive wavelet basis

(mother wavelets), the so-called spindle wavelets (Sect. 6.5). Practical issues about application of the continuous wavelet transform to time–frequency analysis of EEG will be discussed in Sect. 6.4. The last part of the chapter presents data obtained with the continuous wavelet transform of human multichannel EEG, specifically regarding the dynamics of hypersynchronous rhythmic activity in patients with absence epilepsy (Sect. 6.6).

6.2 Oscillatory Activity Prior to Epileptic Seizures

The classical description of the SWD in the multichannel scalp EEG is that the SWD appear abruptly from a normal background activity [4]. However, a gradual increase in power in the low frequencies at frontal locations toward the beginning of the SWD has been found in human patients [5]. Continuous wavelet analysis of the time–frequency structure of the SWD in long-term 5–7 h EEG recordings of WAG/Rij rats performed with the complex Morlet wavelet (2.36) showed that the onset of SWD was preceded by a set of short-lasting rhythmic components with maximum spectral power in the delta (3–5 Hz) and theta/alpha (7–11 Hz) frequency bands [6]. Let us consider the wavelet-based analysis of seizure-precursor EEG activity in more detail.

6.2.1 Description of Experiment

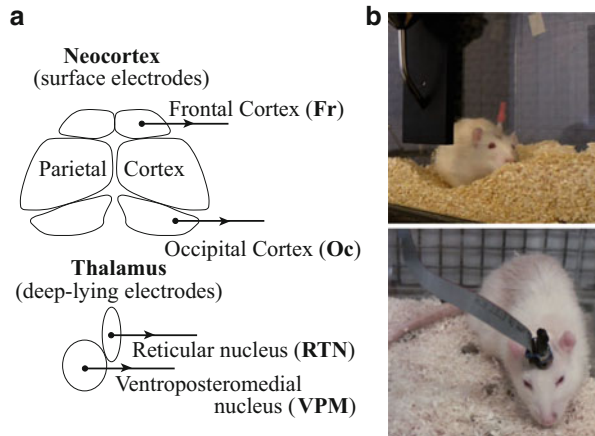
6.2.1.1 Animals

Six male 1-year-old WAG/Rij rats (body weight 320–360 g) were used. The animals were born and raised in the laboratory at the Center for Cognition, Donders Institute of Brain, Cognition and Behavior of Radboud University Nijmegen (Netherlands). They were kept in pairs in standard cages with food and water available ad libitum under a 12–12 h light-dark cycle, with white lights on at 18:00, at a constant ambient temperature of 21 °C. The experiments were conducted in accordance with the legislations and regulations for animal care and were approved by the Ethical Committee on Animal Experimentation of the Radboud University Nijmegen.

6.2.1.2 EEG Recording Design and Equipment

The animals were equipped with six stainless steel electrodes (two pairs of MS 333/2A, Plastic One Inc., Roanoke, VI, USA) for monopolar EEG recordings. The electrodes were identical, insulated with a non-insulated tip (diameter 0.2 mm). Two EEG electrodes were placed epidurally over the cortex in the frontal and occipital cortical areas. Two depth electrodes were implanted into the ventroposteromedial

Fig. 6.1 EEG recording in freely moving WAG/Rij rat. Electrode localization in the brain (a) and illustration of the in vivo experiment (b)



and reticular nuclei of the thalamus [7]. Ground and reference electrodes were placed symmetrically over both sides of the cerebellum. Electrodes were permanently attached to the rat's skull with dental cement. Figure 6.1 illustrates the EEG recording procedure.

The EEG was recorded in freely moving rats in a noise-isolated Faraday cage for 5–7 h in the dark period of the light/dark cycle (see Fig. 6.1b). One day before the EEG recording session, the rats were given 2 h to get used to the recording procedure. They were then moved to custom-made Plexiglas recording cages (25–30 cm wide, 35 cm high). EEG signals were fed into a multichannel differential amplifier via a swivel contact, band-pass filtered between 1 and 500 Hz, digitized with 1,024 samples/s/channel (Data Acquisition Hardware and Software, DATAQ Instruments Inc., Akron, OH) and stored on a hard disk. Recorded EEG signals were filtered at the preset processing stage in the 0.5–49 and 51–100 Hz frequency bands to get rid of high-frequency noise and interfering signals associated with feeding (50 Hz).

6.2.2 Time–Frequency Wavelet Analysis of Cortical and Thalamic SWDs

SWDs were automatically identified in the frontal EEG (the area of SWD amplitude maximum) using the wavelet-based method described in Sect. 7.2. The results of SWD detection in the frontal EEG (where the amplitude of the spike–wave discharges was the highest) were approximated to the thalamic channels (VPM and RTN). Cortical and thalamic records were examined during SWD and before the onset of SWD (pre-SWD epochs, about 3 s prior to SWD onset as defined in the frontal EEG). Non-epileptic control EEG epochs of background activity were also analyzed (from 6 to 12 epochs per animal). Control EEG epochs lasted 10 s.

They did not contain SWDs and included periods of active wakefulness (low-amplitude high-frequency EEG, mixture of theta and beta rhythmic activity), passive wakefulness, light slow-wave sleep (immobile behavior, combined with the presence of intermediate amplitude, slow <6 Hz activity and sleep spindles), and deep slow-wave sleep (immobile behavior, large-amplitude delta <4 Hz waves).

Time–frequency analysis of automatically identified SWDs was carried out using a continuous wavelet decomposition with a complex Morlet mother wavelet. We examined the matrix of wavelet coefficients at each time and frequency in EEG epochs prior to and during SWD. Precursor activity was defined by a gradual increase in the wavelet energy compared to baseline for a minimum of 100 ms observed in the 3 s period preceding the onset of SWD. Rhythmic precursor activity was characterized by high wavelet energy (more than two times higher than the background), which exceeds the threshold for at least 0.3 s. The wavelet energy background level is determined in the period preceding precursor activity. Characteristics of the control EEG (for example, wavelet power) during different kinds of behavioral activity were studied individually in each experimental rat. It was found that delta and theta components were most dominant in SWD precursor activity.

The following time–frequency parameters of SWD precursor activity were extracted independently in the cortex and thalamus by means of wavelet analysis:

1. Mean frequency f_δ or f_θ (Hz) of SWD precursors in their characteristic frequency band (i.e., delta or theta/alpha). The frequency of each precursor type was determined by measuring the peak frequency in the wavelet spectrum (the peak frequency corresponds to the darkest spot in the wavelet spectrum in Figs. 6.2–6.4).
2. Mean duration of SWD precursors (MD, s). In order to localize the precursor in time, we defined the onset and offset of each rhythmic precursor. The onset of the SWD precursor was determined when the wavelet energy in specific frequencies exceeded the mean baseline level for at least 100 ms. The offset of the precursor was determined as the moment when the wavelet energy in the selected frequency band returned to the mean baseline level for this frequency.
3. Difference $\Delta = f_b - f_m$ (Hz) between the SWD frequencies f_b and f_m at the beginning and at the middle, respectively.
4. Time delay T_d (s) between SWD precursors and the onset (the first spike) of the subsequent SWD.
5. Percentage n_k (%) of the two types of SWD precursor, viz., 3–5 Hz (delta) and 7–11 Hz (theta), among the total number of SWDs, viz.,

$$n_k = \frac{N_k}{N_{\text{SWD}}} \times 100\% , \quad (6.1)$$

where N_k is the number of each type of SWD precursor as assessed in the cortex and thalamus and N_{SWD} is the total number of spike–wave discharges.

6. The average durations d and τ of delta and theta/alpha rhythmic precursors (s). The starting point of the precursors was assessed as the time when the wavelet energy in the investigated frequency range (3–5 or 7–11 Hz) exceeded the average energy of the EEG in the corresponding frequency range for at least 100 ms. The end of the precursors was determined as the time when the wavelet energy returned to the baseline level.
7. The number G of cases of coincident presence of delta and theta/alpha components in the pre-SWD.
8. The relative number of cases with simultaneously present delta and theta/alpha from the total number of delta and theta/alpha events, viz.,

$$K = \frac{G}{N_{\theta} + N_{\delta} - G} \times 100\% , \quad (6.2)$$

where N_{θ} and N_{δ} are the numbers of observed delta and alpha/theta events in pre-SWD epoch.

In the control periods, the following parameters were determined automatically using wavelet spectra:

1. The number N_{δ} of delta components in control periods.
2. The mean number N_{δ}/T of delta components per second, where T is the time duration of analyzed EEG in seconds.
3. The mean frequency f_{δ} (Hz) of delta components was measured by averaging the instantaneous frequencies at every sampling point during the full duration of the corresponding delta event.
4. The number N_{θ} of theta/alpha components in control periods.
5. The mean number N_{θ}/T of theta/alpha component events per second, where T is the duration of analyzed periods in seconds.
6. The mean frequency f_{θ} (Hz) of theta/alpha components was measured in a similar way to f_{δ} .

Wavelet analysis was performed in all SWDs detected during 5–7 h of recording. The number of SWDs in rat #23 was 107 (6 h), #24—278 (6 h), #25—59 (7 h), #26—120 (6 h), #28—54 (5 h), #29—124 (6 h). Control periods were randomly chosen artifact-free 10 s periods during active wakefulness, passive wakefulness, light slow-wave sleep, and deep slow-wave sleep (6–12 control periods per rat).

Typically, as already discussed in Sect. 5.3.3, the wavelet spectrum of SWDs in the cortex of WAG/Rij rats showed a local maximum at frequency ~ 10 –11 Hz at the beginning of the SWD and subsequently slowed down to 7–8 Hz in the middle part of a seizure and even lower, to 5–6 Hz, at the end. Descriptive statistics of the frequency modulation of SWDs as recorded in the cortex and thalamus can be found in Table 6.1.

Table 6.1 Averaged frequencies of SWD (mean \pm SD, number of rats $n = 6$) at the beginning and in the middle of the SWD as measured in the cortex and thalamus

	f_b (Hz)	f_m (Hz)	$f_b - f_m$ (Hz)
Cortex	10.1 ± 1.5	7.4 ± 0.8	2.8 ± 0.8
Thalamus	8.5 ± 2.5	6.4 ± 2.4	2.1 ± 0.6

The drop in frequency from the beginning to the middle part of the cortical SWD was statistically evaluated and significant,¹ as was the frequency drop in the thalamus. The frequency at the beginning of the SWD was higher in the cortex than in the thalamus.

6.2.3 *Delta and Theta Precursors of SWD as Measured in the Cortex and Thalamus*

Wavelet-based time–frequency analysis of EEG fragments preceding the spike–wave discharges showed that SWD precursors consisted of several frequency components in the range from 2 to 12 Hz. The two most powerful rhythmic components in frequency bands 3–5 and 7–11 Hz immediately preceded the onset of SWD, considering their predominance and close proximity in time to onset. Theta/alpha precursor activity was found in the cortex and thalamus at the same time, while the delta events appeared in the thalamus and cortex with a small, but significant delay. So the time delay between the delta precursor and the subsequent SWD was longer for the cortex (0.48 ± 0.04) than for the thalamus (0.38 ± 0.04), and this difference was highly significant.

We also calculated the correlations between time–frequency parameters of precursor activity and subsequent SWDs obtained by means of wavelet analysis, in order to study whether there were relations between time–frequency parameters of preictal and ictal EEG. Correlations between the frequency of cortical delta and theta/alpha precursor activity and subsequent SWDs were generally positive and also quite high (delta 0.63, theta/alpha 0.49), while for the thalamus, the coefficients for delta and theta were 0.78 and 0.41, respectively.

Some illustrative examples of delta and theta/alpha precursor activity in the cortex and thalamus can be found in Figs. 6.2 and 6.3. Descriptive statistics of the

¹To estimate the relation between the characteristics of SWD and precursor activity, we used the following statistics. First, Pearson’s correlation coefficients were used to analyze the relation between the characteristics (f_δ , f_θ and corresponding MD) of SWD precursor activity and the frequency f_b . The means per subject were used. Second, Student’s paired t -tests were used to test differences between the characteristics of SWD and precursor activity in the cortex and thalamus. Third, differences between states were analyzed with an ANOVA followed by post-hoc tests, according to Duncan [8].

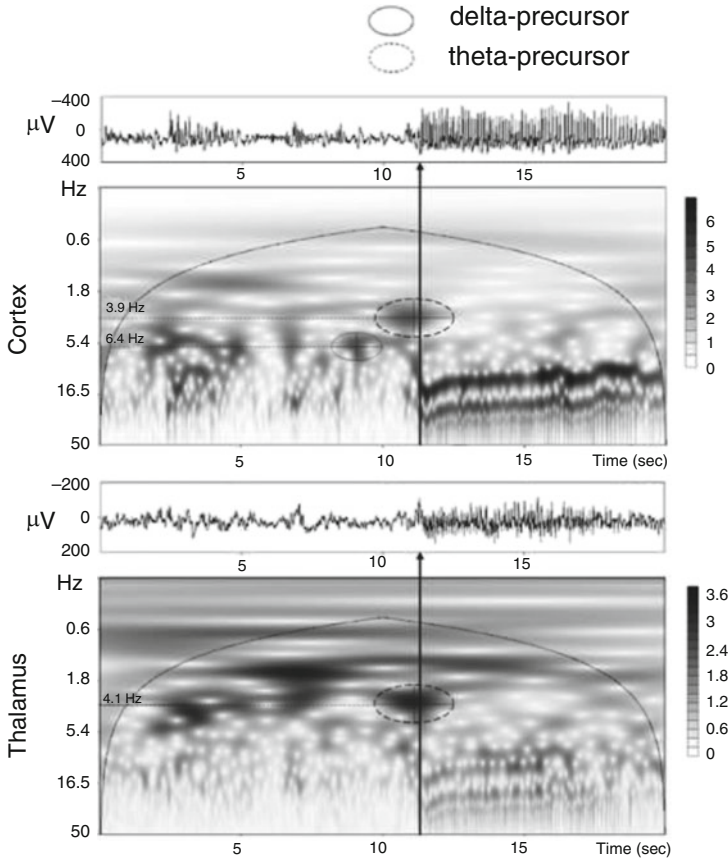


Fig. 6.2 Examples of wavelet surfaces of SWDs simultaneously recorded at the frontal cortex (*upper graph*) and the thalamus, RTN (*bottom graph*). Wavelet spectra were calculated using a complex Morlet mother wavelet with central frequency $\omega_0 = 2\pi$. The onset of the SWD was preceded by 3.9 and 6.4 Hz in the cortex and 4.1 Hz in the thalamus. The *dome-shaped curve* on the wavelet surfaces marks the area of boundary effects (see Sect. 2.3.3). The *ordinate* (frequency) axis has a logarithmic scale. *Arrows* indicate the beginning of the SWD

frequency and duration of delta and theta precursors in the cortex and thalamus are given in Table 6.2.

The respective frequencies f_δ and f_θ of delta and theta/alpha precursor activity in the thalamus were similar to those in the cortex. However, the duration MD of theta precursor activity was slightly longer in the thalamus than in the cortex, and the cortical delta precursor activity lasted longer than the cortical theta precursor activity.

Delta precursor activity in the frontal cortex was found in 90% of all SWDs, and theta/alpha precursor activity was found in 92%. High percentages were also found in the thalamus (VPM), viz., 82 and 83% for delta and theta/alpha precursors,

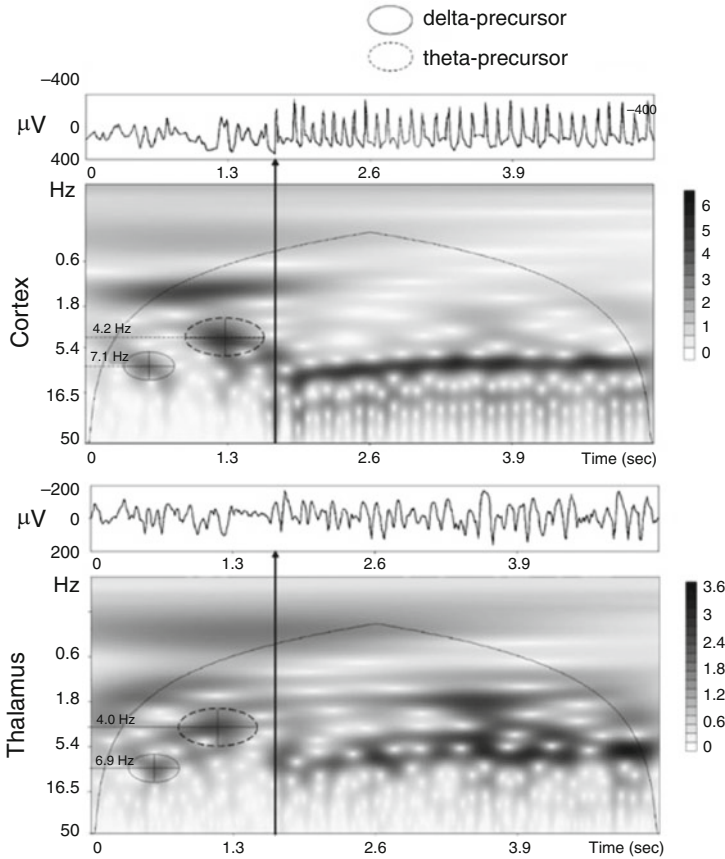


Fig. 6.3 Examples of wavelet surfaces of SWDs simultaneously recorded at the frontal cortex (*upper graph*) and the thalamus, RTN (*bottom graph*). Wavelet spectra were calculated using a Morlet mother wavelet with central frequency $\omega_0 = 2\pi$. The onset of the SWD was preceded by 7.1 and 4.2 Hz in the cortex and 4.0 and 6.0 Hz in the thalamus. The *dome-shaped curve* on the wavelet surfaces marks the area of boundary effects (see Sect. 2.3.3). The *ordinate* (frequency) axis has a logarithmic scale. *Arrows* indicate the beginning of the SWD

respectively. There were no differences in the percentages of SWDs that were preceded by delta and theta/alpha precursors in the cortex and thalamus. The average duration of precursor activity was approximately equal to 0.5 s.

We also investigated whether delta precursor activity was simultaneously present in the cortex and thalamus. It was found that, in 79 % of cases, SWDs were preceded by simultaneous 3–5 Hz precursors in the cortex and thalamus, in 11 % of cases, only in the cortex but not in the thalamus, and in 5 % of cases, only in the thalamus but not in the cortex. Finally, in 5 % of cases, delta precursors were completely absent, in both the cortical and the thalamic EEG. An example of this exceptional situation is shown in Fig. 6.4.

Table 6.2 Time–frequency characteristics of two types of SWD-precursor activity (delta and theta/alpha activity) in WAG/Rij rats (mean \pm SD)

Rat #	Delta (3–5 Hz) SWD precursors			Theta/alpha (7–11 Hz) SWD precursors		
	n_d (% see (6.1))	f_δ (Hz)	d (s)	n_θ (% see (6.1))	f_θ (Hz)	τ (s)
Frontal cortex						
23	89	4.7 \pm 0.6	0.43 \pm 0.04	93	10.2 \pm 0.8	0.39 \pm 0.06
24	88	3.2 \pm 0.4	0.52 \pm 0.02	89	7.6 \pm 2.1	0.48 \pm 0.03
25	93	4.2 \pm 0.7	0.48 \pm 0.02	87	7.9 \pm 0.6	0.45 \pm 0.05
26	87	3.7 \pm 0.8	0.52 \pm 0.05	92	8.2 \pm 1.2	0.54 \pm 0.08
28	89	4.1 \pm 0.5	0.51 \pm 0.10	95	8.5 \pm 1.0	0.48 \pm 0.06
29	92	4.6 \pm 0.5	0.44 \pm 0.03	96	9.3 \pm 1.1	0.41 \pm 0.02
Mean \pm SD	89.7 \pm 2.3	4.1 \pm 0.6	0.48 \pm 0.04	92 \pm 1.4	8.6 \pm 1.0	0.46 \pm 0.05
Thalamus, ventroposteromedial nucleus (VPM)						
23	87	5.3 \pm 1.0	0.41 \pm 0.06	89	9.9 \pm 0.7	0.42 \pm 0.05
24	86	3.0 \pm 0.4	0.54 \pm 0.04	84	7.7 \pm 1.8	0.54 \pm 0.03
25	89	3.9 \pm 0.6	0.50 \pm 0.05	79	8.1 \pm 0.7	0.51 \pm 0.06
26	81	5.1 \pm 1.0	0.62 \pm 0.08	83	8.1 \pm 1.0	0.58 \pm 0.09
28	85	4.4 \pm 0.7	0.48 \pm 0.09	88	8.2 \pm 1.0	0.49 \pm 0.06
29	62	4.3 \pm 0.6	0.45 \pm 0.06	72	9.3 \pm 0.9	0.43 \pm 0.04
Mean \pm SD	81.7 \pm 9.9	4.3 \pm 0.8	0.50 \pm 0.07	82.5 \pm 6.2	8.5 \pm 0.8	0.50 \pm 0.06

A similar study of the co-occurrence of delta and theta/alpha activity was carried out in the control periods in the cortex and in the thalamus in relation to different states (active and passive wakefulness, light and deep slow-wave sleep). The relative number K of co-occurrence of theta/alpha and delta activity was 8.1 % for the cortex and 6.0 % for the thalamus. This difference was not significant, although an effect of state vigilance was found: the co-occurrence was rarer during deep slow-wave sleep than during the other states, yet these three states were not different.

The numbers of delta and theta/alpha events as recorded in the cortex and thalamus in control periods (background EEG) are presented in Table 6.3. We found that the percentage of co-occurrence during the control periods (7.7 %) in the cortex was much lower than that during the precursor activity (79 %).

Thus, analysis of electrical brain activity preceding SWD onset using the continuous wavelet transform has several advantages over traditional FFT. First, the wavelet transform enables reliable detection of non-periodic and non-stationary phasic events (short-lasting rhythmic bursts in EEG). Second, the wavelet transform provides information in the time domain, i.e., information regarding the dynamic changes of spectral components. The above results lead to several interesting conclusions about the SWD precursor activity in the cortical and thalamic EEG, suggesting that seizure-precursor epochs differ from non-epileptic EEG and could be regarded as a transient between non-epileptic and SWD activity. The main finding is that both delta and theta/alpha precursor activities preceded the onset of SWD,

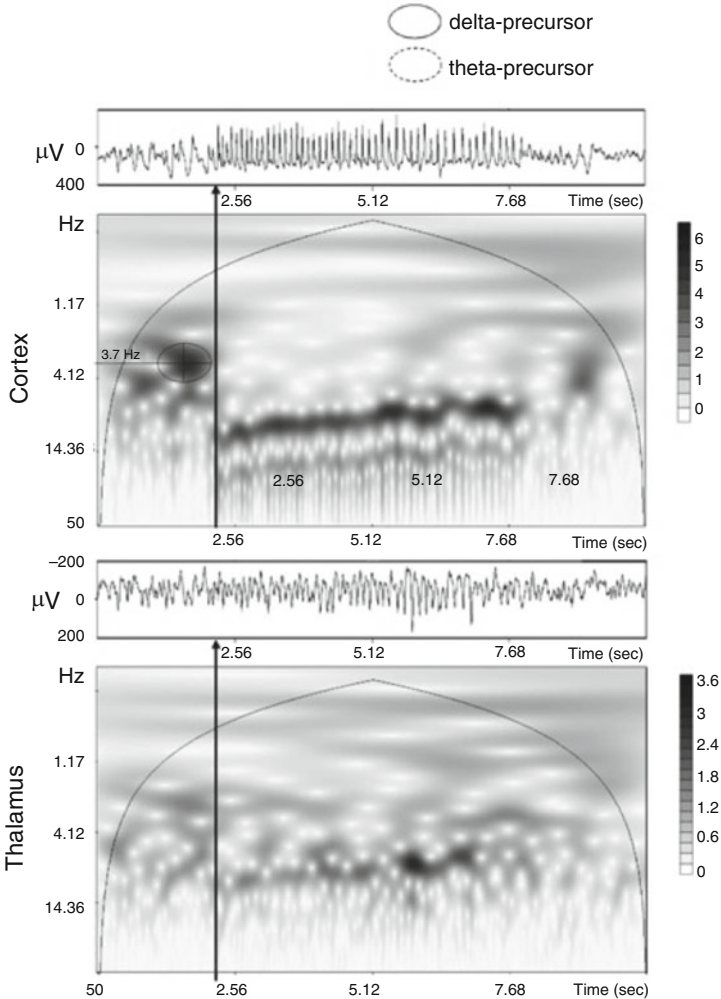


Fig. 6.4 Examples of wavelet surfaces of SWDs simultaneously recorded at the frontal cortex (*upper graph*) and the thalamus, RTN (*bottom graph*). Wavelet spectra were calculated using a Morlet mother wavelet with central frequency $\omega_0 = 2\pi$. Clear precursor activity (3.7 Hz) was present only in the cortex. The *dome-shaped curve* on the wavelet surfaces marks the area of the boundary effects (see Sect. 2.3.3). The *ordinate* (frequency) axis has a logarithmic scale. *Arrows* indicate the beginning of the SWD

and that this combination rarely occurred in control periods. Other findings were the strong association between cortical and thalamic theta/alpha precursor activity and the earlier presence of cortical delta precursors in comparison with thalamic precursors.

Table 6.3 Percentage of co-occurrence of delta and theta/alpha activity in cortex as measured during 2.5–3.0 s periods preceding SWD and during control periods (active and passive wakefulness, light and deep slow-wave sleep)

	Frontal cortex (%)	Thalamus, VPM (%)
Pre-SWD activity	88.9	79.0
Active wakefulness	8.6	6.3
Passive wakefulness	12.9	11.7
Light slow-wave sleep	9.3	4.8
Deep slow-wave sleep	2.2	0.8

The appearance of delta activity in the cortex immediately prior to spike–wave discharges might be regarded as a seizure-related trigger activity, instantiating hypersynchronous discharges in the thalamo-cortical network. More detailed discussion of the neural mechanisms of slow-wave seizure-precursor and the epileptogenic nature of delta and theta/alpha precursors can be found in [6, 9, 10]. It should be emphasized that detection of specific oscillatory patterns, precursors of epileptic events, was only possible with the aid of wavelet-based time–frequency analysis of EEG signals.

6.3 Time–Frequency Analysis of Sleep Spindles and Spindle-Like Oscillatory Patterns

6.3.1 Relationship Between Sleep Spindles, 5–9 Hz Oscillations, and SWDs

Here we consider the characteristics and peculiarities of the time–frequency structure of sleep spindles, i.e., the oscillatory patterns that are the electroencephalographic correlates of slow-wave sleep. Sleep spindles are among the most numerous spontaneous oscillations, abundantly present in electroencephalograms during non-REM sleep in humans and animals [11]. Sleep spindles can be recorded at the cortical surface, and also in the thalamus as brief episodes of 9–14 Hz oscillations. Basic electrophysiological studies have shown that sleep spindle oscillations are triggered by the reticular thalamic nuclei, spread throughout the thalamus, and propagate to the cortex [12–15].

Under certain conditions,² the thalamo-cortical neuronal circuit, which normally produces sleep spindles, could give rise to epileptic spike–wave discharges (SWDs)

²This can happen when the level of neuronal network synchronization becomes too high (hyper-synchronization), or when cortical neurons express too strong an excitation (hyper-excitation) in response to the thalamic input.

[15–21], which are electroencephalographic hallmarks of generalized idiopathic epilepsies, such as absence epilepsy and other syndromes (see Chap. 5).

It is well known that sleep spindles and spontaneous SWDs (but not pharmacologically induced seizures, see, e.g., [16, 18, 19]) are characterized by a similar temporal distribution across the sleep–waking cycle. In particular, both EEG events are predominant in the drowsy state and in the transition from wakefulness to sleep (see, e.g., [22–24]). Sleep spindles are abundant during slow-wave sleep, and the circadian dynamics of SWDs also correlates positively with the dynamics of slow-wave sleep, as was demonstrated in the WAG/Rij rat model of absence epilepsy [22]. In human patients, absence epilepsy is sometimes dismissed as simple “daydreaming”. Absence epilepsy might be considered as a sleep-related disorder, inasmuch as SWDs appear more often when the level of vigilance is low, e.g., passive wakefulness, drowsiness, and light slow-wave sleep in animal models [22, 25, 26], as well as in epileptic patients [27, 28]. Altogether this implies that the occurrence of sleep spindles and SWDs could be controlled by a common circadian timing mechanism that regulates the sleep–wake cycle.

The relationship between SWDs, sleep spindles, and sleep mechanisms is very complicated and not yet well understood. Absence seizures may be initiated by wake-related processes (see [29, 30]). In particular, in Genetic Rats with Absence Epilepsy (GAERS), “SWDs develop from wake-related 5–9 Hz oscillations, which are distinct from spindle oscillations (7–15 Hz)” [31, p. 209]. Five to nine hertz oscillations originate from the cortex (“launched by corticothalamic neurons” [31]), in contrast to sleep spindles, whose pacemaker is well known to be located in the thalamus [18]. Spontaneous medium-voltage 5–9 Hz oscillations are usually present in EEG during waking immobility, but they do not always lead to spike-and-wave discharges [32]. In addition to that, 5–9 Hz oscillations can be recorded in non-epileptic rats and never give rise to SWDs [32].

This section describes the time–frequency properties of two kinds of thalamocortical oscillatory pattern: sleep spindles and 5–9 Hz oscillations [33, 34].

6.3.2 *Experimental Procedure*

EEG analysis was performed by means of the continuous wavelet transform of 24 h EEG recorded in the cortex and thalamus in eight freely moving WAG/Rij rats. The method of EEG recording in rats was described in detail in Sect. 6.2. Criteria for assessing spindle-like patterns in EEG of rats derived from animal EEG research [14, 18, 35]. In WAG/Rij rats, sleep spindles represented a sequence of 8–14 Hz waves. They were characterized by a twofold increase in amplitude as compared to the EEG background and had waxing–waning morphology and a minimal duration of 0.3–0.5 s. For the study, we selected typical fragments of EEG during sleep with well-pronounced sleep spindles.

A typical multichannel recording of a “sleep” EEG is shown in Fig. 6.5. The oscillatory patterns under study (sleep spindles) are marked by dashed frames in the EEG time series. One can see that sleep spindles are most clearly distinguished in

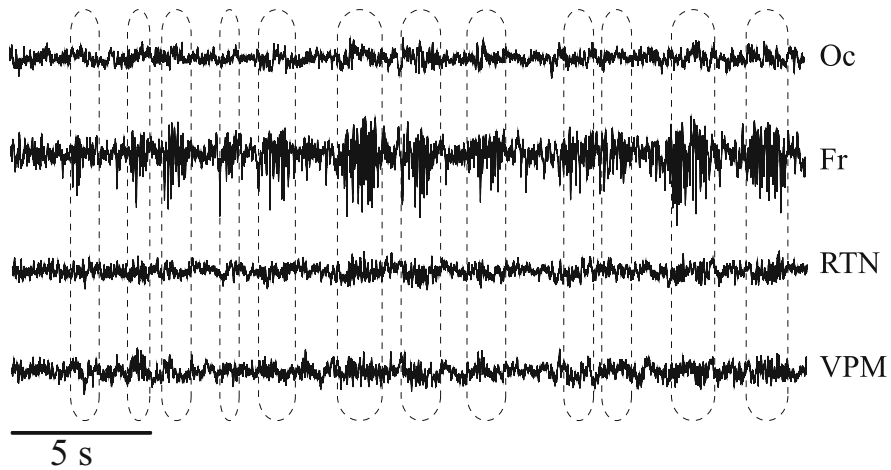


Fig. 6.5 Example of a multichannel EEG recorded during sleep in a symptomatic WAG/Rij rat. The *dashed frames* are selected sleep spindles. Here Fr is the signal recorded in the frontal cortex, Oc in the occipital cortex, RTN in the reticular nucleus, and VPM in the ventroposteromedial nucleus of the thalamus

the frontal cortex (channel Fr, Fig. 6.5), so in further research we used univariate scalar EEG signals recorded in this area.

6.3.3 Time–Frequency Analysis of Spindle-Like Oscillatory Patterns: Comparison of Different Mother Wavelets

In the preliminary stage, we tested several mother wavelet functions for the continuous wavelet transform of sleep EEG and identified the advantages and disadvantages of each of them. We focused our attention on the real MHAT (2.40), and complex Paul (2.37) and complex Morlet (5.1) mother wavelets. It is noteworthy that the wavelet transform with each wavelet basis resulted in wavelet surfaces with specific frequencies f_s that differ from Fourier frequencies f which are commonly used in neurophysiology (see Sect. 2.3.3). More specifically, for the MHAT wavelet, $f_s \approx 3.97f$, for the Paul wavelet with parameter $m = 4$, $f_s \approx 0.71f$, and for the Morlet wavelet with central frequency $\omega_0 = 2\pi$, $f_s \approx f$.

The results of wavelet analysis of the EEG recorded in the frontal cortex during sleep with numerous sleep spindles are shown in Fig. 6.6. This figure shows a typical EEG epoch (Fig. 6.6a) containing several sleep spindles and the corresponding amplitude wavelet spectra $|W(f_s, t)|$, obtained with the mother MHAT (Fig. 6.6b), Paul (Fig. 6.6c), and Morlet (Fig. 6.6d) wavelet functions. The dashed frames indicate the sleep spindles in the EEG and the corresponding regions of the wavelet spectra. Taking into account the fact that the main frequency of sleep spindle

oscillations varied between 10 and 15 Hz (alpha range), this frequency range was selected to analyze the amplitude distribution of the wavelet coefficients.

Analysis and comparison of different mother wavelet functions showed that the complex Morlet wavelet is the optimal mother wavelet function to identify the time–frequency structure of sleep spindles in EEG. The complex Morlet wavelet was therefore used in an automatic system for identification of the sleep spindles (see Sect. 7.5). In the wavelet spectrum obtained by means of the real MHAT wavelet (see Fig. 6.6b), the frequency resolution is low. Correspondingly, the frequency range of sleep spindles in the wavelet spectra is broad and it overlaps with the other types of oscillatory activity in the EEG. At the same time, the real MHAT-based wavelet transform, spikes, and other sharp components in the EEG corresponded to a robust increase in the amplitude $|W(f_s, t)|$ of the wavelet coefficients in the alpha frequency band of interest. The latter feature impedes analysis of oscillatory activity in this range. Furthermore, the shape of the MHAT-based wavelet spectrum does not allow one to track dynamic frequency and amplitude changes in the spindle oscillations. The advantage with the MHAT wavelet is the good temporal resolution, which determines a sharp increase in the amplitude of the wavelet spectrum coefficients when the corresponding oscillatory event appears in the EEG. However, it is a complex matter to classify the sharp jumps in the wavelet spectrum amplitude due to the low-frequency resolution.

A similar situation is observed in the case of the wavelet transform with the Paul mother function ($m = 4$), the results of which are shown in Fig. 6.6c. Likewise, its frequency resolution does not permit precise determination of the dynamical features of the EEG oscillations in the alpha band. In this frequency range in the wavelet surface, we observed many high-amplitude components that are not sleep spindles and complicate sleep spindle analysis.

At the same time, the Morlet mother wavelet with central frequency $\omega_0 = 2\pi$ combines a good resolution both in the frequency and time domains of the EEG signal (see Fig. 6.6d). In the time–frequency wavelet spectrum obtained in the alpha band, we can easily localize patterns corresponding to sleep spindle events, both in the time and the frequency domains. This gives an opportunity to track the variations of frequency and amplitude of the EEG oscillations which are typical for sleep spindles, including the parameter identification in automatic mode (see Sect. 7.5).

Wavelet analysis of a large number of sleep spindles has shown that, in the EEG recordings of WAG/Rij rats, two typical kinds of spindle-like patterns can be picked out using the criterion provided by the fundamental frequency of their wavelet spectrum. As already mentioned above, the fundamental frequency of typical sleep spindles lies in the 10–15 Hz range, and the shape of their oscillations exhibits extreme variability, so the fundamental frequency varies considerably in this frequency range from spindle to spindle. Simultaneously, in the wavelet spectra we found spindle-like oscillatory events, whose shape was close to the that of sleep spindles, but whose fundamental frequencies were in the low-frequency range (5–9 Hz).

Figures 6.7 and 6.8 show EEG epochs, typical wavelet spectra obtained with the Morlet mother wavelet function, and instantaneous energy distributions over

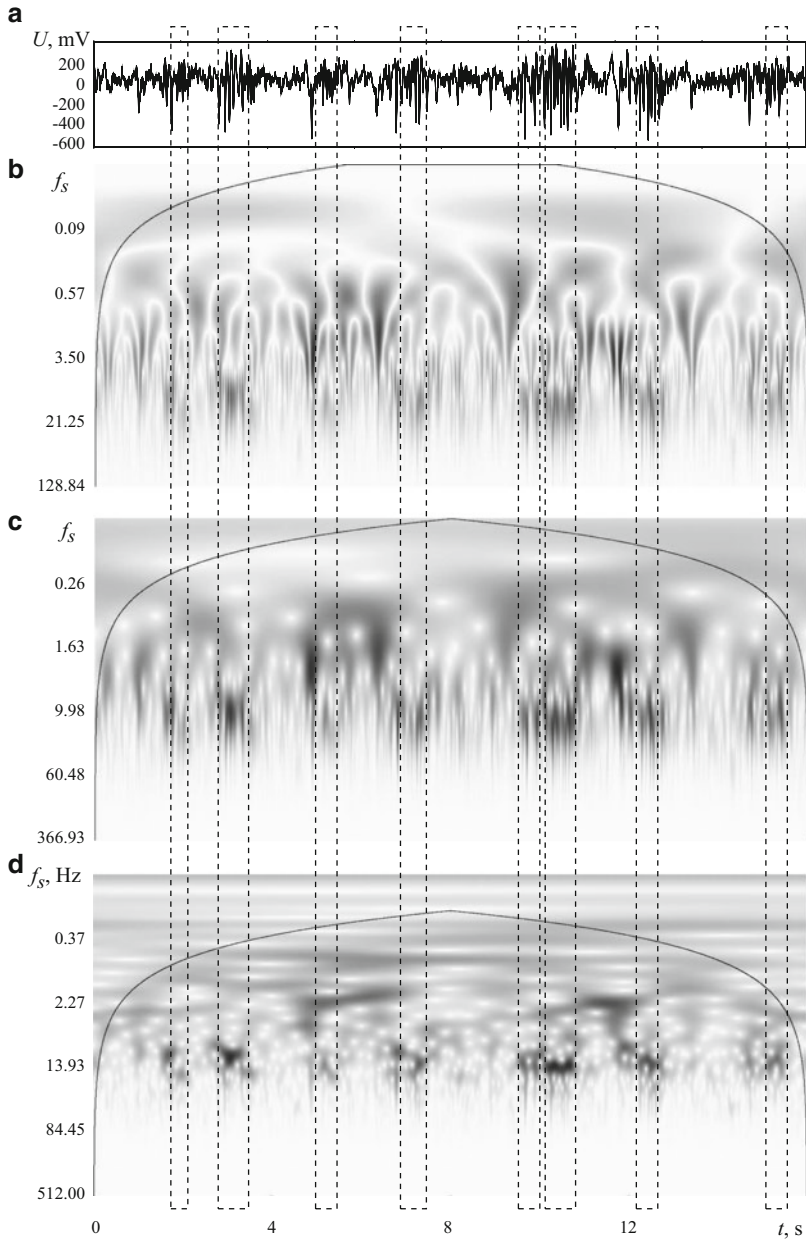


Fig. 6.6 Fragment of EEG during sleep with numerous sleep spindles (marked by *dotted frames*) as recorded at the frontal cortex in a WAG/Rij rat (**a**) and continuous wavelet spectra obtained with different mother wavelets: real MHAT (**b**), complex Paul (**c**), and complex Morlet (**d**). The *dome-shaped curve* on the wavelet surfaces marks the area of boundary effects (see Sect. 2.3.3)

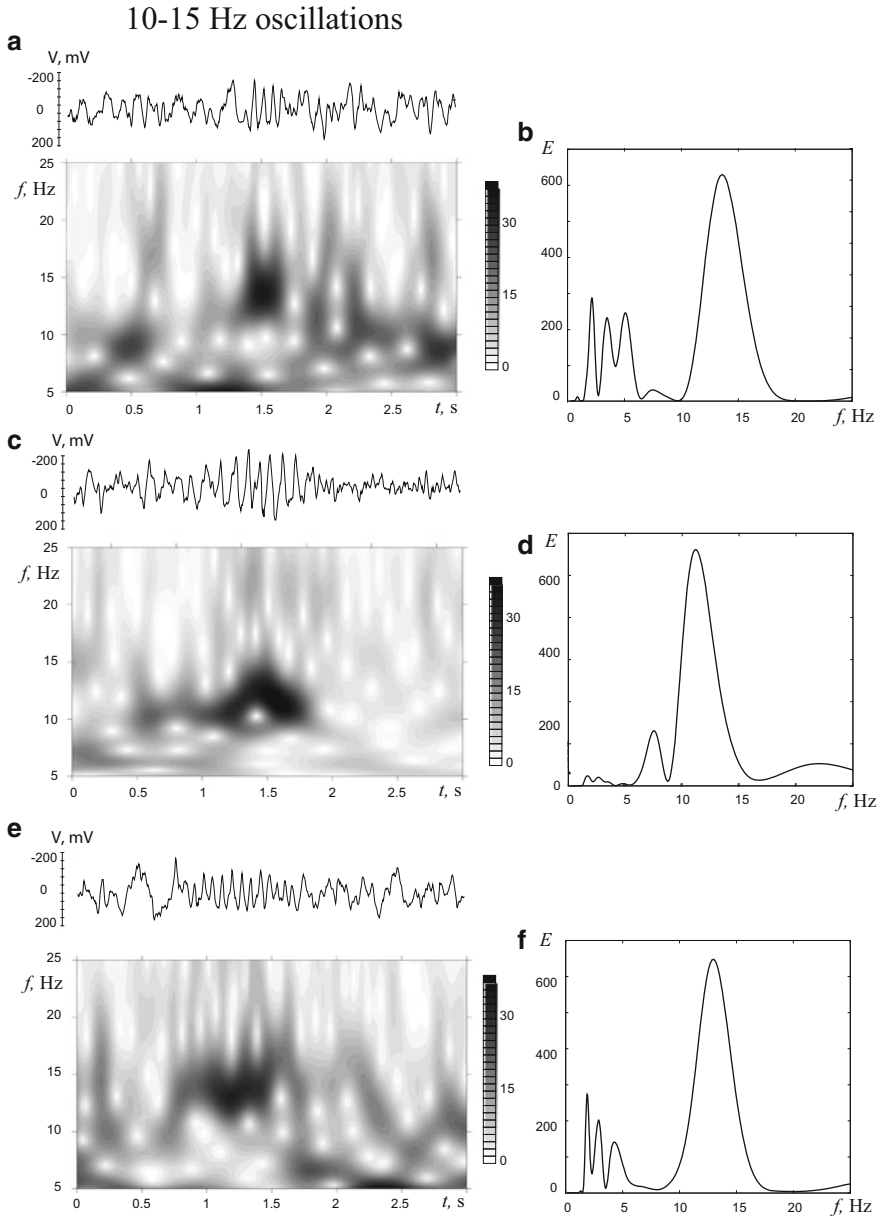


Fig. 6.7 EEG examples of sleep spindles (10–15 Hz) and corresponding Morlet-based wavelet spectra (a), (c), (e). *Right plates* show the distribution of instantaneous wavelet energy $E(f_s)$ (2.33) measured in sleep spindles (b), (d), (f)

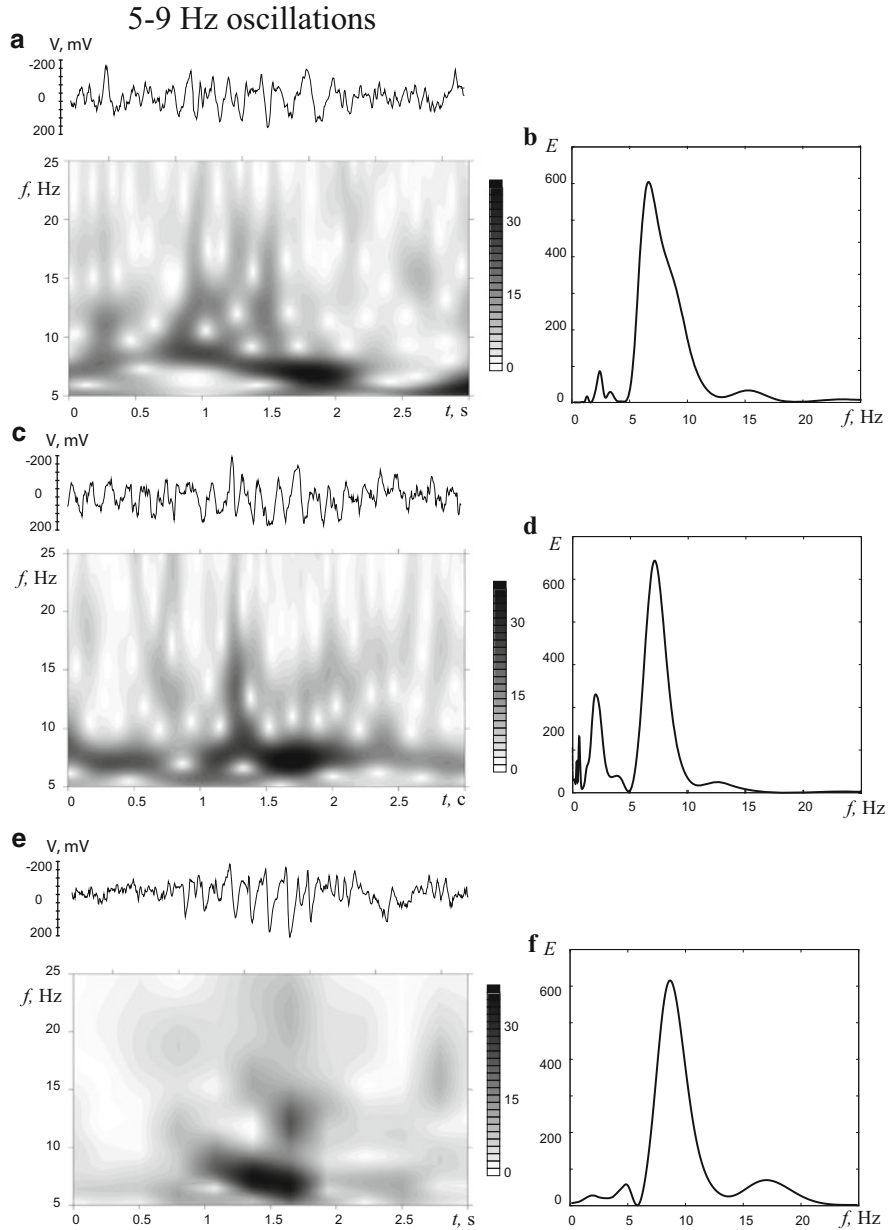


Fig. 6.8 EEG examples of 5–9 Hz oscillations and corresponding Morlet-based wavelet spectra (a), (c), (e). *Right plates* show the distribution of instantaneous wavelet energy $E(f_s)$ (2.33) measured in 5–9 Hz oscillations (b), (d), (f)

Table 6.4 Main time–frequency characteristics of sleep spindles and 5–9 Hz oscillations in EEG registered in the frontal cortex during sleep. N , T , and f are the number, average duration, and mean frequency of analyzed events in the EEG, respectively

Rat #	Sleep spindle			5–9 Hz oscillations		
	N	T (s)	f (Hz)	N	T (s)	f (Hz)
1	3,312	0.8	14.1	1,378	0.73	7.2
2	5,440	0.58	12.6	869	0.84	6.4
3	2,776	0.69	13.2	974	0.85	6.1
4	2,007	0.7	12.8	1,096	0.76	8.3
5	3,145	0.66	14.0	1,511	0.86	7.4
6	4,421	0.64	12.1	1,827	0.81	7.8
Mean \pm SD	3,517 \pm 1,227	0.68 \pm 0.07		1,276 \pm 363	0.81 \pm 0.05	

frequencies for several typical sleep spindles (10–15 Hz) and 5–9 Hz spindle-like oscillations, indicating that peak frequencies of these phenomena lie in two clearly distinctive frequency bands.

Indeed, according to Morlet-based wavelet analysis, sleep spindles in WAG/Rij rats showed a markedly increased wavelet power in the range 10–15 Hz (see Fig. 6.7, where illustrations of typical sleep spindles are shown). The wavelet spectrum of sleep spindles was often contaminated with additional low-frequency components and high-frequency bursts (occasional spikes). There were substantial frequency fluctuations within one spindle train (i.e., intra-spindle frequency variation) and the mean frequency of different sleep spindles also varied (i.e., inter-spindle frequency variations). The average sleep spindle frequency per rat varied from 12.1 to 14.1 Hz (inter-subject variations).

Five to nine hertz oscillations (see Fig. 6.8) are characterized by a spindle-like waveform. The frequency of these oscillations was lower than that in sleep spindles and matched the frequency of epileptic spike–wave discharges, i.e., peaks of wavelet power spectra are in the 7–9 Hz range.

The main time–frequency characteristics of sleep spindles and 5–9 Hz oscillations in EEG registered during sleep are presented for six rodents in Table 6.4. It can be seen that sleep spindles appear in the EEG more frequently in comparison with 5–9 Hz spindle-like oscillations. Note that the number of spike–wave discharges observed in the 6 h EEG recordings under study is estimated to be on average approximately 300 events.

Comparing the instantaneous wavelet spectra $E(f_s)$ obtained with the help of different mother wavelets and presented in Fig. 6.9, we can conclude that only the Morlet wavelet allows one to identify and distinguish between the two kinds of spindle-like activity (sleep spindles and 5–9 Hz oscillations). It is clearly that the use of real MHAT and complex Paul mother wavelets as basis functions does not provide the required frequency resolution (the large width of the corresponding peak in the averaged wavelet spectra in Fig. 6.9), so the peaks corresponding to the 8 and 12 Hz frequencies merge and are not distinguishable using the wavelet analysis. Note that the wavelet energy of the 5–9 Hz oscillations is significantly lower (in fact, two to

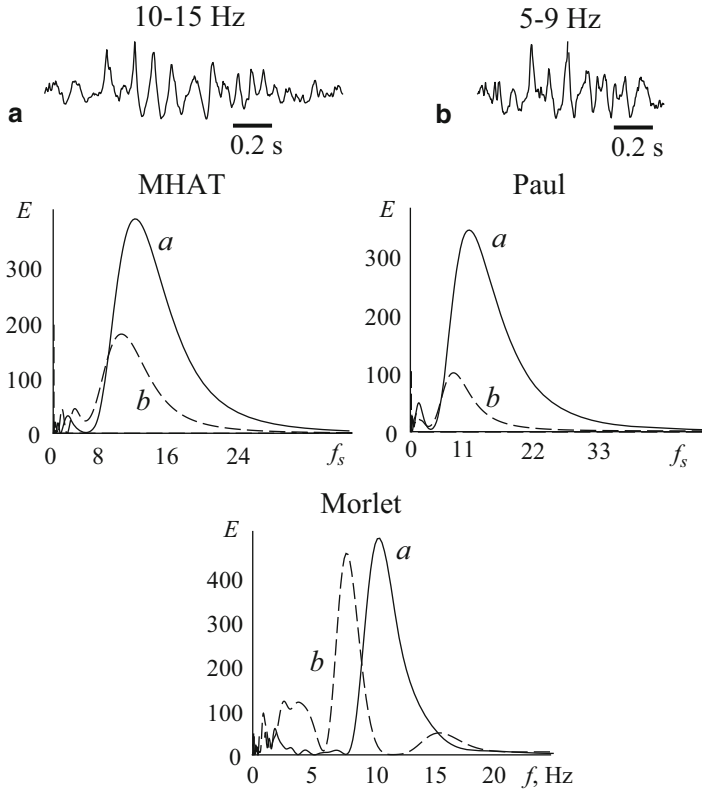


Fig. 6.9 Comparison of energy distributions of the wavelet spectra obtained with the MHAT, Paul, and Morlet mother wavelets ($\omega_0 = 2\pi$) for sleep spindles (10–15 Hz) (**a**, *solid lines*) and 5–9 Hz oscillations (**b**, *dashed lines*) in the frontal cortex

three times lower) than the energy of a typical sleep spindle, so it is difficult to select the low-frequency spindle-like activity in the background EEG and to distinguish it from the more frequent typical sleep spindles. This fact can also greatly complicate the automatic detection of various types of sleep spindles using the above-mentioned mother wavelets.

At the same time, the wavelet analysis with the complex Morlet mother wavelet can effectively separate the two types of spindle-like activity. There are several reasons for this. First, due to the good frequency resolution of the Morlet wavelet, the peaks corresponding to the two kinds of spindles in the wavelet spectra do not overlap. Second, the Morlet-based wavelet spectrum is such that the amplitude of both kinds of spindle-like oscillatory patterns (sleep spindles and 5–9 Hz oscillations) can be compared with each other. As we shall see, this makes it possible to solve the problem of the recognition of these two different kinds of oscillatory patterns in the EEG using the Morlet mother wavelet.

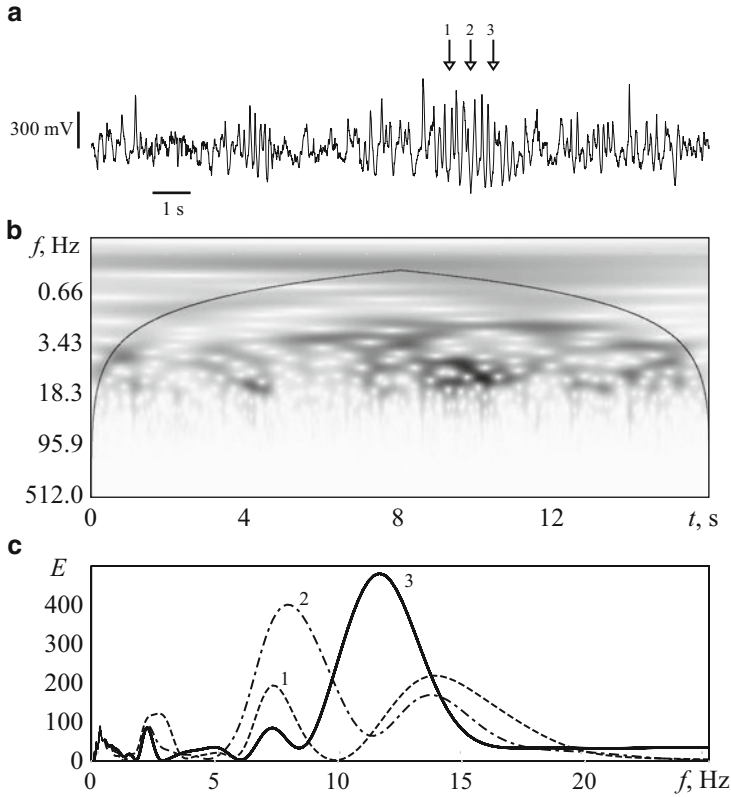


Fig. 6.10 Dynamics of oscillation frequencies within the sleep spindle. EEG signal recorded in the frontal cortex (a), wavelet spectrum obtained with the help of the Morlet wavelet with central frequency $\omega_0 = 2\pi$ (b), and the instantaneous amplitude distributions of wavelet coefficients at different times (indicated by arrows) (c)

We emphasize that balanced time–frequency resolution of the complex Morlet wavelet with $\omega_0 = 2\pi$ allows for effective analysis of frequency dynamics within sleep spindles that would not be possible with other mother functions. Figure 6.10 shows the EEG epoch (Fig. 6.10a) and its wavelet spectrum obtained with the help of the Morlet wavelet (Fig. 6.10b), and the instantaneous amplitude distributions of the wavelet spectrum at different times (Fig. 6.10c), which correspond to the times 1–3 indicated by arrows in Fig. 6.10a. In the given time interval of the EEG, we observe two sleep spindles, but the first one that appears at time $t = 4$ s is short and poorly visible in the EEG signal. Therefore, the analysis was carried out for the second sleep spindle, occurring in the time interval $t = 9$ – 11 s and indicated by arrows.

The most important result of this detailed time–frequency analysis is the fact that the main frequency within spindle oscillations varies significantly, increasing

Table 6.5 Dynamics of intra-spindle frequency and average duration of spindle events. f_1 and f_2 are the average typical frequency of EEG oscillations at the beginning and the end of a sleep spindle, respectively. T is the average duration of the sleep spindles

	T (s)	f_1 (Hz)	f_2 (Hz)	$f_2 - f_1$ (Hz)
WAG/Rij, age 5 months	0.59 ± 0.23	10.28 ± 2.02	11.26 ± 2.26	0.98 ± 1.84
WAG/Rij, age 9 months	0.37 ± 0.08	11.14 ± 2.15	11.30 ± 2.27	0.16 ± 1.44
Wistar, age 7 months	0.32 ± 0.08	12.15 ± 2.0	11.74 ± 1.98	0.59 ± 0.83
Wistar, age 9 months	0.30 ± 0.08	12.45 ± 2.1	13.33 ± 2.06	0.88 ± 1.26

toward the end of the sleep spindle. This is clearly seen in the wavelet surface $|W(f_s, t)|$ and the instantaneous wavelet energy distributions $E(f_s)$ plotted at the three different times. Indeed, the oscillations at the beginning of the sleep spindle are observed with a frequency close to 7.5 Hz (curve 1 in Fig. 6.10c). We then observe an increase in the amplitude of the oscillations and a slow frequency shift towards higher frequencies (curve 2). Simultaneously, oscillatory components with smaller amplitude and frequency close to 14 Hz are present in the wavelet spectrum. By the end of the sleep spindle, there is a rapid increase in the frequency of spindle oscillations to a value of about 12 Hz (curve 3). However, the 7.5 Hz rhythm present at the beginning of the spindle remains, with a reduced amplitude in the wavelet spectra.

6.3.4 Intra-spindle Frequency Dynamics in Epileptic and Non-epileptic Rat Strains

In order to analyze this intra-spindle frequency dynamics, we measured the instantaneous frequency at the beginning (f_1) and at the end (f_2) of each sleep spindle. Table 6.5 presents statistical data for the dynamics of the main frequency during sleep spindle oscillations in WAG/Rij rats (animal model of absence epilepsy, six rodents) and Wistar rats³ (animals without signs of epilepsy, four rodents). It is clear that the growth of the dominant frequency of spindle oscillations is typical ($f_2 - f_1 > 0$) for an inbred strain of epileptic (WAG/Rij) and non-epileptic (Wistar) rats. It should be noted that the dynamics of the intra-spindle frequency of sleep spindles (a gradual increase from the beginning to the end of events) is opposite to the corresponding dynamics of the dominant SWD frequency. The frequency of spike–wave discharges is reduced toward the end of the SWD.

In [36], the mean frequency of oscillations within a spindle obtained by CWT with the Morlet mother wavelet was used as a criterion for dividing sleep spindles into three categories: slow (mean dominant frequency 9.3 Hz), transitional

³Wistar rats are an outbred strain of albino rats belonging to the species *Rattus norvegicus*. This strain was developed at the Wistar Institute in 1906 for use in biological and medical research.

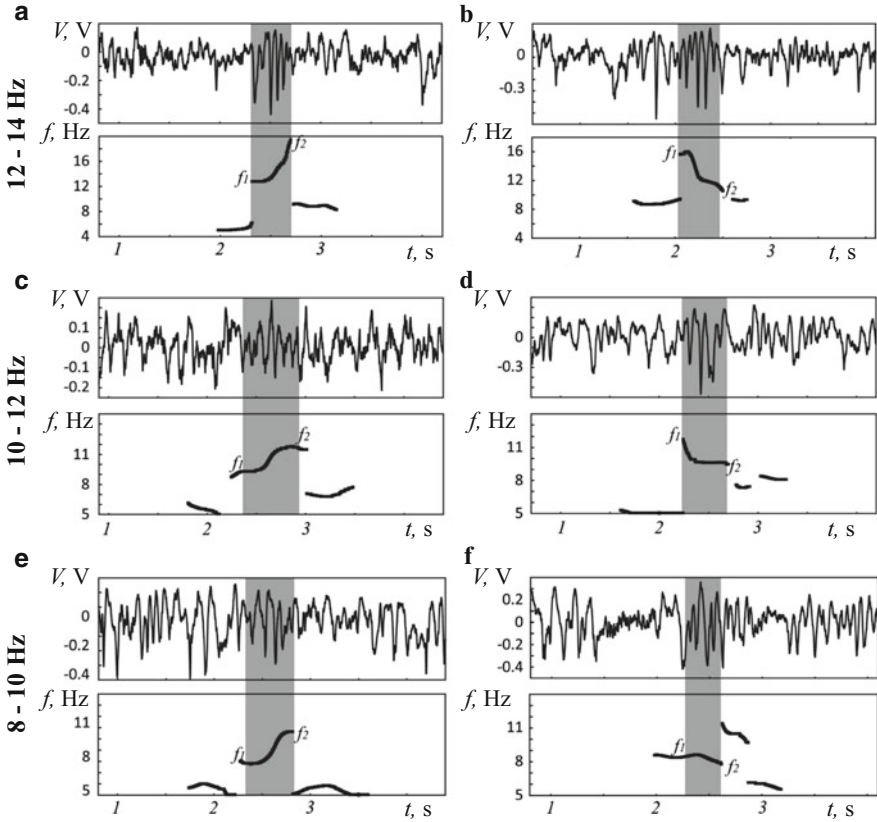


Fig. 6.11 Sleep spindles in the EEGs and the corresponding skeletons of their wavelet surfaces. (a) and (b) Fast spindles (12–14 Hz) exhibiting an increase (a) and decrease (b) in frequency during the spindle event. (c) and (d) Transitional spindles (10–12 Hz). (e) and (f) Slow spindles (8–10 Hz). Each point in the skeleton of the wavelet surface corresponds to a local maximum in the wavelet spectrum (see Sect. 2.3.4). Gray boxes indicate sleep spindle events

(11.4 Hz), and fast (13.5 Hz). Figure 6.11 shows typical examples of each kind of sleep spindle with different inter-spindle dynamics (increase or decrease of intra-spindle frequency) in WAG/Rij rats. Slow and transitional sleep spindles displayed an increase in frequency from the beginning towards the end. It was shown that a higher incidence of epilepsy corresponded to a lower duration of sleep spindles (all types). The mean frequency of transitional and fast spindles was higher in rats with more intensive epileptic discharges. In general, it has also been shown that high epileptic activity in WAG/Rij rats corresponds to the most substantial changes within transitional spindles, whereas changes within slow and fast spindles were moderate.

6.3.5 Age-Related Changes in the Time–Frequency Structure of Sleep Spindles

Furthermore, age-related changes in the typical time–frequency structure of sleep spindles are observed by means of the wavelet spectra consideration. For example, in Wistar rats, the intra-spindle frequency of sleep spindles increased from the beginning to the end ($f_1 < f_2$, $p < 0.0001$), and this effect became more pronounced with age (the difference between f_1 and f_2 in 9-month-old animals was greater than in 7-month-old animals, $p > 0.02$). In contrast to Wistar rats, although the instantaneous frequency of sleep spindles in WAG/Rij rats also increased on average, this effect became poorly defined with age, i.e., $f_2 \approx f_1$. So on average the intra-spindle frequency in WAG/Rij rats remained unchanged during sleep spindles in 9-month-old animals.

We found that the frequency of sleep spindles in WAG/Rij rats with absence epilepsy was lower than in non-epileptic Wistar rats. The presence of slow (< 10 Hz) sleep spindles in rats with absence epilepsy may have important implications (the frequency of sleep spindles due to membrane properties of thalamic neurons, such as imbalanced I_T and I_h currents in TC cells), but this needs to be confirmed in other animal models and in epileptic patients. The frequency content of sleep spindles seems to be underestimated, especially in human patients. The problem is that the frequency is traditionally determined by peak-to-peak calculations or by traditional spectral analysis (fast Fourier transform). Fourier-based frequency estimates have serious limitations when applied to short-lasting transient events in EEG, such as sleep spindles [1, 37]. As emphasized by W. Jankel and E. Niedermeyer in [38]: “as ‘transient nonstationarities’, spindles escape methods of EEG computer analysis”.

We believe that the wavelet-based approach to EEG analysis of sleep spindles in epileptic patients may enhance our knowledge of pro-epileptic changes in sleep EEG that may be useful for diagnostic and prognostic purposes. Studies of the time–frequency structure of sleep spindles, as well as precursors of spike–wave discharges (see Sect. 6.2), taking into account the short duration of these events, could only be carried out with the help of the wavelet transform approach, since it can be optimally configured to operate with such short-length variable oscillatory patterns in the EEG. In Sect. 6.4, we will make some general comments concerning the application of the continuous wavelet transform to time–frequency EEG analysis.

The age-related changes in the dynamics of the intra-spindle frequency described above reflect plastic transformations in the thalamocortical (TC) neuronal network. We now consider these neurophysiological mechanisms in more detail.

Sleep spindles are characterized by an upward-sloping dynamics of the instantaneous frequency during each spindle event only in non-epileptic Wistar rats, but not in epileptic WAG/Rij rats. This ascending frequency dynamics during each spindle event can be accounted for by TC network activity. In fact, it is known that initiation and maintenance of sleep spindles require mutual interactions between two types of thalamic neurons: TC neurons of specific thalamic nuclei (glutamatergic relay cells) and GABA-ergic cells of the reticular thalamic nucleus, the RTN (see references

in [12, 13, 23, 39]). Neurons in the RTN have a propensity to trigger spindle oscillations and fire in bursts at every cycle, acting as pacemaker cells. TC cells receive inhibitory synaptic input from the RTN and produce rhythmic bursts only once in two to four cycles. Cortical neurons of deep layers (corticothalamic cells) effectively control thalamic activity in both RTN and TC neurons via excitatory connections. However, corticothalamic input predominantly excites RTN neurons and feed-forward inhibition of TC cells overcomes direct cortical excitation [40]. This phenomenon is called *inhibitory dominance* of corticothalamic action on TC cells and it is essential for large-scale synchronization of sleep spindles.

Each sleep spindle presents the following sequence of thalamocortical processes [23, 39, 41, 42]:

1. Initial period. The spindle sequence is initiated by the pacemaker cells in the RTN.
2. Waxing (beginning) phase. The first two-to-four bursts of RTN neurons, when TC neurons do not display rebound bursting activity and do not return signals to the RTN.
3. Middle phase. Characterized by mutual recruitment of TC and RTN neurons, when regular spike-bursting in TC was locked in phase with the RTN and cortical neurons.
4. Waning (termination). Characterized by less synchronized activity of thalamic and cortical neurons.

Our data in Wistar rats indicated that, at the beginning of the waxing phase, the instantaneous frequency of cortical sleep spindles was relatively low, but that it gradually rose up during the middle and reached the highest value during the waning phase. The spindle frequency strongly depends on the coupling strength between RTN and TC neurons [43]. In particular, an increased coupling strength in RTN \rightarrow TC neurons resulted in an increase in the spindle frequency in the range 9.5–16 Hz, although in contrast an increase in TC \rightarrow RTN coupling led to a decrease in the spindle frequency by 0.5–2 Hz. The upward-sloping dynamics of the intrinsic spindle frequency in Wistar rats ($f_1 < f_2$) may result from a gradual increased coupling in RTN \rightarrow TC neurons during a spindle (but in the opposite direction, TC \rightarrow RTN). At the end of the sleep spindle, the coupling in RTN \rightarrow TC cells reached a maximum and a further increase in coupling strength led to the excessive cortical synaptic feedback to the thalamus (TC and RTN cells) that is required to terminate the sleep spindle [41, 42]. It is known that cortical neurons are tonically depolarized from the middle to the end of spindles, thus contributing to spindle termination [41].

Our results described in this section and obtained by CWT with the Morlet wavelet indicated that the difference between f_1 and f_2 in Wistar rats increased with age and sleep spindles became longer, suggesting that the propensity of the thalamocortical network to produce long spindle oscillations increases from 7 to 9 months of age. We also found that, in WAG/Rij rats, the intra-spindle frequency did not change during a spindle ($f_1 = f_2$). It seems that the thalamocortical mechanism of spindle maintenance and termination is affected by genetic factors

(predisposition to absence epilepsy), but does not associate with the severity of seizures. In WAG/Rij rats, excitability of the neocortex is known to be increased [21, 44, 45]. Over-intensive cortical feedback to the thalamus in epileptic rats may prevent the ascending dynamics of the intra-spindle frequency. Another mechanism may involve the thalamus (RTN \rightarrow TC neuron associations). The gradual increase in coupling strength in RTN \rightarrow TC neurons that might account for the upward-sloping dynamics of the intra-spindle frequency in non-epileptic rats may be impaired in epileptic rats.

In contrast to Wistar rats, the time–frequency properties of sleep spindles in WAG/Rij rats did not change with age. It seems that age-related aggravation of absence seizures prevented normal developmental changes of sleep spindles in WAG/Rij rats. Epileptic processes in the thalamocortical network underlying age-related aggravation of absence seizures may interfere with the normal mechanisms of sleep spindle development.

In conclusion, these wavelet-based results suggest that (i) the low frequency of sleep spindles and (ii) lack of intra-spindle frequency dynamics could be used as biomarkers for the early (perhaps, preclinical) stage of absence epilepsy.

6.4 Practical Notes Concerning Application of the Continuous Wavelet Transform in Time–Frequency EEG Analysis

The continuous wavelet transform has several advantages over traditional FFT for representing non-periodic and non-stationary signals that have sharp peaks or other kinds of fast events. One limitation of FFT is that it characterizes the EEG signal only in the frequency and not in the time domain, i.e., information regarding the dynamic changes of spectral components. In wavelet space, the EEG signal power is simultaneously represented as a function of time t and frequency f_s . In the case of a real mother wavelet function, the wavelet coefficients W represent the degree of correlation of a prototype wavelet function ψ_0 with the EEG signal on the given time scale s (wavelet frequency $f_s = 1/s$). The wavelet transform with complex mother wavelet can be regarded as a bandpass filter whose transfer characteristic is determined by the mother wavelet, and which also carries information about phase relationships.

The wavelet prototypes (mother wavelets) are wave-like scalable functions which are well localized in both the time and frequency domains [46]. Some mother wavelets provide better resolution in the time domain, and others in the frequency domain. The choice of mother wavelet is of great importance and it is crucial for accurate representation of the EEG signal in the wavelet space (t_0, f_s) . Important characteristics that were taken into account before making a choice of mother wavelet were complex/real, width, and shape of the candidate wavelets ψ_0 .

6.4.1 *Complex or Real Mother Wavelet*

A real wavelet $\psi_0 = \text{Re } \psi_0$ returns information about the amplitudes of the EEG signal and it may be sufficient for isolating EEG spikes or other discontinuities (for example, various artifacts and interferences during EEG registration), but not sufficient for detecting sustained oscillatory processes. A complex wavelet returns information about both amplitudes and phases (see Sect. 2.3.5) and this is more suitable for time–frequency analysis and for representing oscillatory EEG phenomena in wavelet space [46, 47].

6.4.2 *Shape of Mother Wavelet*

Accurate results from the wavelet decomposition are dependent on the shape of the chosen wavelet function, which should be similar to the shape of the analyzed EEG signal [48]. Rectangular functions such as the Haar (2.42) or FHAT (2.41) wavelets are better for representing EEG spikes (and other sharp events in the EEG), while the real Mexican hat (MHAT) wavelet (2.40), which has a smoother shape than the non-smooth Haar and FHAT wavelets, is particularly suitable for detecting epileptic spikes and spike–wave discharges in EEG [48, 49]. Meanwhile, oscillatory EEG patterns can be more accurately represented with complex wavelet functions which are based on smooth harmonic functions, and the Morlet wavelet (2.36) in particular is better suited for the detection of delta, theta, and alpha events, as well sleep spindles, because it mimics the characteristic spindle waveform [37, 48, 50]. Although the Morlet wavelet has no sharp elements equivalent to spikes in SWDs and its shape does not mimic SWDs, it provides the best time–frequency representation and resolution of spike–wave discharges (as well as other oscillatory EEG patterns) in comparison to other mother wavelets (including the sharp-looking Mexican hat wavelet) [37, 51].

6.4.3 *Width of Mother Wavelet*

If a candidate wavelet in Fourier space is too narrow, the frequency resolution will be poor, and if it is wide, the time localization will be less precise. It is also important to take into account the reverse relationship between time and frequency resolution. The higher the frequency resolution, the lower the time resolution and vice versa. The time–frequency resolution can be defined by the shape and width of the mother wavelet function in the frequency domain. In the case of the complex Morlet wavelet, properties of the time–frequency resolution of the wavelet transform can be controlled by changing the main frequency ω_0 , which affects the width and position of the Fourier image of the Morlet wavelet in Fourier space (see (2.36)

and (5.1), Fig. 2.11, and Table 2.1). Actually, in the complex Morlet wavelet family the parameter provided by the central frequency ω_0 determines the shape and the width of the wavelet function in the frequency domain. When $\omega_0 < \pi$, the temporal resolution is high, but little information is available about the frequency content of EEG events (the frequency resolution is low). When $\omega_0 > 4\pi$, the frequency resolution is high, but the time resolution is low. As the Morlet wavelet central frequency ω_0 increases, the properties of the wavelet transform approach the characteristics of the window Fourier transform. We chose the complex Morlet wavelet with $\omega_0 = 2\pi$ as the most appropriate basis, providing optimal time–frequency resolution for the majority of observed EEG phenomena. This basis function was particularly good in localizing the abrupt onset of SWD, as well as gradual amplitude changes during the seizure train. A further advantage in choosing this parameter value $\omega_0 = 2\pi$ is that the frequency f_s of the wavelet transform is equal to the frequency f of the Fourier transform, viz., $f_s = f$, which facilitates the explication and comparison of results.

6.5 Classification of Sleep Spindle Events by Means of Adaptive Wavelet Analysis

The classification of different kinds of oscillations in the EEG and the creation of databases for the reference electroencephalographic patterns are very important and actively investigated problems associated with fundamental research on brain functions [52–54], and with applied tasks such as the development of brain–computer interfaces (BCI) [55–57]. Nowadays various methods have been proposed for solving these problems, based on different mathematical and cybernetic approaches to pattern recognition and classification [52, 58–60].

6.5.1 Construction of Adaptive Wavelet Basis (“Spindle Wavelet”) for Automatic Recognition of Sleep Spindles

As mentioned above (see Sect. 6.3), sleep spindles showed a greater variability in shape, and their electroencephalographic pattern was less stereotypic. This embarrassed the automatic detection of sleep spindles. In [37], a new approach to EEG structure study was developed on the basis of adaptive continuous wavelet analysis [47, 61]. An adaptive wavelet analysis uses as a mother wavelet function some selected EEG epoch which has the highest affinity for the analyzed pattern and serves as a tool for the extraction and recognition of non-standard complex shape oscillations. This strategy, which we refer to as *adaptive wavelet matching*, is to some extent comparable with the matching pursuit technique [62–66], in which a template function is chosen from a stochastic library that contains a set

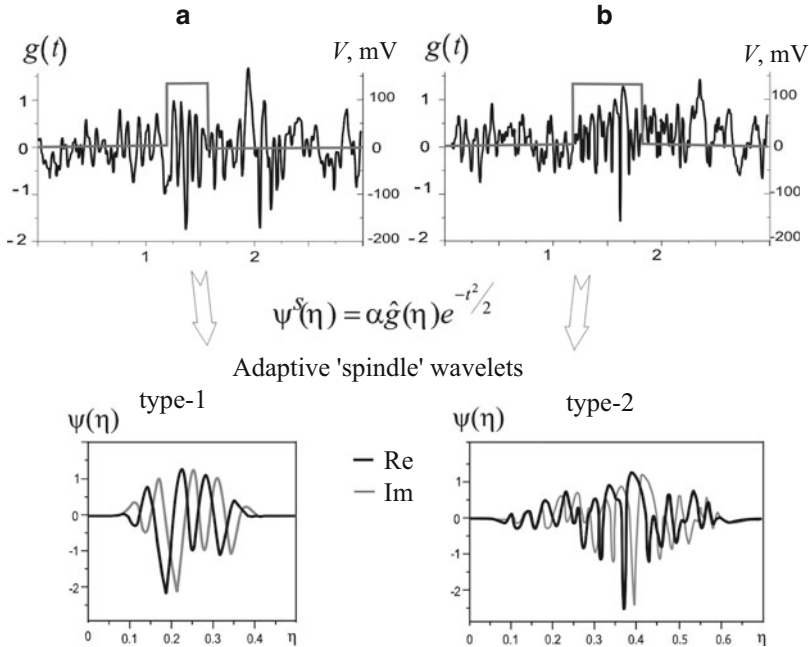


Fig. 6.12 Algorithm used for constructing adaptive *spindle wavelets*. Sleep spindle prototypes $g(t)$ are selected in the native EEG, converted into the complex form and normalized with a Gaussian function. **(a)** Spindle wavelet type 1 and **(b)** type 2. The *black line* corresponds to the real part of the spindle wavelets and the *grey line* to the imaginary part

of Gabor, Dirac, and Fourier basis waveforms. In the case of adaptive wavelet analysis, we do not use preset templates, but our *spindle wavelet* basis functions are adopted directly from the EEG signal. This approach can be used both for effective automatic identification of sleep spindles (see Sect. 7.4) and for standardizing the EEG structure and creating a database of reference electroencephalographic patterns.

For the standardization of sleep spindle patterns, an adaptive wavelet basis function (spindle wavelet) was built using a sleep spindle prototype extracted from the native EEG. Figure 6.12 illustrates this approach to adaptive wavelet construction. The EEG signal was represented by the function $S(t)$. The signal $g(t)$ with eliminated mean value was considered, viz.,

$$g(t) = S(t) - \frac{1}{\Delta T} \int_{\Delta T} S(t) dt , \tag{6.3}$$

and subsequently transformed into the complex form

$$\hat{g}(\eta) = g(\eta) + ig(\eta + T/4) , \quad i = \sqrt{-1} , \tag{6.4}$$

where T denotes the typical period of a sleep spindle oscillation. The time shift between the real and imaginary parts was $T/4$.

In order to construct a localized-in-time wavelet basis $\psi^S(\eta)$, the function $\hat{g}(\eta)$ was normalized with a Gaussian function:

$$\psi^S(\eta) = \alpha \hat{g}(\eta) \exp \left[-\frac{(\eta - T/2)^2}{2} \right], \quad (6.5)$$

where α is the parameter determined from the normalization condition

$$\alpha^2 \int_{-\infty}^{+\infty} |\hat{g}(\eta)|^2 \exp \left[-\frac{(\eta - T/2)^2}{2} \right] d\eta = 1. \quad (6.6)$$

Both *spindle wavelets* fulfilled the requirements for wavelet bases, i.e., continuity, zero mean amplitude, and finite or near finite duration (see Sect. 2.3.1). Note that the same computational procedure is used for the harmonic function, e.g., $\sin(\omega_0 t)$ (or $\cos(\omega_0 t)$), in order to construct the complex Morlet wavelet (see (5.1)).

In order to select a typical spindle template, about 100 candidate spindle templates were chosen in five WAG/Rij rats (15–25 spindles per rat). Each spindle template was tested as a wavelet basis (spindle wavelet) which was used to calculate and analyze the wavelet spectra of sleep spindles. We considered the dependencies of the wavelet spectrum energy $E(t)$ on time t , for a time scale $s = 1.0$. Peaks $E(t) = E_{\max}$ in the wavelet energy dependencies $E(t)$ correspond to sleep spindles with shape similar to the shape of the considered spindle wavelet. Introducing a certain threshold E_k , we could pick out the sleep spindles for which the characteristic energy value exceeded the threshold: $E_{\max} > E_k$. Sleep spindles showed different degrees of conformity to two types of spindle wavelets, e.g., spindle wavelets type 1 and type 2.

6.5.2 Identification of Two Spindle Types with the Aid of Two Adaptive “Spindle Wavelets”

The spindle wavelet which demonstrated the best quality of recognition and provided the maximum number of positive spindle detections, e.g., the one which had the highest affinity to the maximum number of sleep spindles in the EEG of all analyzed experimental animals, was chosen as the *universal* adaptive wavelet basis which best reflects and optimally describes the typical sleep spindle pattern in the epileptic EEG. Spindle wavelets are adopted from spindle prototypes, i.e., from sleep spindle events in the EEG, and therefore embrace the most typical (or generic) features of sleep spindles.

The constructed *universal spindle wavelet* is shown in Fig. 6.12a. A majority of sleep spindles (85–90%) is selected by CWT with this spindle wavelet type.

This spindle type is referred to as type 1, and on the basis of its EEG features, it is considered to represent *normal* spindle oscillations with fundamental frequency 10–14 Hz, which prevail during slow-wave sleep.

The remaining sleep spindles, those which failed to be captured with spindle wavelet 1, were selected using *spindle wavelet 2*, which is shown in Fig. 6.12b. A basis function for spindle wavelet 2 had to be selected for each rat individually (10–20 spindles per subject were tested as mother wavelet). It was found that type 2 sleep spindles comprised 7.9 % of the total number of sleep spindles. These spindles have high power between 12 and 25 Hz. They exhibit a deviant spindle waveform and might be considered as pro-epileptic events (a transitory waveform between sleep spindles and spike–wave discharges) [37].

6.5.3 Two Types of Sleep Spindles and Their Relevance to SWD

There was a clear inconsistency in the population of sleep spindles: those that matched spindle wavelet 1 failed to be captured by spindle wavelet 2. In order to get a better understand of the physiological meaning of this divergence of sleep oscillations, we performed a power spectrum analysis of the two spindle prototypes. Spindle wavelet 1 had a fundamental frequency of 12.2 Hz (see Fig. 6.13) that corresponds precisely to the mean frequency of sleep spindles in rats [35], and in addition, it had a spectral peak at 7 Hz and elevations around 2 and 26 Hz.

In contrast to the spectrum of spindle wavelet 1, the spectrum of spindle wavelet 2 was more complex and its major peak appeared with a frequency of 21 ± 3 Hz. Typically, spindle wavelet 2 showed several sharp peaks at 1, 3, 16.7, and 21.3 Hz, and moderate elevations at 8.5, 11, 24.5, and 27 Hz (see Fig. 6.13). It can be concluded that atypical type 2 sleep spindles can be distinguished from the common type 1 sleep spindles: a powerful beta component can be considered as a hallmark of type 2 spindles by having a larger individual variation.

The occurrence of type 2 sleep spindles with the strong 16–25 Hz component might be accounted for by processes of epileptogenesis taking place in our subjects. Previously, it was shown in [67] by means of EEG coherence analyses that the SWD frequency spectrum was characterized by the fundamental frequency (10–12 Hz) and its second harmonic (20–24 Hz), but also that the onset of SWD was characterized by an increased synchronization in the range 15–16 Hz between bilaterally symmetric cortical areas. Here the peaks with the same frequency (16.7 and 21.3 Hz) were detected in type 2 sleep spindles by means of CWT. It is therefore likely that neuronal synchrony at 16.7 and 21.3 Hz is common to SWD and type 2 sleep spindles. So the type 2 sleep spindles might be considered as a transitory oscillatory waveform between spindle and SWD in the EEG of WAG/Rij rats [37]. Our studies (see [36,37]) have shown that the number of such type 2 events does not exceed 10–15 % of the total number of observed sleep spindles in epileptic EEGs.

As a result, we found by means of adaptive CWT that sleep spindles represent a very heterogeneous group of oscillations, which causes difficulties regarding

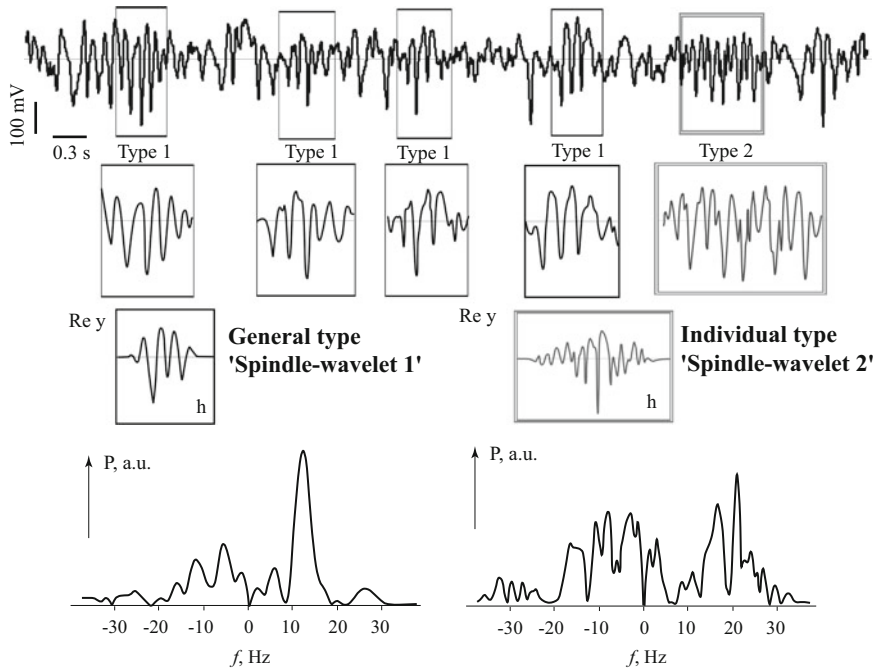


Fig. 6.13 EEG waveforms of sleep spindles in WAG/Rij rats. *Top*: Native EEG in which the majority of sleep spindles comprise characteristic repetitive elements that match spindle type 1. Spindle wavelet type 1 is universal for all the animals. This type of oscillatory activity is a typical sleep spindle. However, 10–15 % of sleep spindles are not recognized by the adaptive wavelet type 1, and their recognition requires one to construct new wavelet bases separately for each animal. This wavelet (referred to as the type 2 spindle wavelet) is characterized by a very complex form which is specific to each animal. Type 2 sleep spindles display larger inter-subject variability and complex structure and can be associated with pro-epileptic activity on the EEG. *Bottom*: Frequency power spectra of spindle wavelets types 1 (*left*) and 2 (*right*). The type 1 spindle wavelet is characterized by a predominant 8–14 Hz frequency component (spindle range). The type 2 spindle wavelet frequency spectrum consists of several frequency components in the spindle and non-spindle range

extraction, recognition, and classification of spindle events in the EEG. In all our rats, almost all sleep spindles (95.5 %) are extracted with joint application of two different types of adaptive *spindle wavelets*. Spindle wavelets are adopted from spindle prototypes, i.e., from sleep spindle events in the EEG, and therefore they embrace the most typical (or generic) features of sleep spindles. The frequency profile of these two types of sleep spindles is crucially different. Note that the type 2 spindle wavelet is characterized by a strong harmonic component (20–25 Hz). The same harmonic component is present in the SWD and is likely to be elicited by spikes (see Sect. 5.3.3). Spikes may also be present in the type 2 spindle sequence. These type 2 sleep spindles exhibit a deviant spindle waveform and they might be considered as pro-epileptic events. We also concluded with the

help of adaptive wavelet analysis that the EEG patterns of sleep spindles and SWDs belong to different families of phasic EEG events with different time–frequency characteristics.

6.6 Synchronous Dynamics of Epileptic Discharges: Application of Time-Scale Synchronization Approach

As already mentioned in Sect. 5.4, there has recently been increased interest in the use of wavelets to study the synchronization phenomena in neuronal networks and ensembles, and in particular, to analyze the synchronization of different areas of the brain. Different cerebral cortex regions are known to operate synchronously under both normal conditions (e.g., cognitive activity) and pathological conditions (Parkinson’s disease, various forms of epilepsy) [68, 69].

One of the most promising applications of wavelets in this context is for diagnosing synchronous activity in complex multifrequency signals, i.e., signals with several fundamental frequencies. In Sect. 2.3.5, we discussed the possibility of using continuous wavelet analysis to study the synchronization of complex oscillations. This approach, well-known as time-scale synchronization, provides an effective method of detection and analysis of the synchronous states in systems of different nature, including the investigation of essentially non-stationary and noisy data.

By way of example, we shall consider the evolution of a hypersynchronous epileptic discharge in EEGs from patients with absence epilepsy, a quite common neurologic disorder associated with total or partial loss of consciousness. We will use a time-scale synchronization approach, based on the continuous wavelet transform with complex Morlet mother wavelet [1, 70].

Absence seizures usually last from a few seconds to tens of seconds, and are accompanied by characteristic spike–wave complexes in EEGs (see also Fig. 5.4b) [71, 72]. Spike–wave discharges recorded during epileptic seizures have a high amplitude and frequency on the order of 3–4 Hz. As is well known, absence seizures are associated with rapid growth of synchronization between different brain regions, and that this in turn leads to the appearance of hypersynchronous spike–wave discharges in EEGs. The source (so-called focus) of epileptic activity and synchronization dynamics before, during, and after spike–wave discharge remains to be elucidated and raises concerns among researchers and clinicians. These issues are closely connected with the very important problem of identifying the epileptic activity source by examination of multichannel EEGs [73, 74].

Attempts to find answers to these questions have been undertaken repeatedly, but in an overwhelming majority of cases, EEG analysis was provided qualitatively by the expert, without applying rigorous mathematical methods. But as experts in neurophysiology have noted [74], the interpretation of the functional condition of the brain by analyzing the qualitative character of the EEG, i.e., the overall pattern

of electrical activity, may lead to unjustified and erratic conclusions, especially in the presence of disease. So, for example, to localize the focus of epileptic activity, experts are guided by their own toolkit, experience, and qualification, rather than using the rigorous methods of mathematical analysis.

The possibilities for accurate solution of this problem using recordings of electrical brain activity in patients with absence epilepsy are considered in [73, 75, 76], but the methods used by the authors depend heavily on the quality of the analyzed EEG signal. This essentially limits the possibilities for applying the offered approaches since, in the overwhelming majority of cases, the researcher or clinician is investigating EEG signals recorded through the skin of the patient's head. Such signals are well known to involve a high level of noise and various artifacts, due to the fact that the skull bones and cutaneous covering significantly distort the shape of the EEG potentials indicating neuronal oscillations. For this reason the spectral structure of EEGs recorded from electrodes placed on the scalp differs from neuronal electrical signals received directly from brain structures by means of depth electrodes. Consequently, application of the time-scale synchronization approach to such experimental data is rather productive and allows one to extract new information about the way the brain operates.

The hardware–software solution Entsefalan produced by the Russian company Medicom-MTD, Taganrog,⁴ consisting of an electroencephalograph analyzer and software for EEG registration and preliminary processing, has been used to register multichannel EEGs in patient volunteers. During EEG registration, patients were subjected to external influences to provoke epileptic attack, e.g., stimulation by audio and photo stimulus with frequency increasing from 3 to 27 Hz and hyperventilation of the lungs, with the latter being the most effective method for provoking seizure.

The EEG registration time was 30 min. During this time, one to five spike–wave discharges were observed in each patient, with average duration close to 2.8 s. The main frequency of SWD oscillations was close to 3 Hz. We considered only signals from 14 electrodes, indicated in Fig. 6.14a by circles. The analyzed EEG signals were unipolar, i.e., they represented a potential difference between an active and indifferent electrodes, viz., electrodes 1 and 2, located on the earlobe of the patient (see Fig. 6.14a). The typical fragment of multichannel EEG containing the spike–wave discharge is presented in Fig. 6.14b. Figure 5.4b illustrates the structure of oscillations during seizure in an EEG from the frontal cortex. The wavelet spectra of the EEG epoch containing the SWD are presented in Figs. 5.5 and 5.6, where showing results of wavelet transforms using different mother wavelets.

As already discussed in Chap. 5, the spike–wave discharge pattern in EEGs recorded from multiple electrodes placed on the scalp differs essentially from the SWD structure in EEGs recorded directly at the brain surface by means of depth electrodes. In particular, the high-frequency component is poorly pronounced—the amplitude of a sharp component (peak) of SWD oscillations is significantly smaller

⁴www.medicom-mtd.com/eng/index.htm

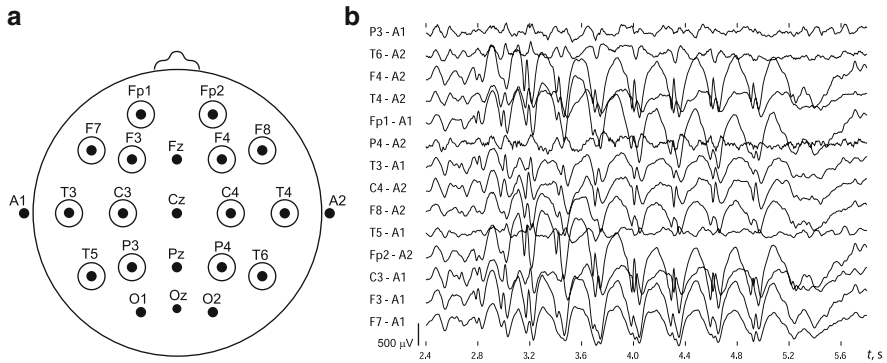


Fig. 6.14 (a) Standard electrode arrangement on the patient's head (10–20 system). Signals from electrodes enclosed by circles were used in synchronization analysis. (b) Example of a typical multichannel EEG showing a spike–wave discharge (2.8–5.2 s)

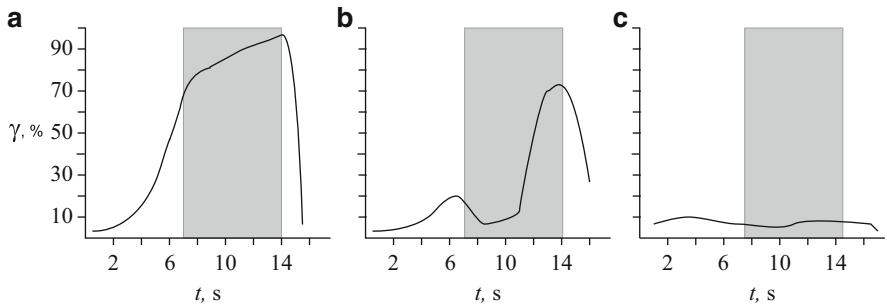


Fig. 6.15 Time-scale synchronization measure versus time for the EEG epoch with spike–wave discharge. (a) Establishment of the synchronization regime at the beginning of the SWD (Fp1 and C4 leads). (b) Synchronization delay (F3 and T5 leads). (c) No synchronization (P3 and C5 leads). The gray rectangle shows the time interval corresponding to the SWD

than the amplitude of a low-frequency (wave) component. At the beginning of the SWD, the greater part of the energy lies in oscillations with frequency close to 3–4 Hz, but later in the SWD the period of spike-and-wave complexes increases, as observed in WAG/Rij rats. The duration of the epileptic seizure in humans was also significantly shorter than the duration of the SWD in laboratory animals (WAG/Rij rats).

To localize a source of spike–wave discharge in patients, the time-scale synchronization (see conditions (2.85) and (2.86)) was investigated pairwise between all the EEG channels shown in Fig. 6.14. Figure 6.15 displays the typical dependence of the time-scale synchronization measure γ (see (2.89)) on time in several cases:

- For pairs of EEG channels between which the time-scale synchronization was observed at the beginning of the epileptic seizure (see Fig. 6.15a).

- For pairs of EEG channels between which synchronization was expressed more weakly and observed after inception of the SWD (see Fig. 6.15b).
- For EEG channels in which time-scale synchronization was not observed (see Fig. 6.15c).

The measure of time-scale synchronization was examined in the frequency range 0.5–10 Hz where the wavelet spectrum energy was highest. It is easy to see that, in the case of absence of synchronization, the measure γ takes small values, and the proportion of synchronized scales does not exceed 5% of the full energy of the wavelet spectrum of the EEG oscillations. This value of the synchronization measure is not equal to zero due to the fact that, at every instant of time, it is possible to find synchronized frequencies. Apparently, this is a normal feature of brain operation since the measure of synchronization calculated for the background EEG epochs exhibits the same behavior.⁵ However, as we approach the beginning of the spike–wave discharge, the time-scale synchronization measure of well-synchronized EEG channels starts to increase (see Fig. 6.15a). This means that the wavelet spectrum energy share corresponding to the synchronized time scales increases, and at the beginning of the spike–wave discharge, the measure of time-scale synchronization reaches $\gamma \approx 90\%$. Such a high level of the time-scale synchronization measure remains throughout the discharge and subsequently, at the end of the SWD, drops to the normal level corresponding to the value of the synchronization measure in control periods without spike–wave discharges. There is another situation where there is also synchronization between EEG channels, but the measure of synchronization begins to grow only after onset of the discharge (see Fig. 6.15b). Finally, in the case of nonsynchronized EEG channels (see Fig. 6.15c), the synchronization measure remains small throughout the discharge.

The results of the search for the focus of epileptic activity and the temporal dynamics of hypersynchronous state formation are presented in Fig. 6.16, where the spike–wave discharge development is shown from the point of view of the synchronization approach. Arrows A–D in Fig. 6.16 indicate typical time moments which correspond to the diagrams of the synchronous state between different pairs of EEG channels. The continuous wavelet analysis involved instantaneous phases in a narrow frequency range of 3–4 Hz, within which the largest fraction of wavelet spectrum energy of spike–wave discharges fell. The lines connect pairs of EEG leads between which synchronization occurred at an instant of time indicated by a corresponding arrow on the EEG fragment plot (see the top of Fig. 6.16).

To reveal the spatial-temporal features of various interacting areas of the brain during epileptic seizure, the time-scale synchronization was estimated at different instants of time during the spike–wave discharge:

- Before the appearance and after the completion of the SWD (Fig. 6.16a, f).
- One second after the start of the SWD (Fig. 6.16b).

⁵Note that intermittency of spontaneously occurring synchronized EEG oscillation epochs has already been described in humans [77].

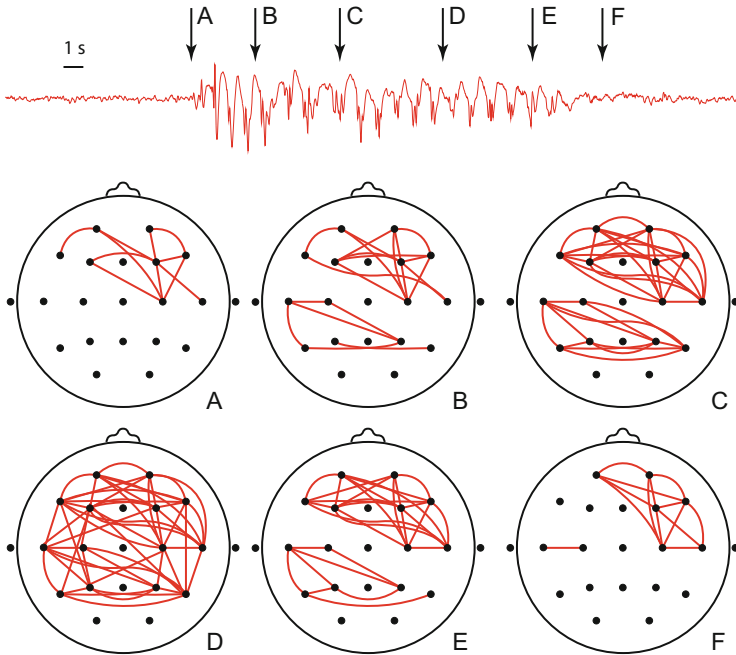


Fig. 6.16 Spatial-temporal dynamics of spike-wave discharge from the point of view of the time-scale synchronization of different brain regions. The number of synchronized areas increases as the spike-wave discharge develops and almost all cortical areas prove to be synchronized by the end of the SWD event. Diagrams correspond to different instants of time indicated by arrows *A–D* on the bipolar EEG recording from the frontal cortex (electrodes F4–A2, see Fig. 6.14)

- One second before the end of the SWD (Fig. 6.16e).
- Three and five seconds after the beginning of the SWD (Fig. 6.16c, d).

The presence of time-scale synchronization in the pair of EEG channels at some instant of time was assumed if the phase-locking condition (2.85) was fulfilled during no fewer than three periods of SWD oscillations (i.e., in this case, not less than 1 s).

Let us analyze the results. It is easy to see that the synchronized region is formed in the frontal cortex a few seconds before the beginning of the spike-wave discharge in the EEG (see Fig. 6.16a). This accords with existing notions about the peculiarities of absence seizures and the results of earlier studies regarding spatial features of spike-wave discharge formation [78, 79]. Westmijse et al. [73] demonstrated that frontal area in the right hemisphere has been primarily involved in the process of synchronization at the beginning of the SWD, i.e. synchronous regime during epileptic activity originated from these local brain area. It should be noted that, at this point in the EEG, there are no typical spike-wave complexes with frequency close to 3 Hz that are typical for epileptic seizures.

At the next examined instant of time (1 s after the SWD begins, see Fig. 6.16b), the spike–wave discharge becomes appreciable in EEG, and the number of synchronized channels increases. The new synchronized leads are located in the immediate vicinity of the epileptic source. In the case considered, a second focus of synchronized epileptic activity forms in the occipital cortex, but synchronous links between the frontal and occipital foci are absent.

After further development of the SWD, the number of synchronized EEG channels proceeds to increase until the two synchronous foci formed at the beginning of the SWD merge into one (see Fig. 6.16c, d), and the synchronization state acquires a generalized character in the brain cortex. This hypersynchronous state extends over all the EEG channels. Soon after formation of the hypersynchronous state, the synchronization regime starts to break down (see Fig. 6.16e). First, synchronization between the frontal and occipital cortexes disappears, whereupon synchronization in the occipital cortex covers a smaller spatial area in comparison with that in the frontal cortex.

Finally, at the end of the SWD, when the spike–wave activity in the EEG has already completely disappeared, synchronization is only observed in a small area of the frontal cortex where the initial epileptic focus was located, i.e., the synchronization area in the epochs preceding the SWD (compare Fig. 6.16d, a). After that the frontal cortex area corresponding to the epileptic focus is also desynchronized for several seconds.

The same dynamics of formation and development of spike–wave discharges was observed for all patients, except for one who was under medication. In all patients, we have identified a steady focus of synchronous activity in the frontal cortex. The additional focus in the occipital cortex has been observed only in some of the patients. Thus, the results of the time-scale synchronization analysis can help, not only to understand the mechanisms of formation of paroxysmal hypersynchronous states during an absence seizure, but also to make predictions. We assume that the participation of the occipital cortex and the presence of the additional synchronous focus during the spike–wave discharge are signs of a progressing clinical course and a negative forecast.

Thus, the time-scale synchronization method based on the application of continuous wavelet analysis with a complex basis was successfully used to describe space-time synchronization of electrical brain activity. Analysis of multichannel EEG recordings by this method not only allowed efficient localization of the source of epileptic activity, but also revealed its distribution patterns and described the process of epileptic activity generalization. These approaches may find application to the solution of other problems such as the detection of links between different brain regions, the search for high-frequency brain activity related to cognitive abilities [80–83], etc.

References

1. A.N. Pavlov, A.E. Hramov, A.A. Koronovskii, E. Sitnikova, V.A. Makarov, A.A. Ovchinnikov, Wavelet analysis in neurodynamics. *Phys.-Usp.* **55**(9), 845 (2012)
2. M. Jobert, C. Tismer, E. Poiseau, H. Schulz, Wavelets: a new tool in sleep biosignal analysis. *J. Sleep Res.* **3**, 223–232 (1994)
3. M.K. van Vugt, P.B. Sederberg, M.J. Kahana, Comparison of spectral analysis methods for characterizing brain oscillations. *J. Neurosci. Methods* **162**, 49–63 (2007)
4. C.P. Panayiotopoulos, Absence epilepsies, in *Epilepsy: A Comprehensive Textbook*, ed. by J.J. Engel, T.A. Pedley (Lippincott-Raven, Philadelphia, 1997), pp. 2327–2346
5. T. Inouye, Y. Matsumoto, K. Shinosaki, A. Iyama, S. Toi, Increases in the power spectral slope of background electroencephalogram just prior to asymmetric spike and wave complexes in epileptic patients. *Neurosci. Lett.* **173**, 197–200 (1994)
6. E.L.M. van Luijtelaar, A.E. Hramov, E. Sitnikova, A.A. Koronovskii, Spike-wave discharges in WAG/Rij rats are preceded by delta and theta precursor activity in cortex and thalamus. *Clin. Neurophysiol.* **122**, 687 (2011)
7. G. Paxinos, C. Watson, *The Rat Brain in Stereotaxic Coordinates*, 4th edn. (Academic, San Diego, 1998)
8. D.S. Moore, G.P. McCabe, *Introduction to the Practice of Statistics*, 6th edn. (W.H. Freeman, New York, 2009)
9. A. Lüttjohann, J.M. Schoffelen, E.L.M. van Luijtelaar, Peri-ictal network dynamics of spike-wave discharges: phase and spectral characteristics. *Exp. Neurol.* **239**, 235 (2013)
10. A. Lüttjohann, E.L.M. van Luijtelaar, The dynamics of cortico-thalamo-cortical interactions at the transition from pre-ictal to ictal LFPs in absence epilepsy. *Neurobiol. Dis.* **47**, 49 (2012)
11. L. De Gennaro, M. Ferrara, Sleep spindles: an overview. *Sleep Med. Rev.* **7**, 423 (2003)
12. A. Destexhe, T.J. Sejnowski, *Thalamocortical Assemblies* (Cambridge University Press, Cambridge, 2001)
13. A. Destexhe, T.J. Sejnowski, *Thalamocortical Assemblies: How Ion Channels, Single Neurons and Large-Scale Networks Organize Sleep Oscillations* (Oxford University Press, Oxford, 2001)
14. E.L.M. van Luijtelaar, Spike-wave discharges and sleep spindles in rats. *Acta Neurobiol. Exp.* **57**(2), 113 (1997)
15. E. Sitnikova, Thalamo-cortical mechanisms of sleep spindles and spike-wave discharges in rat model of absence epilepsy (a review). *Epilepsy Res.* **89**(1), 17 (2010)
16. P. Gloor, Generalized cortico-reticular epilepsies: some considerations on the pathophysiology of generalized bilaterally synchronous spike and wave discharge. *Epilepsia* **9**, 249 (1968)
17. S. Sato, F.E. Dreifuss, J.K. Penry, The effect of sleep on spike-wave discharges in absence seizures. *Neurology* **23**(12), 1335 (1973)
18. M. Steriade, D.A. McCormick, T.J. Sejnowski, Thalamocortical oscillations in the sleeping and aroused brain. *Science* **262**, 679 (1993)
19. G.K. Kostopoulos, Spike-and-wave discharges of absence seizures as a transformation of sleep spindles: the continuing development of a hypothesis. *Clin. Neurophysiol.* **111**(suppl. 2), S27 (2000)
20. H.K.M. Meeren, J.G. Veening, T.A.E. Modersheim, A.M.L. Coenen, E.L.M. van Luijtelaar, Thalamic lesions in a genetic rat model of absence epilepsy: dissociation between spike-wave discharges and sleep spindles. *Exp. Neurol.* **217**(1), 25 (2009)
21. N. Leresche, R.C. Lambert, A.C. Errington, V. Crunelli, From sleep spindles of natural sleep to spike and wave discharges of typical absence seizures: is the hypothesis still valid? *Pflügers Arch. Eur. J. Physiol.* **463**(1), 201 (2012)
22. W.H. Drinkenburg, A.M. Coenen, J.M. Vossen, E.L.M. van Luijtelaar, Spike-wave discharges and sleep-wake states in rats with absence epilepsy. *Epilepsy Res.* **9**(3), 218 (1991)
23. M. Steriade, *Neuronal Substrates of Sleep and Epilepsy* (Cambridge University Press, Cambridge, 2003)

24. E.L.M. van Luijtelaar, A. Bikbaev, Mid-frequency cortico-thalamic oscillations and the sleep cycle: genetic, time of day and age effects. *Epilepsy Res.* **73**, 259 (2013)
25. B. Lannes, G. Micheletti, M. Vergnes, C. Marescaux, A. Depaulis, J.M. Warter, Relationship between spike-wave discharges and vigilance levels in rats with spontaneous petit mal-like epilepsy. *Neurosci. Lett.* **94**(1–2), 187 (1988)
26. A.M. Coenen, E.L.M. van Luijtelaar, Genetic animal models for absence epilepsy: a review of the WAG/Rij strain of rats. *Behav. Genet.* **33**, 635 (2003)
27. P. Kellaway, Sleep and epilepsy. *Epilepsia* **26**(suppl. 1), S15 (1985)
28. L.G. Sadleir, K. Farrell, S. Smith, M.B. Connolly, I.E. Scheffer, Electroclinical features of absence seizures in sleep. *Epilepsy Res.* **93** (2–3), 216 (2011)
29. D. Pinault, T.J. O'Brien, Cellular and network mechanisms of genetically-determined absence seizures. *Thalamus Relat. Syst.* **3**(3), 181 (2005)
30. P. Halasz, A. Kelemen, New vistas and views in the concept of generalized epilepsies. *Deggyogyaszati Szle. Clin. Neurosci.* **62**(11–12), 366 (2009)
31. D. Pinault, A. Slezia, L. Acsady, Corticothalamic 5–9 Hz oscillations are more pro-epileptogenic than sleep spindles in rats. *J. Physiol.* **574**(Pt. 1), 209 (2006)
32. D. Pinault, M. Vergnes, C. Marescaux, Medium-voltage 5–9 Hz oscillations give rise to spike-and-wave discharges in a genetic model of absence epilepsy: in vivo dual extracellular recording of thalamic relay and reticular neurons. *Neuroscience* **105**, 181 (2001)
33. V.V. Grubov, A.A. Ovchinnikov, E. Sitnikova, A.A. Koronovskii, A.E. Hramov, Wavelet analysis of sleep spindles in EEG and development of method of its automatic identification. *Appl. Nonlinear Dyn.* **19**(4), 91 (2011)
34. E. Sitnikova, A.E. Hramov, V.V. Grubov, A.A. Ovchinnikov, A.A. Koronovsky, On-off intermittency of thalamo-cortical oscillations in the electroencephalogram of rats with genetic predisposition to absence epilepsy. *Brain Res.* **1436**, 147 (2012)
35. G. Terrier, C.L. Gottesmann, Study of cortical spindles during sleep in the rat. *Brain Res. Bull.* **3**, 701 (1978)
36. E. Sitnikova, V.V. Grubov, A.E. Hramov, A.A. Koronovskii, Age-related changes in time-frequency structure of EEG sleep spindles in rats with genetic predisposition to absence epilepsy (WAG/Rij). *J. High. Nerv. Act.* **62**(6), 733 (2011)
37. E. Sitnikova, A.E. Hramov, A.A. Koronovskii, E.L.M. van Luijtelaar, Sleep spindles and spike-wave discharges in EEG: their generic features, similarities and distinctions disclosed with Fourier transform and continuous wavelet analysis. *J. Neurosci. Methods* **180**, 304 (2009)
38. W.R. Jankel, E. Niedermeyer, Sleep spindles. *J. Clin. Neurophysiol.* **2** (1), 1 (1985)
39. M. Steriade, The corticothalamic system in sleep. *Front. Biosci.* **8**, D878 (2003)
40. A. Destexhe, D. Contreras, M. Steriade, Mechanisms underlying the synchronizing action of corticothalamic feedback through inhibition of thalamic relay cells. *J. Neurophysiol.* **79**(2), 999 (1998)
41. I. Timofeev, M. Bazhenov, T. Sejnowski, M. Steriade, Contribution of intrinsic and synaptic factors in the desynchronization of thalamic oscillatory activity. *Thalamus Relat. Syst.* **1**, 53 (2001)
42. M. Bonjean, T. Baker, M. Lemieux, I. Timofeev, T. Sejnowski, M. Bazhenov, Corticothalamic feedback controls sleep spindle duration in vivo. *J. Neurosci.* **31**, 9124 (2011)
43. J. Zygierewicz, Analysis of sleep spindles and model of their generation. PhD thesis, Warsaw University, Warsaw, 2000, brain.fuw.edu.pl/~jarek/PHD.pdf
44. U. Strauss, M.H.P. Kole, A.U. Bräuer, J. Pahnke, R. Bajorat, A. Rolfs, R. Nitsch, R.A. Deisz, An impaired neocortical I_h is associated with enhanced excitability and absence epilepsy. *Eur. J. Neurosci.* **19**(11), 3048 (2004)
45. M. D'Antuono, Y. Inaba, G. Biagini, G. D'Arcangelo, V. Tancredi, M. Avoli, Synaptic hyperexcitability of deep layer neocortical cells in a genetic model of absence seizures. *Genes Brain Behav.* **5**(1), 73 (2006)
46. G. Kaiser, *A Friendly Guide to Wavelets* (Springer/Birkhauser, Boston, 1994)
47. A.A. Koronovskii, A.E. Hramov, *Continuous Wavelet Analysis and Its Applications* (Fizmatlit, Moscow, 2003)

48. M. Latka, Z. Wast, A. Kozik, J. West, Wavelet analysis of epileptic spikes. *Phys. Rev. E* **67**, 052902 (2003)
49. H. Adeli, Z. Zhou, N. Dadmehr, Analyses of EEG records in an epileptic patient using wavelet transform. *J. Neurosci. Methods* **123**, 69 (2003)
50. L. Bonfiglio, S. Sello, P. Andre, M.C. Carboncini, P. Arrighi, B. Rossi, Blink-related delta oscillations in the resting-state EEG: a wavelet analysis. *Neurosci. Lett.* **449**, 57 (2009)
51. C. D’Avanzo, V. Tarantinob, P. Bisiacchib, G. Sparacinoa, A wavelet methodology for EEG time–frequency analysis in a time discrimination task. *Int. J. Bioelectromagn.* **11**(4), 185 (2009)
52. E.M. Schmidt, Computer separation of multi-unit neuroelectric data: a review. *J. Neurosci. Methods* **12**, 95 (1984)
53. M. Salganicoff, M. Sarna, L. Sax, G. Gerstein, Computer separations of multi-unit neuroelectric data: a review. *J. Neurosci. Methods* **25**, 181 (1988)
54. A.A. Koronovskii, E.L.M. van Luijtelaar, A.A. Ovchinnikov, E. Sitnikova, A.E. Hramov, Diagnostics and analysis of oscillatory neuronal network activity of brain with continuous wavelet analysis. *Appl. Nonlinear Dyn.* **19**(1), 86 (2011)
55. L. Ke, R. Li, Classification of EEG signals by multi-scale filtering and PCA, in *IEEE International Conference on Intelligent Computing and Intelligent Systems (ICIS’2009)*, Phoenix, 20–22 Nov 2009, pp. 362–366
56. L. Li, D. Xiong, X. Wu, Classification of imaginary movements in ECoG, in *Fifth International Conference on Bioinformatics and Biomedical Engineering (iCBBE)*, Wuhan, 10–12 May 2011, pp. 1–3
57. W.D. Penny, S.J. Roberts, E.A. Curran, M.J. Stokes, EEG-based communication: a pattern recognition approach. *IEEE Trans. Neural Syst. Rehabil. Eng.* **8**, 214 (2000)
58. R. Duda, P. Hart, *Pattern Classification and Scene Analysis* (Wiley, New York, 1973)
59. M.R. Kousarrizi, A.A. Ghanbari, M. Teshnehlab, M. Aliyari, A. Gharaviri, Feature extraction and classification of EEG signals using wavelet transform, SVM and artificial neural networks for brain computer interfaces, in *International Joint Conference on Bioinformatics, Systems Biology and Intelligent Computing, 2009 (IJCBS’09)*, Shanghai, 3–5 Aug 2009, pp. 352–355
60. T. Bassani, J.C. Nievola, Pattern recognition for brain–computer interface on disabled subjects using a wavelet transformation, in *IEEE Symposium on Computational Intelligence in Bioinformatics and Computational Biology (CIBCB’08)*, Sun Valley, 15–17 Sept 2008, pp. 180–186
61. V.A. Gusev, A.A. Koronovskii, A.E. Hramov, Application of adaptive wavelet bases to analysis of nonlinear systems with chaotic dynamics. *Tech. Phys. Lett.* **29**(18), 61 (2003)
62. P.J. Durka, Time–frequency analysis of EEG. PhD thesis, Warsaw University, Warsaw, 1996, brain.fuw.edu.pl/~durka/dissertation/
63. J. Zygierevicz, K.J. Blinowska, P.J. Durka, W. Szelenberger, S. Niemcewicz, W. Androsiuk, High resolution study of sleep spindles. *Clin. Neurophysiol.* **110**, 2136 (1999)
64. P.J. Durka, From wavelets to adaptive approximations: time–frequency parametrization of EEG. *IEEE Trans. Biomed. Eng.* **2**, 1 (2003)
65. P.J. Durka, U. Malinowska, W. Szelenberger, A. Wakarow, K.J. Blinowska, High resolution parametric description of slow-wave sleep. *J. Neurosci. Methods* **147**, 15 (2005)
66. R. Brunelli, *Template Matching Techniques in Computer Vision: Theory and Practice* (Wiley, Chichester, 2009)
67. E. Sitnikova, E.L.M. van Luijtelaar, Cortical and thalamic coherence during spike–wave seizures in WAG/Rij rats. *Epilepsy Res.* **71**, 159 (2006)
68. G. Buzsaki, A. Draguhn, Neuronal oscillations in cortical networks. *Science* **304**, 1926 (2004)
69. N.E. Sviderskaya, *Synchronous Electrical Activity of Brain and Psychic Processes* (Nauka, Moscow, 1987)
70. A.A. Ovchinnikov, T.P. Evstigneeva, A.A. Koronovskii, E. Sitnikova, A.O. Manturov, A.E. Hramov, Dynamics of hypersynchronous epileptic discharges in EEG in patients with absence epilepsy, in *Proceedings of Conference “Nonlinear Dynamics in Cognitive Studies”*, Institute of Applied Physics of Russian Academy of Science, Nizhnij Novgorod, Russian Federation, 2011, pp. 140–142

71. C.P. Panayiotopoulos, Typical absence seizures and their treatment. *Arch. Dis. Child.* **81**(4), 351 (1999)
72. T. Deonna, Management of epilepsy. *Arch. Dis. Child.* **90**(1), 5 (2005)
73. I. Westmijse, P. Ossenblok, B. Gunning, E.L.M. van Luijtelaar, Onset and propagation of spike and slow wave discharges in human absence epilepsy: a MEG study. *Epilepsia* **50**, 2538 (2009)
74. V.V. Gnezditskii, *The Inverse Problem of EEG and Clinical Encephalography* (Taganrog University Press, Taganrog, 2000)
75. P.A. Tass, M.G. Rosenblum, J. Weule, J. Kurths, A. Pikovsky, J. Volkmann, A. Schnitzler, H.-J. Freund, Detection of $n : m$ phase locking from noisy data: application to magnetoencephalography. *Phys. Rev. Lett.* **81**(15), 3291 (1998)
76. P.A. Tass, T. Fieseler, J. Dammers, K.T. Dolan, P. Morosan, M. Majtanik, F. Boers, A. Muren, K. Zilles, G.R. Fink, Synchronization tomography: a method for three-dimensional localization of phase synchronized neuronal populations in the human brain using magnetoencephalography. *Phys. Rev. Lett.* **90**(8), 088101 (2003)
77. P. Gong, A.R. Nikolaev, C. van Leeuwen, Intermittent dynamics underlying the intrinsic fluctuations of the collective synchronization patterns in electrocortical activity. *Phys. Rev. E* **76**(1), 011904 (2007)
78. I.S. Midzianovskaia, G.D. Kuznetsova, A.M. Coenen, A.M. Spiridonov, E.L.M. van Luijtelaar, Electrophysiological and pharmacological characteristics of two types of spike-wave discharges in WAG/Rij rats. *Brain Res.* **911**, 62 (2001)
79. H.K. Meeren, J.P. Pijn, E.L.M. van Luijtelaar, A.M. Coenen, F.H. Lopes da Silva, Cortical focus drives widespread corticothalamic networks during spontaneous absence seizures in rats. *J. Neurosci.* **22**, 1480 (2002)
80. N.E. Sviderskaya, T.N. Dashinskaja, G.V. Taratunova, Spatial organization of EEG activation during the creative processes. *J. High. Nerv. Act.* **51**, 393 (2001)
81. V.N. Dumenko, *High-Frequency Components in EEG and Instrumental Learning* (Science, Moscow, 2006)
82. V.N. Dumenko, The phenomenon of spatial synchronization between the potentials of the cerebral cortex in a wide frequency band 1–250 Hz. *J. Neurosci. Methods* **55**(5), 520 (2007)
83. N.E. Sviderskaya, *Spatial Organization of Electroencephalogram* (VGMA Press, Voronezh, 2008)

Chapter 7

Automatic Diagnostics and Processing of EEG

Abstract This chapter considers basic problems of automatic diagnostics and processing of EEG. We discuss the wavelet-based techniques in order to fully automatize “routine” operations, such as visual inspection of EEG. In addition to that, we exemplify some practical applications of wavelet methods for automatic analysis of pre-recorded signals of neuronal activity (*off-line* diagnostics), and also some examples of EEG analysis in real-time (*on-line*). We also discuss principles of fast and precise detection of transient events in EEG and organization of closed-loop control systems that can be used in BCI. Finally, we consider methods of artifact suppression in multichannel EEG based on a combination of wavelet and independent component analysis.

7.1 Introduction

Electroencephalographic signals (EEG) reflect synchronous synaptic activity produced by different brain areas located close enough to the recording electrode. Thus, EEG recordings can be used as a tool for studying information processing or for monitoring the brain activity and detecting abnormal changes. Importantly, EEG recorded from multiple electrodes placed on the scalp offers a non-invasive low-cost technique with multiple medical and technological applications. Therefore, developing new methods and expert systems for the analysis of EEG signals is an important trend, both in fundamental neuroscience and in clinical practice.

In this chapter we discuss several automatic and semi-automatic methods for processing EEG signals using wavelets. In the past few decades, the wavelet approach has been consolidated as an important tool in studying EEG. This is explained in part by a certain degree of linearity in EEG signals that can be considered as a linear mixture of coexisting oscillatory components of different origin. Thus, nonlinear effects can be neglected in the first approximation, thus allowing linear models of EEGs. This in turn facilitates decomposition of EEG by linear methods like the wavelet transform or independent component analysis

into spectral and/or temporal components containing some desired properties. For example, in Sect. 7.2, we use a wavelet decomposition of EEG to identify specific patterns of absence epilepsy in the gamma frequency band. It appears that this band, which is not the most powerful in the spectrum of spike-wave discharges, is in fact the most representative.

When speaking about automatic or semi-automatic methods, one must distinguish *off-line* and *on-line* processing of EEG. In the first case we deal with a previously recorded EEG with access to the full data set. Thus, for a given time point $t = t^*$, we know not only the “past” ($t < t^*$), but also the “future” ($t > t^*$) data samples. This allows one to compute the wavelet transform normally. In the case of on-line or real time processing, we have two additional difficulties. First, the “future” data samples are not available, which forces special adaptation of the wavelet transform. Second, real time calculations impose strong limitations on algorithm complexity. It must be fast enough to carry out the necessary calculations within the time window between two consecutive data samples.

The use of on-line algorithms is a must in the study of brain-computer interfaces [5, 14, 33, 43, 59, 67, 70, 72, 78, 83, 90, 97, 113, 120, 128, 129, 136]. In particular, the spectral characteristics of the activity of the sensorimotor cortex are related to movements of the limbs. This finding underlies apparatus improving the life-quality of paralyzed patients and can be used for selection of letters or phrases on a screen [33, 57, 71, 98, 109]. Methods capable of diagnosing pathological brain activity in real-time are equally important [84]. In particular, on-line detection of spike-wave discharges could be used to trigger the presentation of external stimuli to study information processing during periods of reduced consciousness [25], or to trigger automatic electrical brain stimulation upon appearance of spike-wave discharges [8]. In Sect. 7.3, we provide an algorithm for real-time diagnostics of epileptic seizures and discuss its experimental implementation.

Advanced automatic methods could significantly improve systems monitoring brain activity. In Sects. 7.4 and 7.5, we consider automatic detection and discrimination of sleep spindles and 5–9 Hz oscillations by means of standard Morlet-based and adaptive wavelet analysis. Then we demonstrate the application of the methods to long-term EEGs. Such methods significantly reduce the time of EEG analysis and errors when dealing with large amounts of data.

The identification of spike-wave discharges and sleep spindles in long recordings offers the possibility of studying their temporal dynamics. In Sect. 7.6, we apply methods of nonlinear dynamics and study on-off intermittency of spike-wave discharges, sleep spindles, and 5–9 Hz oscillations. This allows us to show that the first two patterns are likely to follow deterministic chaotic behavior, whereas 5–9 Hz oscillations exhibit different dynamics. Such findings provide insight into the thalamo-cortical network that lies behind the patterns.

Optimal identification of multiple patterns coexisting in EEG requires fine tuning of many parameters controlling the algorithm. This may be achieved through tedious empirical work or by employing some optimization algorithm. In Sect. 7.7, we discuss serial identification of EEG oscillatory patterns using methods from

optimization theory and adaptive wavelet-based analysis. The method can lead to a significant reduction in identification errors compared to the empirical approach.

Finally, in Sect. 7.8, we study the problem of artifact suppression in multi-electrode EEG recordings from the scalp. Such recordings have multiple artifacts due to eye movements, blinking, muscle activity, etc. There are two major ways to get rid of artifacts:

- Selection of artifact free epochs, which leads to a drastic reduction of available data, and
- Filter-like procedures.

The latter is more attractive, but requires advanced methods. Our wavelet enhanced independent component analysis provides a satisfactory solution to this problem. This method has now become a standard procedure for artifact suppression in EEGs.

7.2 Automatic Identification of Epileptic Spike–Wave Discharges

7.2.1 *General Aspects of Automatic SWD Detection in EEG*

Spike–wave discharges (SWD), typical in cases of absence epilepsy, are represented in the EEG in the form of a two-component complex containing spike and wave (see Sect. 5.3.3, Fig. 5.4). In WAG/Rij rats, the duration of SWDs ranges from 1 to 30 s, and their average number in mature animals is about 15–20 per hour.

At first glance the problem of automatic detection of spike–wave discharges may seem trivial. Indeed, one solution arises directly from the definition of an SWD as an event with oscillation amplitude significantly higher than the background EEG. Thus one could monitor the oscillation amplitude and simply detect events when it overcomes some threshold. However, such a straightforward approach will have poor performance. There are three main reasons. First, besides SWDs, the typical EEG contains other high amplitude patterns, such as sleep spindle waves [112] (see Fig. 5.2, and also Sect. 6.3). Second, the amplitude of the background (desynchronized) EEG can differ essentially with regard to various types of electrical activity (e.g., in sleep and wakeful states). Third, there are SWD-like events with duration less than 1 s that have very similar structure, but are not considered pathological [111]. Thus a more advanced method is required.

In the literature there is a great variety of different methods for recognition of spike–wave discharges. We can separate them into three classes. The first class uses the nonlinear dynamics approach and quantifies different features of EEG signals, such as Lyapunov exponents [2] or entropy [58]. The second class uses artificial neural networks and learning algorithms for data classification [35]. The third class of methods attempts to formalize the definition of the SWD and compares statistical features of different typical epochs in the EEG [12, 81].

It should be noted that some of these methods present the following drawbacks:

- Not applicable for real-time signal processing, e.g., methods based on the calculation of Lyapunov exponents or entropy.
- Low accuracy, e.g., methods estimating statistical properties of different epochs.
- Unstable performance, requiring adjustment of parameters for each individual EEG, e.g., methods based on artificial neural networks.

Applications of the discrete wavelet transform to detection of SWDs has been reported in [118]. Below, we shall discuss methods based on the continuous wavelet transform that provide some benefits over DWT.

7.2.2 *Off-Line Wavelet-Based Algorithm for Automatic Detection of SWDs*

Let us consider an off-line method for automatic detection of epileptic spike–wave discharges in a previously recorded EEG [39, 112]. A practical implementation of this method has been used to detect SWDs in long-term EEG recordings in WAG/Rij rats with a predisposition to absence epilepsy. We used a single-channel EEG recorded from the frontal cortex (the detailed experimental procedure can be found in Sect. 6.2).

Analysis of a large number of SWDs allowed us to reveal some particular features in their time–frequency structure, namely, the occurrence of the corresponding patterns in the EEG was accompanied by a sharp increase in the spectral power in the gamma frequency range (20–50 Hz). Importantly, such an increase does not appear during other strongly pronounced EEG patterns like sleep spindles. Therefore, a sharp increase in the gamma spectrum can serve as a marker for SWDs.

A natural way to detect an increase in the power in the gamma band is to use a wavelet transform. The main idea is to estimate the instantaneous energy of the wavelet spectrum in this frequency band and compare it with a threshold. If the energy exceeds a certain critical value (threshold), then the expert system draws its conclusion with regard to the presence of an SWD [63, 65, 66].

Figure 7.1 shows a typical energy distribution $E(f)$ (see (2.33)) of the wavelet spectrum for an SWD, a sleep spindle, and the background EEG. The fundamental frequency of the SWD oscillations is about 8 Hz, which corresponds to the strongest peak in the wavelet spectrum. However, at low frequencies ($f < 15$ Hz), this peak overlaps with the spectral peak of spindle waves, whence SWD and spindle events may be confused. Nevertheless, SWD epochs show high power at higher frequencies $f > 15$ –20 Hz, i.e., in the gamma frequency band, due to the presence of the second and third harmonics of the fundamental SWD frequency (see Figs. 5.7 and 7.1, harmonics are marked by arrows). Thus each individual peak, a part of the spike-and-wave complex, is displayed in the wavelet spectrum as a local burst in the wavelet power (see, for example, Fig. 5.5).

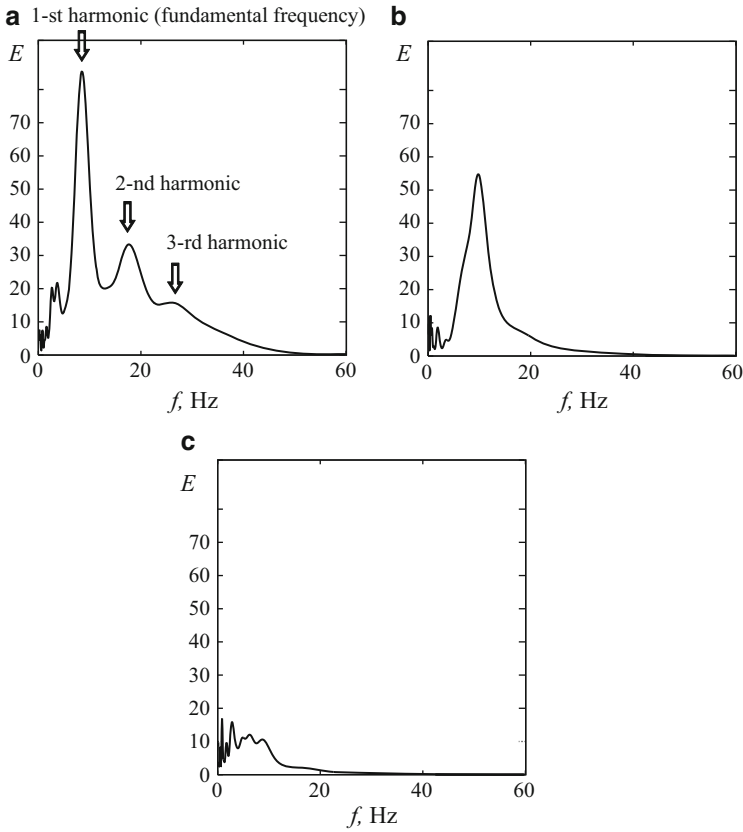


Fig. 7.1 Typical distributions of the wavelet spectrum energy $E(f)$ over frequencies characterizing different oscillatory patterns in WAG/Rij rat EEGs. (a) Spike–wave discharge. *Arrows* mark the fundamental frequency of SWD oscillations and its harmonics. (b) Sleep spindles. (c) Background EEG. Wavelet spectra were calculated using the Morlet wavelet

Let $F_{\text{SWD}} = 30\text{--}50\text{ Hz}$ be the characteristic frequency range of apparent structural differences between spike–wave discharges and other oscillatory patterns. Since we expect an increase in the energy in this frequency range during SWDs, it is convenient to consider the following integral energy:

$$w_{F_{\text{SWD}}}(t) = \int_{F_{\text{SWD}}} |W(t, f)|^2 df . \tag{7.1}$$

If a spike–wave discharge occurs at a certain time t , then the following relation holds:

$$w_{F_{\text{SWD}}}(t) \geq E_k , \tag{7.2}$$

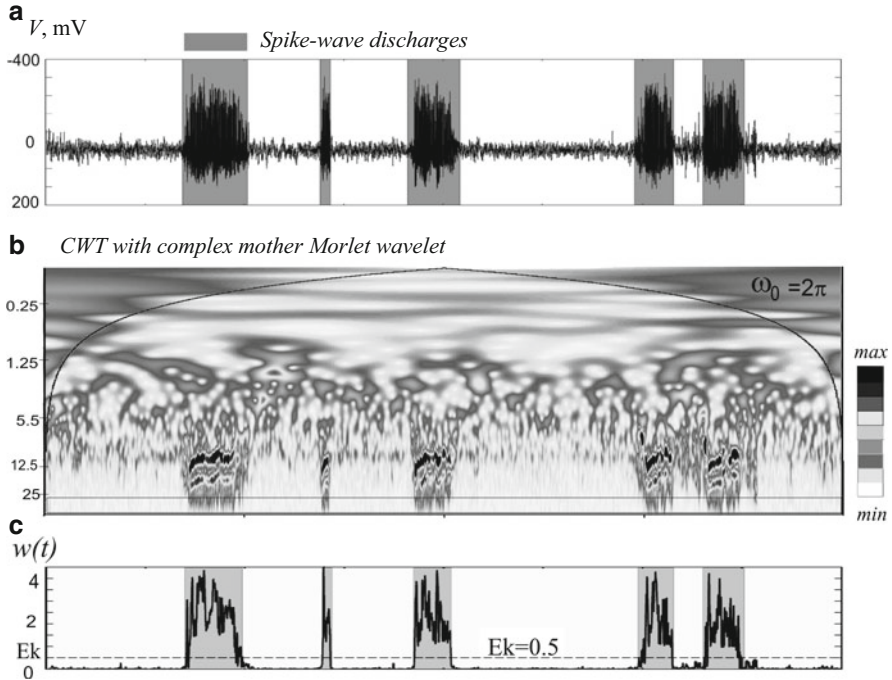


Fig. 7.2 Typical results from automatic recognition of SWDs using a wavelet-based method with a Morlet wavelet with central frequency $\omega_0 = 2\pi$. (a) EEG fragment with spike–wave discharges marked by grey rectangles. (b) Modulus $|W(f,t)|$ of the wavelet spectrum corresponding to this EEG. The dome-shaped curve in the wavelet spectrum outlines a confidence (upper) area in which boundary effects are significant (see Sect. 2.3.3.3). (c) Time-dependence of the instantaneous energy $w(t)$ (7.1) averaged over the characteristic frequency range $F_{\text{SWD}} = 30\text{--}50$ Hz. SWDs were recognized automatically using the value of the wavelet energy $w(t)$ when $w(t) > E_k$, where E_k is the threshold level (dashed line)

where E_k is the experimentally determined threshold energy.

For automated delimitation of epileptic events, we used the method of threshold sorting. Time instants at which the value of w_{F_s} (7.2) exceeded the threshold E_k and did not decrease within the following 1 s were regarded as onsets of epileptic activity. Time instants when the energy level dropped below the threshold were considered as the ends of SWDs.

Figure 7.2a shows an EEG epoch with five spike–wave discharges (grey rectangles) corresponding to epilepsy paroxysms. Figure 7.2b, c illustrate the modulus $|W(f,t)|$ of the wavelet spectrum obtained with the Morlet wavelet (central frequency $\omega_0 = 2\pi$ rad/s) and the corresponding integral energy $w_{F_{\text{SWD}}}(t)$. Identification of SWDs is carried out using the criterion (7.2). The threshold level $E_k = 0.5$ is indicated by the dashed line in Fig. 7.2c. Thus in the integral wavelet spectrum, SWDs (highlighted in grey) are easily recognized by simple thresholding.

Table 7.1 Results of automatic identification of SWD using the CWT with the complex Morlet wavelet ($\omega_0 = 2\pi$ rad/s)

Rat #	Visual detections N_{expert}	Automatic detections			Performance of automatic detections		
		TP	FP	FN	Accuracy $\rho_{\text{SWD}} [\%]$	Sensitivity $\beta [\%]$	Specificity $\delta [\%]$
1	105	105	0	0	100.0	100.0	100.0
2	81	79	2	1	97.5	98.8	97.5
3	249	247	1	2	99.2	99.2	99.6
4	120	117	1	3	97.5	97.5	99.2
5	66	65	2	1	98.5	98.5	97.0
Mean \pm SD					98.5 \pm 1.1	98.8 \pm 0.9	98.7 \pm 1.3

7.2.3 Performance of the Method

The performance of the above-described method has been evaluated by measuring the percentage of true positive/negative and false positive/negative detections. We also computed the sensitivity and specificity of the method. True positives (TP) are defined as the number of correctly detected SWDs. True negatives (TN) are the number of correctly rejected SWD-like events. Then false positives (FP) and false negatives (FN) represent the numbers of events wrongly identified as SWDs and SWDs missed by the method, respectively.

Primarily the accuracy of the automatic recognition of absence epileptic oscillatory patterns was computed as

$$\rho_{\text{SWD}} = \frac{\text{TP}}{N_{\text{expert}}} \times 100 \% , \quad (7.3)$$

where N_{expert} is the number of SWD events selected by an operator, expert in SWD neurophysiology. Table 7.1 summarizes the main results for the automatic identification of spike–wave discharges.

Using $F_{\text{SWD}} = 30\text{--}50$ Hz and $E_k = 0.5$, we achieved successful identification of almost all SWD events in all animals. The obtained accuracy oscillates between 97.5 and 100 % (mean 98.5 %, $n = 5$). The rate of incorrect detections or false positives was below 1.8 %. Thus, SWD events can be faithfully distinguished from the non-epileptic background EEG by the described method. We note that SWDs were automatically recognized with the same parameters (F_{SWD} and E_k) in all animals. Thus the parameter choice is quite robust and requires no further tuning.

The quality of the algorithm’s performance, i.e. correctness of the “binary” solution on the presence/absence of an epileptic event (SWD) was statistically analyzed using a criterion that provided false result with a certain degree of probability: the sensitivity δ and specificity β [16]. The sensitivity and specificity were assessed using the definitions

$$\delta = \frac{TP}{TP + FN} \times 100 \% , \quad (7.4)$$

$$\beta = \frac{TP}{TP + FP} \times 100 \% . \quad (7.5)$$

The first characteristic δ is used to estimate the sensitivity of the method, i.e., the percentage of recognized spike–wave discharges out of the total number in the analyzed EEG fragment. The second characteristic β estimates the percentage of events correctly identified as spike–wave discharges out of the total number of events diagnosed as spike–wave discharges. These characteristics also exceed 98 % (Table 7.1), which is more than acceptable for automatic methods processing neurological signals.

Thus, our findings show that the automatic wavelet-based method for recognition of SWDs may significantly surpass the available standard techniques in terms of accuracy and simplicity of application (no tuning is required). Moreover, the method has a great potential for detection of other oscillatory patterns in EGG.

7.3 Brain–Computer Interface for On-Line Diagnostics of Epileptic Seizures

In Sect. 7.2, we described an *off-line* method for automatic identification and delimiting of epileptic EEG epochs. It is restricted to use with complete (previously recorded) time series. Here we present a description and an experimental verification of a real-time algorithm for detection of SWDs in the EEGs of a genetic rodent model (WAG/Rij rats).

7.3.1 On-Line SWD Detection Algorithm

Diverse EEG patterns belonging to different classes may have similar spectral composition [60, 94]. Therefore, a method used for pattern recognition should adequately distinguish among such patterns with similar frequency content and, in addition, must be numerically efficient to allow hardware or software implementation for on-line EEG analysis [79, 94, 131].

Another significant problem stemming from the on-line data processing is a lack of knowledge of the full time realization. Indeed, at a given time instant t_0 , only the preceding time instants ($t \leq t_0$) are available for the analysis. Thus, the problem of developing a universal method for diagnosis of oscillatory patterns in real-time is extremely complex. Therefore, in this section we provide a brief description of an already existing and tested method for on-line detection of spike–wave discharges [67, 90, 91].

The first problem mentioned above can be reasonably solved by using a complex Morlet wavelet. This wavelet offers optimal selectivity in terms of time-spectral resolution and can distinguish similar oscillatory patterns. The second problem (data restriction to $t \leq t^*$) can be solved if we select a mother wavelet function ψ that decays rapidly in time. Then the definition (2.18) can be replaced by (2.44) with high enough accuracy (for details, see Sect. 2.3.3). In other words, to calculate the wavelet coefficients for a given time scale s at some fixed time instant t^* , we need to have a fragment of signal with $t \in [t^* - T, t^* + T]$. Therefore, we can only determine whether there was an SWD at $t = t^*$ when we reach time $t = t^* + T$, i.e., with a time lag T , which is essentially unremovable using this method. The value of T depends on the mother wavelet and the time scale s (wavelet frequency $f_s \approx 1/s$). In the case of the Morlet wavelet, we can take $T \approx 4$ s.

Let us now discuss the key features of an on-line diagnostic algorithm for detecting oscillatory patterns in EEGs, as proposed in [90, 91]. The method is based on the approach considered in Sect. 7.2. First, the wavelet transform (2.44) is calculated using the Morlet wavelet with central frequency $\omega_0 = 2\pi$ rad/s. Second, a measure of the spectral energy within the frequency range F_{SWD} is introduced (see also (7.1)):

$$w_{F_{\text{SWD}}}(t) = \int_{F_{\text{SWD}}} |W(t, f)| df. \quad (7.6)$$

This is the integral measure of the absolute value of wavelet coefficients over the given frequency domain, i.e., the *wavelet power over domain* (WPOD).

As in Sect. 7.2, we selected the gamma frequency band $F_{\text{SWD}} = 30\text{--}80$ Hz, since it is the most characteristic for distinguishing SWDs and spindle waves. The wavelet power $w_{F_{\text{SWD}}}(t)$ in this frequency range can be calculated with a delay of about 4 s $\approx 4 \times 1/30 \approx 0.14$ s. If $w_{F_{\text{SWD}}}(t)$ shows a drastic growth, then we can mark this time instant as the beginning of an SWD. A similarly rapid decrease in the power marks the end of the SWD. Thus fulfillment of the condition $w_{F_{\text{SWD}}}(t) > E_k$ (see (7.2) in Sect. 7.2) is the basic guideline for detecting an SWD at time $t = t_{\text{current}} - T$.

We note that an EEG is a complex signal, which may have relatively short bursts provoked by motion artifacts, K-complexes, and other events [138]. Then the spectrum of bursting activity can overlap with F_{SWD} and we can observe a rapid growth of the WPOD measure $w_{F_{\text{SWD}}}(t)$, which may exceed the threshold E_k . Thus some bursting activity in EEG can lead to false detection of spike–wave discharges, i.e., *false positive errors* (FP). Figure 7.3a, b show an example of this situation. An EEG epoch has an SWD and an artifact (arrow). Then the WPOD $w_{F_{\text{SWD}}}(t)$ calculated over this epoch shows a strong pulse corresponding to the artifact. The pulse amplitude is significantly higher than the background oscillations of $w_{F_{\text{SWD}}}(t)$ and hence, during on-line processing, we could wrongly detect such a pulse as the marker of an SWD event.

To reduce the number of such false positive detections, we could use a higher value of the threshold E_k . However, this may not help (as in Fig. 7.3b), but merely

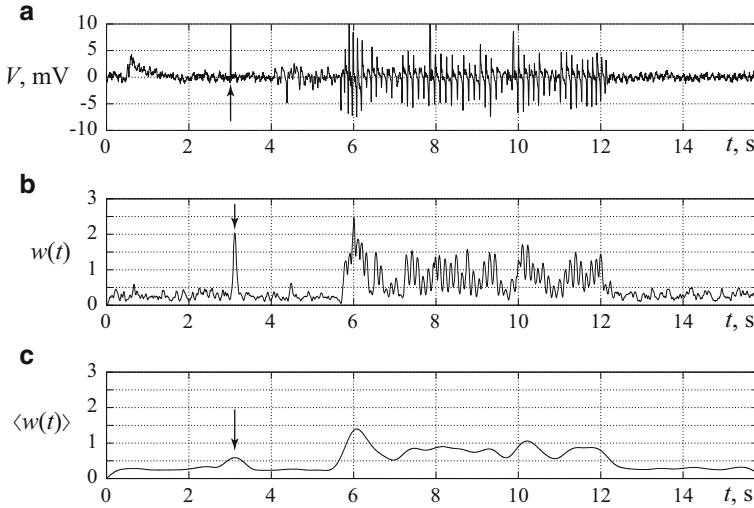


Fig. 7.3 (a) Fragment of an EEG containing a single pulse of high amplitude (*arrow* at 3 s) and a spike–wave discharge (5.5–12.3 s). (b) Instantaneous WPOD energy $w_{F_{\text{SWD}}}(t)$ with an artificial peak (*arrow*) corresponding to the single pulse in the EEG ($F_{\text{SWD}} = 30\text{--}80$ Hz). (c) The artificial peak is attenuated in the time-averaged measure $\langle w_{F_{\text{SWD}}}(t) \rangle$ ($\Delta = 0.2$ s)

increase the number of false negatives. Besides, a higher threshold would introduce an additional time delay into the onset of the SWD. Another way to reduce the number of false positives is to consider an averaged value of $w_{F_{\text{SWD}}}(t)$ over some smoothing window Δ :

$$\langle w_{F_{\text{SWD}}}(t) \rangle = \frac{1}{\Delta} \int_{t-\Delta/2}^{t+\Delta/2} w_{F_{\text{SWD}}}(\tau) d\tau . \quad (7.7)$$

Then the criterion for detecting a spike–wave discharge is

$$\langle w_{F_{\text{SWD}}}(t) \rangle > E_k . \quad (7.8)$$

Figure 7.3c shows this new measure $\langle w_{F_{\text{SWD}}}(t) \rangle$. One can see that the artificial peak becomes much lower, so we can detect SWD events with higher accuracy and exclude incidental short EEG events. Increasing the averaging window Δ , we can achieve more accurate detection (better smoothing of short artificial events). However, averaging introduces an additional delay of order $\Delta/2 = 0.1$ s into the detection of SWD patterns. There is thus a tradeoff between detection accuracy and detection delay.

Figure 7.4 shows a flowchart for implementation of the on-line method for detecting SWDs, called OSDS. To compute the wavelet transform we used the

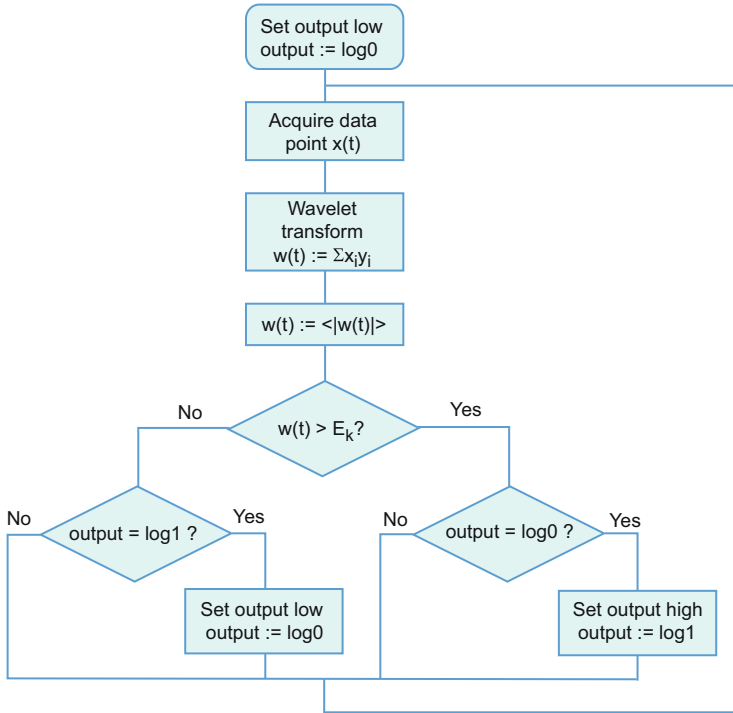


Fig. 7.4 Flowchart of the on-line algorithm for detecting epileptic seizures (OSDS). $w(t)$ is the WPOD (defined by (2.47)), E_k is the threshold for the WPOD, x_i and y_i are the discrete values of the EEG signal and preliminary calculated mother wavelet function, respectively, and $\log 0$ and $\log 1$ are the logical zero (absence of SWD) and one (presence of SWD) of the algorithm output, respectively

fast method based on the vector product (2.47) discussed in Sect. 2.3.3.1. The program calculates the corresponding wavelet power for a given frequency range (30–80 Hz) each time a new data sample is acquired (e.g., every 2 ms for 500 Hz sampling rate). The calculated power is compared with a threshold and a binary output (presence/absence of SWD) is generated.

More precisely, the program performs the wavelet transform for 15 scales (corresponding to frequencies equally distributed in the range 30–80 Hz). Our results show that increasing the number of scales above 15 provides no significant improvement in the algorithm sensitivity, but rather requires additional calculation resources (the calculation time must be kept within 2 ms). The sum of the calculated wavelet power values provides $w_{F_{SWD}}(t)$, which is further averaged and compared to the threshold E_k . The result of the comparison is assigned to the output logical variable

$$V_{out}(t) \in \{\log 0, \log 1\} .$$

At the beginning, it is set to logical zero, i.e., $V_{\text{out}} = \log 0$. As soon as $w_{F_{\text{SWD}}}(t)$ exceeds the threshold E_k , the output is set to logical one, i.e., $V_{\text{out}} = \log 1$. The output is maintained until $w_{F_{\text{SWD}}}(t)$ goes below E_k , at which point the output is switched to logical zero, i.e., $V_{\text{out}} = \log 0$.

We note that the algorithm can also be used to detect other kinds of oscillatory patterns in EEG.

7.3.2 *Experimental Verification of the Algorithm and On-Line SWD Diagnostics*

To test the algorithm, we used differential recordings made in eight rats [90]. The EEG was continuously acquired over 5 h during the light phase (5–15 h).¹ In addition, two of the 8 rats were subject to continuous 24 h recording. Rats were connected to EEG recording leads attached to a swivel contact, which allows registration of the EEG in freely moving animals. Signals were recorded using the WINDAQ recording system (DATAQ Instruments, Akron, OH, USA, www.dataq.com) with a constant sample rate of 500 Hz. Before digitizing, the EEG signal was amplified and filtered by a band pass filter with cutoff frequencies set at 1 and 100 Hz. In addition, a 50 Hz notch filter was applied to reject power line hum. The digitized signal was sent to the OSDS (Fig. 7.4).

Figure 7.5 shows a typical example of on-line SWD detection. Whenever the WPOD $w_{F_{\text{SWD}}}(t)$ exceeds the threshold $E_k = 0.8$, an SWD is detected (Fig. 7.5b). The threshold value E_k should be adjusted for each animal individually. A good initial guess is 2.5–3.5 times the mean WPOD value at normal activity (i.e., non-epileptic background). The algorithm output $V_{\text{out}}(t)$ (Fig. 7.5c) is sent to an additional channel of the WINDAQ recording system. This channel has a digital–analog converter (DAC) with two possible levels: *high* ($\log 1 := +2.5 \text{ V}$) and *low* ($\log 0 := -2.5 \text{ V}$).

The output signal $V_{\text{out}}(t)$ of the OSDS delimits SWD events and, in general, can also control some external device, such as a generator sending some stimuli to the animal's brain. Thus an organized feedback loop can be used, e.g., for studying the effect of external stimuli on epileptic focus, synchronized with the onset of the epileptic neuronal activity.

In experiments, we determined the most adequate individual threshold values E_k using off-line analysis of EEG traces for each rat. One hour EEG fragments were analyzed and E_k was tuned. E_k varied between 0.6 and 1.0 for different animals. This approach allowed us to achieve perfect sensitivity to SWDs for all animals, that is, $\delta = 100\%$ (Table 7.2), i.e., there were no false negative detections. The

¹The experimental system OSDS (*on-line SWD detection system*) was designed and developed at the Donders Institute of Brain, Cognition and Behavior, Radboud University Nijmegen, The Netherlands.

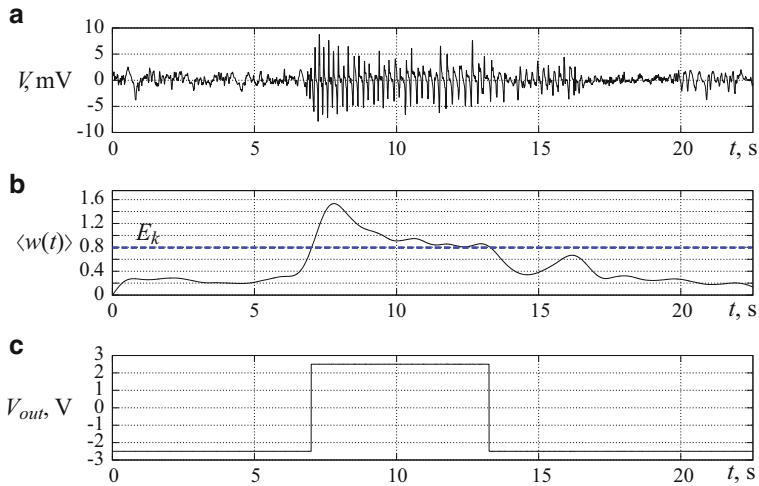


Fig. 7.5 On-line detection of SWDs. (a) Example of an EEG epoch containing SWDs. (b) WPOD averaged power in the 30–80 Hz band. (c) Output of the detection algorithm (OSDS)

mean precision was $\beta = 96.9\%$ (range 94.3–100%, $n = 8$) in the 5 h data set. The average time needed for SWD detection was 1.0 ± 0.55 s following the SWD onset (smoothing window size 500 data points and sample rate 500 samples/s). The SWD detection time is determined primarily by the length of the smoothing window and can be reduced.

The results of the second experimental data set of 24 h EEGs recorded in two rats are presented in Fig. 7.6. The number of incorrectly detected events remains at an acceptably low level throughout the 24 h experiment. The rats had 300–400 SWDs during the 24 h period, with a mean duration of 6.6 s. This agrees with earlier findings in WAG/Rij rats of the same age [111, 126].

Let us now consider the errors in the OSDS algorithm. False negative (FN) errors (SWD events skipped by the algorithm) appear in the first place due to small variations in the dynamics of the brain in response to changes in environmental conditions. In relatively short experiments with properly chosen parameters, FN errors do not appear (Table 7.2). In long-term experiments, FN events are rare and can be observed when the physiological state of the animal changes significantly (Fig. 7.6). The first missed events begin to appear 4–8 h after the beginning of the EEG recording. Such events tend to group together, i.e., within a few hours after registration of the SWD with subthreshold WPOD value, the probability of finding another one becomes greater. At the same time, the total number of unrecognized SWD events remains small (<1% of all detected SWDs).

Another class of errors is false positives (FP), i.e., events wrongly detected as being SWDs. Figure 7.7 illustrates detection of an underdeveloped SWD. Despite the fact that the increase in the WPOD in this case was not as large as during a genuine SWD, it was enough to exceed the threshold and hence lead to false detection of an SWD event. Visual inspection of FP events showed that they

Table 7.2 On-line detection rates of spike-wave discharges in 8 WAG/Rij rats recorded for 5 h

Rat #	Threshold	Window size (data points)	No of visual detections	No of automated detections			Quality of on-line detections		
				TP	FP	FN	Sensitivity β [%]	Precision δ [%]	
1	0.6	600	101	3	0	100	97.1		
2	0.7	500	29	0	0	100	100		
3	0.7	500	43	2	0	100	95.6		
4	0.65	600	66	1	0	100	98.5		
5	0.8	500	44	2	0	100	95.7		
6	0.6	500	66	4	0	100	94.3		
7	0.85	500	115	3	0	100	97.5		
8	0.9	600	56	2	0	100	96.6		
Mean \pm SD			65 \pm 29	2.1 \pm 1.3	0.0 \pm 0.0	100 \pm 0	96.9 \pm 1.8		

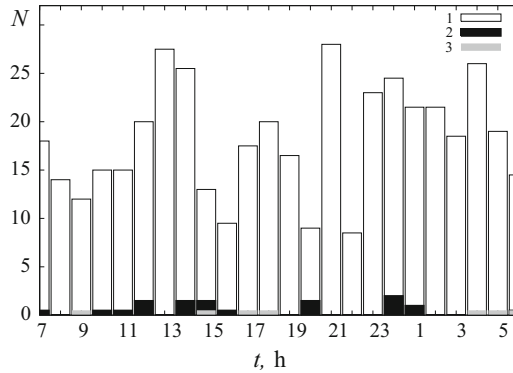


Fig. 7.6 Detection rates of spike-wave discharges for each hour during 24 h recording in two animals. (1) True SWD detections. (2) False positive SWD detections. (3) False negative SWD detections (missed events)

correspond to *intermediate states* or spiky phenomena [32]. It should be noted that, by increasing the size Δ of the smoothing window, the number of false positives can be reduced significantly. However, this will be achieved at the cost of increasing the time lag required for reliable detection of SWD events. The results shown in Table 7.2 were obtained through a compromise between speed of detection and number of FP errors.

The two most important parameters determining algorithm performance are the threshold value E_k and the size Δ of the smoothing window. Figure 7.8 shows the dependence of true detections and missed SWDs on these parameters, as obtained from a 5 h EEG recording. It can be inferred from these maps that there are some areas (combinations of threshold values and smoothing window sizes) for which all SWDs can be detected, while the number of false detections and missed events is kept close to zero. These areas correspond to the threshold $E_k \sim 0.7\text{--}0.9$ and the window size $\Delta \sim 0.4\text{--}0.6$ s.

It should be noted that these maps provide all knowledge required to make an appropriate choice of the two parameters. However, it is not necessary to compute the whole map to find the best parameters, as the area of feasible window sizes does not vary much from animal to animal. It is more practical to establish the number of false detections and missed events for the chosen threshold value and to use the median value of the range as a suitable window size.

7.4 Automatic Detection of Sleep Spindles by Adaptive Wavelets

In Sect. 6.5, we discussed how one can create different types of adaptive wavelet bases, so-called *adaptive spindle wavelets*. Such wavelets are tuned optimally to the structure of various kinds of oscillatory EEG patterns appearing during sleep (sleep

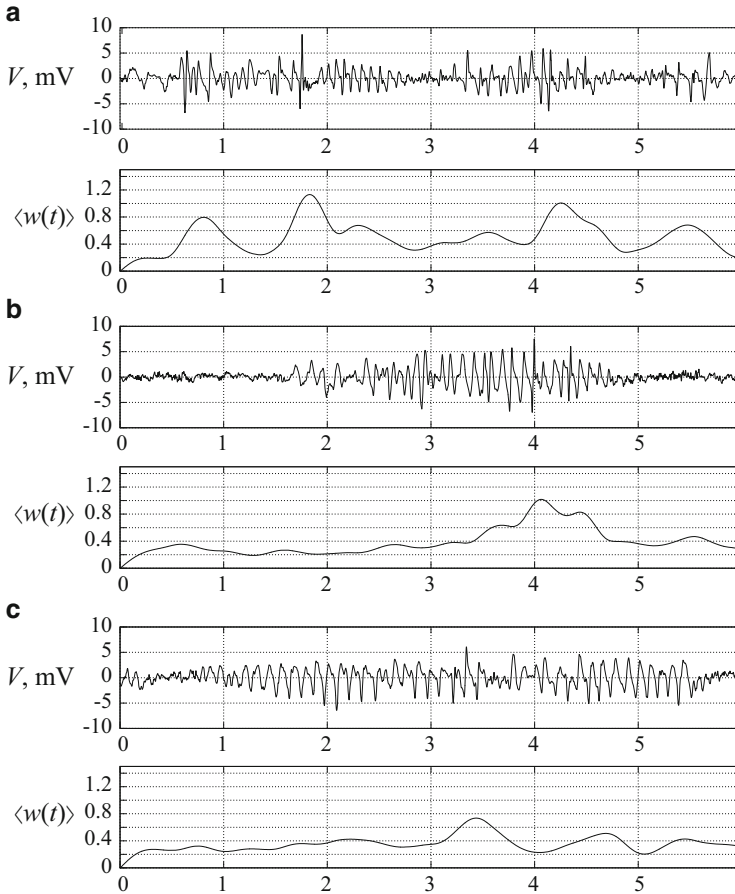


Fig. 7.7 Illustrative examples of typical complexes in EEG (intermediate states) falsely detected as SWDs and corresponding dynamics of the averaged WPOD $\langle w(t) \rangle$ versus time

spindles and 5–9 Hz oscillations). Although the variability in the waveform of sleep spindles was rather high, we were able to distinguish two types of sleep spindles with different shapes, frequency spectra, and times of occurrence (see Fig. 6.13). Sleep spindles showed different degrees of conformity to the two types of spindle wavelets. Type 1 sleep spindles had a typical waveform and predominated during slow-wave sleep. Type 2 spindles had an atypical form and were picked out by the adaptive spindle wavelets 2 which were individual for each rat. These type 2 spindles might be considered as a transitory oscillatory waveform between spindle and SWD in WAG/Rij rat EEGs.

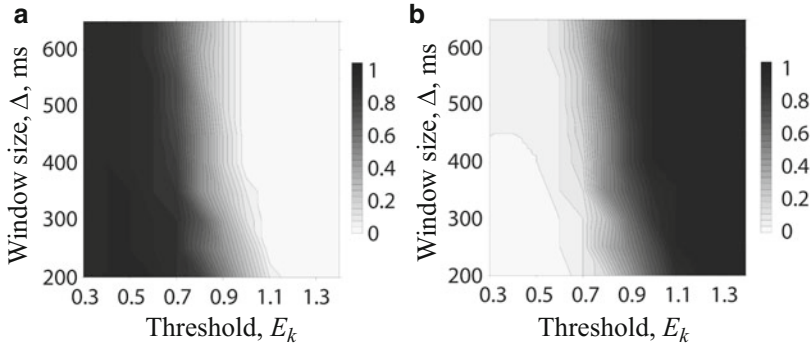


Fig. 7.8 (a) Normalized numbers of true SWD detections. (b) Missed SWDs as a function of window size and threshold

Constructed adaptive wavelet bases can also be used to mark sleep spindle events in the automatic regime [112]. For automatic detection of sleep spindles, we can use the approach discussed in Sect. 7.2, based on the method of threshold sorting (7.2) of the wavelet power $w(t)$, over the typical frequency domain F_S .

Table 7.3 shows separately the results of automatic recognition of sleep spindles of types 1 and 2. The notation is similar to that adopted in Table 7.1. This facilitates comparison with the OSDS algorithm for SWD recognition. Table 7.4 shows the performance of automatic detection of sleep spindles in the EEG by means of the spindle wavelet-based algorithm. When spindle wavelet 1 was used for automatic recognition of spindle events, about 87.4% of sleep spindles (so-called type 1 sleep spindles) were identified correctly in the frequency band $F_{sp1} \in (f_1, f_2) = (7, 14)$ Hz (Tables 7.3A and 7.4). Note that type 1 sleep spindles were recognized with the aid of one common template (spindle wavelet 1). The threshold level E_{k1} for the detection of type 1 sleep spindles was 12.4 for all animals. The remaining sleep spindles, which failed to be captured by spindle wavelet 1, were selected using spindle wavelet 2 in $F_{sp2} \in (20, 25)$ Hz. We found that type 2 sleep spindles comprised 7.9% of the total number of sleep spindles (Tables 7.3B and 7.4). Table 7.3B shows empirically defined thresholds E_{k2} for the identification of type 2 sleep spindles for each animal. Figure 7.9 provides an example of automatic detection of sleep spindles of both types and comparison with detection made by an expert using visual inspection.

The best performance for automatic recognition of sleep spindles is achieved after selecting the optimal wavelet template and adjusting the optimal amplitudes ($E_{k1,2}$) and frequency band (F_S) parameters. Almost all sleep spindles (90–95%) were extracted by the joint application of two different types of adaptive spindle wavelets.

Table 7.3 Automatic identification of sleep spindles with the aid of adaptive wavelet templates (spindle wavelets). The basis function known as spindle wavelet 1 was the same for all animals. Detections of type 1 spindles were made if the wavelet power $w(t)$ in the frequency band $F_{sp1} \in (f_1, f_2) = (7, 14)$ Hz exceeded the threshold E_{k1} . The basis function known as spindle wavelet 2 was chosen for each animal individually. Type 2 spindles were detected when the WPOD $w(t)$ in the frequency band $F_{sp2} \in (f_1, f_2) = (20, 25)$ Hz exceeded the threshold E_{k2} . N_{S1} is the number of sleep spindles missed by the type 1 spindle wavelet. TP is the number of correct detections of sleep spindles, TN the number of correct rejections of sleep spindles, FP the incorrect automatic detections of sleep spindles, and FN the number of events missed by the automatic wavelet-based method. f_{sw2} is the average peak frequency of the spindle wavelet 2 basis

A. Type 1 spindle wavelet

Rat #	Visual detections	Automatic detections			Threshold E_{k1}
	N_{expert}	TP	FP	FN	
1	2,341	2,130	23	281	12.4
2	1,381	1,132	28	110	12.4
3	1,491	1,312	30	149	12.4
4	1,305	1,096	39	104	12.4
5	1,598	1,422	16	144	12.4
Mean \pm SD	$1,623 \pm 416$	$1,418 \pm 419$	27 ± 9	157 ± 72	12.4 ± 0.0

B. Type 2 spindle wavelet

Rat #	N_{S1}	Automatic detections				f_{sw2}	Threshold E_{k2}
		TP	TN	FP	FN		
1	211	140	2,154	70	22	23.3	21.0
2	249	110	1,215	69	21	24	23.5
3	179	164	1,327	30	15	19	18.8
4	209	117	1,175	26	18	17	18.5
5	176	112	1,454	48	14	22	18.5
Mean \pm SD	205 ± 30	129 ± 23	$1,465 \pm 400$	48.6 ± 20.8	18 ± 6	21 ± 3	20.1 ± 2.1

Table 7.4 Performance of automatic detection of sleep spindles by means of the spindle wavelets

Rat #	Type 1 spindle wavelet			Type 2 spindle wavelet		
	Accuracy	Sensitivity	Specificity	Accuracy	Sensitivity	Specificity
	ρ_1 [%]	β [%]	δ [%]	ρ_2 [%]	β [%]	δ [%]
1	91.1	88.4	98.9	66.3	96.9	86.4
2	82.2	91.2	97.6	44.2	94.6	84.0
3	87.8	89.8	97.8	91.6	97.8	91.6
4	83.9	91.3	96.6	56.0	97.8	86.7
5	88.9	90.8	98.9	63.6	96.8	88.9
Mean \pm SD	86.8 ± 3.7	90.3 ± 1.2	97.9 ± 1.0	64.3 ± 17.5	96.8 ± 1.3	87.5 ± 2.9

The merit of the presented method is the pinpoint accuracy of automatic sleep spindle recognition in EEG, which can theoretically reach 100 % by increasing the number of adaptive bases (spindle wavelets). The disadvantage with this approach is its computational complexity, which requires exhaustive testing of a large number of sleep spindle templates for the selection of the optimal basis.

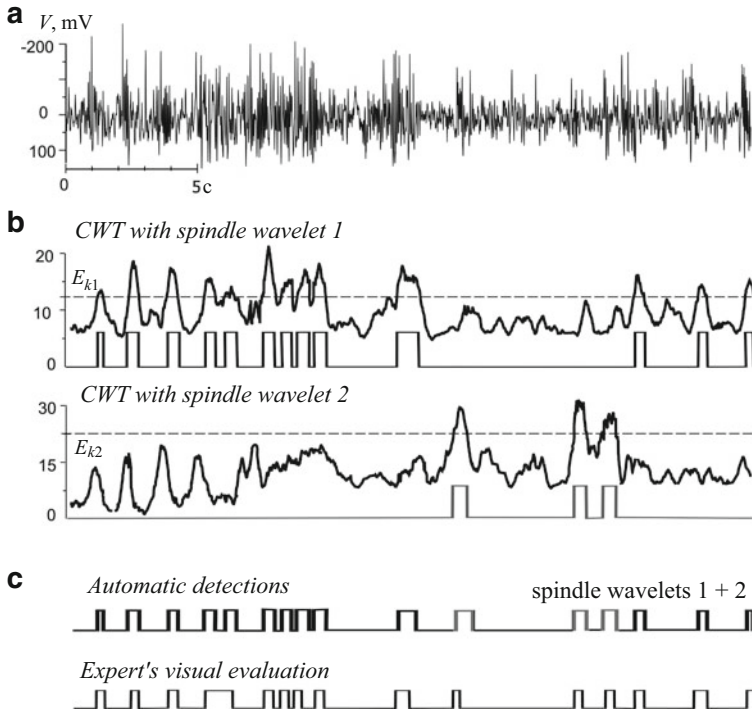


Fig. 7.9 Automatic recognition of sleep spindles with the aid of two spindle wavelets. (a) Example EEG with sleep spindle oscillations. (b) Distribution of wavelet energy $w(t)$ (7.1), as obtained with types 1 and 2 spindle wavelets in the characteristic frequency bands ($F_{sp1,2}$). Type 1 spindle wavelet sleep spindles in $F_{sp1} = 7\text{--}14$ Hz with threshold $E_{k1} = 12.4$. Type 2 in $F_{sp2} = 20\text{--}25$ Hz, threshold $E_{k2} = 21$. (c) Automatic spindle detections (*top*) match expert selections (*bottom*)

7.5 Automatic Detection and Discrimination of 5–9 Hz Oscillations and Sleep Spindles

The method described in Sect. 7.4 is computationally complex. In [114], we suggested a simplified algorithm for automatic recognition and discrimination of 5–9 Hz oscillations and sleep spindles. The method uses the CWT with standard complex Morlet mother wavelet and is based on the method of detection of spike-wave discharges described in Sect. 7.2 (see also (7.1) and (7.2)). This is what we shall now describe.

As mentioned in Sect. 6.3, the wavelet spectrum of spindle-like patterns is characterized by the presence of a peak at 8–15 Hz (see Figs. 6.7 and 6.8). This peak corresponds to the fundamental frequency of spindle waves. However, this frequency is not constant, but usually increases from the beginning to the end of the spindle pattern (see Fig. 6.10). The presence of a spectral peak at 8–15 Hz is a necessary but not a sufficient condition for detecting sleep spindles in EEG. For

example, sleep spindles could often be confused with SWD events, which also have a peak in the 8–15 Hz frequency band. Identification of SWDs, however, can rely on a wavelet measure of the power in the gamma frequency band. Then we can achieve an identification accuracy close to 100 % (see Sect. 7.2). Therefore, in order to reduce errors in the detection of spindle waves, we can first identify SWD events and then set the corresponding EEG segments to zero [112].

Selective detection of sleep spindles (Fig. 6.7) and 5–9 Hz oscillations (Fig. 6.8) is based on measurements of the integral wavelet energy (WPOD) in two frequency bands: $F_s^1 \in [5, 9]$ Hz and $F_s^2 \in [10, 15]$ Hz. The resulting measures $w_1(t)$ and $w_2(t)$ are thresholded (see (7.8)) using levels E_k^1 and E_k^2 , respectively. These levels are chosen empirically to provide the most accurate localization of sleep spindles and 5–9 Hz oscillations in the time domain. We decide on the presence of a sleep spindle if, in the frequency range 10–15 Hz, the wavelet power satisfies $w_2(t) > E_k^2$ and $w_2(t) > w_1(t)$. Thus the criterion is

$$\text{spindle: } w_2(t) > E_k^2 \quad \text{and} \quad w_2(t) > w_1(t) . \quad (7.9)$$

Similarly, 5–9 Hz oscillations must satisfy the condition

$$5\text{--}9 \text{ Hz: } w_1(t) > E_k^1 \quad \text{and} \quad w_1(t) > w_2(t) , \quad (7.10)$$

i.e., the wavelet power $w_1(t)$ in 5–9 Hz exceeds the threshold E_k^1 and is bigger than the power in 10–15 Hz.

In order to determine the end point of each oscillation, we compute the average wavelet power w_0 of the EEG background² for 10 s. Then the value of w_0 is compared to $w_1(t)$ and $w_2(t)$. The end of sleep spindles and 5–9 Hz oscillations is assigned to the instant of time satisfying

$$w_i(t) \leq w_0 , \quad i = 1, 2 , \quad (7.11)$$

i.e., the WPOD $w_i(t)$ becomes comparable to the wavelet energy of the EEG background.

Another difficulty for automatic classification is the presence of rhythmic alpha/theta components in EEG that are related neither to sleep spindles nor to 5–9 Hz oscillations. These rhythmic components correspond to a short-term increase in the instantaneous wavelet energy $w_i(t)$ in the frequency bands F_s^1 and F_s^2 , and may sometimes cause false detections. In order to prevent incorrect detections induced by rhythmic components, the instantaneous wavelet energy $w_i(t)$ can be averaged over a time window Δ (see also (7.7)):

²That is, the EEG epoch which does not contain any oscillatory patterns, i.e., SWD and spindle-like patterns.

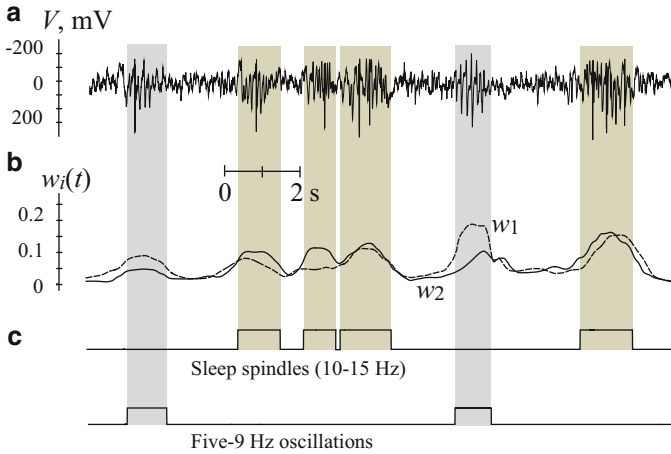


Fig. 7.10 Principles of automatic detection of sleep spindles and 5–9 Hz oscillations in EEG. (a) An epoch consisting of sleep spindles and 5–9 Hz oscillations. (b) Wavelet energy $w_i(t)$ measured in the 5–9 Hz frequency band (*dotted line*) and in 10–15 Hz (*solid line*). (c) Output of the automatic detection algorithm for sleep spindles and 5–9 Hz oscillations

$$\langle w_i(t) \rangle = \frac{1}{\Delta} \int_{t-\Delta/2}^{t+\Delta/2} w(\tau) d\tau . \quad (7.12)$$

Empirically we chose $\Delta = 0.5$ s. Then we can use the average wavelet energy $\langle w_i(t) \rangle$ instead of $w_i(t)$ in (7.9)–(7.11). This procedure improves the quality of automatic detections. It also helps to avoid false detections of short spindle-like events lasting less than 0.5 s.

Figure 7.10 illustrates the procedure for automatic discrimination of sleep spindles and 5–9 Hz oscillations in an EEG fragment. Table 7.5 provides the amplitude and threshold parameters used for selective detection of sleep spindles and 5–9 Hz oscillations in the EEG.

7.6 On–Off Intermittency of Thalamo-Cortical Oscillations

7.6.1 Nonlinear Dynamics of SWDs, Sleep Spindles, and 5–9 Hz Oscillations

Spike–wave discharges are EEG hallmarks of absence epilepsy. SWDs are known to originate from a thalamo-cortical neuronal network that normally produces sleep spindle oscillations. Although sleep spindles and SWD are considered as thalamo-cortical oscillations, the functional relationship between them is not obvious.

Table 7.5 Amplitude, frequency, and threshold parameters counted by the Morlet wavelet-based algorithm for selective detections of sleep spindles and 5–9 Hz oscillations in WAG/Rij rat EEGs. W_{\max} is the maximal energy of the wavelet spectra of analyzed EEG patterns. The central frequency of the Morlet wavelet was $\omega_0 = 2\pi$ rad/s

Rat #	5–9 Hz oscillations		Sleep spindles (10–15 Hz)		Background energy
	W_{\max}	E_k^1	W_{\max}	E_k^2	w_0
1	0.21	0.072	0.20	0.076	0.031
2	0.41	0.115	0.28	0.071	0.028
3	0.43	0.132	0.37	0.124	0.034
4	0.27	0.090	0.24	0.080	0.025
5	0.24	0.088	0.19	0.078	0.028
6	0.26	0.081	0.22	0.069	0.024
Mean \pm SD	0.3 ± 0.09	0.096 ± 0.023	0.25 ± 0.07	0.083 ± 0.021	0.028 ± 0.004

The wavelet-based algorithms for automatic detection of oscillatory events described in the previous sections can be used to study the global temporal dynamics of SWDs, sleep spindles (10–15 Hz), and 5–9 Hz oscillations from the point of view of nonlinear dynamics. In [39, 64, 114], we used the theory of intermittency to evaluate the statistical properties of spindles and SWD events.

Briefly, intermittency is associated with aperiodic switching between so-called regular behavior and chaotic bursts [9, 103]. Applying this concept to EEG, we can relate regular behavior to long-lasting periods of a desynchronized state (background EEG), whereas various kinds of oscillatory events can be considered as chaotic bursts. In healthy human subjects, intermittent EEG behavior is a characteristic feature of spontaneous alpha-range activity 8–13 Hz [31, 47]. It is also observed in seizure activity in patients suffering intractable partial epilepsy [96].

A particular type of intermittent behavior, so called *on–off intermittency* [34, 36, 103], is manifested as an abrupt shift between synchronized and desynchronized states in coupled dynamical systems and networks [10, 11, 38]. On–off intermittency appears in a model system that continually alternates between brief episodes of bursting activity, referred to as the *on*-state, and the quiescent *off*-state [34, 36, 62]. These findings suggest that a similar intermittent mechanism may underlie the temporal dynamics of synchronous thalamo-cortical oscillations, such as SWDs, sleep spindles, and 5–9 Hz oscillations.

To describe intermittent dynamics in EEGs, we used the algorithm described in Sect. 7.5 for detection of SWDs, sleep spindles, and 5–9 Hz oscillations. The method of event detection relies on measuring the distribution of wavelet energy. An increased WPOD $w(t)$ during SWDs, sleep spindles, and 5–9 Hz oscillations is a characteristic feature of synchronized EEG states. We thus consider such epochs as on-states of intermittent behavior (Fig. 7.11). In general, different types of EEG oscillations present different types of on-states (Table 6.4, Sect. 6.3). The temporal dynamics of the investigated oscillatory patterns were examined using statistical analysis of time intervals between consecutive EEG events. These intervals L correspond to the off-phase in the intermittent behavior (Fig. 7.11).

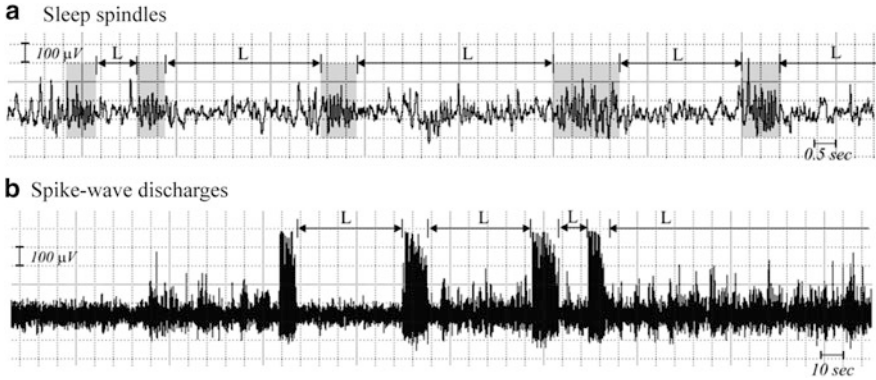


Fig. 7.11 Intermittent dynamics of (a) sleep spindles (grey boxes) and (b) spike-wave discharges. Intervals L between consecutive events have been used for statistical description

We analyzed SWD, sleep spindles, and 5–9 Hz oscillations separately and tested them for power-law dynamics. Under this assumption, the dependence of the number (frequency) $N(L)$ of off-phases on their duration L should obey

$$N(L) = \mu L^\alpha, \quad (7.13)$$

where α is the exponent and μ is the normalization factor. It has been proven that $\alpha = -3/2$ is characteristic of systems with on–off intermittency [15, 34, 36, 39].

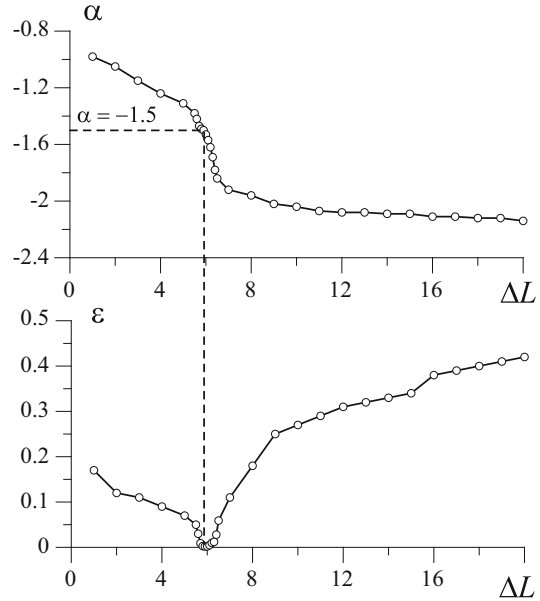
In each individual experiment, the parameter α was calculated by minimizing the root-mean square error ε of empirically obtained distributions $N(L)$ with different bin widths ΔL . Figure 7.12 (upper plot) shows the relationship between the bin width ΔL and the exponent α characterizing the temporal distribution of time periods between consecutive sleep spindles. The value of α decreases from -1.0 to -2.3 with the increase in ΔL . The bottom plot (Fig. 7.12) shows that the root-mean square error ε attains a minimum for $\Delta L \approx 6$ s. For this value of ΔL , we get the exponent $\alpha = -3/2$, which is characteristic of on–off intermittency.

Figure 7.13 shows the distribution of $N(L)$ for SWDs, spindles, and 5–9 Hz oscillations obtained in six animals. Distributions of both inter-SWD and inter-spindle intervals are close to a straight line with $\alpha = -3/2$ on a log–log scale in all experimental animals, i.e., $N(L) \sim L^{-3/2}$. As mentioned above, this type of distribution is known to be a key feature of on–off intermittency [34, 36, 39, 64, 85, 103].

The same analysis of 5–9 Hz oscillations showed that the distributions of inter-oscillation intervals fit a power law with exponent $\alpha = -1$ (Fig. 7.13c). This kind of dynamics was rather uncertain, and it obviously differs from the on–off intermittent behavior of sleep spindles and SWDs.

Although the number of SWDs and sleep spindles varied from rat to rat, these EEG events were distributed in time according to a power law with exponent $\alpha = -3/2$. It is important that on–off intermittent behavior was found in both SWDs

Fig. 7.12 Fitness test for the power law distribution of inter-spindle intervals L for different bin widths ΔL . Data are for sleep spindles. The root-mean square error ε was calculated between the theoretical power law $N(L) = \mu L^\alpha$ and the distribution obtained from experimental data



and sleep spindles, despite the fact that these EEG events differ significantly in their time–frequency profiles (Sects. 5.3 and 6.3).

7.6.2 Intermittent Dynamics of SWDs Under the Influence of a Pro-absence Drug (Vigabatrin)

In order to characterize how pharmacological treatment influences dynamical properties of epileptic activity, we analyzed the EEG recordings in WAG/Rij rats under the influence of a pro-absence drug, vigabatrin, in different doses [39]. Vigabatrin has positive effects in the treatment of generalized epilepsy [4]. However, it has a negative effect in absence epilepsy [77]. Vigabatrin causes a dose-dependent increase in the number and duration of spike–wave epileptic discharges [130], which are characteristic for absence epilepsy.

We tested the distributions of inter-SWD intervals for the presence of on–off intermittency after injection of vigabatrin. In lower doses (125 and 250 mg), vigabatrin decreases the mean length of the laminar phases (so called L intervals), i.e., normal EEG activity decreases. However, distortion of laminar phases provoked by injection of vigabatrin does not disrupt the power law with the characteristic exponent $\alpha = -3/2$ (Fig. 7.14a, b). The pattern of on–off intermittency in drug-injected animals was similar to that observed in control animals (see Fig. 7.13a). Thus, low-doses of vigabatrin do not alter the global dynamics of the epileptic activity.

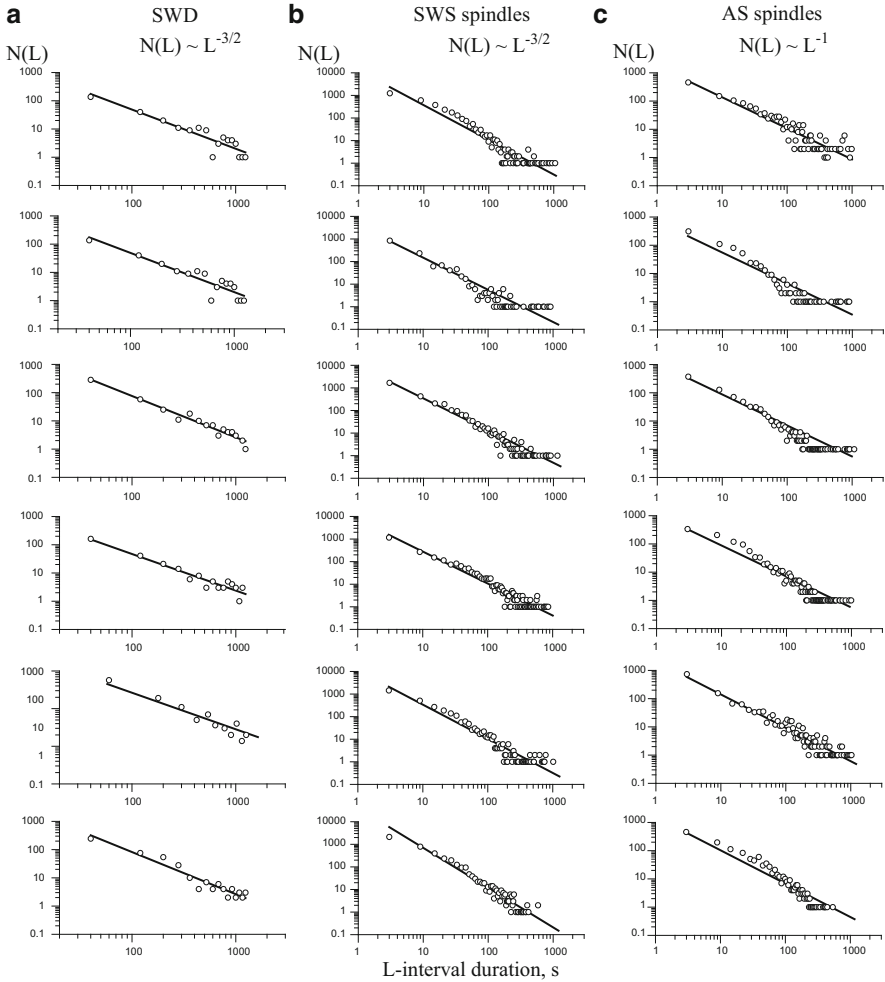


Fig. 7.13 Distributions of time intervals (L intervals) between investigated EEG events plotted on a log-log scale. SWDs (**a**) and sleep spindles (**b**) are best approximated by the power law with exponent $\alpha = -3/2$ in all experiments (ID = 1–6). This is typical for on-off intermittency. Five to nine hertz oscillations (**c**) fit the power law with $\alpha = -1$

Injecting a larger dose of vigabatrin (500 mg) disrupts the on-off intermittency pattern of EEG activity (see Fig. 7.14c). The lengths of inter-SWD intervals become more random and do not follow the line with $\alpha = -3/2$. This may imply that high doses of vigabatrin influence the transition from synchronous EEG states (SWDs) to out-of-phase states (background EEG). Therefore, the intermittency acquires another (probably, more complex) pattern compared to that in control animals.

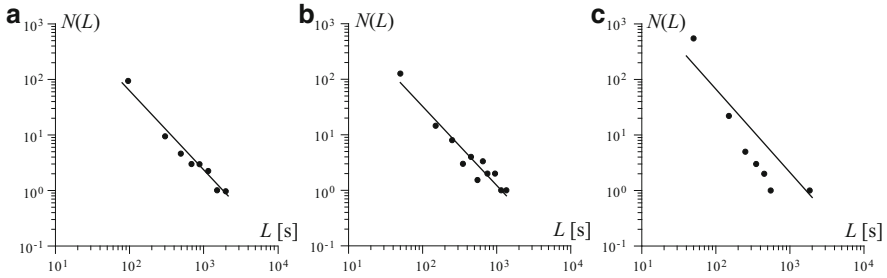


Fig. 7.14 Distributions of inter-SWD intervals after i.p. injections of vigabatrin in doses of (a) 125 mg, (b) 250 mg, and (c) 500 mg (shorter time series compared to Fig. 7.13a have been used). Black circles correspond to experimental data. Straight lines plot the power law $N(L) \sim L^{-3/2}$. In doses greater than 500 mg, vigabatrin significantly changes the distribution of L intervals and on–off intermittency (characteristic for control animals, Fig. 7.13a) is no longer observed

7.6.3 Mechanisms of Intermittent Behavior in the Thalamo-Cortical Neuronal Network

Intermittency in general refers to a wide variety of behaviors, in which almost periodic (oscillatory) dynamics is suddenly interrupted by chaotic bursts. In models of chaotic dynamical systems (such as coupled oscillators and neural networks), the mechanism of intermittency is known to underlie alternations between synchronous and asynchronous regimes [11, 38, 40, 41, 139]. On the basis of the dynamical scenarios, intermittency can be classified into several types: type I, type II, type III, ring, eyelet, and on–off [9, 11, 40, 42, 99].

The results obtained in previous sections on the dynamics of different EEG events demonstrate that:

- The distribution of spindles, 5–9 Hz oscillations, and spike–wave paroxysms is not random.
- The temporal dynamics of sleep spindles and SWDs (but not 5–9 Hz oscillations) follows the law of on–off intermittency.

This is a remarkable finding. Indeed, according to the theory of nonlinear dynamics, on–off intermittency appears in dynamical systems displaying *deterministic* chaos. We know that SWD and sleep spindles are produced by the thalamo-cortical neural network [21, 23, 30, 69, 115, 117]. This implies that this network operates in a regime of deterministic chaos.

It is known that the onset of synchronized phases in systems with on–off intermittency is regulated by an external control parameter or *driving force*. This suggests that the process of synchronization/desynchronization in the thalamo-cortical network should be controlled by a high level hierarchic mechanism (driving force). This driving mechanism may involve the reticular activating system that modulates excitability of thalamo-cortical neurons and is capable of entraining

the network in either sleep-related oscillations or spike–wave paroxysms [116]. Alternatively, this control mechanism might involve the preoptic hypothalamic area, which is responsible for circadian activity and/or sleep–wake transitions, and which is known to be involved in the pathogenesis of absence seizures in WAG/Rij rats [119].

Note that observation of on–off intermittency in thalamo-cortical oscillations is not surprising. Intermittency has been described earlier in spontaneously occurring synchronized EEG oscillations in humans. In particular, the dynamics of synchronized episodes of alpha activity in human EEG had the property of type I intermittency [31]. Gong and colleagues [31, p. 011904-1] assumed that “this kind of dynamics enables the brain to rapidly enter and exit different synchronized states, rendering synchronized states metastable”. Moreover, analysis of shorter aspects of paroxysmal discharges constituting behavioral seizures in human patients suffering partial and traumatic epilepsies revealed type III intermittency [96].

Based on these recent data, we suggest that intermittent behavior may characterize rapid switches between synchronous and asynchronous brain activities. This mechanism may help to avoid unstable oscillatory synchronous regimes that could emerge in the transition from one stable state to another. Intermittent behavior of synchronous EEG patterns implies that their temporal dynamics has a deterministic nature. Such determinism may have clinical interest, allowing long-term prognosis about seizure remission. Further studies in this field may provide effective tools for predicting epileptic activity.

The present results also indicate that the temporal dynamics of 5–9 Hz oscillations is totally different from that in SWDs and sleep spindles. This can be explained by differences in global network mechanisms and in particular the role of the thalamus. The latter does not contribute to the generation of 5–9 Hz oscillations [101, 102], whereas thalamic cellular and intrathalamic network mechanisms are necessary for the initiation of sleep spindles and for the maintenance of SWDs [100, 115, 117].

7.7 Serial Identification of EEG Patterns Using Adaptive Wavelet Analysis

Among the available automatic recognition techniques in neuroscience, wavelet-based approaches are the most powerful. However, they require an appropriate selection of parameters in order to minimize errors of pattern recognition. Indeed, the efficiency of wavelet-based methods can be significantly reduced if some parameters are not optimal. Dealing with the continuous wavelet transform, we should select the mother wavelet and at least two parameters characterizing translation and dilation of the mother wavelet. The problem of parameter selection has been partially addressed in Chap. 4, where we discussed a wavelet approach to spike sorting (see also [74, 93, 106]).

In this section, we shall introduce a special wavelet-based method for pattern identification, which we shall refer to as a serial adaptive wavelet method [86–88]. The advantage of this method is that we may forgo the empirical selection of the wavelet parameters based on optimization theory. Since optimal parameters are computed by means of the proposed technique, the quality of pattern recognition does not depend on the experience of the researcher.

7.7.1 Adaptive Wavelet-Based Technique and the Serial Method

In previous sections, we saw that the continuous wavelet transform with Morlet wavelet provides the best time–frequency resolution of spike–wave discharges and other oscillatory EEG patterns (see also Sect. 6.4). Unlike other wavelets, the Morlet wavelet has an additional parameter ω_0 , called the central frequency, which can be used to adjust the time–frequency resolution. Thus, the Morlet CWT of an arbitrary signal $S(t)$ can be represented as a transform that depends on the scale s , translation t_0 , and central frequency ω_0 :

$$W^S(s, \omega_0, t_0) = \frac{1}{\sqrt{s}} \int_0^T S(t) \psi_{\omega_0} \left(\frac{t - t_0}{s} \right) dt, \quad (7.14)$$

where

$$\psi_{\omega_0}(\eta) = \pi^{-1/4} e^{i\omega_0 \eta} e^{-\eta^2/2} \quad (7.15)$$

is the Morlet wavelet function.

Let us now illustrate the main idea of our adaptive approach. Figure 7.15 sketches the pattern identification problem. Important characteristics of an EEG signal $S(t)$ can be assessed by integrating the instantaneous wavelet amplitudes within some range of scales (see, e.g., Sect. 7.3, and in particular (7.6)):

$$w^S(t) = \int_{s_{\min}}^{s_{\max}} |W^S(s, \omega_0, t_0)| ds. \quad (7.16)$$

An additional smoothing of the function $w^S(t)$ can be performed in order to reduce effects of artifacts (see (7.12)). In the simplest case, we can introduce a filter Z , which provides N_S averages over a sliding window of size N_H [104]:

$$\bar{w}^S(t) = Z(w^S(t), N_S, N_H). \quad (7.17)$$

As a result of pattern identification, a binary (logical) signal $\bar{S}(t)$ is obtained (see Fig. 7.15). The output is logical zero $\bar{S}(t) = 0$ in the absence of any specific oscillatory pattern, while $\bar{S}(t) = 1$ corresponds to intervals containing patterns:

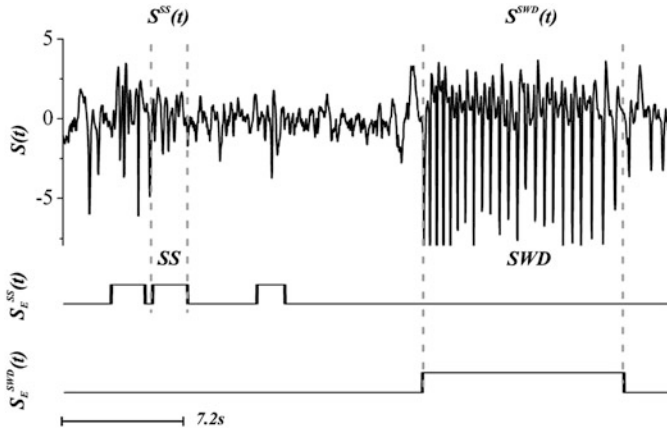


Fig. 7.15 EEG containing sleep spindles (SS) and SWD patterns. Identifications of sleep spindles and SWDs are represented by expert logic signals $S_E^{SS}(t)$ and $S_E^{SWD}(t)$, respectively

$$\bar{S}(t) = C(\bar{w}^S(t), \Theta_L, \Theta_H) = \begin{cases} 1, & \bar{w}^S(t) \in [\Theta_L, \Theta_H], \\ 0, & \text{otherwise,} \end{cases} \quad (7.18)$$

where Θ_L and Θ_H are two thresholds. The value Θ_L provides separation of sleep spindles and spike-wave discharges from the background EEG. The value Θ_H provides selective identification of either sleep spindle or SWD patterns, since these two patterns cannot appear in EEG at the same time and they are characterized by different wavelet energies.

Finally, the standard CWT approach to pattern recognition requires manual or semi-automatic selection and adjustment of the following parameters:

$$P = \{s_{\min}, s_{\max}, \omega_0, N_S, N_H, \Theta_L, \Theta_H\}. \quad (7.19)$$

This tedious problem ($P \in \mathbb{R}^7$) is frequently resolved suboptimally.

The accuracy of pattern recognition can be estimated by comparing the output $\bar{S}(t)$ of the automatic algorithm and the binary signal $S_E(t)$ provided by a human expert after visual exploration of the data. Then the following integral measure can be estimated:

$$E(\bar{S}, S_E) = \frac{1}{T} \int_0^T |\bar{S}(t) - S_E(t)| dt. \quad (7.20)$$

Additional characteristics quantifying the quality of recognition are the number N_E of patterns identified by an expert and the number N_D identified by some standard CWT approach. We shall use several measures quantifying the accuracy

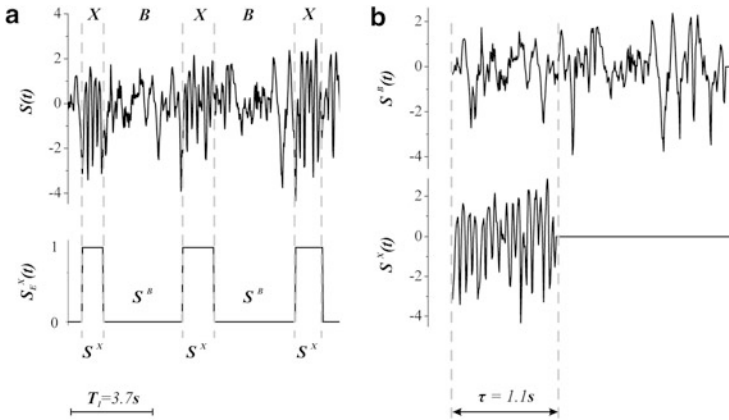


Fig. 7.16 (a) EEG recording containing only one type of pattern (sleep spindle) and (b) the extracted time series formed by background activity $S^B(t)$ and by the detected X patterns $S^X(t)$ (sleep spindle)

of recognition of sleep spindle patterns ρ^{SS} , the sensitivity δ^{SS} , and the specificity β^{SS} (see (7.3)–(7.5)).

Serial identification of EEG patterns involves some aspects of optimization theory [92, 137]. The method assumes that the EEG signal $S(t)$ ($t \in [0, T]$) can be divided into two parts T_1 and T_2 , where $T_1 + T_2 = T$ and $\lambda = T_1/T$. The first part is used to adjust the parameter set P which affects the quality of pattern recognition. This part must contain all types of patterns to be recognized in order to reveal their most essential distinctions from the background EEG. A visual inspection of this part by an expert provides a way to quantify the quality of pattern recognition.

In the adaptive wavelet-based method, we consider instantaneous amplitudes associated with parameters a_j, ω_j that are denoted by $w^S(s_j, \omega_{0j}, t)$. Then filtration and transition to the binary signal $\bar{S}(t)$ are performed using (7.17) and (7.18). Further, we use optimization theory to define parameter values for the most effective and accurate recognition of specific EEG patterns. For this purpose, we consider a multi-parametric approach and introduce a series of $s_j, \omega_{0j}, j \in [1, N_B]$, in order to quantify parameters informing about the complex organization of EEG patterns. The values $s_j, \omega_{0j}, j \in [1, N_B]$, are estimated according to objective functions that maximize distinctions between two investigated patterns (sleep spindle or SWD) and the background EEG activity. Further, the remaining parameters ($\theta_L, \theta_H, N_S, N_H$) are optimized to reduce pattern recognition errors.

Let us consider an arbitrary pattern in EEG which we refer to as pattern X . This may be a sleep spindle, SWD, or another kind of pattern detected by an expert in the signal $S(t), t \in [0, T_1]$ (see Fig. 7.16). At this stage, let us also suppose that we are dealing with a single type of specific oscillatory activity (X pattern) that should be separated from the background EEG activity (indicated by B in Fig. 7.16).

In order to distinguish between $S^X(t)$ and $S^B(t)$, which are associated with X patterns and the background activity, respectively, these fragments of EEG can be extracted and considered as new time series (see Fig. 7.16b). These new time series are further divided into p parts of duration m ($pm = \tau$, where τ is the length of the shorter signal in Fig. 7.16b).

The instantaneous amplitudes of the signal $S^X(t)$ are averaged across each part to get a series of values $v_k^X(s_j, \omega_{0j})$ with $k \in [1, p]$. Using the same algorithm, a series of averaged instantaneous amplitudes $v_k^B(s_j, \omega_{0j})$ is obtained corresponding to the signal $S^B(t)$. The functions $v_k(s_j, \omega_{0j})$ of both series are used to compute an objective function $R_d(s_j, \omega_{0j})$:

$$R_d(s_j, \omega_{0j}) = \frac{\langle v_k^X(s_j, \omega_{0j}) \rangle_k - \langle v_k^B(s_j, \omega_{0j}) \rangle_k}{\sigma(v_k^X(s_j, \omega_{0j}))_k + \sigma(v_k^B(s_j, \omega_{0j}))_k}, \quad (7.21)$$

where angle brackets denote mean values and σ is the standard deviation.

Another way to compute the objective function does not require decomposition and fragmentation of the EEG. An alternative computation of instantaneous amplitudes for signals $S^B(t)$ and $S^X(t)$, the function R_I is introduced as follows:

$$R_I(s_j, \omega_{0j}) = \frac{1}{\tau} \int_0^\tau r_I(s_j, \omega_{0j}, t) dt, \quad (7.22)$$

$$r_I(s_j, \omega_{0j}, t) = \begin{cases} \frac{w^{S^X}(s_j, \omega_{0j}, t) - w^{S^B}(s_j, \omega_{0j}, t)}{w^{S^X}(s_j, \omega_{0j}, t)}, & w^{S^X}(s_j, \omega_{0j}, t) \geq w^{S^B}(s_j, \omega_{0j}, t), \\ \frac{w^{S^X}(s_j, \omega_{0j}, t) - w^{S^B}(s_j, \omega_{0j}, t)}{w^{S^B}(s_j, \omega_{0j}, t)}, & w^{S^X}(s_j, \omega_{0j}, t) < w^{S^B}(s_j, \omega_{0j}, t). \end{cases}$$

Optimal parameters s_j and ω_{0j} of the Morlet mother wavelet are selected according to the values of objective functions given by (7.21) and (7.22). Optimal values of R_d vary between 1.0 and $+\infty$, but for the function (7.22), we should consider appropriate values between 0.3 and 1.0 that can be achieved by stochastic optimization based on Monte Carlo methods or by a simpler method [92, 137] assuming a maximization procedure for R_d or R_I . Selection of the remaining parameters (N_S , N_H , Θ_L , Θ_H) can also be performed to improve the quality of pattern recognition.

At the first stage, fixed values n_S^j and n_H^j of the parameters N_S and N_H are considered, and the parameters Θ_L , Θ_H are optimized according to the minimum of $E(\bar{S}^X, S_E^X)$ or using a general objective function

$$R_\Theta(\Theta_L, \Theta_H, n_S^j, n_H^j) = \frac{1}{2} \left[1 - E(\bar{S}^X, S_E^X) + P(\bar{S}^X, S_E^X) \right]. \quad (7.23)$$

At the fixed values n_S^j and n_H^j , optimal thresholds θ_L^j , θ_H^j are defined according to the maximum of (7.23). Then the next pair of parameters N_S , N_H is selected, viz.,

n_S^{j+1} and n_H^{j+1} , and so on. Parameters can be changed step-by-step or stochastically. Optimal settings are determined by

$$\exists k : P(\bar{S}^X(t, \theta_L^k, \theta_H^k, n_S^k, n_H^k), S_E^X) = \max, \quad t \in [0, T_1]. \quad (7.24)$$

The proposed serial adaptive method assumes a sequential detection of all specific oscillatory patterns that should be recognized in the structure of EEG. The automatic recognition procedure can be performed starting from patterns with the highest energies. In this method, visual inspection of the first part of the EEG signal (T_1) has been done by an expert, and the signals $S_E^{X_j}$ are obtained for each type of specific oscillatory activity. Further, all types of patterns are reordered according to decreasing spectral power.

For the validation of the proposed serial method (the *adaptation stage*), recognition starts from a pattern X_0 characterized by the highest energy. The considered technique is applied to optimize the parameters (s_k, ω_{0k}) , $k \in [1, N_B]_{X_0}$ and then the parameters $(\theta_L, \theta_H, N_S, N_H)$. This procedure is repeated for all remaining types of patterns.

For the full processing mode (the *working stage*), the serial method assumes that the adapted CWT algorithm is applied to the whole of the EEG data and aims to reveal the patterns X_j at the same order j as during the previous stage. In this work, we basically concentrate on two types of oscillatory patterns (sleep spindles and SWD).

7.7.2 Experimental Validation of the Serial Method

In order to compare accuracy of the standard wavelet-based method and the proposed serial technique, we considered EEG signals containing both sleep spindles and SWDs. At the first stage, the standard wavelet-based method was applied with empirically selected parameters. The range of scales in (7.16) was chosen as $\pm 10\%$ of the scale associated with the spectral maximum, $\omega_0 = 2\pi$. Table 7.6 summarizes the results.

Application of the proposed serial adaptive method with the objective function R_d improves recognition abilities of wavelets (see Table 7.7). The accuracy ρ is increased from 71.4 to 87.6% for SS patterns and from 94.1 to 98.3% for SWD patterns. Other measures such as the error E , the sensitivity δ , and the specificity β , confirm the higher efficiency of the adaptive technique. Similar results are achieved for the objective function R_I (see Table 7.8).

Figure 7.17 shows average characteristics obtained with the proposed serial adaptive technique for sleep spindle patterns and which confirm the improvement of recognition abilities using this approach. The results presented demonstrate that a more effective recognition of EEG patterns can be achieved with the adaptive method as compared to the method used previously with the standard CWT-based

Table 7.6 Results of SWD and sleep spindle recognition by the standard CWT-based approach applied to EEGs recorded in 6 rats

Rat #	E [%]		Accuracy ρ [%]		Sensitivity δ [%]		Specificity β [%]	
	SS	SWD	SS	SWD	SS	SWD	SS	SWD
1	18.8	1.6	71.6	100.0	78.0	100.0	100.0	95.0
2	9.3	0.8	92.9	100.0	95.5	100.0	66.7	97.3
3	9.8	1.6	76.0	97.3	83.3	97.3	100.0	97.1
4	4.8	2.3	57.4	67.9	64.2	95.0	96.4	72.5
5	19.9	9.2	58.3	100.0	61.1	100.0	87.1	47.9
6	12.4	1.3	72.0	100.0	78.3	100.0	87.5	95.6
Mean	12.5	2.8	71.4	94.2	76.7	98.7	89.6	84.2
\pm SD	± 5.9	± 3.2	± 13.1	± 12.9	± 12.7	± 2.1	± 12.6	± 20.2

Table 7.7 Results of SWD and sleep spindle recognition by the adaptive CWT-based approach with R_d function for $N_B = 100$

Rat #	E [%]			Accuracy ρ [%]		Sensitivity δ [%]		Specificity β [%]	
	$\alpha(T_1)$	SS	SWD	SS	SWD	SS	SWD	SS	SWD
1	13.4	8.0	0.3	80.4	100.0	83.4	100.0	100.0	100.0
2	9.0	7.0	0.4	87.5	100.0	90.2	100.0	100.0	98.3
3	6.0	7.5	1.3	88.5	100.0	92.7	100.0	94.6	99.8
4	10.8	3.2	0.6	91.7	92.3	96.5	92.9	92.9	98.4
5	18.2	8.3	0.5	91.4	96.8	93.7	96.8	93.6	98.0
6	10.0	10.3	1.1	85.9	100.0	87.9	100.0	93.8	98.4
Mean	11.2	7.4	0.7	87.6	98.1	90.7	98.3	95.8	98.8
\pm SD	± 4.1	± 2.3	± 0.4	± 4.2	± 3.2	± 4.6	± 2.9	± 3.3	± 0.9

Table 7.8 Results of SWD and sleep spindle recognition by the adaptive CWT-based approach with R_l function for $N_B = 100$

Rat #	E [%]			Accuracy ρ [%]		Sensitivity δ [%]		Specificity β [%]	
	$\lambda(T_1)$	SS	SWD	SS	SWD	SS	SWD	SS	SWD
1	13.4	9.0	0.3	85.1	100.0	90.1	100.0	100.0	100.0
2	9.0	8.4	0.3	86.8	100.0	91.5	100.0	100.0	99.0
3	6.0	9.5	2.1	92.3	78.4	95.5	90.6	81.1	99.8
4	10.8	4.9	1.2	80.0	85.7	85.1	100.0	96.4	95.6
5	18.2	8.0	0.5	87.3	96.8	91.0	96.8	93.5	98.0
6	10.0	10.4	0.8	83.3	87.5	85.7	100.0	87.5	99.6
Mean	11.2	8.4	0.9	85.8	91.4	89.8	97.9	93.1	98.7
\pm SD	± 4.2	± 1.9	± 0.7	± 4.1	± 8.9	± 3.9	± 3.8	± 7.5	± 1.7

approach. The objective function R_d provided more effective identifications of the examined patterns in EEG. In this case, the error E is equal to 7.38% for sleep spindles and 0.69% for SWD patterns, respectively. This confirms that the difference between the signals $\bar{S}(t)$ and $S_E(t)$ is reduced. Numerical values of $E(\bar{S}, S_E)$ are controlled by appropriate selections of the thresholds Θ_L and Θ_H .

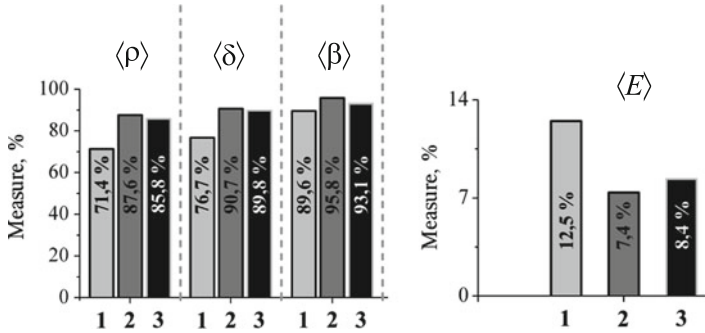


Fig. 7.17 Mean values of all estimated characteristics used for the automatic identification of sleep spindles in EEG. The values 1, 2, and 3 correspond to the standard wavelet approach and to the proposed adaptive technique with objective functions R_d and R_l , respectively

The quality of pattern recognition obviously depends on the duration of the initial time interval T_1 used by an expert to provide a visual identification of specific oscillatory structures. This interval should be long enough to adjust the algorithm parameters, which are subsequently used for detection of patterns in the whole EEG recordings and for further identification of similar oscillatory phenomena in the other time series. The time interval T_1 should contain enough pattern statistics to assess the most informative features. The minimal length of T_1 used in this study was about 10 % of the whole EEG recordings, which corresponds to about 400 sleep spindle patterns. A further increase in T_1 improves the recognition. Thus, a consideration of about 20 % of the entire EEG durations increases the accuracy ρ by 1–2 %. However, this requires twice the duration of data preprocessing by an expert.

7.8 Artifact Suppression in Multichannel EEG Using Wavelet-Enhanced Independent Component Analysis

EEG scalp recordings are widely used in medical practice. Such recordings always have artifacts from eye movements, blinking, muscle activity, etc. The artifact magnitude may be much higher than the underlying neural signals. Thus artifact rejection or suppression is one of the most important preprocessing steps in EEG analysis.

Currently, a widely used way to get rid of artifacts is manual or semi-automatic selection of artifact free data segments or epochs. Although convenient in many cases, this procedure is subjective, requires a high level of skill on the part of the operator, and leads to a significant decrease in the amount of data available for subsequent study. As an example, from a 10 min long EEG of a healthy subject, one usually obtains about a minute of joined artifact-free data. In medical practice,

the massive presence of artifacts in, e.g., EEGs of children [124] or patients with certain injuries [125] makes data reduction even more drastic. Hence, employing a non-cutting, i.e., filter-like procedure for data cleaning becomes indispensable.

In this section we discuss state-of-the-art non-cutting procedures for artifact suppression in multichannel EEG. We introduce a method that uses a wavelet denoising technique to enhance the performance of independent component analysis (ICA). The method, known as wICA and implemented with the wICA Matlab package³ [18], has already proven useful in many applications, such as the study of memory impairment [17], the dynamics of cortical networks [108], obsessive-compulsive disorder [89], brain response to musical stimuli [19], etc.

7.8.1 Independent Component Analysis in EEG Studies

An EEG recording from a single scalp electrode can be considered as a mixture of signals from different brain regions and artifacts. In the first approximation, signals of neural origin can be considered independent of artifacts (for details see, e.g., [51, 55, 56]). With this in mind, a non-cutting method of artifact suppression based on independent component analysis was recently proposed [6]. Later, several modifications of the original algorithm were introduced [3, 28, 44, 45, 49, 50, 52, 54, 82].

ICA tries to separate the recorded EEG signals into statistically independent sources (or components), and then rejects those responsible for artifacts. The majority of EEG applications of ICA focus on the removal of ocular artifacts, where it has been shown to be very useful [28, 54–56, 123, 132, 133]. Currently, ICA is perceived as a potentially robust and powerful method for artifact removal in EEG data and is receiving increasing attention [48, 55, 56, 123–125, 133]. However, there are still several issues that need to be addressed:

- The identification of components responsible for artifacts requires experience on the part of the operator and a priori knowledge about the artifact structure. Besides, an optimal algorithm application is achieved with relatively short (around 10 s) data segments [55]. This counterintuitive result, viz., “more data are not always better”, has been discussed, e.g., in [13], and it assumes a laborious sequential analysis of EEG divided into many short epochs. As a step towards automatic artifact removal, James and Gibson [50] suggested using independent components constrained to be similar to some reference signal incorporating a priori information about the temporal structure of the artifact. Another approach for detection of the components responsible for ocular artifacts uses correlations between electro-oculograms and independent components [28].
- While ICA is now considered an important technique for removing artifacts in EEG signals, there are still few quantitative results showing its advantages and limitations. Existing studies have focused almost exclusively on the spectral

³Available at www.mat.ucm.es/%7Evmarkarov/downloads.php

improvements provided by the ICA decomposition when suppressing typical artifacts. Although it has been proven that ICA-corrected EEGs exhibit a strong reduction in the spectral bands corresponding to artifacts [123, 124], an alert has recently appeared according to which artifact suppression may also corrupt the power spectrum of the underlying neural activity [61, 135]. Thus the question as to how ICA correction distorts the spectrum of the underlying cerebral activity needs to be studied quantitatively.

- One of the most challenging applications of EEGs is the study of cortical circuitry and its reorganization as the brain state changes (see, e.g., [107, 127, 134]). The current literature lacks evaluation of ICA artifact suppression for analysis of synchrony between different electrodes. Non-local characteristics like spectral and partial spectral coherences depend on the phase relation between signals recorded at different electrodes. Thus coherence distortions due to artifacts and their rejection are not generally reducible to power (amplitude) spectrum distortions. Hence, for reliable circuitry analysis, the coherence distortion should also be quantified.

Finally, we would like to draw the reader's attention to intracerebral EEG recordings, also called local field potentials (LFPs). Such recordings are usually made using electrode arrays (collecting up to hundreds of recording tips) that can span single or several neuronal nuclei and provide subcellular spatial resolution and a sampling rate up to 50 kHz. The amount of information generated by such setups is considerable and allows one to study information processing at the mesoscopic level (the level of several interconnected neural nuclei). Recently, we adapted ICA to such studies and were able to reveal functional circuitry and structural organization of cortico-hippocampal pathways [7, 26, 27, 75, 76].

7.8.2 ICA-Based Artifact Suppression

ICA is based on the three following assumptions:

- Experimental data are a spatially stable mixture of the activities of temporarily independent cerebral and artificial sources.
- The superposition of potentials arising from different parts of the brain, scalp, and body is linear at the electrodes, and propagation delays from the sources to the electrodes are negligible.
- The number of sources is no greater than the number of electrodes.

ICA starts with the assumption that L simultaneously recorded EEG signals

$$X(t) = (x_1(t), \dots, x_L(t))^T$$

are linear mixtures of N ($N \leq L$) a priori unknown independent components (sources) $Z(t) = (z_1(t), \dots, z_N(t))^T$, including artifactual components and those of neural origin:

$$X(t) = MZ(t), \quad (7.25)$$

where $M \in \mathcal{M}_{K \times N}(\mathbb{R})$ is the unknown mixing matrix defining weights with which each source is present in the EEG signals recorded on the scalp. Topographic scalp maps of the components (i.e., 3D plots of columns of the matrix M , see examples in Sect. 7.8.4) provide additional information on the localization of the sources. The aim of ICA is to estimate both $Z(t)$ and M from $X(t)$. Technically, two components $z_j(t)$ and $z_k(t)$ are uncorrelated if the expectation of their product can be factorized: $E[z_j z_k] = E[z_j]E[z_k]$. However, this property is necessary but not sufficient for independence. Two components $z_j(t)$ and $z_k(t)$ are independent if and only if their joint probability density can be factorized:

$$p(z_k, z_j) = p(z_k)p(z_j). \quad (7.26)$$

Although (7.26) defines independence, it is computationally unpractical. Therefore other criteria are used, derived from (7.26) (for a review see, [45]).

For ICA, we used the infomax algorithm proposed by Bell and Sejnowski [6] and further modified by Amari et al. [1] and Lee et al. [73]. The algorithm is implemented in the EEGLAB MatLab toolbox [22].⁴ It uses neural networks maximizing the joint entropy and minimizing the mutual information among the output components of a neural processor. For cross-checking, we also employed another ICA implementation, FastICA [46].⁵

Once the algorithm has been applied, we analyze the temporal structure and topography of the components $Z(t)$ (e.g., the ocular artifacts mainly project to frontal sites) and identify among them those components that account for artifacts:

$$Z(t) = (z_1(t), z_2(t), \dots, z_{\text{art}}(t), \dots, z_N(t))^T. \quad (7.27)$$

Then we set the identified artifactual components to zero, $z_{\text{art}}(t) = 0$, obtaining a new component matrix $\hat{Z}(t)$ where the artificial sources have been rejected:

$$\hat{Z}(t) = (z_1(t), z_2(t), \dots, 0, \dots, z_N(t))^T. \quad (7.28)$$

Finally, we reconstruct ICA-corrected EEG signals:

$$\hat{X}(t) = M\hat{Z}(t). \quad (7.29)$$

⁴Available at sccn.ucsd.edu/eeGLAB

⁵Available at www.cis.hut.fi/projects/ica/fastica

Obtained in this way, the new data set $\hat{X}(t)$ represents the ICA estimate of the original artifact-free data.

7.8.3 Wavelet-Enhanced ICA (wICA) for Artifact Suppression

The wavelet transform has been used for analysis of EEGs from the very beginning in different contexts. Throughout this book, we have provided many different applications. Let us now show how wavelets can enhance ICA and greatly improve the performance of artifact suppression.

The WT allows decomposition on multiple scales with further analysis of the wavelet coefficients. For instance, one can suppress (set to zero) some of the coefficients resembling “undesirable” properties in the signal under study. Then inverse WT allows one to restore the original signal, but without these “undesirable” properties. This procedure can be used, e.g., for noise cancelation or denoising. The method known as wICA relies on ICA and makes use of wavelet thresholding, not for denoising the observed raw EEG, but as an intermediate step toward the demixed independent components. This thresholding conserves the time–frequency structure of artifacts and recovers the cerebral activity “leaked” into the components.

When dealing with real EEGs, ICA estimates independent components capturing artificial sources. However, besides strong artifacts, these components can frequently contain a considerable amount of cerebral activity. This may occur, e.g., due to the limitation on the maximal number of independent sources, restriction on temporal independence, or suboptimal algorithm application [13, 55]. Rejection of such components involves the loss of a part of the cerebral activity and, consequently, distortion of the artifact-free EEG [29].

Figure 7.18a gives an example of an independent component $z_1(t)$ found by ICA and identified as corresponding to blinking artifacts. According to the ICA assumptions, this component cannot include other artifacts independent of the ocular ones. The component can be split into a high amplitude artifact $A(t)$ (Fig. 7.18b) and a low amplitude residual neural signal $n(t)$ (Fig. 7.18c):

$$z_1(t) = A(t) + n(t) . \quad (7.30)$$

Note that the ocular artifact vanishes outside of the blinking episodes (Fig. 7.18b). However, the component contains a significant amount of the persisting neural signal (Fig. 7.18a–c).

In the conventional ICA algorithm, the whole component is set to zero, i.e., $z_1(t) = 0$, before the signal recomposition of (7.28) and (7.29). This way, in the ICA-corrected EEG, we lose a part of the cerebral activity:

$$\hat{x}_j(t) = r_j(t) - m_{j1}n(t) , \quad (7.31)$$

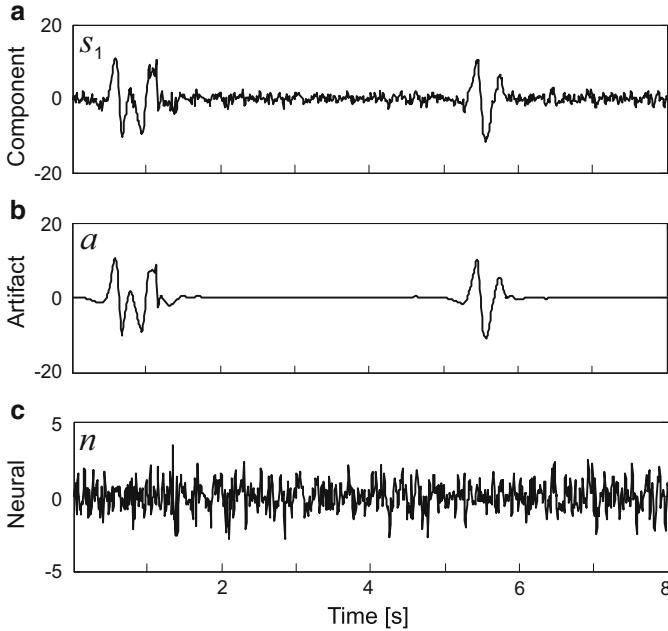


Fig. 7.18 Decomposition of an independent component into artifactual and neural parts. (a) The independent component found by ICA has two episodes of eye blinking (around 0.8 and 5.5 s). (b) Artifactual source presented in the component. (c) Underlying signal of neural origin leaked into the component

where $r_j(t) = x_j(t) - m_{j1}A(t)$ is the artifact-free signal and m_{j1} is the corresponding weight from the mixing matrix M .

Estimating the persisting neural signal $n(t)$, we can further subtract it from the component and thus correct the ICA reconstruction of the artifact-free EEG recording. A priori, as happens in ICA, the decomposition (7.30) of the independent component into artifactual and neural activity is unknown. However, using properties of the signals $A(t)$ and $n(t)$, we can estimate them. Indeed, the artifact $A(t)$ has high magnitude (power) and is localized in the time and/or frequency domains, while $n(t)$ is of low amplitude and has a broad band spectrum (Fig. 7.18b, c). These properties fit well with the wavelet decomposition technique, which provides an optimal resolution in both the time and the frequency domains, without requiring signal stationarity.

The continuous wavelet transform of the sum (7.30) can be written as

$$W^z(s, t_0) = W^A(s, t_0) + W^n(s, t_0), \quad (7.32)$$

where $W^A(s, t_0)$ and $W^n(s, t_0)$ are the wavelet coefficients obtained by the CWT of the artificial and neural parts of the component, respectively. As mentioned above, the coefficients corresponding to artifacts will be of high amplitude and well

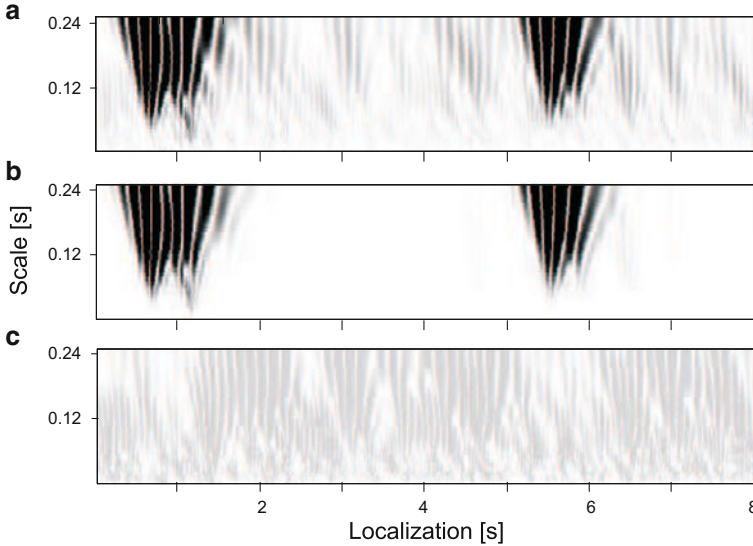


Fig. 7.19 Wavelet representation of the independent component $z_1(t)$ (a) and its parts: artifactual $A(t)$ (b) and neural $n(t)$ (c). *Gray intensity* codifies the absolute value of the wavelet coefficients. The data corresponds to the voltage traces shown in Fig. 7.18

localized in time and scale, while the neural coefficients will be distributed across all scales, and will have a broad spectrum of low energy. To illustrate this, we apply the CWT to the three signals shown in Fig. 7.18.

Figure 7.19 shows the independent component and its parts in the wavelet space. Indeed, the artifactual component $A(t)$ has high amplitude wavelet coefficients (Fig. 7.19b) localized in time windows of the blinking episodes (see also Fig. 7.18), and on long enough scales. The neural part $n(t)$ is small and spreads homogeneously over the whole spectrum of scales and localizations. Accordingly, the decomposition procedure (7.30) can generally be described as a thresholding: all wavelet coefficients above a certain threshold are set to zero, and then the resulting structure is used for the inverse wavelet transformation. Note that the thresholding can also be performed with the DWT, where in addition to (7.32) we get separation of the wavelet coefficients into “artificial” and “neural”, i.e., if $W^A(j, k) = 0$ then $W^n(j, k) = 0$ and vice versa. The described procedure is very similar to the denoising technique proposed by Donoho et al. [24], but here we aim at the opposite goal, i.e., to separate the useful low amplitude and broad band signal from the strong artifacts.

Finally the wavelet enhanced ICA (wICA) algorithm for artifact suppression in EEG is as follows:

- Apply a conventional ICA decomposition to the raw EEG, thus obtaining the mixing matrix M and N independent components $(z_1(t), z_2(t), \dots, z_N(t))^T$.

- Wavelet transform components, obtaining their representations $\{W(j, k)\}_{s_i}$.
- Threshold the wavelet coefficients, i.e., set $W(j, k) = 0$ for those that are higher than the threshold, i.e., $|W(j, k)| > K$.
- Inverse wavelet transform the thresholded coefficients $W(j, k)$, thus recomposing components $\{n_i(t)\}$ consisting of sources of neural origin only.
- Compose the wICA-corrected EEG: $X^*(t) = M(n_1(t), n_2(t), \dots, n_N(t))^T$.

Selection of the threshold value K is an essential element of the algorithm. Here we use the simplest fixed form of threshold:

$$K = \sqrt{2 \log N_t} \sigma, \quad (7.33)$$

where N_t is the length of the data segment to be processed, and

$$\sigma^2 = \frac{1}{0.6745} \text{median}(|W(s, t_0)|^2) \quad (7.34)$$

is the estimator of the magnitude of the neural broad band signal part. As we shall see, this threshold yields a good performance with ocular and heart beat artifacts. Other thresholding strategies (for a review, see [20]) can also be applied, possibly providing better tuning of the algorithm to the particular peculiarities of other artifacts or EEGs.

Note that our algorithm may be completely automatic, since no laborious visual inspection of the independent components followed by selection of those responsible for artifacts is required. The components having no high magnitude artifacts just pass through the wavelet thresholding (steps 2–4) intact, i.e., $n_k(t) = s_k(t)$. This allows for an automatic algorithm application, and consequently its most crucial step 1, to relatively short (say around 10 s) contiguous epochs, as suggested by Jung et al. [55].

7.8.4 Data Collection and Numerical Tools for Testing Connectivity

We assess the performance of artifact suppression by the ICA and wICA methods when applying them to EEGs with two final goals:

- To test the quality of brain signal recovery in the presence of artifacts.
- To quantify the distortions of the EEG power spectrum and spectral coherences introduced by ICA and wICA.

For the first test, we employ semi-simulated recordings, where a priori information on the cerebral signals allows estimation of the recovering quality in the time domain. For the second goal, we use real EEGs. As a reference, in the latter case, we use non-overlapping artifact-free epochs. Such epochs were manually

delimited off-line in the original EEG recordings by a careful inspection of the channel traces [56]. Below, we shall refer to these as control epochs. Once suitable data (ICA/wICA-corrected EEGs and control epochs) have been obtained, posterior spectral and connectivity analyses are applied. Then we compare the derived characteristics (power spectra, coherences) obtained over the same epochs in ICA- and wICA-corrected EEGs with those found for the control.

7.8.4.1 EEG Recordings

For illustration, we considered EEG data acquired following standard guidelines [105] from healthy subjects with their eyes open. The ECI Electro-Cap System with 19 scalp electrodes placed according to the International 10–20 System was used for this purpose. The signals were digitized at a rate of 256 Hz and further filtered (notch filter at 50 Hz, and band pass filter 4–45 Hz).

7.8.4.2 Semi-simulated Data

We manually cut out non-overlapping artifact-free epochs from a real EEG, thereby collecting 15 s clean signals. Then we simulate eye blinking and heart beat artifacts and mix them with the clean EEG, accounting for the artifact morphology, spatial distribution, and scalp topographies using a mixing matrix from a real recording [37]. To reproduce the shape of eye blinking episodes, we use a band pass filtered (1–3 Hz) Poisson random process of 0.3 s per episode. The heart beat is simulated by a pulse train at 1 Hz.

7.8.4.3 Spectrum Estimation

A multi-taper Fourier transform is used for continuous data sets. The algorithm reduces the variance of the spectral estimate by using a set of tapers rather than a unique data taper or spectral window. It is especially effective for short data segments [95, 122]. A MatLab toolbox is freely available [53].⁶

7.8.4.4 Functional Connectivity

To infer on the topological structure of the interaction between different brain regions, a common approach uses spectral coherence (SC) and partial spectral coherence (PSC). To evaluate the SC and PSC we used a customary written Matlab code (based on spectral calculations implemented in the Signal Processing Toolbox).

⁶Available at chronux.org/chronux

The SC is a normalized measure of the cross-spectrum $P_{xy}(\omega) = P_x(\omega)P_y(\omega)$ of two EEG signals $x(t)$ and $y(t)$ recorded at different sites:

$$SC_{xy}(\omega) = \frac{P_{xy}(\omega)}{\sqrt{P_{xx}(\omega)P_{yy}(\omega)}}. \quad (7.35)$$

If the SC equals zero for all frequencies ω , the two processes are linearly independent, i.e., no interaction between the two measured EEG signals exists. $|SC| = 1$ indicates a perfect linear relationship between the two processes, i.e., the dynamics of one signal is completely explained by the other. A significant level of the SC between these extremes, i.e., $0 \leq |SC| \leq 1$, in a certain frequency band implies an association (in terms of synchronization) between the signals, and it is a sign of functional connectivity between the corresponding cortical areas.

The PSC of two EEG signals $x(t)$ and $y(t)$ is given by

$$PSC_{xy|C}(\omega) = -\frac{g_{xy}(\omega)}{\sqrt{g_{xx}(\omega)g_{yy}(\omega)}}, \quad (7.36)$$

where $g(\omega) = P^{-1}(\omega)$ is the inverse matrix of the cross-spectra and C denotes all the other signals. The PSC is also a bounded function, $0 \leq |PSC| \leq 1$. To decide whether two sites are (functionally) coupled directly or not, we apply the same criterion as for the SC.

To conclude positively on the connectivity (synchrony) between two EEG channels, the coherence (either SC or PSC) should be higher than the significance level obtained under assumption of the null hypothesis that time series are statistically independent. In other words, we have to estimate the level of random leakage between the channels. To evaluate the significance level, we use a surrogate data test [110, 121]. The surrogate time series are obtained from the original by randomizing phase relations, keeping the other first order characteristics intact [68].

7.8.5 Suppression of Artifacts by ICA and wICA Methods

Let us first exemplify artifact suppression for the rejection of eye blinking and heart beat artifacts. The eye blinking artifact appears in EEG in the form of large pulses that are well localized in time, and it has the strongest impact on EEG signals. The heart beat artifact appears when an electrode is placed near an artery, and it shows up as a train of short-lasting, relatively low amplitude pulses at a frequency of about 70 beats per minute.

Figure 7.20a shows an example of an EEG taken from a healthy adult subject, instructed to remain in a steady state with the eyes open. The data segment shown has both artifact types we are interested in. Two eye blinking episodes (localized around 3 and 7 s) spread over all channels and affect the frontal sites (from FP1

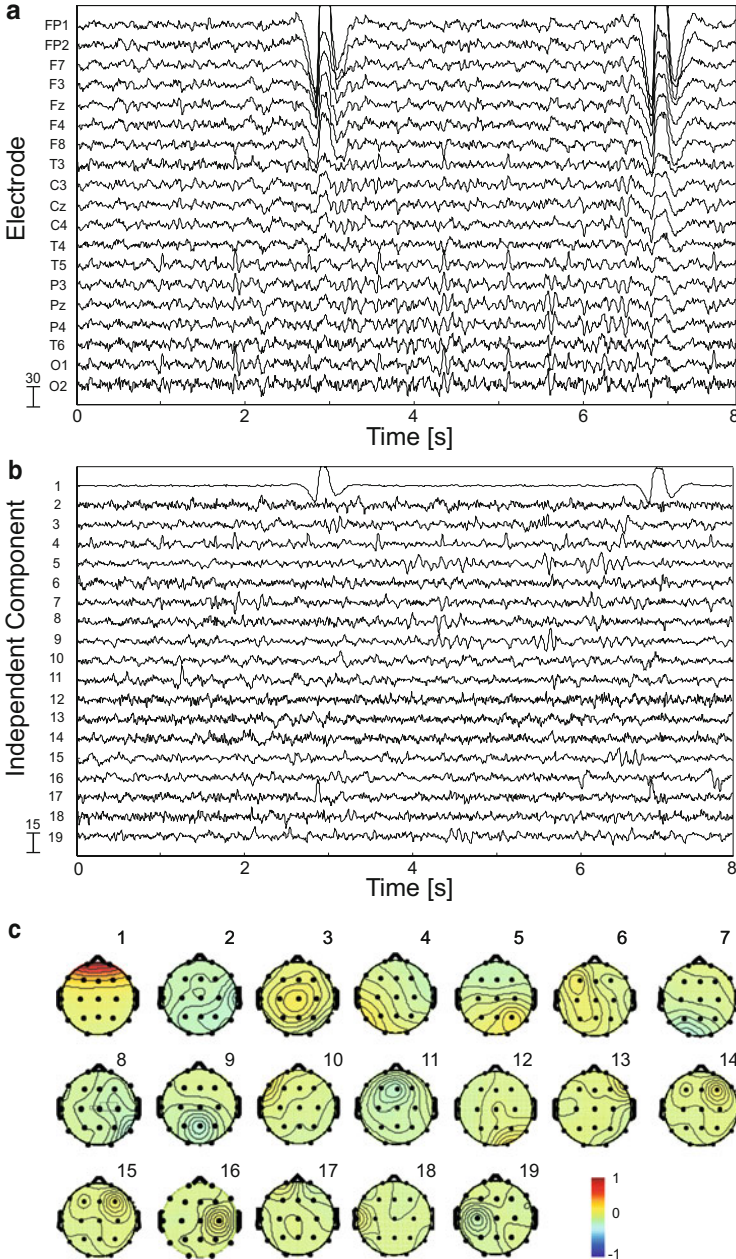


Fig. 7.20 Example of an ICA decomposition of an EEG contaminated by ocular and heart beat artifacts. **(a)** Original EEG data (a segment of 8 s is shown). **(b)** Independent components decomposing the original EEG into 19 sources. The first component is identified as due to ocular artifacts, while the fourth captures the heart beat artifacts. **(c)** Scalp maps showing relative projection strengths of the components over all electrodes. Artifactual components #1 and #4 project most strongly to the frontal and left temporo-occipital areas, respectively

to F8) most strongly. Control segments (for FP1) are taken between consecutive artifact episodes, e.g., at 3.5–6.5 s. The heart beat artifact mainly contaminates the left tempo-occipital electrodes (T3, T5, O1).

The ICA algorithm separates the contributions of the artifactual and neural signals into 19 independent components. The first independent component exhibits strong pulses (Fig. 7.20b) and projects mainly to frontal sites (Fig. 7.20c). This is the “fingerprint” of blinking artifacts whose morphology is characterized by strong short-lasting pulses, and scalp topography shows clear evidence in the frontal sites [55]. Using this a priori knowledge, we identify the first component as being due to the eye blinking artifacts. Similarly, the fourth independent component (Fig. 7.20b) captures the rhythmic pulses from the heart beat artifact. It projects mainly to the left tempo-occipital area (Fig. 7.20c).

Now according to the ICA artifact suppression method, we set the first and the fourth components to zero and reconstruct the EEG recording using (7.29), thus obtaining the ICA-corrected EEG (Fig. 7.21a). Note that, in this way, in accordance with the ICA assumptions, we aim to suppress heart beat and ocular artifacts alone. We also clean the same EEG using the wICA algorithm. Here we skip the manual analysis of the components, but instead apply the automatic wavelet thresholding (steps 2–4) followed by the signal recomposition (step 5). Figure 7.21b shows the EEG corrected by wICA.

Visual inspection of the cleaned EEGs confirms that both methods effectively suppress both artifact types. However, analyzing signals first at the frontal electrodes within artifact-free epochs (outside of blinking episodes), we observe some distortions introduced by the ICA method. The EEG signal cleaned by wICA gives a good match with the artifact-free control signal (Fig. 7.21c). Quantifying the mean squared error in the time domain, viz.,

$$\text{MSE} = E \left[(x_{\text{ICA/wICA}}(t) - x_{\text{control}}(t))^2 \right], \quad (7.37)$$

we get, at FP1, 10.6 and 0.1 μV^2 for ICA and wICA, respectively.

To characterize the quality of the heart beat correction by the two methods, we reconstructed the heart beat artifact at the T5 electrode:

$$A_{\text{heart beat}}(t) = x_{\text{raw}}(t) - \hat{x}_{\text{ICA/wICA}}(t). \quad (7.38)$$

Figure 7.21d shows the artifact estimates provided by the two methods. The artifact reconstructions by ICA and wICA retain about 4.1 and 0.5 μV^2 of the cerebral activity, respectively. We recall that this activity is lost in the corrected EEG. To discard the possibility of a fault due to a particular realization of the ICA algorithm or oddness of the data set, we repeated the same procedure using two different ICA algorithms (Infomax and FastICA) and with different EEG recordings (including recordings where only ocular artifacts were present). Consistently with other studies [13, 80], both ICA algorithms gave similar results when applied to different recordings. Thus we conclude that ICA and wICA methods effectively suppress

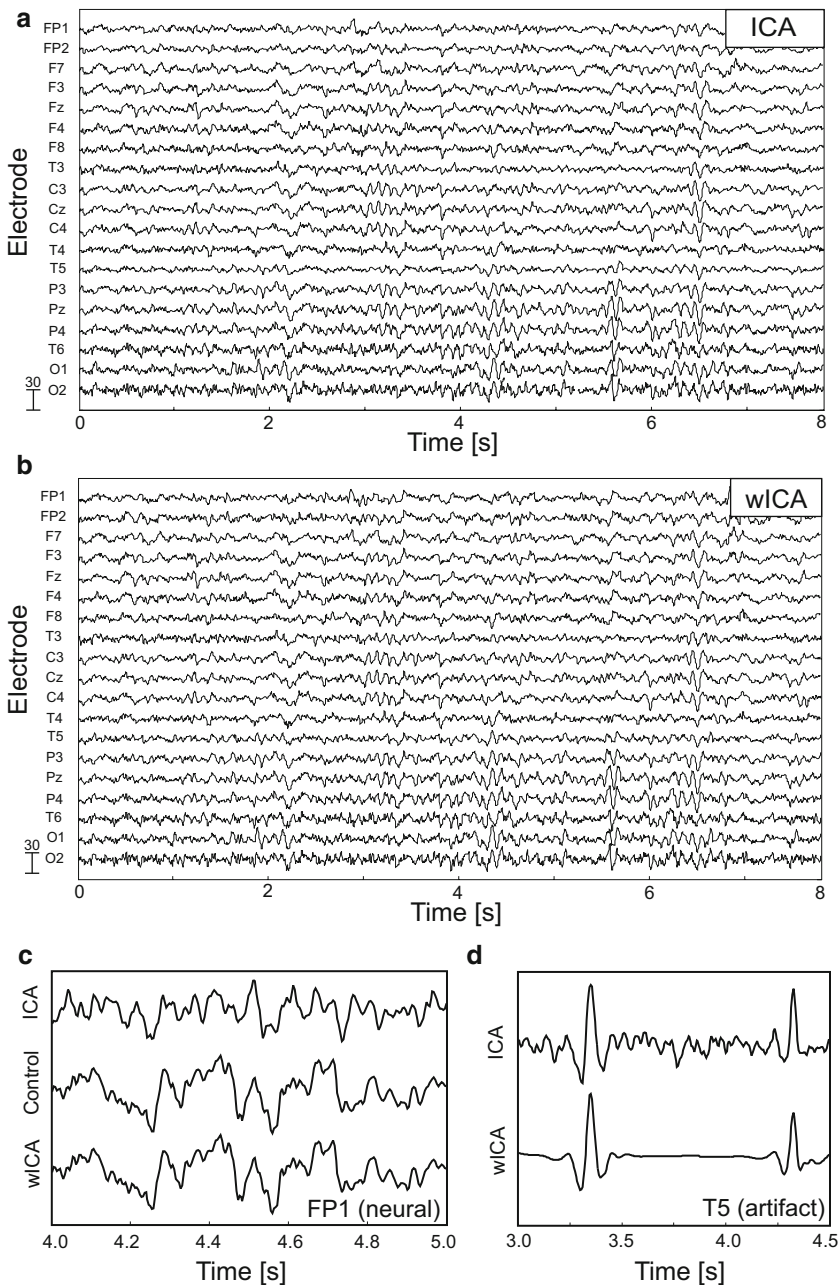


Fig. 7.21 Artifact suppression and signal distortion by ICA and wICA methods. (a) and (b) ocular and heart beat artifacts are effectively suppressed by the ICA (a) and wICA (b) methods (compare with Fig. 7.20a). (c) Zoomed signals during a control (artifact-free) epoch at the FP1 electrode. The wICA-cleaned signal practically reproduces the control signal, while ICA introduces some signal distortions. (d) Estimation of the heart beat artifact at the T5 electrode according to (7.38)

ocular and heart beat artifacts, but outside of the artifact episodes, wICA conserves the cerebral activity much better.

7.8.6 *Recovering Brain Signals in the Presence of Artifacts*

Above we saw that ICA may alter brain signals, while wICA better preserves the brain activity. Let us now quantify in the time domain the distortions introduced by these methods when recovering brain signals in the presence of artifacts. We generate semi-simulated EEG data by mixing joined preselected artifact-free epochs from a real EEG of a healthy subject at rest, and two types of simulated artifacts: ocular and heart beat. The mixture conforms to the artifact morphologies and spatial distributions. Figure 7.22a shows an example of such a recording. The ocular artifacts propagate through frontal sites, and the heart beat is mostly present in the F8 channel.

Following the procedure discussed above, we calculate 19 independent components (Fig. 7.22b), and identify the components numbered 1 and 3 as artificial, due to eye blinking and heart beat, respectively. Note that, as mentioned above, outside of the artifact episodes, the components comprise a considerable amount of cerebral activity that also persists in them during the artifact episodes. This persistent activity degrades the quality of cleaning by ICA, whereas wICA allows one to recover this activity, thereby enhancing the signal cleaning performance. Figure 7.22c illustrates zoomed cerebral activity, simulated artifacts, and ICA/wICA recovered signals. As in Fig. 7.21c, we observe more prominent signal distortion introduced by the ICA method as compared with wICA. This holds for suppression of both ocular and heart beat artifacts.

To quantify the quality of cerebral signal recovery, we calculate the mean squared residual error between the reference (artifact free) EEG in channels FP1 and F8 and those obtained after ICA/wICA processing. Table 7.9 summarizes the results. The presence of ocular and heart beat artifacts in the semi-simulated EEG (not corrected) is characterized by 92.4 and 11.2 μV^2 in the “recorded” signals relative to the control for the FP1 and F8 electrodes, respectively. EEG cleaning by ICA significantly reduces the presence of artifacts in the FP1 channel (by a factor of about nine) and moderately in the F8 channel (by a factor of about one and a half). This corresponds to a reduction of the ocular and heart beat artifacts by 19.4 and 3.5 dB, respectively. wICA further improves the quality of artifact suppression and enhances the performance of ICA by a factor of 6 when separating the cerebral activity from ocular artifacts and by a factor of more than three in the case of heart beat artifacts. Thus for wICA, we have 35.2 and 13.7 dB reductions of the ocular and heart beat artifacts, respectively.

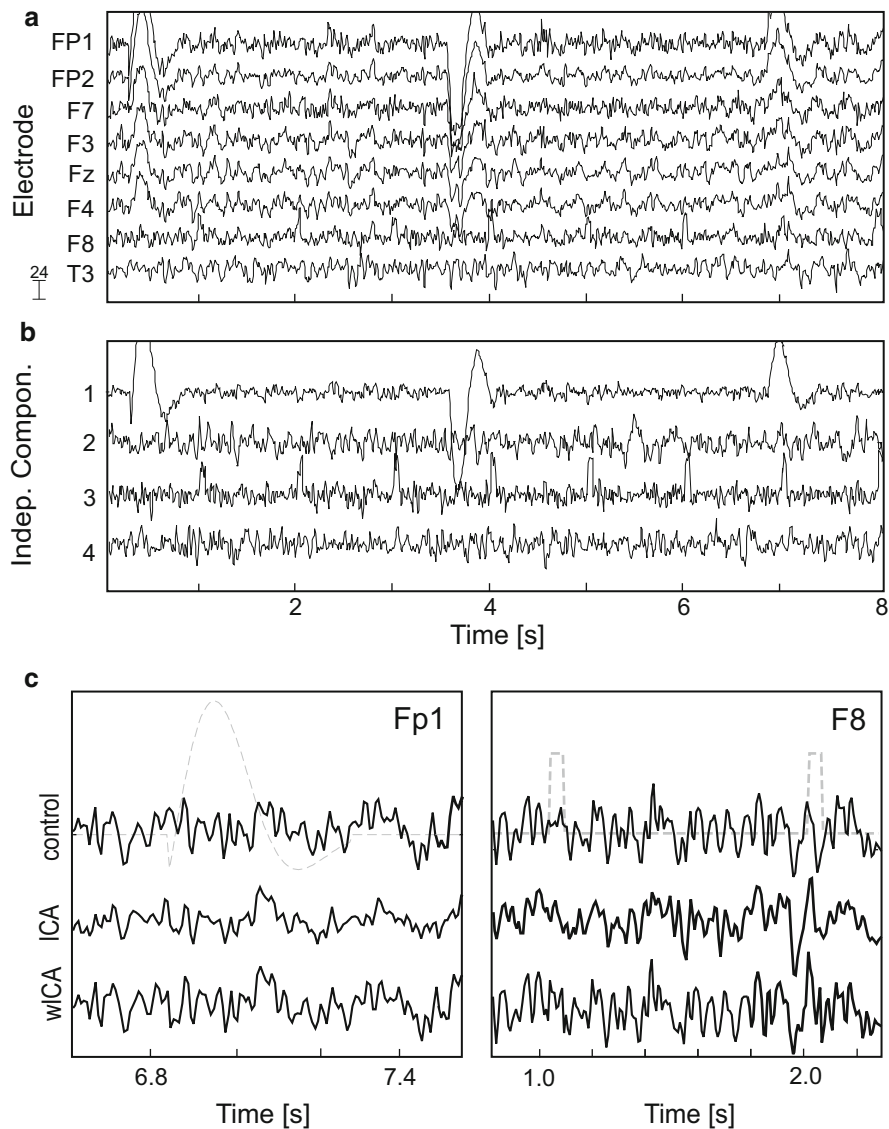


Fig. 7.22 Recovering the brain signal under artifacts on a semi-simulated EEG. (a) EEG segment of 8 s exhibiting ocular (electrodes FP1–F4) and heart beat (electrode F8) artifacts (the first 8 of 19 channels are shown). (b) Independent components as found by ICA (the first 4 of 19 components are shown). Components #1 and #3 correctly pick up the time courses of ocular and heart beat artifacts, respectively. However, a considerable amount of cerebral activity leaks into these components. (c) Zoomed control and ICA/wICA-cleaned signals within ocular (left, Fp1) and heart beat (right, F8) artifact episodes. Time courses of simulated artifacts are shown by dashed gray curves. For both artifact types, ICA-corrected signals deviate considerably more from the reference signals than the wICA-cleaned traces

Table 7.9 Mean squared error for ICA- and wICA-corrected EEGs in the time domain. The first row (not corrected) quantifies the composite strength of ocular and heart beat artifacts present in channels FP1 and F8. The columns show the error in the corresponding channel after artifact suppression by ICA and wICA

	FP1 channel [μV^2]	F8 channel [μV^2]
Not corrected	92.4	11.2
ICA	9.9	7.5
wICA	1.6	2.3

7.8.7 Power Spectrum Distortion

We now consider real EEG recording distortions in the power spectrum of the cerebral activity introduced by artifact suppression. The signal distortions quantified above (see Table 7.9) will generally have an effect on the power spectrum of the cerebral signal:

$$P_{\overline{xx}}(\omega) = P_{rr}(\omega) + \Delta P(\omega) , \quad (7.39)$$

where P_{rr} is the reference power spectrum of the artifact free signal, $P_{\overline{xx}}$ is the spectrum of the signal processed either by ICA or wICA, and P is the spectrum distortion introduced by the methods as a side-effect, which ideally should be equal to zero.

Assuming that the artifacts are expressed in the first independent component (as shown in Fig. 7.20), the power spectrum distortion of the signal introduced by ICA at the j th electrode is given by

$$\Delta P_j(\omega) = -m_{j1}^2 P_m(\omega) , \quad (7.40)$$

where m_{j1} is the corresponding weight from the mixing matrix M , and P_{nn} is the spectrum of the cerebral activity persisting in the independent component (7.30). According to (7.40), the power spectra at all electrodes of the ICA-corrected EEG are underestimated with the same spectral function P_m , but with different factors m_{j1}^2 . Since m_{j1}^2 decays with j for ocular artifacts (Fig. 7.20c), the spectral distortions are higher at the frontal sites. The wICA algorithm drastically reduces the residual cerebral activity in the artifactual component, and hence significantly decreases P_m , thereby providing a potentially better approximation to the power spectrum of artifact-free EEGs.

To quantify the degree of spectral distortions introduced by the artifact suppression methods across different frequency bands, we calculate the mean power density, averaging over ten epochs, and convert it to decibels, for the control (reference) segments before and after ICA and wICA artifact suppression. We repeat the same procedure, changing the length of the data segments used for ICA decomposition, but keeping the same time boundaries for the control epochs. Table 7.10 summarizes the results. The spectrum distortion by ICA (difference between the power densities

Table 7.10 Mean power density in the FP1 channel, evaluated for the control and after artifact suppression by ICA and wICA using the same data epochs

Frequency band	Power density [dB] control	Artifact rejection method	Segment length				
			Power density [dB]				
			4 s	8 s	10 s	15 s	25 s
Theta (4–8 Hz)	21.0	ICA	18.8	16.7	16.6	15.9	15.5
		wICA	20.5	20.4	20.3	19.8	18.9
Alpha (8–13 Hz)	17.9	ICA	16.4	14.2	14.1	13.4	13.2
		wICA	17.8	17.7	17.7	17.6	17.5
Beta (13–30 Hz)	16.1	ICA	13.2	11.7	11.8	10.5	10.3
		wICA	16.1	16.0	16.0	16.0	15.9
Gamma (>30 Hz)	8.6	ICA	5.2	3.6	3.8	2.4	2.1
		wICA	8.6	8.7	8.7	8.7	8.6

evaluated over ICA-corrected and artifact-free signals) increases with the length of the data segment used to estimate the mixing matrix and independent components. Regarding frequencies, the Theta and Alpha bands are less affected, while Beta and Gamma suffer more. wICA preserves the signal better within the artifact-free time windows, and achieves a considerably lower error in the spectrum estimates. Slight distortions are observed in the Theta band, while in the other bands spectral densities are very close to the control values.

We also observe a small decrease in the performance with the increase in segment length used for evaluation of the independent components. To keep this under control, we suggest using segments lasting no more than 15 s. Fixing the length at 10 s (the recommended value for ICA decomposition), we find the absolute values of the spectral distortion, viz.,

$$|\Delta P| = |P_{\text{ICA/wICA}} - P_{\text{ctr}}|, \quad (7.41)$$

to be 4.4, 3.8, 4.3 and 4.8 dB for ICA, and 0.7, 0.2, 0.1, and 0.1 dB for wICA, over the Theta, Alpha, Beta and Gamma bands, respectively. Note that, as predicted in (7.40), the spectrum of the ICA-corrected EEG is always lower than the control spectrum.

7.8.8 *Artifact Suppression and Non-local Characteristics Derived from EEG*

We now investigate the way artifact suppression affects inferences drawn about the interaction (circuitry) between different sites. In the simplest case, synchrony between different electrodes can be picked up by evaluation of spectral and partial spectral coherences (SC and PSC).

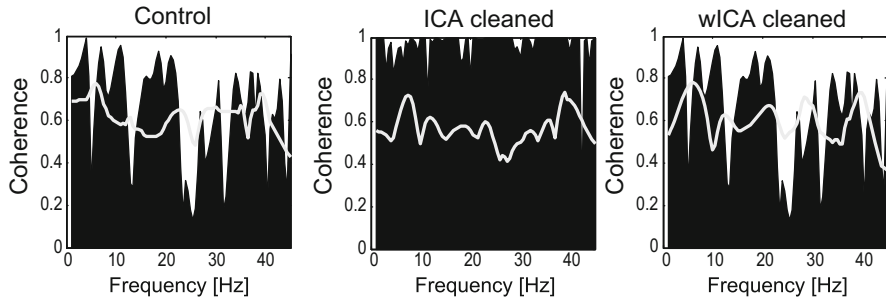


Fig. 7.23 Spectral coherence for a pair of electrodes FP1 and F7 evaluated for the control, and after ICA and wICA artifact suppression. *Gray curves* depict levels of statistical significance. The ICA-corrected EEG shows an overestimated coherence

Figure 7.23 shows an example of the SC evaluated for the pair of electrodes FP1 and F7 under control conditions (using artifact-free epochs), and after ICA and wICA artifact suppression. In each graph, we also plot the level of statistical significance obtained through the surrogate data test. Coherence in a given frequency band above the surrogate level is considered significant and we conclude that there is a functional association between these channels. The coherence calculated over the ICA-corrected EEG is significantly higher than the control over all frequency bands (Fig. 7.23a, b). This overestimation may lead to a spurious hyperconnectivity, i.e., to a false positive conclusion regarding the interaction between the corresponding cortical areas. Artifact suppression by the wICA algorithm involves fewer amplitude and phase distortions of the cerebral part of the EEG and we obtain a coherence estimate very close to the control conditions (Fig. 7.23a, c).

We now test how the results of artifact suppression affect the identification of connectivity patterns between EEG signals. To conclude positively regarding the presence of a connection between a pair of sites, we evaluate the elevation of the PSC above the level of statistical significance provided by the surrogate data test, just as it is shown for ordinary coherence in Fig. 7.23. If positive, this value quantifies the degree of synchrony between the cortical sites, taking into account the dynamics observed at the other electrodes. Figure 7.24 shows the degree of synchrony calculated for the ICA- and wICA-corrected EEG relative to the coherence level under control conditions. No line connecting two cortical sites means perfect concordance with control conditions, whereas red or blue links point to hyper- or hypoconnections compared with control conditions, respectively. ICA data processing generally leads to hyperconnectivity over all frequency bands (see also Fig. 7.23). Application of wICA significantly improves predictions, providing only a few spurious links in the Theta and Alpha bands.

To gain insight into the problem of hyperconnectivity biasing after ICA artifact suppression (Fig. 7.24), we consider a case where neural signals $r_j(t)$ and $r_k(t)$ from two electrodes are statistically unrelated, and consequently have vanishing cross-correlation and coherence. We assume the signals to be corrupted by ocular

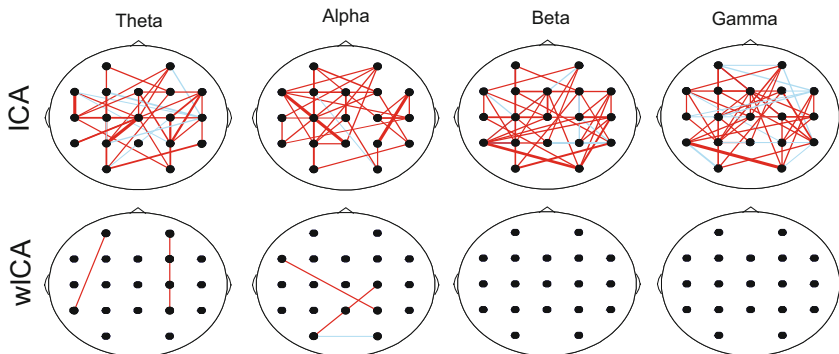


Fig. 7.24 Relative degree of coupling between cortical areas evaluated using partial spectral coherence (PSC). As a reference (zero level), we use the coherence evaluated under control conditions. *Red and blue lines* show spurious hyper- and hypocoherecence links, respectively. The link width defines the strength of the relative association between corresponding sites

artifacts $A(t)$. An application of ICA gives

$$\hat{x}_k(t) = r_k(t) - m_{k1}n(t), \quad \hat{x}_j(t) = r_j(t) - m_{j1}n(t), \quad (7.42)$$

where, as in (7.31), hatted variables correspond to ICA-corrected EEG signals, $r_{j,k}(t)$ are the artifact-free signals, and $n(t) = s_1(t) - A(t)$ is the neural activity persisting in the independent component due to artifacts. From (7.42), we immediately see that, although the artifact-free signals $r_j(t)$ and $r_k(t)$ are uncorrelated, their ICA counterparts \hat{x}_j and \hat{x}_k correlate due to the presence of the common term $n(t)$. Hence we have nonvanishing, spurious coherence:

$$|\text{SC}(\omega)| = \frac{m_{k1}m_{j1}P_{nn}}{\sqrt{P_{\hat{x}_k\hat{x}_k}P_{\hat{x}_j\hat{x}_j}}} \geq 0. \quad (7.43)$$

Thus when the residual neural activity in the component identified as corresponding to artifacts does not vanish, the spectral coherence (and also the partial spectral coherence) can be overestimated after ICA artifact suppression (Fig. 7.24). The wICA algorithm recovers the neural activity persisting in the component, thereby improving the results of the coherence estimate.

7.8.9 Conclusion

In this section we have pursued two complimentary goals:

- To study quantitatively how suppression of artifacts in EEG data distorts the underlying cerebral activity and affects the quality of derived local and non-local characteristics.

- To discuss a method that enhances the performance of the conventional ICA by reducing the EEG distortions due to artifact removal.

First, we have shown that ICA-corrected EEGs may partially lose the record of cerebral activity. Indeed, ICA decomposes the EEG into components of artificial and neural origins and rejects the former. Such a separation is valid for independent, linearly mixed sources when their total number does not exceed the number of recording electrodes [6]. In practice these assumptions can be violated leading to a “leak” of the cerebral activity into components deemed artificial. Complete rejection of such a component thus involves a partial loss of the neural signal. To reduce the distortions in corrected EEGs, we have proposed a wavelet enhanced ICA (wICA) method that allows one recover the cerebral activity leaked into the artificial components.

The wICA method is based on ICA signal decomposition and includes the wavelet thresholding of the independent components as an intermediate step. This step recovers the low amplitude, broad band neural activity persisting in the components identified as responsible for artifacts. Thus, the subsequent deletion of only the artifactual part of the components does not distort the underlying neural activity in the wICA-corrected EEG. Note that wICA not only recovers the cerebral activity outside of the artifact episodes, but it also allows substantial recovery of the neural signal in the presence of artifacts. Another advantage of wICA is its automation. No laborious, ambiguous visual inspection of the independent components is required. Instead, all components are passed through the thresholding procedure, whence only the high magnitude artifacts (e.g., from eye blinking) are cut out. At this point we recall that the proposed use of wavelet analysis, not on raw EEG, but on the independent components has the following important advantage. Artifacts are concentrated in a few components, where the ratio of artifact magnitude to cerebral activity magnitude is much higher than in the artifact-affected electrodes. This greatly improves the quality of artifact detection, and also simplifies the application since fine tuning of the threshold value is not required.

Second, we have quantified the performance of the ICA and wICA artifact suppression methods in the time and frequency domains using semi-simulated and real EEG recordings. Note that quantification of the quality of signal recovery refers to an artifact-free control EEG. In the time domain, we have shown that ICA effectively (by 19.4 dB) eliminates the presence of ocular artifacts and moderately reduces the heart beat artifacts (by 3.5 dB). wICA offers significant improvements, reducing the presence of ocular and heart beat artifacts by 35.0 and 13.7 dB, respectively. In the frequency domain, we have shown that ICA tends to underestimate the EEG power spectrum over all frequency bands. We have estimated the power spectrum loss theoretically and shown that it is a product of the spectrum of the persistent neural activity and the corresponding weight of the mixing matrix. This means, for instance, that spectral loss for ocular artifact suppression is higher in the frontal sites. Calculating the absolute value of the spectral distortion at the FP1 electrode, we found 4.4/0.7, 3.8/0.2, 4.3/0.1 and 4.8/0.1 dB in the Theta, Alpha, Beta and Gamma bands, respectively, for ICA/wICA.

EEG recording is a multichannel technique that provides a natural basis for the study of non-local cerebral dynamics and cortical circuitry. For the first time we have addressed the question of how artifact suppression affects the evaluation of the simplest non-local characteristics, i.e., spectral and partial spectral coherences. Our results suggest that ICA-corrected EEGs may exhibit an overestimated level of coherence, while wICA overcomes this problem, approaching the coherence level found under control conditions. This overestimation may lead to erroneous conclusions regarding the presence of spurious couplings (associations) between the corresponding cortical areas. Indeed, we have shown that the connectivity pattern provided by partial spectral coherence evaluated over ICA-corrected EEG is much denser than under control conditions. wICA solves the problem, showing practically the same connectivity pattern as under control conditions.

References

1. S. Amari, A. Cichocki, H. Yang, A new learning algorithm for blind signal separation, in *Advances in Neural Information Processing Systems 1995*, Denver, vol. 8 (MIT, Cambridge, 1996), p. 757
2. R.G. Andrzejak, G. Widman, K. Lehnertz, C. Rieke, C.E. David, P. Elder, The epileptic process as nonlinear deterministic dynamics in a stochastic environment: an evaluation of mesial temporal lobe epilepsy. *Epilepsy Res.* **44**, 129 (2001)
3. J. Anemüller, T. Sejnowski, S. Makeig, Complex independent component analysis of frequency-domain electroencephalographic data. *Neural Netw.* **16**, 1311 (2003)
4. R.E. Appleton, Vigabatrin in the management of generalized seizures in children. *Seizure* **4**, 45 (1995)
5. T. Bassani, J.C. Nievola, Pattern recognition for brain-computer interface on disabled subjects using a wavelet transformation, in *Proceedings of the 2008 IEEE Symposium on Computational Intelligence in Bioinformatics and Computational Biology, CIBCB'08*, Sun Valley, 15–17 Sept 2008, pp. 180–186
6. A. Bell, T. Sejnowski, An information-maximization approach to blind separation and blind deconvolution. *Neural Comput.* **7**, 1129 (1995)
7. N. Benito, A. Fernandez-Ruiz, V.A. Makarov, J. Makarova, A. Korovaichuk, O. Herreras, Spatial modules of coherent activity in pathway-specific LFPs in the hippocampus reflect topology and different modes of presynaptic synchronization. *Cereb. Cortex* (2013). doi:10.1093/cercor/bht022
8. A. Berenyi, M. Belluscio, D. Mao, G. Buzsaki, Closed-loop control of epilepsy by transcranial electrical stimulation. *Science* **337**(6095), 735 (2012)
9. P. Bergé, Y. Pomeau, C. Vidal, *L'Ordre dans le Chaos* (Hermann, Paris, 1988); P. Bergé, Y. Pomeau, C. Vidal, *Order within Chaos* (Wiley, New York, 1984)
10. S. Boccaletti, D.L. Valladares, Characterization of intermittent lag synchronization. *Phys. Rev. E* **62**(5), 7497 (2000)
11. S. Boccaletti, J. Kurths, G.V. Osipov, D.L. Valladares, C.S. Zhou, The synchronization of chaotic systems. *Phys. Rep.* **366**, 1 (2002)
12. S.V. Bozhokin, N.B. Syvovov, Wavelet-analysis of transient processes in EEG at photostimulation. *Biomed. Electron.* **3**, 13 (2008)
13. G. Brown, S. Yamada, T. Sejnowski, Independent component analysis at the neural cocktail party. *Trends Neurosci.* **1**, 54 (2001)

14. C. Brunner, R. Scherer, B. Graimann, G. Supp, G. Pfurtscheller, Online control of a brain–computer interface using phase synchronization. *IEEE Trans. Biomed. Eng.* **53**, 2501 (2006)
15. J.L. Cabrera, J. Milnor, On–off intermittency in a human balancing task. *Phys. Rev. Lett.* **89**(15), 158702 (2002)
16. G. Casella, L. Roger, *Statistical Inference* (Duxbury, Pacific Grove, 2002)
17. N. Cashdollar, N. Lavie, E. Duzel, Alleviating memory impairment through distraction. *J. Neurosci.* **33**(48), 19012 (2013)
18. N.P. Castellanos, V.A. Makarov, Recovering EEG brain signals: artifact suppression with wavelet enhanced independent component analysis. *J. Neurosci. Methods* **158**, 300 (2006)
19. F. Cong, V. Alluri, A.K. Nandi, P. Toiviainen, R. Fa, B. Abu-Jamous, L. Gong, B.G.W. Craenen, H. Poikonen, M. Huotilainen, T. Ristaniemi, Linking brain responses to naturalistic music through analysis of ongoing EEG and stimulus features. *IEEE Trans. Multimed.* **5**, 1060 (2013)
20. L. Debnath, *Wavelet Transforms and Their Applications* (Birkhauser, Boston, 2002)
21. L. De Gennaro, M. Ferrara, Sleep spindles: an overview. *Sleep Med. Rev.* **7**, 423 (2003)
22. A. Delorme, S. Makeig, EEGLAB: an open source toolbox for analysis of single-trial EEG dynamics including independent component analysis. *J. Neurosci. Methods* **134**, 9 (2004)
23. A. Destexhe, T.J. Sejnowski, *Thalamocortical Assemblies: How Ion Channels, Single Neurons and Large-Scale Networks Organize Sleep Oscillations* (Oxford University Press, Oxford, 2001)
24. D.L. Donoho, I.M. Johnstone, G. Kerkycharian, D. Picardi, Wavelet shrinkage: asymptopia? *J. R. Stat. Soc. (Stat. Methodol.)* **B57**, 301 (1995)
25. W.H. Drinkenburg, M.L. Schuurmans, A.M. Coenen, J.M. Vossen, E.L.M. van Luijtelaar, Ictal stimulus processing during spike–wave discharges in genetic epileptic rats. *Behav. Brain Res.* **143**, 141 (2003)
26. A. Fernandez-Ruiz, V.A. Makarov, N. Benito, O. Herreras, Schaffer-specific local field potentials reflect discrete excitatory events at gamma frequency that may fire postsynaptic hippocampal CA1 units. *J. Neurosci.* **32**, 5165 (2012)
27. A. Fernandez-Ruiz, S. Munoz, M. Sancho, J. Makarova, V.A. Makarov, O. Herreras, Cytoarchitectonic and dynamic origins of giant positive LFPs in the dentate gyrus. *J. Neurosci.* **33**(39), 15518 (2013)
28. A. Flexer, H. Bauer, J. Pripfl, G. Dorffner, Using ICA for removal of ocular artifacts in EEG recorded from blind subjects. *Neural Netw.* **18**, 998 (2005)
29. K. Friston, Modes or models: a critique on independent component analysis for fMRI. *Trends Cogn. Sci.* **2**, 373 (1998)
30. P. Gloor, Generalized cortico-reticular epilepsies: some considerations on the pathophysiology of generalized bilaterally synchronous spike and wave discharge. *Epilepsia* **9**, 249 (1968)
31. P. Gong, A.R. Nikolaev, C. van Leeuwen, Intermittent dynamics underlying the intrinsic fluctuations of the collective synchronization patterns in electrocortical activity. *Phys. Rev. E* **76**(1), 011904 (2007)
32. C.L. Gottesmann, The transition from slow-wave sleep to paradoxical sleep: evolving facts and concepts of the neurophysiological processes underlying the intermediate stage of sleep. *Neurosci. Biobehav. Rev.* **20**, 367 (1996)
33. C. Guger, H. Ramoser, G. Pfurtscheller, Real-time EEG analysis for a brain–computer interface (BCI) with subject-specific spatial patterns. *IEEE Trans. Neural Syst. Rehabil. Eng.* **8**(4), 447 (2000)
34. P.W. Hammer, N. Platt, S.M. Hammel, J.F. Heagy, B.D. Lee, Experimental observation of on–off intermittency. *Phys. Rev. Lett.* **73**(8), 1095 (1994)
35. E. Haselsteiner, G. Pfurtscheller, Using time-dependent neural networks for EEG classification. *IEEE Trans. Neural Syst. Rehabil. Eng.* **8**, 457 (2000)
36. J.F. Heagy, N. Platt, S.M. Hammel, Characterization of on–off intermittency. *Phys. Rev. E* **49**(2), 1140 (1994)

37. H. Hori, M. Aiba, B. He, Spatio-temporal cortical source imaging of brain electrical activity by means of time-varying parametric projection filter. *IEEE Trans. Biomed. Eng.* **51**, 768 (2004)
38. A.E. Hramov, A.A. Koronovskii, Intermittent generalized synchronization in unidirectionally coupled chaotic oscillators. *Europhys. Lett.* **70**(2), 169 (2005)
39. A.E. Hramov, A.A. Koronovskii, I.S. Midzyanovskaya, E.Yu. Sitnikova, C.M. Rijn, On-off intermittency in time series of spontaneous paroxysmal activity in rats with genetic absence epilepsy. *Chaos* **16**, 043111 (2006)
40. A.E. Hramov, A.A. Koronovskii, M.K. Kurovskaya, S. Boccaletti, Ring intermittency in coupled chaotic oscillators at the boundary of phase synchronization. *Phys. Rev. Lett.* **97**, 114101 (2006)
41. A.E. Hramov, A.E. Khramova, A.A. Koronovskii, S. Boccaletti, Synchronization in networks of slightly nonidentical elements. *Int. J. Bifurc. Chaos* **18**(3), 258 (2008)
42. A.E. Hramov, A.A. Koronovskii, M.K. Kurovskaya, O.I. Moskalenko, Type-I intermittency with noise versus eyelet intermittency. *Phys. Lett. A* **375**, 1646 (2011)
43. M. Huang, P. Wu, Y. Liu, L. Bi, H. Chen, Application and contrast in brain-computer interface between Hilbert-Huang transform and wavelet transform, in *The 9th International Conference for Young Computer Scientists, ICYCS*, Zhang Jia Jie, 18–21 Nov 2008, pp. 1706–1710
44. A. Hyvärinen, Independent component analysis: recent advances. *Philos. Trans. R. Soc. A* **371**, 20110534 (2013)
45. A. Hyvärinen, E. Oja, Independent component analysis: algorithms and applications. *Neural Netw.* **13**(4–5), 411–430 (2000)
46. A. Hyvärinen, P. Pajunen, Nonlinear independent component analysis: existence and uniqueness results. *Neural Netw.* **12**, 209 (1999)
47. H. Ito, A.R. Nikolaev, C. van Leeuwen, Dynamics of spontaneous transitions between global brain states. *Hum. Brain Mapp.* **28**, 904 (2007)
48. J. Iriarte, E. Urrestarazu, M. Valencia, M. Alegre, A. Malanda, C. Viteri, J. Artieda, Independent component analysis as a tool to eliminate artifacts in EEG. A quantitative study. *J. Clin. Neurophysiol.* **20**, 249–257 (2003)
49. J. Iriarte, E. Urrestarazu, J. Artieda, M. Valencia, P. Levan, C. Viteri, M. Alegre, Independent component analysis in the study of focal seizures. *J. Clin. Neurophysiol.* **23**(6), 551 (2006)
50. C. James, O. Gibson, Temporally constrained ICA: an application to artifact rejection in electromagnetic brain signal analysis. *IEEE Trans. Biomed. Eng.* **50**, 1108 (2003)
51. C. James, C. Hesse, Independent component analysis for biomedical signals. *Physiol. Meas.* **26**, R15–R39 (2005)
52. C. James, D. Lowe, Extracting multisource brain activity from single EM channel. *Artif. Intell. Med.* **28**, 89 (2003)
53. M. Jarvis, P. Mitra, Sampling properties of the spectrum and coherency of sequences of action potential. *Neural Comput.* **13**, 717 (2001)
54. C. Joyce, I. Gorodnitsky, M. Kutas, Automatic removal of eye movement and blink artifacts from EEG data using blind component separation. *Psychophysiology* **41**(2), 313 (2004)
55. T. Jung, C. Humphries, T. Lee, M. McKeown, V. Iragui, S. Makeig, Removing electroencephalographic artifacts by blind source separation. *Psychophysiology* **37**, 163 (2000)
56. T. Jung, S. Makeig, M. Westerfield, J. Townsend, E. Courchesne, T. Sejnowski, Removal of eye activity artifacts from visual event-related potentials in normal and clinical subjects. *Clin. Neurophysiol.* **11**(10), 1745 (2000)
57. J.F. Kalaska, Neuroscience: brain control of a helping hand. *Nature* **453**, 994 (2004)
58. N. Kannathala, M.L. Choob, U.R. Acharyab, P.K. Sadasivana, Entropies for detection of epilepsy in EEG. *Comput. Methods Biomed.* **3**, 125 (2005)
59. A. Kaplan, J.J. Lim, K.S. Jin, B.W. Park, J.G. Byeon, S.U. Tarasova, Unconscious operant conditioning in the paradigm of brain-computer interface based on color perception. *Int. J. Neurosci.* **115**, 781–802 (2005)

60. L. Ke, R. Li, Classification of EEG signals by multi-scale filtering and PCA, in *IEEE International Conference on Intelligent Computing and Intelligent Systems, ICIS'2009*, Shanghai, 20–22 Nov 2009, pp. 362–366
61. J. Kierkels, G. Boxtel, L. Vogten, A model-based objective evaluation of eyemovement correction in EEG recordings. *IEEE Trans. Biomed. Eng.* **53**, 246 (2006)
62. C.M. Kim, Mechanism of chaos synchronization and on–off intermittency. *Phys. Rev. E* **56**(3, Part B), 3697 (1997)
63. A.A. Koronovskii, A.A. Tyischenko, A.E. Hramov, Turbulent phase distribution during lag synchronization breakage. *Tech. Phys. Lett.* **31**(11), 910 (2005)
64. A.A. Koronovskii, G.D. Kuznetsova, I.S. Midzyanovskaya, E.Yu. Sitnikova, D.I. Trubetskov, A.E. Hramov, Regularities of alternate behavior in spontaneous nonconvulsive seizure activity in rats. *Dokl. Biol. Sci.* **409**, 275 (2006)
65. A.A. Koronovskii, I.M. Minukhin, A.A. Tyischenko, A.E. Hramov, I.S. Midzyanovskaya, Y.E. Sitnikova, E.L.M. van Luijtelea, C.M. Rijn, Application of continuous wavelet transform to analysis of intermittent behavior. *Appl. Nonlinear Dyn.* **15**(4), 34 (2007)
66. A.A. Koronovskii, O.I. Moskalenko, P.V. Popov, A.E. Hramov, Method of allocation of characteristic phases of systems behaviour according time data. Russian Federation Patent No 2337610, Moscow, FIPS, 10.11.2008, Bulletin No 31, 2008
67. A.A. Koronovskii, E.L.M. van Luijtelea, A.A. Ovchinnikov, E.Yu. Sitnikova, A.E. Hramov, Diagnostics and analysis of oscillatory neuronal network activity of brain with continuous wavelet analysis. *Appl. Nonlinear Dyn.* **19**(1), 86 (2011)
68. A. Korzeniewska, M. Manczak, M. Kaminski, K. Blinowska, S. Kasicki, Determination of information flow direction among brain structures by a modified directed transfer function method (dDTF). *J. Neurosci. Methods* **125**, 195 (2003)
69. G.K. Kostopoulos, Spike-and-wave discharges of absence seizures as a transformation of sleep spindles: the continuing development of a hypothesis. *Clin. Neurophysiol.* **111**(Suppl. 2), S27 (2000)
70. M.R. Kousarrizi, A.A. Ghanbari, M. Teshnehlab, M. Aliyari, A. Gharaviri, Feature extraction and classification of EEG signals using wavelet transform, SVM and artificial neural networks for brain–computer interfaces, in *Proceedings of International Joint Conference on Bioinformatics, Systems Biology and Intelligent Computing, IJCBS'09*, Shanghai, 3–5 Aug 2009, pp. 352–355
71. G. Krausz, C. Brunia, C. Neuper, G. Pfurtscheller, Stimulus-preceding negativity and oscillatory changes of the EEG in a non-motor anticipation paradigm. *Int. J. Psychophysiol.* **45**, 124 (2002)
72. R.T. Lauer, P.H. Peckham, K.L. Kilgore, W.J. Heetderks, Applications of cortical signals to neuroprosthetic control: a critical review. *Nat. Med.* **8**, 205 (2000)
73. T. Lee, M. Girolomi, T. Sejnowski, Independent component analysis using an extended infomax algorithm for mixed subGaussian and superGaussian sources. *Neural Comput.* **11**, 417 (1999)
74. J.C. Letelier, P.P. Weber, Spike sorting based on discrete wavelet transform coefficients. *J. Neurosci. Methods* **101**, 93 (2000)
75. V.A. Makarov, J. Makarova, O. Herreras, Disentanglement of local field potential sources by independent component analysis. *J. Comput. Neurosci.* **29**, 445 (2010)
76. J. Makarova, J.M. Ibarz, V.A. Makarov, N. Benito, O. Herreras, Parallel readout of pathway-specific inputs to laminated brain structures. *Front. Syst. Neurosci.* **5**, 77 (2011). doi:10.3389/fnsys.2011.00077
77. J.P. Manning, D.A. Richards, N.G. Bowery, Pharmacology of absence epilepsy. *Trends Pharmacol. Sci.* **24**(10), 542 (2003)
78. S.G. Mason, G.E. Birch, A general framework for brain–computer interface design. *IEEE Trans. Neural Syst. Rehabil. Eng.* **11**(1), 70 (2003)
79. S.G. Mason, R. Bohringer, J.F. Borisoff, G.E. Birch, Real-time control of a video game with a direct brain–computer interface. *J. Clin. Neurophysiol.* **21**(6), 404 (2004)

80. M. McKeown, T. Jung, S. Makeig, G. Brown, Spatially independent activity patterns in functional magnetic resonance imaging data during the stroop color-naming task. *Proc. Natl. Acad. Sci. U.S.A.* **3**, 803 (1998)
81. P.E. McSharry, L.A. Smith, L. Tarassenko, Prediction of epileptic seizures: are nonlinear methods relevant? *Nat. Med.* **9**, 241 (2003)
82. C. Melissant, A. Ypma, E. Frietman, C. Stam, A method for detection of Alzheimer's disease using ICA-enhanced EEG measurements. *Artif. Intell. Med.* **33**, 209 (2005)
83. H.R. Mohseni, A. Maghsoudi, M.B. Shamsollahi, Seizure detection in EEG signals: a comparison of different approaches. *Conf. Proc. IEEE Eng. Med. Biol. Soc. Suppl.* 6724 (2006)
84. F. Mormann, R.G. Andrzejak, C.E. Elger, K. Lehnertz, Seizure prediction: the long and winding road. *Brain* **130**, 314 (2007)
85. Y. Nagai, X.D. Hua, Controlling on-off intermittent dynamics. *Phys. Rev. E* **54**, 1190 (1996)
86. A.I. Nazimov, A.N. Pavlov, A.E. Hramov, V.V. Grubov, A.A. Koronovskii, E. Sitnikova, Adaptive wavelet-based recognition of oscillatory patterns on electroencephalograms. *Proc. SPIE* **8580**, 85801 (2013)
87. A.I. Nazimov, A.N. Pavlov, A.E. Hramov, V.V. Grubov, E. Sitnikova, A.A. Koronovskii, The adaptive method of recognition of specific oscillatory patterns on the basis of wavelet transformation. *J. Commun. Technol. Electron.* **58**, 790–795 (2013)
88. A.I. Nazimov, A.N. Pavlov, A.A. Nazimova, V.V. Grubov, A.A. Koronovskii, E. Sitnikova, A.E. Hramov, Serial identification of EEG patterns using adaptive wavelet-based analysis. *Eur. Phys. J. Spec. Top.* **222**, 2713–2722 (2013)
89. S. Olbrich, H. Olbrich, M. Adamaszek, I. Jahna, U. Hegerla, K. Stengler, Altered EEG lagged coherence during rest in obsessive-compulsive disorder. *Clin. Neurophysiol.* **124**, 2421 (2013)
90. A.A. Ovchinnikov, A. Luttjohann, A.E. Hramov, E.L.M. van Luijtelaar, An algorithm for real-time detection of spike-wave discharges in rodents. *J. Neurosci. Methods* **194**, 172 (2010)
91. A.A. Ovchinnikov, A.E. Hramov, A. Luttjohann, A.A. Koronovskii, E.L.M. van Luijtelaar, Method for diagnostics of characteristic patterns of observable time series and its real-time experimental implementation for neurophysiological signals. *Tech. Phys.* **56**(1), 1 (2011)
92. M. Papadarakakis, N.D. Lagaros, Reliability-based structural optimization using neural networks and Monte Carlo simulation. *Comput. Methods Appl. Mech. Eng.* **191**(32), 3491 (2002)
93. A.N. Pavlov, V.A. Makarov, I. Makarova, F. Panetsos, Sorting of neural spikes: when wavelet based methods outperform principal component analysis. *Nat. Comput.* **6**, 269 (2007)
94. W.D. Penny, S.J. Roberts, E.A. Curran, M.J. Stokes, EEG-based communication: a pattern recognition approach. *IEEE Trans. Neural Syst. Rehabil. Eng.* **8**, 214 (2000)
95. D. Percival, A.T. Walden, *Spectral Analysis for Physical Applications* (Cambridge University Press, Cambridge, 1993)
96. J.L. Perez Velazquez, H. Khosravani, A. Lozano, B.L. Bardakjian, P.L. Carlen, R.A. Wennberg, Type III intermittency in human partial epilepsy. *Eur. J. Neurosci.* **11**, 2571 (1999)
97. G. Pfurtscheller, C. Neuper, C. Guger, W. Harkam, H. Ramoser, A. Schlögl, B. Obermaier, M. Pregenzer, Current trends in Graz brain-computer interface (BCI) research. *IEEE Trans. Neural Syst. Rehabil. Eng.* **8**, 216 (2000)
98. G. Pfurtscheller, R. Scherer, R. Leeb, C. Keinrath, C. Neuper, F. Lee, H. Bischof, Viewing moving objects in virtual reality can change the dynamics of sensorimotor EEG rhythms. *Teleoperators Virtual Environ.* **16**, 111 (2007)
99. A.S. Pikovsky, G.V. Osipov, M.G. Rosenblum, M. Zaks, J. Kurths, Attractor-repeller collision and eyelet intermittency at the transition to phase synchronization. *Phys. Rev. Lett.* **79**(1), 47 (1997)
100. D. Pinault, T.J. O'Brien, Cellular and network mechanisms of genetically-determined absence seizures. *Thalamus Relat. Syst.* **3**(3), 181 (2005)

101. D. Pinault, M. Vergnes, C. Marescaux, Medium-voltage 5–9 Hz oscillations give rise to spike-and-wave discharges in a genetic model of absence epilepsy: in vivo dual extracellular recording of thalamic relay and reticular neurons. *Neuroscience* **105**, 181 (2001)
102. D. Pinault, A. Slezia, L. Acsady, Corticothalamic 5–9 Hz oscillations are more pro-epileptogenic than sleep spindles in rats. *J. Physiol.* **574**(Part 1), 209 (2006)
103. N. Platt, E.A. Spiegel, C. Tresser, On–off intermittency: a mechanism for bursting. *Phys. Rev. Lett.* **70**(3), 279 (1993)
104. W.H. Press, S.A. Teukolsky, W.T. Vetterling, B.T. Flannery, *Numerical Recipes* (Cambridge University Press, Cambridge, 1997)
105. R. Privik, R. Broughton, R. Coppola, R. Davidson, N. Fox, M. Nuwer, Guidelines for the recording and quantitative analysis of electroencephalographic activity in research contexts. *Psychophysiology* **30**, 547 (1993)
106. Q.R. Quiroga, Z. Nadasdy, Y. Ben-Shaul, Unsupervised spike detection and sorting with wavelets and superparamagnetic clustering. *Neural Comput.* **16**, 1661 (2004)
107. E. Rodriguez, N. George, J.P. Lachaux, J. Martinerie, B. Renault, F. Varela, Perception's shadow: long-distance synchronization in the human brain. *Nature* **397**, 430 (1999)
108. N.C. Rogasch, P.B. Fitzgerald, Assessing cortical network properties using TMS-EEG. *Hum. Brain Mapp.* **34**, 1652 (2013)
109. R. Scherer, F. Lee, A. Schlgl, R. Leeb, H. Bischof, G. Pfurtscheller, Toward self-paced brain–computer communication: navigation through virtual worlds biomedical engineering. *IEEE Trans. Biomed. Eng.* **55**, 675 (2008)
110. T. Schreiber, A. Schmitz, Surrogate time series. *Physica D* **142**, 346–382 (2000)
111. E. Sitnikova, E.L.M. van Luijtelaaar, Cortical and thalamic coherence during spike–wave seizures in WAG/Rij rats. *Epilepsy Res.* **71**, 159 (2006)
112. E. Sitnikova, A.E. Hramov, A.A. Koronovskii, E.L.M. van Luijtelaaar, Sleep spindles and spike–wave discharges in EEG: their generic features, similarities and distinctions disclosed with Fourier transform and continuous wavelet analysis. *J. Neurosci. Methods* **180**, 304 (2009)
113. E. Sitnikova, A.A. Koronovskii, A.E. Hramov, Analysis of epileptic activity of brain in case of absence epilepsy: applied aspects of nonlinear dynamics. *Appl. Nonlinear Dyn.* **19**(6), 173–182 (2011)
114. E. Sitnikova, A.E. Hramov, V.V. Grubov, A.A. Ovchinnikov, A.A. Koronovsky, On–off intermittency of thalamo–cortical oscillations in the electroencephalogram of rats with genetic predisposition to absence epilepsy. *Brain Res.* **1436**, 147 (2012)
115. M. Steriade, *Neuronal Substrates of Sleep and Epilepsy* (Cambridge University Press, Cambridge, 2003)
116. M. Steriade, R. McCarley, *A Role for the Preoptic Sleep-Promoting System in Absence Epilepsy* (Plenum, New York, 1990)
117. M. Steriade, D.A. McCormick, T.J. Sejnowski, Thalamocortical oscillations in the sleeping and aroused brain. *Science* **262**, 679 (1993)
118. A. Subasi, Epileptic seizure detection using dynamic wavelet network. *Expert Syst. Appl.* **29**, 343 (2005)
119. N. Suntsova, S. Kumar, R. Guzman-Marin, M.N. Alam, R. Szymusiak, D. McGinty, A role for the preoptic sleep-promoting system in absence epilepsy. *Neurobiol. Dis.* **36**(1), 126 (2009)
120. N.E. Sviderskaya, T.N. Dashinskaja, G.V. Taratunova, Spatial organization of EEG activation during the creative processes. *J. High. Nerv. Activ.* **51**, 393 (2001)
121. J. Theiler, S. Eubank, A. Longtin, B. Galdrikian, D. Farmer, Testing for nonlinearity in time series: the method of surrogate data. *Physica D* **58**, 77 (1992)
122. D. Thomson, Spectrum estimation and harmonic analysis. *Proc. IEEE (Spec. Issue Spectr. Estim.)* **70**, 1055 (1982)
123. S. Tong, A. Bezerianos, J. Paul, Y. Zhu, N. Thakor, Removal of ECG interference from the EEG recordings in small animals using independent component analysis. *J. Neurosci. Methods* **108**, 11 (2001)

124. Y. Tran, A. Craig, P. Boord, D. Craig, Using independent component analysis to remove artifact from electroencephalographic measured during stuttered speech. *Med. Biol. Eng. Comput.* **42**, 627 (2004)
125. E. Urrestarazu, J. Iriarte, M. Alegre, M. Valencia, C. Viteri, J. Artieda, Independent component analysis removing artifacts in ictal recordings. *Epilepsia* **45**, 1 (2004)
126. E.L.M. van Luijteleaer, A.M. Coenen, Two types of electrocortical paroxysms in an inbred strain of rats. *Neurosci. Lett.* **70**(3), 393 (1986)
127. F. Varela, J.P. Lachaux, E. Rodriguez, J. Martinerie, The brainweb: phase synchronization and large-scale integration. *Nat. Rev. Neurosci.* **2**, 229 (2001)
128. V.M. Vaughan, Guest editorial brain-computer interface technology: a review of the second international meeting. *IEEE Trans. Neural Syst. Rehabil. Eng.* **11**(2), 94 (2003)
129. B.M. Velichkovskii, *Cognitive Science. Fundamentals of Cognitive Psychology* (Academy, Moscow, 2006)
130. M. Vergnes, C. Marescaux, G. Micheletti, A. Depaulis, L. Rumbach, J.M. Warter, Enhancement of spike and wave discharges by GABA mimetic drugs in rats with spontaneous petit-mal-like epilepsy. *Neurosci. Lett.* **44**(1), 91 (1984)
131. J.J. Vidal, Real-time detection of brain events in EEG. *Proc. IEEE* **65**, 633 (1997)
132. R. Vigario, Extraction of ocular artifacts from EEG using independent component analysis. *Electroencephalogr. Clin. Neurophysiol.* **103**, 395 (1997)
133. R. Vigario, J. Särelö, V. Jousmäki, H. Hämäläinen, E. Oja, Independent component approach to the analysis of EEG and MEG recordings. *IEEE Trans. Biomed. Eng.* **47**, 589 (2000)
134. A. von Stein, P. Rappelsberger, J. Sarnthein, H. Petsche, Synchronization between temporal and parietal cortex during multimodal object processing in man. *Cereb. Cortex* **9**, 137 (1999)
135. G. Wallstrom, R. Kass, A. Miller, J. Cohn, N. Fox, Automatic correction of ocular artifacts in the EEG: a comparison of regression-based and component-based methods. *Int. J. Psychophysiol.* **53**, 105 (2004)
136. J.R. Wolpaw, N. Birbaumer, D.J. McFarland, G. Pfurtscheller, T.M. Vaughan, Brain-computer interfaces for communication and control. *Clin. Neurophysiol.* **113**, 767 (2002)
137. R. Yuan, D. Yu, F. Liang, Adaptive evolutionary Monte Carlo for optimizations with applications to sensor placement problems. *Stat. Comput.* **18**, 375–390 (2008)
138. D.M. Zenett, A.S. Mikhailov, Mutual synchronization in ensembles of globally coupled neural networks. *Phys. Rev. E* **58**(1), 872 (1998)
139. M.O. Zhuravlev, A.A. Koronovskii, O.I. Moskalenko, A.A. Ovchinnikov, A.E. Hramov, Ring intermittency near the boundary of the synchronous time scales of chaotic oscillators. *Phys. Rev. E* **83**, 027201 (2011)

Chapter 8

Conclusion

Wavelet analysis remains a somewhat exotic method in contemporary neuroscience and neurophysiology. It seems that new mathematical or experimental methods, despite all their benefits and technological advantages, need time to become accepted as a convenient tool for routine applications. It is particularly noticeable in the clinical and biological sciences, where novel mathematical tools must undergo a thorough examination, adaptation, and verification, and only then can they be accepted for practical use. In this context, it should be emphasized that wavelet analysis is suitable for time–frequency analysis of neurophysiological signals, and can also be incorporated into more complex algorithms for experimental data processing that increase the efficacy of data analysis in neurophysiological studies. We believe that the wavelet-based analysis will naturally evolve into a family of standard methods for signal processing in biology and medicine. This does not mean replacement of the conventional by new techniques, but improvement of existing approaches to make wavelet analysis more widely applicable in experimental neuroscience.

The present monograph addresses just a few problems that are frequently encountered in neuroscience and neurophysiology. Even this brief review demonstrates several beneficial ways and promising perspectives for using wavelet analysis in neurophysiological research. Applications of the powerful mathematical analysis of nonlinear dynamics to neuronal systems, both at the micro- and macrolevels of the central nervous system, opens new perspectives for the study of the extremely complex mechanisms of brain functions. At the same time, interpretation of results obtained by this interdisciplinary approach is difficult in the context of neurophysiology due partly to the extreme complexity of the explored object (the nervous system of living organisms), and partly to the difficulty in identifying the appropriate physiological meaning of results obtained by such sophisticated mathematical methods. Here we would like to quote A.M. Ivanitskii and A.I. Lebedev, who commented that “[. . .] the integration of mathematics and physiology gives the best result when the application of a specified mathematical transform is underlain by a fruitful physiological idea” [1]. Indeed, success in developing new data-processing technologies in any interdisciplinary field including contemporary neuroscience

depends on the introduction of new neurophysiological ideas and clearly defined goals, along with appropriate ways to achieve them.

There can be little doubt that the number of neurophysiological studies using wavelet-based methods will continue to grow, because it provides a solution for many challenging problems, such as the principles of information coding and presentation. Further progress in understanding the functions of the central nervous system requires not only the development of experimental research facilities (where considerable progress has been made in the last few decades), but also the introduction of new mathematical methods for decoding neural signals. The extraordinary complexity and intricacy of brain processes make it impossible to decipher neural signals using only the methods of statistical analysis. From the viewpoint of nonlinear dynamics, the adaptation of living systems (organisms and their neural systems) to the environment is accompanied by changes in their dynamics, whereupon neurophysiological signals recorded at this time should be considered as time series of nonstationary processes produced by dynamical systems with an unlimited number of degrees of freedom. If we ignore this fact, we may miss important information about the neural system, whereas understanding adaptive processes facilitates the study of the basic principles of neural activity.

Wavelet analysis can be expressed by the metaphor of a “mathematical microscope”, highlighting the fact that we need to use appropriate magnification in order to disclose certain hidden features that cannot be detected by the naked (or inadequately armed) eye. There is still great (yet hidden) potential for this research tool. The present monograph describes some modifications to the mathematical processing of experimental data and addresses some problems of neural system dynamics, but also tries to inspire the reader by describing the promising new prospects for wavelets in neurophysiological applications. In the coming years, wavelet analysis should become an effective research tool that will help to improve the quality of research in the field of neuroscience.

Reference

1. A.M. Ivanitskii, A.I. Lebedev, *J. High. Nerv. Activ.* **57**, 636 (2007)

Index

A

- Absence epilepsy, 8, 180, 184, 187–189, 191, 193, 194, 198, 211, 212, 222, 231, 233, 235, 242, 243, 254–256, 273, 276
- Accuracy of the automatic recognition, 259
- Action potential, 2, 3, 8, 12, 121, 132, 140, 142, 145
- Active wakefulness, 214, 215, 221
- Adaptive wavelet, 197, 211, 237–242, 254, 255, 267–271, 279, 286
 - matching, 237
- Admissibility condition, 28, 30
- Amplitude, 17, 23, 41–49, 52, 53, 57, 59, 60, 62–65, 80–82, 86, 101, 104, 106, 110, 112–114, 116, 122–130, 132, 143, 147, 151, 154, 183, 184, 187, 189, 192–194, 199, 200, 213, 214, 222–224, 229–231, 236, 237, 239, 242–244, 255, 261, 262, 269, 273, 274, 280, 282, 283, 288, 290–292, 295, 303, 305
- Amplitude modulation (AM), 80, 82
- Amplitude modulation index, 81
- Artifact, 5, 31, 42, 52, 65, 186, 198, 199, 236, 243, 255, 261, 280, 286–301, 304, 305
 - suppression, 8, 9, 198–199, 255, 286–306
- Artificial neural networks, 154–174, 255, 256
- Autocorrelation histogram (ACH), 106–109
- Automatic artifact rejection, 199

B

- Back propagation of errors, 159–160
- Basis function, 35, 64, 65, 194, 196, 228, 238, 240, 270

- BCI. *See* Brain-computer interface (BCI)
- Boundedness condition, 27, 28
- Brain-computer interface (BCI), 6–7, 9, 178, 197, 198, 237, 254, 260–267

C

- Cellular dynamics, 8
- Central nervous system (CNS), 1, 2, 77, 86, 179, 180, 196, 313
- Chaotic attractor, 55, 56
- Chaotic oscillator, 54, 56, 62, 197
- Chaotic signal, 54–56, 58
- Chaotic synchronization, 54, 61
- Chirp, 50
- Classification of neuronal impulses, 8
- Cognitive brain functions, 180
- Complete synchronization, 54, 61
- Complex wavelet, 32, 47, 50, 52, 236
- Continuous approximation, 67, 69
- Continuous wavelet transform (CWT), 8, 25–66, 70, 81, 85, 90, 135, 136, 164, 180, 194, 198, 211, 212, 219, 222, 223, 231, 233–237, 239, 240, 258, 259, 271, 280, 281, 284, 285, 291, 292
- Cortical EEG, 216, 218, 219
- Cross-correlation analysis, 101, 183
- Cross-spectrum, 54, 103, 112, 295

D

- Data compression, 65
- Daubechies wavelet, 68, 71, 135, 155
- Deep slow-wave sleep, 214, 215, 219, 221
- Delta-function, 103
- Delta precursor, 216–218, 220

Delta rule, 159
 Discrete approximation, 67
 Distribution of the energy, 46, 47, 224, 229, 231, 256
 Distribution of the wavelet energy, 29, 231, 274
 DOG wavelet, 33, 34
 Double wavelet analysis, 81–83

E
 Edge effects, 41
 EEG frequency bands, 185
 Electrocardiogram, 35
 Electrocorticogram (ECoG), 179, 181, 182, 196
 Electroencephalogram (EEG), 2, 5–9, 48, 65, 117, 177–201, 21–247, 253–306
 Epileptogenesis, 197
 Epileptic discharges, 2, 193, 198, 232, 242–247, 276
 Evoked potentials, 178, 199, 200

F
 Fast Fourier transform (FFT), 27, 37–41, 184, 219, 233, 235
 Fast sleep spindle, 232
 Father wavelet, 66
 Feedback loop, 6, 264
 FHAT wavelet, 33, 236
 Fourier
 image, 27, 28, 30–33, 37–40, 42, 53, 236
 space, 18, 31, 32, 38, 40, 183, 184, 236
 spectrum, 16, 17, 51, 53, 56–58, 60, 108–110, 117
 Frequency
 band, 31, 43, 44, 60, 94, 101, 104–112, 114, 115, 117, 135, 142, 143, 145–147, 151, 170, 173, 184, 185, 197, 199, 213, 214, 216, 224, 228, 254, 256, 261, 269–273, 295, 301–303, 305
 component, 17, 18, 20, 23, 60, 184, 241
 domain, 18, 25, 28, 32, 91, 101, 106, 183, 184, 186, 193, 194, 196, 224, 235–237, 261, 269, 291, 305
 modulation, 80–82, 84, 85, 215
 modulation index, 81
 Frontal EEG, 213
 Functional space, 26, 67

G
 Gabor transform, 18, 102
 Generalized synchronization, 54, 61

Genetic rat with absence epilepsy (GAERS), 222

H

Haar wavelet, 64, 66–68, 70, 151
 Haloperidol, 194
 Heaviside function, 17, 34
 Hilbert–Huang transform, 3
 Hilbert transform, 56, 57, 95
 Hypersynchronous rhythmic activity, 8, 212
 5–9 Hz oscillations, 196, 222, 227–229, 254, 268, 271–276, 278, 279

I

Independent component analysis (ICA), 9, 198–199, 253, 255, 286–304
 Influence angle of the wavelet transform, 31
 Information encoding, 2, 77, 84, 86–101
 Inhibitory dominance, 234
 Instantaneous amplitude, 48, 64, 80, 81, 230, 282, 283
 Instantaneous energy, 29, 224, 256, 258
 Instantaneous frequency, 48–50, 64, 80, 81, 85, 90, 92, 95, 96, 215, 233, 234
 Instantaneous phase, 54, 56, 57, 60, 62, 64, 245
 Instantaneous wavelet energy distributions, 226, 227, 231
 Instantaneous wavelet spectra, 228
 Intermittency, 245, 274, 277–279
 Interspike interval (ISI), 84, 85, 92, 103, 104
 Intracellular process, 7, 8, 79, 80, 82, 83
 Intra-spindle frequency, 228, 231–235
 Inverse wavelet transform, 29, 45, 292, 293
 Ion concentration, 79

K

Ketamine, 194, 195

L

Lag synchronization, 61, 62
 Light slow-wave sleep, 214, 215, 221, 222
 Local field potentials (LFPs), 2, 122, 123, 125, 182, 186
 Localization condition, 28
 Logarithmic scale, 42, 107, 217, 218, 220

M

Magnetoencephalogram (MEG), 2, 8, 9
 Membrane potential, 78, 79
 Mental control, 6, 7

MHAT wavelet, 33, 42, 46, 167, 190–193, 223–225, 228, 229, 236
 Morlet wavelet, 32, 33, 36, 37, 40–43, 47, 50, 51, 58, 189–195, 212, 223, 224, 228–230, 236, 237, 239, 257–259, 261, 274, 280
 Mother function, 26, 31, 40, 45, 54, 80, 193, 198, 224, 230
 Mother wavelet, 24–29, 32–36, 38, 42, 44, 45, 47, 49, 50, 57, 63, 65, 66, 135, 136, 164, 187–195, 197, 212, 214, 217, 218, 220, 223–231, 235–237, 240, 242, 243, 261, 263, 271, 279, 283
 Movement artifact, 199
 Multichannel EEG, 8, 9, 198, 199, 212, 223, 242–244, 286–304
 Multi-scale analysis, 65–67, 69

N

Neuronal network, 185, 186, 194, 221, 233, 242, 273, 278–279
 Noise, 27, 54, 57, 65, 103, 122, 124, 125, 127–134, 138, 140, 142–149, 151–153, 155, 156, 160–162, 169–174, 186, 187, 195–197, 213, 243
 Non-REM sleep, 221
 Non-stationary process, 3, 31, 63, 314
 Normalization condition, 24, 70, 239

O

Off-line analysis, 5, 264
 On-line algorithm, 254, 263
 On-line SWD detection system (OSDS), 260–265, 269
 On-off intermittency, 197, 254, 273–279
 Orthogonal basis, 64
 Oscillatory pattern, 8, 101, 184, 195–198, 221–235, 254, 257, 259–261, 272, 274, 280, 284
 OSDS. *See* On-line SWD detection system (OSDS)

P

Parametric wavelet sorting, 147–154
 Parseval formula, 27
 Passive wakefulness, 214, 215, 219, 221, 222
 Pattern recognition, 7, 65, 196, 237, 260, 280–283, 286
 Paul wavelet, 32, 33, 40, 223
 PCA. *See* Principal component analysis (PCA)

Phase, 22, 23, 32, 45, 47, 52–64, 78–82, 88, 95, 104, 108, 129, 130, 151, 163, 194, 200, 201, 234–236, 245, 264, 276, 278, 288, 295, 303
 coherent attractor, 55, 57
 height, 78–80, 82
 space, 55
 of spectral component, 54, 64
 synchronization, 54–57, 61, 62, 200, 201
 Phasic neurons, 88, 89
 Power spectrum, 29, 42, 48, 49, 84, 103, 104, 106, 108–110, 165, 185, 186, 240, 288, 293, 301–302, 305
 Principal component analysis (PCA), 124, 130–148, 152–154, 160–162
 Projection of the phase space, 55
 Pyramidal expansion algorithm, 71, 135

R

Random signal, 27
 Real-time detection, 8, 197–198
 of oscillatory patterns, 8, 197–198
 Real wavelet, 22, 34, 193, 194, 236
 Refractive index, 79
 Region of the influence of edge effects, 40–42
 Rhythmic component, 64, 80, 82–85, 90, 92, 195, 197, 199, 212, 272
 in EEG, 195, 197
 RR-interval, 35

S

Scaling function, 66–68, 70
 Scalogram, 29
 Secondary wavelet transform, 81–82
 Sensitivity, 142–146, 259, 260, 263, 264, 266, 270, 282, 284, 285
 Sensory neuron, 2
 Serial identification, 254, 279–286
 Shannon transform, 30
 Short-time Fourier transform, 18, 20, 30, 186
 Skeleton, 47, 49–52, 63, 189, 192, 232
 Sleep spindle, 184, 185, 196, 197, 211, 214, 221–242, 254–257, 267–279, 281, 282, 284–286
 Slow sleep spindle, 221
 Somatosensory information, 87
 Spatial resolution, 2, 182, 288
 Specificity, 259, 270, 282, 284, 285
 Spectral analysis, 4, 17, 18, 21, 25, 48, 103, 108–110, 184, 233
 Spectral components, 18, 23, 30, 54, 57, 59–61, 64, 219, 235

Spectral ridge, 91–93, 95
 Spike, 2, 3, 77, 78, 83–86, 88–97, 100–117,
 121–174, 187–189, 214, 224, 228,
 236, 241, 255, 279
 Spike-wave discharge (SWD), 184, 185,
 187–198, 214, 221, 228, 231, 233,
 236, 240, 242–247, 254–262, 266,
 267, 273, 275, 280, 281
 Spike-wave spindle, 197
 Spindle-like activity, 228, 229
 Spindle wavelet, 212, 238–241, 267–271
 SWD-precursor, 214, 216, 219
 Synaptic neuronal plasticity, 3
 Synchronization measure, 63, 244, 245
 Synchronous state, 8, 63, 242, 245
 System with ill-defined phase, 56

T

Tactile stimulation, 88, 102, 106–113, 116,
 117
 Template matching technique, 197
 Temporal resolution, 102, 116, 182, 200, 237
 Thalamic EEG, 218, 219
 Thalamic nuclei, 2, 221, 233
 Thalamo-cortical neuronal circuit, 221
 Thalamo-cortical oscillations, 273–279
 Theta/alpha precursors, 216–221
 Time domain, 18, 20, 21, 26, 36, 77, 86, 183,
 184, 186, 190, 219, 224, 235, 272,
 297, 299, 301, 305
 Time-frequency analysis, 8, 92, 182–196,
 211–247, 313
 Time-frequency structure, 47, 184, 186, 189,
 190, 193, 196, 212, 233–235, 256,
 290
 Time resolution, 30, 32, 91, 104, 180, 193,
 236, 237
 Time scale, 20, 21, 24–26, 29–32, 35–42,
 44–46, 48, 54, 57–64, 78, 80, 90,
 100, 104, 117, 132–134, 143, 154,
 187, 198, 235, 239, 242–247, 261

Time scale synchronization (TSS), 54, 56,
 61–63, 198, 242–247
 Tonic neurons, 88, 89
 Transitional sleep spindle, 232
 Transmission of information, 87
 Trigeminal neuron, 88, 96–101

V

Vibrissae system, 86, 87
 Vigabatrin, 194, 276–278

W

WAG/Rij rats, 184, 185, 187–190, 192–195,
 197, 211–213, 215, 219, 222–225,
 231–235, 239–241, 244, 255–257,
 260, 265, 266, 268, 274, 276
 Wavelet-based spike classifier (WSC),
 135–136
 Wavelet coherence, 101–117, 196
 Wavelet independent components analysis
 (wICA)
 Wavelet method with super-paramagnetic
 clustering (WMSPC), 141, 142
 Wavelet neuronal network (WNN), 163–166,
 168–174
 Wavelet power over domain (WPOD),
 261–265, 268, 270, 272, 274
 Wavelet shape-accounting classifier (WSAC),
 90, 138–142
 Wavelet transform, 4, 8, 15, 24–72, 78, 80–84,
 90–93, 102–104, 109, 122, 124,
 135–137, 154, 156, 160, 161,
 164–166, 178, 180, 186, 194,
 198–200, 211, 212, 219, 222–224,
 233, 235–237, 243, 253, 254, 256,
 261–263, 280, 290–293
 WAVE wavelet, 34, 136, 168, 190, 191
 Wigner-Ville transform, 3
 Window Fourier transform, 237
 Wistar rats, 96, 231, 233–235